WATER ABOVE THE MOUNTAIN FRONT – ASSESSING MOUNTAIN-BLOCK RECHARGE IN SEMIARID REGIONS

By

Huade Guan

Submitted in Partial Fulfillment
of the Requirements for the

Doctorate of Philosophy in Earth and Environmental Science
with Dissertation in Hydrology

The New Mexico Institute of Mining and Technology
Socorro, New Mexico

December, 2005

To:

Jiya, Harry, and Hansen

Abstract

Mountains provide as much as 90-100% of the freshwater to surrounding basins in arid and semiarid regions because of their distinctive and complex topography, and the consequent effects on precipitation (P) and evapotranspiration (ET). One of the primary objectives of this dissertation is to estimate mountain-block recharge (MBR), an important component of the mountain contribution to groundwater replenishment of surrounding basins, as well as its response to regional climate variability in a semiarid mountain environment of the southwestern U.S. Two major limitations, a lack in understanding hydrologic processes and sparse observation networks, hinder predictive mountain-block hydrologic modeling, and reliable estimation of MBR. Developing approaches to address these limitations is another objective of this dissertation.

A geostatistical algorithm (Auto-Searched Orographic and Atmospheric effects De-trended Kriging, ASOADeK) is first developed for mapping mountain precipitation using sparse gauge data. ASOADeK constructs monthly precipitation maps comparable to PRISM products, and with higher spatial resolution. ASOADeK is also useful for studying regional climatic settings. In arid and semiarid regions, the dominant water flux out of the mountain block is ET. A Topography- and Vegetation-based surface energy partitioning model for ET modeling (TVET) is developed to include the effects of vegetation and topography on mountain-hillslope energy partitioning. The TVET model can be used to map daily potential evaporation and potential transpiration over mountain terrains. The model is also useful for ecohydrologic studies, for example, evaporation and transpiration partitioning of sparsely vegetated ecosystems.

To understand the factors influencing distributed MBR, both generic and specific two-dimensional hydrologic simulations at the hillslope scale were conducted, using the variably saturated hydrologic modeling code, HYDRUS-2D. The results show that the controlling factors for distributed MBR include bedrock permeability, atmospheric forcing (precipitation, and potential evapotranspiration, or PET), vegetation coverage, and soil cover. Among these, bedrock characteristics are the primary control, affecting both the amount and patterns of mountain-block recharge. For bedrock with permeability above a certain threshold ($10^{-15} \sim 10^{-14}$ m^2, equivalent to saturated hydraulic conductivity of $10^{-8} \sim 10^{-7}$ m/sec), local climate conditions (regional climate setting + local orographic modification + elevation-and-slope-aspect effects on P and PET), which determine the water availability at the soil-bedrock interface, are the most important controlling factors. Vegetation strongly affects distributed mountain-block recharge by modifying surface energy balance and soil hydraulic properties. Root-zone soil thickness has a significant influence, especially for the matrix-flow-dominant bedrock (e.g., non-welded tuff). A change of vegetation cover in mountains can lead to a significant change in basin-scale groundwater balance. These results provide criteria for classifying hydrologically similar response units (HRU) in mountain blocks. A framework for the HRU-based approach for quantifying mountain-block recharge is provided. This framework and related sensitivity studies suggest that future efforts should focus on better characterization of mountain bedrock hydraulic properties and better quantification of high-resolution (both temporally and spatially) mountain precipitation estimates.

A simple point-simulation-based approach is applied to map potential mountain-block recharge in two mountain ranges, northern New Mexico. Assuming uniform

bedrock, soil cover and vegetation coverage, the long-term mean downward water flux across the soil-bedrock interface (upper-bound estimate of distributed MBR) can be statistically associated with long-term mean local climate forcing (i.e., mean PET and P). Similarly, the actual ET flux can be related to mean local climate conditions. With these correlations derived from simulations with recharge-optimal bedrock and soil conditions, maps of upper-bound distributed MBR and water yield (or upper-bound of total MBR, i.e., the difference between precipitation and actual ET) are constructed for two mountain ranges with distinctive bedrocks, the southern part of the Sangre de Cristo Mountains and the Jemez Mountains, both in northern New Mexico. The results show that distributed MBR is restricted to the higher elevations in the Sangre de Cristo Mountains, while it is more widely distributed in the Jemez Mountains. The area-weighted average upper-bound distributed MBR is about 35% of the water yield in the Sangre de Cristo Mountains, and 50% in the Jemez Mountain. The results also suggest that previous total MBR estimates (70 mm/yr) for the Sangre de Cristo Mountains are reasonable if the bulk bedrock permeability is close to 1×10^{-14} m^2. For the Jemez Mountains, the results give a total MBR between 70~120 mm/yr, about one half of previous estimates for the San Juan Mountains.

To understand the response of MBR to climate variability, the teleconnections of seasonal precipitation in the mountains in northern New Mexico with PDO (Pacific Decadal Oscillation) and ENSO (El Niño-Southern Oscillation) are investigated. The results suggest a strong correlation between winter and spring precipitation and ENSO and PDO cycles. The summer precipitation, which is dominated by the North American Monsoon, does not have clear correlation with ENSO and PDO cycles. For winter and

spring precipitation, PDO effects are more dominant than ENSO effects. Low PDO effects are strongly dampened by El Niño, and slightly enhanced by La Niña. ENSO modulation of high PDO effects is not as strong as for low PDO effects. The high PDO effect on winter precipitation is enhanced by El Niño, but not much affected by La Niña. PDO and ENSO effects on winter precipitation are modified by topography, with larger anomalies at higher elevations for wetter winters, and larger anomalies at lower elevations for drier winters. The effects of PDO and ENSO effects on distributed MBR are examined by the recharge-climate index functions, which are derived from generic hydrologic simulations. The results suggest that ENSO and PDO associated climate variability can typically lead to a 10~20% change in distributed MBR for the two tested mountainous ranges. Because of its multi-decadal period, PDO effects on MBR may influence groundwater resources in surrounding basins.

Acknowledgements

During my four-year study toward the Ph.D. degree, I have been receiving assistances from many people and agencies. Without their help and support, this dissertation would not have been possible.

First, I would like to acknowledge my advisor, Dr. John Wilson, for his time and effort to shape topics of all chapters in this dissertation. Specifically, Chapter 2 was derived from a term project of John's geostatistics class that John strongly recommended. Otherwise, this chapter, and related Chapter 3, would not be possible for this dissertation. Besides, John's friendly and critical advice has been very helpful in finishing this dissertation. All other professors in my committee have given me a lot of help as well. Every once in a while, Dr. Fred Phillips gave me some literature to read, improving my understanding of mountain-block hydrologic systems. One piece of his advice on modeling Los Alamos hillslope experiments initiated the work for Chapter 6. Dr. Jan Hendrickx brought me through the door into evapotranspiration modeling. His recent advice on distinguishing patch and layer approaches was very valuable for improving expressions of the TVET model (Chapter 4). Dr. Eric Small from University of Colorado at Boulder kindly provided field data to test the TVET model. His critical comments on recharge-climate index relationship significantly improved my understanding of this issue. Dr. Enrique Vivoni helped me with his strong background on hydrometeorology. His advice was very helpful for me to finish Chapter 3, which was initially written as a term project in his hydrometeorology class. His recent comments on Chapter 6 significantly improved the writing of this chapter. I would also like to thank two former committee

members, Dr. Brian McPherson and Dr. Laurel Goodwin (now at University of Wisconsin at Madison), for their time and efforts. Especially, Brian spent a lot of time in first couple of committee meetings and in preparing my candidacy exam.

Besides my committee, Dr. Jirka Šimůnek from University of California at Riverside kindly added new capacity to HYDRUS-2D, and provided me sufficient and prompt support. Dr. Brent Newman from Los Alamos National Laboratory kindly provided hillslope experimental data and sufficient history of the experiments, which directly led to Chapter 6. Some generic simulations in Chapter 5 were also derived from these data. Mr. Marvin Gard from LANL helped to prepare the data. Dr. Oleg Makhnin (Mathematics Department) significantly contributed to the ASOADeK model presented in Chapter 2. Drs. Hongjie Xie and Xiaobing Zhou provided strong GIS and remote sensing supports for some of my dissertation work. Dr. Bruce Harrison helped me improve understanding soil development at the Los Alamos hillslope site.

Special thanks go to Dr. David Gochis (NCAR), Dr. Robert Bowman, Dr. Lynn Brandvold (Bureau), Dr. Peggy Johnson (Bureau), Dr. Grant Meyer (University of New Mexico), Dr. James Cleverly (University of New Mexico), Dr. Andrew Manning (USGS), Dr. Jianjun Xu (NOAA), Mr. Dan Packer (Albuquerque Academy), Mr. Modesto Sanchez (USFS Sandia Range District), and Dr. Peter Mozley. They provided suggestions, data, access to the field sites, and lab space for my study.

I would also like to acknowledge assistance and friendship from my fellow students. They are Bayani Cardenas, Renee Sandvig, Sungho Hong, Weon Shik Han, Benjamin Lechler, Hugo Gutiérrez, David Boutt, Cynthia Connolly, Leslie Clark, Bing

Ye, Sam Earman, and many others. Special thanks also go to people at Inter-library Loan Office of the Skeen Library for their wonderful support.

This dissertation study was supported by SAHRA (Sustainability of semi-Arid Hydrology and Riparian Areas) under the STC Program of the National Science Foundation, Agreement EAR-9876800. The Graduate Student Association of New Mexico Tech provided funding for travel to two conferences.

Table of Contents

List of Tables

List of Figures

List of Appendices

List of Symbols

A	J m^{-2} day^{-1}	available energy for the surface to heat the air and evaporate the water during a time of interest
A_s	J m^{-2} day^{-1}	available energy for the portion of surface with bare soil
A_c	J m^{-2} day^{-1}	available energy for the portion of surface covered by vegetation
A_{it}	J m^{-2} day^{-1}	energy consumed by evaporation of the interception water
A_{sn}	J m^{-2} day^{-1}	energy consumed by snowmelt on the surface
a	Pa^{-1}	empirical coefficient of vapor pressure deficit-dependent function for stomatal resistance
a_s		empirical coefficient for actual solar radiation on the surface
b_s		empirical coefficient for actual solar radiation on the surface
$b_1 \sim b_6$		ASOADeK regression coefficient
c		empirical coefficient of solar radiation-dependent function for stomatal resistance
c_p	J $kg^{-1}°C^{-1}$	specific heat of air at constant pressure
D	Pa	vapor pressure deficit
DI		bedrock surface depression index
d	m	zero plane displacement
d_r		the inverse relative distance of Earth-Sun
E	$kgm^{-2}s^{-1}$	evaporation/transpiration rate for water
ET_0	L/T	potential ET for hypothetical reference grass surface
ETH	L/T	10-day or monthly potential ET
e	Pa	vapor pressure of water
e_a	Pa	partial pressure of water vapor in the air
ele	m	elevation above sea level

$e_s(T)$	Pa	saturated vapor pressure of water at temperature T
e_z	Pa	vapor pressure at the reference height z,
e_0	Pa	vapor pressure at the effective canopy surface
Fr		fraction of surface covered by vegetation
G	J m^{-2} day^{-1}	net downward ground heat flux
H	J m^{-2} day^{-1}	the energy used for heating the air
h	m	vegetation height; or root zone soil water potential
$h_1 \sim h_4$	m	parameters for the Feddes model
h_{50}	m	parameter for the S-shape model
I	W/m^2	the ideal solar irradiance on a surface without considering atmospheric effects
I_{max}	mm	interception capacity of the surface with L=1
I'	W/m^2	equivalent mean solar irradiance on a surface during the daylight hours
I_{sc}	W/m^2	solar constant
It	mm	interception water normalized by total surface
K_x, K_n, K_d		empirical constant for site aridity correction
k		von Karman constant, 0.41
k_c		extinction coefficient for the available energy partition to As
k_{sm}	mm/(day^{0}C)	empirical coefficient for temperature-index snowmelt model
k_T		empirical coefficient for temperature-dependent function of stomatal resistance
L		surface leaf area index, =Lc*Fr
L_c		canopy leaf area index
lw		characteristic length of leaf width

MDD	°C	dew point departure, Tmin-T_D
n	hour	actual sunshine hours
P	mm	precipitation
P_{net}	mm	net active precipitation to the ground surface
P_r	mm	rainfall
P_s	mm	equivalent precipitation of the snowfall
P_m	mm	equivalent precipitation of the snowmelt
PEf		percolation efficiency, a ratio of percolation over net infiltration on a hillslope
PI		percolation index, a ratio of percolation over net interflow on a hillslope
p		parameter of the S-shape model
R_a	Jm^{-2} day^{-1}	net short wave radiation above the atmosphere
R_n	Jm^{-2} day^{-1}	net radiation of the surface
R_{ns}	Jm^{-2} day^{-1}	net short wave radiation absorbed by the surface
R_{nl}	Jm^{-2} day^{-1}	net outgoing long-wave radiation from the surface
R_{s0}	Jm^{-2} day^{-1}	daily radiation on the surface with a clear sky
R_{sun}	Jm^{-2} day^{-1}	actual daily radiation on the surface
r_a	sm^{-1}	aerodynamic resistance to vapor/heat transfer from the leaf surface and the air stream at the reference height
r_c	sm^{-1}	bulk canopy resistance
r_a^a	sm^{-1}	aerodynamic resistance between the top of vegetation and the reference height
r_a^c	sm^{-1}	interleaf aerodynamic resistance
r_a^s	sm^{-1}	sub-canopy aerodynamic resistance
r_s^c	sm^{-1}	bulk stomatal resistance

r_{ST}	sm^{-1}	mean leaf-scale stomatal resistance
r_{ST_min}	sm^{-1}	minimum leaf-scale stomatal resistance
T	°C	air temperature
T_D	°C	dew point
T_d	°C	the temperature for complete vegetation dormancy
T_m	°C	the temperature to initiate snowmelt
T_z	°C	the temperature of the air at some reference height z
T_0	°C	the temperature of the vegetation surface
T_{min}	°C	minimum temperature during the time of interest
T_{max}	°C	maximum temperature during the time of interest
t	second	time
u_h	m/sec	mean wind speed at the canopy height
u_z	m/sec	mean wind speed at the reference height
X	km	UTM easting
Y	km	UTM northing
Z	km	elevation above sea level
z_H	m	roughness length of vegetated surface for heat and vapor
z'_H	m	roughness length of substrate soil for heat and vapor
z_m	m	roughness length of vegetated surface for momentum
z'_m	m	roughness length of substrate soil for momentum
z_0	m	roughness length of vegetated surface
z'_0	m	roughness length of bare substrate
α		Scaling factor of root-water-uptake model; albedo of the surface; or terrain aspect (in ASOADeK model), defined as the direction of the slope orientation, zero to the north,

		increasing clockwise, and 180 to the south
α_w		wind extinction coefficient in the canopy
α_0	$m/s^{0.5}$	empirical coefficient for intra-canopy aerodynamic resistance
β	radians	slope steepness
γ	Pa/°C	the psychrometric constant (= 66 Pa/K)
γ	radians	surface azimuth angle
γ_s	radians	solar azimuth angle, zero due to south
Δ	Pa/°C	the slope of the saturated vapor pressure versus temperature curve
δ	radians	declination of the Earth
θ	radians	solar incident angle on the surface
θ_z	radians	solar zenith angle
λ	$J\ kg^{-1}$	latent heat of the water evaporation
λE	$J\ m^{-2}\ day^{-1}$	the energy for transpiration during the time of interest
ρ_a	$kg\ m^{-3}$	density of the air
ρ_w	$kg\ m^{-3}$	density of the liquid water
φ	radians	latitude
ψ_l	Pa	the leaf water potential
ω	radians	solar hour angle
ω_s	radians	sunset solar hour angle
ω_{s0}	radians	sunset solar hour angle on the horizontal surface

List of Acronyms

ANOVA	Analysis of variance
ASOADeK	Auto-Searched Orographic and Atmospheric effects De-trended Kriging
DEM	Digital Elevation Model
ENSO	El Niño-Southern Oscillation
ET	Evapotranspiration
HRU	Hydrologically-similar Response Unit
LTER	Long-term Ecological Research program
MAE	Mean absolute error
MBR	Mountain-block recharge
MFR	Mountain-front recharge
NCDC	National Climate Data Center
NEXRAD	Next Generation Weather Radar
PDO	Pacific Decadal Oscillation
PE	Potential Evaporation
PRISM	Precipitation-elevation Regression on Independent Slopes Model
PT	Potential Transpiration
SAHRA	Sustainability of semi-Arid Hydrology and Riparian Areas
SNOTEL	Snowpack Telemetry system
TVET	Topography- and Vegetation-based surface energy partitioning model for ET modeling

This dissertation is accepted on behalf of the
Faculty of the Institute by the following committee:

Advisor

August 3, 2005
Date

I release this document to the New Mexico Institute of Mining and Technology.

August 3, 2005
Student's Signature Date

CHAPTER 1 INTRODUCTION

Mountains cover about 25% of the world's continental surface [*Kapos et al., 2000*], with residents accounting for 26% of the global population [*Meybeck et al., 2001*]. Because of their complex topography, and the consequent effects on precipitation and evapotranspiration (ET), mountains serve as water towers for most regions on the Earth. A study of 20 selected catchments worldwide shows that the area-weighted mountain contribution to annual river basin discharge is about 4 times that of the adjacent basin floor [*Viviroli et al., 2003*]. In arid and semiarid regions, mountain contribution can be mush larger [*Meybeck et al., 2001*]. The southwestern United States is a typical example of such an environment.

A dramatic population increase over the past several decades is challenging water management and persistence of ecologic systems in the southwestern United States [*Phillips et al., 2004*]. The contribution of mountains to groundwater replenishment of the adjacent basin aquifer is conventionally called 'mountain-front recharge' (MFR). There are two perspectives from which the MFR is studied, a basin-centered view, and a mountain-centered view [*Wilson and Guan, 2004*]. In basin-centered approaches, MFR is regarded as a boundary condition of the basin aquifer, and is estimated through the hydrologic system in the basin or at the mountain front, avoiding the complex hydrologic processes in the mountain. The basin-centered approaches may give reasonable MFR estimates, but do not represent MFR dynamics, especially its response to climatic

variability and change [*Wilson and Guan, 2004*], and to the increasing anthropogenic disturbances [*Luckman and Kavanagh, 2002*].

Large topographic relief and gradient, and snow and ice storage make mountains sensitive to climatic variability and change. For example, with an increase of 1 ˚C in temperature, the snowline can rise by about 150 meters in elevation [*Beniston, 2003*]. The sensitivity of mountain environments, especially their hydrologic and ecologic conditions, makes them good locations to detect global climate change. A mountain-centered approach, and improved understanding of the mountain hydrologic systems, is thus valuable to understanding mountain responses to climate variability and change, vegetation change, and anthropogenic impacts, and to make predictive modeling possible [*Wilson and Guan, 2004*]. The hydrologic study of mountain environments is termed 'mountain-block hydrology,' as in Wilson and Guan [*2004*], who emphasize the importance of geology, or 'mountain hydrology' as in Bales et al. [*2004*].

A primary objective of this dissertation is to improve our understanding of, and ability to estimate or predict, recharge to mountain-blocks and its response to regional climate variability, in semiarid mountain environments. We refer to this recharge as mountain-block recharge (MBR). It replenishes groundwater within the mountain block, and is ultimately a contribution to MFR. By means of distinguishing different groundwater flow paths, and different locations of recharge, Wilson and Guan [*2004*] separate MFR (total mountain contribution to the adjacent basin aquifer) into direct MFR, and indirect MFR. Direct MFR is the recharge at the mountain front, where the water moves from the surface to the vadose zone and on to the adjacent basin's saturated zone. Indirect MFR is the recharge to the saturated zone in the mountain block, and is further

transferred to the basin aquifer at the mountain front through the subsurface. Indirect MFR is due to, and essentially equal to, mountain-block recharge, and is often a significant component of recharge in arid and semiarid areas [e.g., *Wasiolek 1995; Manning 2002*]. MBR can be distributed over the mountain hillslopes, or be focused on the mountain stream bed or in some cases at the contact of two bedrock outcrops with contrasting permeability, as Earman [*2004*] found in the Chiricahua Mountains in southeastern Arizona.

Focused MBR in streambeds is measurable using stream gauges and other physical and chemical methods along the stream. MBR distributed over mountain hillslopes cannot to be directly measured. Another difficulty of quantifying distributed MBR is that the water that percolates below the root-zone at one location may return back the surface or a stream elsewhere, due to the local soil conditions, geologic structures and topographic relief. This water may subsequently re-recharge at a lower location, as suggested by Earman [*2004*].

This dissertation distinguishes between two types of recharge estimates. In Chapter 7, which focuses on recharge mapping, these are clearly upper-bound estimates, that is, conservative estimates. “Distributed MBR” refers to estimates of water flux that for the first time percolates across the soil-bedrock interface, and is also referred to simply as “percolation.” The second estimate is for “total MBR.” In arid and semi-arid environments, evapotranspiration is the dominant process that “consumes” the water that is brought into the mountain block by precipitation processes [e.g., *Brandes and Wilcox, 2000*]. The long-term difference between precipitation and actual evapotranspiration, gives an estimate for the “water yield,” which is an upper-bound estimate of total MBR.

Two major limitations, a lack in understanding hydrologic processes, and sparse observation networks, hinder predictive mountain-block hydrologic modeling [*Bales et al., 2004*], and reliable estimation of MBR. Developing approaches to address problems due to these two limitations is also the objective of this dissertation.

Chapter 2 develops a geostatistical algorithm (Auto-searched Orographic and Atmospheric effects De-trended Kriging, or ASOADeK) for mountain precipitation estimation, using sparse gauge data and digital elevation model (DEM) data. ASOADeK constructs monthly precipitation maps comparable to PRISM (Precipitation-elevation Regression on Independent Slopes Model) products [*Guan et al., 2005*], and with higher spatial resolution. ASOADeK is also useful for studying regional climatic settings, and studying the effects of large-scale climatic cycles on mountain precipitation variability. It has potential to downscale precipitation products (e.g., Next Generation Weather Radar or NEXRAD) and recover NEXRAD data from mountain beam-blockage shadows.

Chapter 3 looks at the effects of climatic variability on seasonal mountain precipitation in the study area (northern New Mexico). The major findings are that (1) PDO (Pacific Decadal Oscillation) is a more dominant cycle than ENSO (El Niño and Southern Oscillation) controlling precipitation in northern New Mexico. (2) ENSO strongly modulates the low PDO effects on winter and spring precipitation, but not as strongly on the high PDO effects. For low PDO years, El Nino strongly dampens, and La Nina enhances, the negative winter and spring anomalies. For high PDO years, El Nino enhances, but La Nina does not dampen, the positive winter anomaly. (3) It is evident that PDO shifted to its low phase in late 1990s, indicating a larger possibility of drought in the next several decades in the southwestern U.S. (4) The PDO and ENSO effects on winter

precipitation are strongly modified by topography. The connection between seasonal precipitation anomalies and PDO and ENSO cycles is used to study hydrologic responses of the mountains to climatic variability, included in Chapter 7.

In mountain blocks, precipitation is generally the only water input; in arid and semiarid regions, the dominant water flux out of the mountain block is ET. In comparison to precipitation, ET is more difficult to quantify due to complex topography and vegetation coverage, and lack in observation data. ET is a combination of two physically distinctive processes, evaporation (E) and transpiration (T), which do not respond in the same way to environmental conditions and their changes. It is thus important to estimate E and T separately [e.g., *Newman et al., 2004*]. A Topography- and Vegetation-based surface energy partitioning model for hillslope ET modeling (TVET) is developed in Chapter 4, to estimate potential evaporation (PE) and potential transpiration (PT), including the effects of vegetation and topography on mountain hillslopes. TVET also includes the elements of rainfall interception, snow accumulation and snowmelt, and has a site-aridity correction. The actual E and T is estimated by hydrologic modeling using the saturated-unsaturated porous media code HYDRUS, with PE and PT input from TVET. The performance of TVET is tested with observations from two non-mountain environments, one at the basin floor shrub-grass Sevilleta Long Term Ecology Research site, the other at the cottonwood-saltcedar Rio Grande riparian corridor, New Mexico. In this chapter, the modeling of other hydrologic impacts of vegetation, e.g., root-induced preferential flow, is also described.

Chapter 5 focuses on generic numerical simulations of hillslope water partitioning, aimed at an improved understanding of the mountain-block hydrologic processes at the

hillslope scale. These simulations were conducted to investigate the effects of climate, bedrock permeability, surface topography, soil cover, vegetation cover, and bedrock topography on hillslope water partitioning, especially the percolation flux across the soil-bedrock interface. The bulk bedrock permeability has a switch-type effect on distributed MBR. When the permeability is below a threshold, 1.0×10^{-16} m^2 (equivalent to a saturated hydraulic conductivity of 1.0×10^{-9} m/sec) in our study, distributed MBR is negligible. When the permeability is above a higher threshold, $1.0\times10^{-15} \sim 10^{-14}$ m^2 (equivalent to a saturated hydraulic conductivity of $1.0\times10^{-8} \sim 10^{-7}$ m/sec), the amount of distributed MBR can become significant, and depends on climate (modified by local topography), vegetation characteristics, soil characteristics, and the bedrock characteristics (e.g., matrix-flow dominant vs. fracture-flow dominant). With a uniform soil and vegetation cover, the simulations suggest that the percolation (potential distributed MBR) and ET are functions of topography-modified local climate conditions and bedrock characteristics. These functions are used in Chapter 7 to map potential total MBR and distributed MBR in two mountain blocks of northern New Mexico.

Chapter 6 is a series of specific simulations based on two hillslope experiments along a mountainous piñon-juniper and ponderosa pine ecotone in northern New Mexico. These simulations are intended to answer three scientific questions: (1) whether vegetation can be an indicator for distributed recharge in the mountains; (2) how much change in recharge is caused by the woodland encroachment in the Jemez Mountains; (3) why there is little recharge inferred from the field observations at the ponderosa pine site where climate is relatively wet and bedrock is highly permeable.

With the spatially distributed atmospheric boundary conditions from Chapters 2, 3 and 4, and percolation fluxes and ET from the hydrologic simulations of hillslope hydrologic processes in Chapter 5, maps of upper-bound total MBR and distributed MBR of mountain areas in northern New Mexico, are constructed in Chapter 7. An example is shown in Figure 1.1.

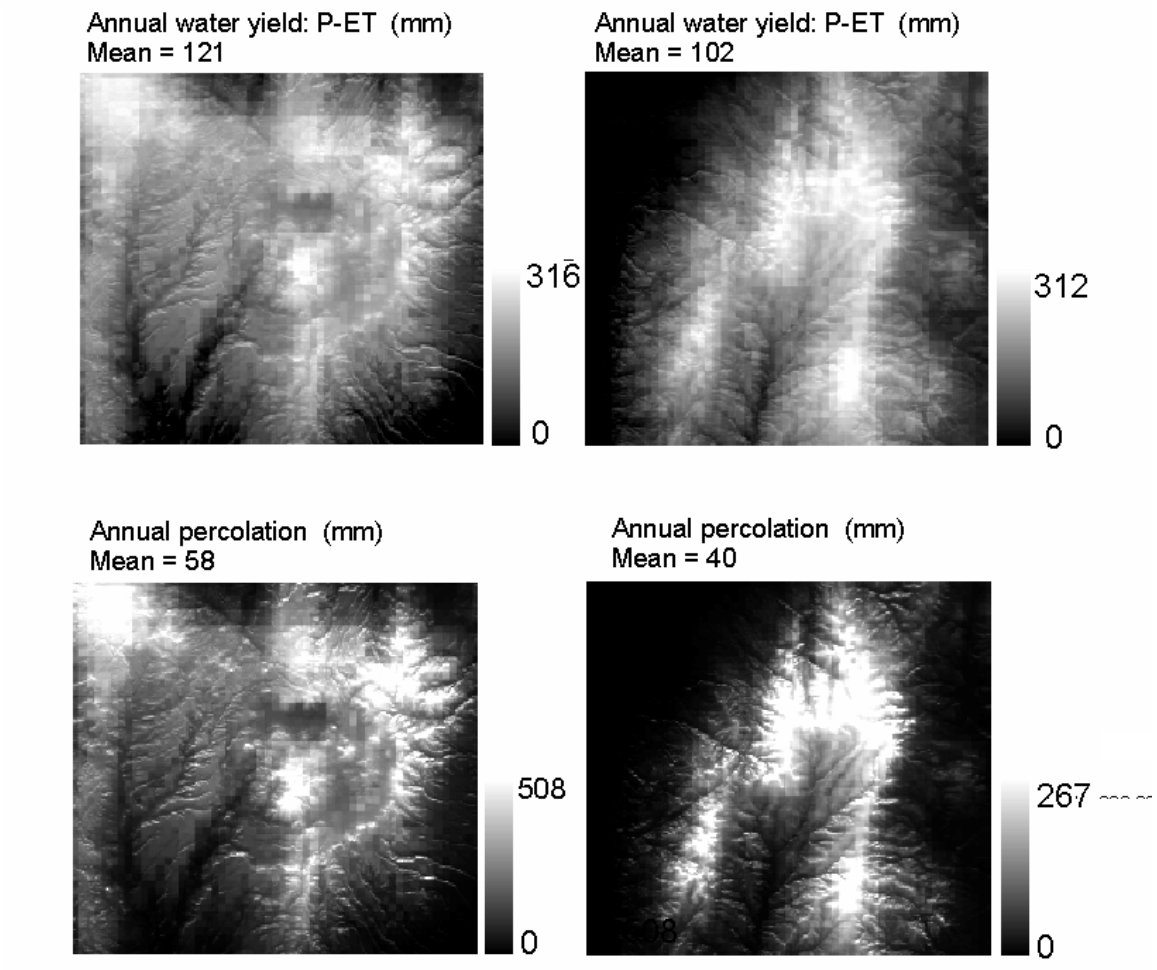

Figure 1.1 An example of upper-bounded total MBR (top) and distributed MBR (bottom) in two mountainous areas, Jemez Mountains (left) and southern part of Sangre de Cristo Mountains (right), northern New Mexico.

The primary study area is located in the mountainous areas of northern New Mexico, including the southern part of the Sangre de Cristo Mountains, the Jemez Mountains, and the southern extension of the San Jan Mountains (Figure 1.2). The Sangre de Cristo Mountains are mainly composed of granitic rock, while the Jemez Mountains are composed of volcanic rocks. The distinct lithology between the two mountain blocks permits investigation of the effects of bedrock type on water partitioning in the mountain block, as well as on MBR. Previous studies suggest that a significant amount of MBR occurs in these regions. Huntley [*1979*] estimated that the MBR in the San Juan Mountains, a similar volcanic range the southern arm of which is just visible in Figure 1.2, is ~200 mm/yr, or about 38% of annual precipitation, and that the MBR in the Sangre de Cristo Mountains is ~70 mm/yr, or 14% of annual precipitation. Wasiolek [*1995*] gave similar estimates of MBR of ~70 mm/yr for the southern part of Sangre de Cristo Mountains. The results of total MBR and distributed MBR from this study are useful tests of the previous MBR estimates in the areas. The study area covers the New Mexico Climate Division 2 of the National Climate Data Center (NCDC), and has nine SNOTEL (Snowpack Telemetry) stations at high elevations with over 20 years of precipitation data. This makes it convenient to test the ASOADeK model, and investigate the effects of climate variability on seasonal precipitation distribution. The study area also includes a field hillslope experiment site (Figure 1.2) from which Dr. Brent Newman from Los Alamos National Lab kindly provided data for numerical simulations in Chapter 6 of this dissertation.

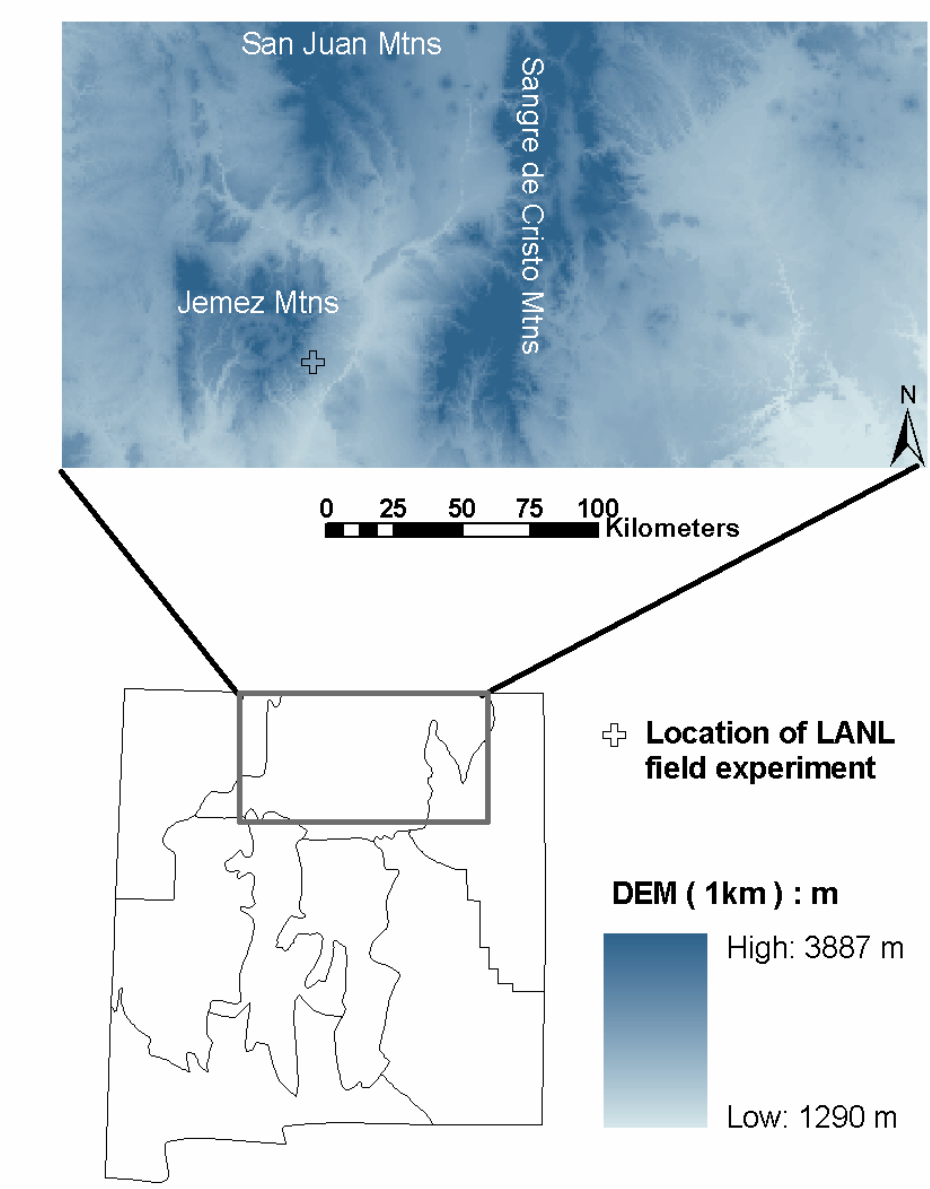

Figure 1.2 The study area in northern New Mexico, including the Sangre de Cristo Mountains in the center, the Jemez Mountains and southern extension of the San Juan Mountains in the west.

References

Bales, R.C., J. Dozier, N. P. Molotch, T. H. Painter, and R. Rice (2004), Mountain Hydrology of the Semi-Arid Western U.S., *CUAHSI Cyberseminar Draft Paper*, Nov 11, 2004.

Beniston, M. (2003), Climate change in mountain regions: a review of possible impacts. *Climatic Change*, 59, 5-31.

Brandes, D., and B.P. Wilcox (2000), Evapotranspiration and soil moisture dynamics on a semiarid ponderosa pine hillslope. *Journal of the American Water Resources Association*, 36(5), 965-974.

Earman, S. (2004), Groundwater recharge and movement through mountain-basin systems of the Southwest: a case study in the Chiricahua Mountains-San Bernardino Valley system, Arizona and Sonora, Dissertation, New Mexico Institute of Mining and Technology.

Guan, H., J.L. Wilson, and O. Makhnin, (2005), Geostatistical Mapping of Mountain Precipitation Incorporating Auto-searched Effects of Terrain and Climatic Characteristics. *Journal of Hydrometeorology* (in press).

Huntley, D. (1979), Groundwater recharge to the aquifers of northern San Luis Valley, Colorado. *Geological Society of America Bulletin*, Part II, 90(8), 1196-1281.

Kapos, V., J. Rhind, M. Edwards, C. Ravilious, and M. Price (2000), Developing a map for the world's mountain forests, in Price, M.F., and Butt, N. (eds.) *Forests in a Sustainable Mountain Environment*, CAB International, Wallingford.

Luckman, B., and T. Kavanagh (2002), Impact of climate fluctuations on mountain environments in the Canadian Rockies. *AMBIO*, 29, 371-380.

Manning, A.H. (2002), Using noble gas tracer to investigate mountain-block recharge to an intermountain basin, Dissertation, University of Utah.

Meybeck, M., P. Green, and C. Vörösmart (2001), A new typology for mountains and other relief classes: an application to global continental water resources and population distribution. *Mount. Res. Dev.*, 21, 34-45.

Newman, B.D., B.P. Wilcox, S. Archer, D.D. Breshears, C.N. Dahm, C.J. Duffy, N.G. McDowell, F.M. Phillips, B. Scanlon (2004), The ecohydrology of arid and semiarid environments: A scientific vision, *CUAHSI Cyberseminar Draft Paper*, Oct. 21, 2004.

Phillips, F.M., J.F. Hogan, and B.R. Scanlon (2004), Introduction and Overview, in *Groundwater Recharge in a Desert Environment: The Southwestern United States*, edited by J.F. Hogan, F.M. Phillips, and B.R. Scanlon, Water Science and Applications Series, vol. 9, American Geophysical Union, Washington, D.C., 1-14.

Viviroli, D., R. Weingartner, and B. Messerli (2003), Assessing the hydrological significance or the world's mountains, *Mountain Research and Development*, 23, 32-40.

Wasiolek, M. (1995), Subsurface recharge to the Tesuque aquifer system from selected drainage basins along the western side of the Sangre de Cristo Mountains near Santa Fe, New Mexico. U.S. Geological Survey Water-Resources Investigations Report 94-4072.

Wilson, J.L., and H. Guan (2004), Mountain-block hydrology and mountain-front recharge, in *Groundwater Recharge in a Desert Environment: The Southwestern United States*, edited by J.F. Hogan, F.M. Phillips, and B.R. Scanlon, Water Science and Applications Series, vol. 9, American Geophysical Union, Washington, D.C., 113-137.

CHAPTER 2 GEOSTATISTICAL MAPPING OF MOUNTAIN PRECIPITATION INCORPORATING AUTO-SEARCHED EFFECTS OF TERRAIN AND CLIMATIC CHARACTERISTICS[1]

2.1 Introduction

Many hydrologic and ecologic studies recognize the importance of characterizing the temporal and spatial variability of precipitation [e.g., *Goodrich et al., 1995*]. This variability is even larger in mountainous regions because of complex topography and orographic effects [*Barry, 1992; Oki et al., 1991; Sturman and Wanner, 2001; Sotillo et al., 2003*]. Orographic effects account for incoming moisture that is forced to rise by the topographic height, leading to more precipitation on the windward side, less precipitation on the leeward side, and more precipitation at higher elevations [refer to *Michaud et al., 1995*, for details on orographic mechanisms]. A lack of adequate gauge stations in mountains and precipitation in the form of snow, very common in mountainous regions during late fall, winter and early spring, complicate data collection and synthesis. Recently, radar has improved the estimation of spatially distributed precipitation; however, beam blockage, underestimation, and non-detection of precipitation are significant problems in mountainous terrains [*Young et al., 1999*]. In addition, a reliable radar algorithm for estimating precipitation as snow is not yet available.

Thus, a reliable precipitation mapping approach based on limited number of gauge data is still desired for mountain areas. Various approaches have been applied to

[1] A revised version of this chapter was accepted by Journal of Hydrometeorology, with co-authors John Wilson and Oleg Makhnin.

map precipitation from gauge observations. They include (1) those ignoring spatial covariance structure and knowledge of precipitation processes (such as orographic effects), e.g., Theissen polygon, and inverse square distance [reviewed by *Goovaerts, 2000*], (2) those considering precipitation spatial covariance structures, e.g., kriging [*Phillips et al., 1992; Goovaerts, 2000*], (3) those considering orographic and/or atmospheric effects on precipitation occurrences, e.g., regression [*Daly et al., 1994; Michaud et al., 1995; Goovaerts, 2000; Drogue et al., 2002*], and (4) those considering both spatial covariance and terrain and/or climatic conditions, e.g., cokriging precipitation with terrain elevation [*Hevesi et al., 1992; Phillips et al., 1992; Goovaerts, 2000*], and de-trended residual kriging [*Phillips et al., 1992; Goovaerts, 2000; Kyriakidis et al., 2001*]. Goovaerts [*2000*] compared seven techniques used to map monthly rainfall data for the Algarve region in Portugal, and concluded that geostatistical kriging methods are better than traditional simple techniques (Theissen, inverse square distance, regression), and methods considering the secondary variables further improved the predictions. Terrain elevation is the most common used secondary variable incorporated in estimating precipitation, based on the physics of orographic effects. However, Goovaerts [*2000*] also found that the benefits of methods incorporating terrain elevation depend on the correlation coefficient between precipitation and elevation. The author proposed a threshold correlation coefficient of 0.75 for useful precipitation-elevation cokriging. Asli and Marcotte [*1995*] also reported that the introduction of secondary information in estimation is worthwhile only for a correlation coefficient above 0.4. This would restrict the usefulness of the terrain elevation in cases where the correlation coefficient is low.

Terrain aspect, and its relationship to moisture sources, also plays a role in orographic effects, and thus should be considered in precipitation estimates [*Hutchinson, 1973; Sturman and Wanner, 2001; Sotillo et al., 2003*]. PRISM (Precipitation-elevation Regression on Independent Slopes Model) provides an approach to couple both terrain elevation and aspect in estimating precipitation [*Daly et al., 1994*]. In PRISM, the terrain is divided into many topographic facets; in each facet the terrain aspect effect is assumed constant. A precipitation-elevation linear regression is constructed for each facet as the precipitation predictor for DEM (digital elevation map) grid cells in that topographic facet. As required for a reliable regression function, each topographic facet must be large enough to include a required number of gauge stations (although there are special algorithms to handle facets that do not meet this requirement). By doing this, PRISM screens out the terrain aspect effects in its regression, which otherwise should be considered but is very often ignored in most other mapping approaches. More recently, PRISM uses weighting functions to incorporate gauge data of neighboring topographic facets for regressions, which involves a sophisticated parameterization [*Daly et al., 2002*]. Sufficient regional climatic knowledge, which is not always available, is required for the PRISM weighting parameterization. In any event, the resolution of PRISM product has been limited by its input DEM grid size (~6km×9km) [*Daly et al., 1994*], although recently, PRISM provides products with a resolution up to ~2 km using a filtering algorithm. In other work, Basist et al. [*1994*] explicitly introduce elevation, slope (terrain steepness associated with the prevailing wind), orientation (relationship between the terrain aspect and the prevailing wind), and exposure (distance between the gauge and the mountain to the upwind direction of the gauge) into annual precipitation regressions.

Similar to PRISM, their approach requires sufficient regional climatic knowledge, and appears to apply for low spatial resolutions.

In this study, we use a multivariate linear regression approach on gauge data to auto-search regional and local climatic settings (i.e., infer the spatial gradient in atmospheric moisture distribution and the effective atmospheric moisture flux direction), and local orographic effects (the effective terrain elevation and the effective terrain aspect). The observed gauge precipitation data are then spatially de-trended by the auto-searched regression surface. The spatially de-trended gauge data are further interpolated by ordinary kriging, to generate a residual precipitation surface. The precipitation map is then constructed by adding the regression surface to the kriged residual surface. This approach is called ASOADeK (Auto-Searched Orographic and Atmospheric effects De-trended Kriging) (Figure 2.1). ASOADek produces high-spatial-resolution precipitation maps explicitly incorporating terrain elevation and aspect, as well as climatic setting, while considering spatial correlation structure across the studied domain. In this paper, ASOADeK is compared to precipitation kriging, precipitation-elevation cokriging, and PRISM estimates, for the long-term monthly average precipitation of a study area in northern New Mexico.

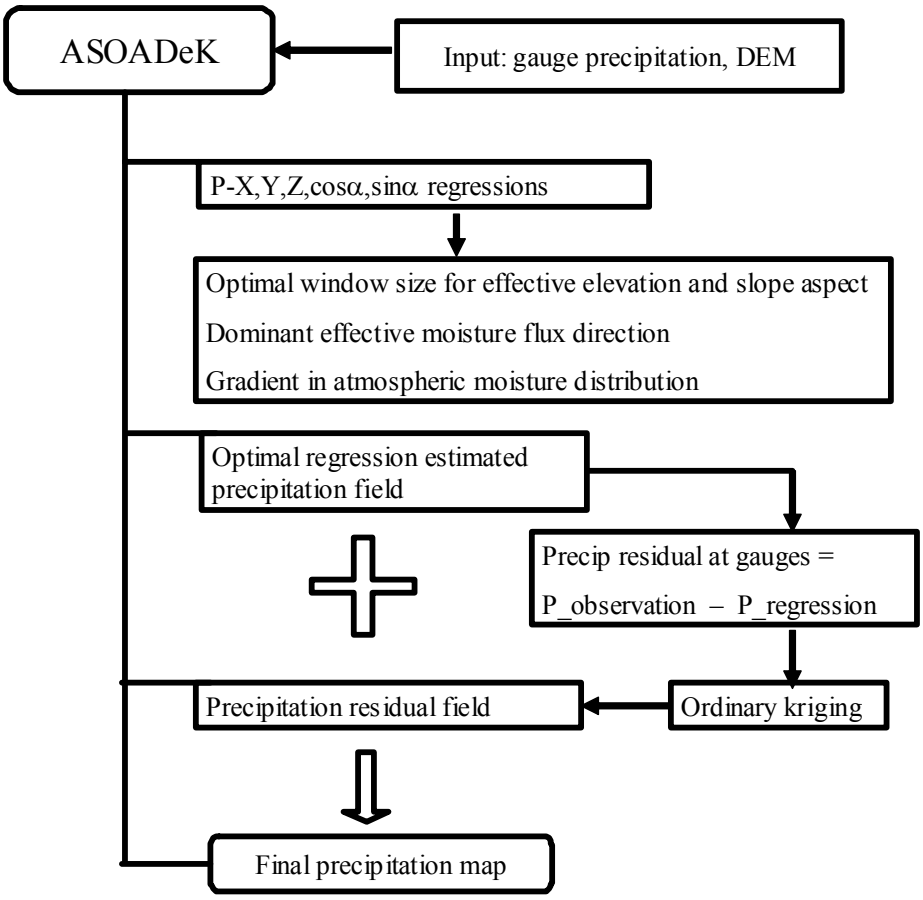

Figure 2.1 Flow chart of the ASOADeK model.

2.2 Methodology

2.2.1 Study area

The study area covers three NCDC (National Climate Data Center) climate divisions (Figure 2.2, DEM + weather stations) in northern New Mexico, with Division 2 as the primary focus (Figure 2.2a). Division 2 is mainly mountains (e.g., Sangre de Cristo) and inter-mountain valleys. The elevation ranges from 1290 to 3887m according to the 1km-resolution DEM map (Figure 2.2b), which was re-sampled from an 60m-resolution DEM [*EDAC, 1996*]. Altogether 74 NCDC weather stations and 9 SNOTEL (SNOwpack TELemetry) stations, which have long-term (>10 year) monthly precipitation data, are

used in this study. The duration of the available data is shown in Figure 2.2c. Division 5 is the central valley along the Rio Grande rift, and Division 6 is the central highlands. The mean annual precipitation, estimated as the averages of available long-term records, is 440, 240, and 410 mm for Division 2, 5 and 6, respectively. We chose Division 2 as the primary study area because it is mostly mountainous terrain, which is appropriate to test ASOADeK for mountain precipitation mapping.

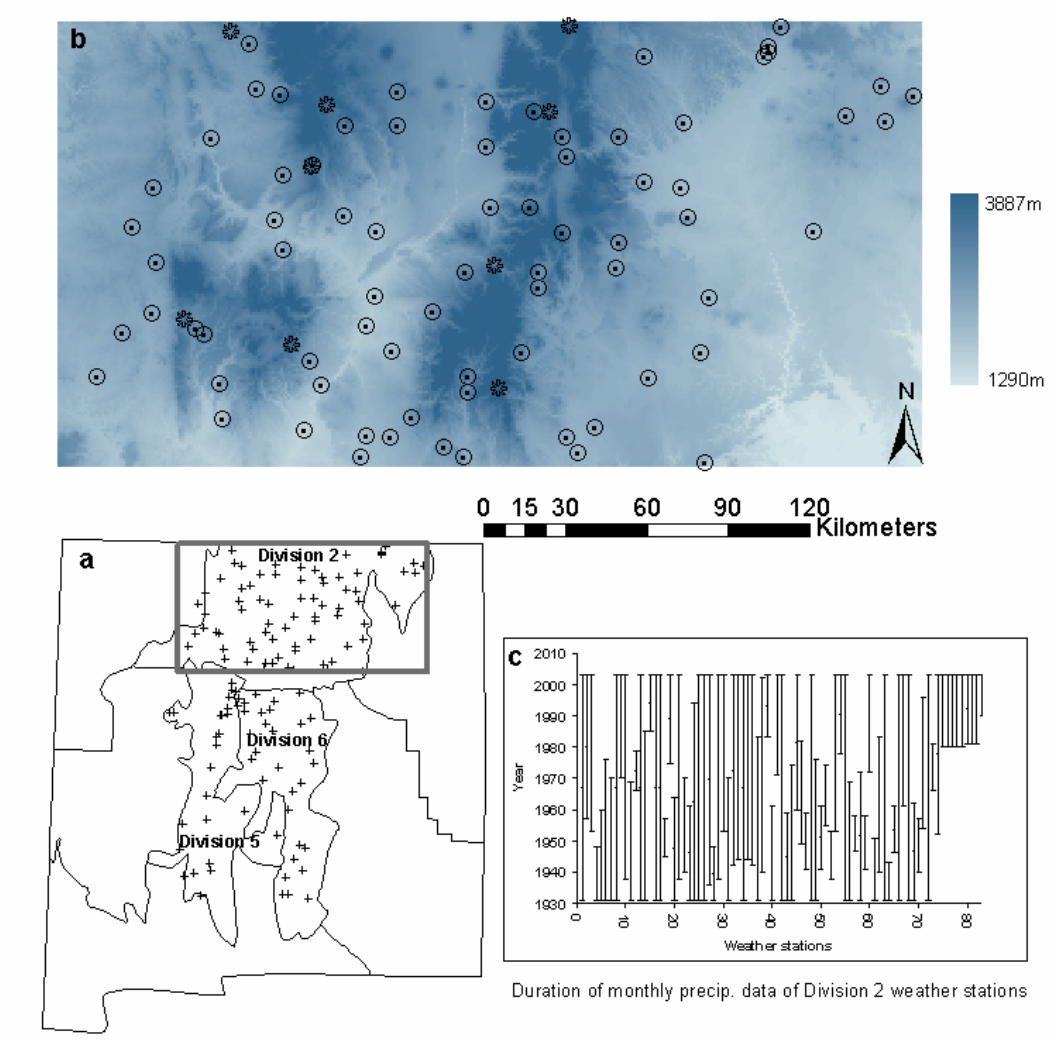

Figure 2.2 Index map showing (a) the three climate divisions in New Mexico, (b) Division 2 DEM map with weather stations (asterisks are SNOTEL stations), and (c) the period of available data.

2.2.2 Auto-searching effective terrain and climatic characteristics

Because of orographic effects the long-term average precipitation (P) is usually well correlated with the terrain elevation (Z). It has also been noticed in other studies that the optimal correlation elevation is not necessary the point elevation, but more often is the effective elevation of a larger area (called the window) surrounding the observation point [*Daly et al., 1994; Kyriakidis et al., 2001*]. The window usually has a square shape. In this study, the window for each gauge is located by comparing the gauge coordinate with the DEM maps of different pixel sizes generated by the ESRI (Redlands, CA) ArcMap GIS tool.

Elevation is not the only orographic factor influencing precipitation; the terrain aspect may also play a role. Orographic effects depend on both terrain characteristics and the moisture flux direction [e.g., *Oki, et al., 1991; Sturman and Wanner, 2001; Sotillo et al., 2003*], the latter varying with seasons. It is difficult to distinguish terrain effects in annual precipitation because the effects of different seasons lump together and partially (or even completely) obscure these effects. Nonetheless, it is reasonable to assume that the mean moisture flux direction does not change much within a short period in the year (e.g. a month). In this short period, the moisture flux-related terrain aspect effects on precipitation should be detectable, and can be used to improve precipitation estimates. In this event, just as effective elevation has an optimal window size, the terrain aspect must also have optimal window sizes demonstrating effective orographic effects. The optimal window size is determined from the best regression that has a minimum residual of the regression estimates with respect to the gauge observations.

Obviously, the availability of atmospheric moisture controls the precipitation distribution. If the moisture flux entering the study area is spatially inhomogeneous, so

too will be the precipitation distribution transverse to the flow path. Our model simplifies this process, representing only a linear spatial gradient in moisture and precipitation (across the flow path). If, on the other hand, the atmospheric moisture depletes enough to cause different precipitation along the flow path, this also leads to a spatial gradient in precipitation distribution. We consider both of these processes together, although they can be separated using the inferred moisture flux direction (see Discussion). In this paper, the atmospheric moisture gradient orientation is defined as zero degrees if it is wetter in the north, increasing clockwise, and 180 degrees if it is wetter in the south. Like moisture flux direction, moisture gradient is inferred from the regression of gauge data, without reference to other data sources.

ASOADeK considers the terrain elevation, the relationship of moisture flux direction and terrain aspect, and the spatial gradient of moisture distribution as independent variables for precipitation estimates. In order for the effects of these variables to be automatically inferred through regression, they are explicitly introduced in regression function. Above-sea-level terrain elevation (Z) in a unit of kilometers is used in this study. Since, the effect of terrain aspect (α) works together with moisture flux direction (ω), they are included into a cosine function, $\cos(\alpha\text{-}\omega)$. The aspect is defined as the direction of the slope orientation, zero to the north, increasing clockwise, and 180 to the south; ω is the source direction of moisture flux, zero from the north, increasing clockwise, and 180 from the south. The UTM easting (X) and northing (Y) of the precipitation gauges, with a unit of kilometers, are used to search the spatial gradient in atmospheric moisture.

$$P = b_0 + b_1 X + b_2 Y + b_3 Z + b_4 \cos(\alpha - \omega) \tag{2.1}$$

Equation (2.1) can be further transformed to

$$P = b_0 + b_1 X + b_2 Y + b_3 Z + b_5 \cos\alpha + b_6 \sin\alpha \qquad (2.2)$$

where $b_5 = b_4 \cos\omega$, and $b_6 = b_4 \sin\omega$, implicitly contain the moisture flux direction. With this equation, the elevation effect is auto-determined by b_3; the spatial gradient in atmospheric moisture is auto-determined by b_1 and b_2; and the moisture flux-dependent aspect effect is auto-determined by b_5 and b_6. The effective moisture flux direction itself can be retrieved from b_5 and b_6. For example, if b_5 and b_6 are both positive, $\omega = atan(b_6/b_5)$. Similarly, the gradient in atmospheric moisture can be retrieved from b_1 and b_2. Five window-sizes for terrain aspect and terrain elevation are considered for each month in the linear regression. The regression with the least MAE (mean absolute error) gives the optimal window sizes for orographic characteristics, and the effective dominant moisture flux direction, as well as the gradient in moisture distribution. The statistical significance of each variable in the regression is evaluated by analysis of the regression variance (ANOVA). These multiple linear regression procedures are the first components of ASOADeK model (Figure 2.1).

2.2.3 Precipitation mapping procedure

2.2.3.1 Construct the optimal regression precipitation map

The regression precipitation map is constructed from the coefficients of the optimal regression function as determined in last section (i.e., known $b_0, b_1, b_2, b_3, b_5,$ and b_6,), and from the terrain elevations and aspects (i.e., X, Y, Z, α; all derived from a DEM) of the optimal window sizes. Since the window size for the terrain elevation may be different from that for the terrain aspect, the regression precipitation map has a spatial resolution of the smaller window size. In this study, long-term average monthly

precipitation maps were constructed. The optimal regression of significant terrain and climatic characteristics is our first order estimate of monthly precipitation.

2.2.3.2 Construct the precipitation residual map

From the optimal regression, and the determined effective orographic windows, the residual ($P_{observation} - P_{regression}$) is calculated for each gauge. With these precipitation residuals, the precipitation residual map can be constructed using ordinary kriging. In this study, GSLIB routines [*Deutsch and Journel, 1998*] were used to calculate the experimental variograms of the precipitation residuals, and to construct the residual maps. The residual map has the same pixel size as the regression precipitation map. In Geostatistics this procedure is called de-trended kriging (also residual kriging) because the regression removes the trend attributed to the deterministic effects of climatic and orographic factors, leaving the residual a near random variable. De-trended kriging is the second component of ASOADeK model. In this paper the variogram models were fitted to the calculated variograms manually (although this step can also be automated using, e.g., a maximum likelihood approach).

2.2.3.3 Construct the final precipitation map

The final monthly precipitation map is obtained by adding the kriged residual map and the regressed precipitation map (Figure 2.1).

2.2.4 ASOADek model testing

Other geostatistic approaches, such as ordinary kriging of observed precipitation, and cokriging of precipitation with terrain elevation, are also applied to the same data and compared to ASOADeK estimates. The theory of kriging and cokriging of precipitation is well demonstrated in the literature [*Hevesi et al., 1992; Daly et al., 1994; Goovaerts, 2000; Kyriakidis et al., 2001*] and is not described here. Cross-validations are done to

evaluate the performance of ASOADeK and other geostatistical approaches. “In cross-validation actual data are dropped one at a time and re-estimated from some of the remaining neighboring data. Each datum is replaced in the data set once it has been re-estimated” [*Deutsch and Journel, 1998*]. For kriging and cokriging, cross validation is done in the kriging processes. For ASOADeK, cross-validation is done from regression through kriging processes, with an assumption that the monthly variogram models do not change with one datum dropped out.

The PRISM monthly mean precipitation product is also compared to ASOADeK. The PRISM data was downloaded from Spatial Climate Analysis Service, Oregon State University [*2003*]. The PRISM data were estimated from the average monthly precipitation over 30 years from 1971-2000, with a spatial resolution of about 4 km. PRISM is not included in the cross-validation, as the necessary information to perform an equivalent and full cross-validation is not available.

2.3 Results

2.3.1 Correlation of precipitation and terrain elevation

We calculated the correlation coefficients for mean monthly precipitation and elevation, using the point elevation for each gauge and the effective DEM elevations for five different window sizes around each gauge (Figure 2.3). The various-resolution DEM maps for the windows were derived from a 60m DEM map using the ERDAS (Atlanta, GA) image processing tool. The *P-Z* correlation is high in the winter months for the mountainous terrain of Division 2. If we adopt a correlation coefficient of 0.75 as the threshold for meaningful cokriging *P* with *Z*, cokriging in Division 2 should only be attempted for a few months. For the central highlands of Division 6, the *P-Z* coefficient is high for all but April and May. The correlation is low for the central valley Division 5,

where the terrain is relatively flat. The best effective elevation windows, maximizing correlation, vary between months for Divisions 5 and 6, while the effective elevation is not sensitive to the window size for Division 2. Combining all three divisions compensates for opposing high and low correlations, losing information for geostatistic estimation. Using combined data in cokriging *P* with *Z* would lead to biased estimates for precipitation.

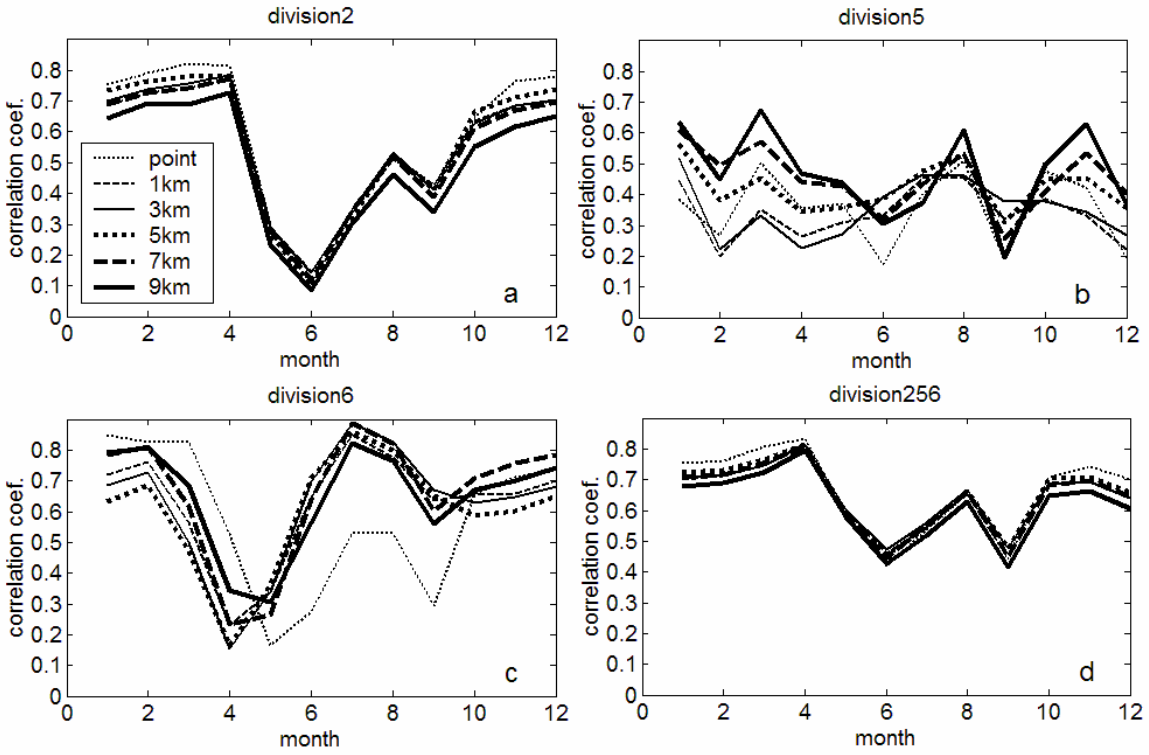

Figure 2.3 Correlation coefficient of mean monthly precipitation and the terrain elevation of various window sizes for NCDC New Mexico Divisions 2 (a), 5 (b), and 6 (c) individually and lumped together (d) (Division 2 includes both NCDC and SNOTEL stations).

2.3.2 Regression of precipitation with terrain and climatic characteristics

Since the effective elevation is not sensitive to window size in Division 2, we used a 1-km DEM elevation window in the following regression analyses of Division 2 precipitation gauge data. For more general situations, cross-combinations of different

window sizes for elevation and terrain aspect should be tested. The regressions included precipitation-elevation (*PZ:* $P = b_0 + b_3 Z$), precipitation-elevation and aspect (*PZA:* $P = b_0 + b_3 Z + b_5 \cos \alpha + b_6 \sin \alpha$), precipitation-elevation, aspect, and spatial gradient of atmospheric moisture (*PZAXY:* $P = b_0 + b_1 X + b_2 Y + b_3 Z + b_5 \cos \alpha + b_6 \sin \alpha$). *PZAXY* is also called ASOADeK regression in this paper. The results are shown in Figure 2.4 and Tables 2.1 and 2.2, and reported below. The general trend is that compared to the *PZ* regression, adding aspect improves the regression fitting, and adding both terrain aspect and atmospheric moisture gradient further improves the regression fitting (Figure 2.4). The relative importance of the three properties varies with months (Table 2.1; note the ANOVA F statistics). For winter months (November through April), both terrain elevation and aspect significantly influence the precipitation distribution. For summer monsoon months (July and August), elevation, terrain aspect, and the spatial gradient of atmospheric moisture all play a role in the precipitation distribution. For the first transition months (May and June), elevation is not an important factor for precipitation processes. For the second transition months (September and October), the elevation is the only factor significantly influencing precipitation distribution.

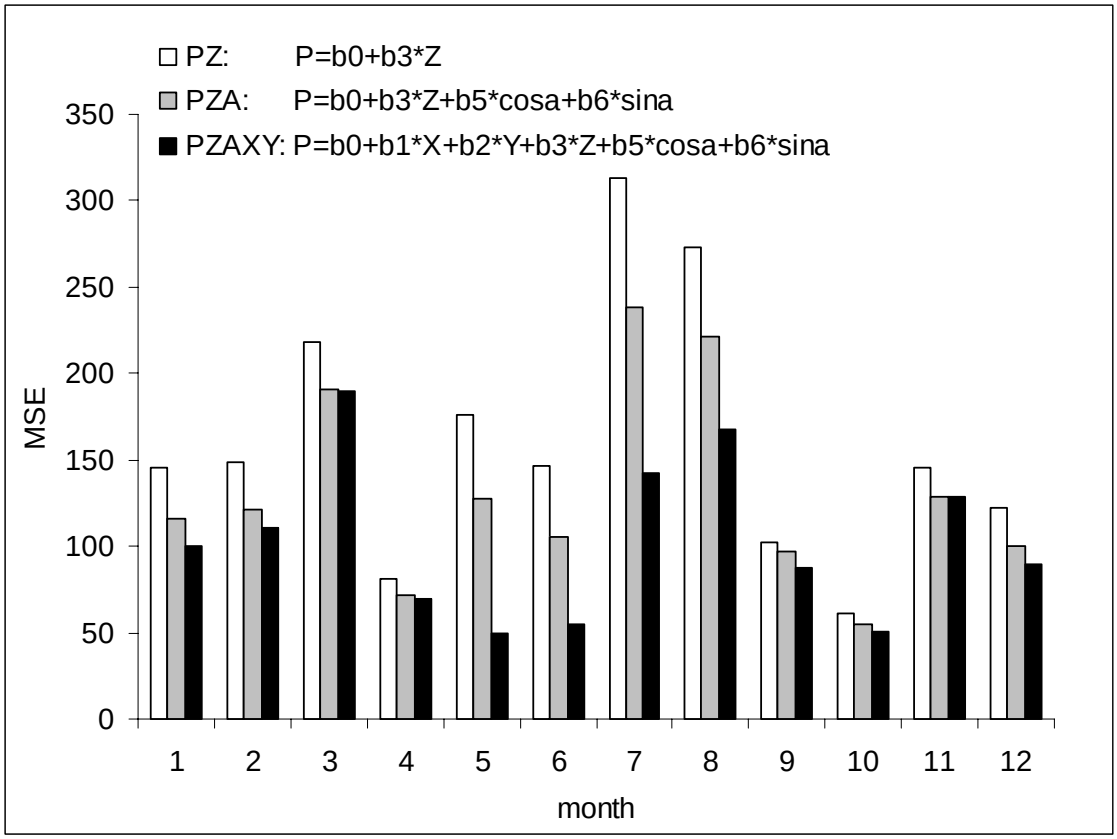

Figure 2.4 Mean squared error of various precipitation (*P*) regression estimates for Division 2.

Table 2.1 R^2 values and F statistical test of ANOVA for significance of various orographic and atmospheric properties in precipitation regressions. For each regression type a boldface F statistic indicates that the variable is significant for that month

Regressions	PZ		PZA		PZAXY	
Month	R^2(%)	Z	R^2(%)	aspect	R^2(%)	X,Y
1	47	***72.39***	59	***11.25***	65	***7.36***
2	53	***90.67***	63	***10.41***	67	4.75
3	55	***99.06***	62	***6.87***	63	1.15
4	60	***119.68***	65	***6.29***	67	2.42
5	8	7.43	36	***16.67***	76	***62.87***
6	2	1.74	31	***16.39***	65	***37.25***
7	11	***10.22***	34	***13.74***	62	***27.79***
8	27	***30.43***	42	***10.30***	58	***13.76***
9	18	***18.13***	25	3.28	34	5.30
10	40	***54.55***	48	5.51	53	4.87
11	47	***71.53***	54	***6.16***	55	1.19
12	49	***78.14***	60	***10.26***	65	***5.79***
$F^{0.005}$		8.33		5.67		5.68

Note: The data in the second column of each regression are ratios of mean of squares for regression due to the variables of interest to mean squared error. $F^{0.005}$ is the critical threshold of 99.5% confidence level, above which adding the variable in regression is significant.
PZ = precipitation-elevation regression
PZA = precipitation-elevation and aspect regression
PZAXY = precipitation-elevation, aspect, and gradient in atmospheric moisture regression

The optimal window size for effective terrain aspect in *PZAXY* regression varies from 3 km to 9km, depending on the month, but is mostly around 5 km (Table 2.2). This is much smaller than the topographic facet used in PRISM [*Daly et al., 1994*]. The effective moisture flux direction, retrieved from *PZAXY* regressions, varies with time, from southwesterly and southerly in winter, transitioning to southeasterly and southerly

in summer (column 3 in Table 2.2). The regression-identified atmospheric moisture gradient also varies with month, suggesting different atmospheric moisture characteristics in the study area through the year. Also note that the wetter direction is not necessarily upwind (see Discussion).

ASOADeK regression results for three selected months (February, May, and August) are shown in Figure 2.5, with comparison to PRISM estimates. Of the three months, February represents the winter season; August is in the summer monsoon season; and May is a transition month in between, and has weak elevation-correlated monthly precipitation. Even without the next step of de-trend kriging of the residual, the ASOADeK regression already shows estimating capacity close to that of PRISM, especially for May.

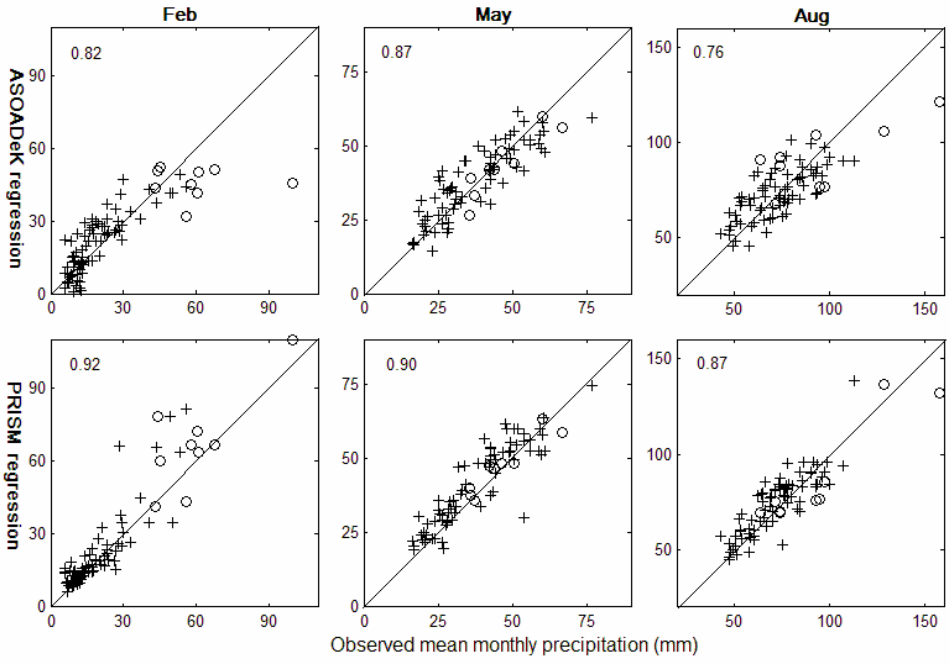

Figure 2.5 Comparison of ASOADeK (*PZAXY*) regression estimates to PRISM estimates for three selected months in Division 2. x-axis is the observed mean monthly precipitation, y-axis is model estimates. Cross legends represent NCDC stations, and circles for SNOTEL stations. The number inside each panel is the correlation coefficient between the estimates and the observations.

Table 2.2 The parameter values of the optimal linear regressions of monthly precipitation from ASOADeK for Division 2, ($P=b_0+b_1X+b_2Y+b_3Z+b_5\cos\alpha+b_6\sin\alpha$)

Month	Aspect window	Moisture flux direction[1]	Moisture gradient[2]	b_0	b_1	b_2	b_3	b_5	b_6	MAE	MAE/P (%)	Mean Precip (mm)
1	9km	213	298	-145.73	-0.062	0.033	27.631	-6.093	-4.009	6.71	29	23.48
2	5km	198	295	-137.11	-0.058	0.027	33.423	-6.789	-2.188	7.13	31	23.08
3	5km	186	279	-80.43	-0.037	0.006	43.788	-9.095	-0.942	9.22	29	31.42
4	5km	180	60	-136.44	0.035	0.020	29.854	-5.361	-0.018	5.90	20	29.52
5	3km	174	86	-93.82	0.144	0.009	13.830	-5.150	0.516	5.37	14	38.54
6	3km	136	121	247.94	0.122	-0.073	9.995	-2.297	2.223	5.70	17	32.97
7	3km	156	134	542.10	0.155	-0.151	26.007	-7.683	3.499	8.92	14	64.91
8	9km	172	145	513.29	0.100	-0.142	35.505	-11.946	1.624	10.38	14	74.59
9	5km	172	154	272.15	0.035	-0.071	16.714	-5.138	0.686	7.06	17	42.60
10	5km	182	195	181.05	-0.012	-0.047	19.227	-4.427	-0.147	5.43	16	33.94
11	5km	180	281	-58.72	-0.047	0.009	29.527	-5.487	-0.016	7.77	31	25.46
12	5km	191	273	-29.08	-0.062	0.003	28.428	-5.369	-1.046	6.37	28	22.51

1. The incoming direction of the moisture flux, zero from the north, increasing clockwise, and 180 from the south.
2. The up-gradient direction of the moisture spatial gradient, zero from the north (i.e., wetter in the north), increasing clockwise, and 180 from the south.

28

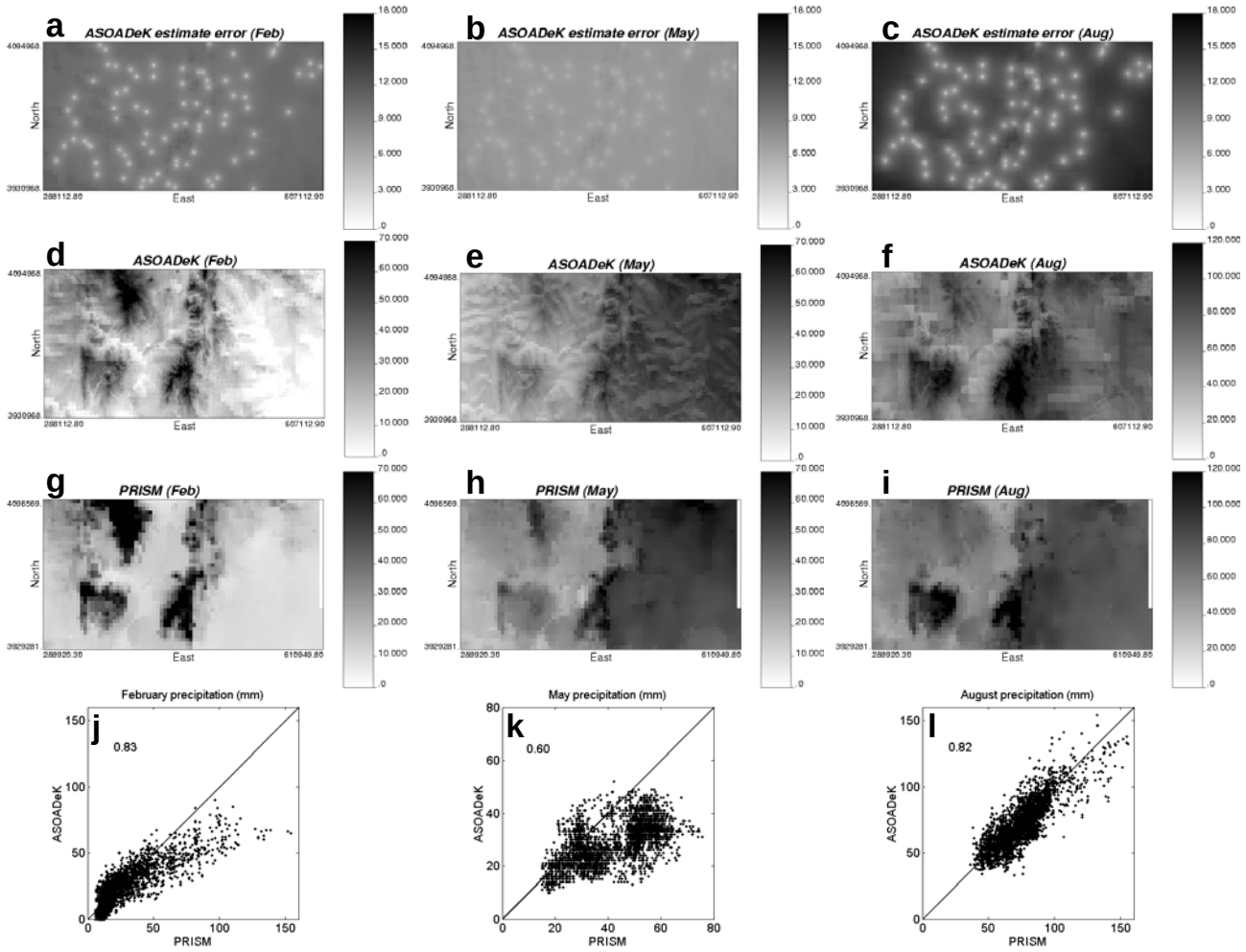

Figure 2.6 ASOADeK-constructed mean monthly precipitation (mm) maps of Division 2 for February, May, and August (d,e,f), with a spatial resolution of 1 km, the respective estimate uncertainty (regression standard error + kriging variance) maps for the three months (a, b,c), the PRISM estimates of the three months (g,h,i) with a spatial resolution of ~4 km, and the scatter plots (j,k,l) between the ASOADeK products and re-sampled PRISM products.

29

2.3.3 ASOADeK precipitation maps

With the regression function and the gauge data, the residuals were calculated. The residual semi-variograms were then modeled (Appendix II) for residual kriging. Adding kriging of the de-trended residual to the repression map leads to the final precipitation maps for each of three months, which are compared to PRISM precipitation maps in Figure 2.6 (c, d, f, g, h, i, j, k, l). The uncertainties of the ASOADeK estimates were calculated as the sum of regression standard error and the kriging variance (Figures 6 a, b, and c). The spatial patterns of precipitation maps from the two approaches agree well. Regarding the estimated precipitation values, ASOADeK estimates for August are consistent with PRISM. For February, ASOADeK gives lower precipitation estimates at the locations with large PRISM precipitation rates. For May, ASOADeK consistently underestimates precipitation compared to PRISM. We also constructed the annual precipitation map by summing all 12-month precipitation maps (not shown). The mean annual precipitation for Division 2 from our map is 445 mm, in good agreement with the arithmetic average of all observations in the division (440 mm). This suggests that for Division 2, the distribution of current gauges (including both SNOTEL and NCDC stations) capture the influence of topography on mean precipitation in the division. However, the mean using only the NCDC stations, 410 mm, is significantly underestimated.

2.3.4 Cross validation

Since all gauge data have been used in the regressions, a good fit to the data does not necessarily indicate a good predicting capacity. Besides, the comparison of the kriging estimates with the observed data used for kriging does not tell how good the estimates are (if the nugget is zero). Cross validations were conducted for various

precipitation estimators, with results shown in Figures 2.7 and 2.8 for three months (February, May, and August). It is not possible with available information to perform cross validations for PRISM in this study. For ASOADeK and other precipitation estimators (*P* kriging, *P-Z* cokriging, *PZ* regression, ASOADeK regression-only) tested in this study, the performance varies between months. For February and May, the ASOADeK regression works better than the precipitation kriging, the *P-Z* cokriging and the *PZ* regression (Figure 2.7). For August, the ASOADeK regression is better than *PZ* regression (Figure 2.7), but poorer than *P* kriging and *P-Z* cokriging. For May, which has a weak *P-Z* correlation, precipitation kriging gives better estimates than *P-Z* cokriging, which is consistent with other studies [*Goovaerts, 2000*]. For all months, ASOADeK estimates, which include both the ASOADeK regression and the kriged residual, are best.

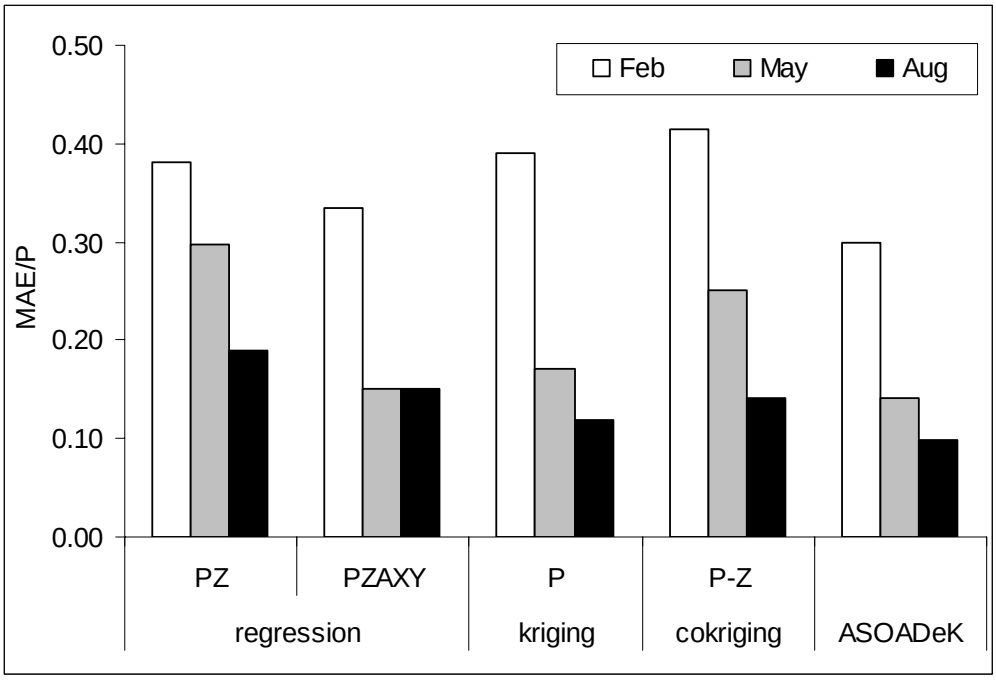

Figure 2.7 Normalized mean absolute error of cross validations for various precipitation estimators in Division 2.

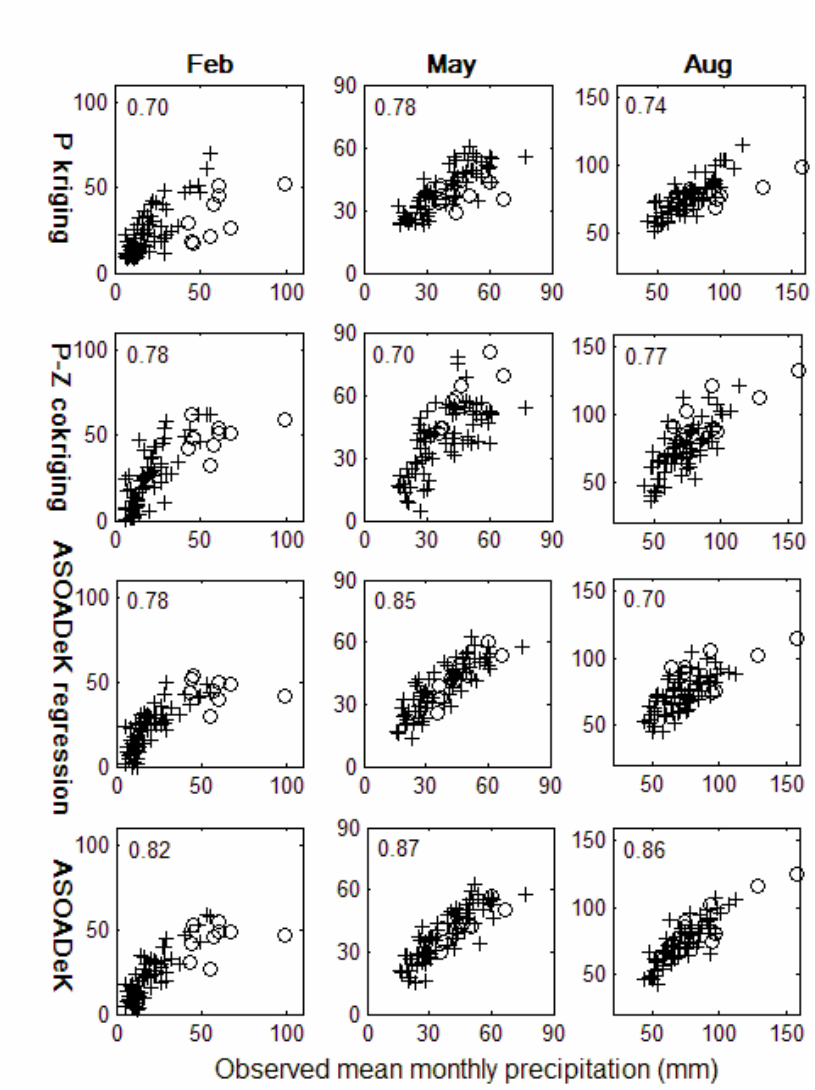

Figure 2.8 Cross validation of precipitation kriging, *P-Z* cokriging, ASOADeK (*PZAXY*) regression, and ASOADeK estimates for three selected months, representing different seasonal climates. x-axis is the observed mean monthly precipitation, y-axis is model estimates. Cross legends represent NCDC stations, and circles for SNOTEL stations, for Division 2. The number inside each panel is the correlation coefficient between estimates and the observations.

2.4 Discussion

2.4.1 ASOADeK auto-searching regional climate setting and local orographic effects

Long-term average precipitation is controlled by the regional climate setting and local conditions. In mountain regions, orographic effects have the strongest influence on precipitation distribution, as once again demonstrated in our study area (Table 2.1). Most precipitation mapping approaches only consider terrain elevation, which alone is not sufficient to represent the orographic effects. In our study area (Division 2), *P-Z* correlation is very low for May and June, and low for monsoon months, indicating elevation is not the dominant orographic factor for these months. In addition to elevation, ASOADeK explicitly introduces terrain aspect, moisture flux direction, and the atmospheric moisture gradient into the multivariate linear regression of gauge data, auto-searching effective orographic and atmospheric characteristics for precipitation mapping, including effective orographic window sizes. These considerations significantly improve the precipitation estimates (Table 2.1 and Figure 2.4).

Although there is no settled scientific opinion about the moisture source of the North American Monsoon [reviewed by *Sheppard et al., 2002*], it is agreed that the moisture (either from the Gulf of California or the Gulf of Mexico) for monsoon precipitation in the southwestern U.S. is developed over Mexico [e.g., *Carleton, 1986; Fawcett et al., 2002; and Bosilovich et al., 2003*]. In other words, in summer monsoon months, the dominant moisture flux in the study area northern New Mexico is southwesterly. The recycling of local moisture source also joins monsoon precipitation in the southwestern United States [*Bosilovich et al., 2003*]. There are also occasionally non-monsoonal summer precipitation events in the study area. Some of these events are

caused by easterly atmospheric moisture flux (NOAA, 2004). The effective moisture flux directions, determined by ASOADeK (Table 2; see Table 1 for significance), are SSE and S, for July and August, respectively, which is apparently the mixture of the two southwesterly and easterly moisture fluxes. For winter months, most of time, Pacific moisture enters North America at latitudes well north of the study area, leading to dry weather in this area [*Sheppard et al., 2002*]. "More favorable conditions for winter precipitation in the southwest U.S. exists when the Pacific High shifts westward, and a low pressure trough forms over the western U.S., allowing Pacific storms to enter the continent at lower latitudes…" [*Woodhouse et al., 1997*]. Thus, the dominant moisture flux of winter months at the study area is southwesterly [*Sellers & Hill, 1974*]. This is more or less captured by ASOADeK, which infers southwesterly to southerly moisture flux direction for the winter months (Table 2).

Now, let's look at the spatial gradient of atmospheric moisture in the study area. If the moisture flux homogeneously enters the whole study area, the only gradient would be due to depletion of atmospheric moisture. The direction of the spatial gradient caused by depleted atmospheric moisture would then agree with flux direction, i.e., more precipitation in the upwind direction of incoming moisture flux. A significant atmospheric moisture gradient that is in disagreement with the effective moisture flux direction, suggests either that the entering moisture flux only covers a part of the study area, or that there are two or more dominant moisture fluxes in the month. The ANOVA analyses of ASOADeK regressions suggest that atmospheric moisture gradient is not important for most winter months and only slightly significant for December and January (Table 2.1). In these months, the ASOADeK-determined spatial moisture gradient is from

the west to the east (drier in the east), with a little deviation from the monthly effective moisture flux direction also determined by ASOADeK (Table 2.2). Whether or not this represents an actual physical process requires further study. For the monsoon months, the moisture spatial gradient is close to the effective moisture flux direction, but still deviates (Table 2.2). This is because there are two circulation patterns that bring moisture for showers and thunderstorms over New Mexico [*NOAA, 2004*]. The first circulation is a strong northward moisture movement from Mexico to New Mexico. The moisture flux direction from this pattern in the study area is southwesterly to southerly. The second circulation is a weak easterly air flow over the study area [*NOAA, 2004*]. The monthly spatial moisture trend obtained from ASOADeK is the apparent result of the mixture effect of these two moisture fluxes. The second weak easterly moisture flux drags the ASOADeK effective moisture flux direction a little eastward away from the first dominant southwesterly moisture flux direction. For the pre-monsoon months (May and June), the moisture spatial gradient is the most significant factor influencing the monthly precipitation distribution in the study area (Table 2.1). In May, the moisture spatial gradient from ASOADeK is orthogonal to the effective moisture flux direction (Table 2.2). This is because in late spring, a northward low-level moisture flux migrates into the central United States from the Gulf of Mexico, causing westward decreasing trend in May precipitation throughout the central and western United States [*Mock, 1996; Higgins et al., 1996 and 1997*]. This low-level moisture flux touches the eastern edge of the study area, leading to an eastward moisture gradient (Table 2.2). ASOADeK successfully captures this climate pattern, and at the same time detects the southerly effective moisture flux direction as well. This northward movement of moisture provides a source for

precipitation in the study area, indicated by the higher monthly precipitation in May than in April and June. It appears from this discussion that, in sufficiently mountainous terrain, and using gauge data alone, the ASOADeK algorithm can be used to infer the effective moisture flux direction and the spatial gradient of atmospheric moisture where the regional climate setting is otherwise unclear.

From the ANOVA analysis (Table 2.1), orographic effects of both terrain elevation and terrain aspect are significant for precipitation during winter and monsoon months. In the transition months, only one factor, either elevation or terrain aspect, plays a significant role. More work is required to reveal whether this is the result of different precipitation processes.

2.4.2 ASOADeK vs. PRISM

Both ASOADeK and PRISM consider terrain aspect in precipitation estimation, but in different ways. In early versions of PRISM the terrain aspect effect was screened out in each topographic facet [*Daly et al., 1994*]. In more recent versions, the aspect effect is described by a weighting function for *P-Z* regression [*Daly et al., 2002*]. The physical mechanism is not well represented. To determine an appropriate weighting function, sufficient knowledge of regional and local climate is needed. In ASOADeK, the terrain aspect effect is explicitly associated with the effective dominant moisture flux direction, well representing the physical mechanism. The moisture flux-dependent aspect effect is also auto-determined in ASOADeK regression without background climate knowledge. Both ASOADeK and PRISM consider the spatial gradient of atmospheric moisture in estimating precipitation distribution. In PRISM, this is achieved by a weighting function in the *P-Z* regression based on distance to the moisture source [*Daly et al., 2002*]. The distance to the moisture source is ambiguous because the moisture flow

path is often tortuous. In addition, for a study area far away from the ocean, the effect of this variable becomes numerically negligible. In ASOADeK, the moisture gradient is automatically searched in high spatial resolution. This allows ASOADeK to represent the actual atmospheric spatial moisture trend in the area of interest, rather than tie it to a distant source of moisture. Regarding spatial resolution, PRISM depends on input DEM resolutions, currently about 4 km, while ASOADeK depends on the minimum of optimal window sizes for various orographic variables from the multivariate regressions. When effective elevation window size is non-sensitive to *P-Z* correlation, such as Division 2 in this study, high spatial resolution precipitation maps can be obtained by prescribing a small window-size for the effective terrain elevations used in the ASOADeK model. Regarding the mapping area, PRISM has been used to estimate precipitation in most areas of northern America, and for all topography types. The current version ASOADeK, however, is used to estimate precipitation for a mountainous area with more-or-less spatially consistent regional climate settings.

Of the three focused study months, the ASOADeK monthly precipitation maps agree well with PRISM for August. However, the February and May estimates for the two models differ (Figure 2.6). This suggests that either ASOADeK underestimates, or PRISM overestimates precipitation for the months, or both. That PRISM appears to overestimate higher February precipitation and slightly overestimate most of the May precipitation, is clearly observed in Figure 2.5. The fairly good cross-validation of ASOADeK May precipitation (Figure 2.7) also suggests that the difference between the two model estimates for May precipitation is due to PRISM overestimates. The ANOVA analysis of ASOADeK regression indicates that atmospheric moisture gradient and

terrain aspect are two major physical factors for May precipitation distribution. Terrain elevation is not a significant predictor of precipitation in this month (Table 2.1). This makes PRISM model (precipitation elevation regression) problematic for this month. In addition, the window size of effective terrain aspect, inferred from ASOADeK regression, is 3 km for May (Table 2.2), far smaller than the topographic facet of the PRISM model. In contrast, the *P-Z* correlation is good for August (Figure 2.3), and the effective terrain window size (9 km) is large (Table 2.2). This probably explains the good agreement between the two models for August precipitation. The PRISM overestimates of some higher precipitation in February are also observed for October through April in the study area (not shown). That ASOADeK underestimates higher February precipitations is observed in Figure 2.7.

Does PRISM actually overestimate winter monthly precipitation (e.g., February) at some locations in the study area? To answer this question, we have to exclude some other causes for the apparent PRISM overestimates of February precipitation shown in Figures 2.5 and 2.6. First, the apparent overestimates could be because of the time periods of observation data for PRISM estimates and those for the estimates in this study are not identical. Both PRISM and our estimates are based on long-term average, i.e., 30 years for PRISM from 1971 through 2000, 11-73 years for our estimates between 1931 and 2003. Comparison of the long-term averages of 1971-2000 to those of available records in the whole time range does show some difference, but not big enough to explain the apparent PRISM overestimates for February shown in Figure 2.5. Besides some PRISM overestimates happen at weather stations where both methods share almost the same data period of 1971-2003. Second, the apparent PRISM overestimates may be an

artifact of data set's elevation range. The elevation of weather stations (1694~3389 m) does not cover the full elevation range of the study area (1290-3887 m), especially with about 500 meters of the higher-end elevation range missing any weather stations. Orographic effects at the high elevations probably deviate from those estimated from the lower elevations. PRISM applies a prescribed universal *P-Z* regression function for the high elevations where observations are lacking, while no adjustments have been done in ASOADeK. This could explain the difference between PRISM and ASOADeK in Figure 2.6, but does not tell which gives better February estimates. The prescribed *P-Z* function in PRISM is not derived locally, and may not represent the situation for our study area. The location with the most severe ASOADeK underestimate is SNOTEL site Hopewell. This site has a point elevation of 3048 meters, but has a larger monthly precipitation rate for winter months than a higher 3389-m-elevation SNOTEL site, Wesner Spring. Hopewell is an outlier site that is not explained by our modeled orographic effects, or represented by other geostatistic approaches (Figure 2.8). If this outlier is excluded, ASOADeK estimates look much better for this and other winter months. PRISM, however, predicts the precipitation at this location well, but overestimates at quite a few other locations (Figure 2.5). We suggest that the apparent winter PRISM overestimates at these locations are due to the non-local vertical extrapolation adjustment; this adjustment in PRISM is better for the monsoon months, as shown in Figure 2.5 and in the scatter plots of August (Figure 2.6).

Similarly, we cannot exclude that ASOADeK underestimates monthly precipitation at some locations. Besides the outlier, the cross-validation results suggest that ASOADeK still slightly underestimates at a couple of observations for February, and

one for August (Figure 2.8). The linear regression employed in ASOADeK may not capture the precipitation distributions of the whole elevation range, and could be improved by using nonlinear regressions. Of course, the above analysis is based on an assumption that the gauge data (both NCDC weather stations and SNOTEL stations) give unbiased measurement of precipitation amount.

2.4.3 ASOADeK vs. other geostatistic approaches

Precipitation kriging only considers spatial covariance structure of the precipitation distribution; it does not capture the orographic effects. For February when *P-Z* correlation is high, precipitation kriging gives poor estimates (Figures 2.7 and 2.8), while for May and August, when *P-Z* correlation is low, precipitation kriging gives fair estimates (Figures 2.7 and 2.8). *P-Z* cokriging considers both precipitation spatial covariance structures and partial orographic effects, and is often used to map mountainous precipitation [e.g., *Hevesi et al., 1992; Goovaerts, 2000*]. However, cokriging requires high *P-Z* correlation, and the mathematical procedure for cokriging is more complex. For May with a low *P-Z* correlation, *P-Z* cokriging gives poor estimates (Figure 2.8). Comparing MAE of precipitation kriging and *P-Z* cokriging, cokriging gives poorer estimates than kriging for all three closely studied months. This supports a threshold of *P-Z* correlation coefficient of 0.75 for useful cokriging, such as suggested by Goovaerts [*2000*]. For annual average precipitation in which the different terrain aspect effects of various months are compensated and traded off, *P-Z* cokriging may become a good tool for precipitation mapping in the mountainous regions [e.g., *Hevesi et al., 1992*]. For February and May, ASOADeK regressions (that is, without kriged residuals) give better estimates than kriging and cokriging, while for August, ASOADeK regression does not out-compete precipitation kriging and *P-Z* cokriging estimates (Figures 2.7 and 2.8).

This is probably because the summer storms occur more randomly in space, and are more difficult for the regressions to capture. Adding its second component (i.e., de-trended kriging of residuals), ASOADeK gives better precipitation estimates than precipitation kriging and cokriging for all months (Figures 2.7 and 2.8). This is reasonable because, while ASOADeK considers spatial covariance structure, it also gives a more complete accounting of orographic and atmospheric effects, and thus is theoretically superior to precipitation kriging and cokriging.

2.5 Conclusions

The purpose of this study is to introduce a geostatistic method (ASOADeK) to map mountain precipitation using only gauge data, while considering both precipitation spatial covariance structure and orographic and atmospheric effects. Application of ASOADeK to monthly precipitation in a mountainous area of northern New Mexico appears to out-perform traditional kriging and cokriging approaches, and produce a precipitation map comparable to the PRISM product, but with a higher spatial resolution. In contrast to PRISM, a knowledge-based approach, ASOADeK does not require detailed understanding of the regional climatic setting. Instead, it automatically detects orographic factors and the climate setting of the study area, including the spatial gradient of atmospheric moisture and the dominant moisture flux direction.

For the study area in northern New Mexico, ASOADeK successfully captures monthly moisture flux directions over the year, and the spatial moisture gradient for monsoon and pre-monsoon months. ASOADeK also suggests that the significance of orographic effects varies between months. For winter months, the terrain elevation is the primary factor, and the terrain aspect is the secondary factor. For monsoon months, both terrain elevation and aspect have similar impacts on precipitation distribution. However,

only terrain aspect is important for May and June, and only terrain elevation is important for September and October. Further studies are required to reveal whether or not this is related to different precipitation processes between the months. If this is the case, it would suggest that ASOADeK has the capacity not only to map mountainous precipitation, but also to work as a diagnostic tool to help understand meteorological processes. In this sense, ASOADeK appears to use mountainous terrain as an instrument to detect or diagnose climate and weather patterns.

To further test the model, future work will include applications of ASOADeK to other mountain areas, and to higher temporal resolutions (e.g. monthly precipitation of a specific year). With its capacity to map high spatial resolution precipitation, ASOADeK could be used to study climate variability (e.g., teleconnections with the Pacific decadal oscillation, and the El Niño-Southern Oscillation) and its effects on mountainous precipitation distribution, and to recover missed rainfall data in the NEXRAD shadow due to the mountain blockage, and to downscale remotely sensed precipitation products. With its auto-search capacity, ASOADeK has potential as a tool to help identify atmospheric moisture sources (e.g., moisture source of the North American Monsoon).

References

Asli, M., and D. Marcotte (1995), Comparison of approaches to spatial estimation in a bivariate contest. *Mathematical Geology*, 27 (5), 641-658.

Barry, R.G. (1992), Mountain climatology and past and potential future climatic changes in mountain regions. *Mountain Research and Development*, 12(1), 71-86.

Basist, A., G.D. Bell, and V. Meentemeyer (1994), Statistical relationships between topography and precipitation patterns. *Journal of Climate*, **7**(9), 1305-1315.

Bosilovich, M.G., Y.C. Sud, S.D. Schubert, and G.K. Walker (2003), Numerical simulation of the large-scale North American monsoon water sources, *Journal of Geophysical Research-Atmosphere*, 108, no.D16, 8614.

Carleton, A.M. (1986), Synoptic-dynamic character of 'bursts' and 'breaks' in the south-west U.S. summer precipitation singularity. *Journal of Climatology*, 6, 605-623.

Daly, C., R.P. Neilson, and D.L. Phillips (1994), A statistical-topographic model for mapping climatological precipitation over mountain terrain, *Journal of Applied Meteorology*, 33, 140-158.

Daly, C., W. P. Gibson, G.H. Taylor, G. L. Johnson, and P. Pasteris (2002), A knowledge-based approach to the statistical mapping of climate. *Climate Research*, 22, 99-113.

Deutsch, C.V., and A.G. Journel (1998), *GSLIB—Geostatistical Software Library and User's Guide*, Oxford University Press, 2nd edition, 369 pp.

Drogue, G., J. Humbert, J. Deraisme, N. Mahr, and N. Freslon (2002), A statistical-topographic model using an omnidirectional parameterization of the relief for mapping orographic rainfall. *International Journal of Climatology*, 22 (5), 599-613.

EDAC (Earth Data Analysis Center) (1996), 60 meter elevation grid image for the state of New Mexico, Albuquerque, NM.

Fawcett, P.J., J.R. Stalker, and D.S. Gutzler (2002), Multistage moisture transport into the interior of northern Mexico during the North American summer monsoon. *Geophysical Research Letters*, 29 (23), 2094, doi:10.1029/2002GL015693.

Goodrich, D.C., J. Faures, D.A. Woolhiser, L.J. Lane, and S. Sorooshian (1995), Measurement and analysis of small-scale convective storm rainfall variability, *Journal of Hydrology*, 173, 283-308.

Goovaerts, P. (2000), Geostatistical approaches for incorporating elevation into the spatial interpolation of rainfall. *Journal of Hydrology*, 228, 113-129.

Hevesi, J.A., J.D. Istok, and A.L. Flint (1992), Precipitation estimation in mountain terrain using multivariate geostatistics, Part I: structure analysis, *Journal of Applied Meteorology*, 31(7), 661-676.

Higgins, R.W., K.C. Mo, and S.D. Schubert (1996), The moisture budget of the central United States in spring as evaluated in the NCEP/NCAR and the NASA/DAO re-analyses, *Monthly Weather Review*, 124, no.5, 939-963.

Higgins, R.W., Y. Yao, E.S. Yarosh, J.E. Janowiak, and K.C. Mo (1997), Influence of the Great Plains low-level jet on summertime precipitation and moisture transport over the central United States, *Journal of Climate*, 10, 481-507.

Hutchinson, P. (1973), The interaction of relief and synoptic situation on the distribution of storm rainfall in the vicinity of Dunedin. *New Zealand Geography*, 29, 31-44.

Kyriakidis, P. C., J. Kim, and N.L. Miller (2001), Geostatistical Mapping of Precipitation from Rain Gauge Data Using Atmospheric and Terrain Characteristics, *Journal of Applied Meteorology*, 40,1855-1877.

Michaud, J.D., B.A. Avine, and O.C. Penalba (1995), Spatial and elevational variations of summer rainfall in the southwestern United States, *Journal of Applied Meteorology*, 34, 2689-1703.

Mock, C.J. (1996), Climatic controls and spatial variations of precipitation in the western United States. *Journal of Climate*, 9(5), 1111-1125.

NOAA, Special feature (2004), the North American Monsoon system, http://www.srh.noaa.gov/abq/climate/Monthlyreports/July/nams.html, visited August, 2004.

Oki, T., K. Musiake, and T. Koike (1991), Spatial rainfall distribution at a storm event in mountainous regions, estimated by orography and wind direction. *Water Resources Research*, 27(3), 359-369.

Phillips, D.L., J. Dolph, and D. Marks (1992), A comparison of geostatistical procedures for spatial analysis of precipitation in mountainous terrain. *Agricultural and Forest Meteorology*, 58, 119-141.

Sellers, W.D., and R.H. Hill (1974), *Arizona Climate 1931-1972*, 2nd edition, University of Arizona Press, Tucson, AZ, 616 pp.

Sheppard, P.R., A.C. Comrie, G.D. Packin, K. Angersbach, and J.K. Hughes (2002), The climate of the US Southwest. *Climate Research*, 21, 219-238.

Sotillo, M.G., C. Ramis, R. Romero, S. Alonso, and V. Homar (2003), Role of orography in the spatial distribution of precipitation over the Spanish Mediterranean zone. *Climate Research*, 23 (3), 247-261.

Spatial Climate Analysis Service, Oregon State University (2003), Parameter-elevation Regressions on Independent Slopes Model (PRISM), Corvallis, OR, USA.

Sturman, A., and H. Wanner (2001), A comparative review of the weather and climate of the Southern Alps of New Zealand and the Europe Alps. *Mountain Research and Development*, 21(4), 359-369.

Young, C. B., C.D. Peters-Lidard, A. Kruger, M.L. Baeck, B. R. Nelson, A.A. Bradley, and J.A. Smith (1999), An evaluation of NEXRAD precipitation estimates in complex terrain. *Journal of Geophysical Research*, 104 (D16), 19691-19703.

Woodhouse, C.A., and D.M. Meko (1997), Number of winter precipitation days reconstructed from Southwestern tree rings. *Journal of Climate*, 10, 2663-2669.

CHAPTER 3 THE TEMPORAL AND SPATIAL PATTERNS OF ENSO AND PDO EFFECTS ON SEASONAL PRECIPITATION IN A MOUNTAINOUS AREA, NORTHERN NEW MEXICO[2]

3.1 Introduction

In arid and semiarid regions of the world, mountains provide most of the fresh water to surrounding sedimentary basins. In the southwestern United States, a dramatic increase in population over the past several decades challenges water management and threatens the sustainability of ecosystems [*Phillips et al*., *2004*]. This calls for urgent study of the mountain-block hydrology, especially of its response to climate variability and change [*Wilson and Guan*, *2004; Bales et al., 2004*]. The temporal and spatial distribution of mountain precipitation is critical to estimating water partitioning (e.g., evapotranspiration, runoff, and groundwater recharge) and understanding ecological responses. It is, however, difficult to capture because of its large spatial and temporal variability. Some of this variability is associated with the complex terrain of mountains and some with the natural variability of atmospheric conditions. A portion of the atmospheric variability is inherently uncertain, and unpredictable. Another portion of the atmospheric variability is associated with large-scale global atmospheric circulations which are coupled with periodic ocean conditions [*Gershunov and Barnett, 1998*]. The connection between local precipitation and the large-scale ocean-atmosphere systems provides a useful tool for seasonal prediction. El Niño-Southern Oscillation (ENSO) and

[2] A revised and abreviated version of this chapter was submitted to *Geophysical Research Letters*, with coauthors Enrique R. Vivoni and John L. Wilson.

Pacific Decadal Oscillation (PDO) are two major related (not independent) large-scale Pacific Ocean-atmosphere coupling cycles, that have been associated with variability of seasonal precipitation [*Ropelewski and Halpert, 1986, 1987; Kiladis and Diaz, 1989; Redmond and Koch, 1991; Latif and Barnett, 1994; 1996; Higgins et al., 2000; Liles, 2000; Barlow et al., 2001; Castro et al., 2001*].

ENSO is a large scale oceanic and atmospheric coupled phenomenon in the equatorial Pacific Ocean. It is characterized by semi-regular oscillation of the sea surface temperature (SST) and the atmospheric pressure at sea level, with a period typically between 3~7 years. ENSO has three phases: warm (or El Niño), neutral, and cold (or La Niña). When ENSO is in El Niño phase, the SST of the eastern and central equatorial Pacific is warmer than normal. At the mean time, the atmospheric pressure at sea level is lower than normal in the eastern, and higher than normal in the western equatorial Pacific. These patterns are opposite when ENSO is in the La Niña phase [summarized from http://iri.columbia.edu/climate/ENSO/background/basics.html]. Although ENSO is characterized in the equatorial Pacific, its impact on climate is global [*Rasmusson & Wallace, 1983*]. PDO is an ENSO-like pattern of Pacific-related climate variability, with a typical period of 20~30 years. It has two phases, characterized by the SST anomaly in the northern Pacific. The western coast of the northern America has higher than normal SST when PDO is in its high phase, and vise versa for the low PDO phase [summarized from http://tao.atmos.washington.edu/pdo/].

In this chapter, the teleconnection of seasonal precipitation to ENSO and PDO cycles is examined for a mountainous region in northern New Mexico, a typical example of the semiarid mountain areas found in the southwestern United States. The results will

be used to study the effects of climate variability on mountain-block recharge in the study area, discussed in Chapter 7.

For the southwestern U.S., the El Niño-Southern Oscillation (ENSO) has been teleconnected to winter precipitation [e.g., *Andrade and Sellers, 1988; Sheppard et al., 2002*], substantially improving the long-range prediction of seasonal precipitation. Winter precipitation usually increases during El Niño (ENSO warm phase) years, and decreases during La Niña (ENSO cold phase) years. This predictive connection provides a potential tool for water management in this region [*Simpson and Colodner*, *1999*]. Due to orographic effects, precipitation in mountains, as well as its variability, differs from that in the valley. Biased estimates of precipitation may result from the valley-clustered NCDC (National Climate Data Center) gauge data that are commonly used for studying atmospheric connections in the western U.S. [*Kunkel and Angel*, *1999*]. It has also been found that the ENSO system affects regional atmospheric circulation, leading to different degree of orographically-enhanced precipitation between ENSO phases in mountainous terrains [*Dettinger et al*., *2004*].

The ENSO teleconnection with winter precipitation is modulated by the Pacific Decadal Oscillations (PDO) [*Gershunov and Barnett, 1998; Gutzler et al., 2002*]. The teleconnection patterns (i.e. dry winter in La Niña years, and wet winter in El Niño years) are enhanced by constructive relationship between ENSO and PDO, i.e., ENSO warm (cold) phase + high (low) PDO phase, and dampened by destructive relationship between two indexes (ENSO warm (cold) phase + low (high) PDO phase). In these studies, the PDO was considered as a secondary factor, next to ENSO cycles. Only very recently has the PDO effect been independently considered in studies using precipitation data, in a

study of Arizona winter precipitation [*Goodrich*, *2004*], although there are studies using proxy data, mostly tree-rings [e.g., *Biondi et al., 2001*; *Benson et al., 2003; Hidalgo, 2004*]. If the PDO cycle has an effect on winter precipitation that is as strong as ENSO, the possible recent PDO shift from the high phase to the low phase, which is still not clear, will strongly affect the climate and water cycle in the southwestern U.S [*Benson et al., 2003*]. For the ENSO cycle itself, some recent studies suggest that the La Niña signal does not have as strong a connection as the El Niño signal to winter precipitation [*Kunkel and Angel, 1999; Goodrich, 2004*].

For practical purposes, such as water resource management, it is appropriate to have predictive seasonal precipitation information throughout the year, not just for the winter season. However, summer precipitation in the southwestern U.S. is usually not well correlated to ENSO or PDO cycles [e.g., *Andrade and Sellers, 1988; Adams and Comrie, 1997; Sheppard et al., 2002*], although a few studies demonstrate some correlation [*Barlow et al., 2001; Castro et al., 2001*]. Gutzler [*2000*] also reported significant negative correlation between summer rainfall in New Mexico and the large-scale antecedent spring snowpack in the Rocky Mountains, which may indirectly be related to ENSO and PDO cycles.

In summary, current knowledge of teleconnections of seasonal precipitation to ENSO and PDO cycles has some limitation for hydrologic applications. (1) Attention has only been given to winter and summer precipitation, and only winter precipitation is found predictable. (2) PDO has not been investigated independently, but only as a secondary factor to ENSO when using precipitation data. (3) Orographic modification of the teleconnections is not clear, which is however very important for estimating

predictable mountain precipitation and its variability. (4) It is not clear whether PDO shifted to its low phase in the late 1990s. In this chapter, the atmospheric teleconnection between precipitation of all four seasons (fall, winter, spring, and summer) and ENSO and PDO cycles is examined. The effects of the PDO cycle are treated independently from the ENSO cycle. Also the effects of El Niño and La Niña are investigated separately. The ASOADeK model (Chapter 2), a newly-developed high-resolution precipitation mapping tool [*Guan et al., 2005*], is used to study the spatially distributed orographic modulation of ENSO and PDO effects. Finally, based on certain patterns of teleconnections, it is examined whether PDO has shifted to its low phase in late 1990s.

3.2 Methodology

3.2.1 Categorization of ENSO and PDO years

Two approaches have been used to study ENSO and PDO teleconnections with precipitation. In the first approach, the correlation of time series of precipitation and ENSO index [e.g., *Hidalgo and Dracup, 2003*] is investigated, in which it is implicitly assumed both extreme ENSO phases influence precipitation. This approach cannot distinguish the difference between the two hypothetic situations shown in Figures 3.1a and b. The other approach investigates the precipitation anomaly of each ENSO and PDO year category [e.g., *Gershunov and Barnett*, *1998*], often with ENSO-neutral years neglected. With the ENSO-neutral phases excluded, illustrated in Figure 3.1c, misunderstanding can result if, e.g., the situation in Figure 3.1d exists. Figure 3.1d suggests that La Niña does not influence precipitation because precipitation is similar between the La Niña year and the neutral ENSO year. However, without the neutral ENSO years, Figure 3.1c indicates that La Niña causes a drier than normal condition. To

avoid these problems, the category approach including ENSO neutral categories is employed in this study.

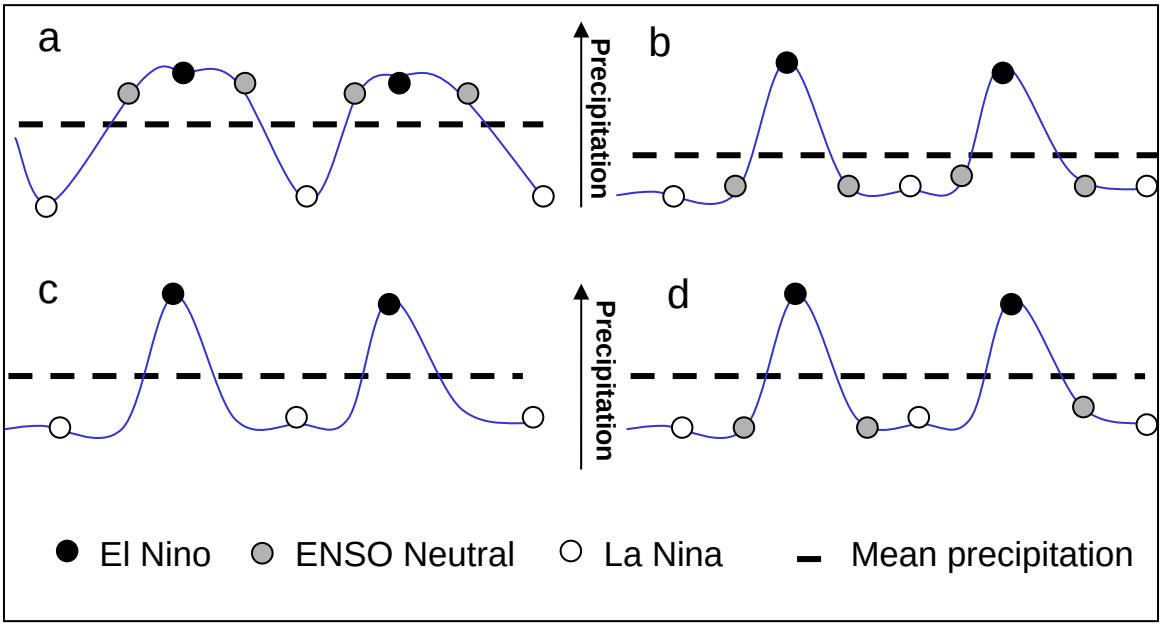

Figure 3.1 Hypothetic situations of ENSO effects on precipitation, showing the temporal precipitation variation (thin lines) around a long term mean precipitation (thick dashed lines). In (a), La Niña leads to dry condition, while El Niño has similar precipitation to neutral ENSO; in (b), El Niño leads to wet condition, while La Niña and neutral ENSO have similar precipitation. By correlation analysis of two time-series data (ENSO index, and precipitation), the situation illustrated in (a) is indistinguishable from that in (b). For the situation illustrated in (d) the La Niña has a similar effect on precipitation as the neutral ENSO phase, and category analysis without including the neutral phase (c) may lead to misunderstanding of the La Niña effect on precipitation.

This chapter investigates the anomalies of mean seasonal precipitation for those years with various combinations of ENSO and PDO phases. Thus, an appropriate identification of ENSO and PDO phases is critical for the data analysis. An ENSO extreme year (El Niño or La Niña) is identified when it meets at least two of three criteria. The first criterion is based on the index from Japanese Meteorological Agency, which is a 5-month running mean of spatially averages sea surface temperature (SST) anomalies over the tropical Pacific: 4°S-4°N, 90°-150°W. An El Niño (La Niña) year is categorized

when the index is above 0.5°C (below -0.5°C) for 6 consecutive months (including OND) (http://www.coaps.fsu.edu/~legler/jma_index.html). The second criterion is based on the index from the Climate Prediction Center of NOAA, which is 3 month running mean of ERSST.v2 SST anomalies in the El Niño 3.4 region (5^oN-5^oS, 120^o-170^oW). The threshold is 0.5°C for at least five consecutive months (http://www.cpc.ncep.noaa.gov/products/analysis_monitoring/ensostuff/ensoyears.html). The third criterion is that the year must agree with that categorized by Gershunov and Barnett [*1998*], in which a similar category-type study, but without including the ENSO neutral years, was completed. The year that does not meet at least two of the three criteria is categorized as of ENSO neutral phase.

As shown in Figure 3.2, a typical ENSO extreme event starts from late spring of the first year, becomes observable in summer, reaches the peak stage in winter, and then decays and dies out in summer of the next year. For the purpose of precipitation prediction, the year in this study is defined from October through the next September as illustrated in the Figure 3.2. The three ENSO year categories (warm, neutral, cold) are further divided according to the PDO phase shift in 1976 [*Mantua et al., 1997; Zhang et al., 1997*], see Table 3.1. Before this year, PDO was in its low phase for our study period 1955-2003. Staring in 1976, it was in its high phase, at least until 1998, when it may have shifted to the low phase [*Climate Impacts Group*, *2005*]. Because there is no consistent opinion among scientists about this recent PDO shift in late 1990s, the years after 1998 are not included in the ENSO + PDO categories of Table 3.1; however they are used to obtain long-term mean precipitation.

The study period (1955-2003) is selected for four reasons. (1) If the time span is extend to earlier years, the available gauges required for studying spatial pattern dramatically decrease (i.e., from over 30 gauges decreased to less than 15). (2) The standard deviation of the 50-year moving average of available gauges is relatively small. (3) There are similar number of years of low PDO (21) and high PDO (23) during 1955-1997. (4) The most recent years (1998-2002) are included to study the possible PDO shift in 1998.

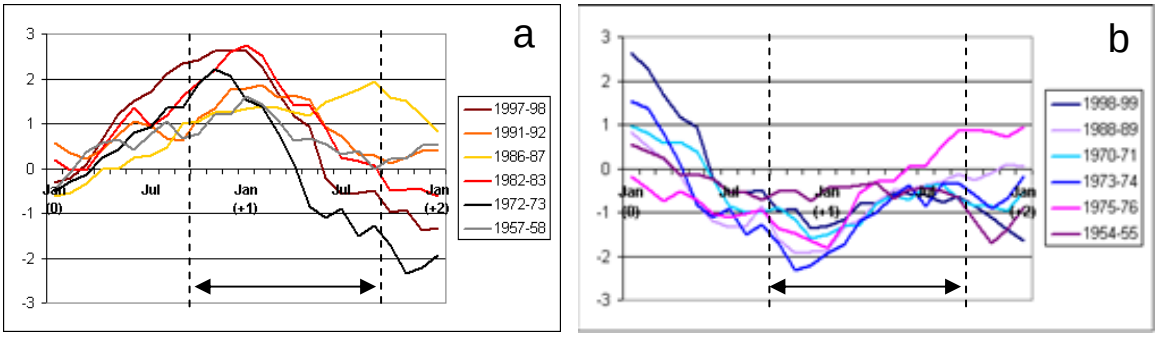

Figure 3.2 The NINO 3.4 index (in units of ˚C) of the six strongest El Niño events (a) and La Niña events (b), which have occurred since 1950 from IRI, Columbia University (http://iri.columbia.edu/climate/ENSO/background/monitoring.html). The dashed lines define the beginning (October of the year) and end (September of the next year) of an ENSO year for the purpose of this study.

Table 3.1 Year categories based on ENSO and PDO phases (each year covers from October through the next September)

ENSO phases	High PDO	Low PDO
Warm phase (El Niño)	76 82 86 87 91 94 97	57 63 65 68 69 72
Cold phase (La Niña)	84 88	55 64 67 70 71 73 74 75
Neutral phase	77 78 79 80 81 83 85 89 90 92 93 95 96	56 58 59 60 61 62 66

3.2.2 Study area and precipitation data

The study area is located in the northern, New Mexico, U.S.A., covering NCDC (National Climate Data Center) Climate Division 2 (Figure 3.3). The area is topographically characterized by mainly mountains (e.g., Sangre de Cristo Mountains, Jemez Mountains) and inter-mountain valleys. The elevation ranges from 1290 to 3887m according to the 1km-resolution DEM map, which was re-sampled from an EDAC 60m-resolution DEM (EDAC, 1996). Over 130 NCDC weather stations are available in the area (no high-elevation SNOTEL stations are used because of their short time spans). The mean annual precipitation, estimated as the averages of available long-term records (>10 years), is 440 mm. However, for the purpose of this study, only those gauges having a data record period of 1955-2003 (49 years) are used to investigate the temporal structures of ENSO and PDO effects. The spatial structures of the teleconnection effects are investigated by comparing the precipitation map of each ENSO and PDO category to the long-term mean precipitation map (see next section). In order to have as many gauges as possible to construct ASOADeK precipitation maps for each season of each ENSO and PDO category, the gauges for category precipitation mapping are not always co-located with those for the long-term mean precipitation mapping. The gauges that have data available for at least two years of the interested ENSO and PDO phase combination within the period 1955-1997 are used. The gauge distributions of three selected categories are shown in Figure 3.3.

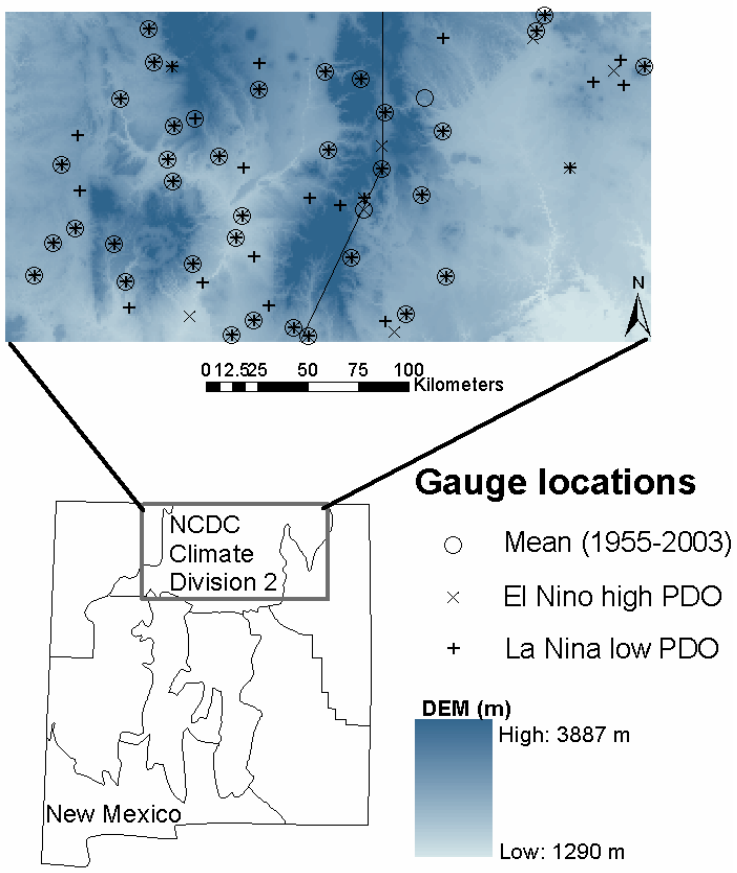

Figure 3.3 The study area in northern New Mexico, U.S.A., with long-term mean gauge distribution, and two selected category mean gauge distributions. The line is an approximate boundary for two different climate sub-regions identified later in this chapter.

3.2.3 Data analyses

The anomaly (significant systemic deviation) of mean seasonal precipitation of a certain ENSO + PDO year category from long-term average is considered as evidence of the teleconnection effect. The deviation was calculated by subtracting the long-term average precipitation from the mean precipitation of each ENSO + PDO year category. To minimize the influence of unpredictable atmospheric variability, the relationship between seasonal anomalies (instead of monthly anomalies) and ENSO + PDO phases was investigated. The seasons were separated as fall (October), winter (November, December, January, February, March), spring (April, May, June), and summer (July,

August, September). We included November and March into the winter season for two reasons. First, precipitation could be in the form of snow in this region during these months. Second, precipitation amount for these five months are highly correlated to one another (not shown). The summer season was defined as July, August, and September, due to the North American Monsoon in the study area.

The procedures for determining the seasonal precipitation anomaly of each ENSO + PDO category is summarized in Appendix III. The deviation of seasonal precipitation of each ENSO + PDO category from the long-term seasonal precipitation was calculated simply by summing the monthly deviations. To see how well the long-term mean represents the long-term average precipitation in the region, the standard deviation of 50-year moving average of the seasonal precipitation was calculated for 22 gauges with long term records (mostly from 1931-2003). The average standard deviation over the 22 gauges gave 1.2, 3.5, 3.1, and 4.4 mm for October, winter, spring, and summer, respectively. The seasonal deviation was considered as an anomaly for the season only when the gauge-average deviation of the study area exceeded the gauge-average standard deviation of the long-term moving averages; the anomaly was set to zero, otherwise.

To test whether the anomalies derived from gauges with both long-term mean and category mean data available are representative for the study area, and to examine the spatial pattern of the teleconnections and the orographic modulations of ENSO and PDO effects, ASOADeK (Chapter 2) was used to construct mean monthly precipitation maps of four selected ENSO + PDO categories, as well as long-term mean monthly precipitation. These four categories were El Niño + high PDO, La Niña + low PDO, neutral ENSO + high PDO, and neutral ENSO + low PDO. The relevant ASOADeK

regressions and precipitation residual variogram modeling are included in Appendix IV. The gauges for category mapping are not necessarily collocated with long-term mean gauges, as shown in Figure 3.3. The category mean precipitation maps were then compared to the long-term mean precipitation maps, pixel by pixel, to discover any systematic spatial features of the precipitation anomalies. Once again the total seasonal anomaly was analyzed. Because the elevation range of available gauges for each category does not cover the whole elevation relief of the study area (Figure 3.4), only those pixels within the elevation range (1500-2700m) in which most gauges are located were used for studying the spatial patterns of anomalies.

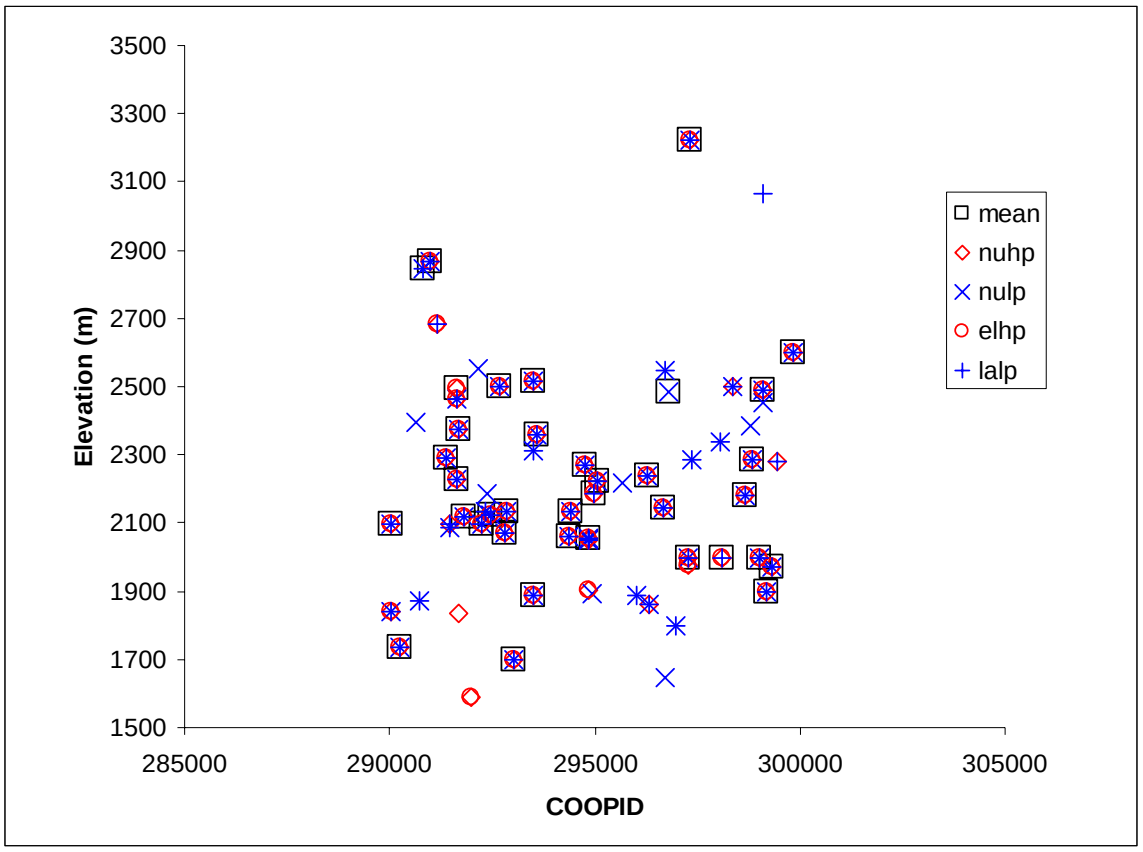

Figure 3.4 The elevations of gauges used for ASOADeK mapping, mean = long-term mean gauges, nuhp = neutral ENSO + high PDO gauges, nulp = neutral ENSO + low PDO, elhp = El Niño + high PDO gauges, and lalp = La Niña + low PDO gauges. COOPID is the NCDC weather station identification number.

3.3 Results and Discussion

3.3.1 Temporal patterns of the ENSO and PDO effects on seasonal precipitation

The seasonal pattern of ASOADeK-estimated anomalies is consistent with that of the gauge-average anomalies for the selected ENSO PDO categories (Figure 3.5). Of the four seasons, winter and spring precipitation anomalies are consistently connected to ENSO and PDO cycles. Suppose we specify that the seasonal anomaly is significant if it exceeds 10% of the long-term mean seasonal precipitation. For the three categories with the high PDO phase, both winter and spring have significant positive anomalies (10~20% seasonal precipitation). For the three categories with the low PDO phase, both categories with ENSO neutral and La Niña have significant negative winter and spring precipitation anomalies (~10% winter precipitation, and ~20% spring precipitation). The category of El Niño + low PDO does not have a significant winter precipitation anomaly, although it has a very small negative spring anomaly (~5%). It appears that the PDO signal is dominant in winter and spring precipitation anomalies in the study area, with wetter winter and spring for high PDO, and dry winter and spring for low PDO. ENSO modulates low PDO effects, but does not much affect high PDO effects, on winter and spring precipitation anomalies. El Niño strongly dampens, and La Niña enhances, negative winter and spring precipitation anomalies during the low PDO years (Figure 3.5). For the high PDO years, El Niño enhances the positive winter precipitation anomaly, but decreases the positive spring precipitation anomaly (Figures 3.5 and 3.6). (In Figure 3.5, La Niña effect on winter and spring precipitation of high PDO years is similar to El Niño. However, this result should not be considered significantly without further investigation as there is only two-year data in this category.)

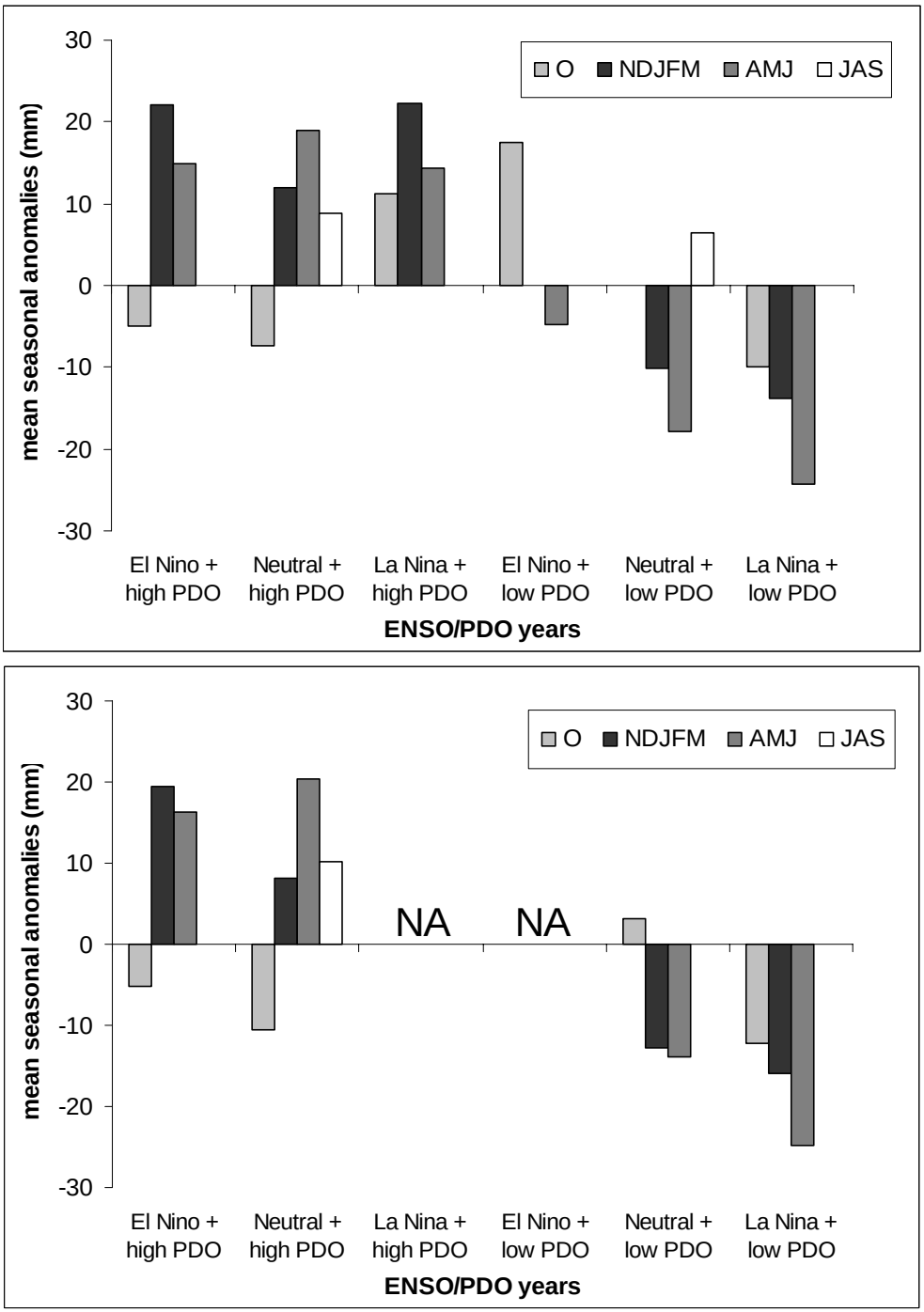

Figure 3.5 The seasonal precipitation anomaly of each ENSO PDO category, averaged over all available gauges (top), and averaged over all pixels with elevations of 1500 ~2700 m from ASOADeK model results (bottom).

Spatially averaged over the study area, summer precipitation does not seem to connect well with ENSO and PDO cycles. It also does not appear to relate to the

antecedent winter precipitation either (Figure 3.5), both seasons being contained in the same study year. A wetter-than-normal winter in the study area does not lead to a drier-than-normal summer. However, if the spatial sub-regions (i.e., the eastern part and western part of the study area in Figure 3.3) are considered, for the category of neutral ENSO + high PDO the summer precipitation anomalies are negatively correlated to the precedent winter precipitation anomalies (Figure 3.6 b & d). But this relationship becomes weaker for other categories--for example, as seen in Figure 3.7 b and d, and j and l, for two low PDO categories, the winter in the eastern sub-region is drier than the neutral ENSO + high PDO (Figure 3.6b), but the summer (Figure 3.7 d and l) does not appear to be wetter than the latter (Figure 3.6d). This suggests that for neutral ENSO + high PDO the summer precipitation anomalies are associated with large-scale climatic cycles, instead of the local correlation to the preceding winter.

It is worth noting that during the destructive phases of ENSO and PDO cycles October is significantly wetter (anomaly = 30~50% monthly precipitation) than normal, especially for the El Niño + Low PDO phase combination (Figure 3.5). We hypothesize that the atmospheric conditions of the destructive ENSO and PDO phases may facilitate tropical storms invading the study area, bringing additional moisture for October precipitation. The tropical storm activity associated with ENSO and PDO has been suggested earlier [e.g., *Englehart and Douglas*, *2001*]. The hypothesis here is supported by the fact that two of the total three eastern Pacific tropical storms in the Octobers of 1955~97, migrating to the north of 30˚N between 103˚W and 114˚W, occurred in 1957 and 1972, the years with El Niño and low PDO phases (analyzed from NOAA data set operated by Unisys, http://weather.unisys.com/hurricane/e_pacific/index.html).

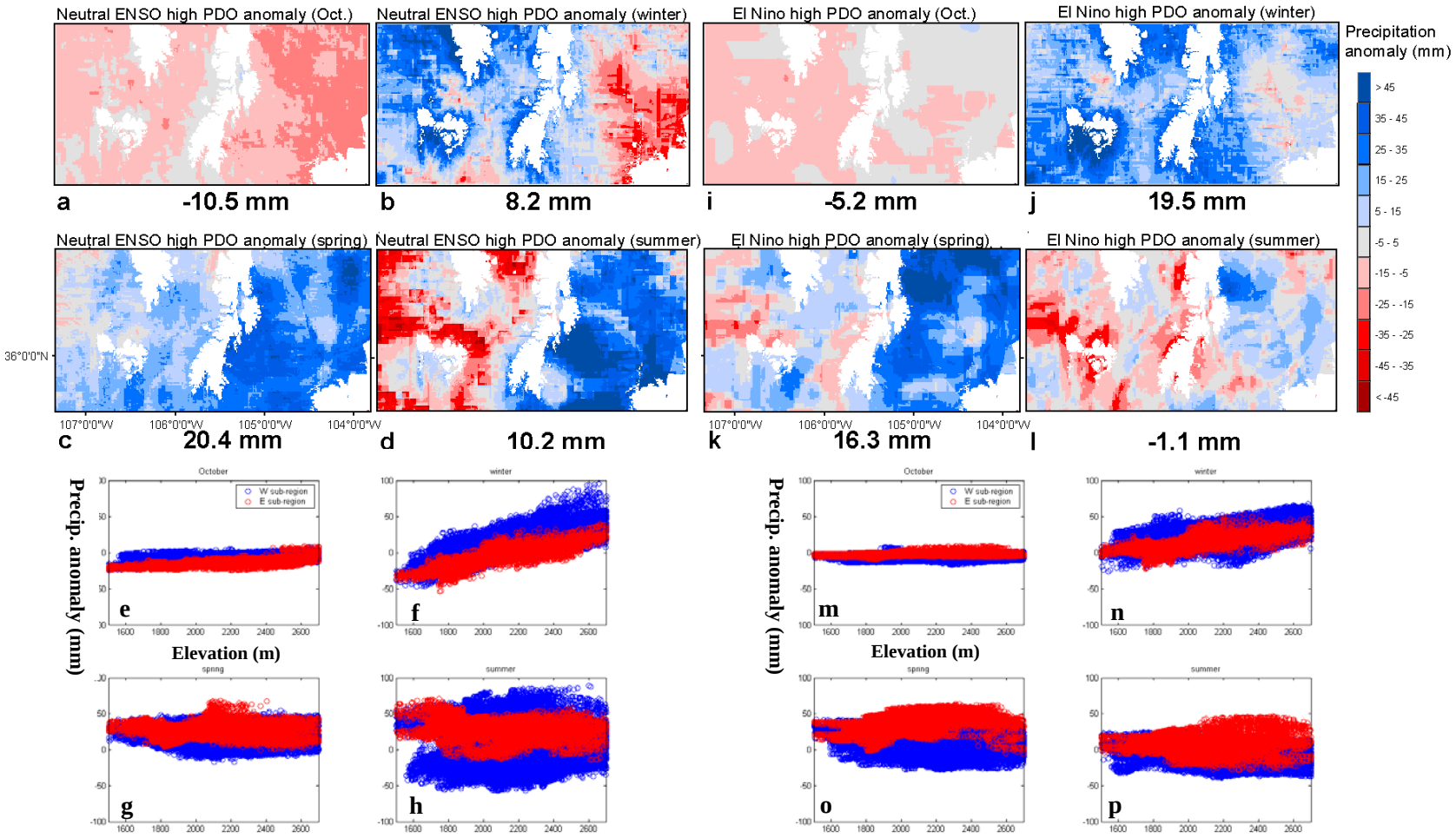

Figure 3.6 The seasonal anomaly maps of October, winter, spring, and summer derived from ASOADeK for categories of neutral ENSO + high PDO (a,b,c,d), and El Niño + high PDO (i, j, k,l), where the number are the mean anomalies over all pixels, the white pixels are elevation beyond the range of 1500~2700m; and the plots of pixel precipitation anomalies vs. elevation for neutral ENSO + high PDO (e,f,g,h), and El Niño + high PDO (m,n,o,p), where red symbols represent pixels in the eastern sub-region, and blue symbols for the western sub-region of the study area, shown in Figure 3.3.

60

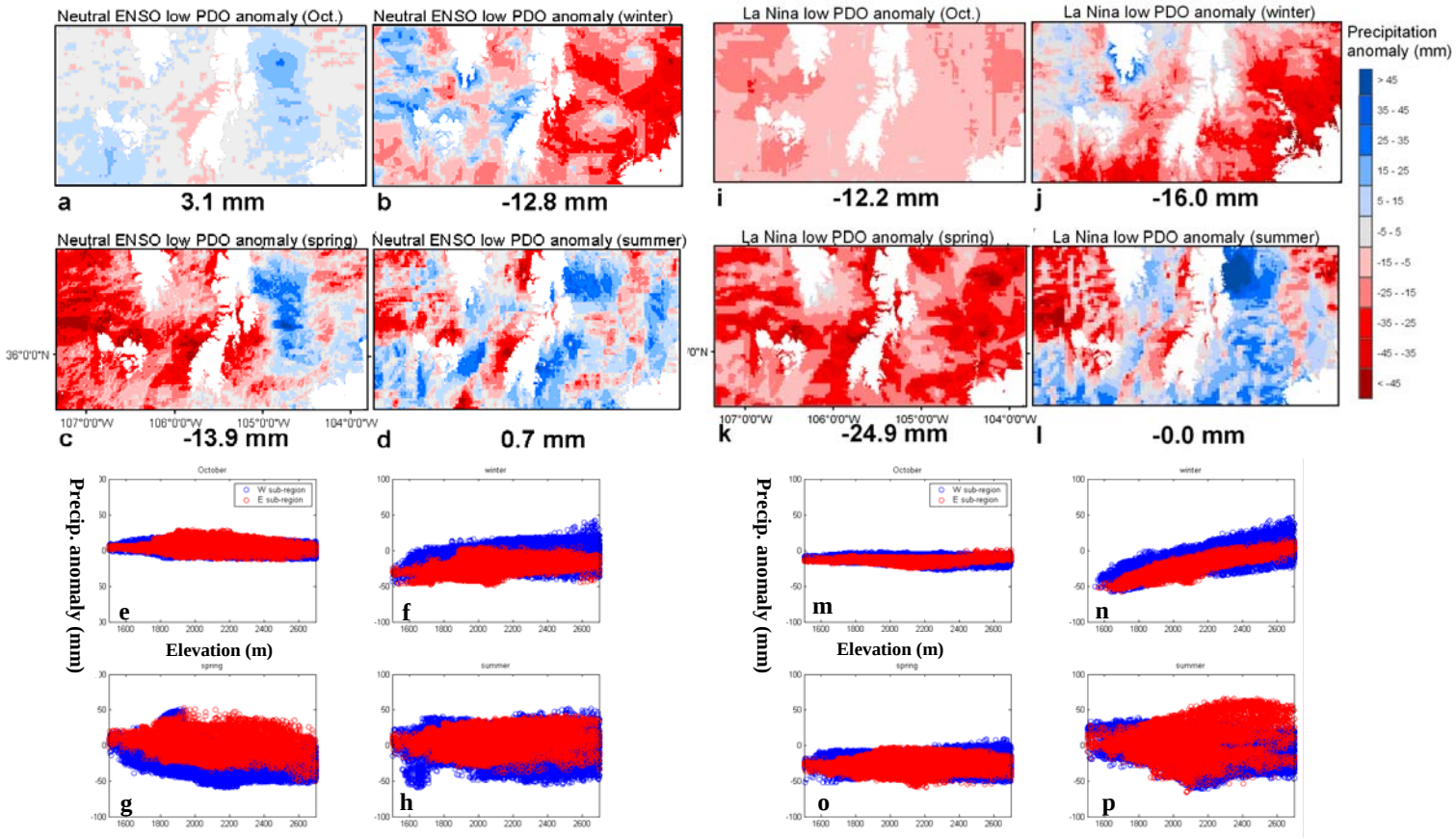

Figure 3.7 The seasonal anomaly maps of October, winter, spring, and summer derived from ASOADeK for categories of neutral ENSO + low PDO (a,b,c,d), and La Niña + low PDO (i, j, k,l), where the number are the mean anomalies over all pixels, the white pixels are elevation beyond the range of 1500~2700m; and the plots of pixel precipitation anomalies vs. elevation for neutral ENSO + low PDO (e,f,g,h), and La Niña + low PDO (m,n,o,p), where red symbols represent pixels in the eastern sub-region, and blue symbols for the western sub-region of the study area, shown in Figure 3.3.

61

3.3.2 Spatial patterns of the PDO and ENSO effects on seasonal precipitation

Spatial patterns of the PDO effects on seasonal precipitation in the study area are shown in Figure 3.6 (a, b, c, d) and Figure 3.7 (a, b, c, d). With neutral ENSO phase, high PDO leads to a wetter-than-normal winter (anomaly = 8mm, Figure 3.6b), with larger anomalies at higher elevations (Figure 3.6f). Spring and summer are overall wetter than normal (Figure 3.6 c, d), but show quite different patterns between the eastern and western sub-regions. Especially for the summer, the eastern sub-region is wetter than normal, while the western sub-region is drier than normal.

With neutral ENSO phase, low PDO leads to a drier-than-normal winter (anomaly = -13 mm, Figure 3.7b). The elevation-dependency becomes much weaker than for high PDO effect (Figure 3.7f). Spring is drier than normal, but showing different patterns between two sub-regions (Figure 3.7c). Low PDO does not seem to affect the summer precipitation much, with slightly positive anomaly to the east of Sangre de Cristo Mtns, and slight negative anomaly to the west (Figures 3.7d).

Spatial patterns of the ENSO effects on seasonal precipitation are investigated by comparing the ENSO extreme phases with constructive PDO phases to ENSO neutral phase with the same PDO. Comparison of Figure 3.6 (a, b, c, d) and (i, j, k, l) tells the El Niño effects, and comparisons of Figure 3.7 (a, b, c, d) and (i, j, k, l) tells the La Niña effects. Compared to the ENSO neutral phase, El Niño amplifies the positive winter anomaly by 2.5 times (Figure 3.6 b and j), slightly decreases the positive spring anomaly (Figure 3.6 c and k), and strongly modifies the summer anomaly patterns, leading to no significant anomaly throughout the study area (Figure 3.6 d and l). Compared to the ENSO neutral phase, La Niña slightly enhances the negative winter anomaly by one third

(Figure 3.7 b and j), and strongly affect the spring precipitation by doubling the negative anomaly (Figure 3.7 c and k). La Niña does not significantly affect summer precipitation in the study area (Figure 3.7 d and l).

Topography modulations of ENSO and PDO effects are clearly observed in Figures 3.6 and 3.7. Winter precipitation anomalies strongly depend on the elevation. For a wetter-than-normal winter, the anomalies are larger at high elevations. For a drier-than-normal winter, the anomalies are larger at lower elevations. Elevation does not significantly affect precipitation anomalies of the other three seasons (Figure 3.6 and 3.7).

Overall, the ENSO and PDO effects indicated from the spatial precipitation anomalies agree with those from the gauge average results. It should be noted that for some ENSO + PDO categories, the anomalies have different patterns between eastern and western parts of the study area. This is especially true for spring and summer of high PDO phases. The different patterns of precipitation anomalies between the two subregions suggest that they may be controlled by two different climate systems. Including them in one NCDC climate division may not be appropriate [*Guttman and Quayle*, *1996*], and can bias the studies only considering the average division precipitation. It is especially important to distinguish the difference for the study area because the two sub-regions provide water for two different river basins.

3.3.3 Did PDO shift in late 1990s?

Based on the consistent connections between PDO phases and winter and spring precipitation anomalies, we calculated mean seasonal anomalies for two La Niña years (1998 & 1999), and two years of ENSO neutral phase (2000 & 2001). Both year groups have negative winter precipitation anomalies, indicating a low PDO phases (Figure 3.8). This suggests that PDO have shifted to its low phase after 1998. However, the confidence

level of this result is undermined by the inconsistent spring anomaly of the two La Niña years (1998 & 1999). If PDO did shift in 1998, several years of consecutive ENSO low and neutral phases would tend to cause droughts in the southwestern U.S. (Figure 3.8), which was evident from the drought in 1998~2002 [*Hoerling and Kumar*, *2003*] and in 1950s in the southwestern U.S. (Figure 3.9).

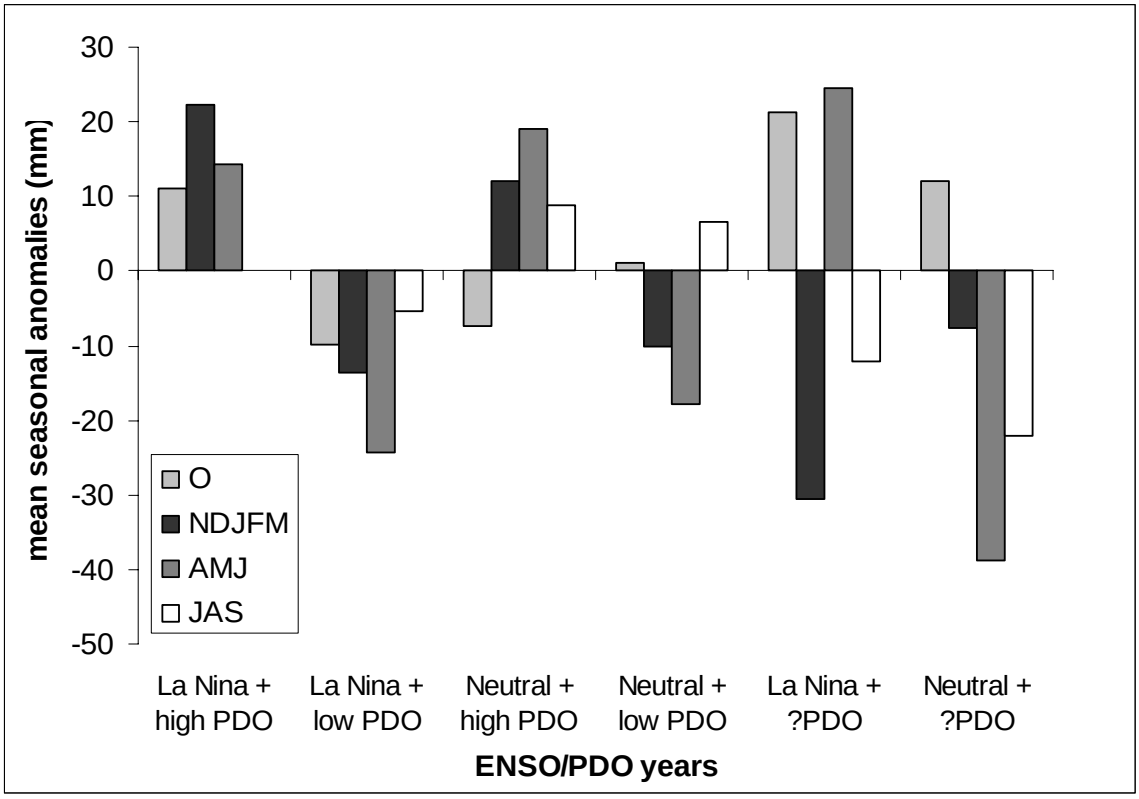

Figure 3.8 The seasonal precipitation anomalies of two years (2000 and 2001) of ENSO neutral phase and unclear PDO phase (sixth column), and two years (1998 and 1999) of La Niña and unclear PDO phase (fifth column), with comparison to seasonal anomalies of categories (first four columns).

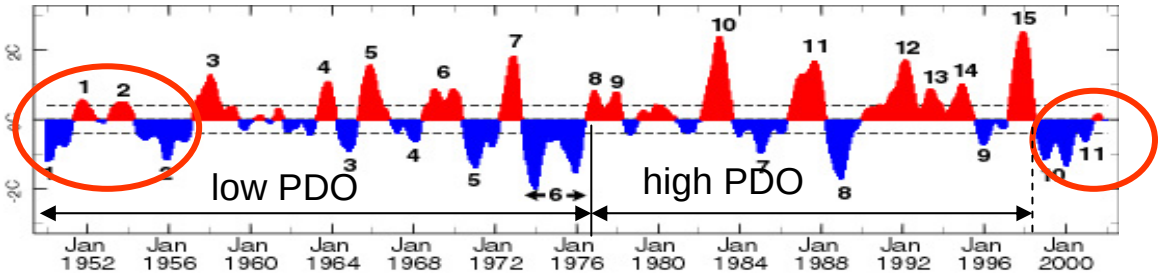

Figure 3.9 Two historical droughts in southwestern U.S. occur in 1950s and in 1998~2002 both occurred in low PDO phase (the historical NINO3.4 Index (y-axis) plot from IRI, Columbia University, http://iri.columbia.edu/climate/ENSO/background/pastevent.html).

3.4 Conclusions

This study examined the teleconnection of seasonal precipitation in a mountainous area of northern New Mexico to ENSO and PDO cycles. The results suggest that the PDO is a more influential factor on winter and spring precipitation in the study area than ENSO, with high PDO leading to a wetter-than-normal winter and spring, and low PDO leading to opposite anomalies. ENSO modulates low PDO effects, but not much affects high PDO periods, for winter and spring precipitation anomalies. El Niño strongly dampens, and La Niña enhances, negative winter and spring precipitation anomalies during the low PDO years. For the high PDO years, El Niño enhances the positive winter precipitation anomaly but decreases the positive spring anomaly. The PDO and ENSO effects on winter precipitation are modified by topography, with larger anomalies at higher elevations for wetter-than-normal winters, and larger anomalies at lower elevations for drier-than-normal winters. Averaged over the study area (one NCDC climate division), the summer precipitation anomaly does usually not connect to either the ENSO and PDO cycles or the precedent winter precipitation anomaly. However, if evaluated in the two sub-regions, the western and eastern portions of the study area, the

summer precipitation anomaly is related to ENSO and PDO for the category of neutral ENSO + high PDO. October is significantly wetter than normal in the years of destructive PDO and ENSO phases, and is possibly associated with the tropical storm tracks. Finally, our results support a PDO shift in 1998, indicating larger possibility of future serious droughts in the southwestern U.S.

References

Adams, D.K., and A.C. Comrie (1997), The North American monsoon. *Bulletin of American Meteorological Society*, 78, 2197-2213.

Andrade, E.R., and W.D. Sellers (1988), El Niño and its effect on precipitation in Arizona and western New Mexico. *Journal of Climatology*, 8, 403-410.

Bales, R.C., J. Dozier, N. P. Molotch, T. H. Painter, and R. Rice (2004), Mountain Hydrology of the Semi-Arid Western U.S., *CUAHSI Cyberseminar draft Paper*.

Barlow, M., S.Nigam, and E.H. Berbery (2001), ENSO, Pacific decadal variability, and U.S. summertime precipitation, drought, and stream flow. *Journal of Climate*, 14, 2105-2128.

Benson, L., B. Linsley, J. Smoot, S. Mensing, S. Lund, S. Stine, and A. Sama-Wojcicki (2003), Influence of the Pacific Decadal Oscillation on the climate of the Sierra Nevada, California and Nevada. *Quaternary Research*, 59, 151-159.

Biondi, F., A. Gershunov, and D.R. Cayan (2001), North Pacific decadal climate variability since 1661. *Journal of Climate*, 14, 5-10.

Castro, C.L., T.B. McKee, and R.A. Pielke Sr. (2001), The relationship of the north American monsoon to tropical and north Pacific sea surface temperatures as revealed by observational analyses. *Journal of Climate*, 14(24), 4449-4473.

Climate Impacts Group (2005), About the Pacific Decadal Oscillation http://www.cses.washington.edu/cig/pnwc/aboutpdo.shtml, visited in 2005.

Dettinger, M., K. Redmond, and D. Cayan (2004), Winter orographic precipitation ratios in the Sierra Nevada--larger-scale atmospheric circulations and hydrologic consequences. *Journal of Hydrometeorology*, 5, 1102-1116.

Englehart, P.J., and A.V. Douglas (2001), The role of eastern North Pacific tropic storms in the rainfall climatology of western Mexico. *International Journal of Climatology*, 21, 1357-1370.

Gershunov, A., and T.P. Barnett (1998), Interdecadal modulation of ENSO teleconnections. *Bulletin of the American Meteorological Society*, 79, 2715-2725.

Goodrich, G.B. (2004), Influence of the Pacific decadal oscillation on Arizona winter precipitation during years of neutral ENSO. *Weather and Forecasting*, 19, 950-953.

Guan, H., J.L. Wilson, and O. Makhnin (2005), Geostatistical Mapping of Mountain Precipitation Incorporating Auto-searched Effects of Terrain and Climatic Characteristics. *Journal of Hydrometeorology* (in press).

Guttman, N.B., and R.G. Quayle (1996), A historical perspective of U.S. climate divisions. *Bulletin of the American Meteorological Society*, 77, 293-304.

Gutzler, D.S. (2000), Covariability of spring snowpack and summer rainfall across the southwest United States. *Journal of Climate*, *13*, 4018-4027.

Gutzler, D.S., D.M. Kann, and C. Thornbrugh (2002), Modulation of ENSO-based long-lead outlooks of southwestern U.S. winter precipitation by the pacific decadal oscillation. *Weather and Forcasting*, 17, 1163-1172.

Hidalgo, H.G., and J. A. Dracup (2003), ENSO and PDO Effects on Hydroclimatic Variations of the Upper Colorado River Basin, *Journal of Hydrometeorology*, 4(1), 5-23.

Hidalgo, H.G. (2004), Climate precursors of multidecadal drought variability in the western United States. *Water Resources Research*, 40, p.W12504.

Higgins, R.W., A. Leetmaa, Y. Xue, and A. Barnston (2000), Dominant factors influencing the seasonal predictability of U.S. precipitation and surface temperature. *Journal of Climate*, 13, 3994-4017.

Hoerling, M., and A. Kumar (2003), The perfect ocean for drought, *Science*, 299, 691-694.

Kiladis,G.N., and H.F. Diaz (1989), Global climate anomalies associated with extremes of the Southern Oscillation. *Journal of Climate*, 2, 1069-1090.

Kunkel, K. E., and J.R. Angel (1999), Relationship of ENSO to snowfall and related cyclone activity in the contiguous United States. *Journal of Geophysical Research-Atmospheres*, 104(D16), 19425-19434.

Latif, M., and T.P. Barnett (1994), Causes of decadal climate variability over the North Pacific and North America. *Science*, 266, 634-637.

Latif, M., and T.P. Barnett (1996), Decadal climate variability over the North Pacific and North America: Dynamics and predictability. *Journal of Climate*, 9, 2407-2423.

Liles, C., (2000), Relationships between the Pacific decadal oscillation and New Mexico annual and seasonal precipitation. *Proceeding of Second Southwest Weather Symposium, Tucson, AZ, NWS-University of Arizona* – COMET, 7p.

Mantua, N.J. and S.R. Hare, Y. Zhang, J.M. Wallace, and R.C. Francis (1997), A Pacific interdecadal climate oscillation with impacts on salmon production. *Bulletin of the American Meteorological Society*, 78, 1069-1079.

Phillips, F.M., J.F. Hogan, and B.R. Scanlon (2004), Introduction and Overview, in *Groundwater Recharge in a Desert Environment: The Southwestern United States*, edited by J.F. Hogan, F.M. Phillips, and B.R. Scanlon, Water Science and Applications Series, vol. 9, American Geophysical Union, Washington, D.C., 1-14.

Rasmusson, E.M., and J.M. Wallace (1983), Meteorological aspects of the El Nino/Southern Oscillation, *Science*, 222(4629), 1195-1202.

Redmond, K.T., and R.W., Koch (1991), Surface climate and stream flow variability in the western United States and their relationship to large-scale circulation indices. *Water Resource Research*, 27, 2381-2399.

Ropelewski,C.F., and M.S. Halpert (1986), North American precipitation and temperature patterns associated with the El Niño-Southern Oscillation (ENSO). *Monthly Weather Review*, 114, 2352-2362.

Ropelewski,C.F., and M.S. Halpert (1987), Global and regional scale precipitation patterns associated with the El Niño-Southern Oscillation. *Monthly Weather Review*, 115, 1606-1626.

Sheppard, P.R., A.C. Comrie, G.D. Packin, K. Angersbach, and M.K. Hughes (2002), The climate of the US Southwest. *Climate Research*, 21, 219-238.

Simpson, H.J., and D.C. Colodner (1999), Arizona precipitation response to the Southern Oscillation: A potential water management tool. *Water Resource Research*, *35*, 3761-3769.

Wilson, J.L., and H. Guan (2004), Mountain-block hydrology and mountain-front recharge, in *Groundwater Recharge in a Desert Environment: The Southwestern United States*, edited by J.F. Hogan, F.M. Phillips, and B.R. Scanlon, Water Science and Applications Series, vol. 9, American Geophysical Union, Washington, D.C., 113-137.

Zhang, Y., J.M. Wallace, D.S. Battisti (1997), ENSO-like interdecadal variability: 1900-93. *Journal of Climate*, 10, 1004-1020.

CHAPTER 4 MODELING HYDROLOGIC IMPACTS OF VEGETATION COVERAGE ON MOUNTAIN HILLSLOPES, WITH EMPHASIS ON EVAPOTRANSPIRATION

4.1 Introduction

In this chapter, modeling approaches are developed to simulate hydrologic impacts of vegetation on mountain hillslopes. The coupling of climate and vegetation feedback is not considered. The mechanisms of vegetation impacts are separated into two parts. The first part includes those mechanisms above ground, e.g., albedo, surface roughness, stomatal control, rainfall interception, snow and snowmelt. The second part includes those mechanisms underground, e.g., vegetation-induced increased hydraulic conductivity, and root-water-uptake. A variably-saturated hydrologic modeling code (HYDRUS-2D), based on the finite element method, is employed to simulate the hydrologic impacts of the vegetation. The above-ground mechanisms of the vegetation impacts are included in a surface energy partitioning model (TVET, section 4.4), which generates the atmospheric boundary conditions for the HYDRUS modeling. The below-ground mechanisms of the vegetation impacts are represented by HYDRUS model parameters, i.e., modified soil hydraulic properties and the root-water-uptake function and parameterization. A root-macropore model is developed in section 4.7 to represent increased soil hydraulic conductivity due to soil structures modified by the vegetation.

With climate change and local anthropogenic disturbance, vegetation coverage has been changing around the world. In the southwestern United States, shrub encroachment into grassland [*Van Auken, 2000*], expansion of piñon-juniper and

mesquite [e.g., *Allen & Breshears, 1998*], and thickening of ponderosa pine forests [e.g., *Mast et al., 1998*] are common vegetation-coverage transition features over the last several decades. The change in vegetation coverage modifies the near-surface water partitioning, changing groundwater recharge. Gee et al., [*1994*] demonstrate that vegetation is the primary factor controlling the water balance in arid and semiarid environments. In Southwestern basins, the establishment of desert vegetation, due to the drier and warmer climate over the last ten thousand years, has shut off the diffuse recharge [*Walvoord et al., 2002; Walvoord and Scanlon, 2004; Phillips et al., 2004*], except for rare situations of extreme precipitation events [*Kearns and Hendrickx, 1998*]. Thus, a good understanding of the role of vegetation in near-surface water partitioning is important to quantify basin scale groundwater recharge, and to predict the change in recharge with the varying vegetation coverage. Vegetation impacts on hydrologic processes and water resources have recently drawn substantial scientific attention; the topic is one of three integrating research focuses of SAHRA (Sustainability of semi-Arid Hydrology and Riparian Areas), an NSF funded science and technology center [*SAHRA, 2004*].

Let's look at first the mechanisms through which the vegetation influences near-surface hydrologic processes. Vegetation modifies surface albedo, and thus the surface energy balance. It also modifies the surface roughness which affects atmospheric vapor, heat, and momentum transfer near the surface [*Hollinger et al., 1994*]. These two effects influence the magnitude of the atmospheric demand for evapotranspiration. The change in surface energy balance also influences the snowmelt process. Vegetation intercepts precipitation which evaporates (or sublimates) directly from the leaf surface, and never

reaches the ground surface; some of the precipitation captured by the vegetation is carried by stemflow to the ground surface, concentrating infiltration near the trunk and changing spatial infiltration patterns. The most significant effect of vegetation is that vegetation transpires soil water. Transpiration is the significant component of evapotranspiration; it consumes shallow soil water in arid and semiarid regions. Besides the atmospheric demand, transpiration depends on the vegetation physiologic activity, root distribution, and the root-zone soil water potential. Finally, vegetation modifies the soil structure, and changes soil hydraulic properties. The TVET model developed in this chapter includes most mechanisms described above related to surface energy partitioning, while the root-macropore model is intended to capture the hydrologic impacts of root-induced macropores.

In this chapter, Section 4.2 introduces the evapotranspiration processes, and how they are simulated in hydrologic models. Section 4.3 reviews some potential evapotranspiration models, and to what degree they meet the needs for evapotranspiration modeling on mountain hillslopes. A surface energy partitioning model (TVET) is described in Section 4.4, specifically to address the need of mountain hillslope ET modeling. Testing of the TVET model at two hydroecological environments, each with two different vegetation cover, is described in Section 4.5. Comparison of TVET and other models of potential ET is included in Section 4.6. Finally, a root-macropore model for hillslope hydrologic modeling is described in Section 4.7.

4.2 Evapotranspiration (ET) and ET modeling

4.2.1 Evapotranspiration and potential evapotranspiration

Evapotranspiration (ET) is a combination of two distinctive processes, evaporation of water from the soil and wet vegetation surface, and transpiration of soil

water in the whole root zone via plant biological activity. Evaporation depends on water availability on the surface (or in the very shallow top soil layer, ~10cm) and the atmospheric demand. The atmospheric demand for evaporation is the evaporation rate occurring on the wet surface under the investigated atmospheric conditions (available energy and aerodynamic tendency for transferring water vapor from the surface to the ambient bulk air stream). This is often referred to as potential evaporation (PE). Besides soil water availability in the root zone, and atmospheric demand, transpiration is also limited by the plant biophysical activities. Corresponding to PE, potential transpiration (PT) is defined as the transpiration rate of the surface with optimal root-zone soil water. PT depends on both atmospheric conditions and vegetation characteristics. Thus, evaporation and transpiration are two physically different phenomena, while coupled via water and energy balances at the near surface.

Because of the difficulty of technically distinguishing these two processes, they are often lumped together as ET. Similarly, PE and PT are lumped together as PET, or potential ET. PET depends on atmospheric demand and vegetation coverage and status, thus it is not only a function of meteorological conditions (weather), but also a function of vegetation coverage. Sometimes, we want to know only the climate effect on evapotranspiration. FAO (United Nations Food and Agriculture Organization) introduces the reference ET (or ET_0) to meet this need. Reference ET is defined as the potential ET on a reference grass surface (i.e., the surface condition is fixed) [*Allen et al., 1998*]. For hydrologic modeling, PET is a more appropriate quantity than ET_0.

4.2.2 ET modeling

Evapotranspiration is an important and often predominant water balance component in arid and semiarid environments [e.g., *Brandes & Wilcox, 2000*]. With

sporadic precipitation events, ET strongly controls the temporal and spatial distribution of root zone soil moisture, on which appropriate vegetation develops. Good ET estimates are thus critical for quantifying small components (e.g., groundwater recharge) in the water balance equation, and understanding the ecotones observed in semiarid environments, e.g., hillslope vegetation coverage varying with slope orientation. Several types of approaches (e.g., in-situ measurement, remote sensing, hydrologic modeling) have been applied to estimate ET on a surface of interest [*Kite & Droogers*, 2000]. Given the complex topography of mountain hillslopes, hydrologic modeling is one method that can be used to estimate both spatial and temporal distributions of ET.

In hydrologic models, ET can be prescribed as an input boundary condition based on site-specific empirical estimates, or dynamically determined based on the hydraulic condition in the system. For both types of models, PET is an important variable associated with the surface conditions (solar radiation, water vapor deficit, wind speed, air temperature, vegetation cover, etc). In typical near-surface hydrological modeling, ET is determined by PET and the shallow soil water potential or water content [*Simunek, 1998; Guswa et al., 2002; Small, 2005*], in which PET constrains the maximum ET rate on the surface. This type of model calculates actual ET either based on lumped soil water content or water potential [e.g., *Rodriguez_Iturbe et al., 1999*], or distributed soil water content or water potential [e.g., *Simunek, 1998; Guswa et al., 2002*]. HYDRUS-2D, employed in this study, belongs to the latter category.

In HYDRUS, evaporation and transpiration can be simulated separately. Evaporation is modeled by Darcy's law when the surface water potential is below a prescribed threshold (i.e., dry soil); it is equal to the potential rate when the surface water

potential is above the threshold (i.e. wet soil). Transpiration is modeled using either the Feddes or the S-shape root-water-uptake model [*Simunek, 1998*]. Both models define a ratio of T/PT (or α), for each finite element node point, based on the nodal water potential, to determine how much water is extracted for transpiration. The Feddes model employs piece-wise linear functions for the ratio in several water potential ranges [*Feddes, 1978*], shown in equation (4.1). The S-shape model is defined by the ratio in equation (4.2) [*van Genuchten, 1987*]. The implicit assumption of both models is that the T/PT ratio only depends on vegetation type(s) and soil water potential, and is independent of soil type. For the Feddes model,

$$\alpha = \begin{cases} 0 & \text{for } h>h_1 \text{ or } h<h_4 \\ \dfrac{h-h_1}{h_2-h_1} & \text{for } h_2<h<h_1 \\ 1 & \text{for } h_3<h<h_2 \\ \dfrac{h_4-h}{h_4-h_3} & \text{for } h_4<h<h_3 \end{cases} \qquad (4.1)$$

where h is soil matrix potential (more negative for drier soil), and h_1, h_2, h_3, and h_4 are experimental constants, of which h_4 physically corresponds to the wilting point of the vegetation. And for the S-shape model,

$$\alpha = \frac{1}{1+\left(\dfrac{h+h_\phi}{h_{50}}\right)^p} \qquad (4.2)$$

where h and h_ϕ are the soil matrix potential and osmotic potential, h_{50} is the total soil water potential at which α is 50%, and p is an experimental constant. In this formula, no wilting point is applied. Nonetheless, it is easy to apply a wilting point for this model by making α zero when the soil water potential falls below the wilting point (e.g., Chapter 6).

Appropriate PET estimation, the partitioning of PE and PT, and the root water uptake model and its parameterization, are all important for modeling of actual ET, and other near-surface water fluxes. For the purpose of this study, sensitivity analysis is used to find the critical parameters for ET modeling, as discussed in section 4.2.3.

4.2.3 Sensitivity analyses for HYDRUS ET modeling

To test how sensitive the HYDRUS ET modeling response to the parameters and variables, a series of numerical runs based on the Los Alamos hillslope experiment site (Chapter 6) have been completed. The tested conceptual models are types of root-water uptake models, i.e., the Feddes model and the S-shape model. The tested parameters include root distribution, and wilting point. The tested variable is various partitioning of PE and PT.

The modeling domain was a thin slice with dimension of 0.1 cm (width) × 200 cm (depth). The top end was assigned an atmospheric boundary, and the bottom end a free drainage boundary, with two sides no flow boundaries. Two soil profiles were applied. The first one had the soil horizons observed at the Los Alamos hillslope site (Chapter 6, Table 6.3). In this profile, the soil was 100 cm thick underlain by a highly permeable non-welded tuff. The saturated soil bulk hydraulic conductivity was adjusted to account for the macropore effect (§4.7), being equated to *Kz-bulk* in Table A6-1.2. Because

interflow was not simulated, the soil of each horizon was assumed isotropic. The tuff had a saturated hydraulic conductivity about one fifth that of the top soil. The bottom part of the soil (70~100 cm depth) had a saturated hydraulic conductivity three order magnitude lower than the soil horizons above. This low-permeability soil layer impedes downward water movement, and is called the impeding layer in this dissertation. The second soil profile was modified by replacing the impeding layer with the tuff. The atmospheric boundary condition was derived from field measurements at the Los Alamos hillslope experiment site for water year 1994 (Figure 6.2), with minute-based temporal resolution.

Four base cases (two root-water-uptake models, and two soil profiles) were derived from the field experiment, which was conducted on ponderosa pine hillslope at Los Alamos National Laboratory [*Wilcox et al., 1997; Newman et al., 2004*]. Each case had equal PE and PT inputs, and the observed root distribution (see Chapter 6). For the Feddes model, the wilting point was set at -15 m after calibration with observed soil water content (Chapter 6); for the S-shape model the wilting point was prescribed to be -250 m, with h_{50} of -3 m and p of 3. From these base cases, parameters and variables were varied to test their effects on water partitioning, with results shown in Tables 4.1 and 4.2. In the tables, ET is the model-calculated actual ET; percolation is the rate of vertical water movement across the soil-bedrock interface; and runoff is infiltration-excess runoff. In the tables the results showing the greatest sensitivity are in boldface.

ET and percolation appear to be most sensitive to parameter values for situations without an impeding layer. For the Feddes model, the wilting point is the most sensitive parameter; root distribution is the least important parameter; and the effect of potential ET partitioning is somewhere in between. For the S-shape model, the sensitive parameter

is the partitioning of PE and PT, while the root distribution and wilting point do not sensitively influence the simulation results. It should be noted that this analysis is conducted on annual cumulative fluxes. If short-period fluxes are evaluated, the sensitive factors can change. For example, in §4.5.1, a root distribution effect is observed.

Table 4.1 Relative difference of water partitioning from the base cases, resulted from varying parameter values for the hydrologic models with the Feddes root-water-uptake function (fractional change of 0.1 equivalent to 10%)

Simulations *		with impeding layer			without impeding layer		
Base cases	cumulative flux	ET	percolation	runoff	ET	percolation	runoff
PE=0.5PET wp=-15m Rt(.65/.35)	mm/year	514	7	19	367	117	19
varied par.	Fractional change relative to base cases						
wp=-250m		0.049	0.021	***-0.108***	***0.705***	***-0.860***	-0.094
PE=0.8PET		0.014	0.007	-0.024	0.000	-0.036	-0.036
PT=0.8PET		0.009	-0.006	0.034	-0.043	***0.118***	0.007
Rt(2/0.3)		0.006	0.001	-0.017	0.004	-0.008	0.002
PE=0.8,Rt(2/0,3)					0.002	-0.038	-0.024
PT=0.8,Rt(2/0.3)					-0.031	***0.101***	0.025

* In this column, PE=0.5 PET means that PE and PT partition equally; wp is wilting point; and Rt (2/0.3) means the relative root density is 2 for top 30 cm and 0.3 for the depth between 30 cm and 70 cm.

Table 4.2 Relative difference of water partitioning from the base case, resulted from varying parameter values for the hydrologic models with the S-shape root-water uptake function (fractional change of 0.1 equivalent to 10%)

Simulations *		with impeding layer			without impeding layer		
Base cases	accumlative flux	ET	percolation	runoff	ET	percolation	runoff
PE=0.5PET wp=-250m	mm/year	509	7	20	325	145	19
varied par.	Fractional change relative to base cases						
wp=-15m					-0.005	0.000	0.010
wp=-800m					-0.002	-0.002	-0.021
PE=0.8PET					0.078	***-0.149***	-0.046
PT=0.8PET					***-0.213***	***0.351***	0.066
Rt(2/0.3)					0.005	-0.012	-0.017

* Same as Table 4.1.

Calibrated with the observed field soil moisture data in Chapter 6, the wilting point of the ponderosa pine for the Feddes model is about -15 meters (water column). At this site, the matrix soil water salinity is high [*Newman et al., 1998*], which causes a total water potential that is lower (more negative) than the matrix water potential. This is not included in parameterization of the Feddes model. If the salinity in the soil water is included, the wilting point is still around -25 meters. This is larger (less negative) than what is expected for the vegetation in semiarid environments. If a more reasonable wilting point is applied in the Feddes model, ET loss is almost double (Table 4.1). In contrast, the S-shape model can apply any wilting point in a realistic range without significant effects on the water partitioning results. Since the two conceptual models have different sensitivities to the model parameterization and variables, it is valuable to select the one that more appropriately represents the vegetation transpiration processes. Two experiments described below give some insight into this issue.

The first experiment was conducted on the *Pinus taeda L.* trees at the Southeast Tree Research and Education Site in the Sandhills of North Carolina [*Ewers et al., 2001*] (Appendix V). With the reported relationship between the canopy-scale stomatal resistance and the soil water content, the ratio of T/PT (or α) can be related to the soil water potential, using the Penman-Monteith equation (Appendix V). The Feddes model and the S-shape model are then fitted to this derived relationship for α and the water potential. The results show that the S-shape model fits better than the Feddes model (Figure A4-1.1). The other experiment measured the fraction of stem embolism as a function of water potential for desert vegetation at the Cienega Creek Natural Preserve, Pima County, Arizona [*Pockman & Sperry, 2000*]. The embolism is xylem blockage

associated with cavitation due to the dry soil conditions. With an assumption that the ratio of T/PT (or α) is proportional to the fraction of xylem that is not in embolism, the root-water-uptake function can be found. An example for creosote bush is shown in Figure V-2. Again the S-shape model fits the experimentally derived relationship well.

It seems that the S-shape model may represent vegetation transpiration process more appropriately than the Feddes model. For the simulations in this dissertation, the S-shape model is first option for transpiration modeling. However, the S-shape is numerically less stable than the Feddes model (Appendix V). When the S-shape model encounters a numerical problem, the Feddes model is used. If the Feddes model is used, the wilting point is a fitted parameter, rather than the actual wilting point for the vegetation.

The sensitivity analysis for the S-shape root-water-uptake model (Table 4.2) indicates that the surface-characteristic PE and PT partition is important for near-surface hydrologic modeling. However, the surface-characteristic PE and PT partitioning is not available from most common-used potential ET models. In the next section, selected potential ET models are reviewed.

4.3 Potential ET models

Since potential ET determines ET flux in HYDRUS-type hydrologic models, a realistic PET is an important input for the simulations. For the purpose of this study, i.e., water partitioning on mountain hillslopes, three requirements for the PET model are: (1) The PET should represent the atmospheric demand for evapotranspiration on a sloped surface, i.e., the influence of slope steepness and aspect should be included in the PET model. (2) Snow, snowmelt, and rainfall interception affect the available energy for

evapotranspiration of soil moisture. Their effects should be included in the PET model. (3) The vegetation effect should be included in the PET model, e.g., vegetation-coverage-dependent PE and PT partitioning, vegetation-dependent bulk stomatal resistance, and perhaps environmental condition constraints on vegetation transpiration. Four candidate PET models with various degree of complexity, and various degree of capacity to meet the requirements of this study, are described below. They are the Hargreaves, Priestley-Taylor, Penman-Monteith, and Shuttleworth-Wallace models.

4.3.1 Hargreaves model

Hargreaves et al. [*1985a*] give an empirical model based on daily temperature measurements.

$$ET_0 = a\frac{R_a}{\rho_w \lambda}(T_{mean} + b)\sqrt{T_{\max} - T_{\min}} \qquad (4.3)$$

where ET_0 is the potential ET for reference grass surface [*Allen et al., 1998*]; R_a is solar radiation at the top of the atmosphere, in a unit of $Jm^{-2}day^{-1}$; $T_{min,}$ T_{mean} and T_{max} are the mean daily minimum, mean daily average and mean daily maximum temperature (°C); ρ_w is density of the liquid water; λ is latent heat of vaporization ; and a and b are empirical constants, equal to 0.0023 and 17.8, respectively, suggested by Hargreaves and Samani [*1985b*]. Droogers and Allen [*2002*] suggest another set of empirical constant values for the Hargreaves equation, 0.0025 and 16.8 for a and b, respectively [reviewed by *Small, 2005*].

The advantage of this method is that it only requires minimum and maximum daily temperatures. The slope steepness and aspect effects and the vegetation effects are

not directly included in the model. Snow and snowmelt, and rainfall interception effect may be implicitly included in the daily temperatures. The vegetation effect is not captured. The Hargreaves equation is developed for estimating ET_0 for weekly and longer periods [*Hargreaves et al., 2003*]. It is not really appropriate to estimate PET for our modeling of hillslope water partitioning. Nonetheless, it provides a long-term PET (e.g., monthly, annually) for larger spatial scales. The slope steepness and aspect effects can be incorporated into R_a, using an appropriate algorithm.

4.3.2 Priestley-Taylor model

The Priestley-Taylor model is based on energy balance considerations. The equation for potential ET can be written [*Priestley and Taylor, 1972*] as

$$PET = \alpha \frac{\Delta (R_n - G)}{(\Delta + \gamma)\rho_w \lambda} \tag{4.4}$$

where Δ is the slope of the saturated vapor pressure versus temperature curve (Pa/°C), γ is the psychrometric constant (≈ 66 Pa/°C), α is empirical dimensionless constant depending on surface conditions, and is 1.26 for reference ET, R_n is the net incoming radiation, G is the net downward ground heat flux, both in a unit of $Jm^{-2}day^{-1}$; ρ_w is density of the liquid water; and λ is latent heat of vaporization.

The Priestley-Taylor equation appears to lump the effect of aerodynamic resistances, such as found in the Penman-Monteith equation (next section), into the α parameter. It was designed to estimate reference ET for periods of 10 days or longer [*Stewart and Rouse 1976*; reviewed by *Winter et al., 1995*]. Since net radiation is included in the equation, the Priestly-Taylor has the capacity to be extended to represent

slope steepness and aspect effects. But it does not include vegetation effects, snow and snowmelt, and rainfall interception.

4.3.3 Penman-Monteith model

Monteith [*1965*] incorporated a canopy resistance term into the Penman equation [*Penman, 1948*], resulting in the Penman-Monteith (PM) model [reviewed by *Stannard, 1993*]. These approaches account for both energy balance and physical mechanisms for transferring heat, vapor, and momentum. The PM equation is

$$PET = \frac{\Delta (R_n - G) + \frac{\rho_a c_p}{r_a}(e_s(T_z) - e_z)}{\rho_w \lambda \left[\Delta + \gamma (1 + \frac{r_c}{r_a}) \right]} \qquad (4.5)$$

where r_c is bulk canopy surface resistance, which is the resistance that the water vapor has to overcome in the path from the inside of the stomata to the bulk canopy surface, and for reference ET r_c is equal to 69 sm^{-1} [*Shuttleworth, 1993*]; r_a is the resistance to vapor transfer from the bulk leaf surface to the reference height; Δ represents the slope of the saturated vapor pressure versus temperature curve; γ is the psychrometric constant ($\approx$ 66 Pa/K); ρ_a is the air density; c_p is specific heat of air at constant pressure; e_s is the saturated vapor pressure at the reference height where the temperature and wind speed is measured; and e_z is the actual vapor pressure at the reference height. When r_c is zero, the equation reduces to the Penman Equation.

Different vegetation effects on transpiration can be captured by adjusting r_c. In the PM model, r_c conceptually includes the stomatal resistance and the interleaf resistance.

The latter accounts for the resistance against which water vapor is transferred from the leaf surface to the bulk canopy surface. However, the interleaf resistance is often neglected, leading to misinterpretation of the vegetation controls. Eagleson [*2002*] pointed out the problem of neglecting interleaf aerodynamic resistance, and suggested to include this resistance into the bulk canopy surface resistance. As in the Priestley-Taylor equation, the PM equation has capacity to be extended to include slope and aspect effects. The vegetation coverage effects, snow and snowmelt effects are not represented.

The PM equation is applied to the surface with a closed canopy. However, in semiarid environments, the surface is more often partially vegetated. Derived from the PM equation, the FAO-56 dual crop coefficient method [*Allen, 2000*] has the potential to partition PE and PT based on vegetation coverage. The model is semi-empirical, with lumped parameter values available for many crops, but not for natural vegetation types.

4.3.4 Shuttleworth-Wallace model

Shuttleworth and Wallace [*1985*] applied a two-layer model [*Lhomme and Chehbouni, 1999*] to calculate transpiration of the top canopy layer and evaporation of the substrate (e.g., soil) for the sparsely vegetated crop field. The major Shuttle and Wallace (SW) equation to estimate ET from the surface with sparse crops is

$$ET = C_c \, PM_c + C_s \, PM_s \qquad (4.6)$$

where PM_c and PM_s are terms each similar to the Penman-Monteith equations representing transpiration from a closed canopy and evaporation from a bare substrate,

respectively. C_c and C_s are functions of aerodynamic resistances and surface resistances, which have complex formulae.

In the SW model, a Beer's law relation is used to partition energy between the canopy and the bare substrate. A soil surface resistance is assumed for evaporation, which is a counterpart to the vegetation surface resistance for transpiration. The aerodynamic resistance is a linear interpolation between a completely bare surface and a completely vegetation-covered surface. The interleaf aerodynamic resistance is separately considered, which is also suggested by Eagleson [*2002*]. With increased complexity and data requirements compared to the PM equation, the SW model has capacity to represent vegetation coverage effects. The aerodynamic resistances, initially developed for crops, do not seem to be applicable for natural, large vegetation, such as mountain forests. Also, the topographic effect, snow and snowmelt, and rainfall interception are not included in the model.

4.4 A Topography- and Vegetation-based surface energy partitioning for hillslope ET modeling (TVET)[3]

4.4.1 Introduction

Potential ET is important information for hydrologic, ecologic, forest, and agricultural studies. Most potential ET models were developed in flat areas and for agricultural purposes (§4.3). These PET models are not appropriate for mountain hillslopes mainly because a sloped surface may receive different solar radiation per unit surface area (or solar irradiance) from a flat surface, and because the natural vegetation is different from crops in terms of ET characteristics. Here we present an algorithm for 'Topography- and Vegetation-based surface energy partitioning for hillslope ET

[3] This model was formerly named "SEP4HillET". A MATLAB code of the TVET model is attached in Appendix X.

modeling', or TVET. This model is designed to separately obtain daily PE and PT on hillslopes with various fractions of vegetation cover. DEM and remote sensing vegetation coverage (Appendix VI) can be incorporated into the model. The major considerations of TVET include: (a) PE and PT partitioning based on vegetation cover; (b) slope and aspect effects on available energy; (c) environmental effects on transpiration; and (d) rainfall interception and snowmelt. These are achieved by the following steps:

1) Solar radiation is adjusted to account for the slope and aspect effects on the sloped surface, while the shade due to other hills is not considered.

2) Available energy for sensible heat and latent heat is partitioned into that of canopy and of inter-canopy bare soil, according to the fraction vegetation cover and canopy leaf area index, using the layer approach [*Lhomme and Chehbouni, 1999*].

3) The available energy on each part of the surface is further partitioned into sensible heat and latent heat with the Penman-Monteith (§4.3) or Penman equation, using a patch approach [*Lhomme and Chehbouni, 1999*].

4) The aerodynamic resistance and bulk stomatal resistance are calculated with the modified Shuttleworth-Wallace approach [*Shuttleworth and Wallace, 1985*]. The intra-canopy aerodynamic resistance is explicitly parameterized in the model.

5) The stomatal resistance is adjusted by a Jarvis-type [*Jarvis, 1976*] function (optional).

6) Rainfall interception and snowmelt are considered to adjust the amount of available energy.

7) Surface albedo is adjusted to account for effects of fractional vegetation cover and snow cover.

8) A site aridity correction [*Temesgen et al., 1999*] is added to the model for applications in arid and semiarid environments.

All these elements have been published individually, but have not been included in one model. The uniqueness of the TVET model is in its integration of all these elements together to represent the surface energy partitioning on mountain hillslopes, and in how it integrates these elements.

Two major elements included in the TVET model are two-component (vegetation and bare soil) energy partitioning and topography-modified solar irradiation. The topography modification is a simple geometric problem, most of which is represented by existing equations in the literature. New equations are independently developed for the solar hours of north-, east-, and west-facing slopes in the TVET model.

For two-component energy partitioning on sparsely vegetated surfaces, Lhomme and Chehbouni [*1999*] distinguish two approaches. One is the layer (coupled) approach in which the energy and vapor flux interact between two components, such as the SW model [*Shuttleworth and Wallace, 1985*]. The other is the patch (uncoupled) approach in which the energy and vapor flux do not interact between two components, such as the model in Kustas and Norman [*1997*].

In a layer approach, soil under the canopy is not distinguished from that in the inter-canopy space. The canopy is treated as a semi-transparent layer for radiation input to the soil surface. The aerodynamic resistances, for transferring momentum, heat, and vapor from the soil surface, also depend on the canopy vegetation characteristics. Because transpiration from the canopy surface and evaporation from the soil surface are highly coupled, the layer approach has complex formulae. A typical example of the layer

approach is the Shuttle-Wallace model [*Shuttleworth & Wallace, 1985*]. In a patch approach, evaporation of the under-canopy soil is not considered. It treats transpiration from the canopy patch and evaporation from the inter-canopy soil patch independently in terms of available energy (although aerodynamic resistances could be coupled). It usually employs the Penman equation for the soil patch, and the Penman-Monteith equation for the vegetation patch.

Both layer and patch approaches provide approximations of potential evaporation and potential transpiration. The TVET model takes advantage of the merits of both approaches, e.g., the coupling in the layer approach and the simple formulae of the patch approach. In TVET a layer approach is used to partition the available energy and calculate the aerodynamic resistance. The patch approach is then used to derive potential evaporation for the soil component, and potential transpiration for the vegetation component. The problem of inconsistent formulation in literature, noticed by Lhomme and Chehbouni [*1999*], is addressed in the TVET model.

The model in its current form is simpler than it could be, with several assumptions. The major assumptions are: (a) no energy interchanges horizontally between two components (except for rainfall interception); (b) diffuse radiation is not explicitly considered; (c) snow falls only on the inter-canopy bare soil; and (d) snow sublimation is not considered.

4.4.2 Available energy partitioning for partially vegetated surfaces

The energy partitioning for the TVET model is shown in Figure 4.1. The energy balance equation for the surface is expressed by

$$A = R_{ns} - R_{nl} - A_{it} - G \tag{4.7}$$

where A is total available energy for sensible and latent heating at the surface for a period of interest (it is daily for the TVET model, which is applied for all other energy terms except for those with specific descriptions); R_{ns} is the net short-wave radiation to the surface; R_{nl} is the net long-wave radiation leaving the surface; G is the net downward ground heat flux (usually assumed zero for daily time step); A_{it} is the energy used to evaporate intercepted rainfall; all are in a unit of $Jm^{-2}day^{-1}$.

As already discussed in §4.4.1 the TVET model classifies the surface into two components, one covered by the vegetation canopy, the other being bare soil. The available energy at the surface further partitions into energy for these two components (A_s for bare soil, and A_c for the canopy), using a layer approach based on Beer's law (Equations 4.8 and 4.9), in which the soil component is considered under a semi-transparent canopy layer. Please note that the units of A_s and A_c in these two equations are energy per unit total surface area. Snow (if there is any) is assumed to fall only on the bare soil surface, and consumes A_s for snowmelt. The bare soil available energy is

$$A_s = A\, e^{-k_c L} - A_{sn} \tag{4.8}$$

where A is the total available energy; k_c is the extinction coefficient; and L is the bulk surface leaf area index, which is the multiplication of leaf area index of the canopy L_c and the fractional vegetation cover Fr of the surface ($L=L_c*Fr$). A_{sn} is the energy used for

snowmelt. Canopy leaf area index is the one-side leaf surface area of the canopy above the unit area of the canopy-covered ground surface. The canopy available energy is

$$A_c = A\,(1 - e^{-k_c L}) \tag{4.9}$$

As you can see from (4.8) and (4.9), the available energy is partitioned between the two components using a layer approach. However, in the TVET model the canopy is assumed in a patchy form. There are reasons to justify this apparent inconsistency both physically and mathematically. The physical reason is that radiation (both short-wave and long-wave) is in various directions. The radiation that is not vertically incident to the soil component can be intercepted by the canopy. Mathematically, the energy partitioning between the two components depends on both canopy leaf area index and the fractional vegetation coverage, which is included in the bulk surface leaf area index term. It should be noted that the energy terms for both components in these equations are the amount of energy per unit total surface area. It is important to be aware of this because the inconsistency problem noticed by Lhomme and Chehbouni [*1999*] is essentially a problem of defining the surface area on which the energy balance is evaluated.

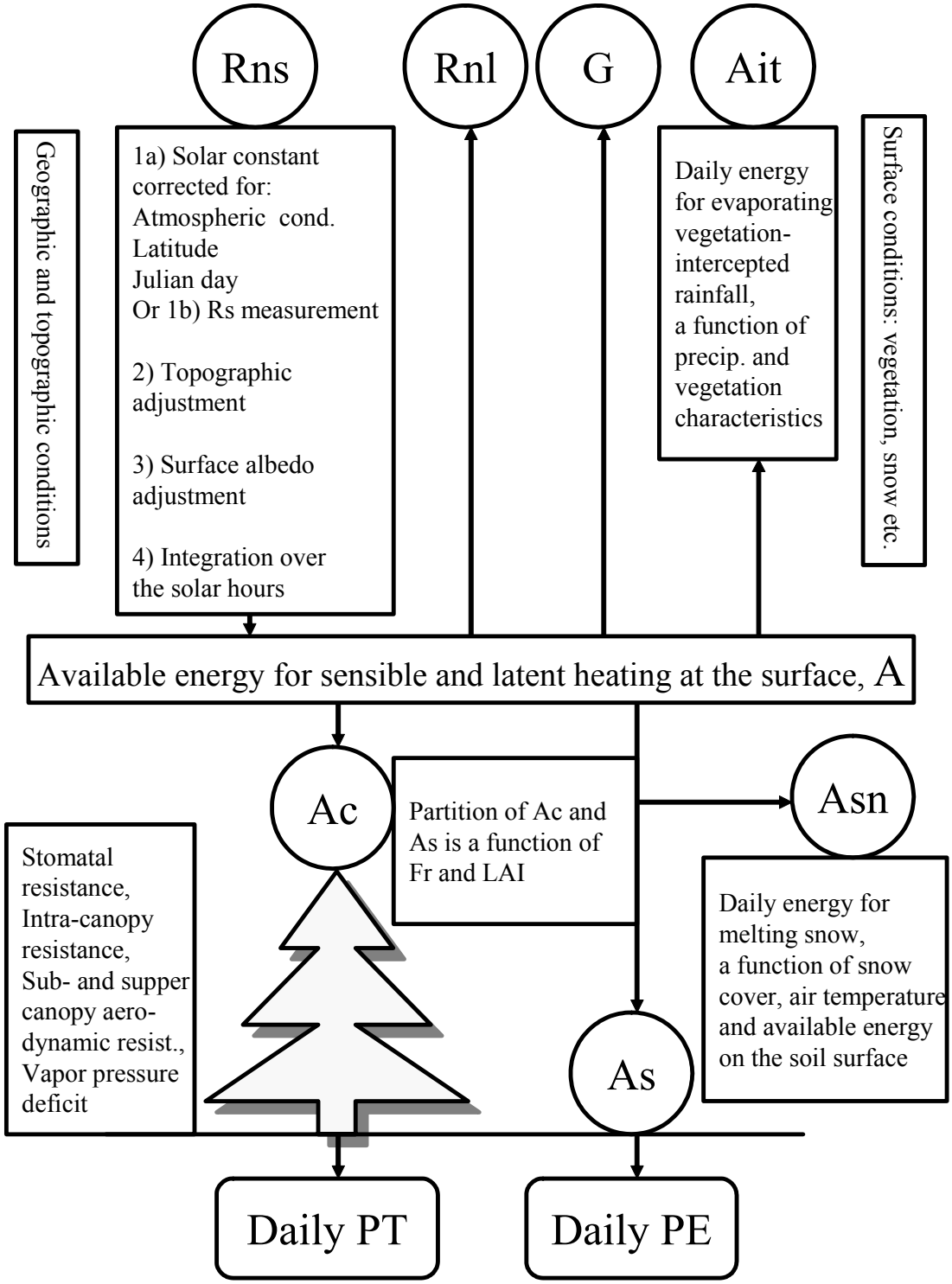

Figure 4.1 Flow chart of the TVET model, showing the energy partitioning components (Fr is surface fractional vegetation cover).

4.4.3 Topography-corrected solar radiation on tilted surfaces

Two major elements of the TVET model are the effects of slope and vegetation on surface energy partitioning. A sloped surface has different solar incident angle than a flat surface, and also has different daily solar illuminating hours. The beam solar radiation on a sloped surface at the top of the atmosphere is given by

$$I = I_{sc} \cos\theta \, d_r \tag{4.10}$$

where θ is the solar incident angle on the target surface, d_r is the inverse relative distance between the earth and the sun, and I_{sc} is the solar constant ($Jm^{-2}s^{-1}$). $\cos\theta$ is given by

$$\begin{aligned} \cos\theta = & \sin\delta \sin\phi \cos\beta - \\ & \sin\delta \cos\phi \sin\beta \cos\gamma + \\ & \cos\delta \cos\phi \cos\beta \cos\omega + \\ & \cos\delta \sin\phi \sin\beta \cos\gamma \cos\omega + \\ & \cos\delta \sin\beta \sin\gamma \sin\omega \end{aligned} \tag{4.11}$$

where δ is the angular position of the sun at solar noon with respect the plane of the equator; φ is latitude; β is the slope of the surface; γ is the surface azimuth angle, with zero due south, negative due east, and positive due west; ω is the solar hour angle, the angular displacement of the sun east or west of the local meridian due to rotation of the earth, negative in the morning, and positive in the afternoon [*Duffie & Beckman, 1991*, p15].

The daily beam radiation at the top of the atmosphere is the integral of equation (4.10) over the period of apparent sunrise to sunset on the surface of interest [*Duffie & Beckman, 1991*, p40].

$$R_a = \int_{t\_sunrise}^{t\_sunset} I_{sc}\, dr \cos\theta\, dt \tag{4.12}$$

or

$$R_a = \frac{12*3600}{\pi} I_{sc}\, dr \int_{\omega\_sunrise}^{\omega\_sunset} \cos\theta\, d\omega \tag{4.13}$$

For a horizontal surface, the sunrise and sunset hour angles are symmetric, with sunset hour angle determined by [*Duffie & Beckman, 1991*, p109]

$$\omega_{s0} = \cos^{-1}(-\tan\phi \tan\delta) \tag{4.14}$$

For a tilted surface, the sunrise and sunset hour angles are difficult to obtain. But we can find them for some specific situations. The sunset hour angle ω_s for a south-facing slope (with $\gamma = 0$) is given by [*Liu and Jordan, 1962*].

$$\omega_s = \min\left[\cos^{-1}(-\tan\phi \tan\delta),\ \cos^{-1}\{-\tan(\phi-\beta)\tan\delta\}\right] \tag{4.15}$$

For a tilted north-facing surface, the sunrise and sunset hour angles are still symmetric, and can be solved from (4.16), (4.17), and (4.18) (see Appendix VII)

$$\tan(\pi/2-\theta_z)=\tan\beta\cos\gamma_s \tag{4.16}$$

$$\sin\gamma_s=\frac{\sin\omega\cos\delta}{\sin\theta_z} \tag{4.17}$$

$$\cos\theta_z=\cos\phi\cos\delta\cos\omega+\sin\phi\sin\delta \tag{4.18}$$

where θ_z is the solar zenith angle, and γ_s is the solar azimuth angle. In these three equations, the three unknowns are θ_z, γ_s, and ω. Other variables are latitude φ, slope angle β, and solar inclination angle δ. The equations can be solved numerically for sunset hour angle ω_s. The sunrise hour angle is negative of the sunset hour angle.

Similar to the north-facing surface, the sunrise and sunset hour angle for the east/west-facing slopes can be solved from the geometrics (Appendix VII).

$$\tan(\frac{\pi}{2}-\theta_z)=\tan\beta\sin\gamma_s \tag{4.19}$$

With equations (4.17), (4.18), and (4.19), we can solve for ω_s. For an east-facing slope, what we solve for here is the sunset hour angle, because the solar azimuth angle is positive. The solar sunrise angle is approximately equal to that of flat surface, i.e., $-\omega_{s0}$. For west-facing slope, we solve for sunrise hour angle, with sunset hour angle equal to ω_{s0}.

By introducing the slope azimuth angle, we can solve the sunrise and sunset hour angle for any tilted surfaces. However, equations for solving sunrise and sunset hour angles become complex for an arbitrary tilted surface. To reduce the complexity, the solar radiation of an arbitrary tilted surface is approximated by linearly interpolating the

values between two of the four special situations (N, E, S and W-facing slopes). For example, if we have a sloped surface facing to the northeast, we calculate the daily solar radiation for north-facing slope and east-facing slope first. Then the two values are interpolated linearly for the sloped surface of interest, which should be improved for more accurate representation of the slope effect.

4.4.4 Daily net radiation on surfaces

4.4.4.1 Net solar radiation

Some of the radiation energy is absorbed and reflected by the atmosphere when it is transmitted to the land surface. The actual daily radiation at the surface is given by [*Allen et al., 1998*]

$$R_{sun} = R_a (a_s + b_s \frac{n}{N}) \tag{4.20}$$

where N is the number of the maximum possible daylight hours on a flat surface; n is the actual hours of the sunshine in the day; a and b are empirical constant, a_s=0.25, b_s=0.50 suggested by Allen et al. [*1998*] for average conditions. The number of daylight hours is derived from the sunset hour angle of the flat surface by [e.g., *Allen et al., 1998*]

$$N = \frac{24}{\pi}\omega_{s0} = \frac{24}{\pi}\cos^{-1}(-\tan\phi\tan\delta) \tag{4.21}$$

At some locations, the measured solar radiation is available. Then measured solar radiation is used and adjusted for the sloped surface.

Some incident solar radiation is reflected from the surface. The net daily solar energy available for the surface is given by

$$R_{ns} = (1-\alpha)R_{sun} \qquad (4.22)$$

where α is albedo of the surface, which is a function of fractional vegetation cover and snow cover.

4.4.4.2 Net long-wave radiation

The long-wave radiation depends on surface temperature and emissivity, and air temperature and emissivity which is associated with atmospheric conditions, such as relative humidity and cloud cover. The daily outgoing net long-wave radiation is empirically given by Allen et al. [*1998*].

$$R_{nl} = (24\times 3600)\,\sigma\,\varepsilon' f\left[\{(273.16+T_{\max})^4 + (273.16+T_{\min})^4\}/2\right] \qquad (4.23)$$

where

R_{nl} = net outgoing long-wave radiation ($Jm^{-2}day^{-1}$)

$\varepsilon' = 0.34 - 0.14\sqrt{e_a/1000}$, net upward emissivity for average condition

$f = 1.35\dfrac{R_{sun}}{R_{s0}} - 0.35$, cloud cover adjustment term

σ = Stefan-Boltmann constant, ($5.6697\times10^{-8}Wm^{-2}K^{-4}$)

T_{max} = maximum temperature during the day (^0C)

T_{min} = minimum temperature during the day (^0C)

e_a = actual vapor pressure (Pa)

R_{s0} = the daily radiation to the surface with a clear sky, given by

$$R_{s0} = (0.75 + 2 \times 10^{-5} ele)\, R_a \tag{4.24}$$

where *ele* = the elevation above sea level, in m.

4.4.5 Two-component model for potential evaporation and potential transpiration

A two-component resistance network model, similar to Shuttleworth and Wallace [*1985*], is adopted for the TVET model (Figure 4.2). The available energy for the canopy and the inter-canopy soil, A_c and A_s (unit: energy per unit total surface area), is further partitioned into latent heat and sensible heat, respectively, using a patch approach. In the patch approach, the available energy needs to be geometrically tied to the surface area of each component. This means that the energy terms for each component have a unit of energy amount per relative surface area of the component. The following two equations connect the layer-approach energy terms on the left-hand side to those of the patch-approach on the right-hand side, by the factor of fractional vegetation cover, for $0 < Fr < 1$.

$$A_c = Fr * (\lambda E_c + H_c) \tag{4.25}$$

$$A_s = (1 - Fr) * (\lambda E_s + H_s) \tag{4.26}$$

where A ($Jm^{-2}day^{-1}$) is the available energy for sensible heat and latent heat per unit total total surface area; λE ($Jm^{-2}day^{-1}$) is the energy for latent heat per unit area of the

component; H ($Jm^{-2}day^{-1}$) is the energy used for heating the air per unit area of the component; subscripts s and c represent the intercanopy soil and the vegetation, respectively; Fr is the fractional vegetation cover.

Application of Penman equation for the soil component, and Penman-Monteith equation for the vegetation component, results in PE (m/day) and PT (m/day) of the total surface (Appendix VIII).

$$PE = \frac{\Delta A_s + (1 - Fr)\frac{\rho_a c_p}{r_a^a + r_a^s}(e_s(T_z) - e_z)}{\rho_w \lambda(\Delta + \gamma)} \tag{4.27}$$

$$PT = \frac{\Delta A_c + Fr\frac{\rho_a c_p}{r_a^c + r_a^a}(e_s(T_z) - e_z)}{\rho_w \lambda\left[\Delta + \gamma(1 + \frac{r_s^c}{r_a^c + r_a^a})\right]} \tag{4.28}$$

where ρ_a is the density of the air; c_p is the specific heat capacity of the air; e_s is the saturated vapor pressure; Δ represents the slope of the saturated vapor pressure versus temperature curve; γ is the psychrometric constant (≈ 66 Pa/K); T_z is the temperature of the air at the reference height z; r_a^a is the aerodynamic resistances between the mean air flow at the canopy height and the reference height shown in Figure 4.2; r_a^s is the aerodynamic resistance between the mean air flow at the canopy height and the soil surface; r_a^c is the aerodynamic resistance between the mean leaf surface to the mean canopy surface; and r_s^c is the bulk canopy stomatal resistance.

The derivation of Equations (4.27) and (4.28) requires $0 < Fr < 1$, as shown in equations VIII-10 and 11. If $Fr = 0$ there is no transpiration in this model (i.e., PT = 0), which is properly preserved by Equation (4.28), and the Penman equation is applied to the entire surface, as properly preserved by Equation (4.27). Thus, Equations (4.27) and (4.28) include the no-vegetation-cover situation of $Fr = 0$. If $Fr = 1$, the Penman Monteith equation is applied to the total surface with canopy-intercepted available energy, which is represented by Equation (4.28). In this situation, all soil is under the canopy. If the Penman equation is applied to the under-canopy soil with the assumption that the term of aerodynamic contribution is negligible, it is represented by Equation (4.27). In this case Equations (4.27) and (4.28) can also be extended to incorporate the situation of $Fr = 1$.

In the TVET model, vegetation effects on surface energy partitioning are well represented. Equation (4.27) is a Penman equation for the wet inter-canopy soil surface, in which the vegetation effect is represented by Fr, r_a^a, r_a^s, and the energy term. The vegetation effect is also included in the energy terms (Equations 4.8 and 4.9). Equation (4.28) is a Penman-Monteith equation for the vegetation part of the surface, in which the vegetation control is represented by Fr, r_a^a, r_a^c, r_s^c, and the energy term.

As mentioned in §4.4.2, the formulae of the TVET model (4.27 and 4.28), derived by the patch approach, is much simpler than the SW model which was derived by the layer approach. Meanwhile, because energy partitioning and transferring of vapor, heat, and momentum are coupled between the two components, the TVET model represents actual processes more appropriately than normal patch models. For example, if Fr is equal to one, Equation (4.26), in its patch model form, does not allow evaporation. This is

obviously not realistic. But, because of the hybrid of layer and patch approaches, Equation (4.27) allows evaporation to occur, with an amount depending on the canopy leaf area index. If *Fr* is equal to zero, Equation (4.28) gives zero transpiration, which is consistent with the modeled situation.

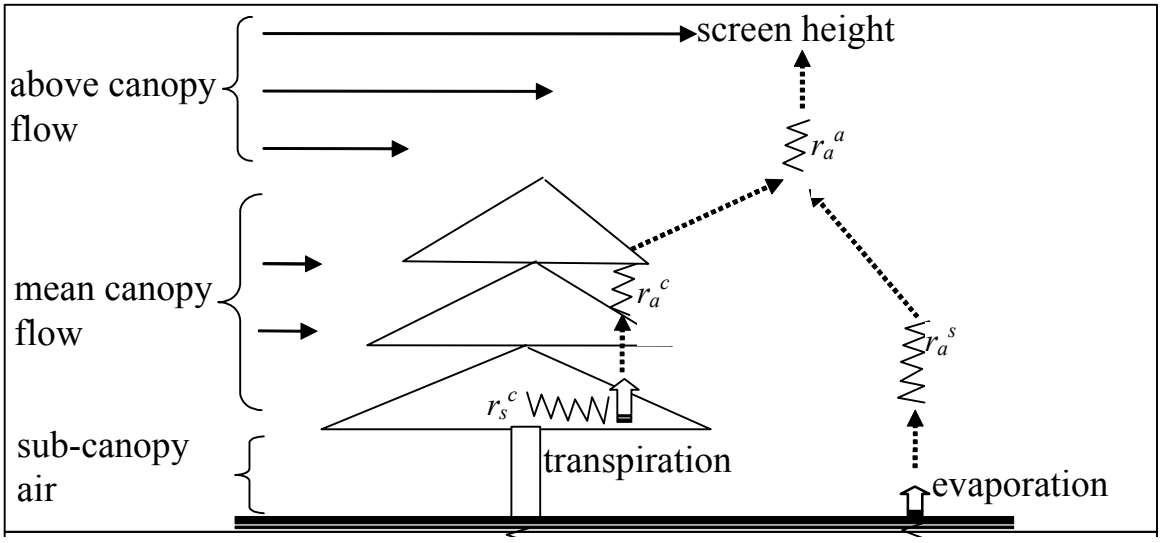

Figure 4.2 Schematic of evaporation from bare-soil and transpiration from vegetation of the open vegetated surface (modified from Shuttleworth and Wallace 1985). Note that the meaning of "s" in r_s^c is "stomatal", different from that in r_a^s, which means "soil component".

4.4.6 Aerodynamic resistances and stomatal resistance

The aerodynamic resistance is a function of wind speed at the reference height, and the surface characteristics (e.g., fractional vegetation cover, vegetation height, canopy leaf area index, etc.). The wind direction and speed are highly variable on mountain hillslopes, and are difficult to quantify. The following derivations of aerodynamic resistances are for a known wind speed at the reference height. However, quantification of topography-related wind field is critical to better estimating aerodynamic resistances and partitioning of sensible heat and latent heat in mountains. This should be among the future efforts to improve the model.

The aerodynamic resistances are linearly interpolated between those for the surface with complete canopy cover and for the surface without canopy cover [*Shuttleworth and Wallace, 1985*], weighted by the equivalent surface leaf area index.

$$\begin{aligned} r_a^a &= \frac{1}{4} L\, r_a^a(\alpha) + \frac{1}{4}(4-L) r_a^a(0) \\ r_a^s &= \frac{1}{4} L\, r_a^s(\alpha) + \frac{1}{4}(4-L) r_a^s(0) \end{aligned} \qquad \text{for } 0 \le L \le 4 \qquad (4.29)$$

$$\begin{aligned} r_a^a &= r_a^a(\alpha) \\ r_a^s &= r_a^s(\alpha) \end{aligned} \qquad \text{for } L > 4 \qquad (4.30)$$

where *(α)* indicates the surface completely covered by vegetation with a canopy leaf area index of 4, and *(0)* indicates the surface is not covered by vegetation. The equations for aerodynamic resistances provided by Shuttleworth and Wallace [*1985*] were originally developed for crops. The TVET model use the following equations (4.31~4.36) for the aerodynamic resistance of the natural surface with *Fr=0* or *Fr=1*.

For the closed vegetation surface, Equation (4.31) is a common way to obtain aerodynamic resistance above canopy [*Campbell and Norman, 1998*].

$$r_a^a(\alpha) = \frac{\ln[(z-d)/z_m]\ln[(z-d)/z_H]}{k^2 u_z} \qquad (4.31)$$

where z is the height of wind and humidity measurements; d is zero plane displacement height; z_m is roughness length of the vegetation governing momentum transfer; z_H is

roughness length of the vegetation governing transfer of heat and vapor transfer; *k* is von Karman's constant; and *u(z)* is wind speed at the reference height *z*. Similar to the above-canopy aerodynamic resistance, the sub-canopy aerodynamic resistance is given by Equation (4.32), assuming that the zero plane displacement is the ground surface (i.e. *d = 0*), and a logarithmic wind speed profile.

$$r_a^s(\alpha) = \frac{\ln[h / z'_m]\ln[h / z'_H]}{k^2 u_h(\alpha)} \tag{4.32}$$

where *h* is the vegetation height; z'_m is roughness length of the soil surface governing momentum transfer; z'_H is roughness length of the soil surface governing transfer of heat and vapor transfer; $u_h(\alpha)$ is the mean wind speed at the canopy height, which is derived from the wind speed profile.

$$u_h(\alpha) = \frac{\ln[(h-d)/z_m]}{\ln[(z-d)/z_m]} u_z \tag{4.33}$$

For the surface without vegetation, it is reasonable to assume that the wind speed at the "canopy" height is equal to that at the reference height. The sub-"canopy" aerodynamic resistance is then given by Equation 4.34, assuming that the zero plane displacement height of the soil surface is negligible with respect to the "canopy" height.

$$r_a^s(0) = \frac{\ln(h / z'_m)\ln(h / z'_H)}{k^2 u_z} \tag{4.34}$$

The above-canopy resistance is the difference between the resistance from the surface to the reference height and the resistance from the surface to the "canopy" height [*Shuttleworth and Wallace, 1985*].

$$r_a^a(0) = \frac{\ln(z/z'_m)\ln(z/z'_H)}{k^2 u_z} - r_a^s(0) \tag{4.35}$$

The interleaf (or intra-canopy) aerodynamic resistance is the resistance for transferring the vapor from the mean leaf surface to the mean canopy surface, which is a function of canopy structure, leaf area index, and the wind speed at the canopy height. Eagleson [*2002*] suggest incorporating the interleaf resistance into the bulk canopy internal surface resistance; while Shuttleworth and Wallace [*1985*] incorporate it into the series of external resistances. The TVET model explicitly includes the interleaf resistance as an external aerodynamic resistance. In this way, the interleaf resistance can be explicitly related to the air flow dynamics (e.g., wind speed), as well as to the canopy effects on modifying air flow. With assumptions that "heat and water vapor are exchanged by molecular diffusion through a laminar layer around the leaves, and that wind speed attenuates exponentially inside the canopy" [*Mo et al., 2004*], the intra-canopy aerodynamic resistance is given by Equation 4.36 [*Choudhury and Monteith, 1988*].

$$r_a^c = \frac{\alpha_w}{4\alpha_0(1-\exp(-\alpha_w/2))}\frac{(l_w/u_h)^{1/2}}{L_c} \tag{4.36}$$

where α_w is the wind extinction coefficient in the canopy; α_0 is a coefficient taken as 0.005 m/s$^{0.5}$; l_w is the characteristic length of leaf width; and L_c is the canopy leaf area index; u_h is the mean wind speed at the canopy height of the surface. The u_h is approximated from the linearly interpolation of the wind speeds at the same height for the closed canopy surface and for the non-vegetated surface. Again, it is assumed that the wind speed at the "canopy" height is equal to that at the reference height for the surface without vegetation. The mean wind speed at the canopy height, for a surface with a fractional vegetation cover *Fr*, is calculated from the linear interpolation by fractional vegetation cover, equation (4.37).

$$u_h = u_z(1 - Fr) + u_h(\alpha)Fr \tag{4.37}$$

Vegetation regulates transpiration rate via its stomata. The stomatal resistance is a function of vegetation type and status. It also responds to the environmental conditions. Jarvis-types functions are adopted to represent these stomatal behaviors (Appendix IX). The mean leaf stomatal resistance is assumed to be a function of vegetation type and the environmental conditions, such as vapor pressure deficit and short-wave radiation, shown in equation (4.38) [*Jarvis, 1976; Stewart, 1988; Lhomme et al. 1998*].

$$r_{ST} = r_{ST\_\min} f_1(D) f_2(I') f_3(T) f(\psi_l) \tag{4.38}$$

where r_{ST_min} is the minimum mean leaf stomatal resistance at optimal conditions; D is the vapor pressure deficit; I' is the incoming solar irradiance; T is the air temperature; and ψ_l is the leaf water potential, where $f(\psi_l) = 1$ for estimating potential transpiration. The bulk stomatal resistance is related to the canopy leaf area index L_c [*Shuttleworth and Wallace 1985*].

$$r_s^c = r_{ST} / L_c \tag{4.39}$$

where r_{ST}, given in (4.38), is the mean stomatal resistance of the leaves (both sides) for $L_c=1$.

4.4.7 Rainfall interception and snowmelt

Both evaporation of intercepted rainfall and snowmelt consume energy. Evaporation of the rainfall interception is not included in either transpiration of the canopy component or evaporation of the inter-canopy bare soil component. Thus the rainfall interception effect on surface energy balance should be considered in the TVET model, as should the snowmelt. A simple model of rainfall interception is applied in the TVET. The snowmelt is modeled by an equally simple temperature-index approach and constrained by the available energy on the bare soil surface.

4.4.7.1 Rainfall interception

The rainfall falling on a vegetated surface does not all reach the ground surface. A substantial portion of the rainfall will be evaporated directly from the canopy. Thus, the amount of intercepted rainfall should be subtracted from the total rainfall when it is applied as the input to the ground surface in the HYDRUS hydrologic model. Also the

evaporation of the intercepted water consumes energy, which will decrease the potential evaporation and transpiration. The intercepted rainfall in given by

$$It = P_r \cos\beta \qquad \text{for } P_r\, cos\beta < I_{max} L \qquad (4.40a)$$

$$It = I_{\max} L \qquad \text{for } P_r\, cos\beta \geq I_{max} L \qquad (4.40b)$$

where P_r is the amount of rainfall (mm) of a rainfall event; I_{max} is the maximum interception capacity of the surface with $L=1$; β is the slope of the surface; and L is the surface leaf area index.

The energy consumed by the intercepted water evaporation is obtained from

$$A_{it} = It\, \rho_w\, \lambda \qquad (4.41)$$

where ρ_w is the liquid water density. The adjusted net precipitation to the ground surface is given by

$$P_{net} = P_r \cos\beta - It \qquad (4.42)$$

Note that now P_{net} is the depth of water on the sloped surface, not on the flat surface as P.

4.4.7.2 Snow and Snowmelt model

It is important to have snow-storage in the model, since snow does not join active liquid-phase hydrological processes immediately. Snow is reported as equivalent water

depth at weather stations, and is not distinguished from the rainfall. A temperature index is applied to partition precipitation into snow and rainfall [*Wigmosta et al., 1994*].

$$P_s = P \qquad \text{for } T_{mean} \le T_{sn} \qquad (4.43b)$$

$$P_r = P \qquad \text{for } T_{mean} > T_{sn} \qquad (4.43b)$$

where T_{mean} is the mean daily temperature; T_{sn} is the specific mean daily temperature above which precipitation is in the form of snow; P is the reported precipitation depth; P_s is the water-equivalent depth of snowfall; and P_r is the rainfall depth. A simple temperature index model is also applied to determine the snowmelt rate when snowmelt occurs [*Dingman, 1994*].

$$P_m = k_{sm}(T_{mean} - T_m) \qquad (4.44)$$

where k_{sm} is an empirical coefficient, 3.6 mm/ (day ^{0}C), from the research at Danville, VT [*Dingman, 1994*]; and T_m is the temperature at which the snowmelt initiates.

Snowmelt is also constrained by available snow (snow water equivalent) and the energy (A_s), which are considered by the model. During the snowmelt, the net active water reaching the ground surface is further adjusted by adding snowmelt to other contributions.

$$P_{net} = P_r \cos\beta - It + P_m \qquad (4.45)$$

4.4.8 Adjustment of PET for disparity of site aridity from reference conditions

We use potential ET for hydrologic modeling input, representing the maximum ET loss that occurs in a specific time period. Almost all the potential ET models were developed for and tested on agricultural irrigation sites. They are used to calculate the potential ET on surfaces with optimal soil water condition. When we use these equations to calculate potential ET for an arid natural environment, some adjustment is recommended [*Temesgen et al., 1999; Hargreaves et al., 2003*]. Two major differences between the actual condition at the arid site and the assumed condition for potential ET at the site (similar to the irrigation site) are the reasons for this type of adjustments. They are: (1) the near-surface atmospheric condition (e.g., daily temperature, relative humidity) at an arid site is quite different from assumed potential surface condition; (2) the near-surface air is often unstable at an arid site. These characteristics of the arid sites often make calculated potential ET unrealistically high. Figure 4.3 shows PM-equation-calculated and TVET-calculated potential ET for grass surfaces with measured atmospheric forcing at Sevilleta (see §4.5.1). The calculated potential ET exceeds 15 mm/day in the summer for 0.5m-tall grass, which is almost double compared to the reference grass ET. Thus the atmospheric condition should be corrected before it is input into a potential ET model which was developed for irrigation environments. As TVET is a potential ET model derived from Penman and Penman-Monteith equations, such a correction is warranted. Daily temperature correction is a simple and applicable approach for most of the PET models.

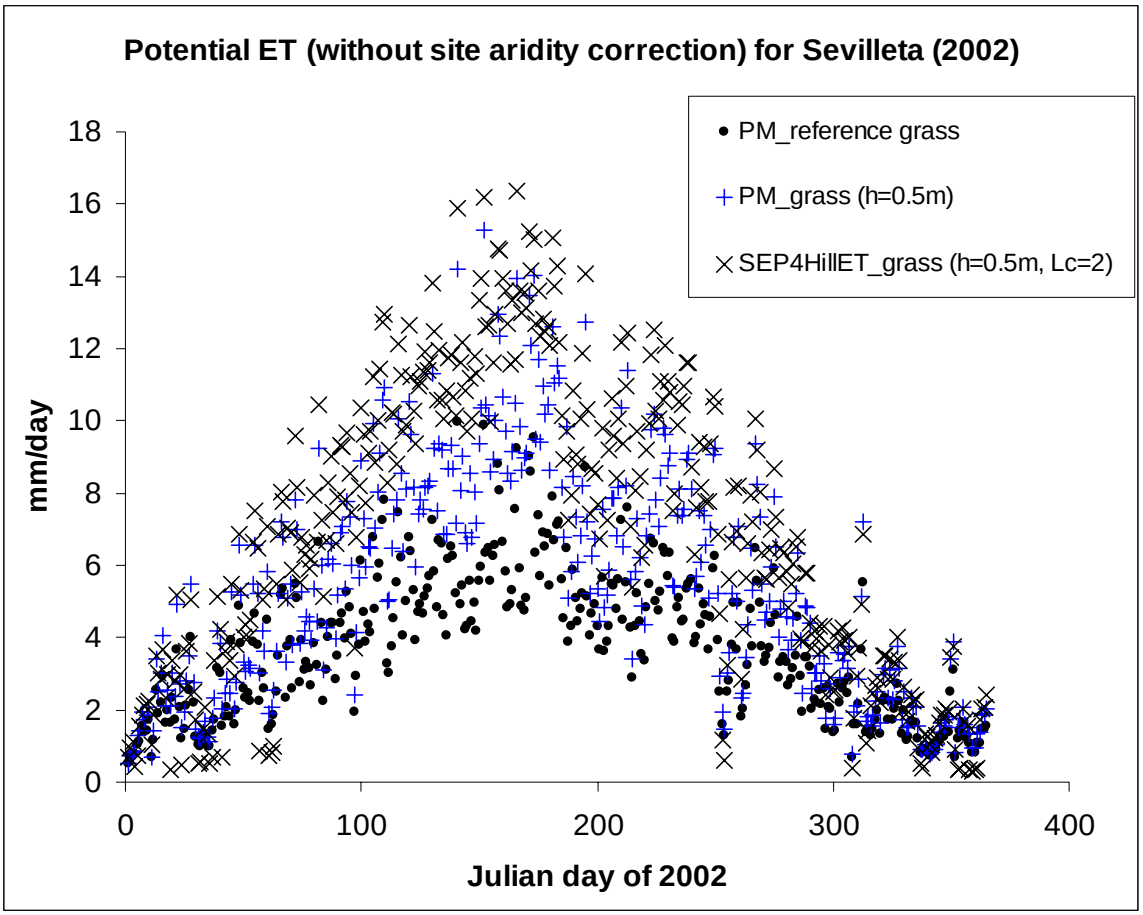

Figure 4.3 TVET-calculated surface potential ET for grass surface (Fr=0.99, h=0.5m, Lc=2, rST_min=130 sec/m) at Sevilleta LTER, 2002, in comparison to PM-equation-calculated potential ET for reference grass (h=0.12m) and for grass surface (h=0.5m).

At irrigated sites or in humid areas, nighttime minimum temperature is very close to the dew point. In an arid environment, there is so little water vapor in the air that the minimum air temperature does not reach the dew point, resulting in a positive T_{min}-T_D, termed as mean dew point departure (*MDD*) by Temesgen et al. [*1999*]. Based on this, Temesgen et al. [*1999*] provided the following equations to adjust T_{min}, T_{max} and T_D , which is used for the site aridity correction in TVET.

$$T_{\max 0} = T_{\max} - K_x (MDD - 2) \qquad (4.46)$$

$$T_{\min 0} = T_{\min} - K_n (MDD - 2) \tag{4.47}$$

$$T_{D0} = T_D + K_d (MDD - 2) \tag{4.48}$$

where *MDD* is the daily mean dew point departure, in ˚C; T_{max0}, T_{min0}, and T_{D0} (˚C) are adjusted temperatures for site aridity; T_{max}, T_{min}, and T_D (˚C) are measured temperatures; K_n, K_x, *and* K_D are empirical constants, for which Temesgen et al. [*1999*] gave as 0.7, 0.4, 0.6, respectively for the arid category, and 0.5, 0.5, and 0.5 for the humid category.

For a site where *MDD* is not available, Jensen et al. [*1997*] suggest an adjustment based on local average climate conditions.

$$T_{bias} = K\left(1 - \sqrt{\frac{P}{ETH}}\right) \tag{4.49}$$

where T_{bias} is the increased maximum temperature, increased minimum temperature, and decreased dew point due to the site aridity, *K* is an empirical constant, which is 4 for Utah, *P* and *ETH* are 10-day or monthly precipitation and PET.

Both adjustments for site aridity are applicable for those PET models with temperature as direct or indirect inputs, e.g., Hargreaves, PM, SW, and TVET models. They are not applicable for the Priestley-Taylor model. Figure 4.4 shows the difference for TVET-calculated potential ET for the shrub surface at Sevilleta, central New Mexico (§4.5.1). However, it should be noted that while the site-aridity correction is necessary for calculating potential ET and for irrigation designs. It should not apply to estimate an

ET rate of a point with condition distinct from its surrounding environment at an arid site (e.g., an evaporation pan placed in the desert environment).

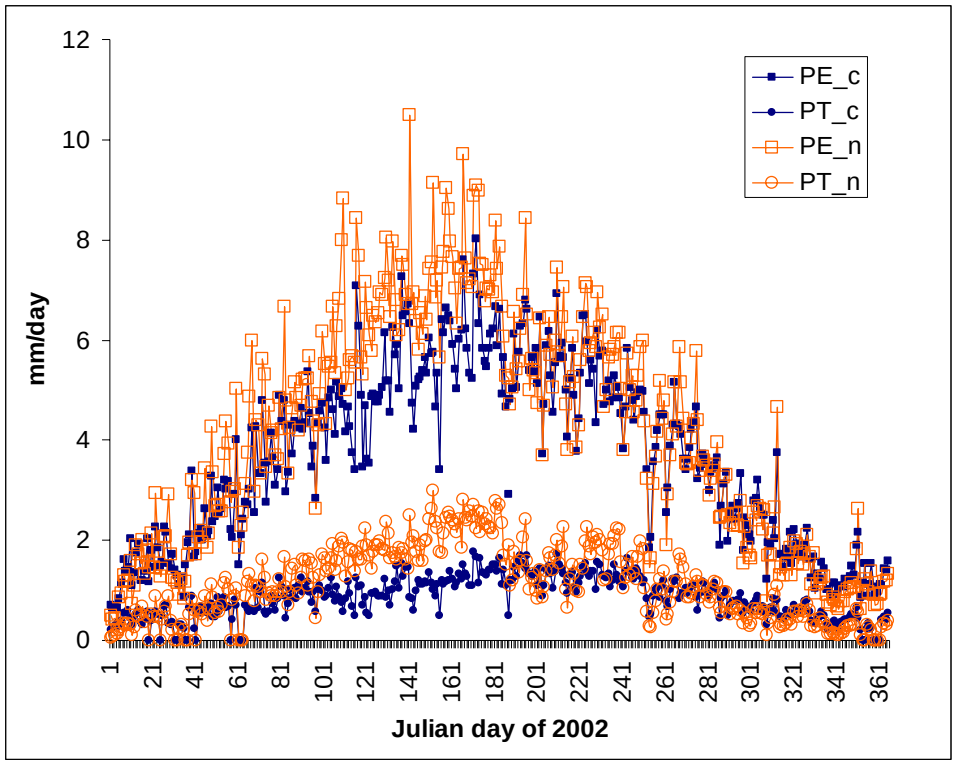

Figure 4.4 Difference in TVET calculated PE and PT for the shrub surface at Sevilleta LTER, 2002, for situations of with (_c) and without (_n) site aridity correction.

4.5 TVET model testing

The TVET model can simulate vegetation and slope controls on PE and PT partitioning. Slope steepness and aspect control PE and PT by their direct influence on solar radiation, which is theoretically straightforward and determined by geometrics. Some results of TVET model showing slope steepness and aspect effects are included in Appendix XI. The functions describing vegetation control on PE and PT are complex. They include the effects of fractional vegetation cover and canopy leaf area index on available energy partitioning between two components, the effects of leaf stomatal resistance and intra-canopy (inter-leaf) aerodynamic resistance on PT, and the effects of

vegetation height and fractional vegetation cover on aerodynamic resistance which affects the latent heat and sensible heat partitioning. Two field studies in essentially flat terrain, one at Sevilleta National Wildlife Refuge (NWR), and the other at the Rio Grande riparian area, are used to test the performance of the vegetation-control functions of the TVET model.

4.5.1 TVET testing with Sevilleta shrub and grass surfaces and the implications

Evaporation alters stable isotopic compositions of both hydrogen and oxygen of water molecules in the soil, while transpiration does not. Based on this, the time-series of stable isotope compositions of the soil water can be used to estimate the partitioning of evaporation and transpiration. Boulanger [*2004*] studied the partitioning of evaporation and transpiration for two surfaces, shrub and grass (Figure 4.5), at the Sevilleta NWR, central New Mexico, using a stable isotope balance model. He measured soil water content and stable isotope compositions of the soil within a week right after a summer precipitation event (Julian day 214 of 2002). The results indicate that subsequent to that event transpiration consumed 16~21% and evaporation consumed 79~84% of post-precipitation soil water at the shrub site. There was no recharge or run-off. At the grass site, these two numbers were 30~48% and 52~70%, respectively. These results can be used to test the vegetation functions of the TVET model.

Boulanger's study gives actual E and T partitioning while TVET gives potential E and potential T partitioning. To make an appropriate comparison, a year of local observations of energy balance components, temperature, precipitation and other meteorological data, where filtered through TVET to produce time-series of PE and PT. HYDUS 1D hydrologic simulations were forced by the times series of precipitation, PE

and PT, to estimate a time series of actual E and T for these two surfaces (shrub and grass). The simulation results, for the period following the rainfall event from which Boulanger collected the samples, are compared to the results from the isotopic study. The simulated results following another two rainfall events during the same year are also examined to see whether the results from the one sampled event are sufficient to represent mean E and T partitioning.

However, it should be noted that the E and T partitioning is very difficult to quantify. The partitioning process depends on weather, vegetation, and soil conditions. The uncertainty in characterizing these conditions will definitely affect an appropriate estimate of E and T partitioning. When numerical modeling is used to investigate E and T partitioning, numerical approximations of evaporation and transpiration processes also lead to uncertainty in modeled E and T values. Appendix XII explores this issue for the HYDRUS modeling code.

With site-specific data input (e.g., Fr = 0.3 for the shrub surface, and 0.55 for the grass surface, Appendix XIII) [*Kurc and Small, 2004*], and the meteorological data (Sevilleta LTER weather station # 40, [*Moore, 2004*]) for the year (2002) in which the Boulanger study was done, as well as parameter values from literature (Appendix XIII), the TVET model was used to determine PE and PT partitioning. The model calculated PE of 81% and PT of 19% for the year at the shrub site, and PE of 64% and PT of 36% for growing season at the grass site (Figure 4.5). The HYDRUS hydrologic modeling domain was a 2-meter column, with the atmospheric boundary (generated from TVET model) at the top, and a free drainage boundary at the bottom. The parameterization of soil properties, root distribution [*Kurc and Small, 2004*], and root-water-uptake model

[*Pockman and Sperry, 2000*] are all based on field or lab measurements, and are given in Appendix XIV. All the modeling inputs (both TVET and HYDRUS) are either based on measurements or from literature (except for the root-water-uptake model parameterization of the grass site), without additional calibration.

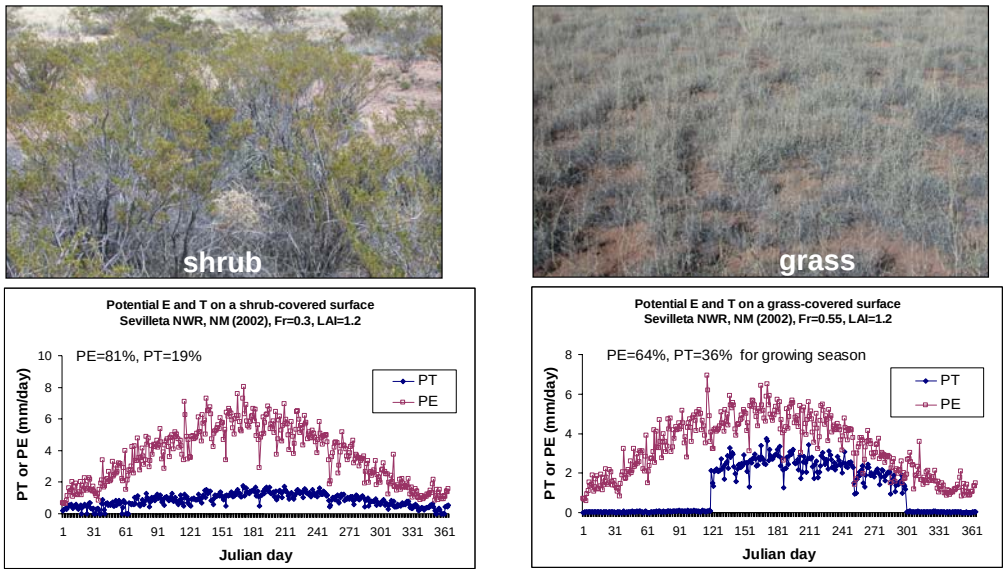

Figure 4.5 TVET-modeled results for shrubland and grassland in Sevilleta NWR, central New Mexico. For the grass land, the grass is assumed active during the growing season (May~October), and dormant during the rest time of the year.

Daily precipitation, model simulated actual E and actual T, simulated soil moisture, and event-based simulated cumulative actual and potential transpiration fractions before and after three rainfall events (on Julian days 214, 254, 261) are plotted in Figure 4.6. The cumulative actual (potential) transpiration fraction of event-based cumulative actual (potential) ET, was calculated from $\Sigma T/\Sigma\{E+T\}$ ($\Sigma PT/\Sigma\{PE+PT\}$). Note that since these are transpiration fractions of total ET, the fraction of potential ET does not have to be larger than the fraction of actual ET, as in Figure 4.6d.

The rainfall event for which the isotopic study was conducted is the one took place on Julian day 214 of the year 2002. At the shrub site, six days after the Julian day 214 event, on the day when Boulanger made his measurement, the cumulative T fraction is 19% (Figure 4.6a). This is in good agreement with the 16~21% from the isotopic results. For this same event at the grass site, the cumulative T fraction is 45% for the six days (Figure 4.6d), within the range of 30-48% suggested by the isotopic measurements. (No literature data are available to derive the root-water-uptake model parameterization for the grass site. The model parameterization was determined based on my subjective conceptualization of the grass (Appendix XIV). The model was not calibrated to fit Boulanger's results.) The good agreement between the modeling results and the isotopic study results for the two surfaces builds confidence in the TVET model.

Now let's examine the simulated E and T partitioning for the other two rainfall events. For the shrub surface the fraction of cumulative T is ~30% for the six days after each event (Figure 4.6b and c), which is significantly larger than 19% of the first rainfall event (on Julian day 214). For the grass surface, the fraction of cumulative T is ~55% for the six days after each event (Figure 4.6e and f), which is also significantly larger than 45% of the first rainfall event. It appears that a single isotopic study, in this case during the week of Julian day 214-220 of 2002, is not sufficient to represent actual E and T partitioning pattern of soil moisture following other rainfall events or over a longer time period.

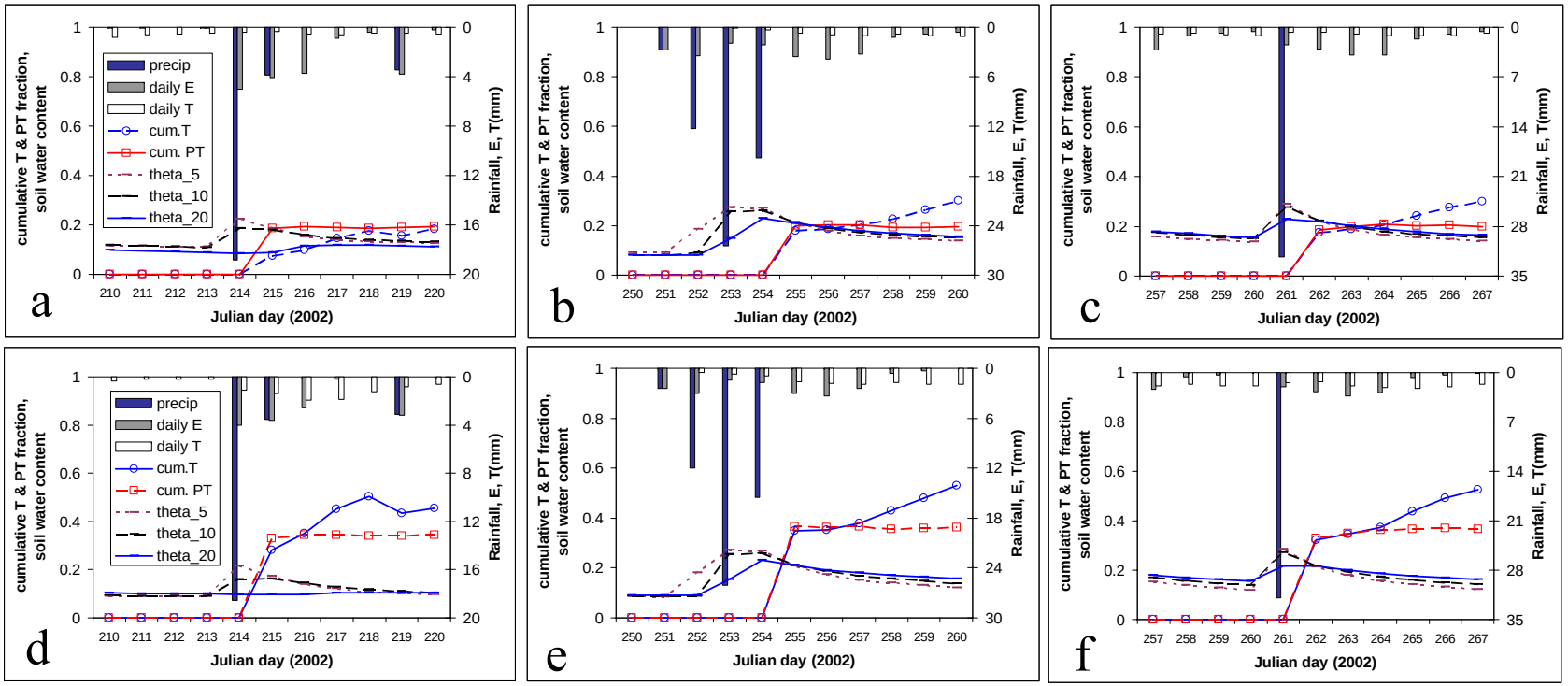

Figure 4.6 Simulated evaporation, transpiration, and soil water content at three depth (5 cm, 10 cm, and 20 cm) near rainfall events for two surfaces: creosotebush (a, b, c) and grass (d, e, f). The fraction of cumulative simulated transpiration and potential transpiration are calculated following the rainfall event at Julian day 214 (a, d), 254 (b, e), and 261 (c, f), respectively.

116

To examine why there are different temporal patterns of E and T partitioning following the rainfall event at Julian day 214, from those following the other two study rainfall events, let's look at the dynamics of E and T partitioning. The daily fraction of actual T is smaller than PT fraction (of the same time period) right after the rainfall event, and increases quickly (Figure 4.6). With a shallower root zone, the grass starts earlier than the shrub to compete for the very-shallow soil water against the evaporation process. The cumulative T fraction exceeds PT fraction for the grass surface a little quicker than for the shrub surface. For the two rainfall events at Julian days 254 and 261, the timing for cumulative T exceeding cumulative PT is similar for the two surfaces, around 3~4 days after the events. This timing is later for the rainfall event of Julian day 214 at the shrub surface. Two small intermediate rainfall events refresh the surface soil water for evaporation (Figure 4.6a), but are not immediately available for transpiration because of relatively deep root zone. However, for the grass surface, with its shallow root zone, the timing is earlier after this rainfall event (214^{th} day) than the other two events. Thus, different root zone depths and precipitation event characteristics help explain the different temporal patterns of E and T partitioning.

Next, let's look at actual E and T partitioning over longer time periods, e.g., on an annual basis (Figure 4.7). From the previous discussion on Figure 4.6, after each rainfall event, the cumulative actual T fraction increases above the PT fraction in a couple days because the surface soil turns dry. This situation of T fraction exceeding PT fraction exists for most of the year, or at least for the growing season. Thus, the long-term mean partitioning of actual E and T is different from the partitioning of potential E and T, with T fraction always larger than PT fraction. For the shrub surface, the T fraction of the

warm season (May~October, E=113mm, T=56mm) is close to that of the whole year (E=138mm, T=74mm), about 35% (Figure 4.7a). This is significantly larger than PT fraction (19%). The PT fraction for the warm season (PE=881mm, PT=205mm) is also similar to that for the whole year (PE=1340mm, PT=311mm). On the grass surface, the T fraction is 49% for the warm season (E=85mm, T=83mm), and 44% for the whole year (E=112mm, T=89mm) (Figure 4.7b). This is also larger than PT fraction of 36% (PE=747mm, PT=417mm) and 26% (PE=1198mm, PT=427mm) for the two periods, respectively.

The E and T partition that Boulanger [*2004*] estimated from soil water several days after one specific rainfall event for the shrub surface (16~21%) and for the grass surface (30-48%) are (coincidentally?) close to a potential partitioning rate for the warm season. They don't appear to apply for the long-term mean of actual E and T partitioning for these two surfaces at Sevilleta, either for the season or the year. Nonetheless, this isotopic study provides valuable information for further assessing E and T partitioning in these environments.

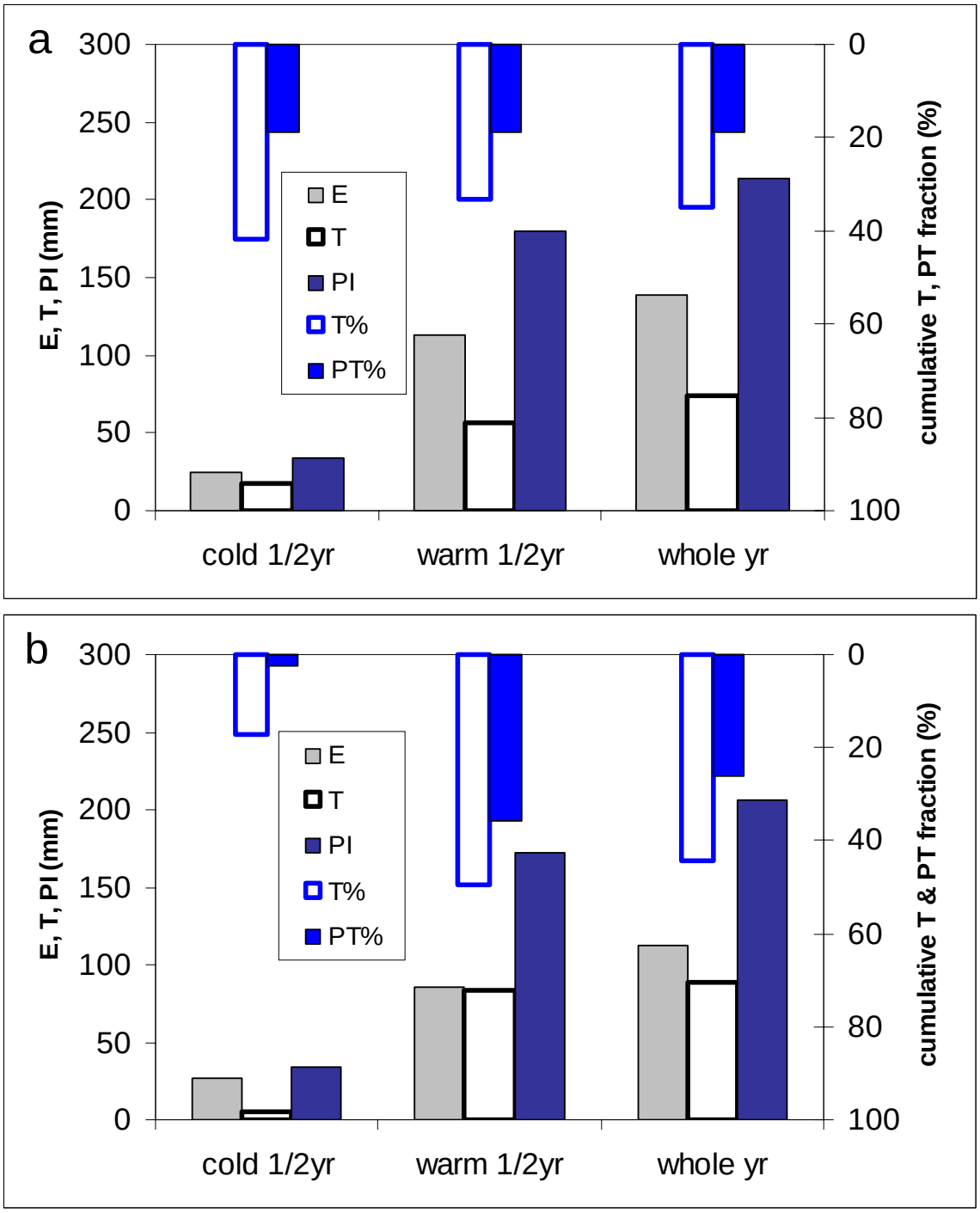

Figure 4.7 Partition of active precipitation water (PI=Precipitation –Interception) into evaporation and transpiration, and cumulative transpiration and potential transpiration, on two surfaces: creosotebush (a) and seasonal grass (b), evaluated for three different periods, with cold ½yr = November ~ April, and warm ½yr = May ~ October.

4.5.2 TVET testing with cottonwood and saltcedar surfaces along Rio Grande riparian corridor and the implications

The other field study, used to test the TVET model, was conducted at the cottonwood flooded site near Belen, and at the saltcedar flooded site on Bosque del Apache, both along the Rio Grande riparian corridor [e.g. *Cleverly et al., 2002*]. Cottonwood and saltcedar are two dominant types of vegetation in this environment. Their consumption of river water via evapotranspiration has been a concern for the water budget of the Rio Grande. Eight study sites have been established to study riparian ET by the Hydrogeoecology Group at the University of New Mexico led by Dr. Clifford Dahm [http://sevilleta.unm.edu/~cleverly/ bosqueET.html, visited July 2004]. Four sites are equipped with micrometeorological measurements, two for cottonwood and the other two for saltcedar. The cottonwood flooded site and the saltcedar flooded site were selected to test TVET model because flooded sites may have ET closer to PET. Cleverly et al. [*2002*] reported that ET at the flooded saltcedar site is 1.6 times that at the non-flooded site. It is reasonable to assume that in some period of the year, the actual ET at these flooded sites is equal or very close to the potential ET. Thus, the actual ET measured at these two flooded sites can be used to test the potential ET derived from the TVET model, i.e., the modeled potential ET should provide an upper bound to the measured actual ET. Different from the 'hard' test given in the last section, the test shown below is 'soft' because the model is calibrated.

Most micrometeorological data were downloaded from Cleverly's website, including precipitation, relative humidity, temperature, wind speed, and actual daily ET estimated from eddy covariance tower. Daily solar radiation data were download from NMSU database [http://weather-mirror.nmsu.edu/stations/, visited in July, 2004],

complimented with weather station #40 of Sevelleta LTER (some data of NMSU database was missed). It should be noted that the solar radiation was measured nearby, which may cause errors for some days in the year. The available vegetation parameters of both the cottonwood site and the saltcedar site included leaf area index and canopy height. However, the fractional vegetation cover, the minimum stomatal resistance, parameters for intra-canopy aerodynamic resistance, the timing of leaf development and deciduousness were not available. Fractional vegetation cover ($Fr = 0.9$), and the characteristic length of leaf width ($l_w = 0.1m$) were prescribed for both sites, and other parameters were adjusted for the year of 2002 (Appendix XIII). For the year of 2003, only the timing of leaf development and senescence were adjusted. Since both cottonwood and saltcedar are deciduous plants, four parameters were used to describe the leaf development and senescence, vg_1 = the day when the plants start to develop leaves, vg_2 = the day when the leaves reach their full stage, vg_3 = the day when the plants start their deciduous stage, vg_4 = the day that the plants stop transpiring, or plants enters dormancy of transpiration (Appendix XIII). The canopy leaf area index and equivalent canopy height were interpolated linearly between the full stage and the dormant stage of transpiration, while the minimum leaf stomatal resistance was exponentially interpolated between the two stages (Appendix XIII).

The modeling results are shown in Figure 4.8 for two sites, with minimum r_{ST} adjusted to fit the observation data at least for some time in the growing season of the year 2002. For the year 2003, only the four timing parameters (vg_1, vg_2, vg_3, vg_4) were adjusted. That the calibrated TVET-modeled PET well bounds the measured ET for the year of 2003 indicates reasonable predicting capability of the TVET model.

Next, let's compare PET of the two types of riparian vegetation. In comparing of the two sites, the transition period between full and dormant stage of transpiration is shorter for the cottonwood, while longer for the saltcedar (Figure 4.9). If the modeled PET represents realistic potential ET for these two sites, the duration for cottonwood at potential full transpiration stage exceeds 5 months, and the duration of saltcedar, however, is only a little over 3 months. Consequently, the maximum water that the vegetation could transpire in a year is about 1250 mm for the cottonwood site and 1000 mm for the saltcedar site.

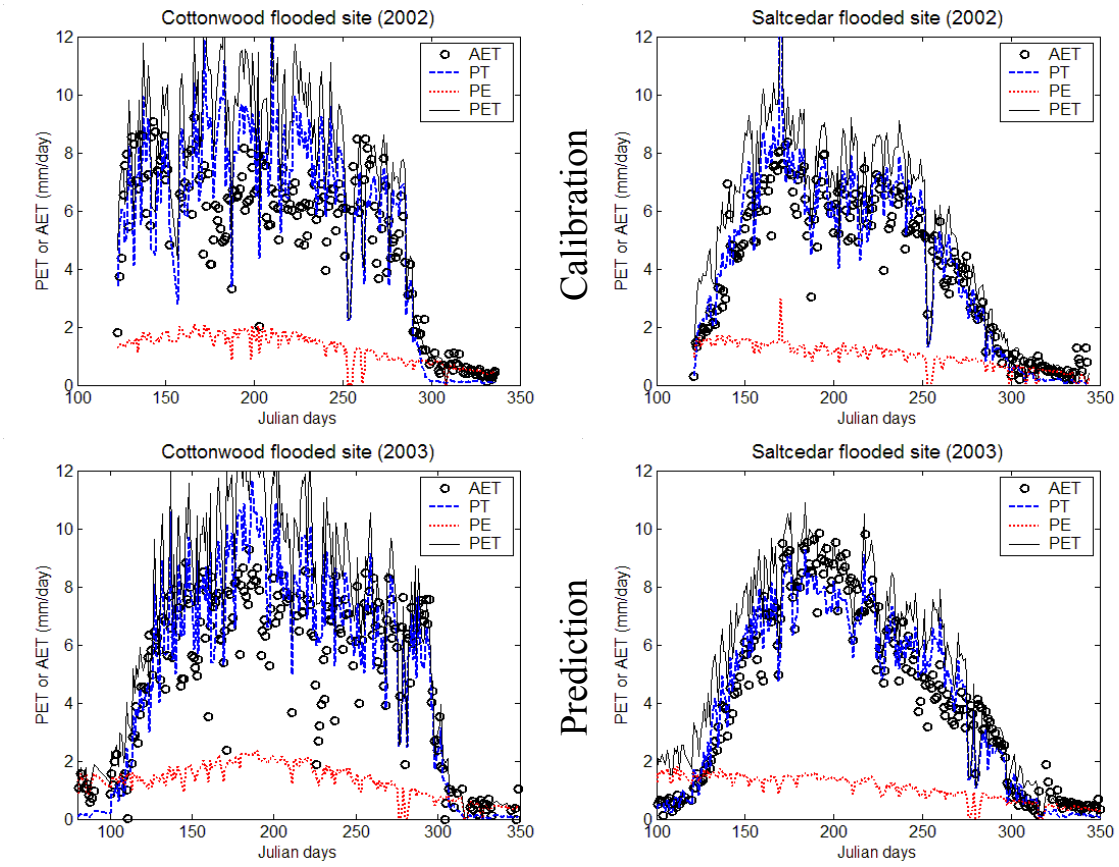

Figure 4.8 The TVET model results for the cottonwood flooded site and the saltcedar flooded site along the Rio Grande, New Mexico. The model was calibrated with 2002 observed actual ET data (top), and used for predicting 2003 potential ET in comparison to the actual ET (bottom).

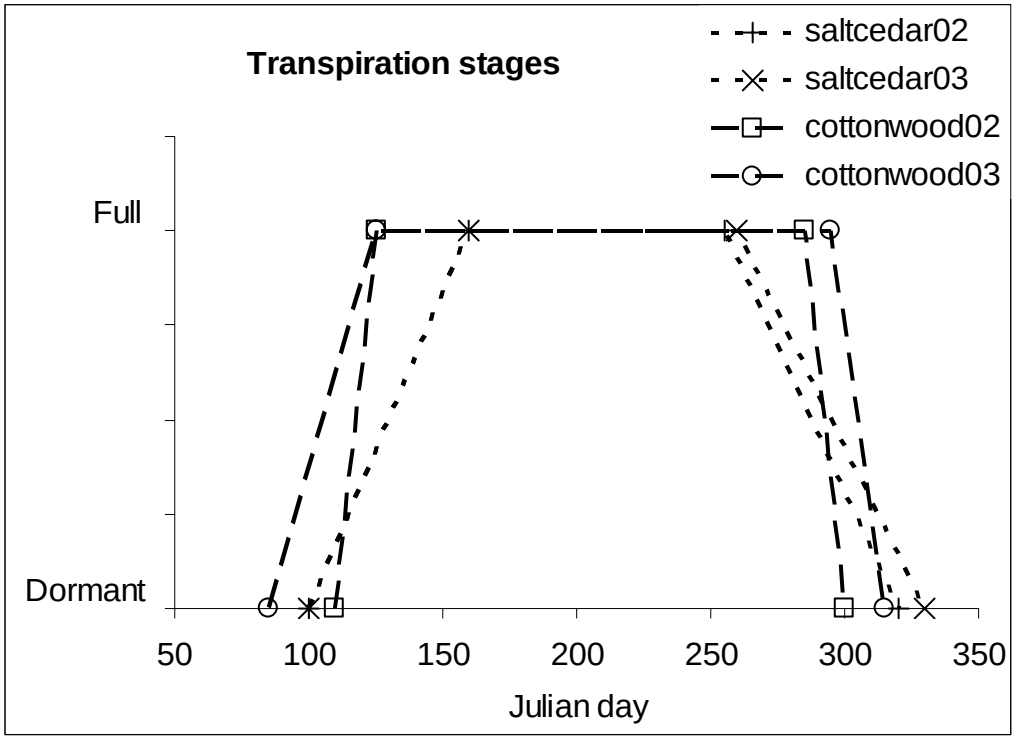

Figure 4.9 TVET-resulted transition of transpiration stages for the cottonwood flooded site and the saltcedar flooded site along the Rio Grande, New Mexico. "02" in the legend means the year 2002, and 03 the year 2003.

4.6 Comparisons of PET models

The comparison of five PET models is shown in Table 1. The models are ordered in the degree of complexity. The Hargreaves model is the simplest one. It will be extended to incorporate slope steepness and aspect effects, and used for situations of low spatial and temporal resolution in this dissertation (Chapter 7). As mentioned earlier, the Priestley-Taylor model cannot be adjusted for site aridity effect, and will not be used in this study.

The PM model was initially developed for the surface with closed vegetation coverage. It is not an appropriate model to generate potential ET for a sparsely vegetated surface. However, if the data are insufficient to capture surface complexity, the reference ET is an acceptable substitute for the surface potential ET. In this situation, the PM model is used in this dissertation. The example case is in Chapter 6, for which the slope effects are negligible, and the PET is calculated in high temporal resolution.

Data requirements for the TVET and SW models are similar if the optional Jarvis-type function in TVET model is turned off. As discussed earlier, the TVET model, a hybrid of the layer and patch approaches, has simpler formulae to the SW model. In addition, the TVET model develops expressions of aerodynamic resistances for naturally vegetated surfaces, and considers the effects of terrain aspect and steepness. TVET will be used in this dissertation for hillslope water partitioning simulations (Chapter 5).

Table 4.3 Data intensity, availability and uncertainty, and the model capacity for selected PET models

Models	Data requirement			Data quality[1]	Model capacity for PET
	meteorological	vegetation	surface		
Hargreaves	T_{max}, T_{min}			5	Weekly or longer, flat surface, can be extended for sloped surface
Priestley-Taylor	T_{mean}			5	Weekly or longer, be extended for sloped surface
	R_n			4	
			G	3	
PM	T_{max}, T_{min}	Height	elev. long. lat.	5	Daily, or hourly, vegetation-type effect, be extended for sloped surface and vegetation coverage effect
	R_n, u, RH		albedo	4	
			r_a	5, 3	
		r_c	G	3	
SW	T_{max}, T_{min}	Height	elev. long. lat.	5	Daily, vegetation-type and coverage effect, be extended for sloped surface
	R_n, u, RH	L	albedo	4	
			r_a^a , r_a^s	4, 3	
		r_a^c, r_s^c		3, 3	
		k_c,	G, r_s^s	3	
TVET	T_{max}, T_{min} , P	Height, L_c	elev. long. lat.	5	Daily, sloped surface, vegetation-type and coverage effects, rainfall interception, snow and snowmelt, environmental stress
			slope par.	5	
	R_n, u, RH	Fr, albedo	albedo	4	
			r_a^a , r_a^s, snow	5, 3	
		r_a^c, r_s^c		3, 3	
		k_c	G	3	
		intercept. par		3	
		Javis-type parameters		1~2	

Note: The numbers between 1~5 are used to relatively represent data availability and uncertainty. The larger the number is, the better the availability and certainty. The parameters listed on the same line have similar data quality. For those lines with two numbers, the first number is data availability to derive the parameter value, and the second is the uncertainty level of the derived parameter value.

125

4.7 Root macropore modeling

4.7.1 Macropore flow and root-induced macropores

Macropore flow in shallow soils is a very common hydrologic phenomenon, drawing much scientific attention [e.g., *Beven & Germann, 1982*]. The term 'macropore' is usually used to describe the pore which has significant larger size than an average matrix pore size, and allows non-equilibrium channeling flow [*Beven & Germann, 1982*]. The macropores can be formed by soil fauna, plant roots, and cracks and fissures and natural soil pipes [*Beven & German, 1982*]. Most macropores are short in length, and discontinuous [*Noguchi et al., 1999*]. Connecting these macropores to form pipe flow requires frequent flow events in the soil [*Noguchi, et al., 1999*], which often occurs in humid regions [e.g., *Burns et al., 1998; Uchida et al., 2004*].

It has long been noticed that vegetation increases soil infiltration capacity for semiarid vegetation cover [reviewed by *Wilcox et al., 2003*]. The San Dimas large lysimeter experiments in California showed that long-term infiltration of vegetated lysimeters were over twice that of bare soil lysimeters [*Patric, 1961*]. A number of factors may account for the increased infiltrability under vegetation canopies [reviewed by *Wilcox et al., 2003*], including modified soil texture due to the canopy-sheltering and higher organic matter content, and a more developed macropore network [*Parsons et al., 1992; Dunkerley, 2000; Bhark & Small, 2003*]. The root-induced preferential flow paths are the major components of a macropore network. For example, Newman et al. [*2004*] observed root macropore flow in a low-permeability (lab measured) soil mantle at a ponderosa pine hillslope (Chapter 6). At one of Renee Sandvig's study sites near Magdalena [*Sandvig, 2005*], it was also observed that the soil surrounding a ponderosa pine root was moist, while dry otherwise, at a depth of about 40 cm (Figure 4.10). This

suggests that root-induced macropore (simplified as root macropore) plays an important role in transmitting water in the root zone. However, the lab measurements of small soil cores, e.g., the common steel ring of a diameter around 5 cm, do not capture the root macropore hydraulic properties because the small volume of core samples disconnects root macropores which were connected in the field (Chapter 6).

With its larger continuity, preferential flow along the perimeter of live and dead roots may play an important role in partitioning of water among surface runoff, ET, interflow and deep percolation (potential groundwater recharge) in semiarid environments. This section discusses numerical representation of root macropore effects.

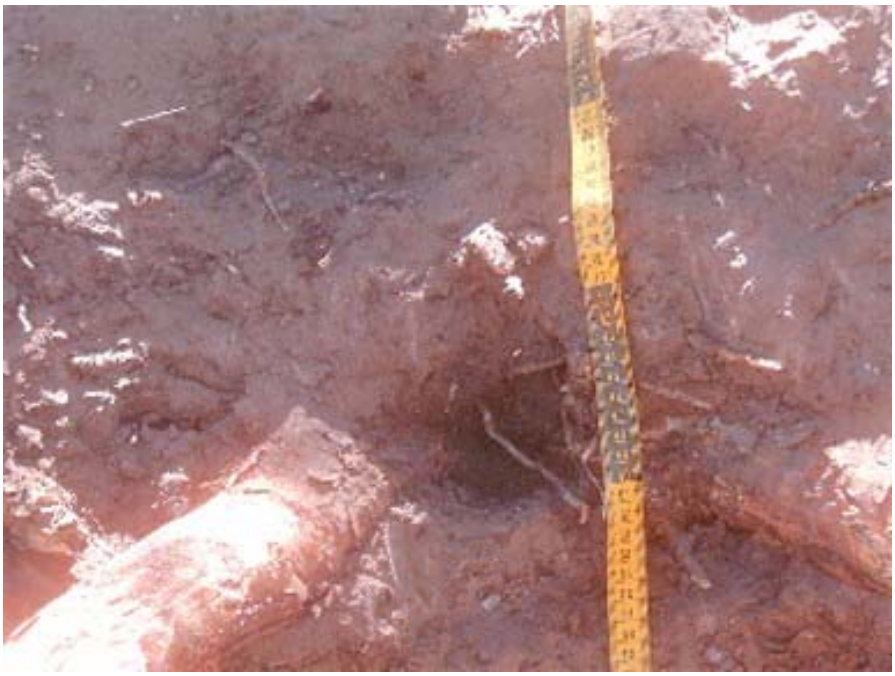

Figure 4.10 Moist soil was observed between these two ponderosa pine roots at a depth of 40 cm.

4.7.2 Root macropore modeling

Hydraulic modeling provides an optional way to estimate the effects of root macropores on water transmission in the shallow subsurface (e.g., root zone). However, modeling root macropore flow is difficult because (1) representation of root orientation and connection is very complex, and (2) the root orientation leads to anisotropic hydraulic conductivity, which is saturation-dependent (when the soil is wet, the water flows preferentially along the root; when it is dry, the water flows along the matrix). Because of complex connection and orientation, a discrete approach is not appropriate to model root macropore flow in this dissertation. Because of distinct hydraulic characteristics between the soil matrix and root macropores, a single continuum model may not be appropriate either. A dual permeability model (§5.2.1) seems to be an appropriate approach to model variably saturated water flow in the soil with root macropores, if the macropore continuum can be represented anisotropically (because of dominant root orientations). Multiple continuums (≥3) models can be used if the different behaviors between different-size macropores are simulated.

4.7.3 A simple root macropore model

Because HYDRUS does not have a dual permeability capability, a crude single continuum model is developed and presented here. This model relates hydraulic conductivity, due to root-induced macropores, to field measured root density. The root density (ρ_r) is often measured on transects, and reported as number of roots per unit area for each root-size class. With the assumption that voids occur surrounding the roots, with an aperture proportional to the root size (Figure 4.11), the volumetric fraction of the roots and their surrounding apertures is given by

$$n_{root} = \sum_{i=1}^{size\_class} [\rho_r^i \frac{\pi}{4}(D_i + 2b_i)^2] \quad (4.50)$$

where ρ_r^i is the root density of root-size class i, D_i is mean root diameter for the class, b_i is mean aperture thickness surrounding the root for the class. The bulk hydraulic conductivity of the soil is then given by

$$K_{bulk} = K_{root} n_{root} + K_{matrix}(1 - n_{root}) \quad (4.51)$$

where K_{root} is the hydraulic conductivity of the fractional area (in 2D transect) occupied by roots and their surrounding voids, and K_{matrix} is the hydraulic conductivity of the fractional area occupied by the soil matrix. K_{matrix} can be measured from the soil core sample. Next, we need to estimate K_{root} of the ensemble of all roots.

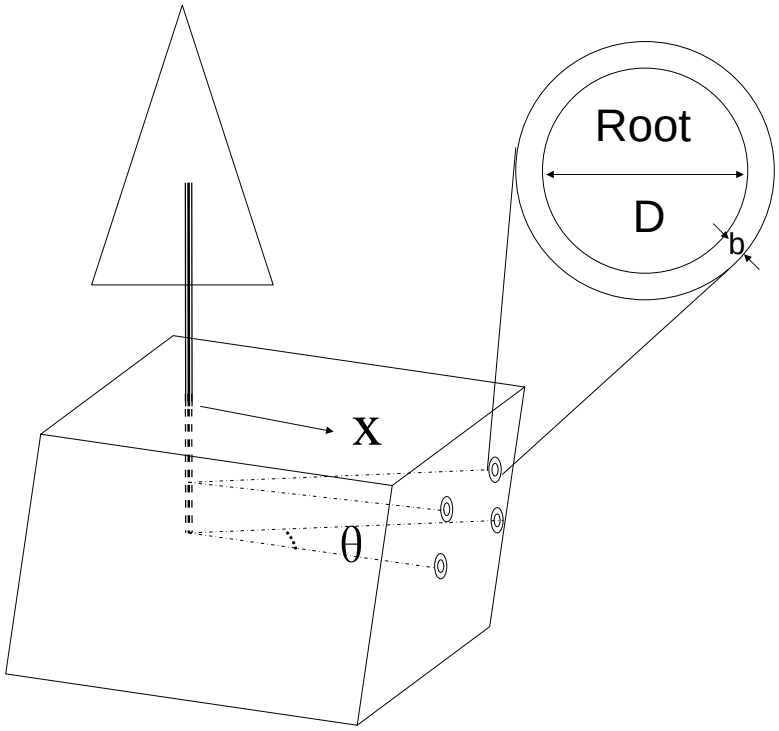

Figure 4.11 Schematic diagram of ideal root distribution, with root radially and uniformly distributed on planes parallel to the slope surface.

K_{root} is saturation-dependent, and difficult to obtain. But, the saturated K_{root} can be calculated by the following steps. First, lets imagine a transect orthogonal to the slope direction (Figure 4.11). Given a hydraulic gradient J under the saturated condition, where $J = -dh/dl$ [*Bear, 1972*], along the longitudinal direction (x) of the slope (Figure 4.11), the volumetric flow rate in one root macropore (parallel to the slope surface) with an angle (θ) to the direction x on the plane parallel to the slope surface, is determined by Equation (4.50), based on Pnueli and Gutfinger [*1992*].

$$Q_i = \frac{J\cos^2\theta}{\tau}\frac{\rho g\pi(D_i+2b_i)^4}{128\mu}\left[1-\left(\frac{D_i}{D_i+2b_i}\right)^4-\frac{\left[1-\left(\frac{D_i}{D_i+2b_i}\right)^2\right]^2}{\ln\left(\frac{D_i+2b_i}{D_i}\right)}\right] \quad (4.52)$$

where J is the hydraulic gradient in direction x (Figure 4.11), θ is the angle between the root and x, τ is the tortuosity of the root, which is defined as the ratio of the actual root length over the linear length. For simplicity, a symbol is used to substitute for the quantity in the big square bracket of (4.52) in the derivation below.

Equation (4.52) gives the saturated volumetric flow along an individual root in the longitudinal direction of the slope. The actual roots are a collection of roots with different sizes and in different directions. First, the roots of different sizes are divided into several root-size classes. Each class has an equivalent root size, i.e., root diameter. Second, it is assumed that roots are distributed uniformly in θ on the planes at different depths parallel to the slope surface. With the simplification and assumption, the volumetric flow rate of one root-size class j, under the saturated condition, is given by

$$Q_j = \int_{-\frac{\pi}{2}}^{\frac{\pi}{2}} \frac{n_j}{\pi} \frac{(J\cos^2\theta)}{\tau} \frac{\rho g \pi (D_j + 2b_j)^4}{128\mu} C_j d\theta = \frac{n_j}{2} \frac{J}{\tau} \frac{\rho g \pi (D_j + 2b_j)^4}{128\mu} C_j \quad (4.53)$$

where n_j is the number of class-j roots observed on the transect, and

$$C_j = \left[1 - \left(\frac{D_j}{D_j + 2b_j}\right)^4 - \frac{\left[1 - \left(\frac{D_j}{D_j + 2b_j}\right)^2\right]^2}{\ln\left(\frac{D_j + 2b_j}{D_j}\right)} \right]$$

The total volumetric flow rate along all roots is the sum of flow rate in all individual root-size classes, given by

$$Q = \sum_{root\_classes} Q_j = \frac{J}{\tau} \frac{\rho g \pi}{256 \mu} \sum [C_j (D_j + 2b_j)^4 n_j] \tag{4.54}$$

Now, we have the volumetric flow rate, due to all root macropores, along the longitudinal direction of the slope. With the total volumetric flow rate and the total root-cross-section areas, the saturated hydraulic conductivity of root macropores is determined by

$$K_{root} = \frac{Q}{JA} = \frac{\rho g \pi}{256 \mu \tau} \frac{\sum [C_j (D_j + 2b_j)^4 n_j]}{\sum [\frac{1}{4} \pi n_j (D_j + 2b_j)^2]} \tag{4.55}$$

This equation gives saturated hydraulic conductivity of root macropores in the longitudinal direction (x) of the slope, assuming that all roots are in planes parallel to the slope surface.

However, the roots may intercept the slope at some angle, rather than be parallel to the slope. In this situation, root macropores contribute to the water flow at z direction, where z is downward orthogonal to x, leading to non-zero hydraulic conductivity in z direction, approximated by

$$Kz_{root} = \frac{\rho g \pi \sin \beta}{256 \mu \tau} \frac{\sum [C_j (D_j + 2b_j)^4 n_j]}{\sum [\frac{1}{4} \pi n_j (D_j + 2b_j)^2]} \tag{4.56}$$

where β is the equivalent root dip angle relative to the slope surface. This situation modifies the saturated hydraulic conductivity in x direction as well, resulting in

$$Kx_{root} = \frac{\rho g \pi \cos\beta}{256\mu\tau} \frac{\sum[C_j (D_j + 2b_j)^4 n_j]}{\sum[\frac{1}{4}\pi n_j (D_j + 2b_j)^2]} \tag{4.57}$$

Similar to equation (4.51), the bulk saturated hydraulic conductivities in x and z directions are given by

$$Kz_{bulk} = Kz_{root} n_{root} + K_{matrix}(1 - n_{root}) \tag{4.58}$$

and

$$Kx_{bulk} = Kx_{root} n_{root} + K_{matrix}(1 - n_{root}) \tag{4.59}$$

For the single continuum model, with (4.58) and (4.59), we can calculate unsaturated bulk hydraulic conductivity based on a soil water retention curve. It should be noted that the bulk hydraulic conductivity obtained this way may be overestimated for some near-saturation conditions (when flow in large macropores stops). Equations (4.56) and (4.57) developed here are also useful for the composite continuum model (with anisotropic properties) and dual permeability model (introduced in §5.2.1). Because the dual permeability model is not available in HYDRUS, and not used for this dissertation, additional parameterization is not discussed.

The root-macropore model presented here explicitly relates the saturated hydraulic conductivity to the root distribution in the soil. It is reasonable to assume that

the increased soil hydraulic conductivity due to the modification of soil structure by the physical, chemical and biological processes of the vegetation, and the soil microbes and animals is positive correlated to the root density in the soil. With this assumption, the root-macropore model can be calibrated to implicitly include other factors leading to further increases of soil hydraulic conductivity.

References

Allen, C.D. and D.D. Breshears (1998), Drought-induced shift of a forest-woodland ecotone: Rapid landscape response to climate variation. *Proceedings of National Academy Sciences of the United States of America*, 95, 14839-14842.

Allen, R.G., Pereira, L.S., Raes, D., Smith, M. (1998), Crop evapotranspiration – Guidelines for computing crop water requirements, Food and Agriculture Organization of the United Nations Irrigation and drainage paper 56.

Allen, R.G. (2000), Using the FAO-56 dual crop coefficient method over an irrigated region as part of an evapotranspiration intercomparison study, *Journal of Hydrology*, 229, 27-41.

Bear, J. (1972), *Dynamics of Fluids in Porous Media*, New York: Dover.

Beven, K. and P. Germann (1982), Macropores and water flow in soils, *Water Resources Research*, 18, no.5, 1311-1325.

Bhark, E.W., and E.E. Small (2003), Association between plant canopies and the spatial patterns of infiltration in shrubland and grassland of the Chihuahuan Desert, New Mexico, *Ecosystems*, 6(2), 185-196.

Boulanger, J.R. (2004), Stable isotope partitioning of evapotranspiration across a shrub-grass ecotone following a precipitation event, Sevilleta National Wildlife Refuge, USA, Master Thesis, New Mexico Institute of Mining and Technology.

Brandes, D., and B.P. Wilcox (2000), Evapotranspiration and soil moisture dynamics on a semiarid ponderosa pine hillslope, *Journal of the American Water Resources Association*, 36(5), 965-974.

Burns, D.A., R.P. Hooper, J.J. McDonnell, J.E. Freer, C. Kendall, K. Beven (1998), Base cation concentrations in subsurface flow from a forested hillslope: The role of flushing frequency. *Water Resources Research*, 34(12), 3535-3544

Choudhury, B.J. and J.L. Monteith (1988), A four-layer model for the heat budget of homogeneous land surfaces. *Quarterly Journal of the Royal Meteorological Society*, 114, 373-398.

Cleverly, J.R., C.N. Dahm, J.R. Thibault, D.J. Gilroy, and J.E.A. Coonrod (2002), Seasonal estimates of actual evapo-transpiration from *Tamarix ramosissima* stands using three-dimensional eddy covariance. *Journal of Arid Environments*, 52, 181-197.

Dingman, S. Lawrence (1994), *Physical Hydrology*, Prentice-Hall, Inc. 575p

Droogers, P. and G. Allen (2002), Estimating reference evapotranspiration under inaccurate data conditions, *Irr. Drain. Sys., 16,* 33-45.

Duffie, J.A., and W.A. Beckman (199), *Solar engineering of thermal processes*, New York, Wiley, 2nd edition, 919p.

Dunkerley, D. (2000), Hydorlogic effects of dryland shrubs: defining the spatial extent of modified soil water uptake rates at an Australian desert site, *Journal of Arid Environment*, 45, 159-172.

Eagleson, P.S. (2002), *Ecohydrology: Darwinian expression of vegetation form and function*, Cambridge University Press.

Feddes, R., P.J. Kowalik, and H. Zaradny (1978), *Simulation of Field Water Use and Crop Yield*, John Wiley & Sons, New York, NY.

Gee, G.W., P.J. Wierenga, B.J. Andraski, M.H. Young, M.J. Fayer, and M.L. Rockhold (1994), Variations in water balance and recharge potential at three western desert sites, *Soil Science Society of America Journal*, 58, 63-72.

Guswa, A. J., M. A. Celia, and I. Rodriquez-Iturbe (2002), Models of soil moisture dynamics in ecohydrology: a comparative study, *Wat. Resour. Res., 38*, 1-15.

Hargreaves, G.L., G.H. Hargreaves, and J.P. Riley (1985a), Irrigation water requirements for Senegal River Basin, *Journal of Irrigation and Drainage Engineering*, 111(3), 265-275.

Hargreaves, G.H., and Z.A. Samani (1985b), Reference crop evapotranspiration from temperature, *Applied Engineering in Agriculture*, 1(2),96-99.

Hargreave, G.H., F.ASCE, and R.G. Allen (2003), History and evaluation of Hargreaves evapotranspiration equation, *Journal of Irrigation and Drainage Engineering*, 129(1), 53-63.

Hollinger, D.Y., F.M. Kelliher, E.D., Schulze, and B.M.M. Köstner (1994), Coupling of tree transpiration to atmospheric turbulence, *Nature*, 371, 60-62.

Jarvis, P.G. (1976), Interpretation of variations in leaf water potential and stomatal conductance found in canopies in field, *Philosophical Transactions of the Royal Society of London Series B-Biological Sciences*, 273, 593-610.

Jensen, D.T., G.H. Hargreaves, B. Temesgen, and R.G. Allen (1997), Computation of ET0 under nonideal conditions, *Journal of Irrigation and Drainage Engineering*, 394-400.

Kearns, A., and J.M.H. Hendrickx (1998), Temporal variability of diffuse groundwater recharge in New Mexico, New Mexico Water Resources Research Institute, Report 309, New Mexico State University, Las Cruse.

Kite, G.W., and P. Droogers (2000), Comparing evapotranspiration estimates from satellites, hydrological models and field data, *Journal of Hydrology*, 229, 3-18.

Kurc, S.A., and E.E. Small (2004), Dynamics of evapotranspiration in semiarid grassland and shrubland ecosystems during the summer monsoon season, central New Mexico, *Water Resources Research*, 40, W09305, doi: 10.1029/2004WR003068.

Kustas, W.P., and J.M. Norman (1997), A two-source approach for estimating turbulent fluxes using multiple angel thermal infrared observations, *Water Resources Research*, 33 1495-1508.

Lhomme, J.P., E. Elguero, A., Chehbouni, and G. Boulet, (1998), Stomatal control of transpiration: Examination of Monteith's formulation of canopy resistance, *Water Resources Research*, 34, 2301-2308.

Lhomme, J. P., and A. Chehbouni (1999), Comments on dual-source vegetation-atmospheric transfer models. *Agriculture and Forest Meteorology*, 94, 269-273.

Liu, B.Y.H., and R.C. Jordan, (1962), Daily insolation on surfaces tilted toward the equator, *ASHRAE Journal*, 3, 53.

Mast, J.N., T.T. Veblen, and Y.B. Linhart (1998), Disturbance and climatic influences on age structure of ponderosa pine at the pine/grass ecotone, Colorado Front Range. *Journal of Biogeography*, 25(4), 743-755.

Monteith, J.L. (1965), Evaporation and environment, in *The State and Movement of Water in Living Organisms*, Sympos. Soc. Exper. Biol. 19, edited by G.E. Fogg, 205-234, Academic, San Diego, California, U.S.A.

Mo, X., S., Liu, Z. Lin, and W. Zhao (2004), Simulating temporal and spatial variation of evapotranspiration over the Lushi basin, *Journal of Hydrology*, 285, 125-142.

Moore, D. (2004), Meteorology Data for the Sevilleta National Wildlife Refuge, NM (1987-2003). Sevilleta Long Term Ecological Research Project Database. http://sev.lternet.edu [July 22nd, 2004].

Newman, B.D, A.R. Campbell, and B.P. Wilcox (1998), Lateral subsurface flow pathways in a semiarid ponderosa pine hillslope, *Water Resources Research*, 34 (12), 3485-3496.

Newman, B.D., B.P. Wilcox, and R.C.Graham (2004), Snowmelt-driven macropore lfow and soil saturation in a semiarid forest, *Hydrological Processes*, 18 (5), 1035-1042.

Noguchi, S., Y. Tsuboyama, R.C. Sidel, and I. Hosoda (1999), Morphological characteristics of macropores and the distribution of preferential flow pathways in a forested slope segment, *Soil Science Society of America Journal*, 63, 1413-1423.

Parsons, A.J., A.D. Abrahams, and J.R. Simanton (1992), Microtopography and soil-surface materials on semi-arid piedmont hillslopes, southern Arizona, *Journal of Arid Environment,* 22, 107-115.

Patric J. H. (1961),The San Dimas large lysimeters, *Journal of Soil and Water Conservation*, 16(1), 13-17.

Penman, H.L. (1948), Natural evaporation from open water, bare soil, and grass, *Proceeding of Royal Society London*, Ser. A., 193, 120-146.

Phillips, F.M., M.A. Walvoord, and E.E. Small (2004), Effects of environmental change on groundwater recharge in the Desert Southwest, in *Groundwater Recharge in a Desert Environment: The Southwestern United States*, edited by J.F. Hogan, F.M. Phillips, and B.R. Scanlon, Water Science and Applications Series, vol. 9, American Geophysical Union, Washington, D.C., 273-294.

Pneuli, D., and C. Gutfinger (1992), *Fluid Mechanics*, Cambridge University Press, 496p.

Pockman, W.T., and J. S. Sperry (2000), Vulnerbility to xylem cavitation and the distribution of Sonoran Desert vegetation, *American Journal of Botany*, 87(9), 1287-1299.

Priestley, C.H.B., and R.J. Taylor (1972), On the assessment of surface heat flux and evaporation using large-scale parameters, *Monthly Weather Review*, 100, 81-92

Rodriguez_Iturbe, I., A. Porporato, L.Ridolfi, V.Isham, and D.R. Cox (1999), Probabilistic modeling of water balance at a point: The role of climate, soil, and vegetation, *Proceedings of Royal Society of London*, Series A, 455, 3789-3805.

Sandvig, R. (2005), Ecohydrological controls on soil-moisture fluxes in arid vadose zones, Master Thesis, New Mexico Institute of Mining and Technology, Socorro, New Mexico.

SAHRA (2004), SAHRA Strategic Plan, unpublished document

Shuttleworth, W.J., and J.S. Wallace (1985), Evaporation from sparse crops-an energy combination theory, *Quarterly Journal of Royal Meteorological Society*, 111: 839-855.

Shuttleworth, W.J. (1993), Evaporation, in Maidment, D.R. (edit): *Handbook of Hydrology*, chapter 4, New York: McGraw-Hill.

Simunek, J., M. Sejna, and M. Th. Van Genuchten (1998), The HYDRUS-1D software package for simulating the one-dimensional movement of water, heat, and multiple solutes in variably saturated media. Version 2.0, IGWMC-TPS-70, Interational Ground Water Modeling Software, International Ground Water Modeling Center, Golden, CO.

Small, E.E. (2005), Climatic controls on diffuse groundwater recharge in semiarid environments of the southwestern United States, *Water Resources Research*, 41 (4), W04012, doi:10.1029/2004WR003193.

Stannard, D.I. (1993), Comparison of Penman-Monteith, Shuttleworth-Wallace, and modified Priestley-Taylor evapotranspiration models for wildland vegetation in semiarid rangeland, *Water Resources Research*, 29(5), 1379-1392.

Stewart, R.B., and W.R. Rouse (1976), A simple equation for determining the evaporation from shallow lakes and ponds, *Water Resources Research*, 12, 623-628.

Stewart, J.B. (1988), Modeling surface conductance of pine forest, *Agric. For. Meteorol.*, 43, 19-37.

Temesgen, B., R.G. Allen, and D.T. Jensen (1999), Adjusting temperature parameters to reflect well-watered conditions, *Journal of Irrigation and Drainage Engineering*, 125(1), 26-33.

Uchida, T, Y. Asano, T. Mizuyama, J.J. McDonnell (2004), Role of upslope soil pore pressure on lateral subsurface storm flow dynamics, *Water Resources Research,* 40(12), p.W12401.

Van Auken, O.W. (2000), Shrub invasions of North American semiarid grasslands. *Annual Review of Ecology and Systematics*, 31, 197-215.

van Genuchten, M. Th. (1987), A numerical model for water and solute movement in and below the root zone. Research Report No 121, U.S. Salinity laboratory, USDA, ARS, Riverside, California.

Walvoord, M., F.M. Phillips, S.W. Tyler, and P.C. Hartsough (2002), Deep arid system hydrodynamics, Part 2: Application to paleohydrologic reconstruction using vados-zone profiles from the northern Mojave Desert, *Water Resources Research*, 38, 1291, doi: 10/1029/2001WR000925.

Walvoord, M.A., and B.R. Scanlon (2004), Hydrologic processes in deep vadose zones in interdrainage arid environments, in *Groundwater Recharge in a Desert Environment: The Southwestern United States*, edited by J.F. Hogan, F.M. Phillips, and B.R. Scanlon, Water Science and Applications Series, vol. 9, American Geophysical Union, Washington, D.C., 15-28.

Wigmosta, M.S., L.W.Vail, and D.P. Lettenmaier, 1994. A distributed hydrology-vegetation model for complex terrain, *Water Resources Research*, v.30, 1665-1679.

Wilcox, B.P., B.D.Newman, D.Brandes, D.W.Davenport, and K. Reid, 1997. Runoff from a semiarid ponderosa pine hillslope in New Mexico, *Water Resources Research*, *33*, no.10, 2301-2314.

Wilcox, B.P., D. D., Breshears, and H.J. Turin, 2003. Hydraulic conductivity in a pinyon-juniper woodland: influence of vegetation, *Soil Science Society of America Journal*, 67, 1243-1249.

Winter, T.C., D.O. Rosenberry, and A.M. Sturrock, 1995. Evaluation of 11 equations for determining evaporation for a small lake in the north central United States, *Water Resources Research*, 31(4), 983-993.

CHAPTER 5 NUMERICAL INVESTIGATION OF WATER PARTITIONING ON MOUNTAIN HILLSLOPES IN SEMIARID REGIONS, WITH EMPHASIS ON WATER PERCOLATION ACROSS THE SOIL-BEDROCK INTERFACE

5.1 Introduction

The previous three chapters (2, 3, and 4) quantify atmospheric boundary conditions in mountains. Now, we will examine the system on and below the ground - a couple of meters below the surface, with a focus on percolation across the soil-bedrock interface. In this chapter, the dynamic near-surface water partitioning processes are investigated via HYDRUS-2D modeling, coupled with the TVET model. Various factors influencing water partitioning are examined, including slope steepness and aspect, bedrock characteristics, soil characteristics, vegetation coverage, and local climate. The considered hydrologic processes include surface runoff, infiltration, evapotranspiration, interflow, macropore flow, and bedrock percolation (water downward moving across the soil-bedrock interface). The objectives are (1) to improve understanding of water partitioning on mountain hillslopes; (2) to determine the dominant factors controlling bedrock percolation and evapotranspiration, providing guidance to classify hydrologically similar response units (HRUs, or hydrotopes as in Jeton and Smith [*1993*] and Gurtz et al. [*1999*]) for large-scale hydrologic modeling in mountains (see Chapter 7); (3) to explore vegetation impacts on mountain hydrologic processes, as well as hydrologic controls on topographically-induced ecotones; and (4) to generate quantitative relationships for mapping mountain-block recharge in Chapter 7.

Hillslope water partitioning has been intensively studied by surface hydrologists [e.g., *Kirkby, 1988; McGlynn et al., 2002; Ridolfi et al., 2003*]. The study shown here is different from most previous studies in that it treats bedrock as a permeable unit, rather than an impermeable barrier, and in that it couples near-surface hydrologic processes to surface and atmospheric boundary conditions. Below is background for this study.

Groundwater hydrologists commonly consider and study the contribution of mountains to groundwater replenishment of the basin at the mountain-front. The few studies that extend to the mountain treat the mountain surface as a prescribed flux boundary, without considering the dynamics of hillslope processes in the shallow soil layer. A recent recharge study at a field infiltration site on Yucca Mountain [*Pan et al., 2005*] indicates that neglecting these shallow-soil hydrologic processes can lead to significant error in simulating groundwater.

In contrast, hillslope hydrologists often focus only on the thin soil layer above the bedrock. Few studies on mountain hillslopes have examined the partitioning of water between shallow processes (surface runoff, ET, interflow, etc.) and deep percolation to the mountain. In this chapter, we use the term "percolation" to describe the downward water flux passing over the soil-bedrock interface, and "interflow" to represent the downslope lateral water movement in the soil. Very often, percolation is neglected based on the estimated low bedrock permeability, the presence of a low permeable soil layer above the bedrock, or the presence of slope-parallel soil pipes above the bedrock. However, observations suggest that this assumption may be naive. For example, considerable rainfall percolates through fractured sedimentary rock into a mountain tunnel at Yura, Wakayama Prefecture, Western Japan [*Shimojima et al., 1993*]. Another

tunnel observation in gneissic bedrock in France demonstrates how fractures improve percolation into the bedrock. In this tunnel, the fracture zones have an average percolation rate of 2.4 mm/day, in contrast to 0.024 mm/day in the host gneiss zone [*Pili et al, 2004*]. Groundwater flow in bedrock of mountain watersheds in North America is reported by Wilson and Dietrich [*1987*], Anderson et al. [*1997*], and Montgomery et al. [*1997*], and in Japan by Onda et al. [*2001*]. Recently, using geochemical and temperature as tracers, Earman [*2004*] demonstrated that bedrock percolation at high elevations contributes to the groundwater at low elevations in the Chiricahua Mountains, Arizona. These observations suggest that there are cases of an appreciable flux of water across the soil-bedrock interface into the underlying deep mountain mass. They also suggest that the bedrock permeability at these sites must be large enough to allow significant percolation to occur.

For a hillslope with bedrock permeable enough for significant percolation, soil water storage determines whether the percolation occurs. Factors, such as local climate, soil surface and bedrock surface topography (slope and depression), slope configurations (plan and profile curvatures), slope aspect, soil properties (matrix and macropores), and vegetation coverage, influence temporal and spatial soil moisture distributions [*Petch, 1988; Crave and Gascuel-Odoux, 1997; Grayson et al., 1997; Yeakley et al. 1998; Puigdefabregas et al., 1998; Gomez-Plaza et al., 2001; Qiu et al., 2001; Freer et al., 1997; Freer et al., 2002; Chaplot and Walter, 2003; Hawke and McConchie, 2003; Ridolfi et al., 2003; and Newman et al., 2004*]. Topography (mainly slope steepness) is one of the most intensively studied factors. Most studies suggest that the topography only affects hillslope soil moisture distribution in wet conditions [e.g., *Puigdefabregas et al.*

1998; Western et al., 1999; Qiu et al., 2003; Ridolfi et al., 2003], while Yeakley [*1998*] report topographic factors assert more control during drier periods at a humid watershed. These studies may inform us that there is a soil moisture range, beyond which, either drier or wetter, the topographic effects on soil moisture become less important. It is recently recognized that bedrock surface topography, as well as ground surface topography, influences soil moisture distribution and subsurface flow in the sediment above the bedrock surface. These effects have been recently studied [*McDonnell, 1997; Noguchi et al. 2001; Freer et al., 2002; Chaplot and Walter, 2003*]. Even though ground surface depression-enhanced recharge has been noticed for a long time [*Lissey, 1968; Hendrickx and Flury, 2001*], the effect of bedrock surface depression on bedrock percolation has not been examined.

All of these studies of hillslope water partitioning focus on soil moisture dynamics and lateral moisture movement, neglecting percolation across the soil-bedrock interface. These issues are revisited in this chapter with a focus on percolation, using high-resolution distributed numerical modeling of the hillslope with stepwise increasing complexities.

5.2 Numerical modeling

The simulations were conducted in two dimensions using HYDRUS-2D [*Simunek et al., 1999*]. In HYDRUS, variably saturated water flow in porous media is simulated using the Richards equation. The unsaturated hydraulic properties of soils and bedrock are represented by van Genuchten functions [*van Genuchten, 1980*]. Evaporation is modeled using a Darcy's law-based extraction function, and transpiration is modeled using either the S-shape or Feddes root-water-uptake model (§4.2.2). Surface runoff is simulated as an infiltration-excess process. (HYDRUS cannot handle saturation-excess

runoff.) HYDRUS also has capacity to model preferential flow in macropores and fractures.

5.2.1 Conceptual model for fracture flow in rocks (or macropore flow in soils)

Altman et al. [*1996*] summarize six conceptual models for simulating water flow through a fractured porous medium. They are equivalent porous medium model (one continuum with one single water retention curve), composite porosity model (one continuum with a composite water retention curve), dual porosity model (two continuums, i.e., matrix and fracture, of which matrix stores but does not transmit water), dual permeability model (similar to dual porosity model, except that the matrix also transmits water), and discrete fracture models with or without matrix. For the purpose of this dissertation, i.e., modeling variably saturated subsurface water flow, the two most appropriate continuum models for macropore flow in soils and fracture flow in bedrock are the composite porosity model and the dual permeability model. The dual porosity model is not appropriate because it does not allow matrix flow, while the matrix is important most of the year in semiarid environments. The fracture (or macropore) flow only occurs during and shortly after some rainfall and snowmelt events. The equivalent porous medium model (or single porous medium) is not used because it lacks capacity to simulate the different hydraulic properties of matrix and fractures (or macropores) and their effects. The discrete fracture models are not considered because of their complexity and computing intensity. Considering availability of numerical codes, computing capacity, and data availability, the composite porosity model was selected for the fracture (and soil macropore) flow in this dissertation, which is available in HYDRUS. The dual

permeability model is under development for HYDRUS, which could be applied in the future.

In the composite porosity model, the fractured rock (or macropore soil) is represented as a uniform continuum with a composite water retention and hydraulic conductivity function [*Simunek et al., 2003*]. In this model, the water pressure in fractures is assumed locally equal to that in matrix. Water flows only through rock matrix at low saturation and through both fractures and matrix at high saturation [*National Research Council, 2001*]. The composite multimodal water retention function developed by Durner [*1994*] is used for the bulk rock.

$$S_e = \sum_{i=1}^{k} w_i \left[\frac{1}{1 + (\alpha_i |\psi|)^{n_i}} \right]^{m_i} \tag{5.1}$$

where S_e is the effective saturation, k is the total number of pore modes, i and w_i are the ith pore mode and its weight, respectively, α, m, n are van Genuchten parameters [*van Genuchten, 1980*], where $m = 1 - 1/n$, and ψ is the soil water potential.

The relative hydraulic conductivity is then calculated using numerical evaluation of Mualem's [*1976*] predictive model.

$$K_r(\theta) = S_e^{\tau} \left[\int_0^{\theta} \frac{d\theta}{\psi} \Big/ \int_0^{\theta_{sat}} \frac{d\theta}{\psi} \right]^2 \tag{5.2}$$

where K_r is the relative hydraulic conductivity (dimensionless), and θ is volumetric water content, and τ is an empirical pore-connectivity parameter.

Two modes of pore distributions are used to represent the fractured granite, one for fractures and the other for the rock matrix. The rock matrix van Genuchten hydraulic parameters are adopted from Gimmi et al. [*1997*]. The weight of fractures in (5.1) is determined so that the hydraulic conductivity of the equivalent continuum approaches the prescribed saturated conductivity of fractured rock at saturated condition, and the rock matrix unsaturated hydraulic conductivity when it is far away from saturated condition. This model assumes that fracture (macropore) flow occurs when the matrix is saturated, which does not completely capture actual fracture (macropore) flow characteristics. In reality, fracture (macropore) flow may occur when the matrix is unsaturated. This approximation is reasonably accurate for fracture flow, because of bedrock's low matrix porosity for water storage, but is not as accurate for soil macropore flow.

5.2.2 Conceptual model for steepness-dependent surface runoff

In Chapter 4 we saw that slopes modify atmospheric boundary conditions at the surface. Slope steepness may also directly influence water partitioning near the surface. For example, overland runoff moves down-gradient more quickly on a steep slope than a moderate slope. Physically, the steepness-dependent runoff process can be attributed to two major mechanisms: (1) the fraction of gravitational energy used for downward movement is larger on a steeper slope; (2) the surface water retention capacity is smaller on a steeper slope because infiltration-excess water quickly runs off on a steeper slope. Since the current version HYDRUS-2D immediately takes away infiltration-excess runoff, not allowing runoff to propagate downslope, its runoff only depends on the

infiltration capacity of the soil. It does not capture these two steepness-dependent mechanisms. A conceptual model of equivalent ponding depth is constructed to represent the steepness-dependent surface retention capacity. A pseudo-soil layer in the model is used to mimic steepness-dependent runoff process.

The surface retention capacity can be approximated by an equivalent surface water ponding depth. Water ponding on the surface is caused by available water (precipitation and/or lateral inflows) exceeding infiltration capacity. It is affected by the surface roughness. For simplicity, the surface roughness is assumed to have a sinusoidal form (Figure 5.1), and is described by the function

$$y = d\cos(\frac{2\pi}{L}x) + a + bx \tag{5.3}$$

where d is the amplitude of the sinusoidal shape, L is the periodic length of the shape, b is the slope (tangent of slope angle)，a is a constant, x is the horizontal location in slope direction.

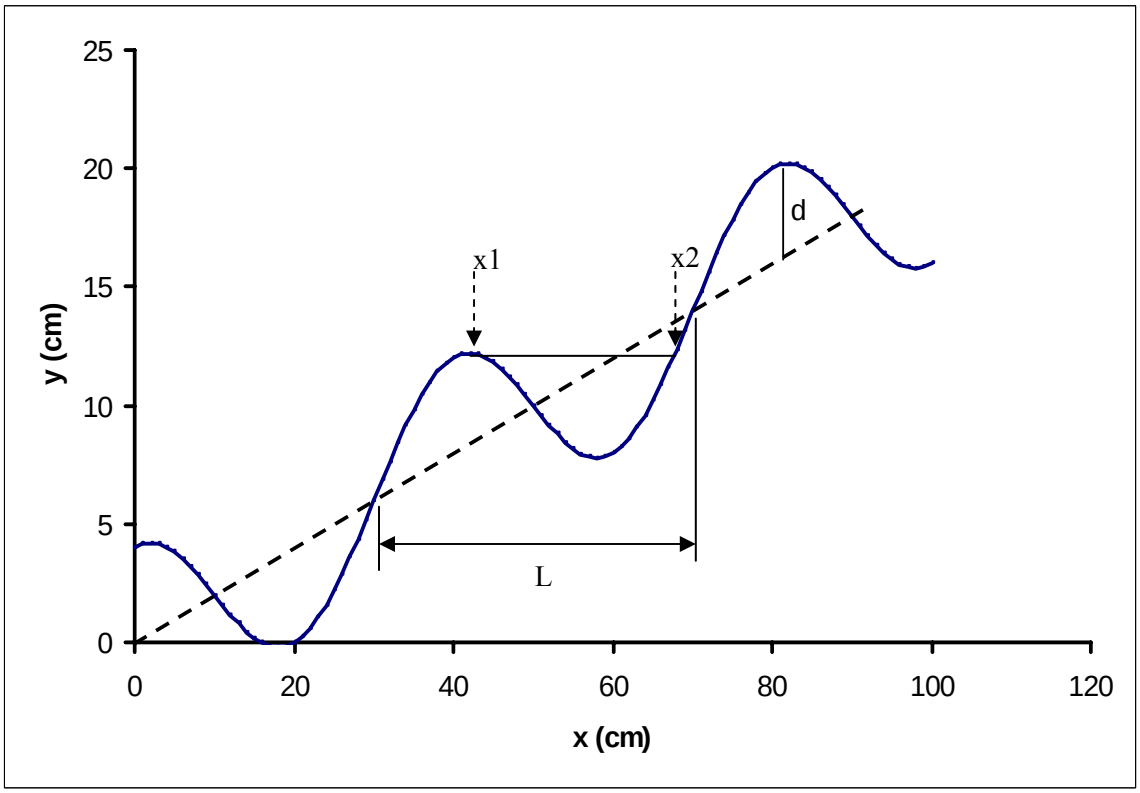

Figure 5.1 Schematic diagram showing ponding depth due to roughness on the slope surface (*a = 0, b = 0.2, d = 4 cm, L = 40 cm* for equation 5.3).

The surface ponding volume in the 2D cross section for each periodic element is

$$V = \int_{x1}^{x2} y_1 dx - \int_{x1}^{x2} y dx \qquad (5.4)$$

where y is the microtopography, y_1 is the maximum pond free surface elevation, and x_1 and x_2 are the location where the maximum pond free surface intercepts with the microtopography. x_1 is obtained from the equation of $\frac{dy}{dx} = 0$, or

$$\frac{-2\pi d}{L}\sin(\frac{2\pi}{L}x_1) + b = 0 \qquad (5.5)$$

For this condition, y_1 is the value of y at $x = x_1$; x_2 is the next location where $y = y_1$. The effective ponding depth is obtained by

$$D = \frac{V}{L} \qquad (5.6)$$

It turns out that D is dependent on d, L, and the slope b (*tangent* of slope angle). For $d=2$ and $L=20$ (any consistent units), D is 1.284, 0.793, and 0.443 for a slope of 0.1, 0.2, and 0.3, respectively. For $d = 4$ and $L= 40$, D is 2.568, 1.586, and 0.886 for the three slopes, respectively.

HYDRUS-2D does not explicitly support surface ponding. It does not allow continuous surface runoff either. A pseudo soil layer on top of the actual soil profile with an extremely high saturated hydraulic conductivity and a pore thickness equivalent to ponding water depth mimics the mechanisms for steepness-dependent surface runoff process. The pore thickness is multiplication of the pseudo layer thickness and its porosity. For example, a 5cm-thick pseudo layer with a porosity of 0.5 approximates an equivalent ponding depth of 2.5 cm on a 0.2 slope. The downslope end of the pseudo layer is prescribed as a seepage boundary, which allows the pseudo layer to hold water when the pseudo layer becomes unsaturated. The unsaturated pore water (the maximum amount close to the equivalent ponding depth) in the pseudo layer eventually infiltrates into the underlying modeled soil.

This approximation approach is used to mimic steepness-dependent runoff processes. It has only been applied to §5.5, which has atmospheric boundary conditions of high a temporal resolution necessary to capture infiltration-excess runoff.

5.2.3 Modeling hillslope hydrologic processes

Various hydrologic processes occur inter-dependently on mountain hillslopes (Figure 5.2). To understand hillslope water partitioning, it is appropriate to simulate all these processes simultaneously, which is, however, complex and data and computationally intensive. Very often, some processes are studied while neglecting some other processes that are less important to understanding the issue of interest. In this way, a cause and effect relationship is more easily obtained. This chapter first focuses on soil water partitioning at the soil-bedrock interface, i.e., partitioning of interflow at the interface, and percolation across the interface, without considering complex surface conditions. The related factors affecting water partitioning at the interface are bedrock permeability, soil water availability (i.e., the rate of soil water replenishment from the surface), slope steepness, bedrock topography, and soil characteristics. For this purpose, steady-state simulations are conducted to understand effects of these factors on water partitioning at the soil-bedrock interface (§5.3).

Steady-state simulations do not represent the whole picture of the hillslope hydrologic system. Additional transient simulations considering all processes (except for sublimation) shown in Figure 5.2 are conducted to approach a better understanding of the system. Two temporal resolutions of atmospheric boundary conditions, one daily (§5.4), the other of minute-time steps (§5.5), are applied in the transient simulations. The daily-step atmospheric boundary conditions are generated from the TVET model, which are intended to study the effects of slope (steepness and aspect) and vegetation coverage

effect on hillslope water partitioning. Since the daily atmospheric boundary condition is too coarse in temporal resolution to capture infiltration-excess runoff, a minute-based atmospheric condition is applied to investigate the effects of precipitation characteristics and slope steepness on hillslope water partitioning. All simulations are conducted in two dimensions.

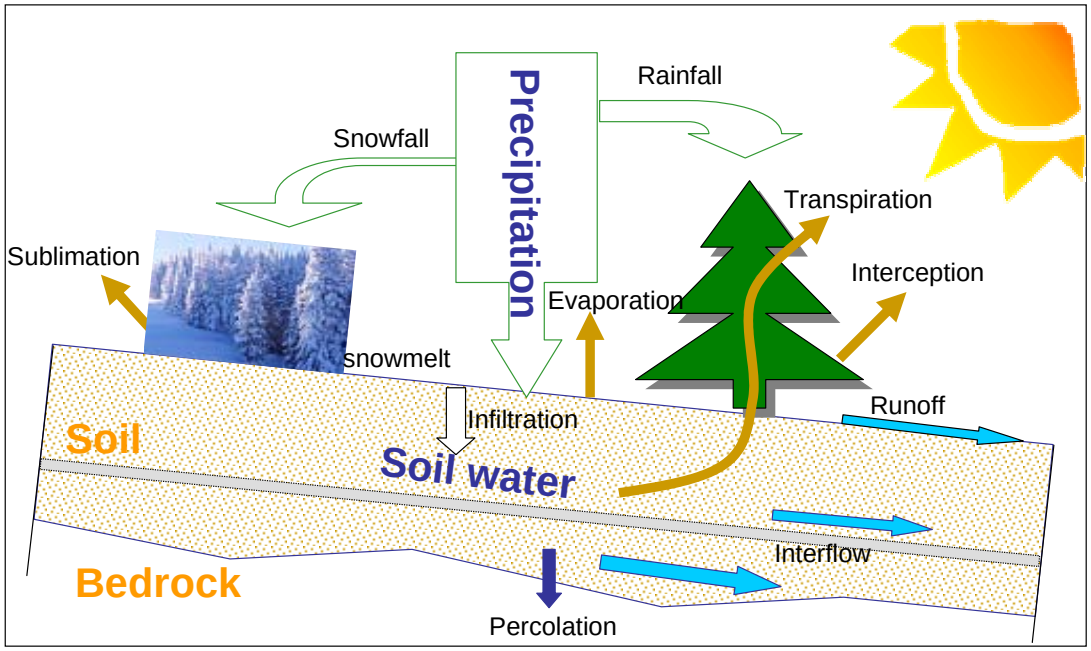

Figure 5.2 Schematic diagram showing the complex hillslope hydrologic system consisting of various inter-dependent hydrologic processes (snow sublimation is not considered in this dissertation).

5.3 Steady-state simulations

5.3.1 Numerical setting

The objectives of the steady-state simulations were to study how bedrock characteristics, slope steepness, and soil characteristics affect soil water partitioning at the soil-bedrock interface, for a given water availability. The water availability defined here was infiltration prescribed from the surface. ET was not simulated; the prescribed

infiltration was net infiltration. For these objectives, infiltration rate, bedrock permeability, bedrock surface roughness, slope steepness, and soil cover were varied in the simulations.

The conceptual setting for this series of 2D simulations is shown in Figure 5.3. Interflow and percolation were modeled in steady state; water availability was prescribed at the surface with a uniform infiltration rate. The infiltration rate was low (0.03~0.3 mm/day, reasonable for semiarid mountain regions) low enough to not exceed infiltration capacity of the top soil. A no-flow condition was prescribed for the upslope side, free drainage (or unit downward hydraulic gradient) for the bottom boundary, and a seepage face for the downslope side. 100-meter-long inclines (term exchangeable with the term 'slope') with various steepnesses (shown as tangent of the slope angle: 0.05~0.3) and soil types were studied. Various depressions were made on the bedrock (Figure 5.4) to investigate their effects on water partitioning. The depression index (DI), a dimensionless value illustrated in Figure 5.4, was used to measure the degree of bedrock surface depression. One meter of soil cover (one or more homogeneous layers) of uniform thickness was draped over one-meter of fractured bedrock. With the free drainage condition below, this simulated a much deeper block of bedrock, mimicking a water table far below the free drainage boundary. A sensitivity study was performed to test this assumption, showing that one-meter-thick bedrock is appropriate to represent the hydrologic state of homogenous bedrock of a larger thickness. Hydrological properties (in this dissertation, hydraulic conductivity of 1 m/sec is equivalent to hydraulic permeability of 1×10^{-7} m^2) of fractured rock and soils applied in simulations are shown in

Table 5.1, where the soil properties were adopted from Carsel and Parrish [*1988*], the bedrock properties were derived from Gimmi et al. [*1997*].

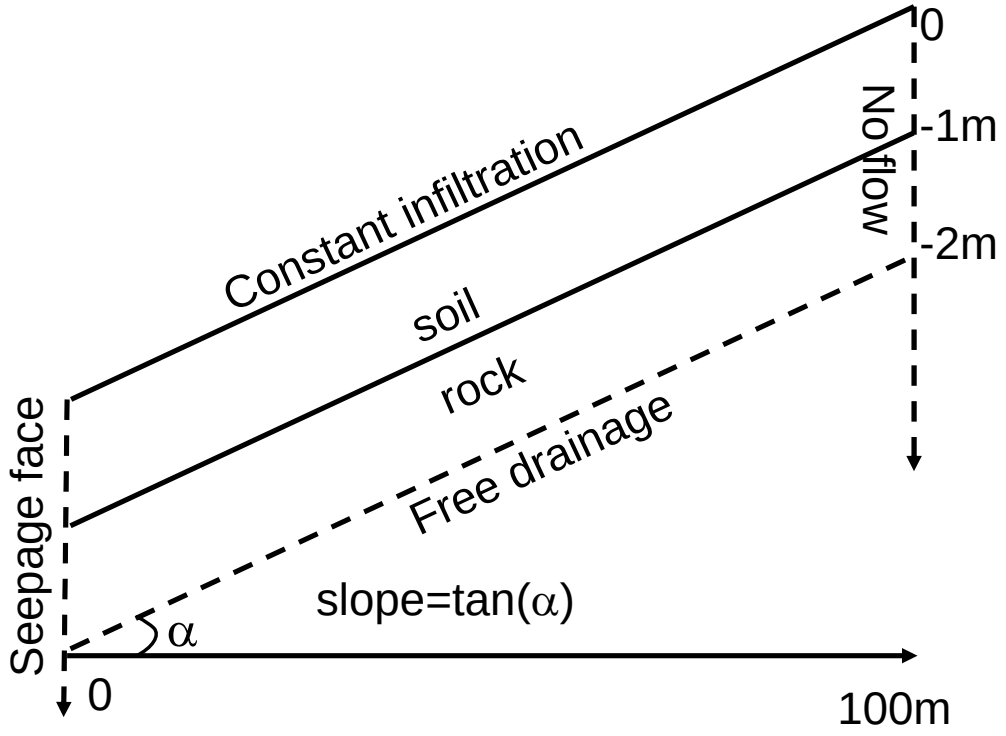

Figure 5.3 Conceptual hillslopes emphasizing shallow soil layer and underlying shallow bedrock in simulations

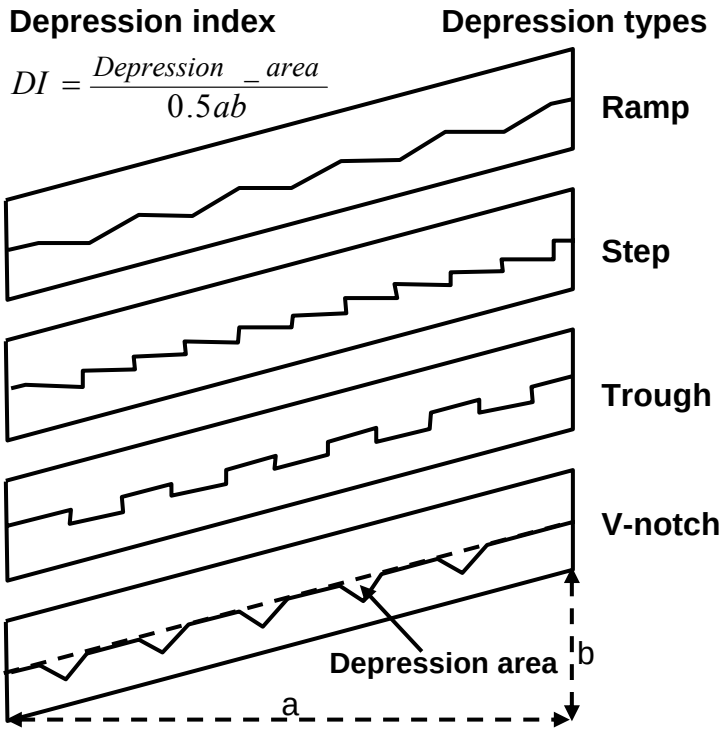

Figure 5.4 Modeled depression types and depression index (DI)

Table 5.1 Hydraulic properties (van Genuchten parameters) of materials applied in the steady-state simulations

	θ_r	θ_s	α_1 (1/cm)	n_1	k^d (m^2)	$w_2{}^e$	α_2 (1/cm)	n_2
Granite[a]	0	0.008	1.13×10^{-4}	1.77	1.0×10^{-16}	0.07	0.0131	4.23
Sand[b]	0.045	0.43	0.145	2.68	8.3×10^{-12}	NA	NA	NA
Sandy loam	0.065	0.41	0.075	1.89	1.2×10^{-12}	NA	NA	NA
Silt	0.034	0.46	0.016	1.37	6.9×10^{-14}	NA	NA	NA
Silty clay[c]	0.07	0.36	0.005	1.09	5.6×10^{-15}	NA	NA	NA

[a] Some properties of the granite(θ_s, k, and w_2) vary between simulations
[b] The soil textural classifications are according to Soil Conservation Service
[c] Silty clay is written in a shortcut of 'clay' in the text and figures
[d] The permeability of bulk rock (including contribution of matrix and fractures (or macropores)
[e] w_2 is the weight of fractures in Durner's [1994] model (§5.2.1); other parameters with subscript 2 are van Genuchten parameters of the fractures (or macropores).

5.3.2 Results and discussion

Since evapotranspiration was not explicitly considered, the prescribed infiltration rate determines the soil water availability at the soil-bedrock interface for a hillslope with a given bedrock. A quantity, defined as the ratio between the infiltration rate and the bedrock saturated hydraulic conductivity, is used to measure relative water availability. The results of this series of simulations show how net infiltration partitions into interflow and percolation at the soil-bedrock interface. The water fluxes were measured from the simulations at three 10-meter intervals, 40-50 m, 60-70 m, and 80-90 m measured from the down-slope side. To quantify water partitioning between interflow and percolation, a percolation index (*PI* = *percolation* ÷ *interflow*) was used to present simulation results, where percolation is the amount of water flowing across bottom bedrock boundary of each sampled interval, and interflow is a net increase in the amount of water flowing downslope within each sampled interval. Conceptually, *PI* gives relative amount of percolation versus net interflow. When percolation equates to net interflow, *PI* is one. When percolation is different from net interflow, *PI* can be any number between *0* and $+\infty$. Thus, *PI* numerically amplifies the difference between percolation and interflow, and is a useful index when the two quantities are similar in magnitude. To avoid the problem of a possible divide by zero for *PI*, another parameter called percolation efficiency *(PEf* = *percolation* ÷ *infiltration*) is also used, where the infiltration is the amount of water flux prescribed at the soil surface, and percolation the amount of water percolating into the bedrock. Conceptually, the percolation efficiency tells the fraction of infiltration water that percolates into the bedrock immediately below. If contribution of lateral flow

to percolation is negligible, such as situations in the steady state simulations, the percolation index has a value between zero and one (or 0% ~100%).

5.3.2.1 Relative water availability effect and bedrock permeability threshold

First, we focus on the relative water availability effects (i.e., the ratio of infiltration rate over the saturated bedrock conductivity) on water partitioning at the soil-bedrock interface, while the slope steepness, soil cover characteristics, and bedrock surface topography remain fixed. Simulations on an incline with sandy loam soil, ramp-type depression with a *DI* (Figure 5.4) of 0.1 and a slope of 0.3, were conducted under various infiltration rates and bedrock permeabilities. The results are shown in Figure 5.5. With a specific infiltration rate, the percolation efficiency increases with the bedrock permeability, and reaches essentially 100% after the bedrock permeability exceeds some critical value. This critical value depends on the infiltration rate, with a lower value for a lower infiltration rate. A dimensionless quantity mentioned earlier, relative water availability (R) defined as the ratio of infiltration over saturated bedrock hydraulic conductivity, is related to percolation efficiency (Figure 5.6). The percolation efficiency decreases with an increase of relative water availability (R), and can be fitted with a S-shape function of the $logR$.

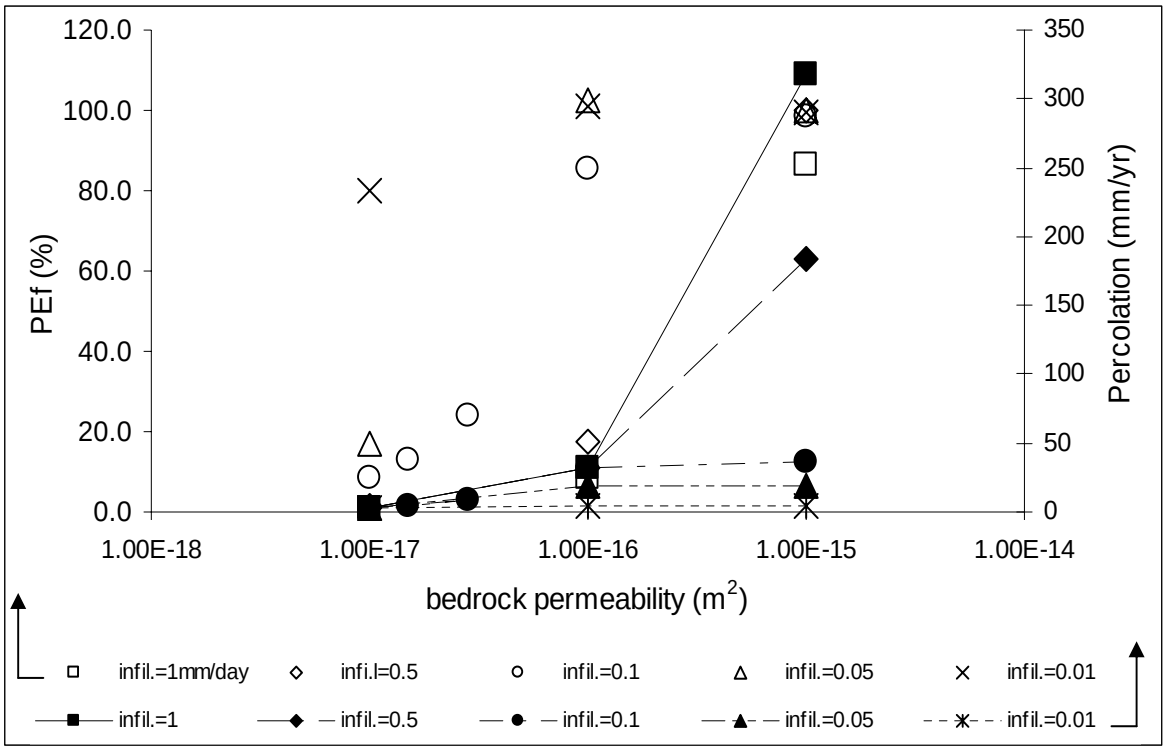

Figure 5.5 Bedrock permeability control on percolation efficiency (open symbols, *PEf*= percolation/infiltration) and the amount of percolation (solid symbols) at various infiltration rates (mm/day), measured at mid-slope (60-70m) with slope=0.3, ramp-type depression *DI*=0.1, soil=sandy loam.

For the practical purpose, the absolute amount of percolation is more meaningful than the relative number (i.e., percolation efficiency). When the bedrock permeability is as low as 1.0×10^{-17} m^2, the percolation is below 3.2 mm/year no matter what the infiltration rate is. For this situation, the soil-bedrock interface is saturated with water. In practice, where the water availability is highly transient in semiarid regions, the soil-bedrock interface is unsaturated most of the year. The percolation becomes negligible for this low-permeability bedrock. For an infiltration rate over 0.1 mm/day, bedrock having a permeability of 1.0×10^{-16} m^2 allows a percolation rate larger than 30 mm/year, which is significant in semiarid areas. Thus, we tentatively define a bedrock permeability threshold for significant recharge of 1.0×10^{-16} m^2. In any event, these simulations do not

account for the effects of temporal variation in infiltration input, and the competition for soil moisture by ET. As shown later, the threshold becomes larger when more complex hillslope hydrologic processes are considered.

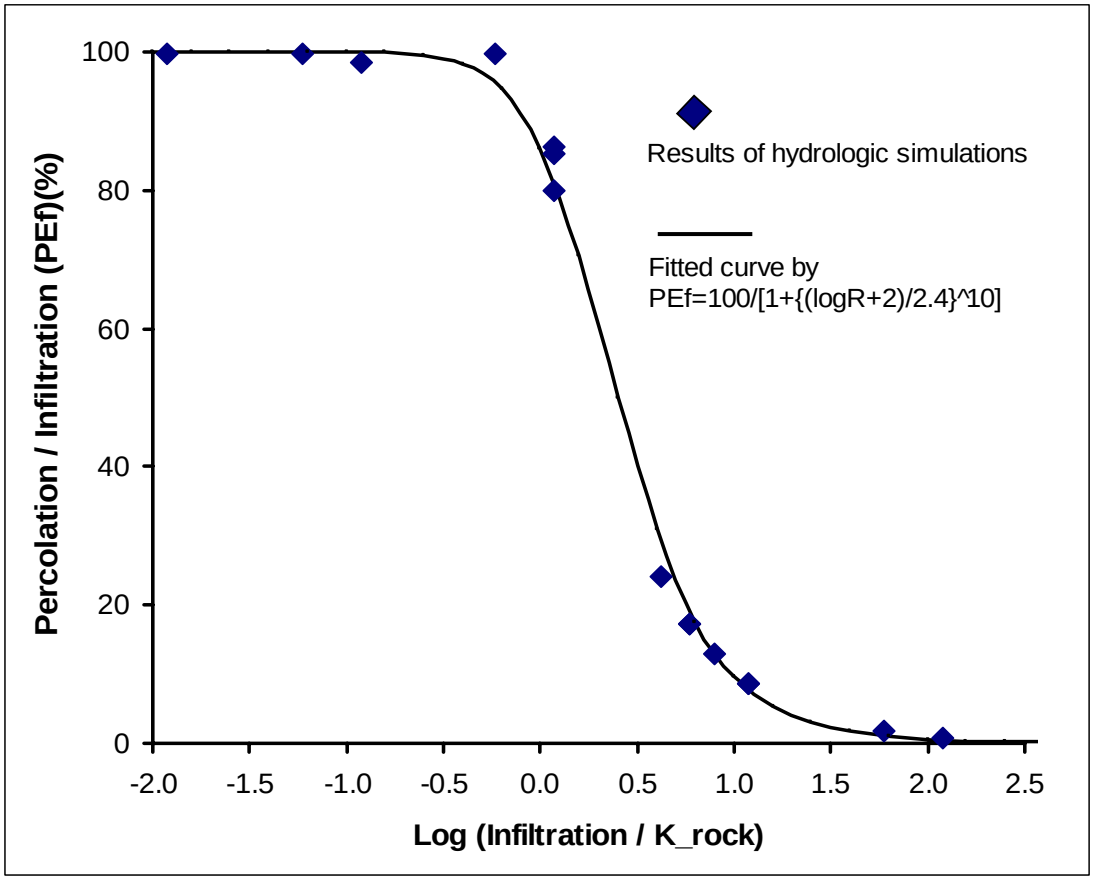

Figure 5.6 Percolation efficiency as a function of relative water availability for simulations with slope=0.3, ramp-type depression *DI*=0.1, soil=sandy loam, and various values of bedrock permeability and infiltration rates (shown in Figure 5.5).

5.3.2.2 Slope steepness effect

The two major interfaces on our slopes are the ground surface and the soil-bedrock interface. Steady-state simulations are not able to capture the slope steepness effect on water partitioning between runoff and infiltration at the ground surface because

runoff is not simulated. This section looks at the slope steepness effect on water partitioning at the soil-bedrock interface.

Simulations of six slopes (0.05~0.3) with two types of soil covers were conducted for a bedrock permeability of 1.0×10^{-16} m^2 and an infiltration of 0.1 mm/day ($R \approx 1$) (Figure 5.7). There were no bedrock depressions in these simulations which were designed to look at the effect of slope steepness. A slope steepness effect is observed for all three 10m-long sampling intervals with sandy loam-cover slopes, while it is only observed for the upper sampling intervals with silt-cover slopes (Figure 5.7). With a slope effect, the percolation index decreases with slope steepness, as more water moves downhill as interflow. For the lower sampling intervals on the silt-cover slopes, the soil is so wet that the bedrock permeability limits percolation. For these situations, as the fracture flow has been fully initiated (Figure 5.7d, when water potential is larger than -8 cm), the slope steepness effect becomes negligible.

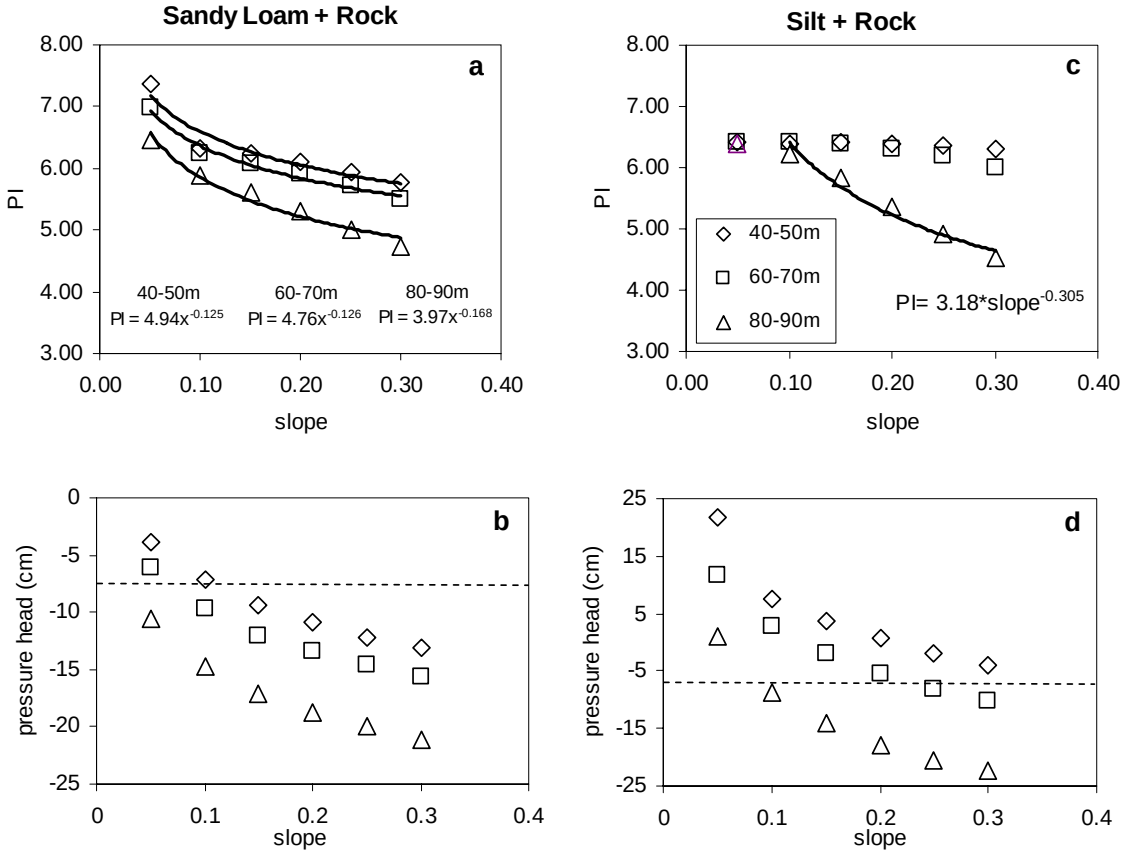

Figure 5.7 Slope effect on percolation index (PI=percolation/interflow), and the respective water pressure at the soil-bedrock interface, for sandy loam-covered slopes (a) and (b), and silt-covered slopes (c) and (d), with DI=0, bedrock k=1×10^{-16}m^2, and infiltration=0.1 mm/day. Diamonds = 40-50m (downslope), squares = 60-70m, and triangles = 80-90m (upslope) hillslope intervals. Power law regression fits of PI to slope are shown in a and c. The dashed line in b and d is the threshold pressure head needed to fully activate flow in the bedrock fractures.

The relationship between *PI* and slope fits power functions very well for the simulation cases in which water pressure head at the soil-rock interface is below -8 cm, while this relationship does not hold when water pressure head is above -8 cm (Figure 5.7). This indicates that water pressure distribution is an important factor affecting water partitioning. For inclines covered with sandy loam (Figure 5.7a), *PI* of each slope at the three intervals increases downslope, although the slope doesn't change. This is obviously because water pressure at the soil-bedrock interface increases downslope, and thus

increases the actual hydraulic conductivity of the fractured rock, resulting in an increase of *PI*. For inclines covered with silt, the water pressure at the soil-bedrock interface also increases downslope. However, there is no difference of *PI* between intervals (40-50m) and (60-70m) for each slope for steepness below 0.2 (Figure 5.7c). This is because of the non-linear change of fracture rock hydraulic conductivity with the soil water pressure (not shown). There is a water pressure head window (-8 to -400 cm, not shown) in which the hydraulic conductivity of the bedrock changes dramatically with the water pressure. When the water pressure at the soil-bedrock interface is within this window, it significantly affects water partitioning. When the change of the water pressure is outside of this window, the effect on water partitioning (in terms of percolation index) is negligible. In arid and semiarid regions, the soil moisture regime at the soil-bedrock interface is outside the drier end of this window most of the year.

Since the slope effect on water partitioning at the soil-bedrock interface is due to its effect on water pressure distribution at the soil-bedrock interface, it is the slope of bedrock surface, rather than that of ground surface, that influences water partitioning at the soil-bedrock interface. Although these mechanisms are not that important to the absolute amount of percolation flux, they shed light on understanding the slope steepness control on the hillslope soil moisture distribution.

To further test how the slope steepness effect varies with soil water conditions, additional simulations were conducted with two other infiltration rates (0.028 mm/day and 0.3 mm/day), one lower and one higher, for the sandy loam-covered inclines, with results shown in Table 5.2 (2^{nd} major column). As the condition becomes drier ($R \approx 0.3$) or wetter ($R \approx 3$), the slope steepness effect on soil water partitioning disappears. This

result is similar to the slope steepness effect on hillslope soil water distribution, inferred from literature (§5.1).

Table 5.2 Percolation index (PI) and the amount of percolation, measured at the 60-70 m hillslope location of one-meter-thick sandy loam-covered inclines, with bedrock permeability of 1.0×10^{-16} m^2 at various infiltration rates

R[a]	Infiltration mm/day	Slope effect (DI=0) Slope	PI	Percolation mm/yr (mm/day)	Depression effect (slope=0.3) DI[b]	PI	Percolation mm/yr(mm/day)
0.32	0.028	0.1	∞	10.3 (0.028)	0.000	∞	10.3 (0.028)
		0.2	∞	10.3 (0.028)	0.042	∞	10.4 (0.028)
		0.3	∞	10.3 (0.028)	0.092	∞	11.0 (0.028)
1.16	0.1	0.1	6.2	31.7 (0.087)	0.000	5.5	31.1 (0.085)
		0.2	5.9	31.5 (0.086)	0.042	6.0	31.4 (0.086)
		0.3	5.5	31.1 (0.085)	0.092	6.4	31.7 (0.087)
3.47	0.3	0.1	0.41	31.8 (0.087)	0.000	0.41	31.8 (0.087)
		0.2	0.41	31.8 (0.087)	0.042	0.41	31.8 (0.087)
		0.3	0.41	31.8 (0.087)	0.092	0.42	31.8 (0.087)

[a] R is the ratio of infiltration rate over saturated bedrock hydraulic conductivity
[b] DI is depression index of trough-type depressions, explained in Figure 5.3
∞ >10000

PI is a relative number index. It doesn't give the actual amount of percolation or how it changes with slope steepness, which is of greater interest for practical applications. If the absolute amount of percolation is evaluated, the slope steepness effect on water partitioning at the soil-bedrock interface is essentially negligible (Table 5.2 2nd major column).

5.3.2.3 Soil cover effect

By their different water-holding capacities (i.e., water retention characteristics) and hydraulic conductivities, soils can affect water partitioning at the soil-bedrock interface. To understand the effects of different soil-characteristics, both single-soil cover and double-soil cover were employed. The double-soil cover is composed of a major soil layer (85cm thick) and a coarser (sand) or finer (clay) interlayer soil (15 cm) between the major soil layer and the bedrock. The slopes have no bedrock depressions. The simulation results are shown in Figure 5.8. At upper sampled intervals, where soil water pressure should be lower, the percolation is always larger for double soil-cover slopes than for single soil-cover slopes, even when the soil above the soil-bedrock interface is clay (the hydraulic conductivity is still orders magnitude larger than underlying bedrock). At the lower sample interval, where soil has higher saturation at the interface, the difference in percolation index is smaller between inclines with different soil covers. The slope effect seems to be smaller on slopes with complex soil cover than simple soil cover. The effect of soil thickness on percolation is not significant, mainly because evapotranspiration and runoff are not explicitly included in the simulations.

Similar to the slope steepness effect, the soil cover effect on water partitioning at the soil-bedrock interface is negligible in terms of the absolute percolation amount (not shown).

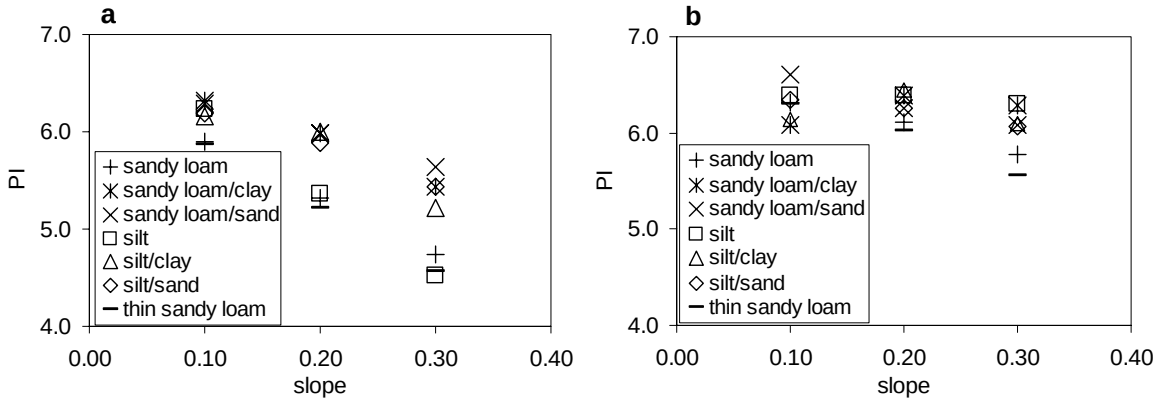

Figure 5.8 Effect of soil cover characteristics on percolation index (PI) at upslope (a: 80-90 m) and downslope (b: 40-50 m) locations, with DI=0, bedrock k=1×10^{-16}m^2, and infiltration=0.1 mm/day. The total thickness of the soil cover is 1 meter, except for the thin sandy loam cover, which is 35 cm. For the two-layer soil cover, the first or top soil is 85 cm thick, and the second soil, 15 cm thick, lies on the bedrock.

5.3.2.4 Bedrock surface depression effect

Bedrock surface topography influences hillslope interflow [e.g., *Freer et al., 2002*]. Usually, continuous bedrock depressions form hollows for saturated interflow, leaving water less contact time with the bedrock for percolation to occur. Isolated bedrock depressions store soil water, which should enhance percolation. This section examines the effect of isolated bedrock depressions on percolation.

Each of four types of depression (Figure 5.4) was applied on inclines with a slope of 0.3. Again we examine conditions for three 10-meter intervals (40-50, 60-70, 80-90m). Two different depression magnitudes were employed for Step, V-notch, and Trough types. Generally, depressions on the rock surface facilitate percolation, especially at the upslope locations where the soil has low saturation (Figure 5.9). Of the four depression types, Step and Ramp types are not actually depressions, but roughness which changes local slope steepness. Trough and V-notch types are real depressions. For these two

depression types, the percolation index can be linearly related to depression index (Figure 5.10).

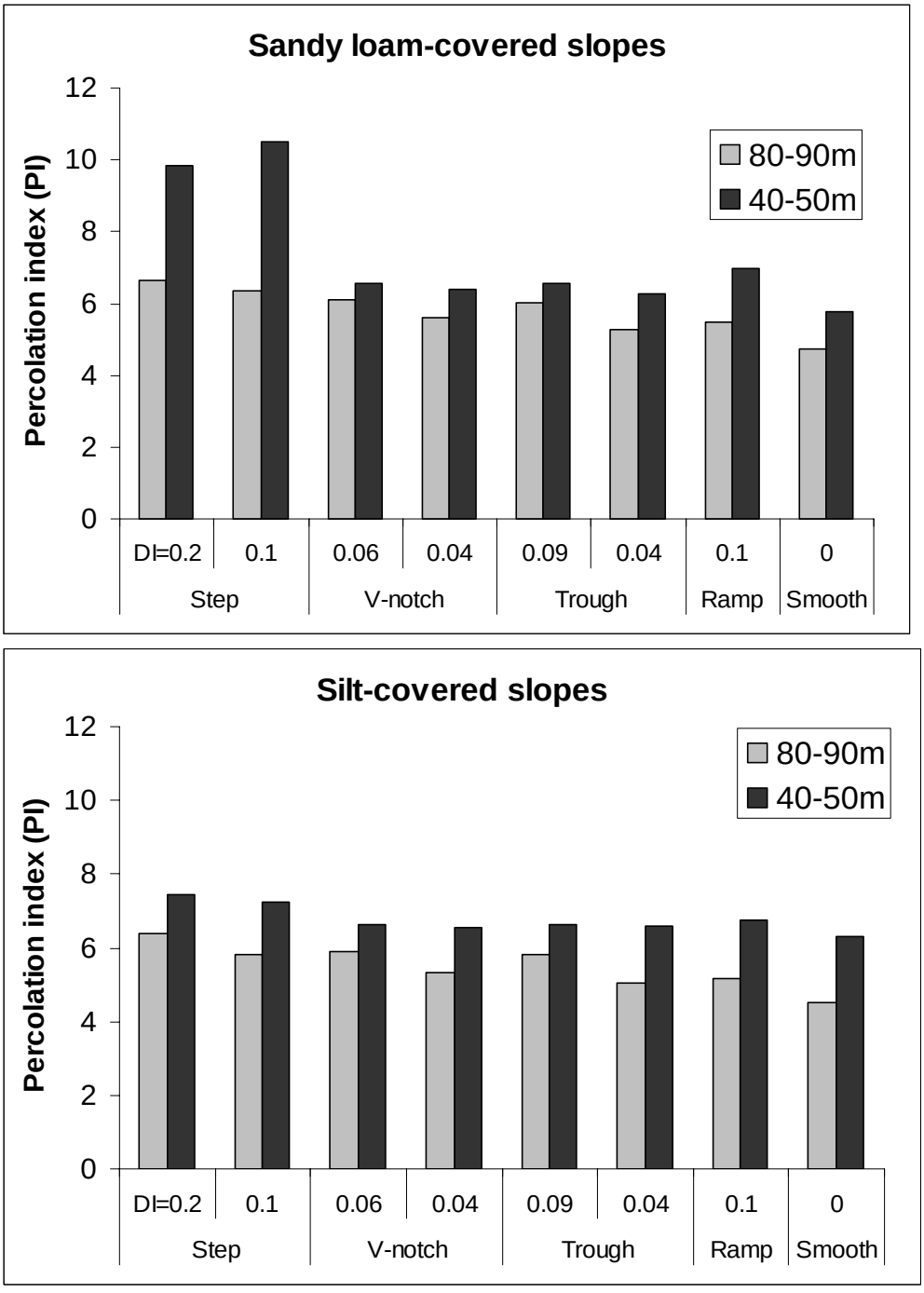

Figure 5.9 Simulated percolation index of the slopes with bedrock depressions of different types and magnitudes for sandy-loam soil cover (top) and silt soil cover (bottom) at two sampling locations, 80-90 m interval and 40-50 m interval. (The large PI for step-type depressions on the sandy loam-covered slopes may be due to the numerical problems.)

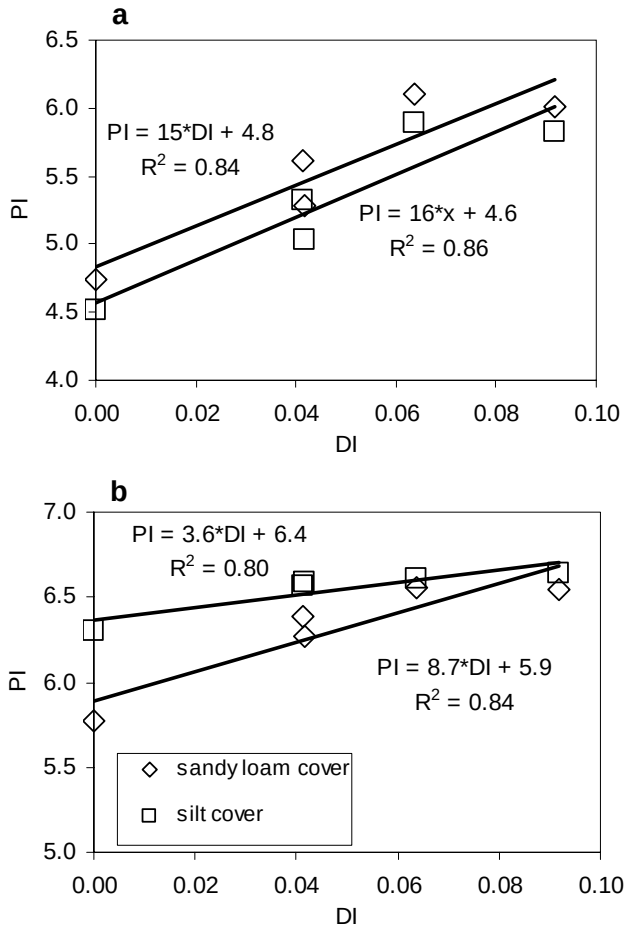

Figure 5.10 Percolation index (*PI*) as a function of depression index (*DI*) for trough and V-notch type bedrock surface depressions at upslope (a: 80-90 m) and downslope (b: 40-50 m) locations, with slope=0.3, bedrock k = $1\times10^{-16}m^2$, and infiltration=0.1 mm/day. The solid lines are regression fits of PI and DI

However, if the depression effect is evaluated by the absolute percolation, it is negligible (see, e.g., Table 5.2). It should be noted that the simulations assume homogenous bedrock properties, with small scale depression (a depth of a few tens centimeters). For a large-scale depression with correlated (collocated) fractures, the percolation should be significantly facilitated, but this situation is not captured by the simulations in this study.

5.3.2.5 Summary of the steady state simulations

This section examined the effects of slope steepness, soil cover characteristics, bedrock surface topography on water partitioning at the soil-bedrock interface, while assuming steady flow. In terms of percolation index, the results indicate that all three factors influence percolation, but only for a certain range of relative water availability (R), where R is the ratio of net infiltration over the saturated bedrock hydraulic conductivity. For the two factors (slope steepness and bedrock depression) that were specifically examined for various relative water availabilities, effects are observed for R close to one. At a drier or wetter condition, neither of them affects percolation index. In terms of absolute percolation, none of these factors (slope, soil, and bedrock topography) cause a significant difference. The primary controls on percolation are bedrock permeability and water availability. For bedrock with bulk permeability above 1.0×10^{-16} m^2, the percolation can be significant.

However, it should be noted that the steady-state simulations with constant infiltration inputs do not capture the effects of temporal variation in infiltration input, evapotranspiration loss, and the fast fracture flow when the fracture occurs at the bedrock depressions. Nor does it capture three-dimensional flow focusing effects. In the next sections we'll include temporal variation and ET, but this dissertation does not consider discrete fracture flow or 3D effects.

5.4 Transient simulations with daily atmospheric boundary conditions

In the steady state simulations, surface conditions were not considered. Simulations in this section couple surface conditions with the shallow subsurface hydrologic processes on mountain hillslopes. The effects of terrain aspect and vegetation coverage on hillslope water partitioning were emphasized of this series of simulations. The TVET model was used to generate daily atmospheric boundary conditions for shallow subsurface hydrologic modeling. The hydrological processes considered in the simulations included precipitation, interception, snow and snowmelt, infiltration, interflow, ET, and percolation (Figure 5.2). Runoff was not modeled because the daily atmospheric boundary condition was not temporally short enough to capture infiltration-excess runoff (i.e., precipitation intensity from the daily atmospheric forcing is always smaller than top soil infiltration capacity), and because saturation-excess runoff could not be modeled by HYDRUS.

5.4.1 Numerical setting

The examined factors included bedrock characteristics, slope aspect, soil thickness, vegetation cover, and precipitation characteristics. Two types of bedrock, matrix-flow-dominant non-welded tuff and fracture-flow-dominant granite, were considered. The effects of two extreme slope aspects, north-facing and south-facing, were examined. Two different thickness soils, one 30 cm and the other 100 cm, were used in the simulations. The effects of various vegetation-cover conditions were investigated. Four years (1991~1994 water years, including one El Niño year) of consecutive micrometeorological measurements near South Baldy, Magdalena Mountains of central New Mexico (Figure 5.11), were used for the simulations. For simplicity, slope

steepness and soil types were fixed. The bedrock surface depressions were also not applied because of their apparent negligible effect on percolation (§ 5.3).

To reduce computational load, a section 20-cm long and 200-cm thick was applied. To mimic hillslope conditions, a continuous side-end boundary was applied to this small slice (Appendix XV). The domain was composed of two layers (bedrock covered with soil) (Appendix XV). The material properties are shown in Table 5.3. Other conditions are given in Appendix XV. For each of the 16 hypothetical slopes (slope aspects soil thickness, fractional vegetation cover, and bedrock type were varied between modeled slopes), two simulations were performed with four-year atmospheric forcing. One was set up to simulate the condition at the top of the 100m slope of the previous section, with a no-flow boundary at the upgradient side; the other was designed to simulate the condition at the midslope, with continuous slope boundary at both sides of the simulated slice (Appendix XV). The metric for percolation along the slope was defined by the geometric mean of the percolation from the topslope slice and the midslope slice. In this section (§5.4), all simulations were performed with atmospheric forcing of four consecutive years (1991~1994 water years). The initial condition for each simulation was obtained by a couple of times of periodic forcing of the same climate condition (i.e., four-year time series).

Table 5.3 Hydraulic properties (van Genuchten parameters) of materials applied in the daily-step transient simulations

	θ_r	θ_s	α_1 (1/cm)	n_1	k (m^2)	w_2	α_2 (1/cm)	n_2
Granite	0	0.008	1.13×10^{-4}	1.77	1.0×10^{-15}	0.15	0.0131	4.23
Tuff	0	0.28	0.0014	1.42	5.8×10^{-14}	NA	NA	NA
Loam	0.078	0.43	0.036	1.56	2.9×10^{-13}	NA	NA	NA

Figure 5.11 The photo of South Baldy (~3250m), Magdalena Mountain, the central New Mexico, taken in the summer of 2001, showing distinctive vegetation coverage on two opposite slopes (the tree-covered slope is north-facing).

5.4.2 Results and discussion

The objectives of this series of simulations were: (1) to understand the effects of vegetation coverage, slope aspect, bedrock, soil thickness, and climate patterns on

hillslope water partitioning with a focus on percolation; (2) to understand the distinctive vegetation coverage between north-facing and south-facing slopes on South Baldy, Magdalena Mountains (Figure 5.11); and (3) to estimate the distributed mountain-block recharge on these two slopes.

5.4.2.1 Effects of slope aspects, vegetation cover, bedrock, and soil thickness

The cumulative percolation during the whole four-year simulation period, together with the cumulative precipitation and active water (rainfall – interception + snowmelt), is plotted against time (Figure 5.12). The difference between the cumulative precipitation (P) and active water (pI) represents rainfall interception loss, derived from the TVET model. The lag in response of the active water curve to the increasing slope of the precipitation curve suggests snow storage and snowmelt later. Annually (four-year) averaged percolation for various slope conditions is plotted in Figure 5.13. These results indicate that all examined factors (bedrock, soil thickness, vegetation coverage, slope aspect, and climate pattern) influence percolation.

Compared to the less-permeable fracture-flow dominant granite, permeable tuff strongly facilitates percolation (Figures 5.12 and 5.13). Bedrock not only affects the percolation amount, but also the percolation temporal pattern. Cumulative percolation into the tuff grows gradually (Figure 5.12 c&d) compared to the fractured granite which grows abruptly in steps (Figure 5.12 a&b). The abrupt increases in cumulative percolation correspond to snowmelt in the spring of 1992 (following an El Niño winter), and the monsoon seasons of 1991 and 1993. The monsoon seasons of 1992 and 1994 do not lead to significant percolation (Figure 5.12). The big snowmelt in spring of 1992 is associated with a positive anomaly of snowfall in the previous El Niño winter (1991-1992) (Chapter 3). Removal of vegetation decreases transpiration (not shown here, see

Appendix XV), thus increasing the percolation, especially for the slope with a thick-soil cover (Figures 5.12, 5.13). Slope aspect modifies potential ET and influences percolation, with a significantly larger percolation on the north-facing slope than the south-facing slope. Soil thickness controls water storage capacity on the hillslope. A thicker soil leads to a smaller percolation (Figures 5.12, 5.13). This effect is more significant on the slope with the more permeable bedrock, and with more deep-root vegetation. The effect of soil thickness becomes insignificant on the granite slope with no vegetation coverage.

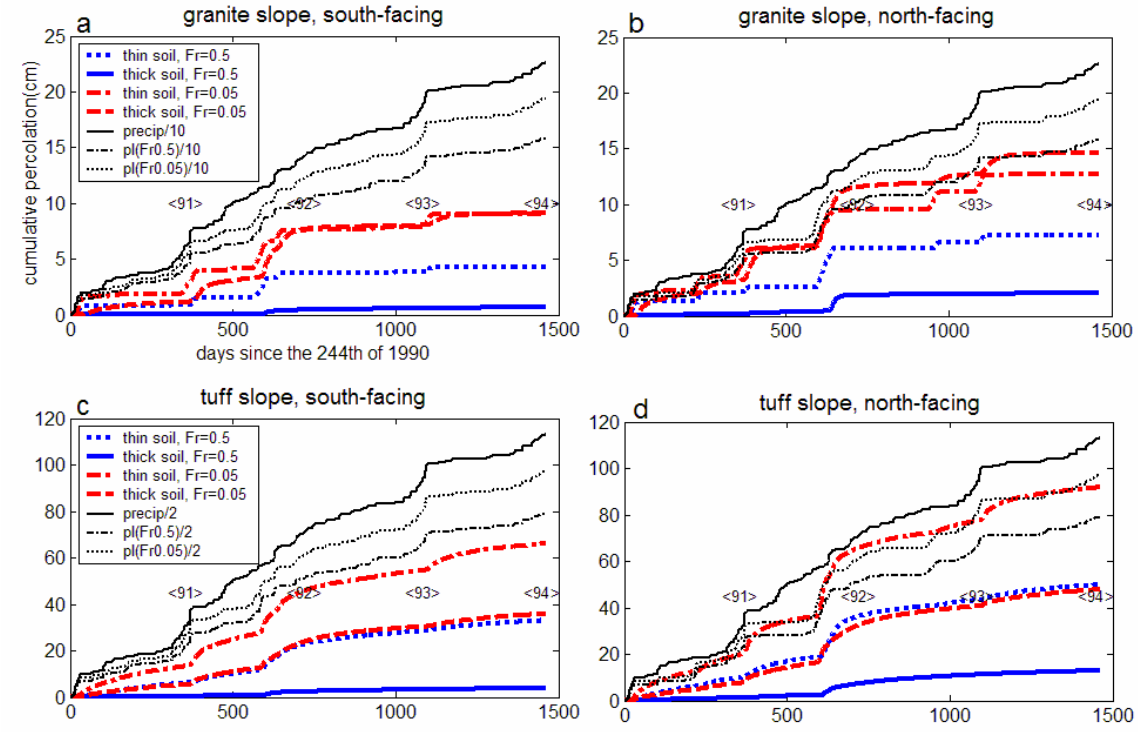

Figure 5.12 The cumulative amount of percolation together with the precipitation and active water (pI) on the surface in the four-year period for various slope conditions, a) south-facing 20˚ slope with granite bedrock, b) north-facing 20˚ slope with granite bedrock, c) south-facing slope with tuff bedrock, and d) north-facing slope with tuff bedrock. Fr is the fractional vegetation cover, thin soil = 30 cm, thick soil = 100 cm, '<xx>' is the location of monsoon season (July, August, and September), 'xx' is the year. Note the different vertical scale for tuff v. granite results.

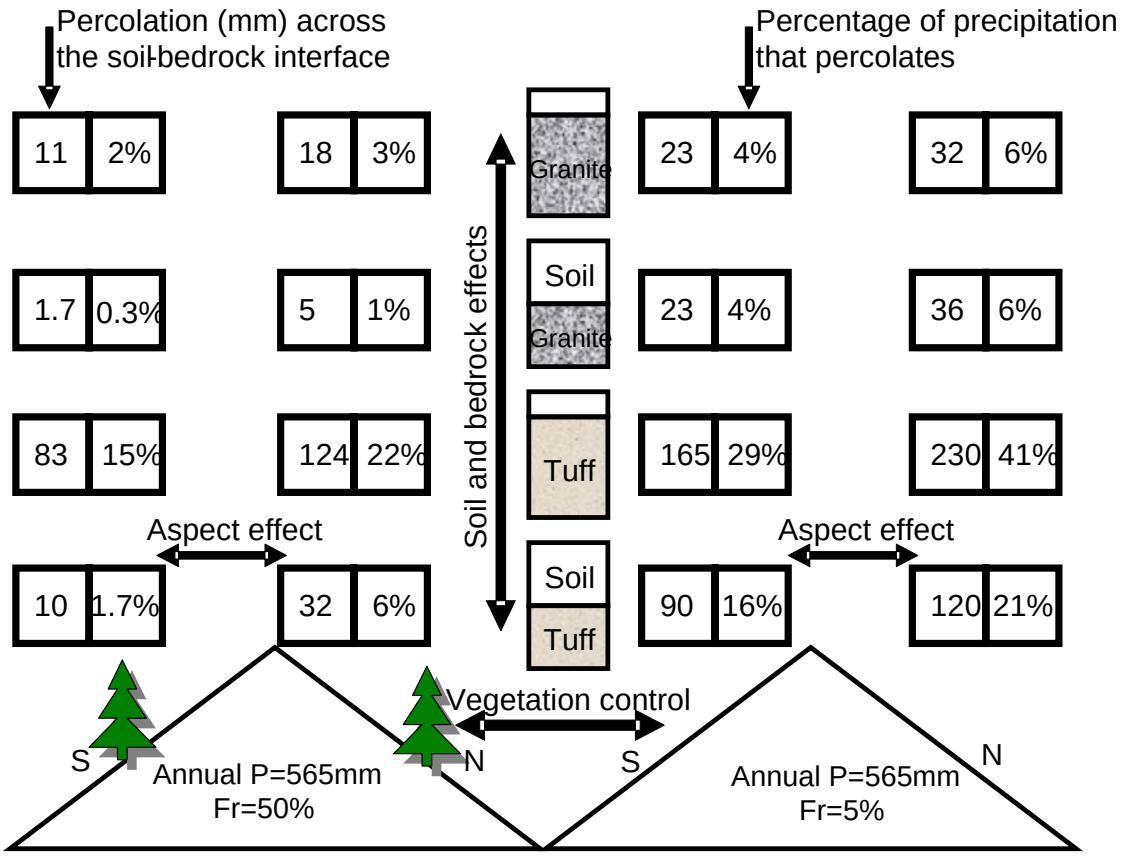

Figure 5.13 Annually averaged simulation results showing the effects of vegetation coverage, slope aspects, bedrock characteristics, and soil thickness on the percolation across the soil-bedrock interface on a hypothetical hillslope with a slope angle of 20˚ (Fr is the fractional vegetation cover).

If we define a percolation of 10 mm/yr as a significant contribution to recharge, the fractured-granite (1.0×10^{-15} m^2) slopes, with a climate condition similar to South Baldy, Magdalena Mountains, NM, have recharge near the threshold. Thus, we should modify previously-determined bedrock permeability threshold, 1.0×10^{-16} m^2 from steady state simulations, to 1.0×10^{-15} m^2 for these transient simulations.

5.4.2.2 Why distinctive vegetation cover on two opposite-aspect slopes?

Distinctive vegetation covers develop on two opposite-aspect slopes of South Baldy, Magdalena Mountains (Figure 5.11). The north-facing slope is covered by dense conifer trees, while the south-facing slope is covered by seasonal grasses. Similar phenomena (i.e., terrain-aspect induced ecotones) are very common in mountain terrains [e.g., *McMahon, 1998*]. A common hypothesis is that compared to the south-facing slope, the north-facing slope has less evaporative demand, and thus more soil moisture to support dense vegetation. This is tested by the TVET model coupled with shallow subsurface hydrologic modeling.

Time-series of root zone soil moisture are critical in the test of this hypothesis. Since vegetation modifies soil moisture, it is not appropriate to test the hypothesis by examining soil moisture state between the slopes with current vegetation coverage. Thus, let's assume the vegetation (Fr = 50% conifer trees) and soil thickness (30 cm or 100 cm) were initially identical on the two opposite-aspect slopes. Two soil covers with different thickness (one 30 cm, the other 100 cm) were applied in the simulations, with two different underlying bedrocks (Table 5.3). The simulation results of top slope runs were used for the following analyses. Water potential at the depth of 20 cm was examined for the thin soil slope, and that of 40 cm for the thick soil slope. Only the duration of dry periods are shown, with three levels of dryness-strongly dry, moderately dry, and weakly dry (Figure 5.14). The strongly dry condition is equivalent to soil water potential below -70 m; the moderately dry condition equivalent to water potential between -50 and -70 m; the weakly dry condition equivalent to water potential between -30 and -50 m. Because bedrock does not seem to affect root-zone dryness duration from the simulations, Figure

5.14 only displays simulation results of the granite slopes, with the results of tuff slope included in Appendix XVI.

The results suggest that soil moisture changes more frequently for slopes with shallow soil cover than thick soil cover. The difference in soil water potential between two slopes is amplified for thin-soil-cover slopes, and dampened for thick-soil-cover slopes. Strongly dry root zone soil lasts for one month during the growing season on the south-facing thin-soil-cover slope, which may kill or seriously weaken the trees that were assumed to exist in the simulations. Based on these results, it seems that the thin soil on the south-facing slope could explain the distinctive vegetation coverage on two opposite-aspect slopes. Here, we did not consider the interaction between soil development and the vegetation. We discuss this issue in Chapter 6.

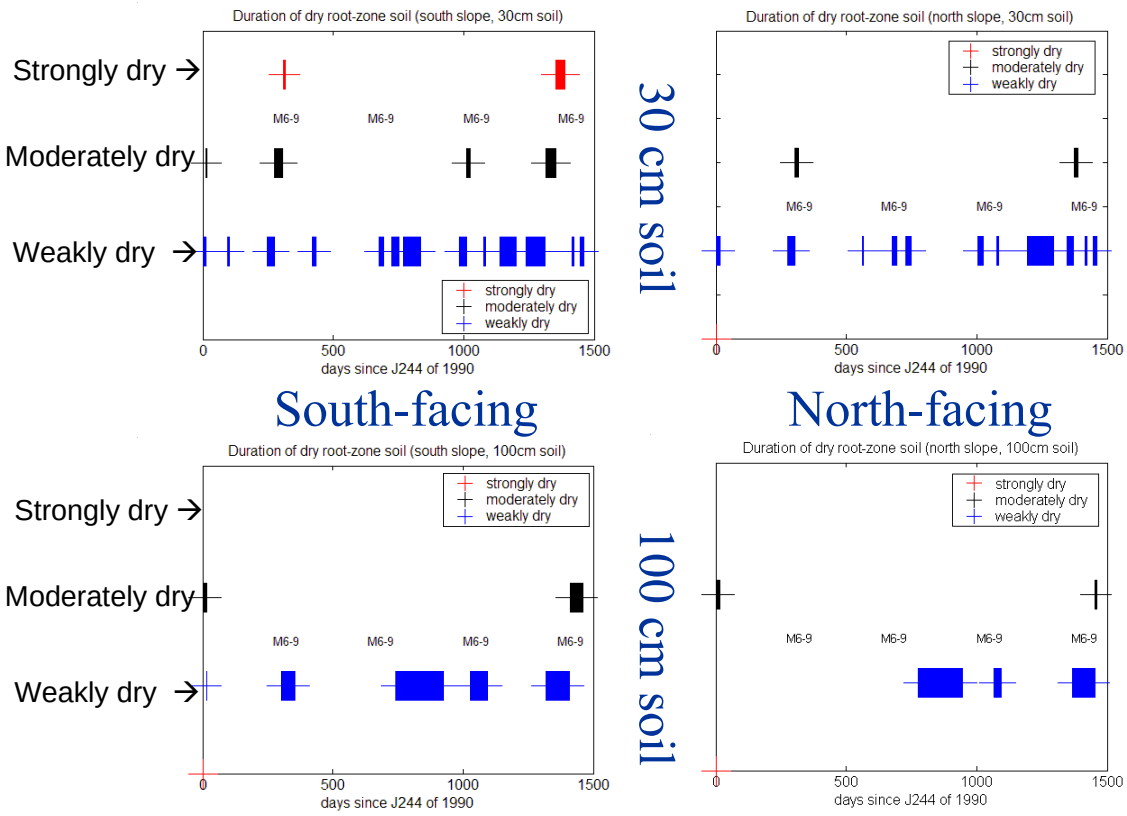

Figure 5.14 The duration of dry root-zone soil for hypothetical slopes of 50% vegetation coverage (conifer trees), and of slope angle of 20˚, with two opposite slope orientations and two types of soil thickness. The bedrock is granite. For the 30-cm soil, soil water potential at 20 cm depth is examined from the simulations. For the 100-cm soil, soil water potential at 40 cm depth is examined.

5.4.2.3 What is percolation on the two opposite-aspect slopes?

What are then the recharge potentials on these two slopes? To answer this question, two additional simulations were conducted for the south-facing slope with a thin-soil cover, and with atmospheric condition for seasonal grass (May-October) derived from TVET (Appendix XVII). The results are compared to those of the north-facing slope with tree cover (Figure 5.15). It is interesting that the potential recharge on the two slopes is similar, in contrast to the big difference if the same vegetation cover occurs on the two slopes (Figure 5.13). These results appear to demonstrate how the vegetation

adapts to the local climate conditions and impacts hydrologic processes on mountain environments. Detailed discussion is included in Appendix XVIII. It should be noted that only climate and vegetation interaction are included here, leaving soil response and feedback not considered. The soil response to climate and vegetation conditions is discussed in Chapter 6.

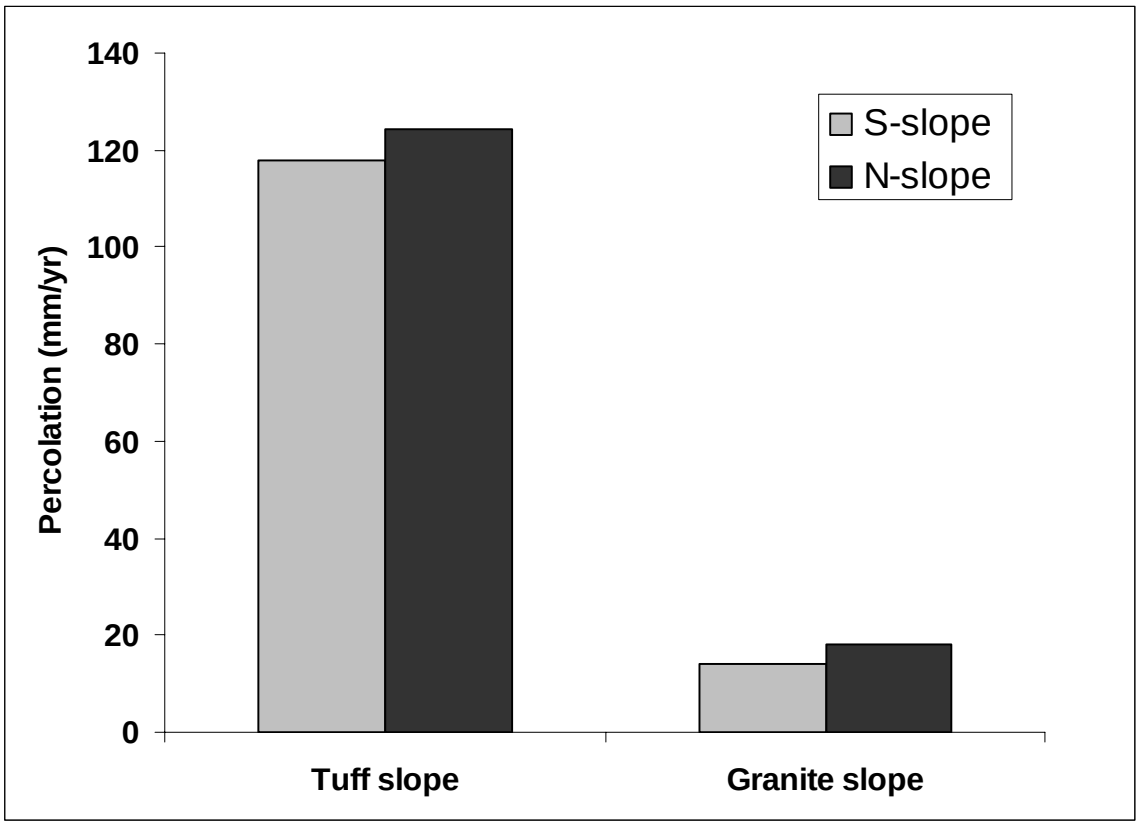

Figure 5.15 Simulated annual percolation at south-facing slope with seasonal grass (Fr=0.5), and north-facing slope with conifer tree (Fr=0.5), both with a 30-cm soil.

5.5 Transient simulations with minute-based atmospheric boundary conditions

Slope steepness does not appear to significantly affect water partitioning at the soil-bedrock interface (§5.3). However, it may affect water partitioning at the surface

where active water partitions into runoff and infiltration. One objective of this section is to examine this effect using a high temporal resolution atmospheric input (precipitation and PET).

The results of daily-step transient simulations (§5.4) suggest that bedrock permeability, soil thickness, vegetation coverage, slope aspect, and climate conditions all affect percolation on mountain hillslopes. Slope aspect takes effect by modifying climate conditions (i.e., PET and P). Climate in mountains is also modified by terrain elevation. Their effects can be lumped together into the regional climate conditions and, with fixed bedrock, soil cover, and vegetation coverage, the climate effect on hillslope water partitioning can be examined. The other objective of this section is obtain quantitative percolation and ET functions of local climate conditions (modified by topography) for mountain-block recharge mapping in Chapter 7. The idea here is to find relationships for percolation and climate conditions, and for actual ET and climate conditions. The relationships are then projected to obtain percolation and ET maps, based on climate condition maps (Chapter 7).

5.5.1 Numerical setting

The atmospheric boundary was derived from micrometeorological observations at the Los Alamos ponderosa pine hillslope experiment site in northern New Mexico [*Wilcox et al., 1997*] (Chapter 6). The mean annual precipitation was about 520 mm, and annual PET was about 1350 mm. The PET was calculated from Penman-Monteith equation (Chapter 4). Three-water-year data series (1994~1996, see Chapter 6, Figure 6.4), of which 1995 was El Niño year (Chapter 3), were used in the simulations. The mean climate condition of these three years is close to the long-term mean condition in the area (Figure 5.25, Table 5.5). Climate conditions of the three water years varied

(Figure 6.4), having annual PET/P ratios of 2.6, 1.8, and 3.1, respectively. To generate more varied climate conditions, mimicking the large spectrum of topography-modified local climate conditions in mountains, PET was varied by a multiplication of 0.75, 0.5, and 0.35 for each of the three years, while keeping the same temporal variation patterns. The precipitation time series was fixed as the observations of the Los Alamos experimental site. In this way 12 climate conditions, with different ratio of PET/P, were obtained. As you can see here, PET and P are de-coupled from the topography. This is appropriate for this section because our objectives here are to find the relationships between percolation (also actual ET) and the climate conditions. The topography effects on percolation and water yield will be investigated later in Chapter 7 by using topography modified climate conditions (PET and P).

For computational reasons, a 30-cm slope section with a thickness of 200 cm was applied in the simulations with a continuous slope boundary (Appendix XIX). The soil thickness was fixed at 30 cm. The material properties are shown in Table 5.4. As mentioned in §5.2.2, a pseudo layer was placed on the top of the physical soil layer to mimic infiltration-excess surface runoff. Because it was not appropriate to model evaporation from this pseudo layer, ET was simulated as transpiration. This should not significantly change the modeling results given the thin soil cover. Each of the four hypothetical slopes (combination of two slope steepness and two bedrock types) were modeled at two locations (topslope and midslope, Appendix XIX). For each location, 12 simulations (Table XX-1 of Appendix XX) were performed with 12 re-scaled climate conditions (each having a duration of one water year) derived from the three-year observations. In this section (§5.5), the simulations were performed with atmospheric

forcing of each hypothetical water year. The initial condition for each simulation was obtained by periodic forcing of the same climate condition (i.e., times series of each water year).

Table 5.4 Hydraulic properties of materials applied in the minutely-step transient simulations

	θ_r	θ_s	α_1 (1/cm)	n_1	k (m^2)	w_2	α_2 (1/cm)	n_2
Granite	0	0.008	1.13×10^{-4}	1.77	1.0×10^{-14}	0.14	0.1	5
Tuff	0	0.28	0.0014	1.42	1.0×10^{-14}	NA	NA	NA
Silt with macropore	0.034	0.48	0.016	1.37	6.95×10^{-13}	0.05	0.83	3
Pseudo layer	0.034	0.48	0.016	1.37	6.95×10^{-10}	0.1	32	3

5.5.2 Results and discussion

The steady-state simulations do not capture the effect of slope steepness on water partitioning. The series of simulations (Appendix XX) with minute temporal inputs examines the slope steepness effect on runoff and percolation under various hypothetical local climate conditions, which were generated from three-year observations by uniformly rescaling the PET time series. The simulations capture the steepness effect on surface runoff generation, with a larger runoff on a steeper slope, and slightly larger at the location of mid-slope than top-slope (Figure 5.16). The results also indicate that the most effective factor on runoff is precipitation, with a twice as much runoff generation in the 1994 water year (with a lot of summer storms, Chapter 6) as in the 1996 water year. The evaporative demand weakly, but consistently, decreases runoff generation. The runoff generation on a slope underlain by fractured granite is more variable than that on permeable tuff (also see the cumulative runoff plots in Appendix XX).

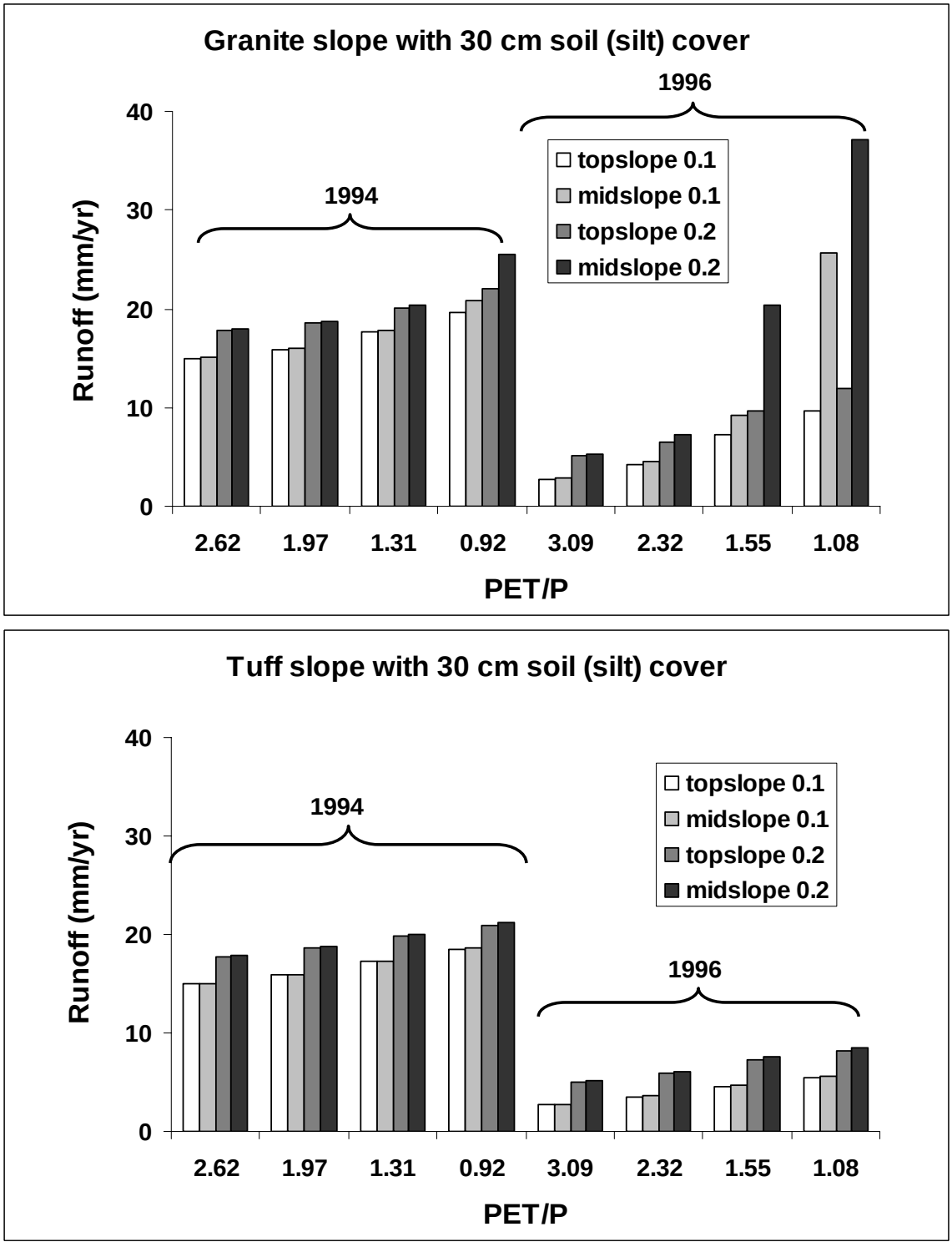

Figure 5.16 The cumulative surface runoff for a hypothetical granite slope (top) and tuff slope (bottom), under various conditions. The climate conditions were generated by rescaling observation-based PET using factors of 0.75, 0.5, and 0.35, for each water year.

The simulated cumulative annual percolation is summarized in Figures 5.17~20. Figure 17 shows slope steepness effects on percolation under various climate conditions. In comparison of simulated percolations for two slope steepnesses, the percolation at the topslope location is smaller for a steeper slope, while at the mid-slope location it is larger for a steeper slope. This is physically reasonable. On a steeper slope, lateral downslope soil water movement is stronger. The topslope location loses more water to interflow, and leaves less water for percolation. At the midslope location, the soil receives more water laterally from upslope, which enhances percolation. If we use geometric mean of the percolation at the two relative slope locations for the average percolation for the slope, there is little slope steepness effect.

Figures 5.18~20 show cumulative percolation (geometrical average of the two locations; note the different scales in the three figures) for slopes with two different degrees of steepness, and two types of underlying bedrock. In agreement with previous simulations, percolation into the matrix-flow-dominant tuff is significantly larger than that into the fracture-flow-dominant granite (even though their bulk saturated hydraulic conductivity is the same). This suggests that unsaturated flow into the matrix-flow-dominant bedrock is important. For all examined slopes, average climate conditions (measured by PET/P) have a dominant effect on percolation. For granite slopes, significant percolation occurs when PET/P is below 1.5. For tuff slopes, significant percolation may occur for a ratio as large as 2.5 (Figure 5.17).

The temporal pattern of the cumulative percolation indicates that percolation into the granite is more sensitive to the precipitation characteristics; while for tuff slope, the effect of precipitation characteristics is less significant. This is probably related to the

different porosities of the two bedrocks (Table 5.4). The effect of climate variability on groundwater recharge is observed here, with significant snowmelt-induced recharge in water year 1995 (from October of 1994 through September of 1995) with 1994-1995 El Nino winter (note that this was defined as 1994 in Chapter 3), while snowmelt is not important for the other two water years (1994, and 1996). It should be noted that these simulations were based on observations at one location, which did not capture the snowmelt effect on recharge at higher elevations. As snow contribution to the total precipitation increases with elevation, snowmelt-induced recharge would increase with elevation.

What do the minutely-based simulations tell us about the bedrock permeability threshold for significant percolation (>10mm/yr). For the three years of observed atmospheric forcing (i.e., 100% PET in Figures 5.18~20), both fractured granite and tuff slopes have percolation smaller than 10 mm/yr for the 1994 and 1996 water years, and larger than 10 mm/yr for the 1995 water year. On average, the bedrock permeability (1.0×10^{-14} m^2) prescribed for both granite and tuff should be around the threshold for significant recharge. It is clear from Figures 5.17~20, that the bedrock permeability threshold for significant recharge depends on local climate conditions.

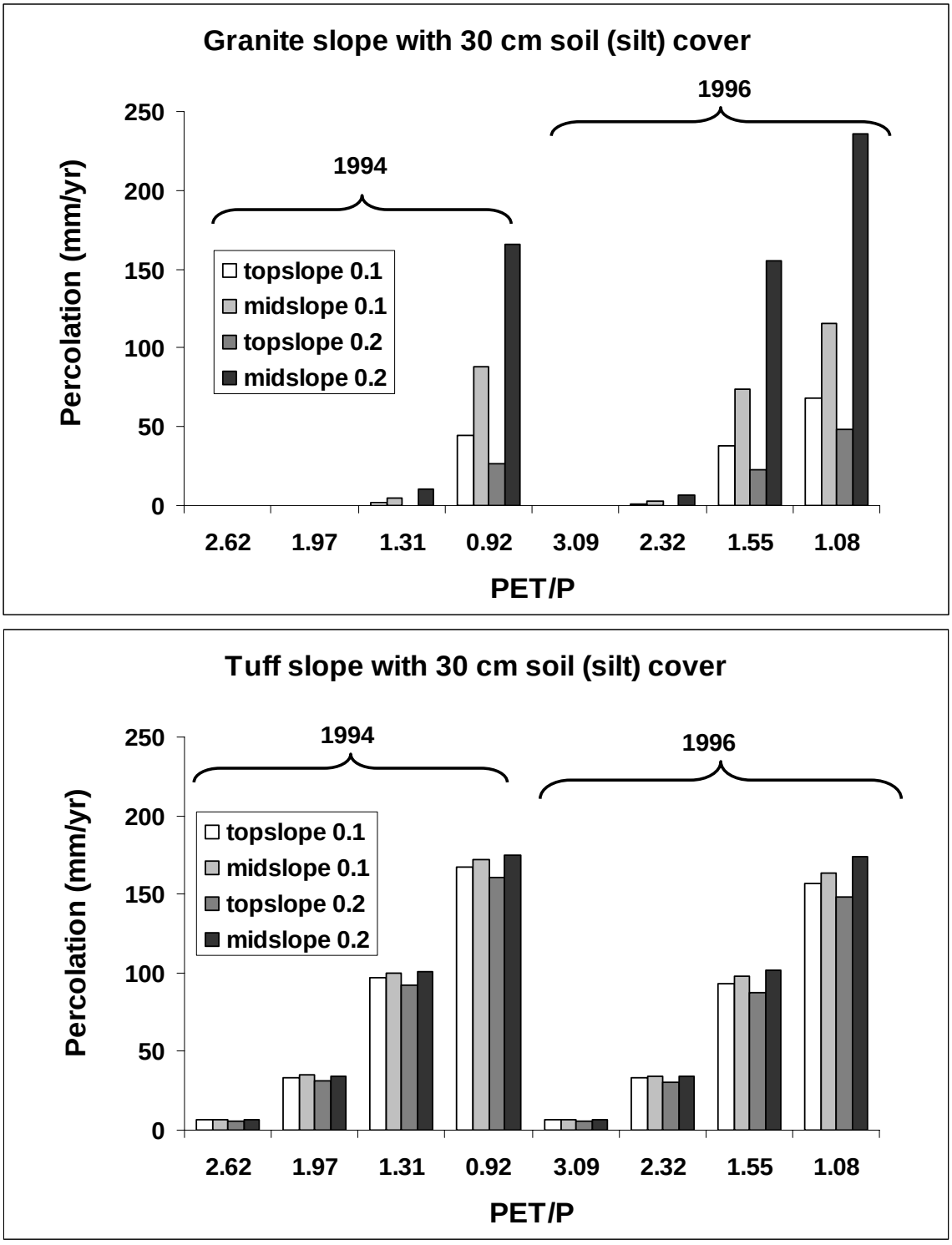

Figure 5.17 The cumulative percolation for a hypothetical granite slope (top) and tuff slope (bottom), under various conditions. The climate conditions were generated by rescaling observation-based PET using factors of 0.75, 0.5, and 0.35, for each water year.

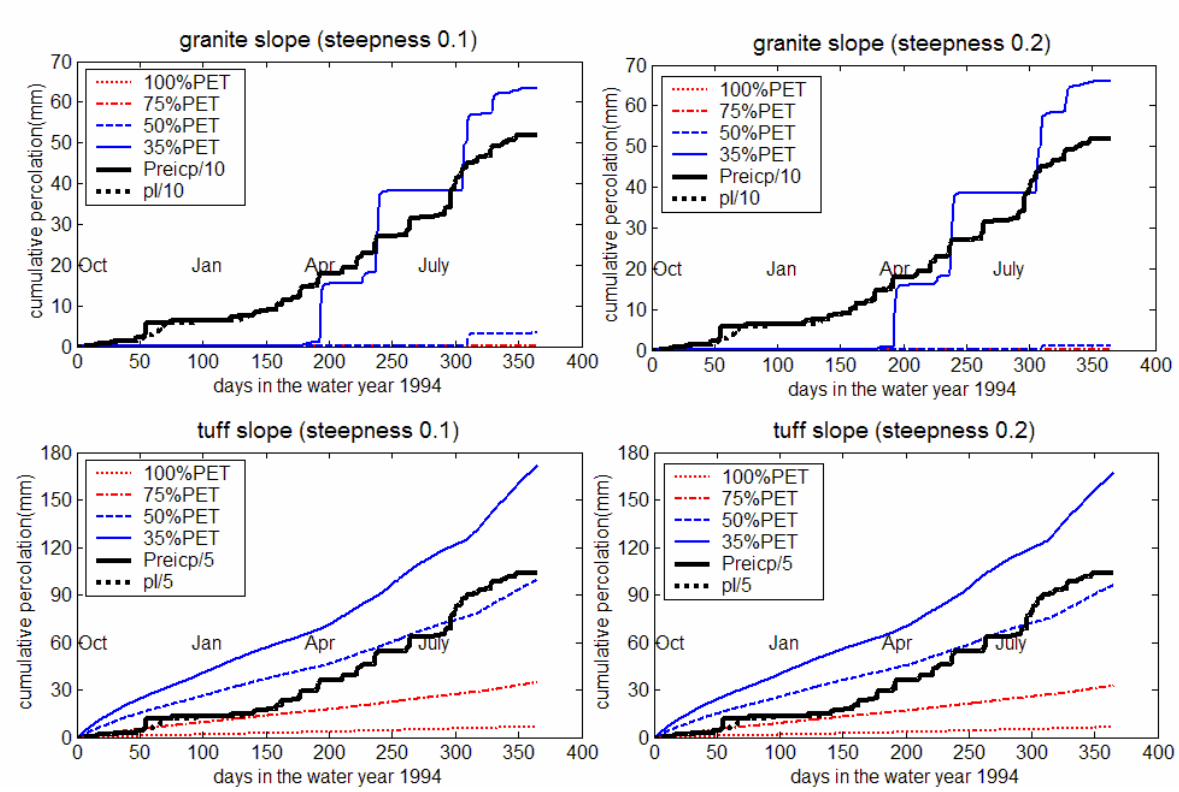

Figure 5.18 Simulated cumulative percolation (geometric mean of the topslope and midslope) under various synthetic climate conditions for the 1994 water year, together with the cumulative precipitation, and active water (pI, or rainfall + snowmelt), for two degrees of slope steepness, and two types of bedrock.

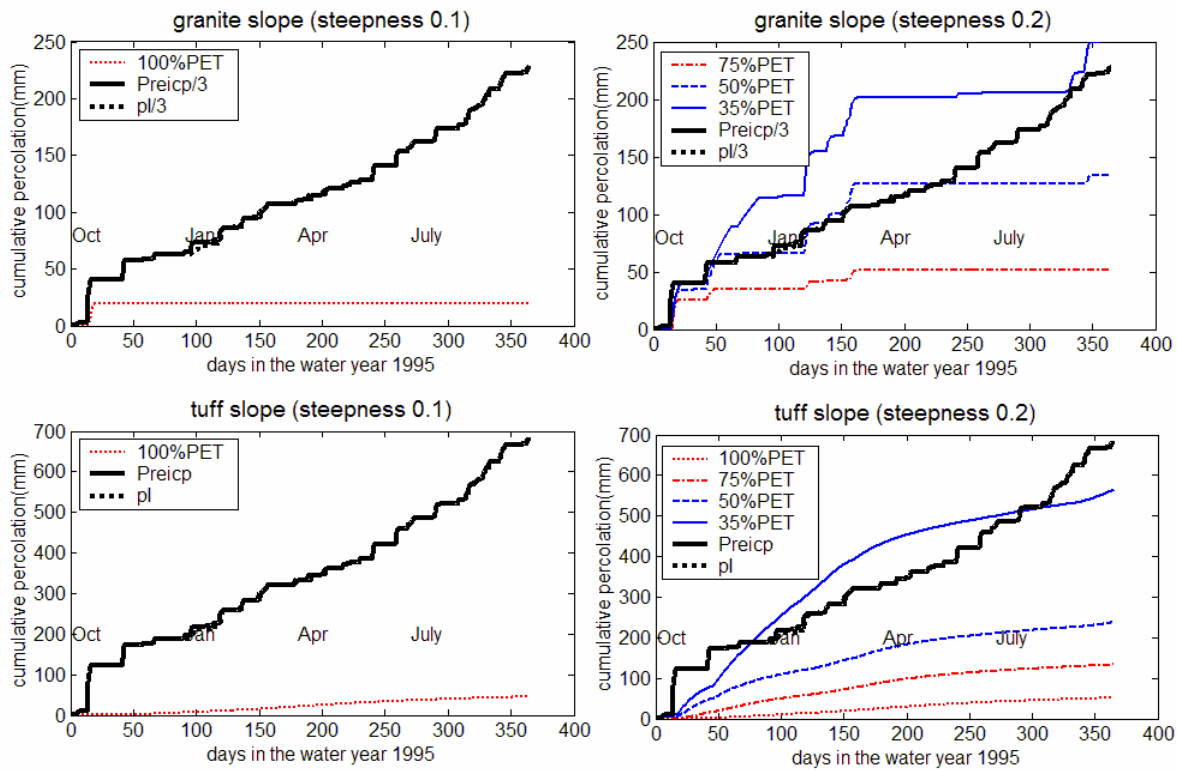

Figure 5.19 Same as 5.18, but for the 1995 water year. Some simulation runs are missed because of numerical stability problems of HYDRUS.

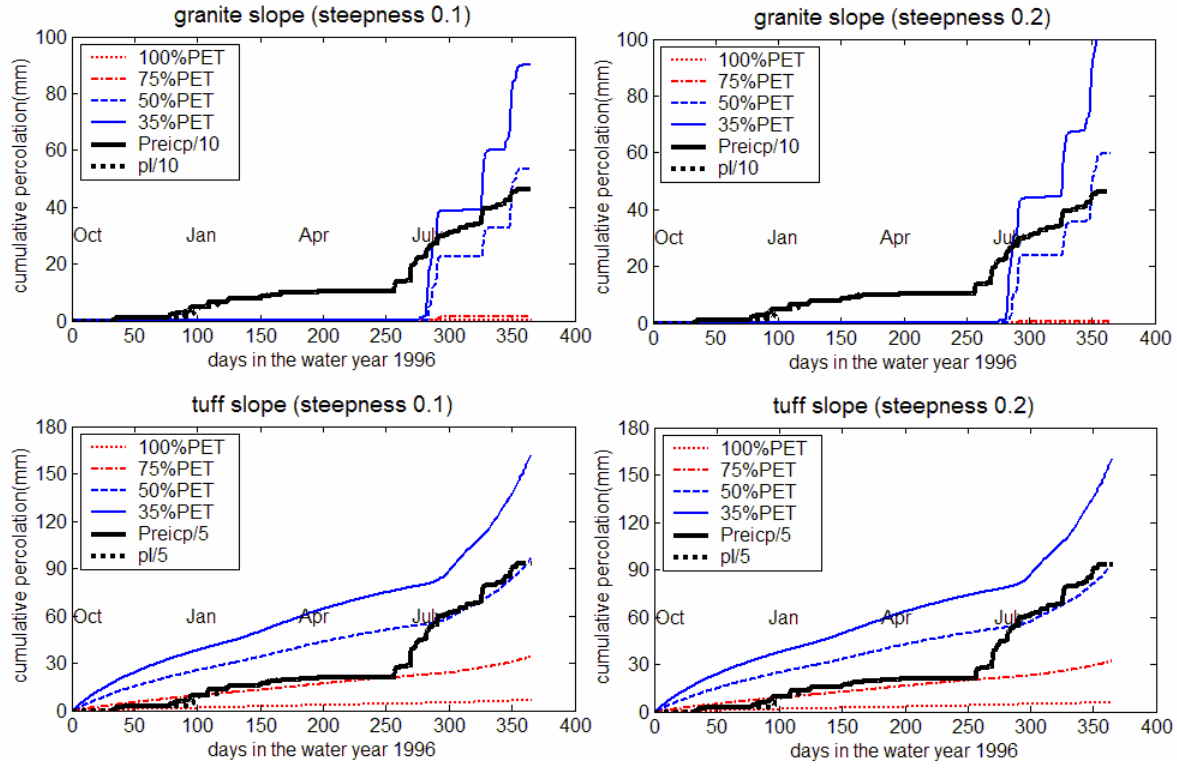

Figure 5.20 Same as Figure 5.18, but for the 1996 water year.

5.6 Discussion

Water partitioning at the soil-bedrock interface along hillslopes depends on various conditions, such as bedrock characteristics, slope steepness and aspect, local climate condition, soil characteristics, and vegetation coverage, etc. Below is a discussion of issues raised by both the generic steady-state simulations and the transient simulations.

5.6.1 Bedrock permeability effect on percolation and its characterization

It is often assumed that most types of bedrock are not permeable enough to allow water percolation. However, significant percolation on hillslopes underlain by the fractured granite is observed in our steady-state simulations with a bulk bedrock permeability of 1.0×10^{-16} m^2 or greater (Figure 5.5 and Table 5.2). In the transient simulations of semiarid mountain regions with daily atmospheric forcing, significant percolation (1~5% annual precipitation) is observed for fracture-flow dominant bedrock with a permeability of 1.0×10^{-15} m^2 (Figure 5.13). In the transient simulations with minute-based atmospheric forcing, the simulated permeability for both fracture-flow dominated and matrix-flow dominated bedrock is 1.0×10^{-14} m^2, and allows significant percolation under a normal semiarid climatic conditions. (Some minute-based simulations with bedrock permeability of 1.0×10^{-15} m^2 were also performed. The percolation was negligible for most of the various PET/P ratios). This is probably because the simulations with minute-based atmospheric forcing captures runoff water loss from the hillslopes (Figure 5.16), which is usually associated with larger storm events. In daily-atmospheric forcing simulations, none of this water runs off, and some contributes to percolation, instead. The permeability threshold for significant percolation is apparently related to

local climate conditions, as well as the bedrock hydraulic properties (Figure 5.17). For the matrix-flow-dominant bedrock (e.g., non-welded tuff), the permeability threshold for significant percolation is smaller, as shown in Figures 5.18~20 with significantly larger percolation for tuff slopes than granite slopes under the same climate condition. In summary, for semiarid mountains, bedrock with permeability between 1.0×10^{-15} m^2 and 1.0×10^{-14} m^2 has a potential for significant distributed recharge.

Bedrock with bulk permeability above these values is common [*Snow, 1979; Caine & Tomusiak, 2003*]. For example, Snow [*1979*] reported permeability around 1.0×10^{-14} m^2 for most of the 5862 tests on fractured crystalline rocks. In addition to tectonic factors, weathering and unloading often cause more fractures in rocks near the surface, which increase bedrock permeability. Thus, studies are required to look at the mechanism of water partitioning at the soil-bedrock interface, instead of simply neglecting the possible bedrock percolation process.

Since bedrock permeability is the primary control for percolation on mountain hillslopes, it is important to have good characterization and quantification of mountain-bedrock permeability for reliable mountain-block recharge estimates. However, estimation of effective bedrock permeability for transmitting water in mountains is a big challenge. The complex geologic structures and bedrock fracture networks (occurrence and connection) make it difficult to obtain representative bedrock permeability of interested scales from point measurements. Conventional pumping tests are extremely difficult to apply in mountains. Compared to the matrix-flow-dominant bedrock (e.g., non-welded tuff), the effective permeability of fracture-flow-dominant bedrock (e.g., crystalline bedrock) is more difficult to estimates. The major difficulties are: (1) the

fracture zone is difficult to locate in mountains; (2) the connection of fractures in the mountain block is difficult to obtain; (3) relationship between observed fractures and effective permeability is not clear; (4) upscaling of permeability derived from small zones to a larger area is not clear. Although many efforts have been made to address these difficulties [e.g., Snow, 1969; Witherspoon et al., 1980; Long & Witherspoon, 1985; Liu et al., 2000; Odling, 2001; Winter & Tartakovsky, 2001], it is still not clear how we can obtain reliable estimates of effective mountain-bedrock permeability.

Recently, Caine & Tomusiak [*2003*] coupled field fracture characterization and numerical modeling (FracMan) for estimating fractured bedrock permeability of the Turkey Creek Watershed, Colorado Rocky Mountain Front Range. Wilson [*2005*] used air permeameters measuring permeability of numerous non-welded tuff outcrops in the Pajarito Plateau of the Jemez Mountains. These efforts of intensive field measurements provide good information for estimating effective permeability of the mountain block. Measurements of water seepage rate from mountain tunnels [e.g., Pili et al., 2004] also provide valuable information for estimating bedrock permeability. Besides direct field measurements, some geophysical techniques can be used to estimate fractured bedrock permeability. For example, Boado [*1997*] proposed to relate the hydraulic properties of fracture bedrock to seismic attributes. In spite of these progresses, quantification of mountain-bedrock permeability is still a big challenge, and of large uncertainty.

Given the importance of bedrock permeability in estimating percolation over mountain hillslopes, a better characterization of bedrock hydraulic properties in mountains is among future needs for better mountain-block recharge estimates.

5.6.2 Slope steepness and aspect effects

Due to the gravitational force, it is assumed more water flows laterally along the slope as runoff and interflow when the slope steepness increases. Consequently, the percolation would decrease with slope steepness. It is observed in the steady-state simulations that *PI* (= *percolation* ÷ *interflow*) decreases with the slope steepness, at least for some situations (Figure 5.7). However, this effect is not significant in terms of the percolation amount (Table 5.2). An observable effect of slope steepness on surface runoff generation is shown in the transient simulations (Figure 5.16), i.e., larger runoff occurs on a steeper slope. A similar effect on percolation, however, is not observed (Figure 5.17). The difference in effect on surface runoff and percolation is due to the different response time of two processes. Surface runoff is a quick process, and captures the slope steepness effect by fast partitioning of active precipitation water on the surface. Percolation is a slow process. Any effect of slope-steepness on infiltration at the surface is filtered by the dynamic soil water storage (mainly through evapotranspiration), before reaching the soil-bedrock interface, where the percolation occurs. As a result, slope steepness is not a significant factor on percolation.

The simulations suggest that slope steepness does not significantly affect the percolation. However slope aspect does have an effect given sufficiently permeable underlying bedrock (Figure 5.13). This is because of modification of local climate by the slope aspect (steepness as well), leading to more solar energy on a south-facing slope than on a north-facing slope. This indicates that the effect of slope aspect on percolation is mainly from their influence on the surface energy partitioning, not on their influence on the water partitioning at the soil-bedrock interface. The effect of slope steepness works in a similar way. Thus, the slope aspect effect is more important than slope

steepness; and the effect is more dominant in winter and spring than in summer (Appendix XI).

5.6.3 Soil thickness effect

Soil works as temporal storage for infiltration water (rainfall and snowmelt) on mountain hillslopes. If it is absent, water quickly runs off, leaving less water for percolation. This situation is not simulated in this dissertation. In some cases, a low-permeability soil horizon in the soil cover may impede downward water movement to the soil-bedrock interface, leading to little percolation (Chapter 6). In this chapter, the effect of soils with permeability orders magnitude larger than the underlying bedrock is examined. For a thick soil cover, the water-storage capacity is larger. Consequently, vegetation transpiration competes for more water against percolation (Figures 5.12 and 5.13). The soil thickness effect becomes smaller when the deep-rooted vegetation coverage is smaller. This is evident from observations that percolation is insensitive to soil thickness when the evapotranspiration is not modeled (Figure 5.8), or when ET is modeled and the vegetation is removed from granite slopes (Figure 5.13).

5.6.4 The effect of local climate conditions

The steady-state simulations demonstrate that the relative water availability (R= the ratio of net infiltration rate over saturated bedrock hydraulic conductivity) at the soil-bedrock interface can be used to estimate the limitation factor for percolation. When R is far larger than one, bedrock permeability is the limitation. When R is far smaller than one, water availability is the limitation. The local climate condition, which determines the soil water availability, controls the percolation for a hillslope with permeable bedrock (Figures 5.12, 5.17~20). In this study, PET/P (the ratio of annual potential ET over precipitation) is used to characterize the local climate condition. The ratio of PET/P is

modified by terrain steepness and aspect, terrain elevation, and vegetation coverage. For a matrix-flow-dominant bedrock ($k=10^{-14}$ m^2), a local climate condition with an annual PET/P smaller than 2.3 can lead to significant annual percolation (>10 mm), insensitive to precipitation characteristics. For a fracture-flow-dominant bedrock ($k=10^{-14}$ m^2), the annual PET/P has to be smaller than 1.5 for a significant annual percolation (>10 mm), and the effect is sensitive to precipitation characteristics (Figure 5.17).

5.6.4.1 Estimation of recharge from local climate conditions

Since the topographic effects on percolation are mainly from its influences on the surface energy partitioning (§5.6.2), they can be lumped into the effect of local climate conditions. If the function of recharge and climate conditions (e.g., PET/P ratio) is obtained, the topographic effects on recharge can be estimated from the topography-dependent local climate conditions.

Can we use a simple climate index, such as the aridity index (PET/P), to estimate recharge? Small [*2005*] used synthetic time series of climatic variables (PET and P), derived from precipitation gauges throughout the southwestern United States, to model diffuse recharge. He concluded that long-term mean PET/P is not an appropriate indicator for estimating diffuse recharge. The major reason is that besides the PET/P ratio, recharge also depends soil types, PET and P seasonality, and storm size distribution (duration, intensity, and precipitation interval). Nonetheless, the variability of climatic seasonality is relatively small for a small study area (e.g., the northern NM mountains in this dissertation). The seasonality effect should be not as much important as in Small's [*2005*] study. The recharge-aridity index function can be a good way to estimate local long-term mean recharge for a certain bedrock and soil condition. Below are two simulation studies that test this assumption.

The first is the study of daily-step simulations (§5.4). These simulations were conducted on hillslopes of loam (30cm) + fractured granite (170cm) with topography- and vegetation-modified climate conditions (numerical setting exactly as § 5.4.1) for four consecutive water years (Figure 5.13). The simulated four water years had quite different seasonal precipitation. For example, the winter of 1992 water year was an El Nino winter, with significant larger snow precipitation than other years. Consequently, the simulated recharge of this water year mostly occurred in spring snowmelt season (Figure 5.12 a&b). However, this type of seasonal variability does not break the relationship between annual recharge and annual climate index (Figure 5.21). This result supports the assumption that for a small region, seasonality is not important for the recharge-climate index relationship.

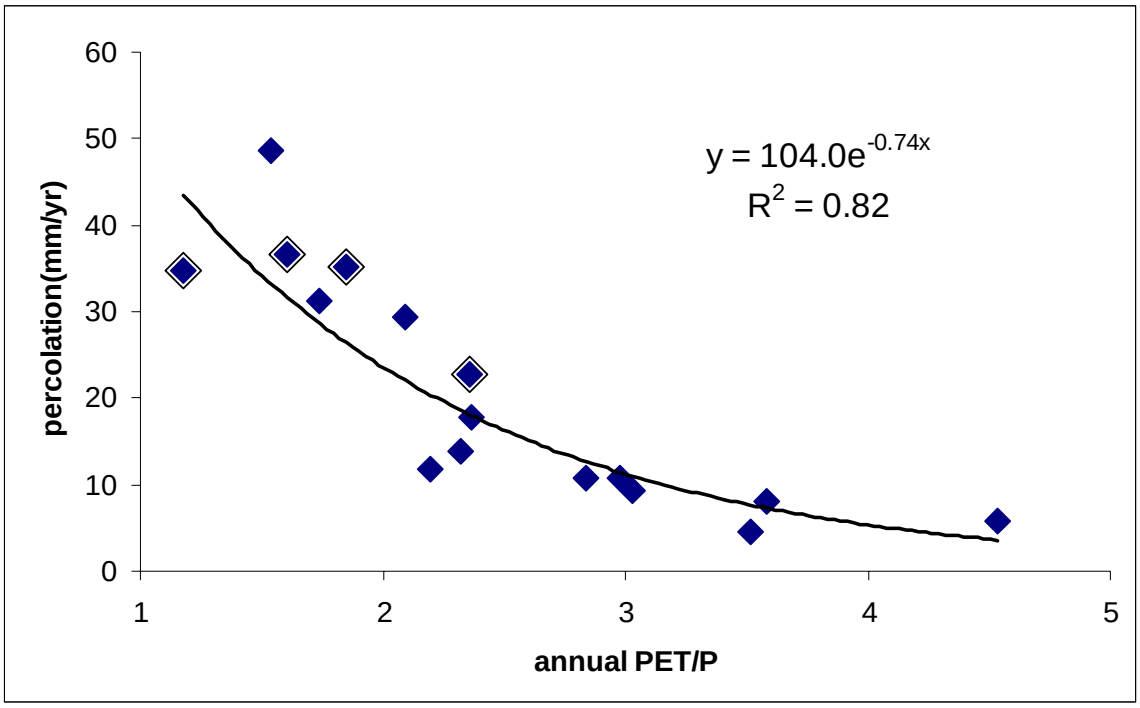

Figure 5.21 Simulated annual percolation (1991~1994) on a hypothetic fractured-granite ($k = 1.0 \times 10^{-14}$ m^2) slope with a 30cm-loam cover, as a function of annual PET/P modified by topography and vegetation. The four distinguished points are percolation of 1992 water year.

The second study is to compare the numerical simulation result to Sandvig's [*2005*] field study. Using soil chloride profiles, Sandvig's [*2005*] estimate of the long-term mean recharge at her ponderosa pine sites (PET/P = 3.7) in central New Mexico is about 2.3 mm/yr. If the climate index can be used an indicator for recharge, we should expect similar percolation from the numerical simulations forced by a climatic boundary with aridity index of 3.7. Because no high-temporal-resolution climate data is available for this site, which is important to simulate recharge (§5.6.6.1), the minute-time-step micrometeorological observations at Los Alamos, are rescaled by the PET/P ratio for Sandvig's ponderosa pine site. This is done for each of the three years. Note that the observed PET/P ratios are different for the three years (Figure 6.4), the rescaling factors are also different.

Based on the soil profile description of Sandvig's [2005] sites 10 and 11, the model soil profile is composed of sandy-loam (0~30 cm depth), loam (30~70 cm), and silt (70~200 cm), with hydraulic properties embedded in HYDRUS. Although at 30~70 cm, clay content is usually high for the ponderosa pine site, the tree root increases the hydraulic conductivity of the bulk soil. This is why loam is prescribed at this depth interval. The root distribution is prescribed in the top 70 cm of the profile, with relative root density based on observations at the Los Alamos ponderosa-pine hillslope site (i.e, 0.65 at 0~30cm, and 0.35 at 30~70cm). The root-water-uptake model is prescribed as the S-shape model (h50=-500 cm, p=2), which was calibrated at the Los Alamos ponderosa pine site (Chapter 6). Two series of 1D simulations are conducted using HYDRUS-1D (Appendix XXI). In the first series, the simulations are conducted in sequence with initial condition inherited from the previous year. In the second series, the simulations are

conducted for each individual year, with soil column in equilibrium to the atmospheric forcing of the specific year.

The first series simulation results estimate that percolation is 2.2, 3.9, and 5.2 mm/yr for the three water years, respectively. The mean annual percolation is 3.8 mm/yr, close enough to Sandvig's [*2005*] estimate (~2.3 mm/yr) for the ponderosa pine sites (Appendix XXI). The agreement between the simulation result and the estimate based on field observations gives us more confidence in using climate index for estimating local recharge. However, in the second series simulations for Sandvig's [*2005*] ponderosa pine sites, the simulated annual recharge are 0.7, 7.8, and 2.2 mm/yr for the hypothetical 1994, 1995 and 1996 water years (all having the same aridity index) (Appendix XXI). This suggests that some climatic characteristics other than the mean PET/P ratio control recharge. If it is not the precipitation seasonality, it must be characteristics of storm size distribution. Thus, the recharge-climate index is not appropriate to estimate recharge of an individual year. It is used for estimating long-term mean recharge based on long-term mean climate index.

5.6.4.2 Recharge-aridity index functions for the northern New Mexico

With an assumption of uniform soil (30 cm macropored silt) and bedrock (fractured granite or non-welded tuff), the recharge-climate index relationship can be derived for the northern New Mexico from the minute-step simulations (§5.5 ,Figure 5.22). The relationship can be fitted with equations 5.7 and 5.8 for granite slopes and tuff slopes, respectively.

$$Percolation\,(\frac{mm}{year}) = 1222.2\exp(-2.766\frac{PET}{P}) \qquad (5.7)$$

for granite slopes, and

$$Percolation\,(\frac{mm}{year}) = 1230.9\exp(-1.771\frac{PET}{P}) \tag{5.8}$$

for tuff slopes, where PET is annual potential ET and P is annual precipitation, both in units of mm.

Similarly, the annual evapotranspiration is also a function of local climate conditions and underlying bedrock (Figure 5.23), with fitted linear regression equations (5.9) and (5.10) for granite slopes and tuff slopes, respectively.

$$ET = -30.3 + 0.660P + 0.149PET \tag{5.9}$$

for granite slopes, where *ET*, *P* and *PET* are in mm/year, and

$$ET = -80.4 + 0.584P + 0.186PET \tag{5.10}$$

for tuff slopes.

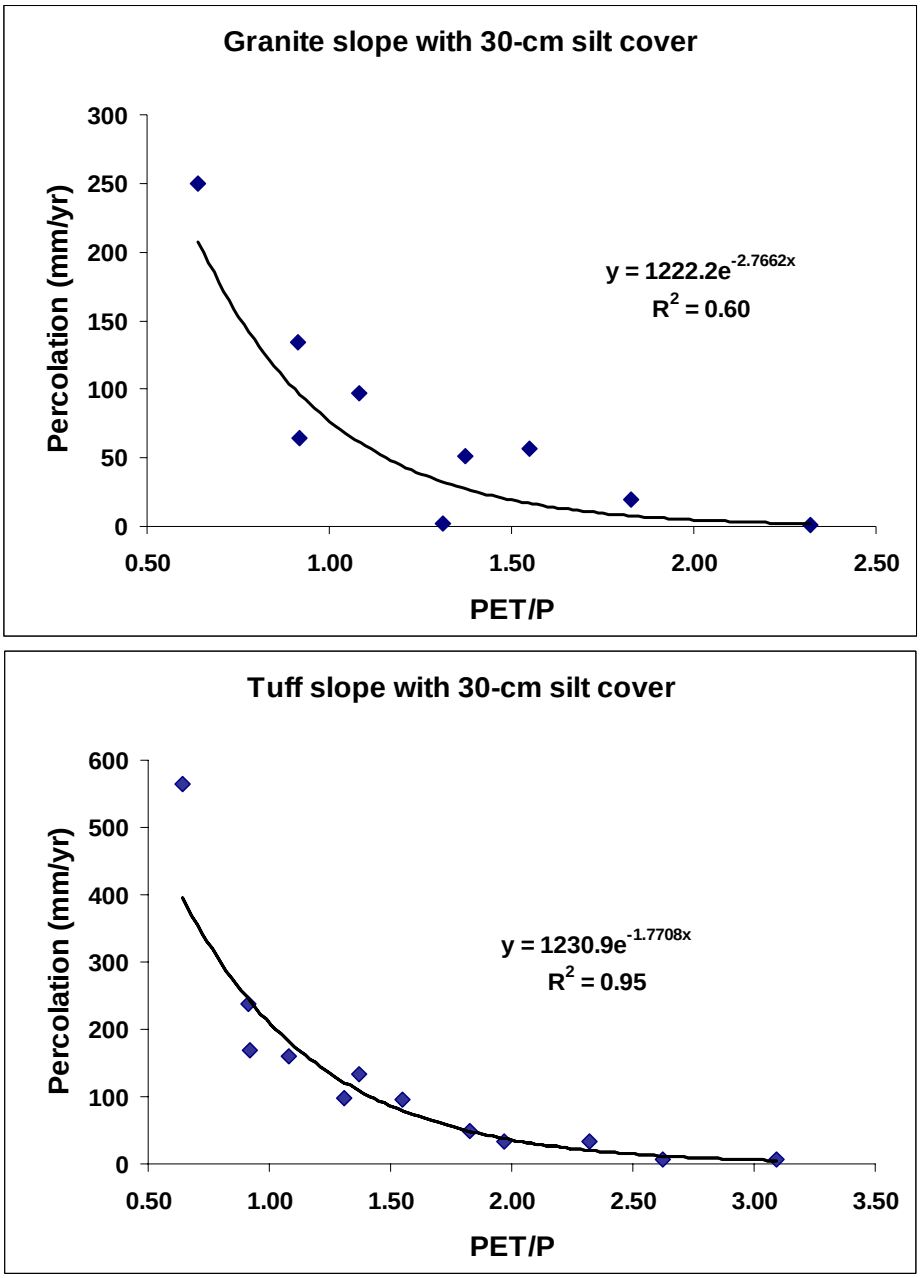

Figure 5.22 The cumulative percolation as an exponential function of local climate condition on a hypothetical granite slope (top) and tuff slope (bottom), with 30-cm soil cover. Each data point corresponds to average simulation results (i.e., averaged over 0.1 and 0.2 slope steepness) for each climate condition.

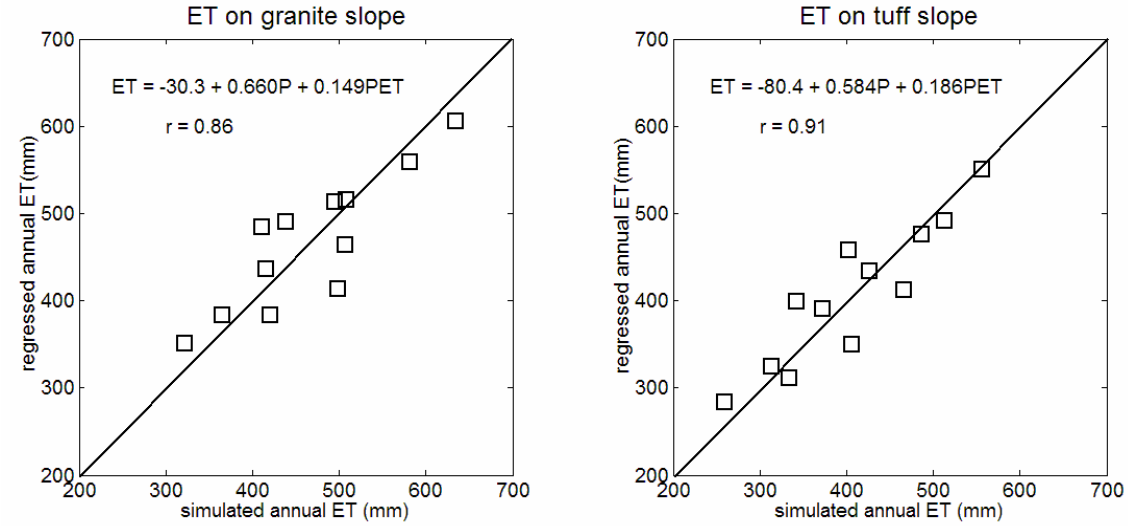

Figure 5.23 Regression-estimated annual ET as a function of local climate condition vs. model simulated annual ET for a hypothetical granite slope (left) and tuff slope (right), with 30-cm soil cover. Each data point corresponds to average simulation results (i.e., averaged over 0.1 and 0.2 slope steepness) for each climate condition.

As discussed in §5.6.4.1, the recharge-climate index function is used for estimating the long-term mean recharge from the long-term mean local climate condition. Are the statistics derived from 3-year-climate-based simulations (§5.5) representative of the effects of long-term climate variability? To test whether the 3-year-climate-based simulations are representative, a long-term (1948~2004) simulation is completed using daily climate data of NCDC Los Alamos weather station (COOP 295084). This station (2262m) is a little lower than the Los Alamos ponderosa hillslope site (2315m), where the minute-step micrometeorological observations were made. It is reasonable to assume precipitation seasonality and storm size distribution are similar to the Los Alamos ponderosa pine site. Potential ET is assumed to be the same as the Los Alamos ponderosa pine site, and not change between years. The Penman-Monteith-equation-calculated hourly PET of 1996 water year at the Los Alamos ponderosa pine site (Figure 6.4) is

degraded to daily time step for long-term simulations of the NCDC weather station. The annual PET/P from 1948 through 2004 is shown in Figure 5.24.

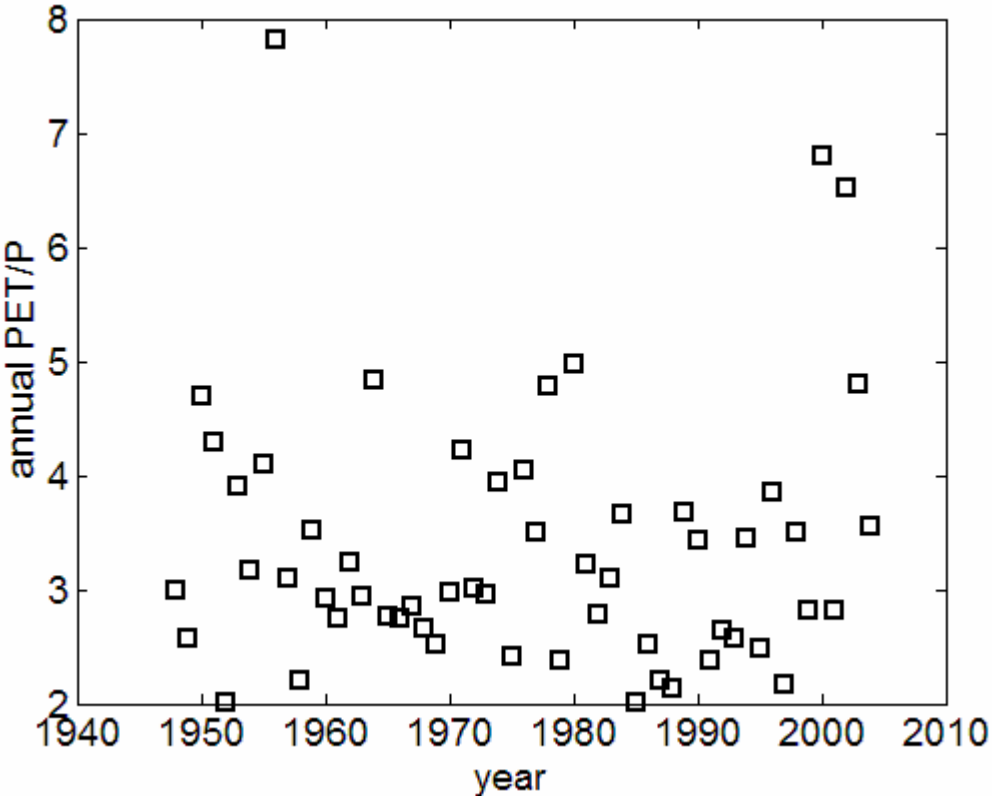

Figure 5.24 Annual PET/P at NCDC Los Alamos weather station (COOP 295084).

The simulated 1D soil column is composed of 30-cm macropored silt and 170-cm non-welded tuff (Table 5.4). HYDRUS-2D is used because HYDRUS-1D does not have composite function for modeling macropored silt. The simulation with the 57-year climate forcing is done sequentially (i.e., the initial condition of a year inherits from the end of the previous year), with simulated annual percolation shown in Figure 5.25. It is observed that annual percolation negatively responds to the annual PET/P ratio, but with some time lag (there should be less time lag for fractured-granite slopes). This is another reason that the recharge-climate index relationship is not appropriate for estimating

recharge of an individual year. The three water years (1994~1996), that were used to derive the recharge-climate index functions, have climate condition and recharge very close to the long-term mean values (Table 5.5).

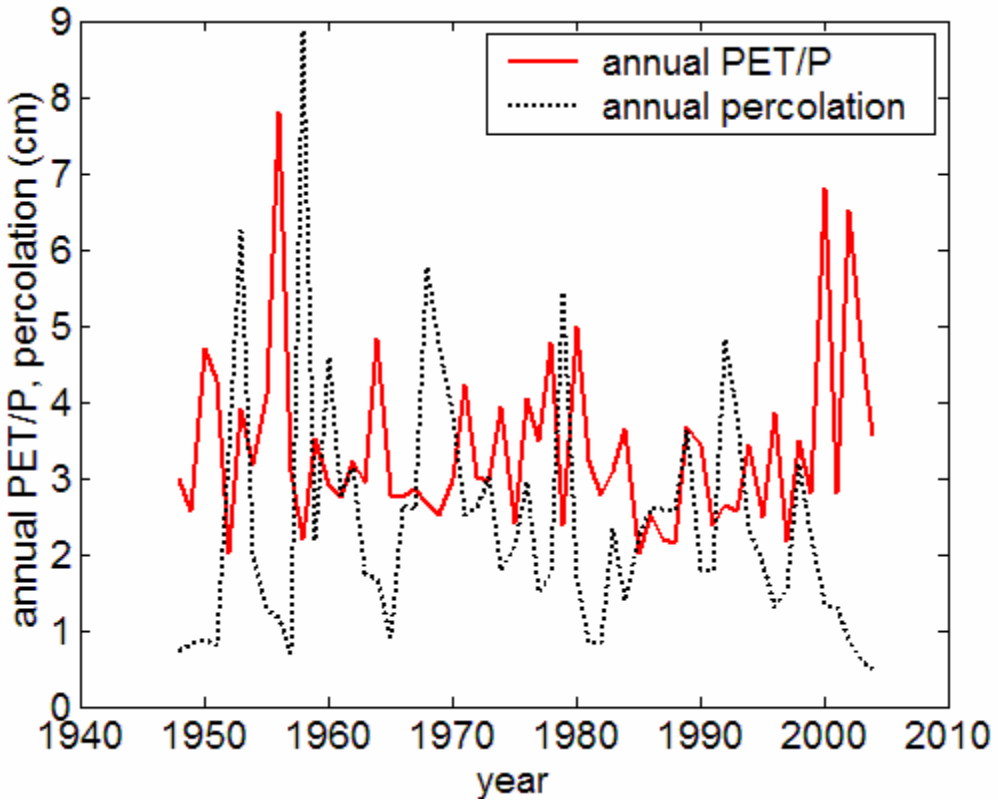

Figure 5.25 The HYDRUS-2D simulated annual percolation of a 1D column (30 cm macropore silt + 170 cm tuff) with daily precipitation observed at the NCDC Los Alamos weather station, in comparison to the annual PET/P ratio. The daily PET was prescribed identical between years.

Table 5.5 The mean climate condition and simulated percolation of a 1D column (30 cm macropore silt + 170 cm tuff) with daily atmospheric forcing observed at the NCDC Los Alamos weather station

mean	57years	three years
PET (mm/yr)	1433	1433
P (mm/yr)	463	456
PET/P	3.10	3.14
Percolation (mm/yr)	24.1	18.4

We can also find the relationship (an exponential function) between the simulated annual percolation and the annual aridity index (solid line in Figure 5.26). The results of the three water years locate near the solid line, which again indicates the climate of the three selected water years is representative of the long-term mean conditions.

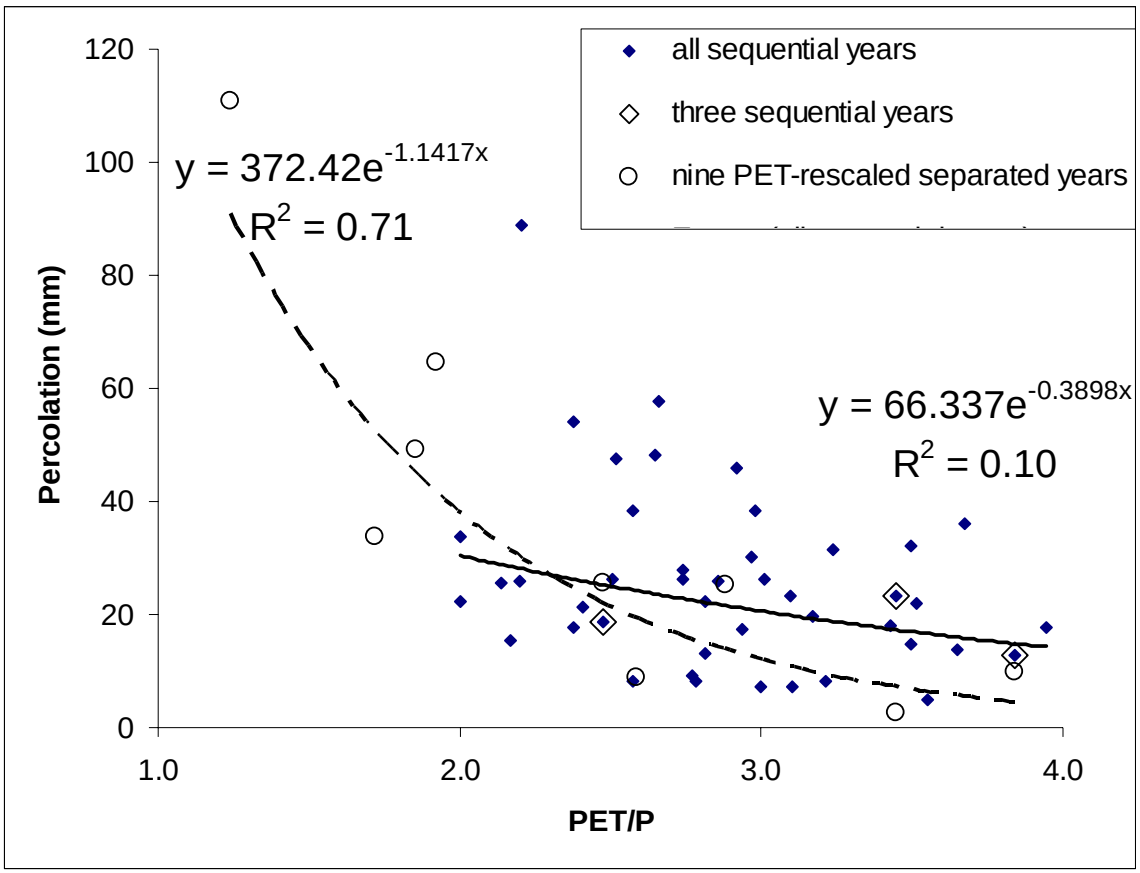

Figure 5.26 The simulated (macropored silt + tuff) annual percolation with daily precipitation observed at the NCDC Los Alamos weather station vs. annual PET/P (the data point with PET/P over 4 are neglected). The three open diamonds are for the three water years (1994, 1995, and 1996). The nine open circles are for separated PET-rescaled (100%PET, 75%PET, and 50%PET) 1994, 1995, and 1996 water years. The solid line is the exponential function fit of solid diamonds; the dashed line is exponential function fit of open circles.

Can we use the solid line in Figure 5.26 to estimate recharge of the nearby location with significant different topography-modified climate conditions? The answer is No. This is because the solid line is derived from one location with a certain mean

climate condition. One year of low PET/P ratio, very often having a dry initial condition following a high PET/P year, does not often lead to a high annual recharge. This is different from the situation at a location with low long-term mean PET/P ratio (e.g., north-facing slopes). Thus, even though we do simulations with sequential long-term atmospheric forcing at one location, we only produce one data point (mean PET/P, mean percolation) for generating the recharge-climate index function.

To estimate spatial recharge distribution of a mountainous area with various local mean climate conditions, we need to re-scale the point climate condition to mimic a range of mean climate conditions in the mountains. Simulations forced by these rescaled climate conditions will give recharge estimates for locations with similar mean climate conditions. The circles in Figure 5.26 are simulated percolations for re-scaled climate conditions based on the three-water-year data. The three rescaled conditions are 100%PET, 75%PET, and 50%PET, respectively, with fixed precipitation time series. Based on these circles, an exponential function is found to relate mean annual recharge to mean annual climate conditions. Now, let's test this function with mean annual percolation from sequential simulations of three-water-year forcing at Los Alamos hillslope site.

Because the climate is re-scaled to wetter conditions than the NCDC Los Alamos weather station (PET/P=3.1), the Los Alamos hillslope site (PET/P=2.4) is used to test the resulted function. The atmospheric forcing of 1994~1996 water years is used sequentially (as done in §5.4) in the simulation to obtain mean annual percolation. If the initial condition in equilibrium with a neutral ENSO year 1996 (or 1994) water year is used (i.e., periodic forcing of 1996 (or 1994) water year is performed to obtained the

initial condition), the simulated mean annual percolation is 34 (or 42) mm/yr. The fitted function (dashed line in Figure 5.26) estimates a mean annual percolation of 23 mm/yr. The error can be due to the noise in the fitted function or the difference in climate characteristics between the NCDC station and the Los Alamos hillslope site. A longer climate data set would be helpful to obtain a more statistically representative recharge-climate index function for long-term mean recharge estimation. Nonetheless, the difference between fitted and simulated recharge is less than 50% of the simulated values. This is not too bad for recharge estimation.

In summary, the recharge-climate index relationship can be used to estimate long-term mean recharge. It is not appropriate for estimating recharge of an individual year. Rescaled PET/P is necessary to find the recharge-climate index function for a mountain region, where local climate conditions are strongly modified by topography. The three water years (1994~1996 water years) have a climate condition close to the long-term-mean condition in the study area. However, because the three-year climate record does not include all variability of long-term climatic characteristics (mainly storm size distribution pattern), the fitted recharge-aridity index function has error for recharge estimation. It tends to underestimate mean recharge because the short time span does not usually include extreme events, especially sequential events that often lead to large recharge. To make the function more statistically representative, a longer climate record is recommended for obtaining the function in the future.

Nonetheless, since it is long-term mean recharge being considered in the recharge-aridity index function, the effect of rare extreme events on the long-term mean recharge should be small by averaging over a long time period. (This is different from the

situation on the basin floor, where recharge only occurs for some extreme events [e.g., *Kearns and Hendrickx, 1998*]. Because the long-term mean recharge is very close to zero, the contribution of recharge due to few extreme events can be important). Thus, the equations 5.7~10, derived from the three-year minute-time-step simulations, is reasonably representative to the study area. They will be used in Chapter 7 to estimate mountain-block recharge of the Sangre de Cristo Mountains and the Jemez Mountains.

5.6.4.3 Locally derived empirical functions for recharge-climate index relationships

The simulated percolation for granite and tuff slopes (§5.5) can be also fitted with power-law functions (Figure 5.27). They are

$$Percolation = \frac{66.99}{PET^{3.57}} P^{3.57} \qquad (5.11)$$

for slopes of fracture-flow dominant bedrock (e.g. granite), and

$$Percolation = \frac{200.68}{PET^{2.76}} P^{2.76} \qquad (5.12)$$

for slopes of matrix-flow dominant bedrock (e.g., tuff) slopes, where P, PET, and percolation are in units of mm/yr.

These functions are similar to some empirical equations used to estimate various types of mountain-front recharge [*Wilson and Guan, 2004*]. For example, Maxey-Eakin

[*1949*] developed an empirical function for the White River Basin, Nevada, (transformed by Wilson and Guan [*2004*])

$$MFR = 9 \times 10^{-9} P^{3.72} \qquad (5.13)$$

where MFR is approximately equivalent to MFR_1 in Wilson and Guan [*2004*], i.e., the sum of conventional mountain-front recharge and mountain-block recharge. The power is close to the percolation equation of slopes with fracture-flow dominant bedrock, (5.11).

Maurer and Berger [*1997*] estimated an empirical regression for mountain water yield (including surface runoff and subsurface flow, approximately equivalent to MFR_2 in Wilson and Guan [*2004*]) at Carson Basin, Nevada,

$$MFR_2 = 2.84 \times 10^{-5} P^{2.43} \qquad (5.14)$$

where P is the mean annual precipitation in mm per year. The power is similar to the percolation equation for slopes of matrix-flow dominant bedrock, 5.12.

Equations 5.11 and 5.13 do not represent the same quantities. Neither do the equations 5.12 and 5.14. Nonetheless, the similarity between the two equations indicates that some basic physical processes that are captured by the hydrologic simulations of this study may be also implicitly included in those empirical equations. It should be noted that the similarity is only in the functional form. If the parameterization is considered, they are significantly different. Equations 5.11 and 5.12 tell us that the parameterization of those empirical equations strongly depends on bedrock characteristics and annual

potential ET. This suggests that the transferability of those empirical equations is problematic. The approach used to generate the functions in this study could be used to re-parameterize the empirical recharge equations, such as Maxey-Eakin equation, when they are applied in other regions. Equations 5.11 and 5.12 also tell us that recharge is influenced by both annual potential ET and precipitation, and their relationship, not only annual precipitation.

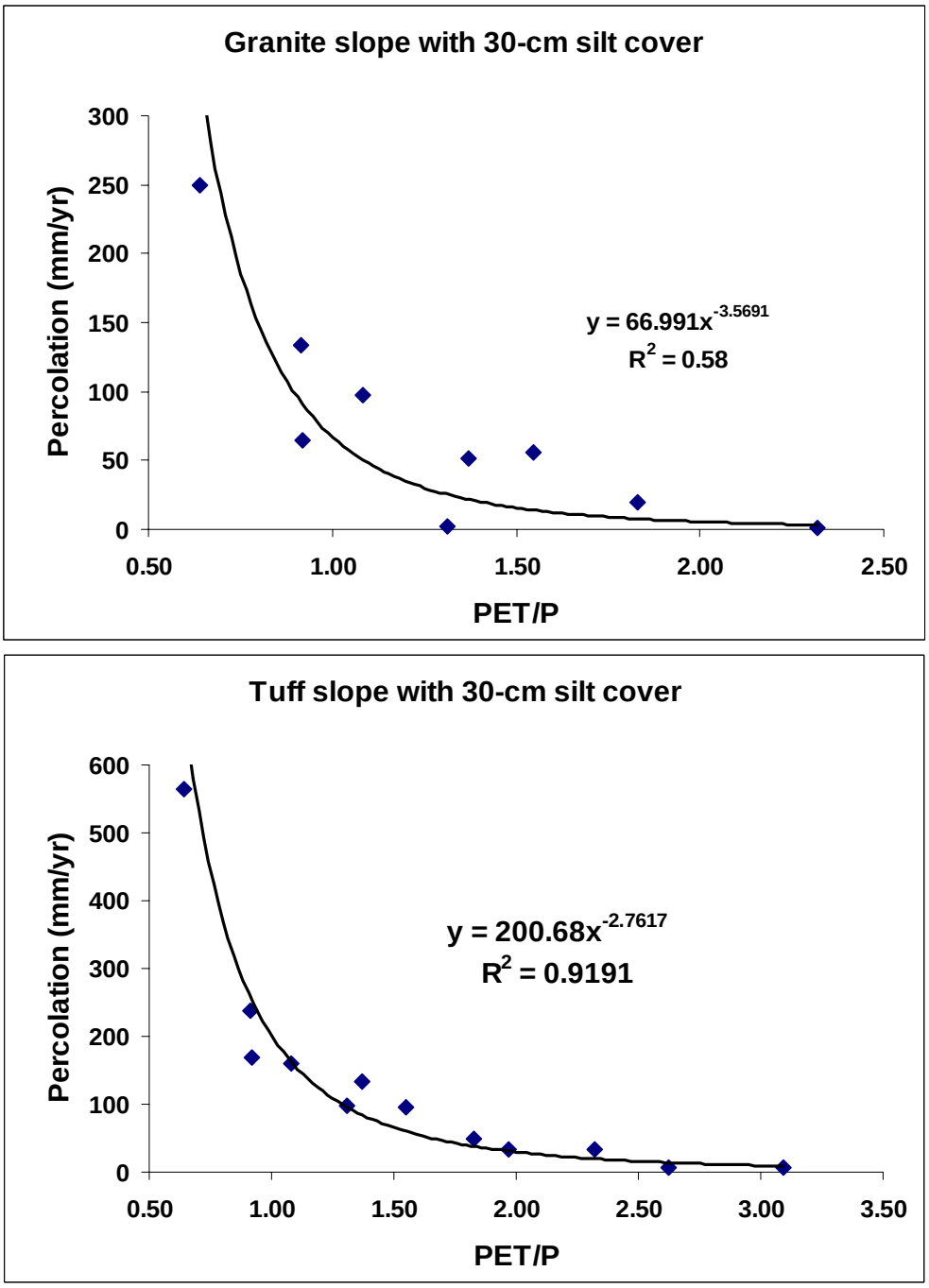

Figure 5.27 The cumulative percolation as a power-law function of local climate condition on a hypothetical granite slope (top) and tuff slope (bottom).

5.6.5 Vegetation coverage effect

Vegetation influences near-surface water partitioning via various mechanisms (§4.1). The effect of watershed vegetation control on water yield has been studied for several decades [e.g., *Bosch and Hewlett, 1982; Dugas et al., 1998; Wilcox et al., 2005*]. For 94 watershed experiments reviewed by Bosch and Hewlett [*1982*], all but one had increased water yield after vegetation removal (mostly in the first and second years). However, Wilcox et al.'s study [*2005*] of nine small watersheds in the Edwards Plateau, Texas, over a period of 13 yeas show that changes in woody plant cover has little effect streamflow from these watershed. All these studies quantified water yield change by measuring the streamflow, without considering percolation (or recharge) into the underlying bedrock. The simulations here reveal how vegetation control affects recharge. From the transient simulations (§5.4) with the atmospheric boundary condition provided by TVET, the percolation increases several to ten times when the vegetation is removed (Figure 5.13). It should be noted that the soil structure and geomorphic changes due to the vegetation removal were not represented in the simulations. Nonetheless, the results should be applicable to the first couple of years after vegetation change. The increased annual percolation is about 2~5% annual precipitation for the fractured granite slope, and 15~20% annual precipitation for the highly permeable tuff slope, and the number varies with soil thickness. This demonstrates that the increased water yield due to the vegetation removal partitions into both streamflow and deep percolation, and does so in a way that depends on both the soil and the underlying bedrock characteristics. Some studies showing negligible change in streamflow after vegetation removal may not necessarily mean negligible change in percolation and therefore in water yield.

Apparently, the vegetation effect is closely related to other factors that influence near-surface water partitioning. The establishment of vegetation is determined by climate conditions, terrain location (elevation, slope aspect and steepness), soil development, etc. For example, vegetation on different slopes is often different, with denser vegetation on the slope with thicker soil and less PET, leading to similar soil water state between the slopes, and similar recharge potential. Thus, locations with dense vegetation coverage usually have a larger potential to increase water yield (precipitation-ET) by vegetation removal. Vegetation also modifies soil structure, and thus the soil hydraulic properties. This effect is investigated in Chapter 6.

5.6.6 Effects of numerical simulations on recharge estimates

The uncertainty of numerical modeling, due to the conceptual model and model parameterization, is an important issue. Here we try to show two aspects of this issue. One is related to the temporal resolution of the atmospheric forcing. The other is the modeling dimensions, i.e., 1D versus 2D.

5.6.6.1 Uncertainty due to the temporal resolution of the atmospheric forcing

Simulations of three different temporal resolution of the atmospheric forcing have been completed in this chapter. They are steady-state, daily-step, and minute-time-step simulations. The bedrock permeability threshold for significant recharge, estimated from the three series of simulations, increases from 10^{-16} m^2 to 10^{-14} m^2. It is reasonable to assume that higher-temporal-resolution simulations give estimates closer to the actual values. In this case, the permeability threshold of 10^{-14} m^2 estimated from the minute-time-step simulations is more reasonable for the semiarid environments. Simulations of low-resolution atmospheric forcing miss hydrological dynamics on mountain hillslopes.

For example, when daily atmospheric forcing is used, the simulation may overestimate recharge on mountain hillslopes because infiltration-excess runoff is captured by the simulation and some of it is redirected into percolation.

To test how serious this problem is, percolation fluxes of (macropored silt + bedrock) columns from minutely-based forcing are compared to those from daily-based forcing. The simulations of minutely-based forcing are from §5.5. With the same soil and bedrock, and daily atmospheric forcing degraded from the minutely-based forcing, 1D simulations were performed using HYDRUS-2D (HYDRUS-1D does not have composite function for macropored silt and fractured granite). For tuff slopes, simulated percolation is larger for daily-forcing simulations than for minute-time-step simulations, for PET/P ratio over 1.0. The difference becomes smaller when PET/P ratio is below one. It seems that minutely- (or hourly-) based forcing is necessary to estimate distributed recharge on mountain hillslopes, where infiltration-excess runoff is important. For granite slopes, the difference should be larger (not as many results available to evaluate as for tuff slopes because of a numerical instability problem). That the daily-step simulations do not capture infiltration-excess runoff probably accounts for this difference.

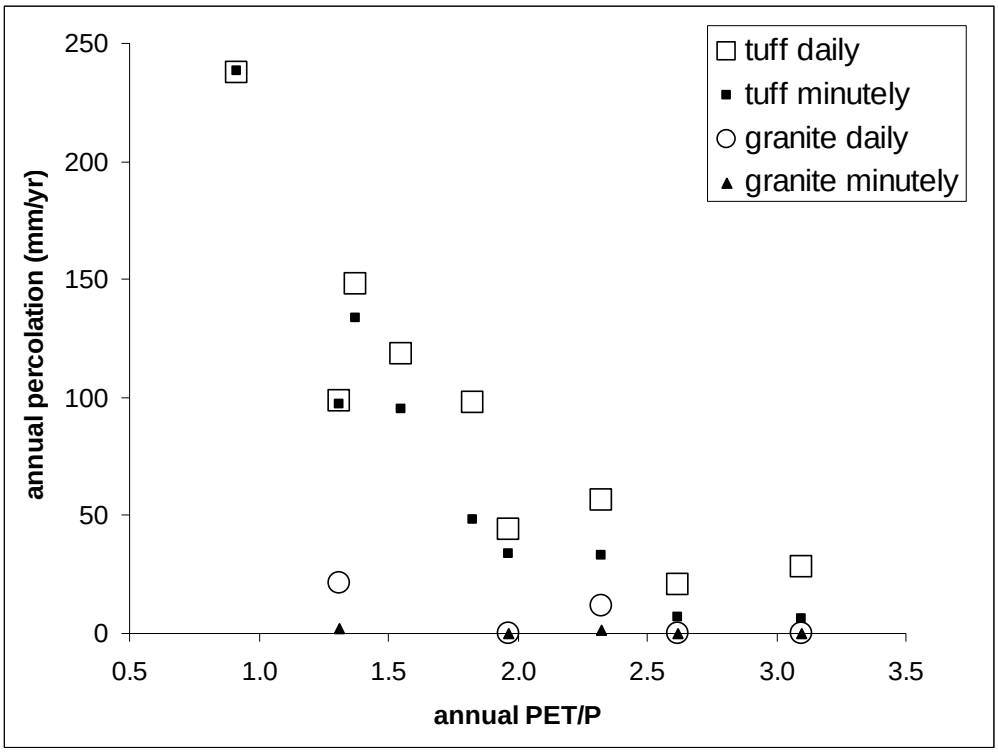

Figure 5.28 Simulated annual percolation as a function of annual PET/P ratio from models with minutely-based atmospheric forcing vs. daily-based atmospheric forcing, for tuff and granite slopes (overlain by 30 cm macropored silt).

High-temporal-resolution precipitation products are critical to numerically simulate recharge in mountains. Given the large spatial precipitation variability in mountains, precipitation products of high-spatial-resolution are similarly important for estimating mountain-block recharge [e.g., *Blindish & Barros, 2000*].

5.6.6.2 One-dimensional modeling vs. two-dimensional modeling

There are two reasons that HYDRUS-2D, instead of HYDRUS-1D, is used for simulations of hillslope water partitioning. First, two dimensions are needed to investigate lateral downslope flow. HYDRUS-2D allows us to look at the slope-dependent surface runoff, interflow and percolation. Second, HYDRUS-2D has some new capacities (e.g., composite function), which are not available for HYDRUS-1D. To

test how important the 2D simulations are to estimate percolation on mountain hillslope, the results of 2D simulations are compared to those of 1D simulations.

Because HYDRUS-1D does not have capacity for the composite function (§5.2.1), the daily-step transient simulations of tuff slopes based on South Baldy conditions (§5.4) are conducted. The results are compared to the 2D simulations. The HYDRUS2D simulations are: (1) north-facing 20 degree slope, with 30 (or 100cm) loam soil and underlying tuff, a total thickness of 200cm, at two locations (topslope and midslope) (Appendix XVI); (2) south-facing 20 degree slope, with 30 (or 100cm) loam soil and underlying tuff, a total thickness of 200cm, at two locations (topslope and midslope) (Appendix XVI). Corresponding HYDRUS-1D simulations are: (1) north-facing 20 degree slope (characterized by its climate condition), with 30 (or 100cm) loam soil and underlying tuff; and (2) south-facing 20 degree slope (characterized by its climate condition), with 30 (or 100cm) loam soil and underlying tuff.

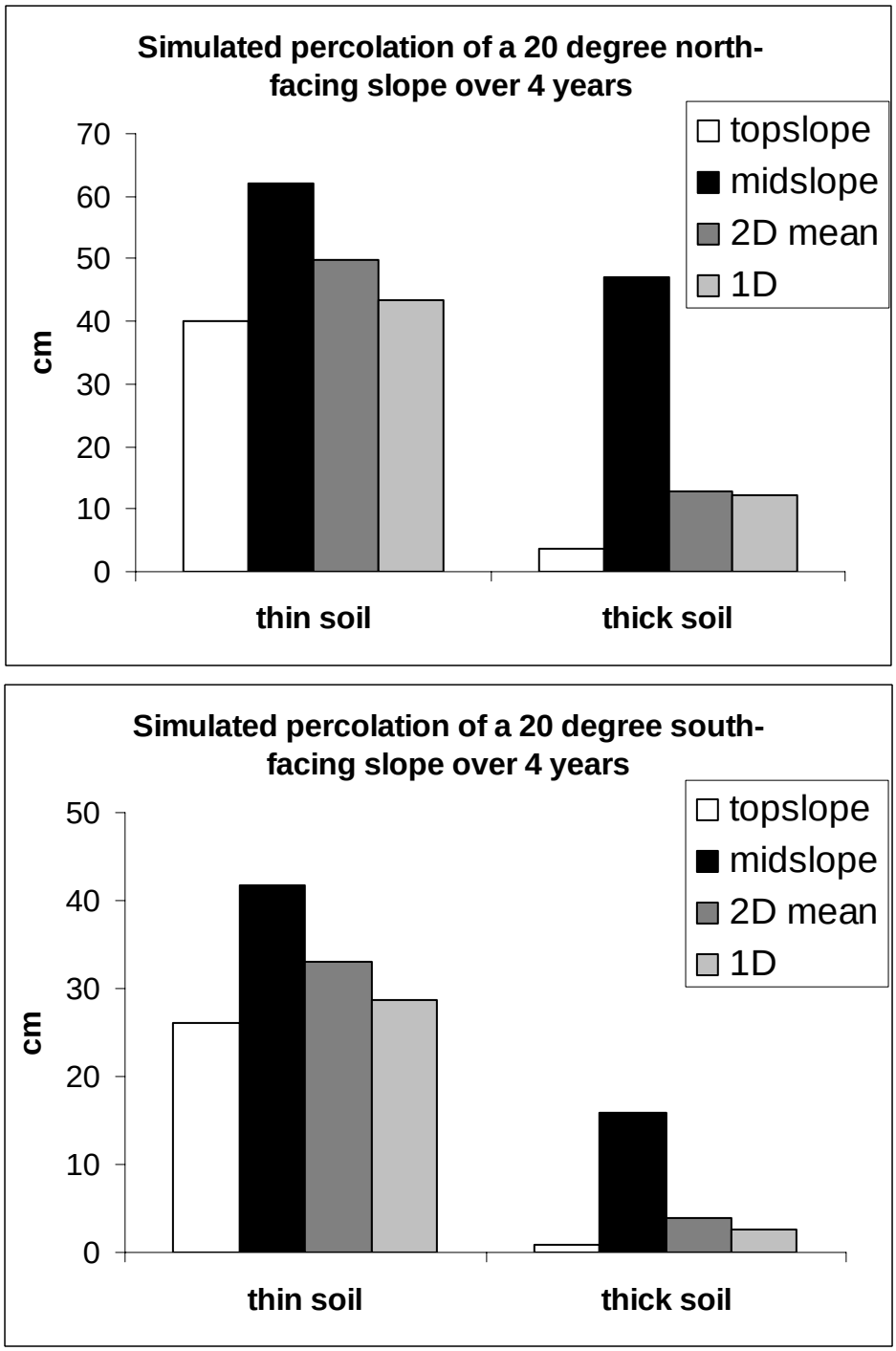

Figure 5.29 Simulated percolation over a 4-year modeling period on a hypothetic 20 degree slope (Fr=50%, conifer forest) with underlying tuff (properties see section 5.4.1) for both north-facing (top) and south-facing conditions (bottom).

The percolation from 1D simulations is between that from 2D topslope and midslope simulations (Figure 5.29). This is reasonable because 1D does not simulate lateral flow. The 2D topslope loses some water via lateral flow, while the midslope gains some water from the upgradient direction. If the geometric mean of the topslope and midslope simulation results is used for the metric of actual percolation of the slope, 1D simulation underestimates the percolation by ~15% for the examined 20 degree slopes. The difference depends on soil thickness, with smaller difference for thick-soil slopes. Because the difference is caused by lateral flow, the difference between 1D and 2D simulations should be negligible for slopes with small slope steepness. The steepness threshold, for significant difference between 1D and 2D modeling, should be dependent of the soil types and bedrock characteristics. Further simulations are required to find out what is the steepness threshold for a specific slope condition.

In general, 2D simulations give different percolation from 1D simulations on mountain hillslopes. The magnitude of the difference depends on slope location, slope steepness and soil thickness (examined), and probably also on soil type and bedrock characteristics (not examined). For a slope with a small steepness and/or thick soil cover, 1D simulations should give similar results (percolation) to spatially averaged 2D simulations.

5.7 Conclusions

This chapter examines various factors influencing percolation across the soil-bedrock interface on mountain hillslopes via generic steady-state and transient modeling. The factors investigated include bedrock characteristics, soil characteristics, vegetation characteristics, slope steepness and aspect, and climate conditions. Two primary controlling factors are bedrock permeability and the water availability at the soil-bedrock

interface. The results suggest a bedrock permeability threshold of $10^{-15} \sim 10^{-14}$ m^2 for significant percolation to occur in the arid and semiarid environments. This threshold is even smaller for matrix-flow dominant bedrock, such as non-welded tuff. Water availability at the interface is determined by local climate conditions (characterized by precipitation amount and patterns and respective PET amount and patterns), soil characteristics, and vegetation coverage. Slope steepness has some effects on water partitioning at the ground surface, however, it does not appear to significantly affect percolation across the soil-bedrock interface. The effects of slope steepness and aspect on percolation are more realized by modifying the local climate conditions. Thus, the slopes aspect effect is more important than slope steepness; and the effect is more dominant in winter and spring than in summer. In most situations, as in this study, percolation is a slow process (even slower than ET) on mountain hillslopes. Evapotranspiration, associated with soil thickness, vegetation coverage, and slope orientation, strongly influences percolation. Precipitation provides the ultimate water source for percolation. The effects of precipitation patterns on percolation depend on bedrock characteristics, with fracture-flow-dominant bedrock more sensitive to precipitation temporal patterns.

Finally, all of these factors interact together on mountain hillslopes, determining percolation across the soil-bedrock interface. The relation between percolation and each individual factor is highly nonlinear. This suggests that numerical simulations coupling all the factors and processes are needed to estimate the percolation. Since bedrock permeability and local climate are two primary factors controlling percolation on mountain hillslopes, besides the integrated hydrologic modeling, future efforts should be

placed to a better characterization of mountain bedrock hydraulic properties, and a better quantification of high-resolution (both temporally and spatially) mountain precipitation.

The recharge-climate index function is appropriate to estimate long-term mean local recharge for an area with similar soil and bedrock characteristics. Based on the minute-time-step simulations with rescaled atmospheric forcing, the recharge-aridity index functions are obtained for the hypothetical Sangre de Cristo Mountains (fractured granite with bulk permeability of 1×10^{-14} m^2) and the Jemez Mountains (non-welded tuff with bulk permeability of 1×10^{-14} m^2) of the northern New Mexico. These functions will be used in Chapter 7 to estimate mountain-block recharge in these two mountain blocks.

References

Altman, S.J., B.W. Arnold, R.W. Barnard, G.W. Barr, C.K. Ho, S.A. McKenna, and R.R. Eaton (1996), Flow calculations for Yucca Mountain groundwater travel time (GWTT-95). SAND96-0819, Sandia National Laboratories, Albuquerque, NM.

Anderson S.P., W.E. Dietrich, D.R. Montgomery, R. Torres, M.E. Conrad, and K. Loague (1997), Subsurface flow paths in a steep unchanneled catchment. *Water Resources Research*, 12, 2637-2653.

Bindlish, R., and A.P. Barros (2000), Disaggregation of rainfall for one-way coupling of atmospheric and hydrologic models in regions of complex terrain. *Global and Planetary Change*, 25, 111-132.

Boadu, F.K. (1997), Relating the hydraulic properties of a fractured rock mass to seismic attributes: theory and numerical experiments. *International Journal of Rock Mechanics and Mineral Science*, 34, 885-895.

Bosch, J.M., and J.D.Hewlett (1982), A review of catchment experiments to determine the effect of vegetation changes on water yield and evapotranspiration. *Journal of Hydrology*, 55, 3-23.

Caine, J.S., and S.R.A. Tomusiak (2003), Brittle structures and their role in controlling porosity and permeability in a complex Precambrian crystalline-rock aquifer system in the Colorado Rocky Mountain Front Range. *GSA Bulletin*, 115(11), 1410-1424.

Carsel RF, and R.S. Parrish (1988), Developing joint probability distributions of soil water retention characteristics. *Water Resources Research*, 24, 755-769.

Chaplot, V, and C. Walter (2003), Subsurface topography to enhance the prediction of the spatial distribution of soil wetness. *Hydrological Processes*, 17, 2567-2580.

Crave, A., C. Gascuel-Odoux (1997), The influence of topography on time and space distribution of soil surface water content. *Hydrological Processes*, 11, 203-210.

Dugas, W.A., R.A. Hicks, and P. Wright (1998), Effect of removal of *Juniperus ashei* on evapotranspiration and runoff in the Seco Creek watershed. *Water Resources Research*, 34(6), 1499-1506.

Durner W. (1994), Hydraulic conductivity estimation for soils with heterogeneous pore structure. *Water Resources Research*, 30, 211-223.

Earman, S. (2004), Groundwater recharge and movement through mountain-basin systems of the Southwest: a case study in the Chiricahua Mountains-San Bernardino Valley system, Arizona and Sonora, Dissertation, New Mexico Institute of Mining and Technology.

Freer, J., J. McDonnell, K.J. Beven, D. Brammer, D. Burns, R.P. Hooper, and C. Kendal, (1997), Topographic controls on subsurface storm flow at the hillslope scale for two hydrologically distinct small catchments. *Hydrological Process*, 11, 347-1352.

Freer, J., J.J. McDonnell, K.J. Beven, N.E. Peters, D.A. Burns, R.P. Hooper, B.Aulenbach, and C. Kendall (2002), The role of bedrock topography on subsurface storm flow. *Water Resources Research*, 38(12), 1269, doi: 10.1029/2001WR000872.

Gimmi T., M. Schneebeli, H. Fluhler, H. Wydler, and T. Baer (1997), Field-scale water transport in unsaturated crystalline rock. *Water Resources Research*, 33, 589-598.

Gomez-Plaza, A, M. Martinez-Mena, J. Albaladejo, and V.M. Castillo (2001), Factors regulating spatial distribution of soil water content in small semiarid catchments. *Journal of Hydrology*, 253, 211-226.

Grayson, R.B., A.W. Western, and F.H. Chiew (1997), Preferred states in spatial soil moisture patterns: local and nonlocal controls. *Water Resource Research*, 33, 2897-2908.

Gurtz, J., A. Baltersweiler, and H.Lang (1999), Spatially distributed hydrotope-based modeling of evapotranspiration and runoff in mountainous basins. *Hydrological Processes*, 13(17), 2751-2768.

Hawke, R.M., and J.A. McConchie (2003), Variability of in situ moisture measurements and implications for modeling hillslope processes. *Environmental and Engineering Geoscience*, 9, 213-223.

Hendrickx, J.M.H., and M. Flury (2001), Uniform and preferential flow mechanisms in the vadose zone, in *Conceptual Models of Flow and Transport in Fractured Vadose Zone*, National Academy Press, Washington D.C., 149-187.

Jeton, A.E., and J.L. Smith (1993), Development of watershed models for two Sierra Nevada basins using a geographic information system. *Water Resources Bulletin*, American Water Resources Association, 29(6), 923-932.

Kearns, A., and J.M.H. Hendrickx (1998), Temporal variability of diffuse groundwater recharge in New Mexico, *New Mexico Water Resources Research Institute, Report* 309, New Mexico State University, Las Cruse.

Kirkby, M. (1988), Hillslope runoff processes and models. *Journal of Hydrology*, 100, 315-339.

Lissey A. (1968), Surficial mapping of groundwater flow systems with application to the Oak river Basin, Manitoba. Ph.D. thesis, University of Saskatchewan, 141p.

Liu, E., J.A. Hudson, and T. Pointer (2000), Equivalent medium representation of fractured rock. *Journal of Geophysical Research*, 105, 2981-3000.

Long, J.C.S., and P.A. Witherspoon (1985), The relationship of the degree of interconnection to permeability in fracture networks. *Journal of Geophysical Research*, 90, 3087-3098.

Maurer, D.K., and D. L. Berger (1997), Subsurface flow and water yield from watersheds tributary to Eagle Valley hydrographic area, west-central Nevada, *U.S. Geological Survey Water-Resources Investigation Report 97-4191*.

Maxey, G.B., and T.E. Eakin (1949), Ground water in White River Valley, White Pine, Nye, and Lincoln Counties, Nevada. *Nevada Department of Conservation and Natural Resources Water Resources Bulletin, no. 8*.

McDonnell J.J., (1997), Comment on "The changing spatial variability of subsurface flow across a hillside" by Ross Woods ad Lindsay Rowe. *Journal of Hydrology* (NZ) 36, 97-100.

McGlynn, B.L., J.J. McDonnel, and D.D. Brammer (2002), A review of the evolving perceptual model of hillslope flowpaths at the Maimai catchments, New Zealand. *Journal of Hydrology*, 257, 1-26.

McMahon, D.R. (1998), Soil, landscape and vegetation interactions in a small semi-arid drainage basin: Sevilleta National Wildlife Refuge, New Mexico, Master Thesis, New Mexico Institute of Mining and Technology.

Montgomery D.R., W.E. Dietrich, R. Torres, A.P. Anderson, J.T. Heffner, K. Loague (1997), Hydrologic response of a steep, unchanneled valley to natural and applied rainfall. *Water Resources Research*, 33, 91-109.

Mualem Y. (1976), A new model for predicting the hydraulic conductivity of unsaturated porous media. *Water Resources Research*, 12, 513-522.

National Research Council (2001), *Conceptual models of flow and transport in the fractured vadose zone*. Washington, DC: National Academy Press.

Newman, B.D., B.P. Wilcox, and R.C. Graham (2004), Snowmelt-driven macropore flow and soil saturation in a semiarid forest. *Hydrological Processes*, 18, 1035-1042.

Noguchi, S., Y. Tsuboyama, R.C. Sidle, and I. Hosada (2001), Subsurface runoff characteristics from a forest hillslope soil profile including macropores, Hitachi Ohta, Japan. *Hydrological Processes*, 15, 2131-2149.

Odling, N.E. (2001), The scaling of hydraulic conductivity in rock fracture zones. *Geophysical Research Letters*, 28, 3019-3022.

Onda Y., Y. Komatsu, M. Tsujimura, and J. Fujihara (2001), The role of subsurface runoff through bedrock on storm flow generation. *Hydrological Processes*, 15, 1693-1706.

Pan, L, K. Zhang, Y-S. Wu, and G.S. Godvarsson (2005), Percolation through fractured porous media under transient infiltration: reconciling measured and predicted seepage into a mined openning, Earth Sciences Division Director's Review, Lawrence Berkeley National Laboratory, April, 2005.

Petch RA. (1988), Soil saturation patterns in steep, convergent hillslopes under forest and pasture vegetation. *Hydrological Processes*, 2, 93-103.

Pili, E., F. Perrier, and P. Richon (2004), Dual porosity mechanism for transient groundwater and gas anomalies induced by external forcing, *Earth and Planetary Science Letters*, 277, 473-480.

Puigdefabregas J, G.D. Barrio, M.M. Boer, L. Gutiérrez, A. Solé (1998), Differential responses of hillslope and channel elements to rainfall events in a semi-arid area. *Geomorphology*, 23, 337-351.

Qiu, Y., B.J. Fu, J. Wang, and L.D. Chen (2001), Spatial variability of soil moisture content and its relation to environmental indices in a semi-arid gully catchment of the Loess Plateau, China. *Journal of Arid Environments*, 49(4), 723-750.

Ridolfi, L., P. D'Odorico, A. Porporato, and I. Rodriguez-Iturbe (2003), Stochastic soil moisture dynamics along a hillslope. *Journal of Hydrology*, 272, 264-275.

Sandvig, R. (2005), Ecohydrological controls on soil-moisture fluxes in arid vadose zones, Master Thesis, Earth and Environmental Science, New Mexico Institute of Mining and Technology, Socorro, New Mexico.

Shimojima E., T. Tanaka, R. Yoshioka, Y. Hoso (1993), Seepage into a mountain tunnel and rain infiltration. *Journal of Hydrology*, 147, 121-151.

Šimůnek, J., M. Sejna, M.Th. van Genuchten (1999), The HYDRUS-2D software package for simulating two-dimensional movement of water, heat, and multiple solute in variably saturated media. Version 2.0, IGWMC-TPS-53, International Ground water Modeling Center, Colorado School of Mines, Golden, Colorado, 251p.

Šimůnek, J., N.J., Jarvis, M.Th. van Genuchten, and A. Gardenas (2003), Review and comparison of models for describing non-equilibriium and preferential flow and transport in the vadose zone. *Journal of Hydrology*, 272, 14-35.

Small, E.E. (2005), Climatic controls on diffuse groundwater recharge in semiarid environments of the southwestern United States, *Water Resources Research*, 41 (4), W04012, doi:10.1029/2004WR003193.

Snow, D.T. (1969), Anisotropic permeability of fractured media. *Water Resources Research*, 5, 1273-1289.

Snow DT. (1979), Packer injection test data from sites on fractured rock, LBL (Lawrence Berkeley Lab)-10080.

Van Genuchten, M. Th. (1980), A closed-form equation for predicting the hydraulic conductivity of unsaturated soils. *Soil Science Society of America Journal*, 44, 892-898.

Western, A.W., R.B. Grayson, G. Bloschl, G.R. Willgoose, and T.A. McMahon (1999), Observed spatial organization of soil moisture and its relation to terrain indices. *Water Resource Research*, 35(3), 797-810.

Wilcox, B.P., B.D. Newman, D. Brandes, D.W. Davenport, and K. Reid (1997), Runoff from a semiarid ponderosa pine hillslope in New Mexico. *Water Resources Research*, *33*, no.10, 2301-2314.

Wilcox, B.P., M.K. Owens, R.W. Knight, and R.K. Lyons (2005), Do woody plants affect streamflow on semiarid karst rangelands? *Ecological Applications*, 15(1), 127-136.

Wilson C.J., and W.E. Dietrich (1987), The contribution of bedrock groundwater flow to strom runoff and high pore pressure development in hollows. *IAHS Publication*, 165, 49-59.

Wilson, J.L., and H. Guan (2004), Mountain-block hydrology and mountain-front recharge, in *Groundwater Recharge in a Desert Environment: The Southwestern United States*, edited by J.F. Hogan, F.M. Phillips, and B.R. Scanlon, Water Science and Applications Series, vol. 9, American Geophysical Union, Washington, D.C., 113-137.

Winter, C.L., and D.M. Tartakovsky (2001), Theoretical foundation for conductivity scaling. *Geophysical Research Letters*, 22, 4367-4369.

Witherspoon, P.A., J.S.Y. Wang, K. Iwai, and J.E. Gale (1980), Validity of cubic law for fluid flow in a deformable rock fracture. *Water Resources Research*, 16, 1016-1024.

Yeakley J.A., W.T. Swank, L.W. Swift, G.M. Hornberger, H.H. Shugart (1998), Soil moisture gradients and controls on a southern Appalachian hillslope from drought through recharge. *Hydrology and Earth System Sciences*, 2, 41-49.

CHAPTER 6 MODELING INVESTIGATION OF WATER PARTITIONING ALONG A SEMI-ARID MOUNTAINOUS ECOTONE AND ITS IMPLICATION

6.1 Introduction

Generic simulations were presented in Chapter 5 to gain an improved understanding of near-surface water partitioning on mountain hillslopes in arid and semiarid environments. This chapter focuses on specific hydrologic simulations of two hillslope sites along a mountainous ecotone at the Los Alamos National Laboratory. The mountain ecotones are very sensitive to the climatic variability and change. For example, Allen & Breshears [*1998*] found that ponderosa pine forest in a 2378-ha portion of Frijolito Mesa, Bandelier Wilderness of the Jemez Mountains decreased from ~37% to ~15% during a <5 year period of 1950's drought, replaced by the piñon-juniper woodland. Even though the climate returned to the normal condition after the drought, the ecotone has not recovered the pre-drought location. Does this ecotone shift cause significant change in mountain-block recharge of the Jemez Mountains?

Sandvig [*2005*] studied a transect of various vegetation zones (from shrub, grass, juniper, to ponderosa pine) on the basin floor on the central New Mexico. She found that through interaction of climate, vegetation, and soil, each vegetation ecosystem has significantly different vadose-zone dynamics and recharge rate from the neighboring zones. For example, estimated from soil chloride profiles, the mean recharge rate is 2.3 mm/yr for the ponderosa pine zone and 0.5 mm/yr for the juniper site. Thus, she suggests that, on basin floors, vegetation types can be used as an indicator for recharge estimation.

Can vegetation also be an indicator for recharge in the mountain environment? Answering this question is the primary objective of this chapter.

The two hillslope sites studied in this chapter are representatives of piñon-juniper woodlands and ponderosa pine forests. These two vegetation coverage types are among a larger elevation-dependent vegetation spectrum in the Jemez Mountains (Table 6.1). The two hillslope sites are along the ponderosa pine and piñon-juniper ectone. If the recharge is a function of ecosystem, the large ecotone shift in the Jemez Mountains [*Allen & Breshears, 1998*] may lead to significant change in basin-scale groundwater recharge. Examining the significance of mountain vegetation change on basin-scale groundwater balance is the second objective of this chapter.

Table 6.1 Elevation-dependent vegetation types in the Jemez Mountains [from *Allen, 1989*]

Elevation	General vegetation communities
1600-1900 m	Juniper grasslands
1900-2100 m	Piñon-juniper woodlands
2100-2300 m	Ponderosa pine forests
2300-2900 m	Mixed conifer forest of ponderosa pine, Douglas-fir, white fir, aspen, and limber pine
2900-3500 m	North-facing slopes: Spruce-fir forests of Engelmann spruce and corkbark fir
	South-facing slopes: local areas of high elevation grasslands

The generic simulations in Chapter 5 suggest that the two primary controls on percolation across the soil-bedrock interface are soil water availability near the interface and the bedrock permeability. The threshold bedrock permeability for potential

significant percolation is about 10^{-15}~10^{-14} m^2 in arid and semiarid environments (Chapter 5). However, field observations of bedrock water content at the Los Alamos ponderosa pine (precipitation 450~700 mm/yr), which has a highly permeable tuff bedrock (saturated hydraulic conductivity, $K_s = 1.8\times10^4$ mm/yr, or permeability $k = 5.8\times10^{-14}$ m^2), suggest only negligible percolation to the bedrock [*Wilcox et al., 1997*]. At this same site, slope parallel macropore flow was observed in a clay-rich soil horizon [*Wilcox et al., 1997; Newman et al., 2004*]. The sum of surface runoff and interflow through the soil was estimated to be 10~60 mm/year, and little water was believed to percolate the bedrock [*Wilcox et al., 1997*]. The rest returned to the atmosphere through ET [*Brandes and Wilcox, 2000*]. A low-permeability barrier at or above the soil-tuff interface was thought to impede the downward movement of water into the highly permeable tuff [*Wilcox et al., 1997*]. The inconsistency of estimated percolation at this field site and our generic modeling predictions (Chapter 5) may be due to the simplified generic modeling setting and the high permeability of the modeled soils in contrast to soils in the field situation. At the ponderosa pine site, for example, based on lab soil core measurement, the Bt soil horizon has a permeability as low as 2.5×10^{-17} m^2 (or K_s = 8 mm/year), much smaller than the underlying bedrock. Understanding why little recharge occurs at the ponderosa pine site, and for what conditions the recharge can be significant in this environment, is the third objective of this chapter.

6.2 The study sites

Besides the distinct vegetation coverage, the two Los Alamos study sites have significantly different soil characteristics. The soil profile of the ponderosa pine site is relatively uniform, with high-clay-content horizons. The soil is about one meter thick [*Wilcox et al., 1997, Newman et al., 1997*]. In contrast, the soil thickness at the piñon-

juniper site varies significantly and has a mean thickness of 70-80 cm, or ~30 cm thinner than the ponderosa pine site [*Davenport et al., 1996*]. Both sites are located on relatively flat surfaces (~5% slope steepness), minimizing topographic effects on water partitioning.

6.2.1 The ponderosa pine site

The ponderosa pine site, located at the Los Alamos National Laboratory, northern New Mexico, with an elevation of 2315 m, is covered by sparse ponderosa pine trees (Figure 6.1) with under-story short grasses. The north hillslope marked in Figure 6.1 is the focus of this chapter. The southeast-facing north hillslope has a steepness of about 6%. The soil cover is fairly uniform, about 100 cm, with horizons including A, Bw, Bt, CB [*Wilcox et al., 1997*]. Roots occur in the top 70 cm of the soil with A, Bw, and Bt horizons [*Newman et al., 2004*]. The lab-measured soil unsaturated hydraulic properties are given in Table 6.2. Root distribution data are provided in Table 6.3.

Table 6.2 Fitted van Genuchten model parameters for laboratory measurements of soil and bedrock samples typical of the study site (original measurement data were provided by Dr. Brent D. Newman)

Sample #	Depth (cm)	Horizon	α (1/cm)	n	θ_s	θ_r	K_s (m/s)
2-2.5	6	A	0.015	1.33	0.44	0.06	7.5E-07
3-7.0	18	Bw	0.017	1.14	0.39	0.06	5.7E-09
4-11.0	28	Bt	0.004	1.75	0.37	0.11	6.3E-08
5-17.0	43	Bt	0.0045	1.15	0.40	0.08	2.5E-10
7-29.0	74	CB	0.016	1.11	0.47	0.06	7.1E-09
8-33.0	84	CB	0.009	1.14	0.47	0.06	1.3E-09
RE16-98-0107*		R	0.0014	1.42	0.28	0	5.8E-07

Note: According to Dr. Brent D. Newman, this sample was from Tshierege member, subunit 3 of the Bandelier Tuff, not from the study site. But it was estimated to be the most representative of the shallow tuff at the study site [*Newman, 2003*].

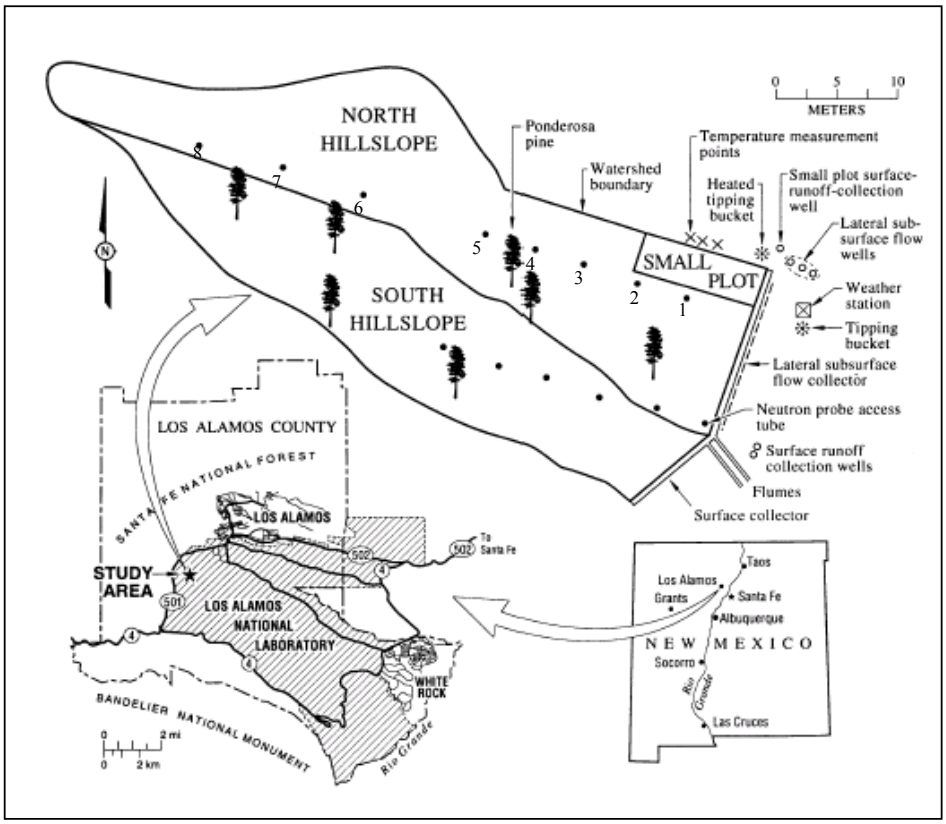

Figure 6.1 The location map of the study site (from Wilcox et al., 1997). The numbers next to neutron probe access tubes will be referred in the text.

Table 6.3 Root distribution at the study site [*Newman et al., 2004*]

Horizons	Roots per m^2 by size class				
	<1mm	1-2mm	2-5mm	5-10mm	>10mm
A+BW	414	281	57	19	14
Bt	244	163	89	22	15
CB	4	8	0	0	0

6.2.2 The piñon-juniper site

The piñon-juniper site (latitude 34.30˚N, longitude 106.27˚W), about 8 km to the east of the ponderosa pine site, is located at the Mesita del Buey of the Pajarito Plateau,

Northern New Mexico. The site is of an elevation of 2140m, with 50% covered by Colorado piñon pine and one-seed juniper [*Davernport et al., 1996; Wilcox et al., 2003*]. The soils, developed from Bandelier Tuff, are mainly in texture of sandy-loam or loam, and have experienced very little erosion [*Davernport et al., 1996; Wilcox, 1994*]. Some measurements of unsaturated hydraulic conductivity were performed at the top of the soil profiles [*Wilcox et al., 2003*], but no comprehensive hydrologic properties of the soil profiles have been measured at this site. Based on the unsaturated hydraulic conductivity measurements, the top soil is modeled as loam with macropores (Figure 6.2). There is no quantitative description of root distribution at this site. Based on qualitative descriptions [*Tierney and Foxx, 1987*], most roots distribute within the depth of 60 cm. Figure 6.3 shows the conceptualized root density function for the site.

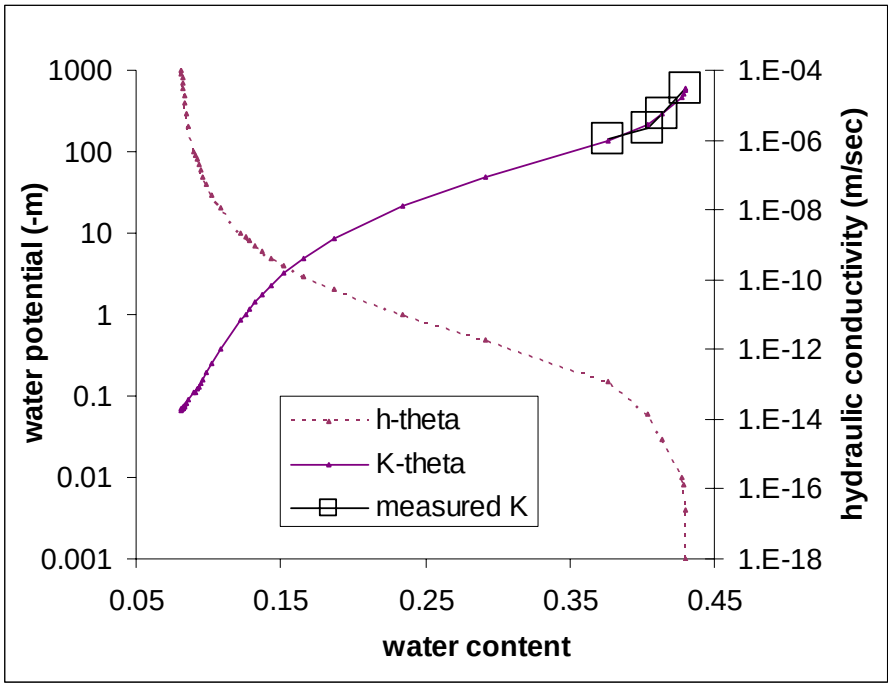

Figure 6.2 The macropored loam unsaturated hydrologic characteristic curves, with K-theta curve fitted to the measurements.

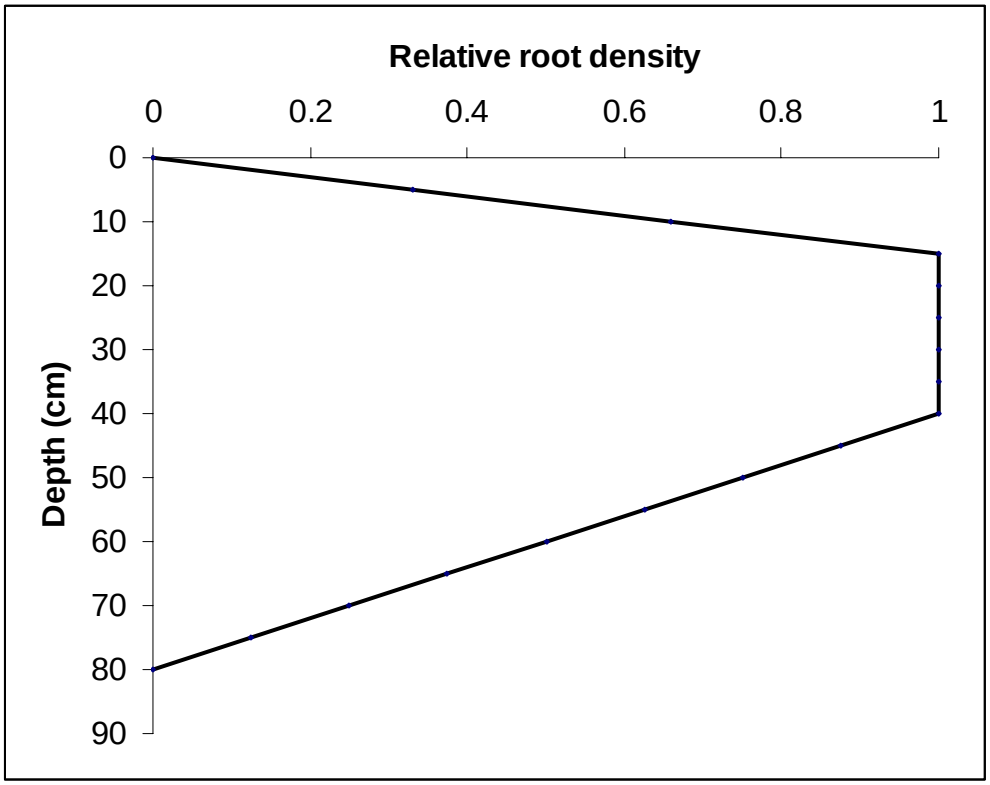

Figure 6.3 Conceptualized relative root density function for the piñon-juniper site [based on *Tierney and Foxx, 1987*].

6.3 Meteorological data and data processing

6.3.1 Meteorological observation and data processing for the ponderosa pine site

Micrometeorological data were measured at the ponderosa pine site every 15 minutes, with the instruments installed at a height of about 2 meters above the ground. The data include solar radiation, wind speed, relative humidity, and temperature. The precipitation was measured at one-minute intervals. Surface runoff and interflow were also monitored onsite every 15 minutes, and measured at one-minute intervals when there was flow. Soil moisture at various locations and depths were measured a few tens of times during each year [*Wilcox et al., 1997*].

The precipitation data (heated gauge data) was used to generate a time-series of active water (or potential infiltration, PI) available for infiltration, which is the sum of rainfall and snowmelt. The total precipitation from Oct. 1993 through Aug. 1998 was 2590 mm, with an annual mean of 527 mm. The recorded precipitation was classified into rainfall and snowfall based on the mean daily temperature [*Wigmosta et al., 1994*]. The snowmelt was estimated by a temperature-index model [*Dingman, 1994*]. The potential ET (PET) was estimated by Penman-Monteith equation (§4.3.3) for a hypothetic reference grass surface using the collected data for solar radiation (15 ~ 60-minute temporal resolution), temperature, and relative humidity. Because wind speed was not measured above the ponderosa trees, the measured wind speed was not used, but instead assigned a mean value of 2 m/sec [*Allen et al., 1998*]. The potential ET (based on reference grass) during the night (8pm~6am) was approximated to zero. The estimated total PET from Oct. 93 through Aug. 98 was 6486 mm, with an annual mean of 1319 mm, about 2.5 times the precipitation during this period. The three years of data (1994~1996 water years, each water year from the previous October through September), used for HYDRUS simulations, are shown in Figure 6.2. The seasonality of PET was similar from year to year, while potential infiltration (rainfall + snowmelt) varied among the years. The ratios of PET/P (same as PET/PI over the whole water year) were 2.5, 2, and 3 for 1994, 1995, and 1996 water years respectively.

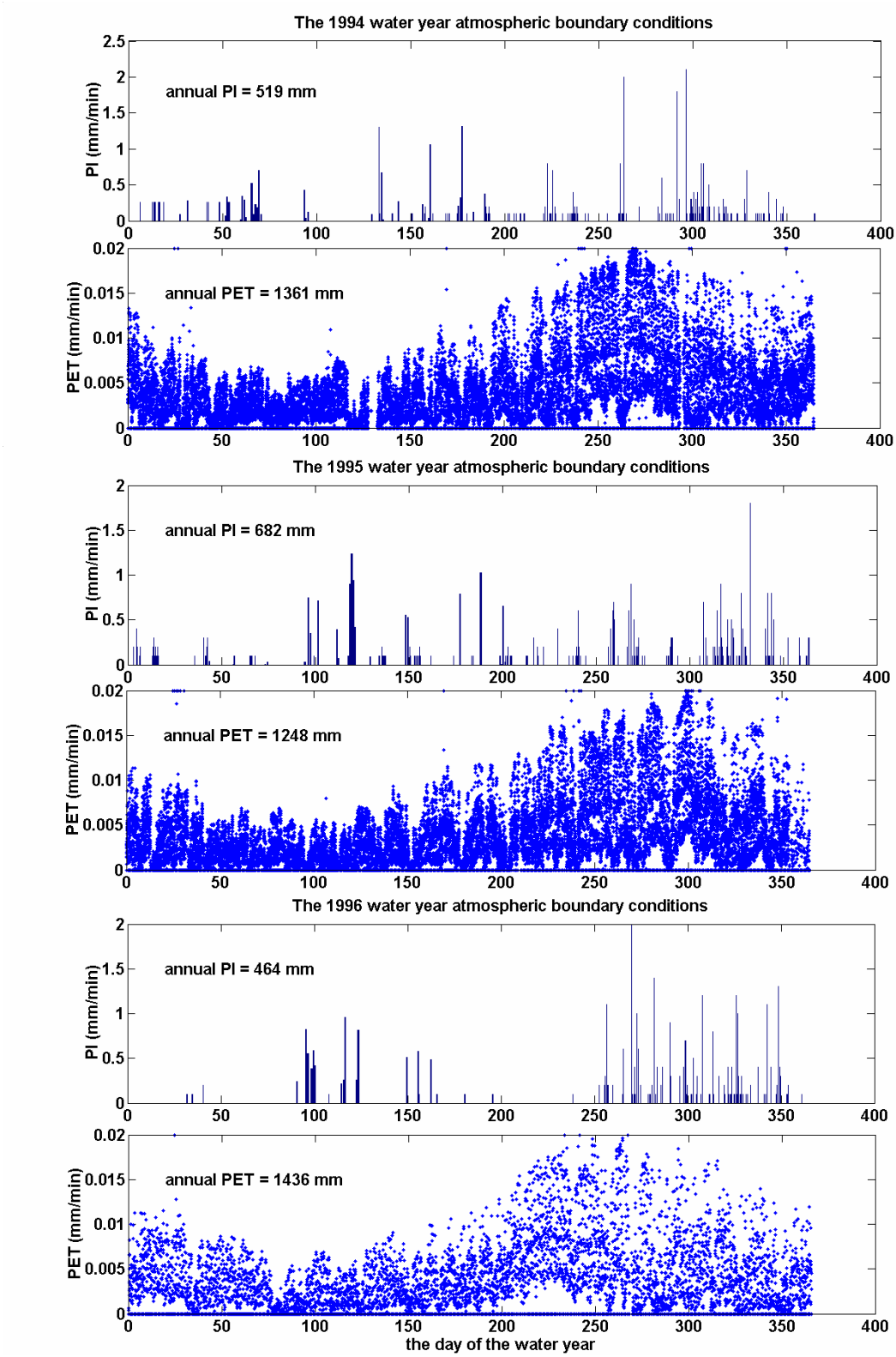

Figure 6.4 The atmospheric boundary condition for three water years (94, 95, and 96). The time interval for 94 and 95 is every 15 minutes, and for 96 is every 60 minutes, causing different appearance of the PET plots. PI is based on measure P and calculated as the sum of rainfall and snowmelt. PET is calculated using Penman Monteith model.

6.3.2 Meteorological observation and data processing for the piñon-juniper site

The meteorological data were recorded from the "erosion plot", about 264m west of the piñon-juniper site. Although a tipping bucket station was installed at the piñon-juniper site, it did not have a winter precipitation record. The summer precipitation recorded at the tipping bucket station was similar to that of the "erosion plot" station. Different from high-temporal-resolution micrometeorological data for the ponderosa pine site, daily-step micrometeorological data is used for simulations of the piñon-juniper site. From our previous discussion in §5.6.6.1, the infiltration-excess runoff is not simulated in the modeling of daily-step atmospheric forcing. This problem is solved by subtracting observed runoff (Figure 6.5, some runoff events were removed because they did not match any rainfall events) from the precipitation (or snowmelt) data.

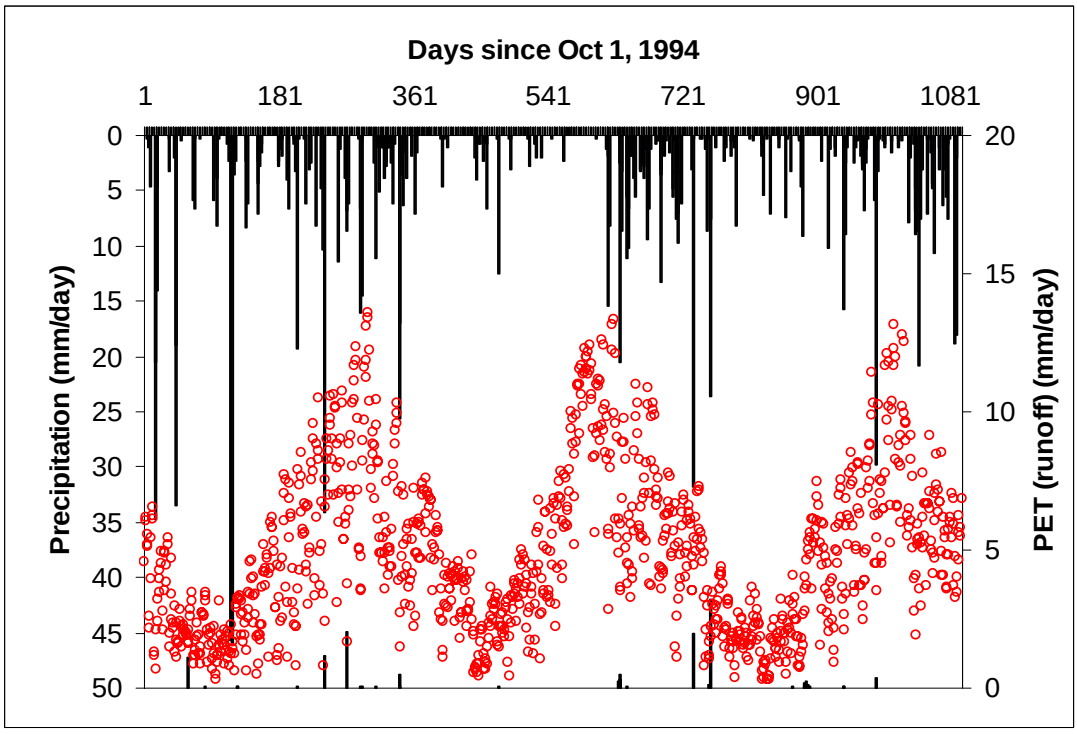

Figure 6.5 Daily precipitation (rainfall + snowmelt), daily potential ET, and daily runoff at the Piñon-Juniper site for the water years 1995~1997. Note that 1995 water year is an El Nino year.

Table 6.4 Annual precipitation, potential ET, and aridity index at the piñon-juniper site for the three water years

water years	P(mm)	PET(mm)	PET/P
1995	613	1698	2.8
1996	267	2004	7.5
1997	442	1653	3.7

The atmospheric forcing of the three water years (Table 6.4, Figure 6.5) is derived from the "erosion plot" station. Potential ET is estimated using the Penman-Monteith equation. The mean annual precipitation of the three years is 440 mm, which is a little wetter than the long-term mean precipitation (~400 mm/yr). The water year 1995 is extremely wet, and 1996 is extremely dry. The three-year mean PET/P ratio is 4.1, located in the climate ranges for the juniper ecosystem (Appendix XVIII).

6.4 Numerical simulations of the ponderosa pine site

6.4.1 Simulation settings

Due to a limited computational capacity, only a one-meter-wide section at the northern hillslope (Figure 6.1) at the ponderosa site was simulated (Figure 6.6). Because the thickness of soil cover and individual horizons vary a little with location, the simulated hillslope section was generated based on the soil cover at the third neutron probe access tube upslope from the down gradient end on the north hillslope (Figure 6.1). The section was one meter wide and two meters thick, with four soil horizons (A: 10cm, Bw: 20cm, Bt; 40 cm, and CB: 30 cm thick) according to Wilcox et al. [*1997*], and with a root zone in the top three soil horizons, according to Newman et al. [*2004*] (Figure 6.6). The soil hydraulic properties (Table 6.5) and root distribution was homogeneous for each

soil horizon. A prescribed constant gradient, 0.5 sin(2β), where β is the slope angle, was assigned to each side of the soil layers, mimicking a continuous hillslope condition (Appendix XV). The top end of the domain was prescribed with the atmospheric boundary condition (§6.3.1), and the bottom was the free drainage boundary (Figure 6.6). The root-macropore effect, modifying soil hydraulic properties, was represented by the conceptual model described in §4.7 (Appendix XXII). Evapotranspiration was modeled as described in §4.2. Runoff was modeled as an infiltration-excess process, without considering downslope propagation. The initial condition for the 1994-water-year simulations was obtained by rerunning the same 1994 climate forcing several times, to achieve a quasi-steady state of periodic climate forcing. For those simulations of 1995 and 1996 water years, the initial condition was inherited from the previous water year.

Table 6.5 The van Genuchten model parameters of the four soil horizons and the underlain bedrock for the simulations

Horizon	α (1/cm)	n	θ_s	θ_r
A	0.015	1.33	0.44	0.06
Bw	0.017	1.14	0.39	0.06
Bt	0.0045	1.15	0.44*	0.08
CB	0.016	1.11	0.47	0.06
R (tuff)	0.0014	1.42	0.28	0

* The saturated volumetric water content is changed from lab-measured value of 0.4 (Table 6.2) to 0.44 to match the observed soil water content in the field. The saturated hydraulic conductivities are either from Table 6.2, or Appendix XXII, dependent of the conceptual models (discussed in §6.4.2).

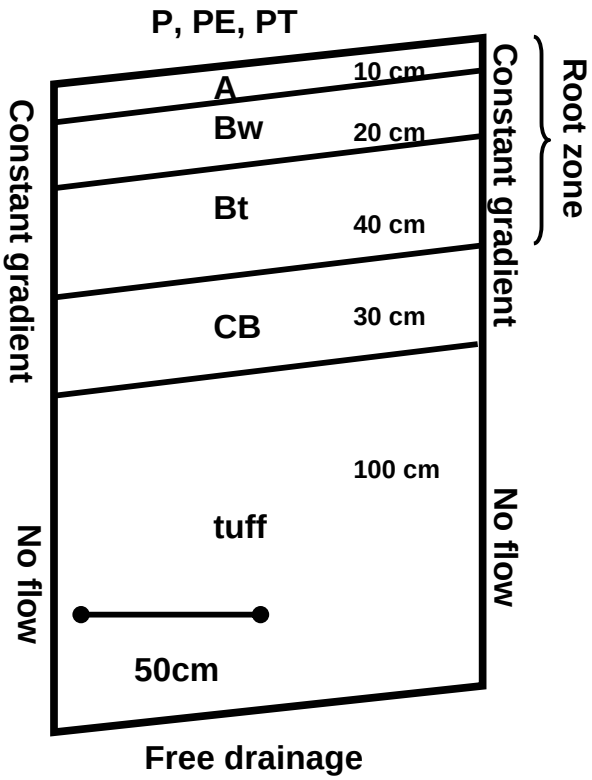

Figure 6.6 Schematic cross-section of the 2D, 1-meter-wide simulation settings. Continuous boundary is assigned at both site of the section for the soil horizons.

Because of the relatively deep root zone (~70 cm), transpiration should be modeled separately from evaporation, which requires separate PE and PT input for the HYDRUS model. However, PE and PT partition was not available from Penman-Monteith equation that was used to generate PET. To assess the uncertainty of PE and PT partitioning for hydrologic simulation results, sensitivity analyses were done specifically for this site (§6.4.2). Similarly, an appropriate root density function may be also important to simulate soil moisture variation, although it does not appear to significantly influence cumulative root-zone water partitioning (i.e., ET, percolation, and runoff, as in §4.2.3). This root density function may not necessarily be the observed root density

profile for this site, which has both deep-rooted and shallow-rooted vegetation. Thus, sensitivity analyses of the root distribution function were also conducted.

6.4.2 Model calibration

From the lab measurements (Table 6.2), the lowest-permeability soil existed at 40 cm depth within the Bt horizon, where the root macropore flow was observed [*Newman et al., 2004*]. Thus, the root macropore effect should be included in the model, using the simple root macropore model described in §4.7. The observed surface runoff (simulated as a non-propagated infiltration excess process) and soil water content were used to hand calibrate the models.

The root macropores were numerically represented by two approaches (Appendix XXII). In one approach, each soil horizon with root macropores was represented as a single continuum with anisotropic hydraulic conductivity (this model is referred to as *X*). The advantage of this conceptual model is that it has a capacity to represent root-induced anisotropic saturated hydraulic conductivity. But this model may overestimate bulk unsaturated hydraulic conductivity. In the other approach, the soil horizon was represented as a composite continuum (referred to as *CC*) with a composite water retention and hydraulic conductivity function. This conceptual model captures the abrupt change in bulk hydraulic conductivity (§5.2.1) before and after macropore flow is initiated. But it does not represent root-induced anisotropy (although this could, in principle, be done using HYDRUS). Also it should be noted that the composite model allows macropore flows only when the matrix is close saturated conditions, which may not well capture the actual macropore flow.

A single continuum (referred to as *SC*) with homogeneous and isotropic properties, based on lab-measured hydraulic properties (Table 6.2), i.e., without

considering root macropores, was also modeled as a control simulation in comparison to other models considering root macropores. For the *X*-series simulations, because the anisotropy depends on the effective root dip angle (β), three equivalent root dip angles were prescribed to find the one most closely representing the root macropore effects.

Since root macropores strongly influence the infiltration capacity of the soil, measured surface runoff is used to test the models (Figure 6.7). Time-series of surface runoff events and the amount of cumulative runoff are compared. The *SC* model strongly overestimates observed surface runoff, suggesting the importance of the macropore effect which is not captured by the small soil core lab measurements. All other models consider the root macropore effect and capture major observed runoff events. In terms of cumulative runoff, the results suggest that the *X2* model with equivalent root dip angle of 15° is the optimal one for this study site. Thus, conceptual model *X2* will be used in this study.

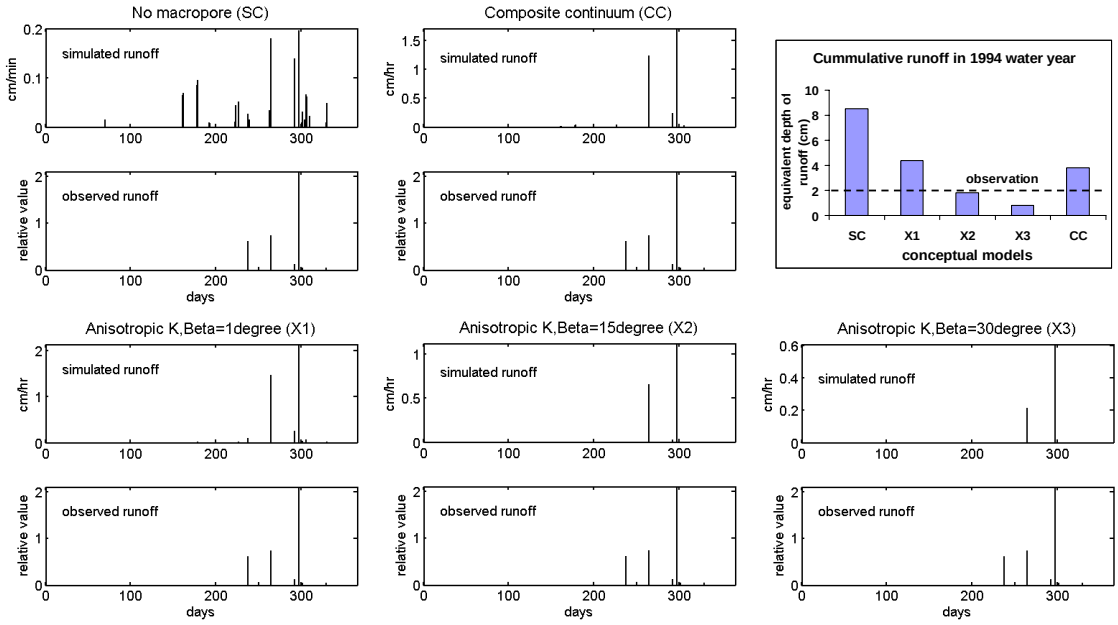

Figure 6.7 Modeling ponderosa site runoff for the 1994 water year with various conceptual models, in comparison to observations. Modeling results are shown in the top graph of each panel, with observation in the bottom graph of the panel. The top right graph shows the cumulative annual runoff from the models with comparison to the observation. Please note that the observed runoff was recorded in one-minute temporal resolution. Because the unit in the runoff database was not appropriately recorded, only the relative amount is plotted here to show the timing of runoff events. The observed cumulative runoff is obtained from Wilcox et al. (1997). Interflow, which was small both for the observations and the simulations, is not shown.

However, this does not necessarily mean that the *X* conceptual model is superior to the *CC* model for this study site. This is because the parameterization (Appendix XXII) of the root macropore model has not been tested, especially the value of b_i (§4.7). In this study, annulus aperture b_i was prescribed as 2.7% of the root diameter. For *CC* model, it is also possible to calibrate the b_i value and make the modeling result better fit to the observed runoff. Nonetheless, the calibration results show that the *X* model with bi=2.7%Di and β=15°, captures the soil infiltration capacity at this site, which is indicated by good match of the simulated runoff to the observation.

The ET model and model parameterization were tested and calibrated with measured soil water contents. Because of its better numerical stability (than the S-shape model), the Feddes model was used during the calibration. The uncertainties due to partitioning of PE and PT, root distribution, and wilting point, were analyzed; and the model was calibrated (Figure 6.8). Comparison of simulation results in Figure 6.8c and d indicates that the soil moisture variability is not sensitive to root density at this site. Comparison of simulation results in Figure 6.8a and b indicates that the soil moisture variability is not sensitive to partitioning of PE and PT either. The results are most sensitive to the wilting point of the Feddes model (Figure 6.8). The calibrated value of wilting point for this site is -15 meters (Figure 6.8c and d). This wilting point is very wet for vegetation in semiarid environments. This may indicate Feddes model does not simulate transpiration when the soil is dry (Appendix V). In later simulations, an S-Shape model, that was calibrated to be more or less equivalent to the Feddes model, was used whenever it was numerically possible (Figure 6.9). The prescribed partitioning of PE (~70% PET) and PT (~30% PET) was used for the further simulations, roughly equivalent to the fractional coverage of the ponderosa pine trees at this study site. The root density (A+Bw have 0.65 relative density, and Bt has 0.35 relative density) close to the observations (Table 6.3) was used for further simulations.

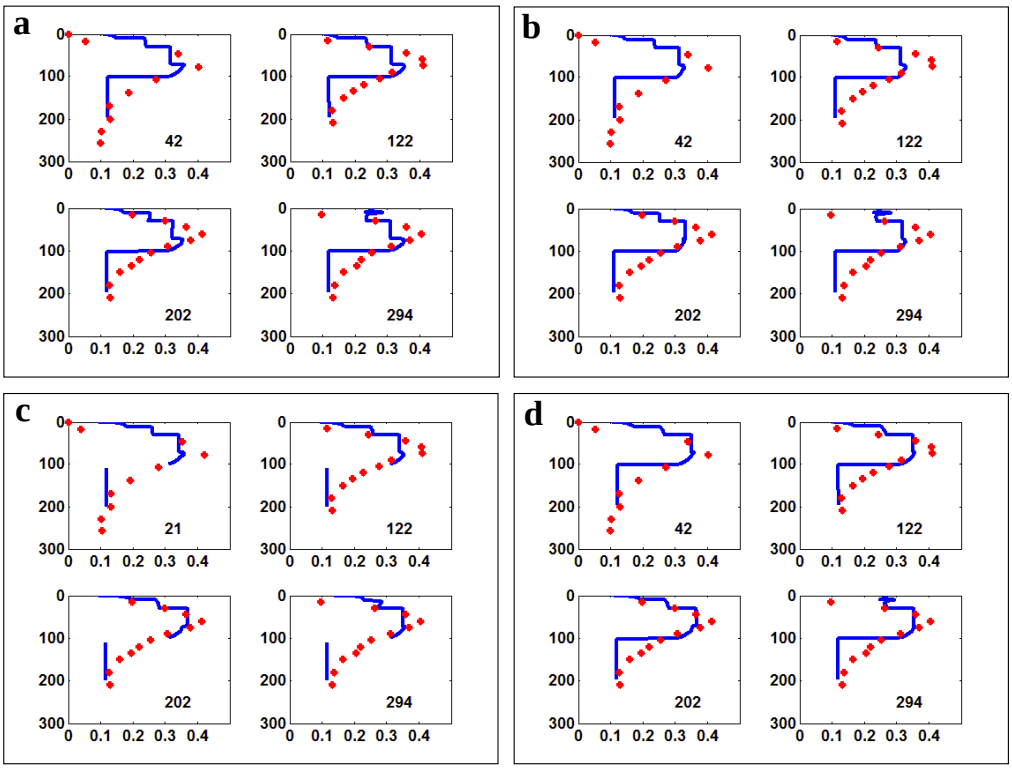

Figure 6.8 The simulated soil water content profile (lines) at four times of the 1994 water year with various ET model parameterizations, in comparison to observations (stars). (a): PE = 50%PET, PT = 50%PET, wilting point of the Feddes model (§4.2.2) h4 = -50m, Root density A+Bw = 0.59, Bt = 0.4; (b): PE = 70%, PT = 30%, h4 = -50m, Root density A+Bw = 2.0, Bt = 0.3; (c): PE = 70%, PT = 30%, h4 = -15m, Root density A+Bw = 0.65, Bt = 0.35; (d): PE = 70%, PT = 30%, h4 = -15m, Root density A+Bw=2.0, Bt=0.3. The number inside each panel is the day of the 1994 water year when the soil moisture was measured.

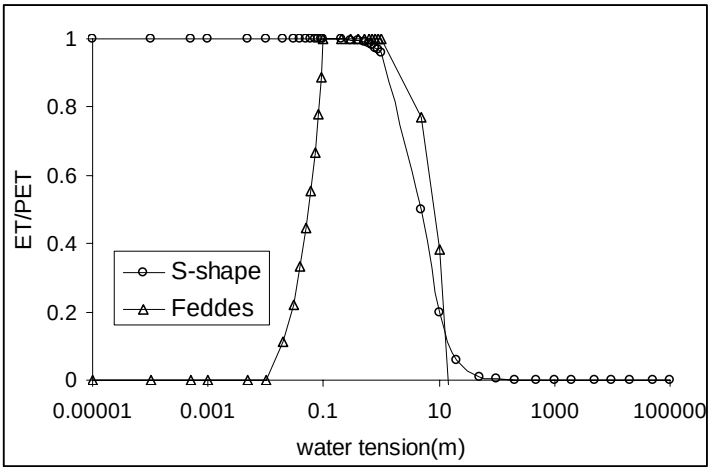

Figure 6.9 The calibrated S-shape root-water-uptake model (h50=-500 cm, p=2, wilting point =-25000 cm) vs. the calibrated Feddes model (wilting point = -1500 cm).

6.5 Numerical simulations of the piñon-juniper site

Due to incomplete data (e.g., soil hydraulic property data is largely lacking) and heterogeneity of soil profile at this site, it is difficult to calibrate the root-water-uptake model with the observed soil moisture data (not shown). Instead, literature-reported root-water-uptake model parameterization is used. To cope with the uncertainty, two root-water-uptake functions are used. One (Figure 6.10a) is derived from Pockman & Sperry's [*2000*] xylem embolism study of the one seed juniper (*Juniperus monosperma*) (§4.2.3, Appendix V). The other (Figure 6.10b) is derived from Cruiziat et al. [*2002*] for *Juniperus verginiana*. *Juniperus verginiana* is a widely distributed conifer growing both in xeric and mesic environments [*Cruiziat et al., 2002*], which has a weaker root-water-uptake capacity than one seed juniper. It is used to mimic the root-water-uptake function of piñon trees (Figure 6.10b). Thus these two functions bound two ends of the root-water-uptake capacities at the piñon-juniper site.

Similarly, three sets of soil profiles are used in the simulations to deal with the soil heterogeneity at the piñon-juniper site. One (top soil + sandy loam + tuff) is used for mimicking sandy soil, another (top soil + silt + tuff) for clayish soil, and (topsoil + loam + tuff) for an average soil characteristics at the site. The soil hydraulic properties are shown in Table 6.6. The soil profile thickness is determined by the observed mean soil thickness at the site [*Davenport et al., 1996*]. The top soil is prescribed to be 10-cm thick, with the rest 70 cm of either sandy loam, loam, or silt The simulations are performed in (effectively) one-dimension (0.1cm*200cm) using HYDRUS-2D (HYDRUS-1D does not have capacity for the top macropored soil). For the small slope steepness (~5%), and thick soil (~80 cm) at this site, one dimensional simulations should be appropriate to investigate distributed recharge (§5.6.6.2).

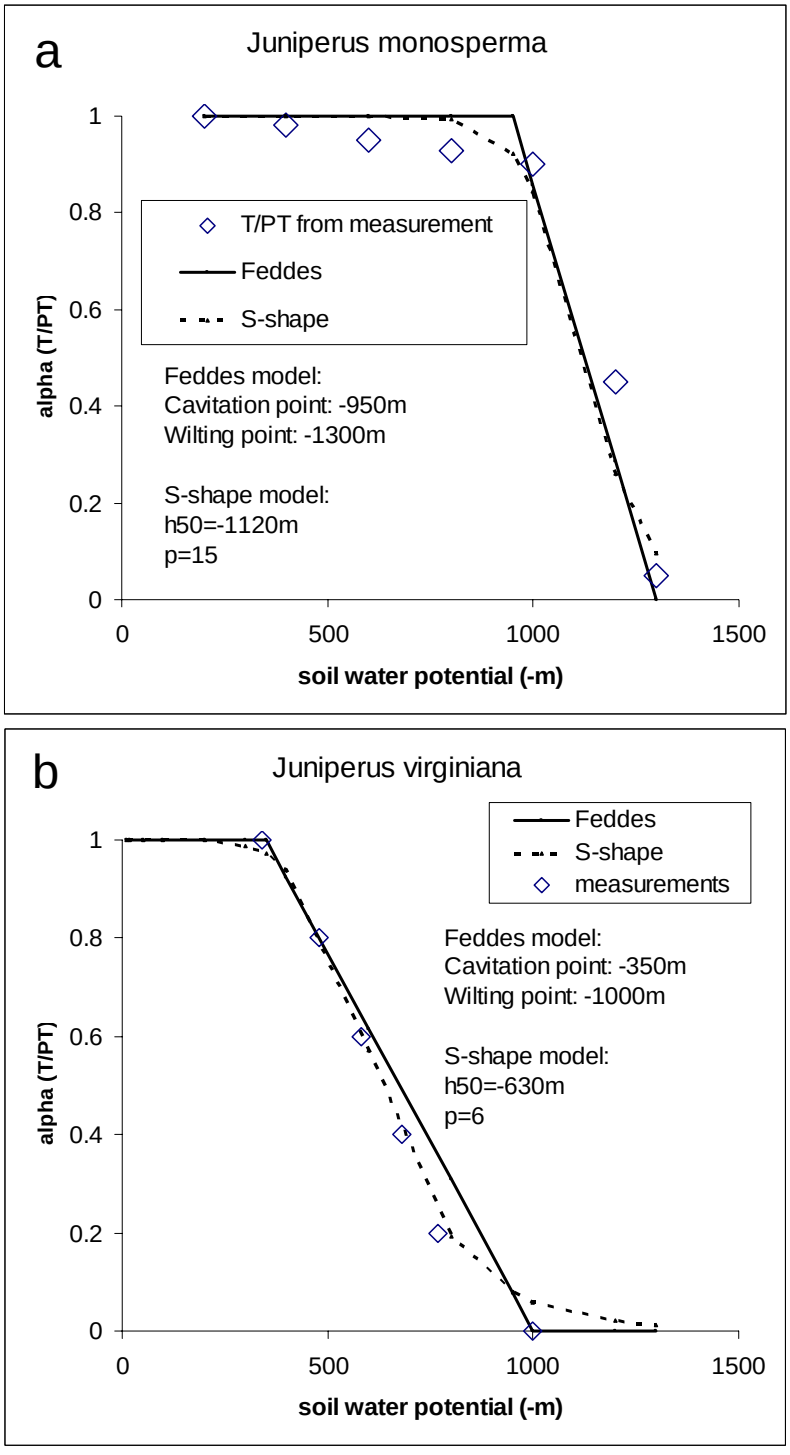

Figure 6.10 The root-water-uptake model parameterizations fitted to the measurements for two juniper species: (a) *Juniperus monosperma*, (b) *Juniperus verginiana*. *Juniperus monosperma* is the one-seed juniper at the piñon-juniper site. *Juniperus verginiana* is a widely distributed conifer growing both in xeric and mesic environments [*Cruiziat et al., 2002*], which is used to mimic the root-water-uptake function of piñon trees.

Table 6.6 The van Genuchten model parameters of the soils and the underlain bedrock for simulations of the piñon-juniper site

	θ_r	θ_s	α_1 (1/cm)	n_1	k (m^2)	w_2	α_2 (1/cm)	n_2
macropored loam (top soil)	0.078	0.43	0.036	1.56	3.10×10^{-12}	0.05	0.6	3
sandy loam*	0.065	0.41	0.055	1.72	1.23×10^{-12}	NA	NA	NA
loam	0.078	0.43	0.036	1.56	2.89×10^{-13}	NA	NA	NA
silt	0.034	0.46	0.016	1.37	6.94×10^{-14}	NA	NA	NA
tuff	0	0.28	0.0014	1.42	5.80×10^{-14}	NA	NA	NA

* The α and n values were modified from the default values in HYDRUS, to make simulations stable.

6.6 Modeling results

6.6.1 Simulation results of the ponderosa pine site

With the calibrated root-macropore model and ET model, additional simulations of the ponderosa site were conducted for each of the three water-year atmospheric forcings. Because of the low soil matrix permeability (Table 6.2), the below-root-zone soil and bedrock water content should be in equilibrium with long-term (e.g., several years) atmospheric forcing. The 1994 water year (ENSO neutral phase) atmospheric condition was assumed to be close to long-term average condition. Several repeated simulations were conducted with the 1994 water year atmospheric forcing, aimed at obtaining the quasi-steady-state water content of the tuff to match the observations (Figure 6.11).

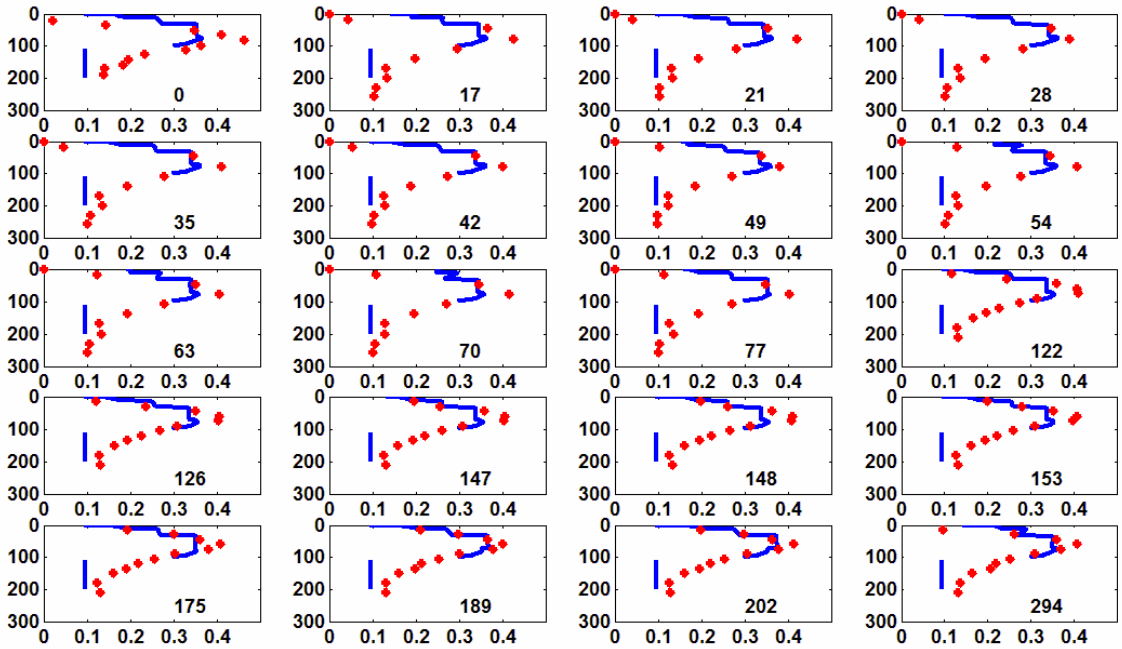

Figure 6.11 The ponderosa site simulated soil water contents (lines) at various days (the number in each panel) in quasi-equilibrium with the atmospheric forcing for the 1994 water year, in comparison to the 1994 observations (stars).

The simulated annual percolation into the tuff at the ponderosa site is about 5 mm (~1% of the precipitation). The simulated evapotranspiration accounts for 94% of annual precipitation, in agreement with previous analyses of the field data [*Brandes and Wilcox, 2000*]. Simulations with atmospheric forcing for the 1995 and the 1996 water years were also performed. The initial conditions of 1995 and 1996 water years were inherited from the simulations of previous water years. The percolation into the tuff was similar to that of 1994 water year, involving less than 1% of annual precipitation (Table 6.7, columns #2~4). From these simulations, it appears that the recharge (percolation) at this location is not significant, consistent with Wilcox et al. [*1997*].

Wilcox et al. [*1997*] suggested that a low permeable impeding layer restricts downward water movement into the bedrock at the ponderosa pine site. They gave three candidate layers: (1) CB horizon, (2) the base of Bt horizon, (3) a thin 'smear' of

translocated clay at the soil-tuff interface. At this site, the lowest permeability of the soil matrix occurs at a depth of about 40 cm in Bt horizon (Table 6.2). However, the observed soil water in the field appears ponded at a depth of 70 cm, around the interface of Bt and CB horizons. The matrix soil hydraulic conductivity cannot explain an impeding layer at this site. The absence of root macropores at depths below 70 cm may lead to a bulk low permeable layer. If this is the case, then the base of Bt horizon and CB horizon play the same role as long as the roots are absent at these depths. To test this hypothesis, two further simulations with modified CB horizon were conducted. In the first simulation, the CB horizon was replaced with tuff, leading to a 70 cm thick soil with root macropores, and results in significantly enhanced percolation (Table 6.7, column #5). In the second simulation, the CB horizon was replaced with the Bt horizon including root macropores, resulting in similar enhanced percolation (not shown). The simulated percolation, for the situation with root zone directly contacting the tuff, increases to ~20% of the annual precipitation. This suggests that the low-permeability soil between the root zone and the underlying tuff behaves as an impeding layer preventing significant percolation into the bedrock.

6.6.2 Simulation results of the piñon-juniper site

The simulated percolation at the piñon-juniper site is small (~1mm/yr; see Table 6.7 column #6), and is insensitive to the two types of root-water-uptake models and their parameterizations described in Figure 6.10. The different soil types affect percolation flux (Figure 6.12), with finer soil having consistently reduced percolation (Figure 6.12). However, the simulations did not consider macropore flow at the piñon-juniper site. Thus, the long-term mean percolation at this site could be larger than 1 mm/yr.

Table 6.7 Simulated water partitioning fluxes (in equivalent depth mm/year) at the studied hillslope

	Ponderosa pine			Ponderosa pine[1]	Piñon-juniper	Ponderosa at PJ site[2]
Water year	1994	1995	1996	1994	1995~1997	1995~1997
Infiltration	506	637	467	506	436	436
ET	490	598	435	379	436	432
Runoff	18	49	0	18	NA	NA
Percolation	<5	<5	<5	108	~1	~3
ET/P (%)	93.5	87.3	93.0	72.3	~100	99
Percolation/P (%)	<1	<1	<1	20.6	<1	<1

1. Assumes root zone directly contacts the underlying tuff by replacing the CB horizon with tuff (PET/P=2.5), the root-macropored modified soil has a vertical saturated hydraulic conductivity of ~2.5×10^{-6} m/sec.
2. Assumes ponderosa pine were at the piñon-juniper site with climate condition similar to what it is today (PET/P=4.1), the loamy soil has a saturated hydraulic conductivity of 2.9×10^{-6} m/sec.

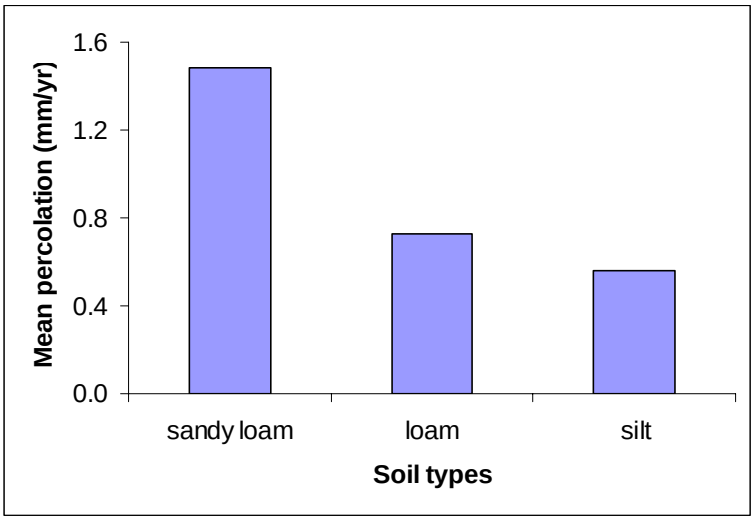

Figure 6.12 Simulated mean annual percolation over the three water years (1995~1997) for various soil types at the piñon-juniper site.

From Allen & Breshears' [1998] study, appreciable amount of ponderosa pine forest was replaced by piñon-juniper woodland in 1950s' drought, and has not recovered even the climate returned back to the pre-drought condition. Since the piñon-juniper site locates near the ponderosa pine and piñon-juniper ecotone, it is reasonable to assume that with the current climate condition at the piñon-juniper site, ponderosa pine could exist earlier. By comparing the percolation in the hypothetic ponderosa pine coverage and the actual piñon-juniper coverage at the studied piñon-juniper site, we are able to examine how much impact on mountain-block recharge that the vegetation coverage change could lead to.

We have completed the simulations for piñon-juniper-covered situations (Table 6.7 column #6). With the climate forcing, soil profile (top soil + loam + tuff) of the piñon-juniper site, and ponderosa-characterized root distribution (Table 6.3) and root-water-uptake model (Figure 6.9), percolation are simulated (Table 6.7 column #7). The percolation of the ponderosa-covered surface is three times of the piñon-juniper-covered surface.

6.7 Discussion

6.7.1 Can vegetation be an indicator of recharge in the Jemez Mountains?

The simulated mean annual percolation at the ponderosa pine site and the piñon-juniper site is similar. This suggests that, at least in this case, vegetation itself cannot be an indicator for distributed recharge. Besides climate condition and vegetation coverage type, the soils are different between the two sites. On one hand, the wetter climate at the ponderosa pine site tends to increases recharge in comparison to the piñon-juniper site. On the other hand, the clay-rich soil at the ponderosa pine site impedes percolation and reduces recharge. Thus, both vegetation types and soil characteristics should be

considered for recharge estimation. One immediate question is whether the difference in soil covers between the two sites is a coincident or a common relationship. If the thick clay-rich soil at the ponderosa pine forest is a common phenomenon, distributed recharge should be small, and probably close to that of the lower-elevation piñon-juniper woodlands. This would challenge the conventional perspectives that recharge increases with elevation in mountains.

Can we find some physical mechanisms leading to different soil covers at the two sites? The soil thickness at each site should be the snapshot of long-term soil accumulation and erosion processes. At both sites, the soils developed in Bandelier Tuff, and on a relatively flat surface (6% for ponderosa pine, and 4% for piñon-juniper). Erosion processes should not be dominant at the two sites [*Wilcox, 1994*]. Accumulation processes include the accumulation of aerosols and the weathering of the underlying bedrock. The major agent for weathering is water. If we assume at the beginning that the soils at both sites were thin, and the climate was similar to what we have today, the percolation into the tuff at the ponderosa pine would be 100 mm/yr, in comparison to 1 mm/yr at the piñon-juniper site. With the distinctive percolation rates, the weathering of tuff at the ponderosa pine would be much stronger than at the piñon-juniper site. This would explain why the ponderosa pine site has a thicker soil than the piñon-juniper site. Also, the higher rate of downward movement of the soil water at the ponderosa pine site leaches down clay from the top layer of the profile, leading to thicker Bt horizon at the ponderosa pine site than that at the piñon-juniper site [*Newman et al., 1997*]. If the picture described here represents the actual processes, under stable geomorphologic condition, the ponderosa pine forest will eventually develop thick clay-rich soils in the

Jemez Mountains. The clay-rich soil impedes percolation, leaving more water for vegetation transpiration. This may explain the thickening of ponderosa pine forest after recent fire suppressions [e.g., *Allen et al., 2002*].

Nonetheless, most mountain hillslopes experience significant erosion processes, often breaking the above mechanisms. For example, at Los Alamos, on a 200-m hillslope near the east of West Jemez Road, soil thickness reduces from over 200 cm to only 75 cm [*Reneau & McDonald, 1996,* p84]. Thick soils, in some cases due to quick local deposition [Reneau *& McDonald, 1996,* p120], have low clay content. At locations where the erosion processes are important for the soil development, or the soil is formed by quick deposition, the impeding soil layer may be absent under the ponderosa pine, leading to significant amount of percolation into the bedrock. The significant percolation can also occur at locations where the impeding layer is locally damaged.

Significant difference in percolation is found between two hypothetical ponderosa pine hillslopes (Table 6.7 columns # 5 and 7) with two climate conditions. The soil thickness and bulk vertical direction soil hydraulic conductivity are similar between the two hypothetical hillslopes (Table 6.7 footnotes). Thus, the difference in climate conditions (prescribed PET/P = 2.5 for column #5, and = 4.1 for column #7 of Table 6.7) should account for the big difference in percolation. This suggests that the climate index is a more important indicator than the vegetation-cover characteristics for estimating recharge in the mountain environment. This result is different from implications from Sandvig's [*2005*] basin floor study, in which vegetation can be used as an indicator for recharge estimates. The inconsistency of between this study and Sandvig's [*2005*] study can be due to that the climate gradient in a basin-floor ecosystem is very small, quite

different from that in the mountain. Due to the large topographic gradient, climate gradient is large in mountainous environments, leading to big difference in recharge. In this situation, vegetation can not work as a recharge indicator.

6.7.2 How would recharge change due to woodland encroachment into the ponderosa pine forest in the Jemez Mountains?

Although vegetation alone cannot be used as an indicator for estimating recharge in mountains, under the same soil and climate conditions, different vegetation coverage types appear to have different recharge (Table 6.7, columns #6 and 7). This can be used to estimate the impact of recent vegetation coverage change on percolation, the basin-scale water balance. Allen & Breshears [*1998*] found that ponderosa pine forest decreased from 37% to 15% during the 1950s' drought in their study area, a 2378-ha portion of Frijolito Mesa, Bandelier Wilderness of the Jemez Mountains. The dead ponderosa pine forest was replaced by piñon-juniper woodland. It is reasonable to assume that the climate condition of piñon-juniper encroachment in Allen & Breshears' [*1998*] study area is similar to the piñon-juniper site described in §6.2.2 because both are near the ponderosa pine and piñon-juniper ecotone. If we assume that the soil profile in Allen & Breshears' [*1998*] study area is similar to the piñon-juniper site at the Mesita del Buey of the Pajarito Plateau in this study, the distributed MBR change due to the woodland encroachment can be estimated. Based on different recharge potential of the two vegetation types (Table 6.7, columns # 6 vs. 7), the recharge in Allen & Breshears' [*1998*] study area would reduce by 1×10^4 m^3/yr. The area-weighted recharge reduction of the encroachment area is 30 times the diffuse recharge of grassland, 5 times the diffuse recharge of juniper land, and equal to the diffuse recharge of the ponderosa pine surface

estimated by Sandvig [2005] on the basin floor. Thus, it is important to consider vegetation-change-induced recharge alteration for estimating basin-scale water balance.

6.7.3 The effect of root-induced macropore flow in near-surface water partitioning

The results of this study indicate the important role of root-induced macropores in near-surface water partitioning. When lab-measured soil hydraulic conductivity of the ponderosa pine site (the *SC* model) was applied in the model, the simulation overestimated runoff by 4 times (Figure 6.4). This indicates that core scale samples are not large enough to capture macropore effects at the site, consequently underestimating the infiltration capacity. The apertures surrounding vegetation roots can serve as preferential flow paths, behaving as macropores, as observed at the study site [*Newman et al., 2004*]. Because they have a characteristic length larger than the size of the core samples, the hydraulic effects of the roots are not captured by core measurements. In this study, we related root-induced macropores to the observed root density. With incorporated root-macropores, the model represented the soil infiltration capacity (inferred from the simulated infiltration-excess runoff) for the study site. The root-induced macropores increase the bulk saturated hydraulic conductivity of the soil. Their hydrologic effects are more important for the soil with low permeability, e.g., the soil at the studied ponderosa pine site. Also, it should be noted that the root-induced macropore may not only include the apertures surrounding the roots, but also include the opening from decayed roots, and the bioactivity results of the worms and other soil organisms living on the roots [*Freckman and Virginia, 1989*]. All these can be related to root distribution, and can be implicitly included in the root macropore model provided in this study (§4.7).

Because of root-macropore modification, the clay-rich root-zone soil of the ponderosa pine site has bulk vertically saturated hydraulic conductivity close to the loam soil. Without roots in the CB horizon, the soil hydraulic conductivity is about three order magnitude lower (Table XXII-2). This permeability contrast explains the observed soil moisture distribution at the ponderosa pine site. Dramatic increase in percolation when below-root-zone CB horizon is missed suggests that CB horizon is an impeding layer for recharge at the studied ponderosa pine site.

6.7.4 Implications for the root-water-uptake model

This study also sheds light on the root-water-uptake model in HYDRUS ET modeling (§4.2.2). Two root-water-uptake models, Feddes and S-shape, are provided in HYDRUS to calculate the scaling factor for transpiration. Application of the Feddes model gave a calibrated (§6.4.2) wilting point of -15 meters (water potential) for the ponderosa pine, too wet for the vegetation in semiarid environments. This suggests that the scaling factor that linearly decreases with the soil water potential in the Feddes model probably does not represent root-water-uptake process of the ponderosa pine. If this is the case, the simulations using the Feddes model and the measured vegetation wilting point would overestimate transpiration, as demonstrated in Chapter 4. The S-shape model, on the other hand, assumes a nonlinear decrease of the scale factor with the soil water potential, which may better represent the physics of the root-water-uptake processes. These results are consistent with what we discuss in Chapter 4. However, for piñon and juniper, both the Feddes and S-shape model fit to the measurements, and have similar effects on modeled percolation.

For rigorous root-zone hydrologic modeling, appropriate conceptual model and parameterization are critical to simulate root-zone water partitioning. However, a

comprehensive dataset for testing root-water-uptake model and its parameterization is still not available yet. The results discussed above, based on a very limited number of observations, suggest that the S-shape model is a more reasonable approach to represent root-water-uptake model. The commonly-used Feddes model probably does not appropriately mimic root-water-uptake process for some vegetation species. Additional experiments and observations should be among future efforts for testing vegetation-species-dependent root-water-uptake models.

6.8 Conclusions

Numerical simulations of water partitioning were performed on ponderosa and piñon-juniper sites along a semiarid ecotone near Los Alamos National Laboratory in the Jemez Mountains. The results suggest that, by itself, vegetation coverage is not an appropriate indicator for estimating recharge in mountains. Due to the large climate gradient in mountains, the climate has the dominant effect on distributed mountain-block recharge. Soil is another factor, which should be considered for estimating recharge. This study indicates that distributed recharge at the studied ponderosa pine site is very small (< 1% of annual precipitation), similar to that of the lower and drier piñon-juniper site. The low-permeability soil, between the overlying root zone and underlying bedrock, impedes downward movement of water into the highly permeable tuff at the ponderosa pine site.

The results also suggest that root macropores play an important role in transmitting water at the ponderosa pine site. If the ponderosa hillslope has a thin soil cover, with root-zone directly contact underlying permeable bedrock, the distributed recharge can be as large as 20% of the annual precipitation at the studied ponderosa pine site. The recent woody plants (piñon and juniper) encroachment into the ponderosa pine forest in the Jemez Mountains could lead to significant change in the distributed

mountain-block recharge, of an area-weight amount from several to tens times basin-floor diffuse recharge in the central New Mexico. Thus, vegetation change in the mountains in semiarid regions can significantly impact basin-scale groundwater balance.

Two root-water-uptake models, the Feddes model and the S-shape model, are specifically examined using the field observation data. Our modeling results suggest that for the ponderosa pine, the S-shape model better represents the root-water-uptake process of the ponderosa pine than the Feddes model. For the piñon-juniper, both models can be used to represent actual root-water uptake processes.

References

Allen, C.D. (1989), Changes in the landscape of the Jemez Mountains, New Mexico, Ph.D. dissertation, Berkeley, University of California, 346p.

Allen, C.D., and D.D. Breshears (1998), Drought-induced shift of a forest-woodland ecotone: Rapid landscape response to climate variation. *Proceedings of the National Academy of Sciences of the Untied States of America*, 95(25), 14839-14842.

Allen, C.D., M. Savage, D.A. Falk, K.F. Suckling, T.W. Swetnam, T. Schulke, P.B. Stacey, P. Morgan, M. Hoffman, and J.T. Klingel (2002), Ecological restoration of Southwestern ponderosa pine ecosystems: A broad perspective, *Ecological Applications*, 12(5), 1418-1433.

Allen, R.G., L.S. Pereira, D. Raes, and M. Smith (1998), Crop evapotranspiration – Guidelines for computing crop water requirements, *Food and Agriculture Organization of the United Nations Irrigation and drainage paper 56*.

Brandes, D., and B.P. Wilcox (2000), Evapotranspiration and soil moisture dynamics on a semiarid ponderosa pine hillslope, *Journal of the American Water Resources Association*, 36(5), 965-974.

Cruiziat, P., H. Cochard, and T. Ameglio (2002), Hydraulic architecture of trees: main concepts and results. *Annals of Forest Science*, 59(7), 723-752.

Davenport, D.W., B.P. Wilcox, and D. D. Breshears (1996), Soil morphology of canopy and intercanopy sites in a piñon-juniper woodland, *Soil Science Society of America Journal*, 60(6), 1881-1887.

Dingman, S. L. (1994), *Physical Hydrology*, Prentice-Hall, Inc. 575p.

Freckman, D.W., and R.A. Virginia (1989), Plant-feeding nematodes in deep-rooting desert ecosystems, *Ecology*, 70(6), 1665-1678.

Newman, B.D., A.R. Campbell, and B.P. Wilcox (1997), Tracer-based studies of soil water movement in semi-arid forests of New Mexico, *Journal of Hydrology*, 196, 251-270.

Newman, B.D. (2003), personal communication, Los Alamos National Laboratory, New Mexico.

Newman, B.D., B.P. Wilcox, and R.C. Graham (2004), Snowmelt-driven macropore flow and soil saturation in a semiarid forest, *Hydrological Processes*, 18, 1035-1042.

Pockman, W.T., and J. S. Sperry (2000), Vulnerbility to xylem cavitation and the distribution of Sonoran Desert vegetation, *American Journal of Botany*, 87(9), 1287-1299.

Reneau, S. L., and E.V. McDonald (1996), Landscape history and precesses on the Pajarito Plateau, Northern New Mexico, LANL report, LA-UR-96-3035.

Sandvig, R. (2005), Ecohydrological controls on soil-moisture fluxes in arid vadose zones, Master Thesis, Earth and Environmental Science, New Mexico Institute of Mining and Technology, Socorro, New Mexico.

Tierney, G.D., and T.S. Foxx (1987), Root lengths of plants on Los Alamos National Laboratory Lands, LANL report, LA-10865-MS, 59p.

Wigmosta, M.S., L.W. Vail, and D.P. Lettenmaier (1994), A distributed hydrology-vegetation model for complex terrain, *Water Resources Research*, 30, 1665-1679.

Wilcox, B.P. (1994), Runoff and erosion in intercanopy zones of pinyon-juniper woodlands. *Journal of Range Management*, 47 (4), 285-295.

Wilcox, B.P., B.D. Newman, D.Brrande, D.W. Davenport, and K. Reid (1997), Runoff from a semiarid ponderosa pine hillslope in New Mexico, *Water Resources Research*, 33(10), 2301-2314.

Wilcox, B.P., D.D. Breshears, and C.D. Allen (2003), Ecohydrology of a resource-conserving semiarid woodland: Effects of scale and disturbance. *Ecological Monographs*, 73(2), 223-239.

CHAPTER 7 MOUNTAIN-BLOCK RECHARGE IN TWO MOUNTAIN AREAS, NORTHERN NEW MEXICO

7.1 Introduction

In the previous two chapters, highly resolved hydrologic modeling improves our understanding of water partitioning on mountain hillslopes, especially factors influencing percolation across the soil-bedrock interface. How does this understanding help to produce applied estimates of mountain-block recharge?

Let's first recall how mountain-block recharge has been estimated previously, as reported in the literature. Mountain-block recharge, without distinction between distributed and focused components, was estimated empirically by a lumped water balance on the mountain, with estimated precipitation into, and ET and runoff leaving, the mountain block [e.g., *Huntley, 1979*], or with an empirical relationship of ET and runoff with the precipitation [e.g., *Maxey and Eakin, 1949*]. These studies neglect the effects of spatial variability in precipitation, bedrock, soil, vegetation, and topography, and the dynamics of hydrologic processes in the mountain block. Huntley [*1979*] estimated a mountain-block recharge about 200 mm/yr in San Juan Mountains, and about 70 mm/yr in Sangre de Cristo Mountains, southern Colorado. McAda and Wasiolek [*1988*] estimated a mountain-block recharge of less than 30 mm/yr (roughly estimation from the their results) in the southern part of Sangre de Cristo Mountains, and about 30 mm/yr in the eastern part of Jemez Mountains. Several years later, Wasiolek [*1995*] re-estimated the mountain-block recharge as 70 mm/yr in the Sangre de Cristo Mountains.

These estimates suggest that a lot of mountain-block recharge is occurring in these areas, but with a large uncertainty.

Recently, Flint et al. [*2004*] proposed a GIS-based basin characterization model (BCM) to account for the effects of spatial variability on potential recharge. The model "uses a mathematical deterministic water-balance approach that includes the distribution of precipitation and the estimation of potential evapotranspiration, along with soil water storage and bedrock permeability" [*Flint et al., 2004*]. The BCM model provides an approach to evaluate basin-wide recharge potential. It skips finer-scale hydraulic dynamics in the soil, especially the ET processes. This limits it to estimating recharge on the complex and dynamic mountain hillslope systems. For example, the BCM suggests no recharge if potential ET exceeds precipitation. However, the high-resolution hydrologic simulations (Chapter 5) indicate that, on an annual basis, recharge can occur under the condition that potential ET is twice that of precipitation.

Another study conducted in Switzerland [*Gurtz et al., 1999*] employs the hydrotope concept (hydrologically similar response units, or HRU) to estimate water partitioning in humid mountainous basins. The model (PREVAH) (precipitation-runoff-evapotranspiration-hydrotope) has five sub-models, a snow model, an interception model, a model of soil water storage and depletion by evapotranspiration, a runoff generation model, a discharge concentration and a flood routing model. PREVAH first classifies the study area into numerous sub-catchments. In each sub-catchment, hydrotopes are identified based on the river system, levels of meteorological input variables (e.g., 100 m elevation interval), topography (elevation, aspect, and steepness), land surface cover, and the soil properties. The simulation is then conducted for each hydrotope. It is not clear

from the referenced paper how the hydrotopes of each sub-catchment laterally connect. The most promising aspect of this hydrotope approach is tremendous decrease in computational cost. For example, the Thur River catchment, with an area of 1703 km^2, has 170,300 grid cells (100m × 100m), but only 2486 HRUs in Gurtz et al. [*1999*]. If a digital topography map of 500m × 500m (e.g., DEM) is used, the number of HRUs reduces to 1208. However, PREVAH lumps the soil water storage effect on evapo-transpiration by using Penman-Monteith equation with stomatal resistances as a function of lumped soil moisture. This simplification loses the capacity to represent soil moisture dynamics, which is important to quantify percolation flux across the soil-bedrock interface, especially in semiarid climates.

In this chapter, a framework for mountain-block hydrology modeling is described (§7.2), aimed at quantifying the temporal and spatial distribution of distributed mountain-block recharge. However, due to the restriction of time and computational capability, application of the distributed mountain-block hydrology modeling is beyond the scope of this dissertation. A simplified mapping approach is proposed (§7.3), and applied for two mountain areas in northern New Mexico (§7.4 and 7.5). The results give bounding estimates for the total mountain-block recharge and distributed mountain-block recharge (Chapter 1). Finally, climate variability effects on mountain-block recharge are examined in §7.6.

7.2 Mountain-block recharge modeling

Two future options for distributed mountain-block recharge modeling are described in Figures 7.1 and 7.2. Fully distributed three-dimensional (3D) hydrologic modeling is proposed in the first option (Figure 7.1). The model output will give temporal and spatial distribution of ET, distributed MBR, and runoff. Estimates of focused MBR

depend on whether or not streamflow is simulated in the model. In comparison to the fully distributed mountain-block hydrologic modeling, the most promising aspect of the hydrotope-based modeling is that it greatly reduces the computational cost [e.g., *Gurtz et al., 1999*]. In this option, the mountain-block is divided into many hydrotopes according to topography, bedrock, soil thickness, vegetation, as well as local climate conditions [e.g., *Jeton and Smith, 1993*]. The hydrotopes are connected based on topographic relationships. High-resolution hydrologic modeling is conducted in 2D cross-sections, simultaneously for each hydrotope. The hydrotopes communicate at prescribed time steps. The output from the hydrotope-based model is the same as the grid-based model, except that the output hydrologic state variables are distributed in units of hydrotopes, instead of grids.

For both future options, the atmospheric boundary could be generated using the ASOADeK and TVET models, or their equivalents. It is difficult to obtain distributed precipitation data in the mountains. On one hand, weather stations are sparse in mountainous terrain, and require a reliable interpolation approach to obtain precipitation maps. On the other hand, common NEXRAD and satellite precipitation products have low spatial resolutions, and fail to capture precipitation spatial variability in mountains, which could lead to significant error in hydrologic simulations [e.g., *Bindlish & Barros, 2000*]. The ASOADeK model (Chapter 2) can be used to generate temporally average precipitation maps over the mountains based on gauge data. In the future, available NEXRAD and satellite precipitation products will be downscaled using the ASOADeK regression, and fused into gauge-interpolated precipitation maps.

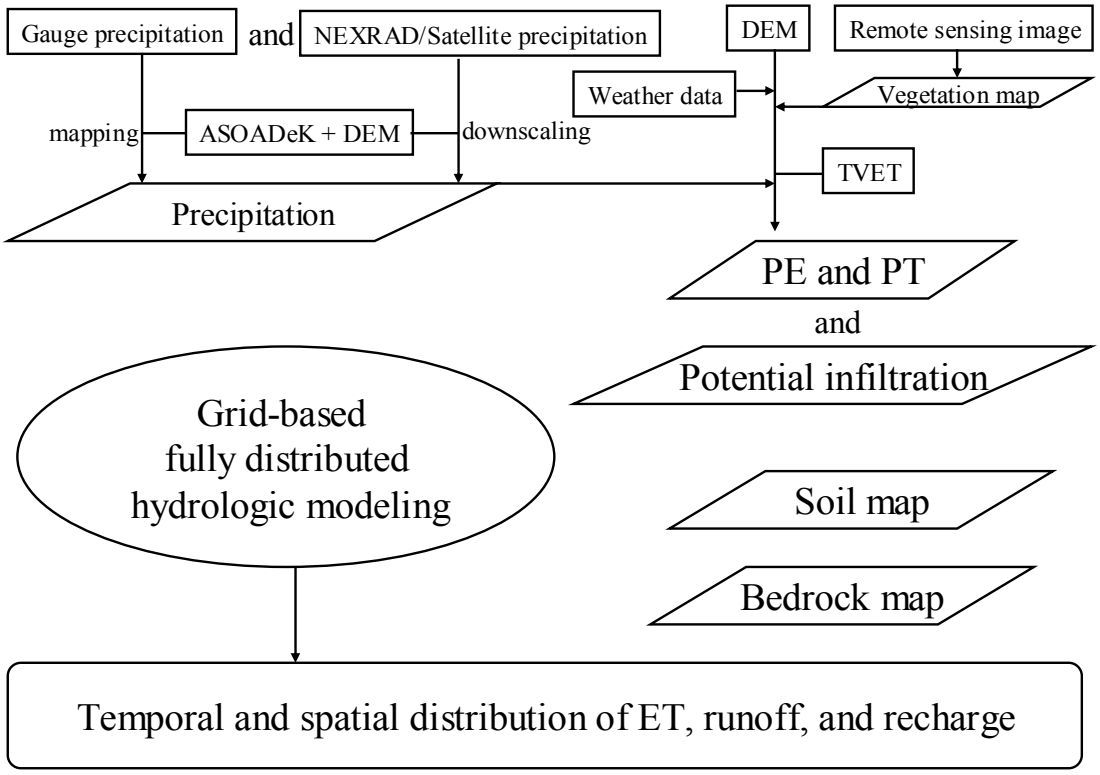

Figure 7.1 Grid-based distributed mountain-block recharge modeling.

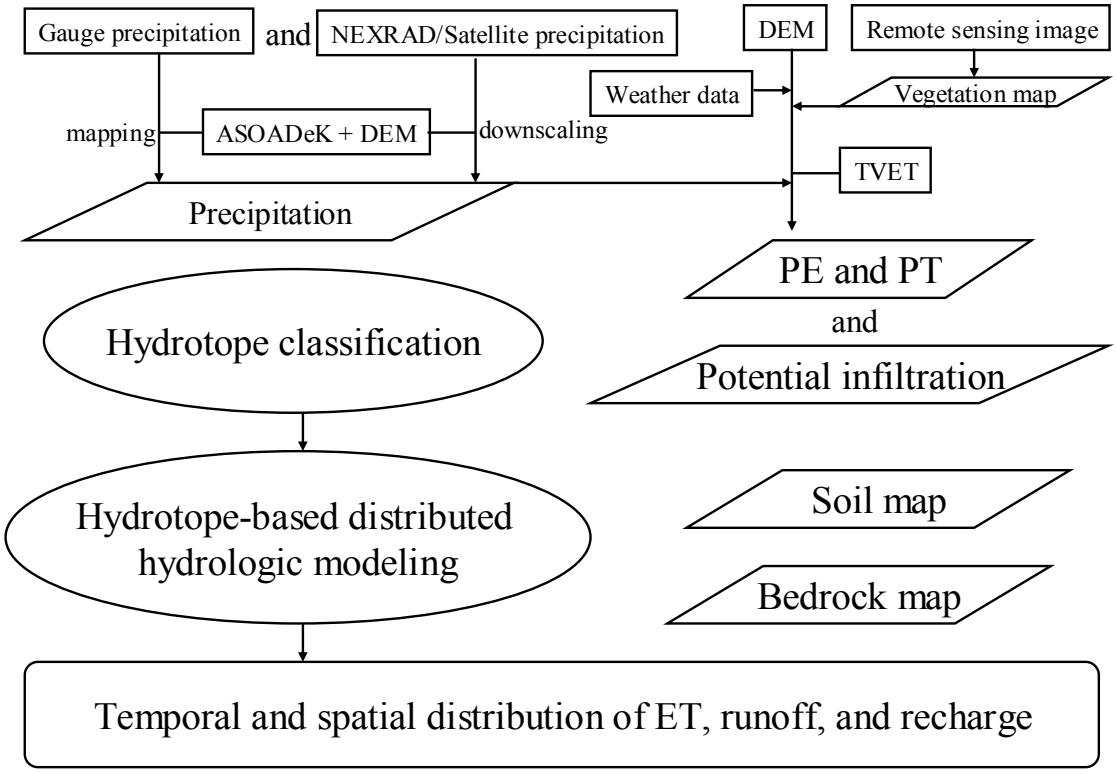

Figure 7.2 Hydrotope-based distributed mountain-block recharge modeling.

The TVET model can be then used to generate spatially and temporally distributed potential E and potential T, as well as potential infiltration, from DEM, weather data, remote sensed vegetation maps, and ASOADeK-downscaled NEXRAD (or other remotely sensed data) precipitation maps. The weather data (e.g., temperature, relative humidity, wind speed, etc.) usually come from ground-based observations, which again require certain types of interpolation. ASOADeK-like models will also be developed to map these weather variables. With these spatially distributed time-series weather variables, TVET will construct time-series of active water for infiltration and runoff on the ground surface, potential evaporation, and potential transpiration for each pixel.

7.3 Simplified mapping approach for mountain-block recharge

As a demonstration of the promise of these advances, a simplified mapping approach is applied to map mountain-block recharge in two mountainous areas of northern New Mexico (Figure 7.3). However, as we saw in Chapters 5 and 6, the factors influencing near-surface water partitioning on mountain hillslopes are many; the processes are complex and interrelated; and their effects on percolation are highly nonlinear. It is not feasible to use a simplified approach to map realistic mountain-block recharge. Nonetheless, we can estimate the maximum possible mountain-block recharge (or upper-bound MBR in this dissertation) with some approximations, and begin to explore the mapping strategies. The long-term mean distributed MBR is upper-bounded by the percolation. The long-term mean total MBR is upper-bounded by the difference between long-term mean precipitation (P) and actual evapotranspiration (ET), which is referred to as “water yield”. In literature, the word “water yield” has two meanings. One is the stream-flow attributed by an area of interest [e.g., Bosch & Hewlett, 1982]; the

other is the difference of P and ET in an area of interests [e.g., *Maurer & Berger, 1997*]. The second meaning is adopted in this dissertation because it appropriately represents the mountain contribution to basin-scale water balance (both surface and subsurface).

To reduce complexity, the spatial variability of soil and vegetation is not considered. Soil is assumed to be thin and with macropores, which optimizes conditions for percolation. Bedrock is assumed uniform, and with a larger permeability, e.g., 1.0×10^{-14} m^2 for both fractured granite in Sangre de Cristo Mountains, and non-welded tuff in Jemez Mountains. This assumption is probably close to the actual mean bedrock permeability in Jemez Mountains. For example, nine laboratory measurements (constant head or falling head permeameters) of tuff matrix permeability from the Jemez Mountains range from 10^{-17} to 10^{-12} m^2 [*Newman, 2003*]. From numerous air mini-permeameter measurements of tuff matrix in the eastern flank (Pajarito Plateau) of the Jemez Mountains, the permeability of glassy nonwelded tuff ranges from $10^{-12.4}$ to $10^{-11.9}$ m^2, that of crystallized nonwelded tuff from $10^{-12.9}$ to $10^{-11.3}$ m^2, and that of welded tuff from $10^{-13.3}$ to $10^{-12.3}$ m^2 [*Wilson, 2004*].

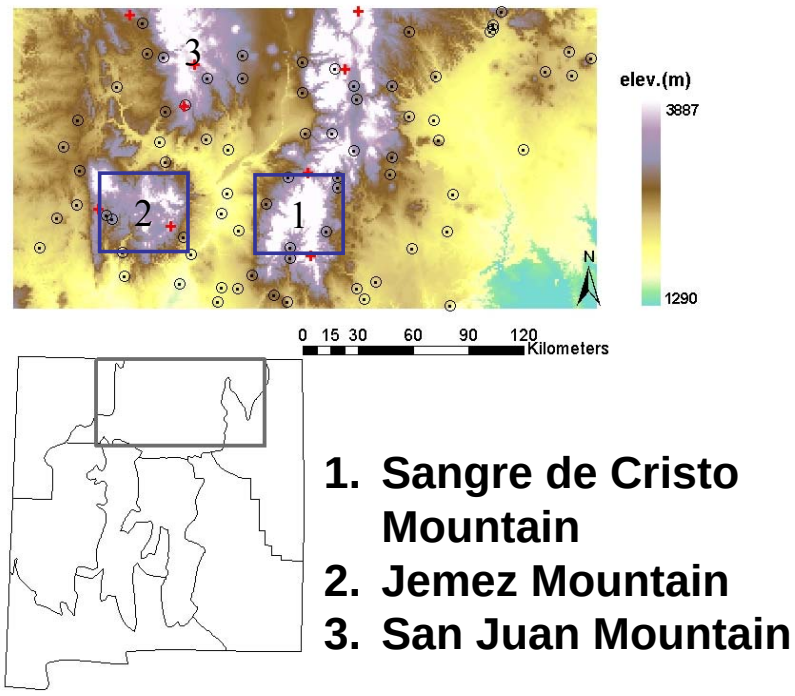

Figure 7.3 Two study mountainous areas: southern part of Sangre de Cristo Mountains and Jemez Mountains. The circles and crosses are precipitation gauges used for precipitation mapping for the area.

For the granitic-rock-dominated Sangre de Cristo Mountains, few permeability measurements have been done. However, some testing of fractured crystalline bedrock in other areas suggests 10^{-14} m^2 is very possible for the Sangre de Cristo Mountains. For example, Caine and Tomusiak [*2003*] estimate permeability of 10^{-13} to 10^{-14} m^2 for intensively fractured crystalline rock in Turkey Creek Watershed of the Front Range of the Rocky Mountains, using the FracMan model. Snow's [*1979*] classical study reports bulk permeability of 10^{-14} m^2 for most of the fractured crystalline rocks that he considered, measured using packer tests.

However, it should be noted that the bedrock permeability is one of the primary factors determining percolation on mountain hillslopes (Chapter 5). The uncertainty in

bedrock permeability estimates will strongly affect the estimated mountain-block recharge. The results in the following of this chapter should be carefully applied to estimating actual MBR in northern New Mexico. The big assumption here is the bulk bedrock permeability of 10^{-14} m^2. If the mean actual bedrock permeability deviates from this value, which is very possible, the estimated recharge will change. Nevertheless, if the mean actual bedrock permeability over the studied mountain-blocks is smaller than 10^{-14} m^2, which is also very possible, the upper-bound MBR estimated in the following should apply for the study area.

With these assumptions for vegetation, soil, and bedrock, the percolation is controlled only by slope steepness and topography-modified local climate condition. As we found in Chapter 5, slope steepness' direct control on percolation at the soil-bedrock interface is not important, leaving the climate condition as the major control factor. The distributed mountain-block recharge (i.e., percolation across the soil-bedrock interface) is then investigated at a point location. Climate conditions are varied to account for different local climates modified by topography (e.g., elevations, terrain aspect, etc.). Similar approaches have been used to quantify basin scale diffuse recharge at the basin floor [e.g., Fayer et al., 1996; *Kearns and Hendrickx 1998; Small, 2005*].

The prediction functions are derived in Chapter 5 for the two studied mountain blocks with their different bedrock types. Equations 5.7 and 5.8 are for estimating percolation in granitic Sangre de Cristo Mountains and non-welded tuff Jemez Mountains, respectively; and equations 5.9 and 5.10 are for estimating actual annual ET in the two mountain ranges, respectively. Since percolation and ET regression equations were derived from the simulated results independently, they are related but not strictly

constrained by each other. When they are applied to one pixel, the sum of percolation and ET could exceed the total precipitation into that pixel, which is not necessarily realistic. Nonetheless, when the results are averaged over an area consisting of numerous pixels, the relationship between percolation and water yield (P-ET) is reasonable (i.e., percolation < water yield). With these regression functions, the percolation map and the water yield maps can be generated if maps of annual precipitation and potential ET are available. For simplicity in further discussion, this procedure is called the point-simulation-based approach.

7.4 Annual precipitation and potential ET mapping

The long-term average annual precipitation map for the study area is constructed by summing monthly precipitation maps from the ASOADeK model (Chapter 2), with a pixel size of 1 kilometer (Figure 7.4). Hargreaves' 1985 equation (Chapter 4, equation 4.3) is used to estimate long-term-average monthly PET maps, which are then summed together to generate the annual PET map for the study area.

Since Hargreaves equation was developed for flat areas, it should be modified for the mountain terrains. The mean solar radiation at the top of the atmosphere (R_a) in the equation is adjusted to account for the effects of the terrain slope steepness and aspect by using terrain functions of the TVET model. The model calculates the ratio of *Ra* on sloped surface to that of the flat surface as a function of slope steepness and aspect, and the time of the year for the study area (Figure 7.5). The slope steepness and aspects are derived from a 60-m DEM.

Besides *Ra*, the monthly mean daily temperatures (minimum and maximum) are needed to calculate potential ET for each month. In the study area, the mean daily maximum temperature is well correlated to the terrain elevation. The correlation

coefficient is not sensitive to the DEM window size, except for the 60-m window (Figure 7.6). The relative low correlation coefficient for the 60-m window is an artifact of the rough geographical coordinate records of the NCDC weather stations. Physically, the 60-m DEM elevation should have similar correlation coefficient as elevations of other spatial resolution. Thus, 60-m DEM elevations are used to estimate monthly mean daily maximum temperature for the study area using the regression function derived from gauge data. The correlation coefficient between monthly mean daily minimum temperature is high for warm seasons, but not for cold seasons (Figure 7.7). The linear regression functions are used to estimate monthly mean daily minimum temperature for the warm season months (April ~ September) using the 60-m window DEM. The mean daily minimum temperature is interpolated from the gauge observations by kriging for the remaining months (October ~ March).

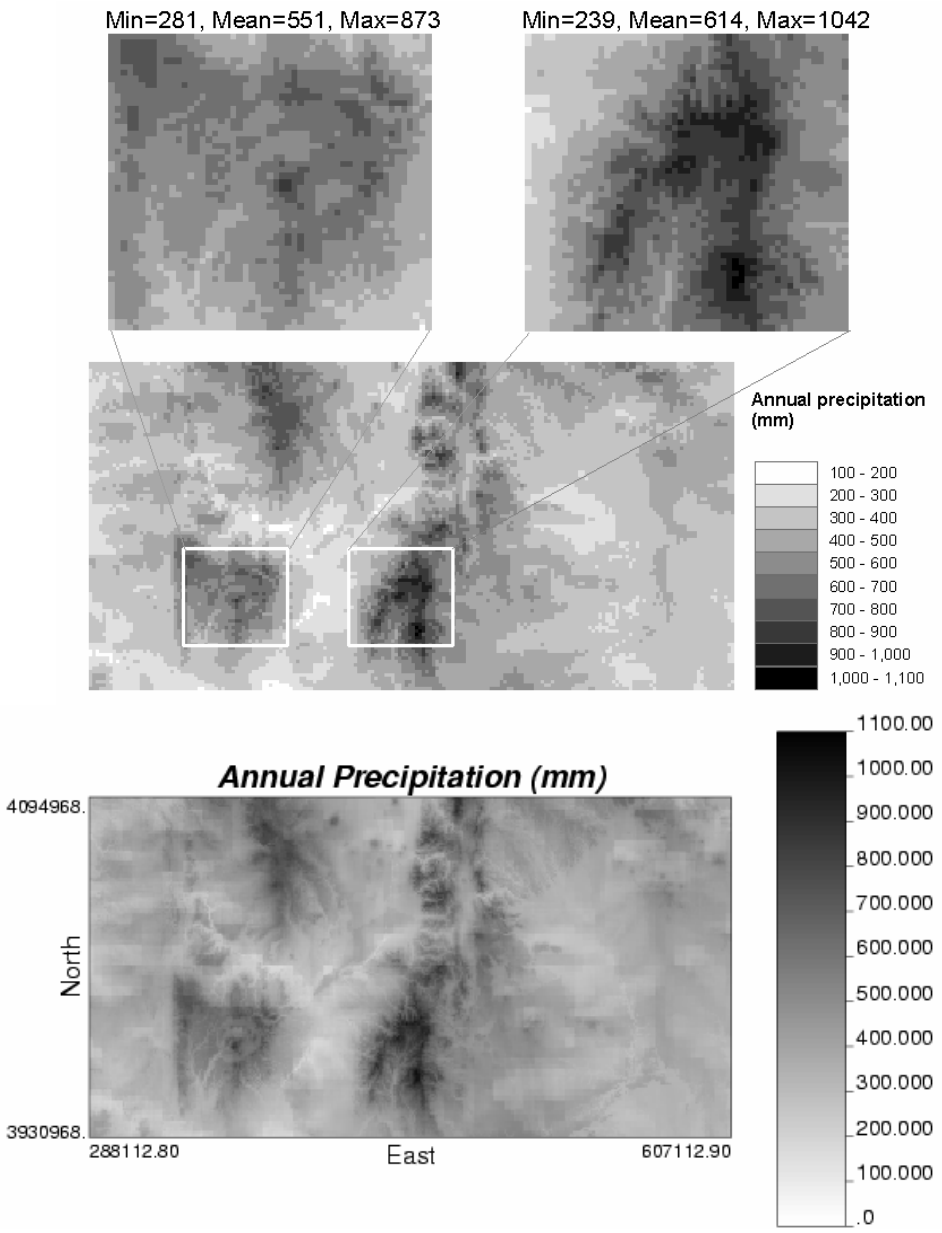

Figure 7.4 The long-term-average annual precipitation (top) in the study area, northern New Mexico, with insets of two focused study mountain blocks, derived from ASOADeK-generated precipitation map of 1 km resolution (bottom) (sum of the 12 monthly ASOADeK precipitation, Chapter 2).

With monthly mean daily minimum temperature maps, daily maximum temperature maps, and terrain-correction coefficient for *Ra*, the monthly potential ET is mapped with a pixel size of 60 meter. These monthly PET maps are summed to obtain the annual PET map (Figure 7.8).

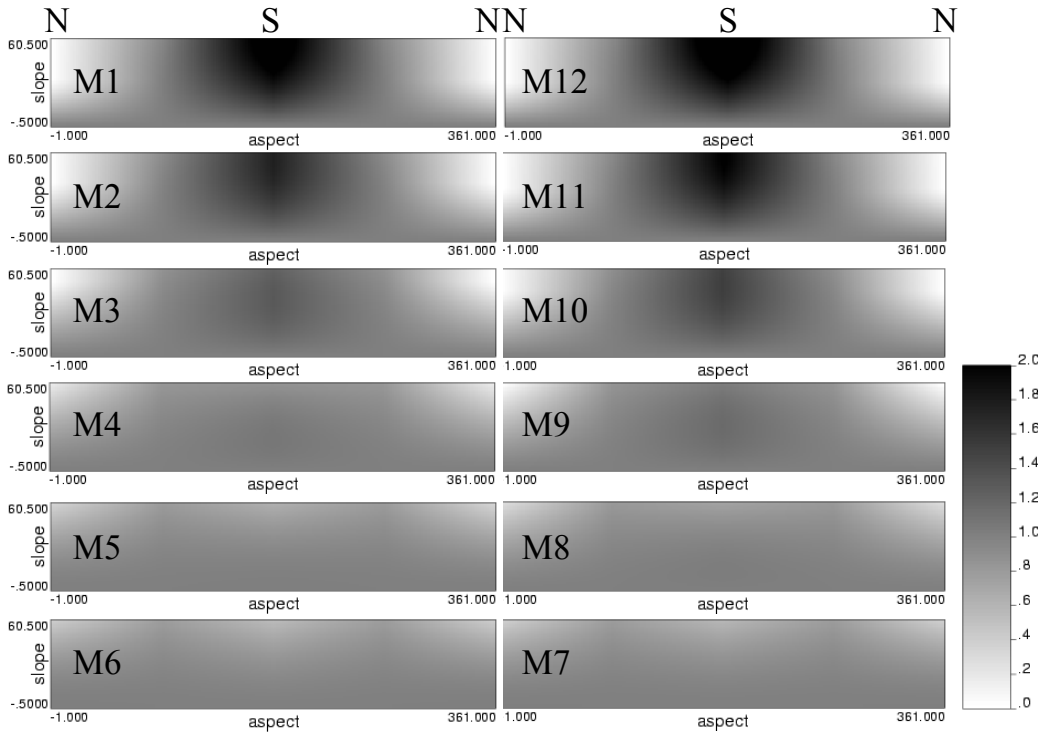

Figure 7.5 The TVET model calculated the ratio of solar radiation at the top of the atmosphere on a sloped surface to that on the flat surface as a function of slope steepness (vertical axis, in degree) and slope aspect (horizontal axis, in degree, zero due south) for 12 months (from January (M1) through December (M12) in the year, for a location in northern New Mexico.

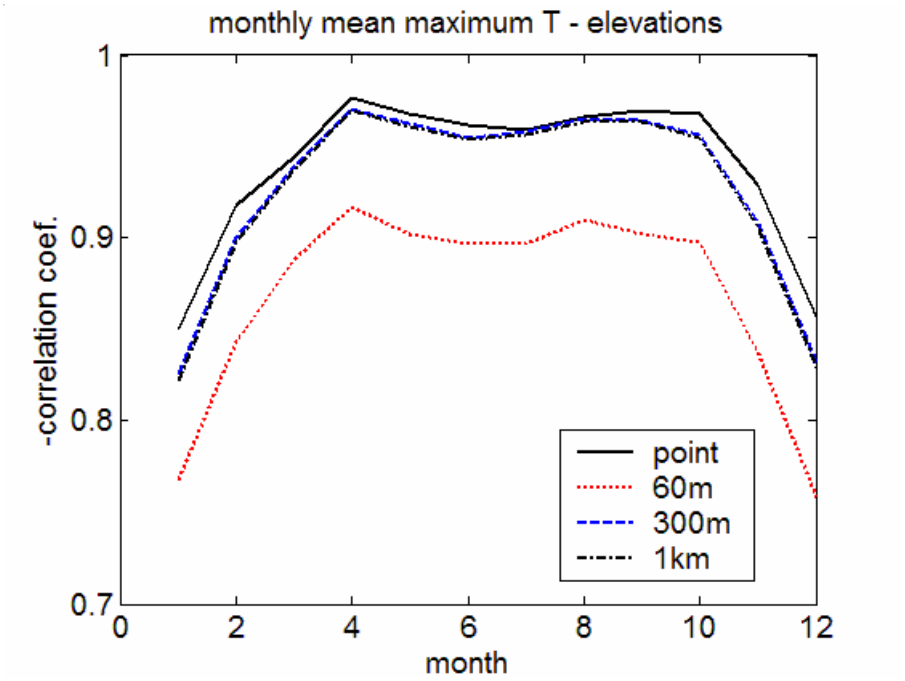

Figure 7.6 The Pearson correlation coefficient of monthly mean daily maximum temperature and the elevation for various window sizes in the study area, northern New Mexico.

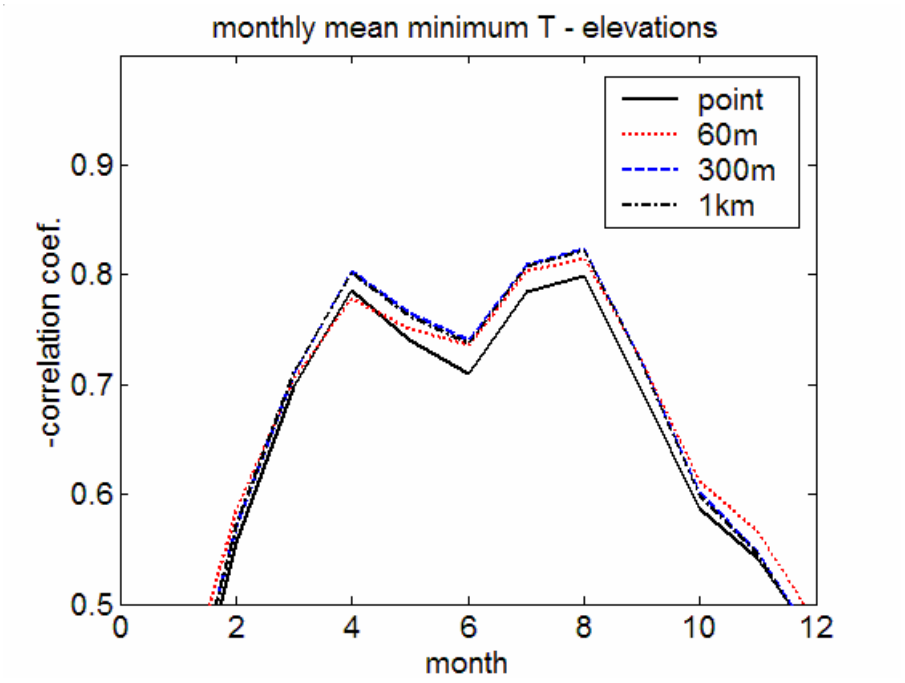

Figure 7.7 The Pearson correlation coefficient of monthly mean daily minimum temperature and the elevation for various window sizes in the study area, northern New Mexico.

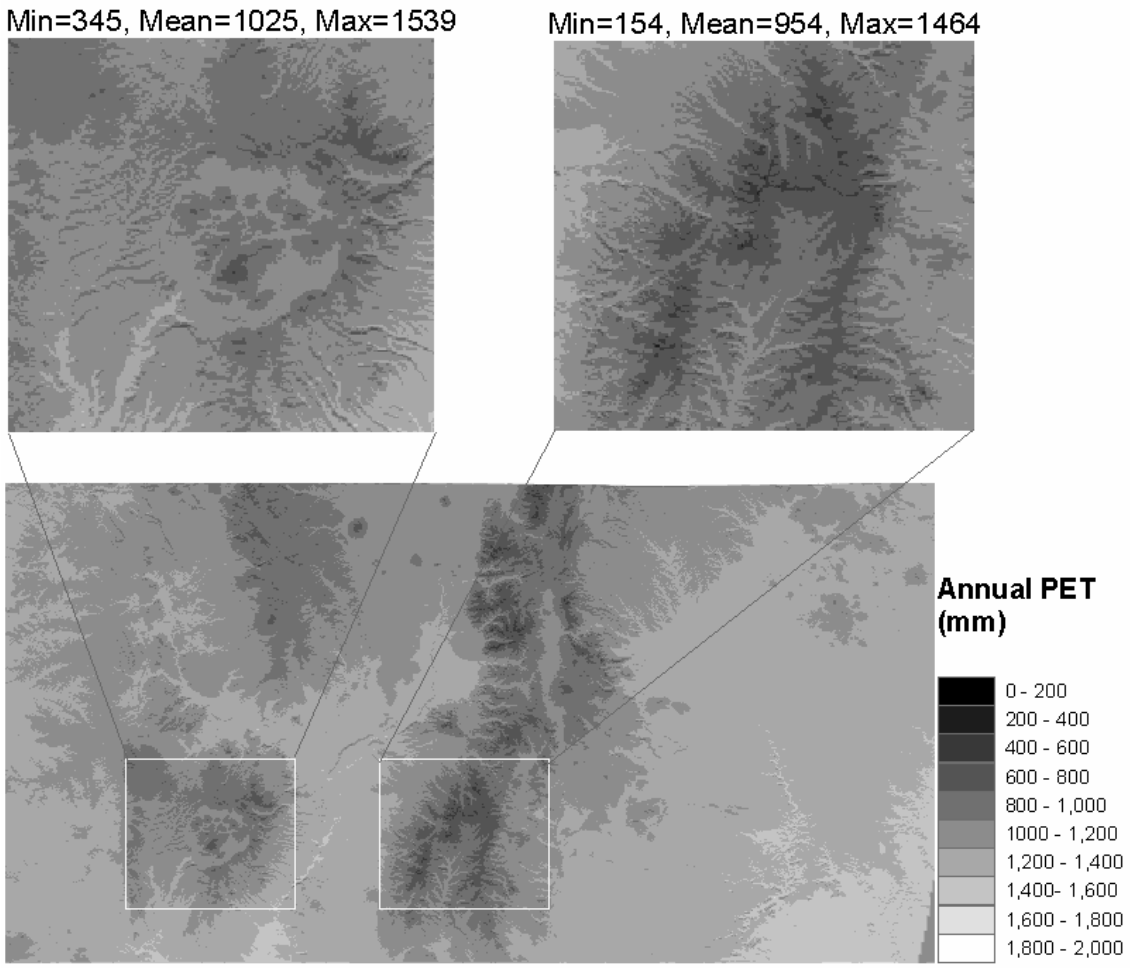

Figure 7.8 The annual potential ET map (sum of the 12 monthly ET maps) with insets of two focused study mountain blocks. The original data has a spatial resolution of 60 m.

7.5 Mountain-block recharge in Jemez Mountains and Sangre de Cristo Mountains

As discussed earlier in Chapter 5, the annual percolation is a function of mean local climate conditions (characterized with annual PET/P ratio) for given bedrock if soil and vegetation characteristics are uniform. Similarly, the actual annual ET is also a function of local climate conditions. Now that we have the topography-modified local climate conditions, annual P (Figure 7.4) and annual PET (Figure 7.8), over the two mountain blocks, we can generate percolation maps and water yield maps (P-ET) using Equations 5.7~10 for the two mountain blocks. The water yield maps place an upper limit on amount of total mountain-block recharge, i.e., the total of distributed and focused MBR. The percolation maps provide an estimate of distributed MBR that is biased toward the high side.

The generated percolation maps and water yield maps are shown in Figure 7.9, with the mean value averaged over the whole map area of each study mountain block. To test whether this mean value is representative, the means over various elevation ranges are also calculated from the maps (Figure 7.10). The distributed MBR does not significantly change between the elevation range of 1500m and above (i.e. the whole map area) and that of 2000m and above (Figure 7.10). This suggests that the mean value for the whole mapped area is representative for the studied mountains. This is also true for the mean of water yield (Figure 7.10).

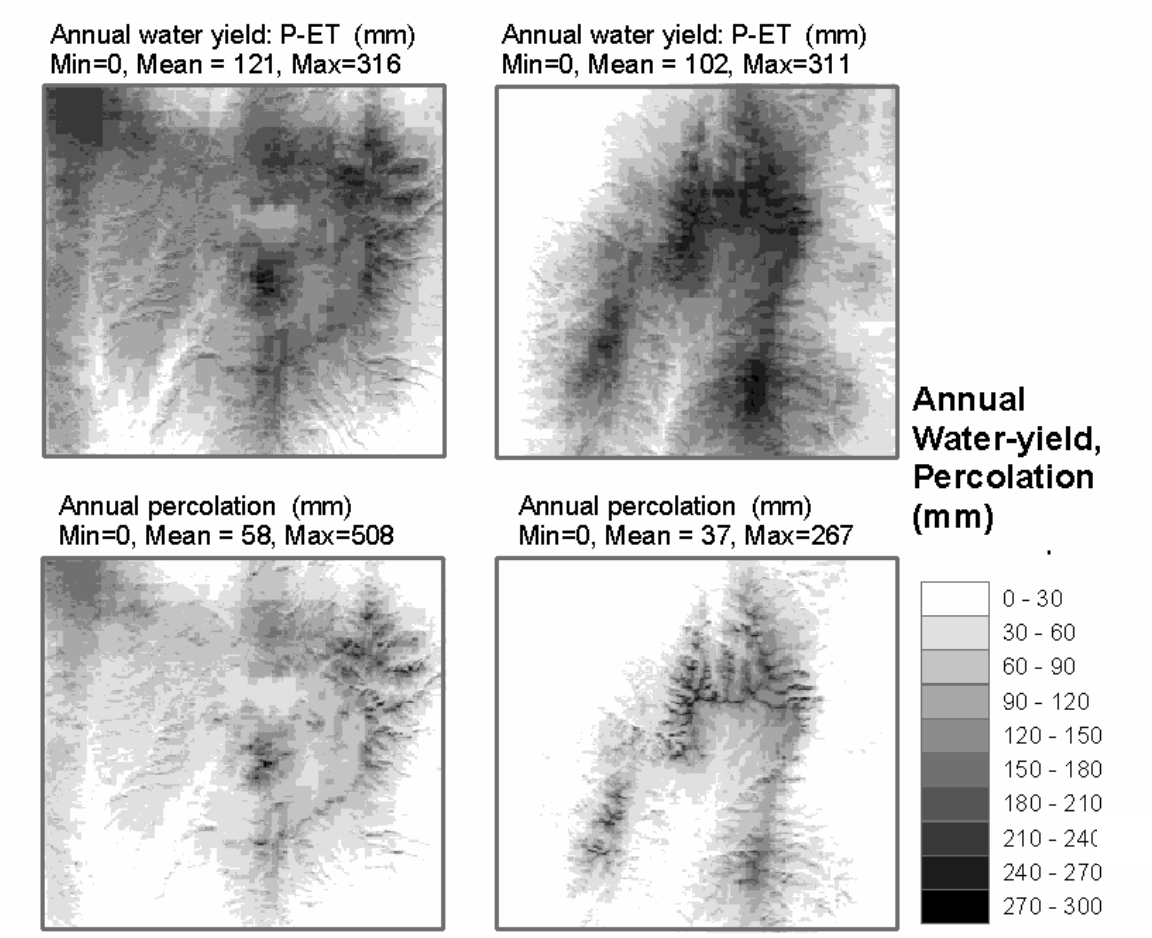

Figure 7.9 The water yield (upper bound of total MBR) maps and percolation maps for Jemez Mountains (left) and Sangre de Cristo Mountains (right). The minimum, mean, and maximum values for each map are numbers evaluated over the whole mapped area.

Compared to the precipitation maps (Figure 7.4) and potential ET maps (Figure 7.8), the recharge maps (Figure 7.9) clearly suggest the effects of bedrock hydraulic properties. The Sangre de Cristo Mountains have a larger annual precipitation and a smaller potential ET than Jemez Mountains, which could lead to a larger recharge. However, the water yield in the Sangre de Cristo Mountains is smaller than Jemez Mountains, either for the whole mapped region (Figure 9), or for specific elevation ranges (Figure 7.10). So is the distributed MBR (Figures 7.9 and 7.10). In terms of spatial patterns, the distributed MBR in Sangre de Cristo Mountains is limited to the high-

elevation zone, while it extends to lower elevations in Jemez Mountains (Figure 7.9). The distributed MBR accounts for about 50% the water yield in Jemez Mountains, and about 35% in Sangre de Cristo Mountains. This indicates that a larger fraction of water yield joins streamflow (not necessary runoff out of the mountains) in the Sangre de Cristo Mountain than in Jemez Mountains.

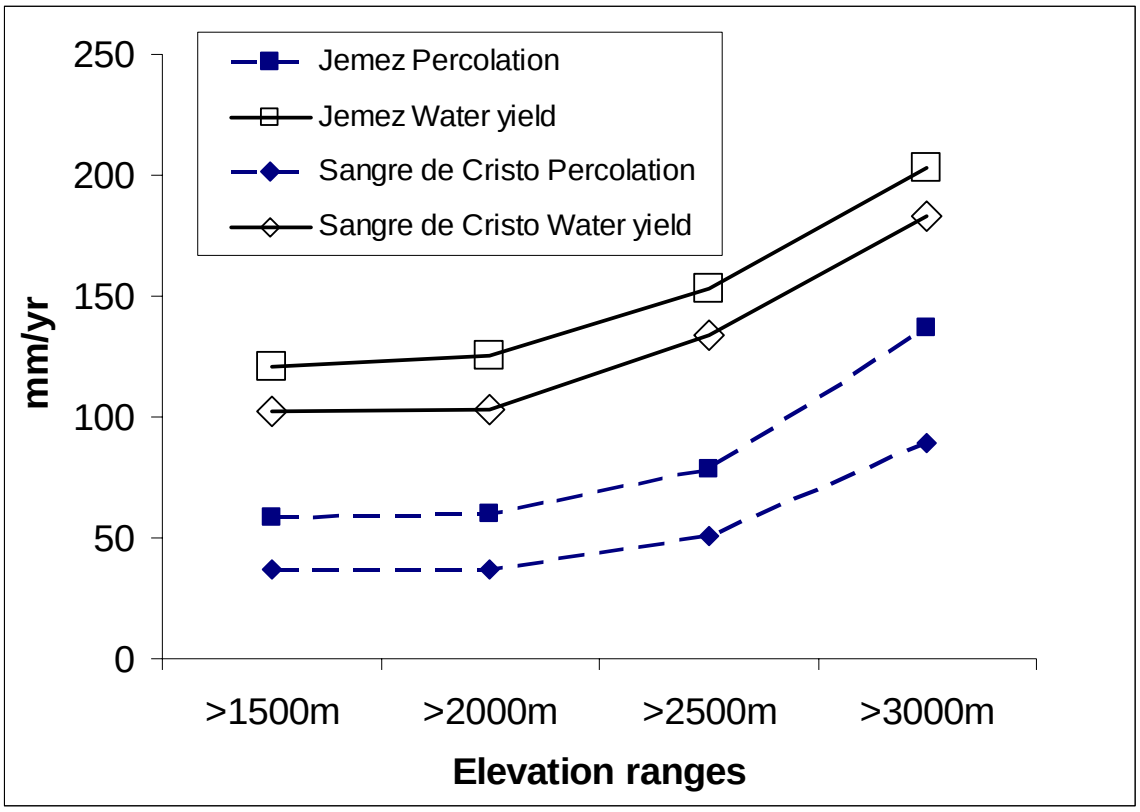

Figure 7.10 Mean annual percolation and water yield (upper bound of total MBR) of the two study mountain blocks, average over various elevation ranges.

Both distributed MBR and water yield increases with elevation (Figures 7.10 and 7.11) in the two study mountainous areas. The patterns of recharge (and water yield) – elevation relationship are similar for the two areas (Figure 7.11 right column), with recharge (water yield) starting at a lower elevation in Jemez Mountains than in Sangre de

Cristo Mountains. The large spread of recharge (water yield) at a same elevation demonstrates topography-induced variability in precipitation and potential ET.

The percolation and water yield maps provide estimated upper bounds of distributed MBR and total MBR, respectively. They can be compared to previously published MBR estimates for these mountains. In Sangre de Cristo Mountains, total MBR has been estimated about 70 mm/year [*Huntley, 1979; Wasiolek, 1995*]. That is below the (upper bound) estimate for water yield from this study (Figure 7.9), suggesting that the previous estimate is reasonable (but not necessary close the actual MBR). This study also suggests that the distributed MBR in Sangre de Cristo Mountains cannot exceed 40 mm/year (Figure 7.9).

There is no independent MBR estimate for the whole Jemez Mountains. We can give a range based on the MBR estimates for surrounding mountains. Since the Jemez Mountains are mainly composed of volcanic bedrock, with a large fraction of non-welded tuff (highly permeable), they are more permeable than the crystalline rock Sangre de Cristo Mountains. So the MBR in Jemez Mountains should be larger than MBR in the Sangre de Cristo Mountains. Because the volcanic San Juan Mountains (Figure 7.3), to the north of Jemez Mountains, have a wetter climate, the MBR estimate for San Juan Mountains [*Huntley, 1979*; §7.1] should give an upper bound of MBR in Jemez Mountains. Based on previous studies, total MBR at Jemez Mountains falls in the range of 70~200 mm/year. The modeled water yield for the Jemez Mountains in this study (Figure 7.9) reduces this range to 70~120 mm/year. The mean distributed MBR in Jemez Mountains cannot exceed 60 mm/year (Figure 7.9).

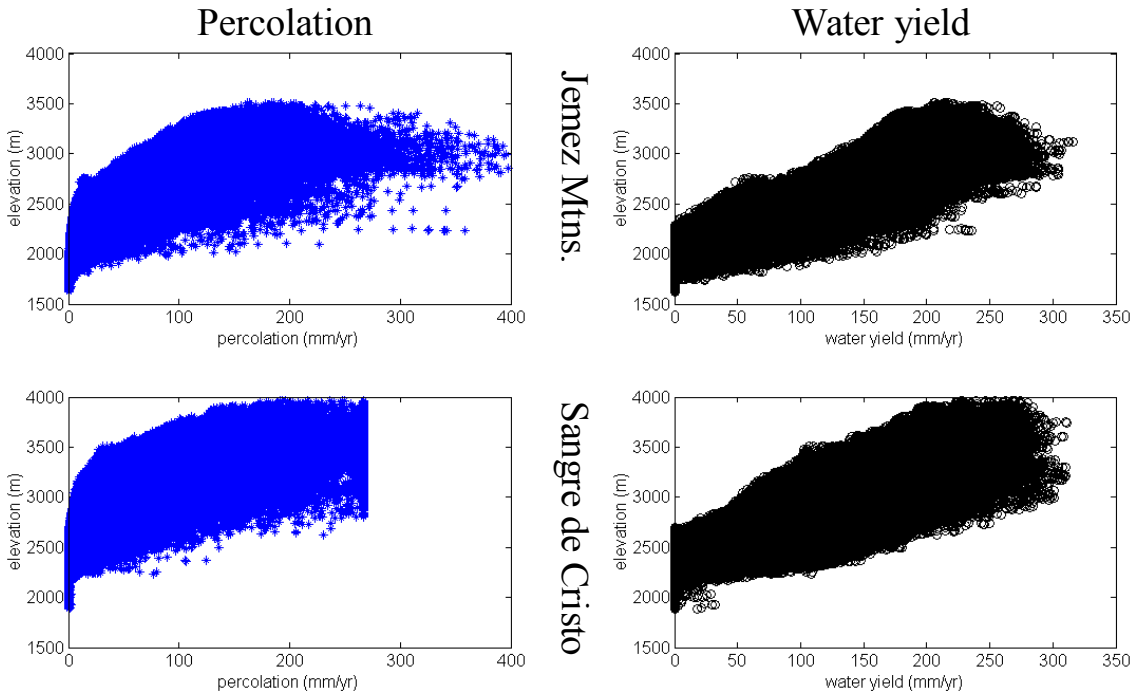

Figure 7.11 The estimated percolation (x axis) varies with elevation (y axis) for Jemez Mountains (top) and Sangre de Cristo Mountains (bottom) in the left column, and the water yield distribution with elevation for the two mountainous areas in the right column.

7.6 Response of mountain-block recharge to climate variability in the Jemez and Sangre de Cristo Mountains

How does the mountain-block recharge respond to climate variability associated with the ENSO and PDO cycles, as found in Chapter 3? The category-mean annual precipitation maps of that chapter are used to construct percolation maps and water yield maps for the two studied mountain ranges, with the crude assumption that the temperature (or potential ET) does not change significantly between different ENSO + PDO categories.

As discussed in Chapter 3, SNOTEL gauge data were not used to map category-mean precipitation, leading to a larger uncertainty at high elevations where no NCDC gauge data were available. The precipitation anomalies were not mapped for this high elevation zone in Chapter 3. However, in order to examine climate variability effects on mountain-block recharge, the high-elevation data must be used here, with assumption that the bias of high-elevation precipitation estimates are similar between categories. In addition, it is assumed that the bias of high-elevation precipitation estimates linearly translates into the bias in recharge between ENSO + PDO categories, which is canceled out when the recharge difference is calculated. An example shown in Appendix XXIII indicates that this assumption is reasonable.

With these assumptions, the difference in maximum distributed MBR from the long-term mean climate conditions is mapped for two selected ENSO + PDO categories (Figure 7.12). The Jemez Mountains are more sensitive to climate variability than the Sangre de Cristo Mountains. Higher elevations are more sensitive than lower elevations (Figures 7.12 and 7.13). Averaged over the studied mountainous areas, El Nino + high PDO increases distributed MBR in Jemez Mountains by ~17% in comparison to the long-term mean climate conditions, while La Nina + low PDO decreases distributed MBR by ~19%. In the Sangre de Cristo Mountains, El Nino + high PDO increases distributed MBR by ~10% in comparison to the long-term mean climate conditions, and La Nina + low PDO decreases distributed MBR by ~15%. It appears that distributed recharge in the Jemez Mountains is more sensitive to climate variability and change than in the Sangre de Cristo Mountains. This is probably related to the different topography patterns between the two mountain blocks. For plateau-characterized Jemez Mountains, there are

many relatively high-elevation pixels which have significant change in annual precipitation in ENSO and PDO cycles; while for the mountain-characterized Sangre de Cristo Mountains, the number of these pixels are smaller. As a result, the overall mean distributed MBR is more sensitive to the climate change in the Jemez Mountains. However, this result should not apply to individual pixels between the two mountains.

Because processes within the mountain block dampen the variability of water partitioning at the soil-bedrock interface, the relatively high frequency ENSO-associated climate variability may not affect the groundwater table in the mountains. The low frequency PDO-associated climate variability may transmit its effects to the bedrock aquifer in the mountains, and even the surrounding basin aquifers. For example, with a semi-discrete dynamic model, Duffy [*2004*] demonstrated that a change in climate forcing in the Los Pinos Mountains, of central New Mexico, would affect the Rio Grande water table 20-km-away in roughly 50 years. Because of wetter climate conditions than the Los Pinos Mountains, subsurface water transmits through the mountain blocks faster in the Jemez and Sangre de Cristo Mountains. Thus, climatic decadal variability (i.e. PDO) could affect groundwater resources in the surrounding basins in north New Mexico, where the two studied mountain ranges are located. The sensitivity of MBR to climate variability also sheds light on the vulnerability of groundwater resources to potential future climate change.

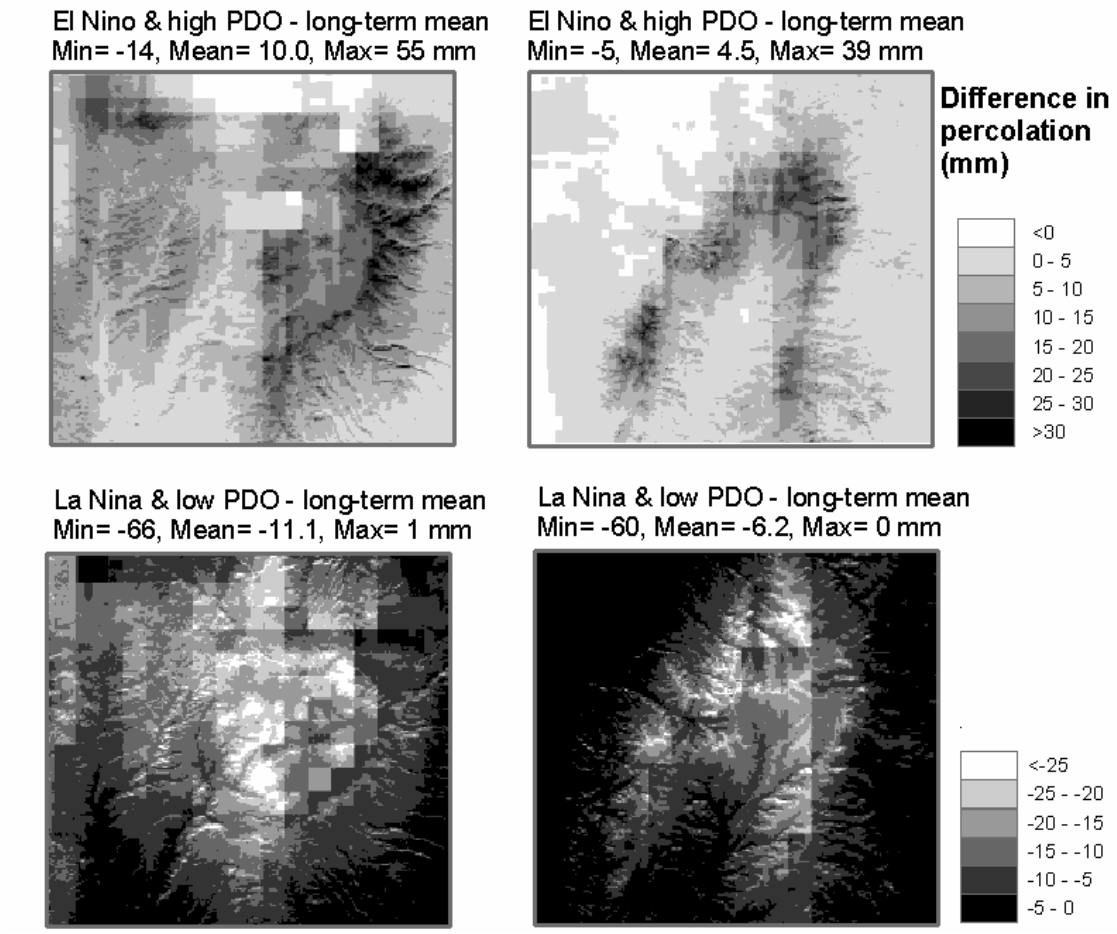

Figure 7.12 The difference in distributed MBR of two selected ENSO+PDO categories (El Nino + high PDO on the top, and La Nina + low PDO at the bottom) from the long-term mean climatic condition, for the two studied mountains (Jemez on the left, and Sangre de Cristo on the right). Note the change in sign of the differences for the two climate conditions.

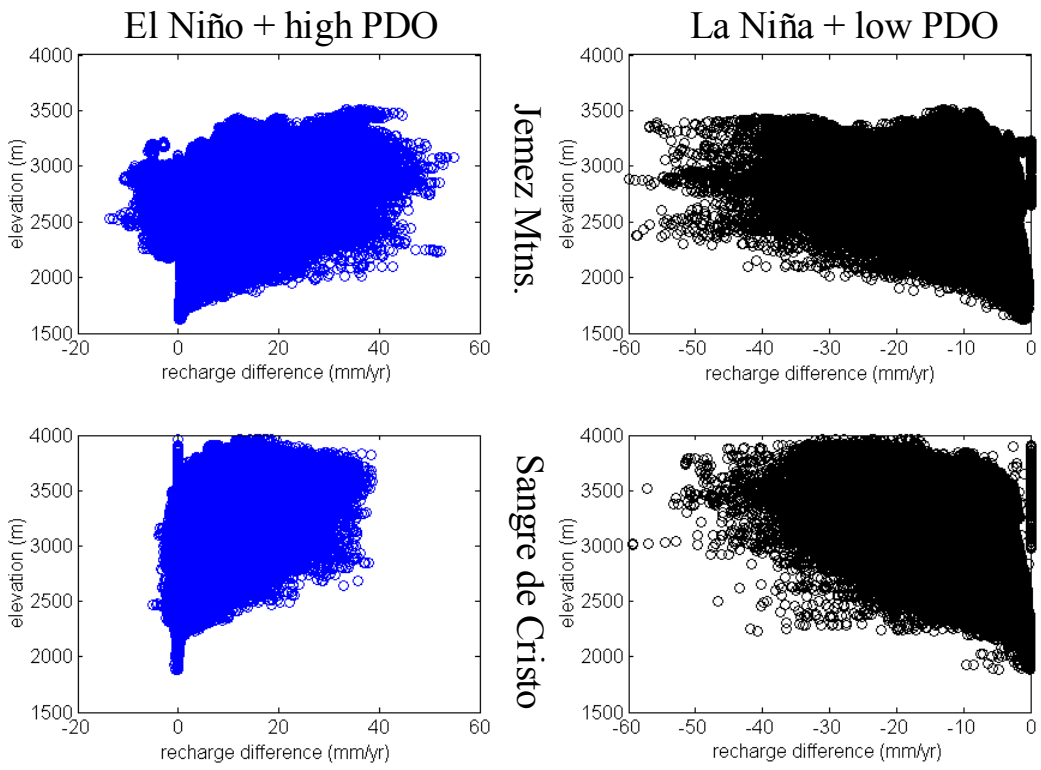

Figure 7.13 The difference of distributed MBR (x-axis) of two selected ENSO+PDO categories (El Nino + high PDO on the left, and La Nina + low PDO on the right) from the long-term mean climatic condition, for the studied mountains (Jemez on the top, and Sangre de Cristo at the bottom) as a function of elevation (y-axis).

7.7 Conclusions

This chapter describes three optional numerical approaches to estimate mountain block recharge, with different degrees of complexity. They are the fully distributed 3D mountain-block hydrologic model, the hydrotope-based distributed hydrologic model, and the simplified point-simulation-based approach. Because of its distributed nature and low computational cost, the hydrotope-based model is recommended for the future exploration of mountain-block recharge. The ASOADeK and TVET models are useful to

generate atmospheric boundary conditions for the mountain block hydrology modeling for all three approaches.

The point-simulation-based approach is applied in two mountain areas, the Jemez Mountains and the Sangre de Cristo Mountains, northern New Mexico. For the Jemez Mountain, the results suggest that total mountain-block recharge is less than 120 mm/year, with distributed MBR (bounded by percolation) being about 50% of the total MBR (bounded by water yield). Coupled with previous studies in the surrounding mountain areas, the total MBR in the Jemez Mountains should be between 70~120 mm/year. For the Sangre de Cristo Mountains, the total MBR is less than 100 mm/year, suggesting that the previous estimate of 70 mm/year is reasonable. The spatial patterns of MBR are different for the two mountain blocks, with MBR limited to the higher elevations in the Sangre de Cristo Mountains while spreading over elevations in the Jemez Mountains.

The results also suggest that ENSO and PDO cycles associated climate variability can lead to a 10~20% change in MBR for the two mountainous areas. Although this amount of variability occurs at the shallow soil-bedrock interface, some of it, especially that associated with decadal climate variability, may also affect the groundwater replenishment rate to the underlying mountain bedrock aquifer, and the surrounding basins. In terms of MBR averaged over whole mountain ranges, the Jemez Mountains are more sensitive to the climate variability and change than the Sangre de Cristo Mountains.

References

Bindlish, R., and A.P. Barros (2000), Disaggregation of rainfall for one-way coupling of atmospheric and hydrologic models in regions of complex terrain. *Global and Planetary Change*, 25, 111-132.

Bosch, J.M., and J.D.Hewlett (1982), A review of catchment experiments to determine the effect of vegetation changes on water yield and evapotranspiration. *Journal of Hydrology*, 55, 3-23.

Caine, J.S., and S.R.A. Tomusiak (2003), Brittle structures and their role in controlling porosity and permeability in a complex Precambrian crystalline-rock aquifer system in the Colorado Rocky Mountain Front Range. *GSA Bulletin*, 115(11), 1410-1424.

Duffy, C.J. (2004), A semi-discrete dynamical model for mountain-front recharge and water balance estimation: The Rio Grande, *Eos Trans*. AGU, 85(17), Jt. Assem. Suppl., Abstract H42B-06.

Fayer, M.J., G.W. Gee, M.L. Rockhold, M.D. Freshley, and T.B. Walters (1996), Estimating recharge rates for a groundwater model using a GIS, *Journal of Environmental Quality*, 25, 510-518.

Flint, A.L., L.E. Flint, J.A. Hevesi, and J.M. Blainey (2004), Fundamental concepts of recharge in the Desert Southwest: a regional modeling perspective, in *Groundwater Recharge in a Desert Environment: The Southwestern United States,* edited by J.F. Hogan, F.M. Phillips, and B.R. Scanlon, Water Science and Applications Series, vol. 9, American Geophysical Union, Washington, D.C., 159-184.

Gurtz, J., A. Baltersweiler, and H.Lang (1999), Spatially distributed hydrotope-based modeling of evapotranspiration and runoff in mountainous basins, *Hydrological Processes*, 13(17), 2751-2768.

Huntley, D. (1979), Groundwater recharge to the aquifers of northern San Luis Valley, Colorado. *Geological Society of America Bulletin*, *Part II*, *90*, no.8, 1196-1281.

Jeton, A.E., and J.L. Smith (1993), Development of watershed models for two Sierra Nevada basins using a geographic information system, *Water Resources Bulletin*, American Water Resources Association, 29(6), 923-932.

Kearns, A., and J.M.H. Hendrickx (1998), Temporal variability of diffuse groundwater recharge in New Mexico, *New Mexico Water Resources Research Institute, Report* 309, New Mexico State University, Las Cruse.

Maurer, D.K., and D.L. Berger (1997), Subsurface flow and water yield from watersheds tributary to Eagle Valley hydrographic area, west-central Nevada, *USGS Water-Resources Investigations Report* 97-4191, 56p.

Maxey, G.B., and Eakin T.E. (1949), Ground water in White river valley, White Pine, Nye, and Lincoln Counties, Nevada*, Nevada Department of conservation and Natural Resources Water Resources Bulletin,* no. 8, 59p.

McAda, D.P., and M. Wasiolek (1988), Simulation of the regional geohydrology of the Tesuque aquifer system near Santa Fe, New Mexico, *U.S. Geological Survey Water-Resources Investigations Report 87-4056*, 71p.

Newman, B.D. (2003), Personal communication. Los Alamos National Laboratory, Los Alamos, New Mexico.

Small, E.E. (2005), Climatic controls on diffuse groundwater recharge in semiarid environments of the southwestern United States, *Water Resources Research*, 41 (4), W04012, doi:10.1029/2004WR003193.

Snow, D.T. (1979), Packer injection test data from sites on fractured rock, *LBL (Lawrence Berkeley Laboratory, Energy and Environment Division) Report*. No. 10080 (197911), 15p.

Wasiolek, M. (1995), Subsurface recharge to the Tesuque aquifer system from selected drainage basins along the western side of the Sangre de Cristo Mountains near Santa Fe, New Mexico. *U.S. Geological Survey Water-Resources Investigations Report* 94-4072.

Wilson, J.E. (2004), Characteristics of faults in nonwelded ignimbrites from the Pajarito Plateau and implications for fluid flow, Ph.D. Dissertation, New Mexico Institute of Mining and Technology, Socorro, New Mexico.

CHAPTER 8 SUMMARY, CONCLUSIONS, AND RECOMMENDATIONS

Near-surface water partitioning in mountains via highly resolved hydrologic modeling is studied in this dissertation, aimed at understanding factors and mechanisms controlling mountain-block recharge, and estimating mountain-block recharge in semiarid regions. Reliable atmospheric boundary conditions (precipitation and potential evapotranspiration) are required for mountain-block hydrologic modeling. The first part of the dissertation (Chapters 2~4) described the development of models to quantify the atmospheric boundary conditions in mountains. The second part of the dissertation (Chapters 5~7) included generic and specific hillslope-scale hydrologic simulations, and mountain-block recharge estimation of a typical semiarid mountainous region. Below are summaries of each piece of work in the dissertation, with its conclusions, uniqueness, strengths and weaknesses, and recommendations for future efforts.

8.1 The ASOADeK model

The ASOADeK model (Chapter 2) considers both precipitation spatial covariance, and orographic and atmospheric effects, in estimating precipitation distribution. The ASOADeK model was applied to map monthly precipitation for a mountainous area in semi-arid northern New Mexico. The effective moisture flux directions and spatial moisture trends identified by the optimal multiple linear regressions, using only gauge data, agree with the regional climate setting. When compared to a common precipitation mapping product, PRISM, the ASOADeK summer precipitation maps of the study area

agree well with the PRISM estimates, and with higher spatial resolution. The ASOADeK winter maps improve upon PRISM estimates. ASOADeK gives better estimates than precipitation kriging and precipitation-elevation cokriging because it considers orographic and atmospheric effects more completely.

A strength of the ASOADeK model is its auto-search capacity. With precipitation gauge data, the model auto-determines the climatic setting, and automatically includes both atmospheric and orographic effects for precipitation mapping. Another strength of the model is the high-resolution precipitation product. A weakness of the ASOADeK model are its assumption that the effective atmospheric moisture flux direction is uniform throughout the area of interest, and that the atmospheric moisture gradient monotonously increases from one side to the other side of the area. These assumptions make the model less applicable for mapping event-based mountain precipitation, but they can be relaxed in future versions of the ASOADeK model.

Future work will include applications of ASOADeK to other mountainous areas, and to higher temporal resolutions (e.g., monthly precipitation of a specific year). With its capacity to map spatially high resolution precipitation, ASOADeK could be used to study climate variability effects on mountainous precipitation distribution (e.g., teleconnections with the Pacific decadal oscillation, and the El Niño-Southern Oscillation, as in Chapter 3). With its auto-search capacity, ASOADeK regression has potential for recovering missed rainfall data in the NEXRAD shadow due to the mountain blockage, and for downscaling low spatial-resolution precipitation products. It also has potential as a tool to help identify atmospheric moisture sources (e.g., moisture source of the North

American Monsoon). The model could be also useful to study mountain glaciers, and paleoclimate [*Meyer, 2005*].

8.2 The TVET model

The TVET model separately calculates daily potential E and potential T for partially vegetated hillslopes. It includes slope steepness and aspect effects, and vegetation-cover effects, while quantifying surface energy partitioning. A geometric relationship is used to determine the instantaneous solar incident angle and apparent daily solar hours on a sloped surface, which primarily determines the amount of available energy for surface sensible and latent heating. The available energy is partitioned into one part for the vegetation-covered surface fraction, and the other for the inter-canopy bare soil fraction. Application of the Penman equation for the bare soil part, and the Penman-Monteith equation for the canopy part, with a resistant network for vapor and heat transfer, results in daily potential E and potential T for the surface. The model also includes Jarvis-type functions, rainfall interception, snow and snowmelt, and a site aridity correction. Coupled with near-surface hydrologic models, the TVET model successfully reproduced evaporation and transpiration partitioning measured by an isotopic study on two vegetated surfaces at the Sevilleta LTER.

The individual elements of the TVET model have been published. The uniqueness of TVET is that it couples all these components together. Besides, the model also develops new equations for some of the aerodynamic resistances, and for daily solar radiation on north-, east-, and west-facing slopes. Coupled with near-surface hydrologic modeling, the model is useful for improving understanding of ecohydrological systems, near-surface water partitioning, and vegetation impacts on hydrologic processes. The model has the potential to take spatially distributed data (e.g., vegetation coverage, DEM

topography) in order to generate spatial distributed PE and PT for large-scale hydrologic modeling.

Two major components in the TVET are topographic and vegetation coverage effects on surface energy partitioning. Some other model elements, such as rainfall interception, snow cover and snowmelt, are relatively weak. Even for the topographic effects, only the shadow due to the slope itself is considered in the model. The shade due to other hills is not included. These weak aspects of the model should be improved.

The model cannot tell the difference between east-facing and west-facing slopes if it is not fed with different temperatures. The maximum solar radiation occurs in the west-facing slope in the afternoon when the daily temperature closes to its maximum. This solar radiation and temperature relationship optimizes ET on the west-facing slope. However, this relationship does not exist for east-facing slope. Thus, there is a difference in PE and PT between east-facing slope and west-facing slope [e.g., *Burnett, 2004*]. Using daily temperatures, without considering this temporal relationship, the current TVET model cannot capture the difference between east-facing and west-facing slopes. Measurements of temperatures, relative humidity, and other variables on different aspect slopes would help address this problem, but less data-demanding approaches are needed. In the current version of TVET, mean wind speed at the canopy height is interpolated between two end-situations, and terrain-aspect effect is interpolated between four specific aspect slopes. These interpolations should be tested and improved in the future version.

For the future work, in addition to these model improvements, new applications of the TVET models are recommended. It can be used to study evaporation and transpiration partitioning of various ecosystems, to study topography-induced ecotones and their

response to climate variability and change, and to study vegetation impacts on hydrologic processes and water yield.

8.3 Hillslope water partitioning simulations

Spatially high-resolution hillslope hydrologic simulations with various degrees of temporal resolution have been conducted to understand hillslope water partitioning in semiarid environments. The uniqueness of these simulations is that the bedrock is treated as a permeable layer in the model. For the transient simulations, the model is closely coupled with surface conditions.

The major findings from the simulations are that (1) in arid and semiarid environments, the bedrock permeability threshold for significant recharge is between 1.0×10^{-15} m^2 and 1.0×10^{-14} m^2, with matrix-flow dominant bedrock having a lower threshold; (2) slope steepness affects surface runoff, but has much less influence on percolation at the soil-bedrock interface; (3) topography affects recharge mainly by modifying atmospheric conditions (precipitation and potential ET) and vegetation coverage; (4) vegetation adapts to surface conditions, and strongly impacts near-surface water partitioning; consistent with previous studies, water yield will increase shortly after the vegetation removal; (5) vegetation root associated macropores strongly affect water transmission in the near surface, especially in clay-rich soil horizons; (6) clay-rich soil lacking roots behaves as an barrier for distributed recharge; and (7) unconnected bedrock surface micro-depressions (cm scale) do not significantly improve recharge.

The simulations do not exclude the possibility of bedrock surface macro-depressions (meter scale) enhancing recharge, especially if the depressions are connected. Also, the simulations haven't tested the slope profile and curvature effects on hillslope

water partitioning. Although macropore flow and fracture flow have been included in some of the simulations, they could not exactly represent the fast flow that occurs in the field. Future work is recommended to improve the simulations by including these situations, and more appropriate conceptual models for macropore flow (e.g., dual-permeability model or discrete fracture simulation).

The hypothesis of an ecohydrologically elastic range was originated from the hydrologic simulations of two slope-induced ecosystems (Appendix XVIII), and is worth of further exploration. This hypothesis describes that within a certain range of climate conditions, vegetation interacts with soil hydrologic conditions, leading to similar soil hydrologic states. The hypothesis is complementary to Sandvig's [*2005*] field studies. Sandvig [*2005*] examined vadose zone soil water flux for four ecosystems with different vegetation covers in central New Mexico, and found that vadose zone hydrologic processes are related to vegetation types on basin floor. Because of the topographic relief in mountains, local climate conditions vary in a short distance, providing a good situation for testing the hypothesis. With the large climate gradient, mountains also provide situations for testing the climate range beyond which vegetation cannot be used as an indicator for estimating recharge. This hypothesis, if rested, is useful for predicting future climate change impacts on vegetation cover, and consequently on water resources.

With certain bedrock, soil cover, and vegetation coverage, recharge is predictable from topography-modified local climate conditions. The relationship between recharge and local climate conditions may be worth of further study, which could provide some basis for transfer of some empirical MBR equations.

8.4 Mountain-block hydrologic modeling and mountain-block recharge

Various factors, including bedrock permeability, local climate condition (modified by topography), soil-cover characteristics, and vegetation-cover characteristics, influence mountain-block recharge. The effects of these factors interact to each other; and their relative significance varies with conditions. Thus, integrated hydrologic modeling is required to simulate the whole system for estimating mountain-block recharge. Three approaches with different degrees of complexity are described for estimating mountain-block recharge. They are the fully distributed 3D mountain-block hydrologic model, the hydrotope-based distributed hydrologic model, and the simplified point-simulation-based approach.

With the simplified point-simulation-based method, it is found that total MBR of the Jemez Mountains is less than 120 mm/year, with 50% attributed to the distributed MBR. Coupled with previous studies in the surrounding mountain areas, the total MBR in the Jemez Mountains should be between 70~120 mm/year. For the Sangre de Cristo Mountains, the total MBR is less than 100 mm/year, suggesting that the previous estimate of 70 mm/year is possible. The spatial patterns of MBR are different for the two mountain blocks, with MBR limited to the high elevations in the Sangre de Cristo Mountains while diffused in the Jemez Mountains. However, it should be noted that these results were based on hydrologic simulations, in which various climate conditions were characterized with different PET/P ratio but with fixed annual P. The simulated recharge may be different from the recharge forced by actual climate conditions on the mountain, where not only annual PET/P but also annual P varies. Besides, the modified Hargreaves model for potential ET, used in the simplified method of MBR estimation, has not been

tested for mountainous terrains. Future testing with field measurement or remote sensing results is valuable.

Besides the weakness discussed above, the point-simulation-based approach in this dissertation does not yet consider the variability of soil and vegetation cover. In the future, it will be appropriate to estimate mountain-block recharge via distributed hydrologic modeling. The hydrotope-based hydrologic model considers distributed hydrologic properties of the mountain block, and lumps small variability within each hydrologically-similar response unit. Because of its distributed nature and low computational cost, the hydrotope-based distributed mountain-block hydrologic modeling is recommended for the future testing.

Since bedrock permeability and local climate are two primary controls influencing mountain-block recharge, besides integrated hydrologic modeling, future efforts should be also placed to a better characterization of mountain bedrock hydraulic properties, and a better quantification of high-resolution (both temporally and spatially) mountain precipitation.

8.5 Climate variability and its effects on mountain-block recharge

Teleconnection of mountain precipitation to ENSO and PDO cycles were examined for the mountainous region of northern New Mexico. The major findings are that (1) PDO is a more dominant factor than ENSO on winter and spring precipitation in the study area. (2) Low PDO effects, but not high PDO effects, on winter and spring precipitation are modulated by ENSO; El Niño strongly dampens, and La Niña enhances, negative anomalies of winter and spring precipitation during the low PDO years; in high PDO years, positive winter precipitation anomaly is enhanced by El Niño. (3) The PDO

and ENSO effects on winter precipitation are modified by topography. And (4) the PDO may have shifted to its low phase in later 1990s.

The simulated MBR from the simplified point-simulation-based approach suggests that the precipitation variability associated with large-scale climatic cycles can lead to 15~20% change in MBR averaged over the Jemez Mountains, and 10~15% change in MBR in Sangre de Cristo Mountains. The amount of variability was inferred from the modeled change in percolation, which may not be reflected at the groundwater table because of the system buffering effects. Nonetheless, the modeled variability sheds light on how MBR responds to climate change.

Future work is recommended to study other hydrologic responses (e.g., streamflow, snow coverage, etc.) and ecologic responses (e.g., vegetation coverage) to the climate variability and change. Besides, only precipitation variability was related to the large-scale climatic cycles in this dissertation. Temperature was assumed to be constant with climatic cycles. Future work is also recommended to study the temperature variability, as well as the potential effects of the global trend toward warming. Potential future temperature change affects potential ET, and proportion of snowfall in the total precipitation [*Earman, 2004*]. Both effects influence groundwater recharge in the mountains.

References

Burnett, B.N. (2004), Aspect and microclimatic influences on hillslope geomorphology, northeastern Arizona. Master Thesis, Earth and Planetary Sciences, University of New Mexico, Albuquerque, New Mexico.

Earman, S. (2004), Groundwater recharge and movement through mountain-basin systems of the Southwest: a case study in the Chiricahua Mountains-San Bernardino Valley system, Arizona and Sonora, Dissertation, New Mexico Institute of Mining and Technology.

Meyer, G. (2005), Personal communication, Earth and Planetary Sciences, University of New Mexico, Albuquerque, New Mexico.

Sandvig, R. (2005), Ecohydrological controls on soil-moisture fluxes in arid vadose zones, Master Thesis, Hydrology, New Mexico Institute of Mining and Technology, Socorro, New Mexico.

Appendices

This section includes reference materials and appendices for major chapters of the dissertation. The figures, tables, and equations are numbered using a format like ‘V-1’, where the capital Roman indicates the appendix number. The figures, tables, and equations of the main text of this dissertation are numbered using a format like ‘5.1’, where the first number indicates the chapter number.

Appendix I References

Adams, D.K., and A.C. Comrie (1997), The North American monsoon. *Bulletin of American Meteorological Society*, 78, 2197-2213.

Allen, C.D. (1989), Changes in the landscape of the Jemez Mountains, New Mexico, Ph.D. dissertation, Berkeley, University of California, 346p.

Allen, C.D. and D.D. Breshears (1998), Drought-induced shift of a forest-woodland ecotone: Rapid landscape response to climate variation. *Proceedings of National Academy Sciences of the United States of America*, 95, 14839-14842.

Allen, R.G. (2000), Using the FAO-56 dual crop coefficient method over an irrigated region as part of an evapotranspiration intercomparison study. *Journal of Hydrology*, 229, 27-41.

Allen, R.G., L.S. Pereira, D. Raes, and M. Smith (1998), Crop evapotranspiration – Guidelines for computing crop water requirements. *Food and Agriculture Organization of the United Nations Irrigation and drainage paper 56*.

Altman, S.J., B.W. Arnold, R.W. Barnard, G.W. Barr, C.K. Ho, S.A. McKenna, and R.R. Eaton (1996), Flow calculations for Yucca Mountain groundwater travel time (GWTT-95). SAND96-0819, Sandia National Laboratories, Albuquerque, NM.

Anderson S.P., W.E. Dietrich, D.R. Montgomery, R. Torres, M.E. Conrad, and K. Loague (1997), Subsurface flow paths in a steep unchanneled catchment. *Water Resources Research*, 12, 2637-2653.

Andrade, E.R., and W.D. Sellers (1988), El Niño and its effect on precipitation in Arizona and western New Mexico. *Journal of Climatology*, 8, 403-410.

Asli, M., and D. Marcotte (1995), Comparison of approaches to spatial estimation in a bivariate contest. *Mathematical Geology*. 27 (5), 641-658.

Bales, R.C., J. Dozier, N. P. Molotch, T. H. Painter, and R. Rice (2004), Mountain Hydrology of the Semi-Arid Western U.S., *CUAHSI Cyberseminar draft Paper*.

Barlow, M., S.Nigam, and E.H. Berbery (2001), ENSO, Pacific decadal variability, and U.S. summertime precipitation, drought, and stream flow. *Journal of Climate*, 14, 2105-2128.

Barry, R.G. (1992), Mountain climatology and past and potential future climatic changes in mountain regions. *Mountain Research and Development*, 12(1), 71-86.

Basist, A., G.D. Bell, and V. Meentemeyer (1994), Statistical relationships between topography and precipitation patterns. *Journal of Climate*, 7(9), 1305-1315.

Bear, J. (1972), *Dynamics of Fluids in Porous Media*, New York: Dover.

Beniston, M. (2003), Climate change in mountain regions: a review of possible impacts. *Climatic Change*, 59, 5-31.

Benson, L., B. Linsley, J. Smoot, S. Mensing, S. Lund, S. Stine, and A. Sama-Wojcicki (2003), Influence of the Pacific Decadal Oscillation on the climate of the Sierra Nevada, California and Nevada. *Quaternary Research*, 59, 151-159.

Beven, K. and P. Germann (1982), Macropores and water flow in soils. *Water Resources Research*, 18(5), 1311-1325.

Bhark, E.W., and E.E. Small (2003), Association between plant canopies and the spatial patterns of infiltration in shrubland and grassland of the Chihuahuan Desert, New Mexico, *Ecosystems*, 6(2), 185-196.

Bindlish, R., and A.P. Barros (2000), Disaggregation of rainfall for one-way coupling of atmospheric and hydrologic models in regions of complex terrain. *Global and Planetary Change*, 25, 111-132.

Biondi, F., A. Gershunov, and D.R. Cayan (2001), North Pacific decadal climate variability since 1661. *Journal of Climate*, 14, 5-10.

Boadu, F.K. (1997), Relating the hydraulic properties of a fractured rock mass to seismic attributes: theory and numerical experiments. *International Journal of Rock Mechanics and Mineral Science*, 34, 885-895.

Bosch, J.M., and J.D.Hewlett (1982), A review of catchment experiments to determine the effect of vegetation changes on water yield and evapotranspiration. *Journal of Hydrology*, 55, 3-23.

Bosilovich, M.G., Y.C. Sud, S.D. Schubert, and G.K. Walker (2003), Numerical simulation of the large-scale North American monsoon water sources. *Journal of Geophysical Research-Atmosphere*, 108, no.D16, 8614.

Boulanger, J.R. (2004), Stable isotope partitioning of evapotranspiration across a shrub-grass ecotone following a precipitation event, Sevilleta National Wildlife Refuge, USA, Master Thesis, New Mexico Institute of Mining and Technology.

Brandes, D., and B.P. Wilcox (2000), Evapotranspiration and soil moisture dynamics on a semiarid ponderosa pine hillslope, *Journal of the American Water Resources Association*, 36(5), 965-974.

Burnett, B.N. (2004), Aspect and microclimatic influences on hillslope geomorphology, northeastern Arizona. Master Thesis, University of New Mexico.

Burns, D.A., R.P. Hooper, J.J. McDonnell, J.E. Freer, C. Kendall, and K. Beven (1998), Base cation concentrations in subsurface flow from a forested hillslope: The role of flushing frequency. *Water Resources Research*, 34(12), 3535-3544

Caine, J.S., and S.R.A. Tomusiak (2003), Brittle structures and their role in controlling porosity and permeability in a complex Precambrian crystalline-rock aquifer system in the Colorado Rocky Mountain Front Range. *GSA Bulletin*, 115(11), 1410-1424.

Carleton, A.M. (1986), Synoptic-dynamic character of ‘bursts’ and ‘breaks’ in the south-west U.S. summer precipitation singularity. *Journal of Climatology*, 6, 605-623.

Carsel R.F., and R.S. Parrish (1988), Developing joint probability distributions of soil water retention characteristics. *Water Resources Research*, 24, 755-769.

Castro, C.L., T.B. McKee, and R.A. Pielke Sr. (2001), The relationship of the north American monsoon to tropical and north Pacific sea surface temperatures as revealed by observational analyses. *Journal of Climate*, 14(24), 4449-4473.

Chaplot, V., and C. Walter (2003), Subsurface topography to enhance the prediction of the spatial distribution of soil wetness. *Hydrological Processes*, 17, 2567-2580.

Choudhury, B.J. and J.L. Monteith (1988), A four-layer model for the heat budget of homogeneous land surfaces. *Quarterly Journal of the Royal Meteorological Society*, 114, 373-398.

Cleverly, J.R., C.N. Dahm, J.R. Thibault, D.J. Gilroy, and J.E.A. Coonrod (2002), Seasonal estimates of actual evapo-transpiration from *Tamarix ramosissima* stands using three-dimensional eddy covariance. *Journal of Arid Environments*, 52, 181-197.

Climate Impacts Group (2005), About the Pacific Decadal Oscillation http://www.cses.washington.edu/cig/pnwc/aboutpdo.shtml, visited in 2005.

Crave, A., and C. Gascuel-Odoux (1997), The influence of topography on time and space distribution of soil surface water content. *Hydrological Processes*, 11, 203-210.

Cruiziat, P., H. Cochard, and T. Ameglio (2002), Hydraulic architecture of trees: main concepts and results. *Annals of Forest Science*, 59(7), 723-752.

Daly, C., R.P. Neilson, and D.L. Phillips (1994), A statistical-topographic model for mapping climatological precipitation over mountain terrain. *Journal of Applied Meteorology*, 33, 140-158.

Daly, C., W. P. Gibson, G.H. Taylor, G. L. Johnson, and P. Pasteris (2002), A knowledge-based approach to the statistical mapping of climate. *Climate Research*, 22, 99-113.

Davenport, D.W., B.P. Wilcox, and D. D. Breshears (1999), Soil morphology of canopy and intercanopy sites in a piñon-juniper woodland. *Soil Science Society of America Journal*, 60(6), 1881-1887.

Dettinger, M., K. Redmond, and D. Cayan (2004), Winter orographic precipitation ratios in the Sierra Nevada--larger-scale atmospheric circulations and hydrologic consequences. *Journal of Hydrometeorology*, *5*, 1102-1116.

Deutsch, C.V., and A.G. Journel (1998), *GSLIB—Geostatistical Software Library and User's Guide*, Oxford University Press, 2nd edition, 369 p.

Dingman, S. L. (1994), *Physical Hydrology*, Prentice-Hall, Inc. 575p.

Drogue, G., J. Humbert, J. Deraisme, N. Mahr, and N. Freslon (2002), A statistical-topographic model using an omnidirectional parameterization of the relief for mapping orographic rainfall. *International Journal of Climatology*, 22(5), 599-613.

Droogers, P. and G. Allen (2002), Estimating reference evapotranspiration under inaccurate data conditions. *Irr. Drain. Sys., 16,* 33-45.

Duffie, J.A., and W.A. Beckman (1991), *Solar engineering of thermal processes*, New York, Wiley, 2nd edition, 919p.

Duffy, C.J. (2004), A semi-discrete dynamical model for mountain-front recharge and water balance estimation: The Rio Grande, *Eos Trans*. AGU, 85(17), Jt. Assem. Suppl., Abstract H42B-06.

Dugas, W.A., R.A. Hicks, and P. Wright (1998), Effect of removal of *Juniperus ashei* on evapotranspiration and runoff in the Seco Creek watershed. *Water Resources Research*, 34(6), 1499-1506.

Dunkerley, D. (2000), Hydorlogic effects of dryland shrubs: defining the spatial extent of modified soil water uptake rates at an Australian desert site. *Journal of Arid Environment*, 45, 159-172.

Durner W. (1994), Hydraulic conductivity estimation for soils with heterogeneous pore structure. *Water Resources Research*, 30, 211-223.

Eagleson, P.S. (2002), *Ecohydrology: Darwinian expression of vegetation form and function*, Cambridge University Press.

Earman, S. (2004), Groundwater recharge and movement through mountain-basin systems of the Southwest: a case study in the Chiricahua Mountains-San Bernardino Valley system, Arizona and Sonora, Dissertation, New Mexico Institute of Mining and Technology, Socorro, New Mexico.

EDAC (Earth Data Analysis Center) (1996), 60 meter elevation grid image for the state of New Mexico, Albuquerque, NM.

Englehart, P.J., and A.V. Douglas (2001), The role of eastern North Pacific tropic storms in the rainfall climatology of western Mexico. *International Journal of Climatology*, 21, 1357-1370.

Fayer, M.J., G.W. Gee, M.L. Rockhold, M.D. Freshley, and T.B. Walters (1996), Estimating recharge rates for a groundwater model using a GIS, *Journal of Environmental Quality*, 25, 510-518.

Fawcett, P.J., J.R. Stalker, and D.S. Gutzler (2002), Multistage moisture transport into the interior of northern Mexico during the North American summer monsoon. *Geophysical Research Letters*, 29(23), 2094, doi:10.1029/2002GL015693.

Feddes, R., P.J. Kowalik, and H. Zaradny (1978), *Simulation of Field Water Use and Crop Yield*, John Wiley & Sons, New York, NY.

Flint, A.L., L.E. Flint, J.A. Hevesi, and J.M. Blainey (2004), Fundamental concepts of recharge in the Desert Southwest: a regional modeling perspective, in *Groundwater Recharge in a Desert Environment: The Southwestern United States,* edited by J.F. Hogan, F.M. Phillips, and B.R. Scanlon, Water Science and Applications Series, vol. 9, American Geophysical Union, Washington, D.C., 159-184.

Freckman, D.W., and R.A. Virginia (1989), Plant-feeding nematodes in deep-rooting desert ecosystems. *Ecology*, 70(6), 1665-1678.

Freer, J., J.J. McDonnell, K.J. Beven, N.E. Peters, D.A. Burns, R.P. Hooper, B.Aulenbach, and C. Kendall (2002), The role of bedrock topography on subsurface storm flow. *Water Resources Research*, 38(12), 1269, doi: 10.1029/2001WR000872.

Freer, J., J. McDonnell, K.J. Beven, D. Brammer, D. Burns, R.P. Hooper, and C. Kendal, (1997), Topographic controls on subsurface storm flow at the hillslope scale for two hydrologically distinct small catchments. *Hydrological Process*, 11, 347-1352.

Gee, G.W., P.J. Wierenga, B.J. Andraski, M.H. Young, M.J. Fayer, and M.L. Rockhold (1994), Variations in water balance and recharge potential at three western desert sites. *Soil Science Society of America Journal*, 58, 63-72.

Gershunov, A., and T.P. Barnett (1998), Interdecadal modulation of ENSO teleconnections. *Bulletin of the American Meteorological Society*, 79, 2715-2725.

Gimmi T., M. Schneebeli, H. Fluhler, H. Wydler, and T. Baer (1997), Field-scale water transport in unsaturated crystalline rock. *Water Resources Research*, 33, 589-598.

Gomez-Plaza, A, M. Martinez-Mena, J. Albaladejo, and V.M. Castillo (2001), Factors regulating spatial distribution of soil water content in small semiarid catchments. *Journal of Hydrology*, 253, 211-226.

Goodrich, D.C., J. Faures, D.A. Woolhiser, L.J. Lane, and S. Sorooshian (1995), Measurement and analysis of small-scale convective storm rainfall variability. *Journal of Hydrology*, 173, 283-308.

Goodrich, G.B. (2004), Influence of the Pacific decadal oscillation on Arizona winter precipitation during years of neutral ENSO. *Weather and Forecasting*, *19*, 950-953.

Goovaerts, P. (2000), Geostatistical approaches for incorporating elevation into the spatial interpolation of rainfall. *Journal of Hydrology*, 228, 113-129.

Grayson, R.B., A.W. Western, and F.H. Chiew (1997), Preferred states in spatial soil moisture patterns: local and nonlocal controls. *Water Resource Research*, 33, 2897-2908.

Guan, H., J.L. Wilson, and O. Makhnin (2005), Geostatistical Mapping of Mountain Precipitation Incorporating Auto-searched Effects of Terrain and Climatic Characteristics. *Journal of Hydrometeorology* (in press).

Gurtz, J., A. Baltersweiler, and H.Lang (1999), Spatially distributed hydrotope-based modeling of evapotranspiration and runoff in mountainous basins. *Hydrological Processes*, 13(17), 2751-2768.

Guswa, A. J., M. A. Celia, and I. Rodriquez-Iturbe, 2002. Models of soil moisture dynamics in ecohydrology: a comparative study, *Wat. Resour. Res., 38*, 1-15.

Guttman, N.B., and R.G. Quayle (1996), A historical perspective of U.S. climate divisions. *Bulletin of the American Meteorological Society*, *77*, 293-304.

Gutzler, D.S. (2000), Covariability of spring snowpack and summer rainfall across the southwest United States. *Journal of Climate*, *13*, 4018-4027.

Gutzler, D.S., D.M. Kann, and C. Thornbrugh (2002), Modulation of ENSO-based long-lead outlooks of southwestern U.S. winter precipitation by the pacific decadal oscillation. *Weather and Forecasting*, 17, 1163-1172.

Hargreave, G.H., F.ASCE, and R.G. Allen (2003), History and evaluation of Hargreaves evapotranspiration equation. *Journal of Irrigation and Drainage Engineering*, 129(1), 53-63.

Hargreaves, G.L., G.H. Hargreaves, and J.P. Riley (1985a), Irrigation water requirements for Senegal River Basin. *Journal of Irrigation and Drainage Engineering*, 111(3), 265-275.

Hargreaves, G.H., and Z.A. Samani (1985b), Reference crop evapotranspiration from temperature. *Applied Engineering in Agriculture*, 1(2),96-99.

Hawke, R.M., and J.A. McConchie (2003), Variability of in situ moisture measurements and implications for modeling hillslope processes. *Environmental and Engineering Geoscience*, 9, 213-223.

Hendrickx, J.M.H., and M. Flury (2001), Uniform and preferential flow mechanisms in the vadose zone. *Conceptual Models of Flow and Transport in Fractured Vadose Zone*, National Academy Press, Washington D.C., 149-187.

Hevesi, J.A., J.D. Istok, and A.L. Flint (1992), Precipitation estimation in mountain terrain using multivariate geostatistics, Part I: structure analysis. *Journal of Applied Meteorology*, 31(7), 661-676.

Hidalgo, H.G., and J. A. Dracup (2003), ENSO and PDO Effects on Hydroclimatic Variations of the Upper Colorado River Basin. *Journal of Hydrometeorology*, 4(1), 5-23.

Hidalgo, H.G. (2004), Climate precursors of multidecadal drought variability in the western United States. *Water Resources Research*, 40, p.W12504.

Higgins, R.W., A. Leetmaa, Y. Xue, and A. Barnston (2000), Dominant factors influencing the seasonal predictability of U.S. precipitation and surface temperature. *Journal of Climate*, 13, 3994-4017.

Higgins, R.W., K.C. Mo, and S.D. Schubert (1996), The moisture budget of the central United States in spring as evaluated in the NCEP/NCAR and the NASA/DAO re-analyses. *Monthly Weather Review*, 124(5), 939-963.

Higgins, R.W., Y. Yao, E.S. Yarosh, J.E. Janowiak, and K.C. Mo (1997), Influence of the Great Plains low-level jet on summertime precipitation and moisture transport over the central United States. *Journal of Climate*, 10, 481-507.

Hoerling, M., and A. Kumar (2003), The perfect ocean for drought. *Science*, *299*, 691-694.

Hollinger, D.Y., F.M. Kelliher, E.D., Schulze, and B.M.M. Köstner (1994), Coupling of tree transpiration to atmospheric turbulence. *Nature*, 371, 60-62.

Huntley, D. (1979), Groundwater recharge to the aquifers of northern San Luis Valley, Colorado. *Geological Society of America Bulletin*, Part II, 90(8), 1196-1281.

Hutchinson, P. (1973), The interaction of relief and synoptic situation on the distribution of storm rainfall in the vicinity of Dunedin. *New Zealand Geography*, 29, 31-44.

Jarvis, P.G. (1976), Interpretation of variations in leaf water potential and stomatal conductance found in canopies in field. *Philosophical Transactions of the Royal Society of London Series B-Biological Sciences*, 273, 593-610.

Jensen, D.T., G.H. Hargreaves, B. Temesgen, and R.G. Allen (1997), Computation of ET0 under nonideal conditions. *Journal of Irrigation and Drainage Engineering*, 394-400.

Jeton, A.E., and J.L. Smith (1993), Development of watershed models for two Sierra Nevada basins using a geographic information system. *Water Resources Bulletin*, American Water Resources Association, 29(6), 923-932.

Kapos, V., J. Rhind, M. Edwards, C. Ravilious, and M. Price (2000), Developing a map for the world's mountain forests, in Price, M.F., and Butt, N. (eds.) *Forests in a Sustainable Mountain Environment*, CAB International, Wallingford.

Kearns, A., and J.M.H. Hendrickx (1998), Temporal variability of diffuse groundwater recharge in New Mexico, New Mexico Water Resources Research Institute, Report 309, New Mexico State University, Las Cruse.

Kiladis,G.N., and H.F. Diaz (1989), Global climate anomalies associated with extremes of the Southern Oscillation. *Journal of Climate*, 2, 1069-1090.

Kirkby, M. (1988), Hillslope runoff processes and models. *Journal of Hydrology*, 100, 315-339.

Kite, G.W., and P. Droogers, (2000), Comparing evapotranspiration estimates from satellites, hydrological models and field data. *Journal of Hydrology*, 229, 3-18.

Kunkel, K. E., and J.R. Angel (1999), Relationship of ENSO to snowfall and related cyclone activity in the contiguous United States. *Journal of Geophysical Research-Atmospheres*, *104*(D16), 19425-19434.

Kurc, S.A., and E.E. Small (2004), Dynamics of evapotranspiration in semiarid grassland and shrubland ecosystems during the summer monsoon season, central New Mexico. *Water Resources Research*, 40, W09305, doi: 10.1029/2004WR003068.

Kustas, W.P., and J.M. Norman (1997), A two-source approach for estimating turbulent fluxes using multiple angel thermal infrared observations. *Water Resources Research*, 33, 1495-1508.

Kyriakidis, P. C., J. Kim, and N.L. Miller (2001), Geostatistical Mapping of Precipitation from Rain Gauge Data Using Atmospheric and Terrain Characteristics. *Journal of Applied Meteorology*, 40, 1855-1877.

Latif, M., and T.P. Barnett (1994), Causes of decadal climate variability over the North Pacific and North America. *Science*, 266, 634-637.

Latif, M., and T.P. Barnett (1996), Decadal climate variability over the North Pacific and North America: Dynamics and predictability. *Journal of Climate*, 9, 2407-2423.

Lhomme, J. P., and A. Chehbouni (1999), Comments on dual-source vegetation-atmospheric transfer models. *Agriculture and Forest Meteorology*, 94, 269-273.

Lhomme, J.P., Elguero, E., Chehbouni, A., and Boulet, G. (1998), Stomatal control of transpiration: Examination of Monteith's formulation of canopy resistance. *Water Resources Research*, 34, 2301-2308.

Liles, C. (2000), Relationships between the Pacific decadal oscillation and New Mexico annual and seasonal precipitation. *Proceeding of Second Southwest Weather Symposium, Tucson, AZ, NWS-University of Arizona* – COMET, 7p.

Lissey A. (1968), Surficial mapping of groundwater flow systems with application to the Oak river Basin, Manitoba. Ph.D. thesis, University of Saskatchewan, 141p.

Liu, B.Y.H., and R.C. Jordan (1962), Daily insolation on surfaces tilted toward the equator. *ASHRAE Journal*, 3, 53.

Liu, E., J.A. Hudson, and T. Pointer (2000), Equivalent medium representation of fractured rock. *Journal of Geophysical Research*, 105, 2981-3000.

Long, J.C.S., and P.A. Witherspoon (1985), The relationship of the degree of interconnection to permeability in fracture networks. *Journal of Geophysical Research*, 90, 3087-3098.

Luckman, B., and T. Kavanagh (2002), Impact of climate fluctuations on mountain environments in the Canadian Rockies. *AMBIO*, 29, 371-380.

Manning, A.H. (2002), Using noble gas tracer to investigate mountain-block recharge to an intermountain basin, Dissertation, University of Utah.

Mantua, N.J. and S.R. Hare, Y. Zhang, J.M. Wallace, and R.C. Francis (1997), A Pacific interdecadal climate oscillation with impacts on salmon production. *Bulletin of the American Meteorological Society*, 78, 1069-1079.

Mast, J.N., T.T. Veblen, and Y.B. Linhart (1998), Disturbance and climatic influences on age structure of ponderosa pine at the pine/grass ecotone, Colorado Front Range. *Journal of Biogeography*, 25(4), 743-755.

Maurer, D.K., and D. L. Berger (1997), Subsurface flow and water yield from watersheds tributary to Eagle Valley hydrographic area, west-central Nevada. *U.S. Geological Survey Water-Resources Investigation Report 97-4191*.

Maxey, G.B., and T.E. Eakin (1949), Ground water in White river valley, White Pine, Nye, and Lincoln Counties, Nevada. *Nevada Department of conservation and Natural Resources Water Resources Bulletin, no. 8*, 59p.

McAda, D.P., and M. Wasiolek (1988), Simulation of the regional geohydrology of the Tesuque aquifer system near Santa Fe, New Mexico. *U.S. Geological Survey Water-Resources Investigations Report 87-4056*, 71p.

McDonnell, JJ. (1997), Comment on "The changing spatial variability of subsurface flow across a hillside" by Ross Woods ad Lindsay Rowe. *Journal of Hydrology* (NZ) 36, 97-100.

McGlynn, B.L., J.J. McDonnel, and D.D. Brammer (2002), A review of the evolving perceptual model of hillslope flowpaths at the Maimai catchments, New Zealand. *Journal of Hydrology*, 257, 1-26.

McMahon, D.R. (1998), Soil, landscape and vegetation interactions in a small semi-arid drainage basin: Sevilleta National Wildlife Refuge, New Mexico, Master Thesis, New Mexico Institute of Mining and Technology.

Meybeck, M., P. Green, and C. Vörösmart (2001), A new typology for mountains and other relief classes: an application to global continental water resources and population distribution. *Mount. Res. Dev.*, 21, 34-45.

Meyer, G. (2005), Personal communication, University of New Mexico, Albuquerque, New Mexico.

Michaud, J.D., B.A. Avine, and O.C. Penalba (1995), Spatial and elevational variations of summer rainfall in the southwestern United States. *Journal of Applied Meteorology*, 34, 2689-1703.

Mo, X., S. Liu, Z. Lin, and W. Zhao (2004), Simulating temporal and spatial variation of evapotranspiration over the Lushi basin. *Journal of Hydrology*, 285, 125-142.

Mock, C.J. (1996), Climatic controls and spatial variations of precipitation in the western United States. *Journal of Climate*, 9(5), 1111-1125.

Monteith, J.L. (1965), Evaporation and environment, in *The State and Movement of Water in Living Organisms*, Sympos. Soc. Exper. Biol. 19, edited by G.E. Fogg, 205-234, Academic, San Diego, California, U.S.A.

Montgomery D.R., W.E. Dietrich, R. Torres, A.P. Anderson, J.T. Heffner, K. Loague (1997), Hydrologic response of a steep, unchanneled valley to natural and applied rainfall. *Water Resources Research*, 33, 91-109.

Moore, D. (2004), Meteorology Data for the Sevilleta National Wildlife Refuge, NM (1987-2003). Sevilleta Long Term Ecological Research Project Database. http://sev.lternet.edu [July 22nd, 2004].

Mualem Y. (1976), A new model for predicting the hydraulic conductivity of unsaturated porous media. *Water Resources Research*, 12, 513-522.

National Research Council (2001), *Conceptual models of flow and transport in the fractured vadose zone*. Washington, DC: National Academy Press.

Newman, B.D. (2003), personal communication. Los Alamos National Laboratory, New Mexico.

Newman, B.D., A. R. Campbell, and B.P. Wilcox (1997), Tracer-based studies of soil water movement in semi-arid forests of New Mexico. *Journal of Hydrology*, 196, 251-270.

Newman, B.D, A.R. Campbell, and B.P. Wilcox (1998), Lateral subsurface flow pathways in a semiarid ponderosa pine hillslope. *Water Resources Research*, 34 (12), 3485-3496.

Newman, B.D., B.P. Wilcox, and R.C. Graham (2004), Snowmelt-driven macropore flow and soil saturation in a semiarid forest. *Hydrological Processes*, 18, 1035-1042.

Newman, B.D., B.P. Wilcox, S. Archer, D.D. Breshears, C.N. Dahm, C.J. Duffy, N.G. McDowell, F.M. Phillips, B. Scanlon (2004), The ecohydrology of arid and semiarid environments: A scientific vision, *CUAHSI Cyberseminar Draft Paper*, Oct. 21, 2004.

NOAA (2004), Special feature: the North American Monsoon system, http://www.srh.noaa.gov/abq/climate/Monthlyreports/July/nams.html, visited August, 2004.

Noguchi, S., Y. Tsuboyama, R.C. Sidel, and I. Hosoda, (1999), Morphological characteristics of macropores and the distribution of preferential flow pathways in a forested slope segment. *Soil Science Society of America Journal*, 63, 1413-1423.

Noguchi, S., Y. Tsuboyama, R.C. Sidle, and I. Hosada (2001), Subsurface runoff characteristics from a forest hillslope soil profile including macropores, Hitachi Ohta, Japan. *Hydrological Processes*, 15, 2131-2149.

Odling, N.E. (2001), The scaling of hydraulic conductivity in rock fracture zones. *Geophysical Research Letters*, 28, 3019-3022.

Oki, T., K. Musiake, and T. Koike (1991), Spatial rainfall distribution at a storm event in mountainous regions, estimated by orography and wind direction. *Water Resources Research*, 27(3), 359-369.

Onda Y., Y. Komatsu, M. Tsujimura, and J. Fujihara (2001), The role of subsurface runoff through bedrock on storm flow generation. *Hydrological Processes*, 15, 1693-1706.

Pan, L.H. et al. (2005), Lawrence Berkerly National Laboratory Internal Review Report (unpublished).

Parsons, A.J., A.D. Abrahams, and J.R. Simanton (1992), Microtopography and soil-surface materials on semi-arid piedmont hillslopes, southern Arizona. *Journal of Arid Environment,* 22, 107-115.

Patric J. H. (1961), The San Dimas large lysimeters. *Journal of Soil and Water Conservation*, 16(1), 13-17.

Penman, H.L. (1948), Natural evaporation from open water, bare soil, and grass. *Proceeding of Royal Society London*, Ser. A., 193, 120-146.

Petch RA. (1988), Soil saturation patterns in steep, convergent hillslopes under forest and pasture vegetation. *Hydrological Processes*, 2, 93-103.

Phillips, D.L., J. Dolph, and D. Marks (1992), A comparison of geostatistical procedures for spatial analysis of precipitation in mountainous terrain. *Agricultural and Forest Meteorology*, 58, 119-141.

Phillips, F.M., J.F. Hogan, and B.R. Scanlon (2004), Introduction and Overview, in *Groundwater Recharge in a Desert Environment: The Southwestern United States*, edited by J.F. Hogan, F.M. Phillips, and B.R. Scanlon, Water Science and Applications Series, vol. 9, American Geophysical Union, Washington, D.C., 1-14.

Phillips, F.M., M.A. Walvoord, and E.E. Small (2004), Effects of environmental change on groundwater recharge in the Desert Southwest, in *Groundwater Recharge in a Desert Environment: The Southwestern United States*, edited by J.F. Hogan, F.M. Phillips, and B.R. Scanlon, Water Science and Applications Series, vol. 9, American Geophysical Union, Washington, D.C., 273-294.

Pili, E., F. Perrier, and P. Richon (2004), Dual porosity mechanism for transient groundwater and gas anomalies induced by external forcing, *Earth and Planetary Science Letters*, 277, 473-480.

Pneuli, D., and C. Gutfinger (1992), *Fluid Mechanics*, Cambridge University Press, 496p.

Pockman, W.T., and J. S. Sperry (2000), Vulnerbility to xylem cavitation and the distribution of Sonoran Desert vegetation. *American Journal of Botany*, 87(9), 1287-1299.

Priestley, C.H.B., and R.J. Taylor (1972), On the assessment of surface heat flux and evaporation using large-scale parameters. *Monthly Weather Review*, 100, 81-92

Puigdefabregas J, G.D. Barrio, M.M. Boer, L. Gutiérrez, A. Solé (1998), Differential responses of hillslope and channel elements to rainfall events in a semi-arid area. *Geomorphology*, 23, 337-351.

Qiu, Y., B.J. Fu, J. Wang, and L.D. Chen (2001), Spatial variability of soil moisture content and its relation to environmental indices in a semi-arid gully catchment of the Loess Plateau, China. *Journal of Arid Environments*, 49(4), 723-750.

Rasmusson, E.M., and J.M. Wallace (1983), Meteorological aspects of the El Nino/Southern Oscillation. *Science*, 222(4629), 1195-1202.

Redmond, K.T., and R.W., Koch (1991), Surface climate and stream flow variability in the western United States and their relationship to large-scale circulation indices. *Water Resource Research*, 27, 2381-2399.

Ridolfi, L., P. D'Odorico, A. Porporato, and I. Rodriguez-Iturbe (2003), Stochastic soil moisture dynamics along a hillslope. *Journal of Hydrology*, 272, 264-275.

Rodriguez_Iturbe, I., A. Porporato, L.Ridolfi, V.Isham, and D.R. Cox (1999), Probabilistic modeling of water balance at a point: The role of climate, soil, and vegetation. *Proceedings of Royal Society of London*, Series A, 455, 3789-3805.

Ropelewski,C.F., and M.S. Halpert (1986), North American precipitation and temperature patterns associated with the El Niño-Southern Oscillation (ENSO). *Monthly Weather Review*, 114, 2352-2362.

Ropelewski,C.F., and M.S. Halpert (1987), Global and regional scale precipitation patterns associated with the El Niño-Southern Oscillation. *Monthly Weather Review*, 115, 1606-1626.

SAHRA (2004), SAHRA Strategic Plan, unpublished document.

Sandvig, R. (2005), Ecohydrological controls on soil-moisture fluxes in arid vadose zones, Master Thesis, New Mexico Institute of Mining and Technology, Socorro, New Mexico

Sellers, W.D., and R.H. Hill (1974), *Arizona Climate 1931-1972*, 2nd edition, University of Arizona Press, Tucson, AZ, 616 p.

Sheppard, P.R., A.C. Comrie, G.D. Packin, K. Angersbach, and J.K. Hughes (2002), The climate of the US Southwest. *Climate Research*, 21, 219-238.

Shimojima E., T. Tanaka, R. Yoshioka, Y. Hoso (1993), Seepage into a mountain tunnel and rain infiltration. *Journal of Hydrology*, 147, 121-151.

Shuttleworth, W.J. (1993), Evaporation, in Maidment, D.R. (edit): *Handbook of Hydrology*, chapter 4, New York: McGraw-Hill.

Shuttleworth, W.J., and J.S. Wallace (1985), Evaporation from sparse crops-an energy combination theory. *Quarterly Journal of Royal Meteorological Society*, 111, 839-855.

Simpson, H.J., and D.C. Colodner (1999), Arizona precipitation response to the Southern Oscillation: A potential water management tool, *Water Resource Research*, *35*, 3761-3769.

Šimůnek, J., M. Sejna, and M. Th. Van Genuchten (1998),The HYDRUS-1D software package for simulating the one-dimensional movement of water, heat, and multiple solutes in variably saturated media. Version 2.0, IGWMC-TPS-70, Interational Ground Water Modeling Software, International Ground Water Modeling Center, Golden, CO.

Šimůnek, J., M. Sejna, and M.Th. van Genuchten (1999), The HYDRUS-2D software package for simulating two-dimensional movement of water, heat, and multiple solute in variably saturated media. Version 2.0, IGWMC-TPS-53, International Ground water Modeling Center, Colorado School of Mines, Golden, Colorado, 251p.

Šimůnek, J., N.J., Jarvis, M.Th. van Genuchten, and A. Gardenas (2003), Review and comparison of models for describing non-equilibriium and preferential flow and transport in the vadose zone. *Journal of Hydrology*, 272, 14-35.

Small, E.E. (2005), Climatic controls on diffuse groundwater recharge in semiarid environments of the southwestern United States. *Water Resources Research*, 41 (4), W04012, doi:10.1029/2004WR003193.

Snow, D.T. (1969), Anisotropic permeability of fractured media. *Water Resources Research*, 5, 1273-1289.

Snow, D.T. (1979), Packer injection test data from istes on fractured rock, LBL (Lawrence Berkeley Laboratory, Energy and Environment Division) Rpt. No. 10080 (197911), 15p.

Sotillo, M.G., C. Ramis, R. Romero, S. Alonso, and V. Homar (2003), Role of orography in the spatial distribution of precipitation over the Spanish Mediterranean zone. *Climate Research*, 23(3), 247-261.

Spatial Climate Analysis Service, Oregon State University (2003), Parameter-elevation Regressions on Independent Slopes Model (PRISM), Corvallis, OR, USA.

Stannard, D.I. (1993), Comparison of Penman-Monteith, Shuttleworth-Wallace, and modified Priestley-Taylor evapotranspiration models for wildland vegetation in semiarid rangeland. *Water Resources Research*, 29(5), 1379-1392.

Stewart, J.B. (1988), Modeling surface conductance of pine forest. *Agric. For. Meteorol.*, 43, 19-37.

Stewart, R.B., and W.R. Rouse (1976), A simple equation for determining the evaporation from shallow lakes and ponds. *Water Resources Research*, 12, 623-628.

Sturman, A., and H. Wanner (2001), A comparative review of the weather and climate of the Southern Alps of New Zealand and the Europe Alps. *Mountain Research and Development*, 21(4), 359-369.

Temesgen, B., R.G. Allen, and D.T. Jensen (1999), Adjusting temperature parameters to reflect well-watered conditions. *Journal of Irrigation and Drainage Engineering*, 125(1), 26-33.

Tierney, G.D., and T.S. Foxx (1987), Root lengths of plants on Los Alamos National Laboratory Lands, LANL report, LA-10865-MS, 59p.

Uchida, T, Y. Asano, T. Mizuyama, and J.J. McDonnell (2004), Role of upslope soil pore pressure on lateral subsurface storm flow dynamics. *Water Resources Research,* 40(12), p.W12401.

Van Auken, O.W. (2000), Shrub invasions of North American semiarid grasslands. A*nnual Review of Ecology and Systematics*, 31, 197-215.

van Genuchten, M. Th. (1980), A closed-form equation for predicting the hydraulic conductivity of unsaturated soils. *Soil Science Society of America Journal*, 44, 892-898.

van Genuchten, M. Th. (1987), A numerical model for water and solute movement in and below the root zone. Research Report No 121, U.S. Salinity laboratory, USDA, ARS, Riverside, California.

Viviroli, D., R. Weingartner, and B. Messerli (2003), Assessing the hydrological significance or the world's mountains. *Mountain Research and Development*, 23, 32-40.

Walvoord, M., F.M. Phillips, S.W. Tyler, and P.C. Hartsough (2002), Deep arid system hydrodynamics, Part 2: Application to paleohydrologic reconstruction using vados-zone profiles from the northern Mojave Desert. *Water Resources Research*, 38, 1291, doi: 10/1029/2001WR000925.

Walvoord, M.A., and B.R. Scanlon (2004), Hydrologic processes in deep vadose zones in interdrainage arid environments, in *Groundwater Recharge in a Desert Environment: The Southwestern United States*, edited by J.F. Hogan, F.M. Phillips, and B.R. Scanlon, Water Science and Applications Series, vol. 9, American Geophysical Union, Washington, D.C., 15-28.

Wasiolek, M. (1995), Subsurface recharge to the Tesuque aquifer system from selected drainage basins along the western side of the Sangre de Cristo Mountains near Santa Fe, New Mexico. U.S. Geological Survey Water-Resources Investigations Report 94-4072.

Western, A.W., R.B. Grayson, G. Bloschl, G.R. Willgoose, and T.A. McMahon (1999), Observed spatial organization of soil moisture and its relation to terrain indices. *Water Resource Research*, 35(3), 797-810.

Wigmosta, M.S., L.W. Vail, and D.P. Lettenmaier (1994), A distributed hydrology-vegetation model for complex terrain. *Water Resources Research*, 30, 1665-1679.

Wilcox, B.P., B.D. Newman, D.Brrande, D.W. Davenport, and K. Reid (1997), Runoff from a semiarid ponderosa pine hillslope in New Mexico. *Water Resources Research*, 33(10), 2301-2314.

Wilcox, B.P., D. D., Breshears, and H.J. Turin (2003), Hydraulic conductivity in a pinyon-juniper woodland: influence of vegetation. *Soil Science Society of America Journal*, 67, 1243-1249.

Wilcox, B.P., M.K. Owens, R.W. Knight, and R.K. Lyons (2005), Do woody plants affect streamflow on semiarid karst rangelands? *Ecological Applications*, 15(1), 127-136.

Wilson C.J., and W.E. Dietrich (1987), The contribution of bedrock groundwater flow to strom runoff and high pore pressure development in hollows. *IAHS Publication*, 165, 49-59.

Wilson, J.E., (2004), Characteristics of faults in nonwelded ignimbrites from the Pajarito Plateau and implications for fluid flow, Ph.D. Dissertation, New Mexico Institute of Mining and Technology.

Wilson, J.L., and H. Guan (2004), Mountain-block hydrology and mountain-front recharge, in *Groundwater Recharge in a Desert Environment: The Southwestern United States*, edited by J.F. Hogan, F.M. Phillips, and B.R. Scanlon, Water Science and Applications Series, vol. 9, American Geophysical Union, Washington, D.C., 113-137.

Winter, T.C., D.O. Rosenberry, and A.M. Sturrock (1995), Evaluation of 11 equations for determining evaporation for a small lake in the north central United States. *Water Resources Research*, 31(4), 983-993.

Winter, C.L., and D.M. Tartakovsky (2001), Theoretical foundation for conductivity scaling. *Geophysical Research Letters*, 22, 4367-4369.

Witherspoon, P.A., J.S.Y. Wang, K. Iwai, and J.E. Gale (1980), Validity of cubic law for fluid flow in a deformable rock fracture. *Water Resources Research*, 16, 1016-1024.

Woodhouse, C.A., and D.M. Meko (1997), Number of winter precipitation days reconstructed from Southwestern tree rings. *Journal of Climate*, 10, 2663-2669.

Yeakley J.A., W.T. Swank, L.W. Swift, G.M. Hornberger, H.H. Shugart (1998), Soil moisture gradients and controls on a southern Appalachian hillslope from drought through recharge. *Hydrology and Earth System Sciences*, 2, 41-49.

Young, C. B., C.D. Peters-Lidard, A. Kruger, M.L. Baeck, B. R. Nelson, A.A. Bradley, and J.A. Smith (1999), An evaluation of NEXRAD precipitation estimates in complex terrain. *Journal of Geophysical Research*, 104 (D16), 19691-19703.

Zhang, Y., J.M. Wallace, and D.S. Battisti (1997), ENSO-like interdecadal variability: 1900-93. *Journal of Climate*, 10, 1004-1020.

Appendix II ASOADeK regression de-trended precipitation residual semivariogram models

The experimental omni-directional semivariograms of monthly ASOADeK regression-detrended precipitation residuals were calculated by GSLIB routine "gamv". Three semivariogram models, Spherical, Exponential, and Gaussian, were parameterized to fit the experimental semivariograms. The exponential model best fit the experimental variograms for all twelve months. The results are shown in Figure II-1. The fit parameters are included in Table II-1.

Table II-1 Fit semivariogram models and parameterization of 12 monthly precipitation residuals

Month	Model*	Nugget (mm^2)	Sill (mm^2)	Range (m)
1	2	0	85	22000
2	2	0	85	22000
3	2	0	180	22000
4	2	20	50	18000
5	2	15	30	19000
6	2	0	50	50000
7	2	0	130	40000
8	2	0	180	50000
9	2	20	50	25000
10	2	0	42	20000
11	2	40	80	15000
12	2	0	90	15000

Model: 1=Spherical, 2=Exponential, 3=Gaussian

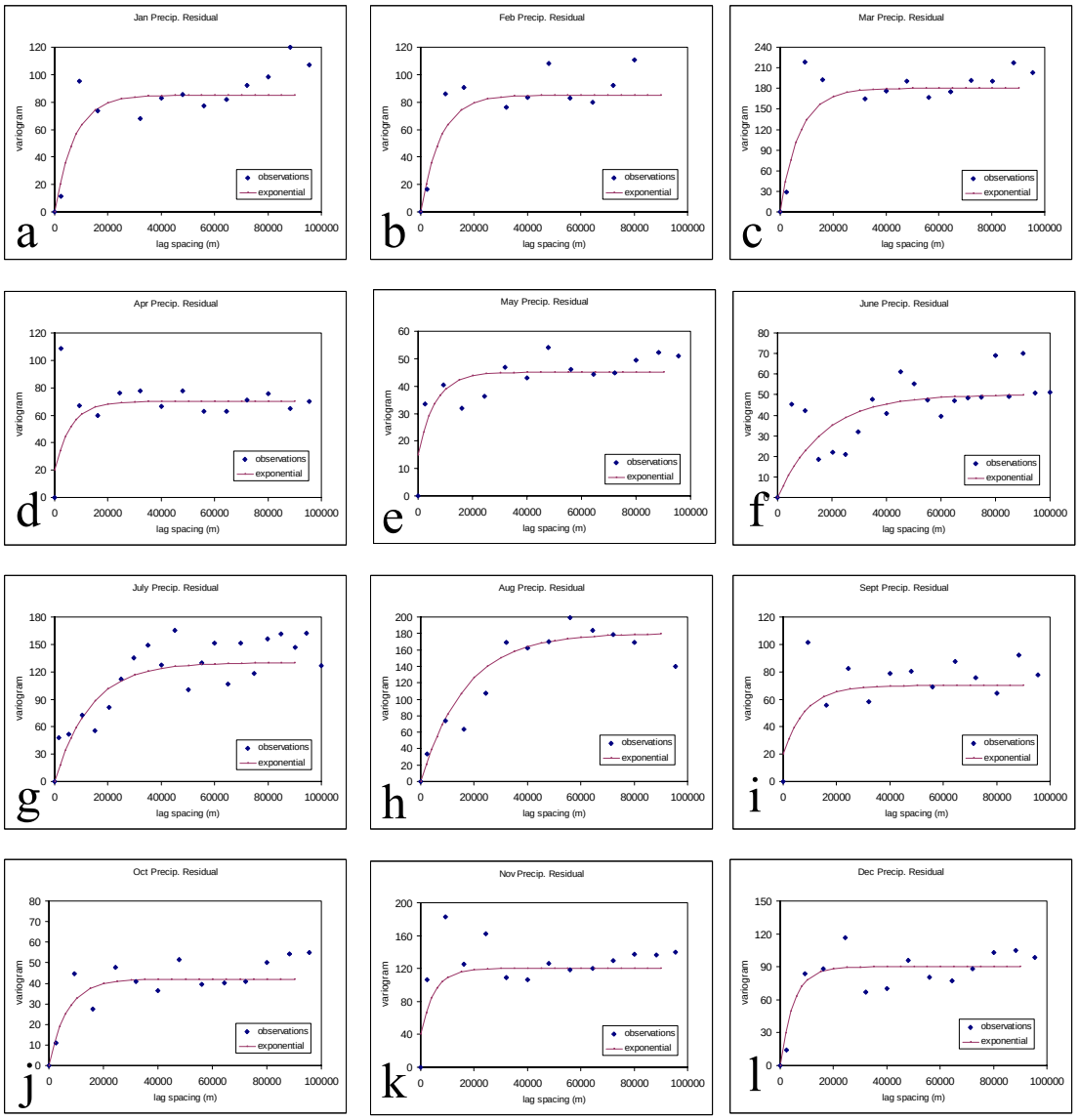

Figure II-1 The semi-variogram models fit to the experimental semi-variograms of ASOADeK regression de-trended precipitation residuals for January through December (a through l).

Appendix III Procedures for seasonal anomaly calculation

This appendix describes the steps for determining seasonal precipitation anomalies from gauge data.

1. For 22 gauges with consecutive data length over 50 years (mostly 1931~2003)
    a. Calculate the 50-year moving averages of monthly precipitation. For each gauge, there are *12 n* data, where *n* is the number of moving averages. The number varies between gauges.
    b. Sum the monthly precipitation to get the seasonal precipitation. Now for each gauge, there are *4 n* data.
    c. Find the standard deviation of 50-year moving averages of each of the four seasons for each gauge. Now each gauge has 4 data.
    d. Find the mean standard deviation of 50-year moving average over all 22 gauges for four seasons.

2. For each ENSO + PDO category
    a. Find the gauges which have both at least two-year data of the category, and the long-term data of 1955~2003 (at most 5 years of data missed)
    b. Calculate the category-mean monthly precipitation and long-term mean monthly precipitation for each gauge.
    c. Sum the mean monthly precipitation to mean seasonal precipitation for each gauge. This is done for both category mean, and long-term mean.
    d. Find the difference in mean seasonal precipitation between the category and the long-term average.
    e. Find the mean (averaged over all available gauges) of the difference of seasonal precipitation for four seasons, as wells as the standard deviation of the difference.
    f. The mean seasonal anomaly is the mean difference if the mean difference exceeds the mean standard deviation found in 1.d.; and zero otherwise.

Appendix IV ASOADeK regressions and de-trended precipitation residual semivariogram models for various ENSO + PDO categories

This appendix includes ASOADeK regression parameters of monthly mean precipitation for various ENSO + PDO categories, as well as the long-term average (Tables IV-1 ~ 5). The semivariogram models of ASOADeK de-trended precipitation residuals for each category are also included (Tables IV-6 ~10).

The ranges of semivariogram models in this chapter are much larger than those in Appendix II. Two situations account for these differences. For the long-term mean precipitation residual, most semivariograms were fit with the spherical model (Table IV-6), while all model types were exponential in Appendix II (Table II-1). The spherical model tends to have a larger range than the exponential model. For ENSO + PDO categories, the number of years of which precipitation data were used for calculating category was small. The mean precipitation of each gauge had a larger portion of variability that was not captured by the ASOADeK regression. This renders larger ranges in the variogram models (Table IV-7 through IV-10).

Table IV-1 The parameter values of the ASOADeK regression ($P=b_0+b_1X+b_2Y+b_3Z+b_5\cos\alpha+b_6\sin\alpha$) for long-term mean monthly precipitation (1955~2003)

Month	Aspect window[1]	b_0	b_1	b_2	b_3	b_5	b_6	MAE
1	5	-177.066	-0.048	0.047	11.260	-4.912	-3.052	4.3
2	4	-181.678	-0.021	0.043	15.733	-4.376	-2.914	4.4
3	3	-160.480	-0.002	0.035	19.584	-5.243	-1.643	5.2
4	3	-141.197	0.028	0.029	15.355	-3.122	-0.271	4.1
5	4	-157.603	0.133	0.028	11.492	0.756	-3.820	5.3
6	5	120.563	0.132	-0.043	12.825	2.415	-1.527	4.8
7	2	469.495	0.140	-0.132	29.321	-3.285	0.028	9.0
8	3	364.050	0.080	-0.098	30.549	-5.436	0.329	8.2
9	4	85.565	0.033	-0.021	10.197	-0.001	-2.858	4.1
10	5	-47.354	-0.009	0.015	10.019	-3.135	-1.682	3.2
11	5	-147.387	-0.022	0.039	10.180	-4.493	-2.740	4.0
12	2	-48.009	-0.024	0.012	12.916	-3.885	-1.465	3.7

Note: 1 = 1 km, 2 = 3 km, 3 = 5 km, 4 = 7 km, 5 = 9 km

313

Table IV-2 The parameter values of the ASOADeK regression ($P=b_0+b_1X+b_2Y+b_3Z+b_5\cos\alpha+b_6\sin\alpha$) for Neutral ENSO + high PDO category mean monthly precipitation (1955~1997)

Month	Aspect window[1]	b_0	b_1	b_2	b_3	b_5	b_6	MAE
1	3	-232.342	-0.076	0.058	24.209	-7.101	-2.662	5.9
2	3	-116.409	-0.040	0.024	25.069	-4.216	-3.836	5.8
3	3	-256.616	-0.012	0.055	31.309	-4.612	-3.477	6.4
4	1	-109.261	0.022	0.020	20.017	1.694	0.583	5.4
5	2	-62.344	0.185	-0.002	17.118	-3.333	1.899	6.9
6	2	399.364	0.167	-0.114	12.379	-3.519	-0.417	5.5
7	4	526.895	0.186	-0.155	31.683	-8.408	-2.947	10.0
8	4	466.232	0.233	-0.148	46.289	-10.156	-0.437	11.7
9	4	485.728	0.089	-0.133	23.565	-2.058	-5.978	8.3
10	2	118.444	-0.029	-0.031	19.802	-1.432	-3.360	4.8
11	2	-42.873	-0.046	0.013	17.712	-2.484	1.375	5.7
12	4	-149.323	-0.037	0.034	21.675	-1.221	-4.698	4.2

Note: 1 = 1 km, 2 = 3 km, 3 = 5 km, 4 = 7 km, 5 = 9 km

314

Table IV-3 The parameter values of the ASOADeK regression ($P=b_0+b_1X+b_2Y+b_3Z+b_5\cos\alpha+b_6\sin\alpha$) for Neutral ENSO + low PDO category mean monthly precipitation (1955~1997)

Month	Aspect window[1]	b_0	b_1	b_2	b_3	b_5	b_6	MAE
1	5	-89.730	-0.042	0.021	18.193	-1.993	-4.547	5.0
2	5	-194.728	-0.033	0.046	17.816	-6.613	-4.247	5.3
3	3	-21.850	-0.023	-0.001	25.315	-3.174	-3.177	5.2
4	3	-253.059	0.027	0.056	15.669	-2.668	-0.792	5.3
5	2	-68.321	0.177	-0.001	8.329	-7.124	-1.143	6.2
6	1	233.407	0.160	-0.072	7.870	-3.394	3.873	5.4
7	2	539.596	0.193	-0.158	33.213	-11.953	7.162	10.7
8	5	812.731	0.100	-0.213	35.615	-12.782	3.613	13.2
9	1	-67.914	-0.036	0.026	5.451	-0.108	3.417	7.0
10	2	18.711	-0.027	0.003	6.340	-4.503	1.639	6.6
11	5	-110.306	-0.044	0.030	9.480	-1.053	-2.268	2.9
12	4	21.021	-0.035	-0.005	14.876	-1.121	-2.888	4.9

Note: 1 = 1 km, 2 = 3 km, 3 = 5 km, 4 = 7 km, 5 = 9 km

315

Table IV-4 The parameter values of the ASOADeK regression ($P=b_0+b_1X+b_2Y+b_3Z+b_5\cos\alpha+b_6\sin\alpha$) for El Niño + high PDO category mean monthly precipitation (1955~1997)

Month	Aspect window[1]	b_0	b_1	b_2	b_3	b_5	b_6	MAE
1	3	-39.587	-0.066	0.011	19.026	-5.761	-1.018	5.4
2	3	-184.153	-0.003	0.039	20.217	-4.014	-1.164	4.0
3	3	-247.632	0.018	0.048	33.406	-5.372	-3.451	6.5
4	3	-71.397	0.044	0.009	19.043	-3.395	1.667	6.3
5	5	-511.674	0.124	0.121	4.852	-8.407	-1.983	7.3
6	3	-93.940	0.223	0.003	11.226	-3.374	1.311	8.2
7	3	607.410	0.195	-0.177	33.867	-9.528	-1.236	8.1
8	2	349.932	0.041	-0.086	24.339	-6.658	7.514	11.5
9	3	-21.934	0.032	0.006	9.310	0.778	1.378	4.5
10	5	-137.469	0.019	0.032	11.871	-5.883	-2.479	4.6
11	5	-44.284	-0.056	0.014	21.373	-4.112	-4.238	6.7
12	3	130.383	-0.030	-0.031	12.407	-3.055	-0.606	5.4

Note: 1 = 1 km, 2 = 3 km, 3 = 5 km, 4 = 7 km, 5 = 9 km

316

Table IV-5 The parameter values of the ASOADeK regression ($P=b_0+b_1X+b_2Y+b_3Z+b_5\cos\alpha+b_6\sin\alpha$) for La Niña + low PDO category mean monthly precipitation (1955~1997)

Month	Aspect window[1]	b_0	b_1	b_2	b_3	b_5	b_6	MAE
1	2	-231.230	-0.062	0.057	21.032	-4.567	-3.285	5.3
2	2	-66.301	-0.056	0.015	21.774	-3.846	-1.468	5.2
3	3	-173.755	-0.025	0.037	22.936	-3.905	-0.337	5.0
4	3	-129.279	-0.002	0.025	20.095	-4.196	-0.118	3.8
5	2	-67.538	0.117	0.005	8.968	-4.073	-0.049	5.1
6	3	-96.750	0.129	0.011	10.020	-4.817	-0.381	6.6
7	2	646.436	0.182	-0.182	33.795	-5.102	7.603	11.7
8	2	503.144	0.084	-0.137	32.985	-7.067	3.273	8.5
9	2	321.803	-0.009	-0.070	0.837	-2.429	2.760	7.6
10	4	87.330	-0.002	-0.022	9.416	-0.291	-2.297	5.2
11	4	-193.214	0.003	0.041	18.725	-2.547	-3.865	3.8
12	5	-258.562	-0.048	0.063	21.745	-3.802	-2.782	4.9

Note: 1 = 1 km, 2 = 3 km, 3 = 5 km, 4 = 7 km, 5 = 9 km

317

Table IV-6 Fit semivariogram models and parameterization of 12 monthly precipitation residuals of long-term mean (1955~2003)

Month	Model*	Nugget (mm^2)	Sill (mm^2)	Range (m)
1	2	10	21	50000
2	1	8	21	50000
3	1	15	28	40000
4	1	5	24	60000
5	2	20	25	50000
6	1	13	25	50000
7	1	0	135	50000
8	1	0	110	65000
9	2	0	26	60000
10	1	0	22	50000
11	1	10	15	50000
12	1	10	12	40000

Model: 1=Spherical, 2=Exponential, 3=Gaussian

Table IV-7 Fit semivariogram models and parameterization of 12 monthly precipitation residuals of neutral ENSO + high PDO

Month	Model*	Nugget (mm^2)	Sill (mm^2)	Range (m)
1	2	0	55	60000
2	2	5	50	60000
3	2	20	35	40000
4	2	20	40	60000
5	2	15	65	60000
6	1	5	35	50000
7	2	40	150	80000
8	1	55	200	70000
9	2	10	100	60000
10	2	10	30	60000
11	2	20	35	60000
12	2	10	20	50000

Model: 1=Spherical, 2=Exponential, 3=Gaussian

Table IV-8 Fit semivariogram models and parameterization of 12 monthly precipitation residuals of neutral ENSO + low PDO

Month	Model*	Nugget (mm^2)	Sill (mm^2)	Range (m)
1	2	10	40	50000
2	2	5	35	50000
3	2	10	35	40000
4	1	5	50	40000
5	2	15	70	60000
6	2	20	30	50000
7	2	30	190	80000
8	1	55	260	40000
9	2	30	45	30000
10	2	10	75	70000
11	2	5	10	50000
12	2	10	27	50000

Model: 1=Spherical, 2=Exponential, 3=Gaussian

Table IV-9 Fit semivariogram models and parameterization of 12 monthly precipitation residuals of El Niño + high PDO

Month	Model*	Nugget (mm^2)	Sill (mm^2)	Range (m)
1	2	15	28	50000
2	2	0	22	50000
3	2	20	40	40000
4	1	0	75	60000
5	2	10	100	50000
6	1	60	70	50000
7	2	20	95	80000
8	2	35	150	80000
9	2	10	25	30000
10	2	0	30	50000
11	2	20	40	40000
12	2	10	40	40000

Model: 1=Spherical, 2=Exponential, 3=Gaussian

Table IV-10 Fit semivariogram models and parameterization of 12 monthly precipitation residuals of La Niña + low PDO

Month	Model*	Nugget (mm^2)	Sill (mm^2)	Range (m)
1	2	20	35	50000
2	2	20	20	50000
3	2	10	27	40000
4	2	5	20	50000
5	2	12	30	50000
6	1	17	40	50000
7	2	30	170	80000
8	2	40	80	55000
9	2	40	45	30000
10	2	20	40	50000
11	2	3	17	40000
12	2	10	33	40000

Model: 1=Spherical, 2=Exponential, 3=Gaussian

Appendix V The root-water-uptake model and numerical stability problem of the S-shape model

Given appropriate atmospheric boundary condition, an appropriate root-water-uptake model is important to simulate transpiration flux. However, the model and its parameterization are rarely available for naturally vegetated surfaces. In this appendix, two measurements are used to derive the root-water-uptake model. From these observations, the relationship between the root-water-uptake function and the soil water potential is derived. The two models, the Feddes and S-shape models, are then fitted to the derived relationship. The results indicate that the S-shape model may be more appropriate to represent the physical process of transpiration. Finally, the numerical stability problem of the S-shpae model is discussed.

Root-water-uptake function for Pinus taeda L. derived from a field study

Ewers et al., [*2001*] measured sap flux of 11- to 13- year-old *Pinus taeda L.* at the Southeast Tree Research and Education Site in the Sandhills of North Carolina, on an infertile, well drained, sandy soil. The sap flux was then scaled to mean canopy stomatal conductance. The soil moisture was measured using automated time domain reflectometry (TDR) at 0.05, 0.1, 0.25, 1.0, and 1.9 m depths. With the effects of sunlight, vapor pressure deficit, and temperature screened out, an empirical function of mean canopy stomatal conductance and soil water content is defined (Equation V-1).

$$G_{SRB} = j + k \ln \theta_R \qquad \text{(V-1)}$$

where G_{SRB} is the mean canopy stomatal conductance at conditions with optimal daily sunlight, temperature, and vapor pressure deficit, with a unit of $mmolm^{-2}s^{-1}$, θ_R is root-surface-area weighted soil water content, j and k are the fitted constants, 413.1 (unitless) and 114.5 (unitless) respectively. The unit of conductance is converted to ms^{-1}, by a factor of $2.4*10^{-5}$, shown below.

$$1\frac{mmol}{m^2 s} = \frac{10^{-3} mol}{m^2 s} * \frac{24*10^{-3} m^3}{mol} = 2.4*10^{-5} m/s \qquad \text{(V-2)}$$

where $24*10^{-3}$ m^3/mol is from the V/n ratio of the ideal gas, where n is the amount of air in the unit of moles, and V is the respective volume of the n mole air under the standard pressure. The ratio is about 24.5 L/mol at 25°C, and 22.4 L/mol at 0°C

The equation (V-1), coupling with the Penman-Monteith equation (§4.3.3), is used to obtain the relationship between actual transpiration and soil water content with average atmospheric conditions for the experimental site. Since no soil hydraulic property is available for this experimental site, sandy-loam (based on the descriptions of Ewers et al., [2001]) is used to find the function relating transpiration and soil water potential. With a assumption that transpiration is at the potential rate when the soil is saturated, the ratio of T/PT can be obtained for the soil at various saturations. The result is plot in Figure V-1, with comparison to two fit root-water-uptake models. It seems that the S-shape model represents the root-water-uptake function of Ewers's study site better than the Feddes model.

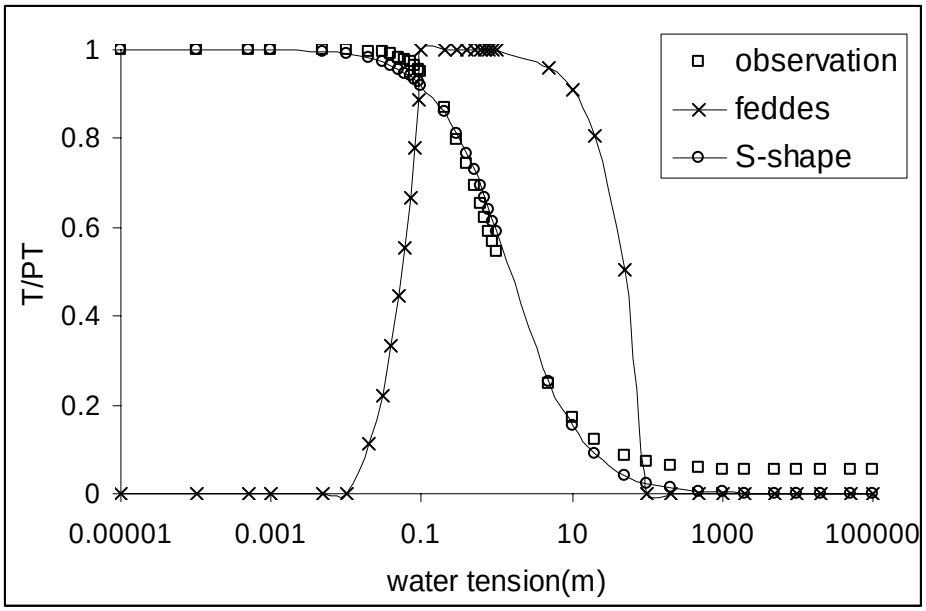

Figure V-1 Root-water-uptake function calculated from Ewers [2001], with comparison to the S-shape model (h50=-1.5m, p=0.9) and Feddes model (h1=-0.1, h2=-0.25, h3=-2, and h4=-100m).

At this study site, annual precipitation is 1210 mm [Ewers et al., 2001]. The fitted *p* value (Figure V-1) for this humid site is 0.9, while van Genuchten [1987] suggested 3.0 for a site with salinity stress. For a site at semi-arid environment, the *p* value should be between 1 and 3.

Root-water-uptake function for creosotebush derived from a lab study

Pockman & Sperry [*2000*] measured hydraulic conductivity of the vegetation stems at various water potentials in the stems of Arizona creosotebush (*Larrea tridentata* (DC.) Coville), as well as some other woody species. With assumption that the root has similar response to the soil water potential, the root-water-uptake relationship with the soil water potential was derived. Fitting the two models, the Feddes (not shown) and S-shape models, to the derived root-water-uptake relationship, shows that the S-shape model fits the observation-derived relationship better. The fitting results are shown in Figure V-2.

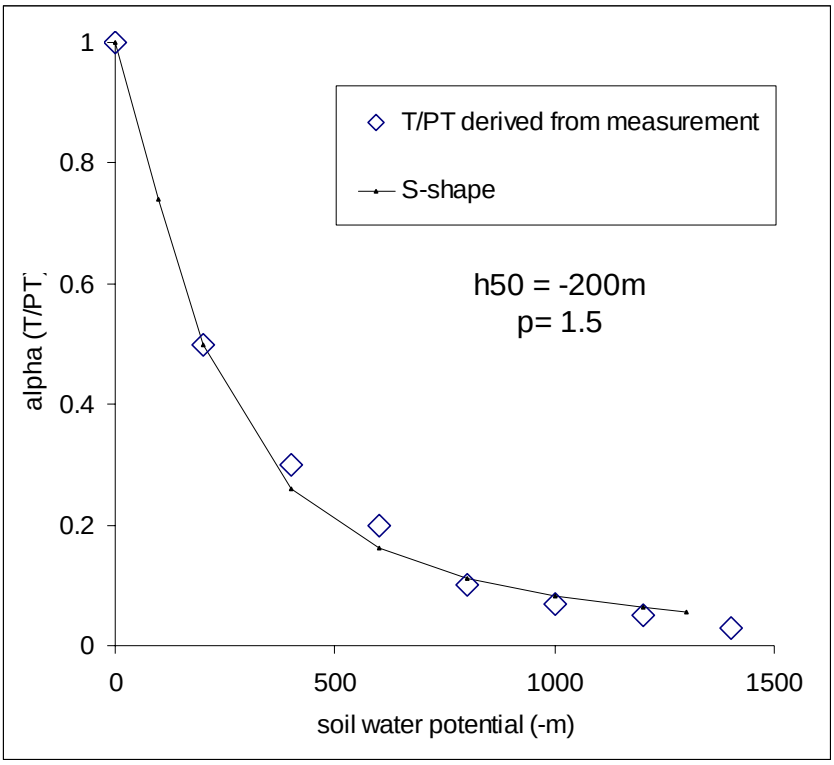

Figure V-2 The S-shape root-water-uptake function fit to the lab measurements for creosotebush by Pockman & Sperry [*2000*].

Potential numerical problem of S-shape model

The numerically instabilities in HYDRUS can occur with the S-shape model. In my experience, the instability usually occurs when the soil is dry, and the problem is more serious for a coarse texture soil. When the soil is dry, the total available soil water for transpiration is little. For the Feddes model, the α value (§4.2.2) linearly decreases to zero, for which HYDRUS can eventually meet the need of requirement (e.g., $\alpha * PT$). For the S-shape model, the α value decreases much slower than the Feddes model when the soil is dry. This may cause numerical instability.

To understand this problem, let's image that at some point, the soil water is not enough to meet the requirement for transpiration ($\alpha * PT$). The program decrease the soil water potential so that the α value becomes smaller. At the meantime, the soil water

content becomes smaller because of the decreased soil water potential. The numerical instability problem occurs if the soil water content decrease faster than the α value with the soil water potential. This situation does not occur for the Feddes model (Figures V-3 and V-4). For the S-shape model, it may occur. And it is more possible to happen for coarse texture soils. For example, the instability problem was observed for the sandy loam in Figure V-3. This problem could be solved by an increased p value of the S-shape model, which increases dropping rate of the α value. For example, a hillslope water partitioning simulation encountered problem when I used h_{50} of -2 m and p of 0.9 (Figure V-3). However, when I modified the parameters to -3 m and 2 (Figure V-4), respectively, the numerical problem disappeared. Another way to solve the problem is to apply wilting point in the S-shape model, shutting the transpiration process when the soil is dry (In current commercial version HYDRUS, no wilting point is applied for the S-shape model).

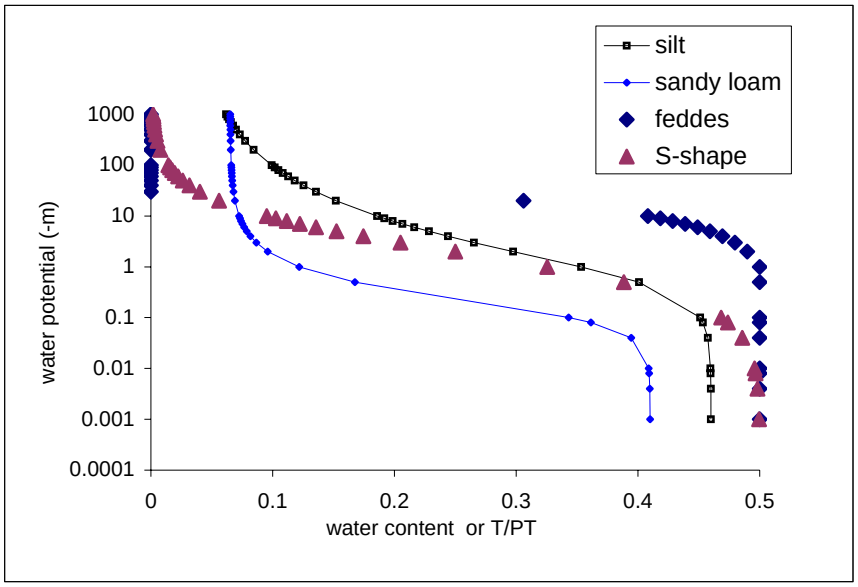

Figure V-3 The soil water retention curves for silt and sand loam, and normalized T/PT curves for Feddes model (h3=-1m, h4=-50m) and S-Shape model (h50=-2m, p=0.9).

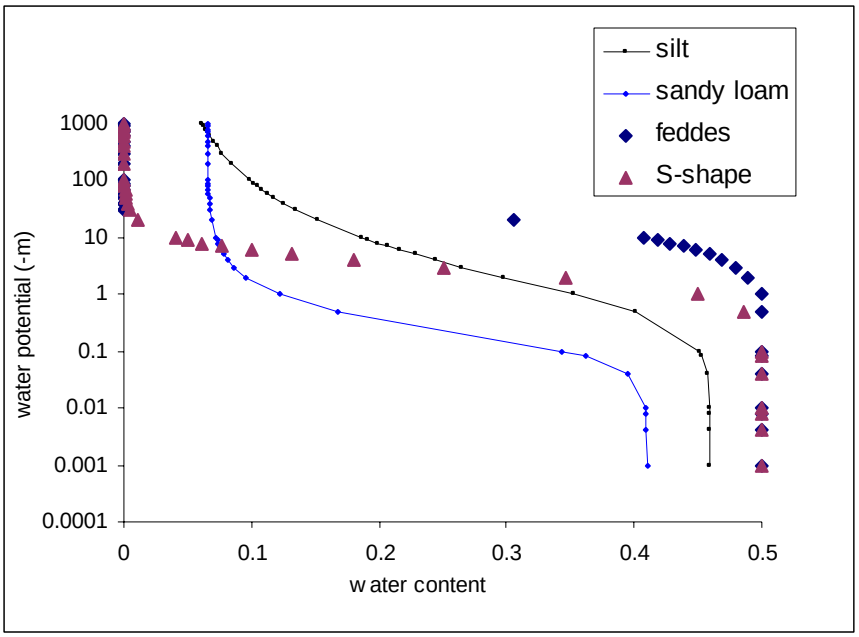

Figure V-4 The soil water retention curves for silt and sand loam, and normalized T/PT curves for Feddes model (h3=-1m, h4=-50m) and S-Shape model (h50=-3m, p=2).

Reference

Ewers, B.E., R. Oren, K.H. Johnsen, and J.J. Landsberg (2001), Estimating maximum mean canopy stomatal conductance for use in models, *Canadian Journal of Forest Research*, 31, 198-207.

Pockman, W.T., and J. S. Sperry (2000), Vulnerbility to xylem cavitation and the distribution of Sonoran Desert vegetation, *American Journal of Botany*, 87(9), 1287-1299.

van Genuchten, M. Th. (1987), A numerical model for water and solute movement in and below the root zone. Research Report No 121, U.S. Salinity laboratory, USDA, ARS, Riverside, California.

Appendix VI Assessment of the applicability of three common models for estimating fractional vegetation cover from remote sensing imagery in a semi-arid environment[1]

1. Introduction

Land surface vegetation cover classification and quantification is used in studies of ecology, hydrology, meteorology, land cover and land use, and global climate change. Characterization of vegetation cover includes vegetation types, leaf area index (LAI), land surface vegetation coverage, vegetation height, etc. The remote sensing technique is used to characterize the temporal and spatial distribution of surface vegetation cover because of its efficiency, large-area coverage, and the availability of spatially and temporally continuous data sets. However, spatial resolution of a remotely sensed image is generally not enough to map individual vegetation, mixing is a very common phenomenon. A pixel classified as vegetation often contains a portion of soil or *vice versa*. To accurately estimate the coverage of vegetation in a region using remote sensing data, especially for those of moderate to low resolution, unmixing analysis is needed to estimate the vegetation fraction (*Fr*) at a subpixel level. Many algorithms have been developed to estimate the fractional vegetation cover within a pixel (Huete, 1986; Smith et al. 1990; Roberts, 1991; Roberts et al., 1993, 1998; Choudhury et al., 1994; Wittich & Hansing, 1995; Gillies et al., 1997; Carlson & Ripley, 1997; Gutman & Ignatov, 1998; Asner & Heidebrecht, 2002). Most of these algorithms can be grouped into one of three common *Fr* models: the linear reflectance model, the linear NDVI model, and the quadratic NDVI model. The Normalized Difference Vegetative Index, NDVI, is itself

[1] This chapter is in revision for *Remote Sensing of Environments*, with coauthors: John L. Wilson, Hongjie Xie, and Xiaobing Zhou.

intrinsically non-linear in reflectance. The names of the NDVI based *Fr* models come from whether the *Fr* estimate is linear or quadratic in term of the NDVI. We test and compare the linear reflectance and NDVI-based models for a semiarid environment using remote sensing data.

The linear spectral mixture model (referred to as the linear reflectance model) is a common method used to obtain fractional vegetation cover within a pixel from the remote sensing imagery. It is defined as

$$\sum_j (R_{ij} X_j) = R_i \ , \qquad \text{(VI-1)}$$

with constraint equation

$$\sum_j X_j = 1 \ , \qquad \text{(VI-2)}$$

where R_{ij} is the reflectance of the *j-th* end-member for band *i*, X_j is the fractional surface area covered by *j-th* end-member, R_i is the total reflectance of the pixel of band *i*. The fundamental principle of this model is that the emitted or reflected energy from a multi-component surface is a radiometrically decipherable combination of the energy radiated from each component in proportional to its areal percentage. Thus, the spectral reflectance recorded for a pixel at any single band is the linear combination of the spectral reflectance of the spectrally distinctive surface features (end-members) contained in the pixel weighed by their respective areal proportions (e.g., Adams, Smith, & Johnson, 1986; Karnieli et al., 2002). Spectral signatures of all available visible and near infrared bands can be used to estimate the fraction cover of the end-members in each pixel (Sabol,

Adams, & Smith, 1992). The linear reflectance model has been applied to obtain soil and rock cover (Adams, Smith, & Johnson, 1986; Ramsey and Christensen. 1998), snow cover (Zhou & Li, 2003), and vegetation cover (Smith et al. 1990; Roberts, 1991; Roberts, Smith, & Adams, 1993; Roberts et al., 1998; Asner & Heidebrecht, 2002) of the surface. For vegetation cover, two to three end-members are usually applied depending on the surface vegetation types and structures. In semiarid environments, the vegetation types and structures are simple; we can often use only two end-members for a specific time period, i.e., one vegetation end-member and one soil end-member, j=1,2, with X_1=Fr, X_2=1-Fr. This simplicity is one reason why we test the Fr models in a semiarid environment.

Other common methods for spectral mixture analysis relate fractional vegetation cover Fr to nonlinear transformations of multiple-band spectral signatures. Based on correlation analysis, Gertner et al. (2002) found that of the seven tested nonlinear multi-band transformations of Landsat TM images NDVI has the highest correlation with Fr. Table VI-1 shows several published Fr-NDVI linear and quadratic models. For simplicity, we refer to these as the linear NDVI model and the quadratic NDVI model, respectively, while realizing that any model based on NDVI is intrinsically non-linear in terms of spectral reflectance. The linear NDVI model is expressed as (Wittich & Hansing, 1995; Gutman & Ignatov, 1998)

$$Fr = \frac{NDVI - NDVI_0}{NDVI_\infty - NDVI_0} , \qquad \text{(VI-3)}$$

and the quadratic NDVI model is (Gillies et al., 1997; Choudhury et al., 1994; Carlson & Ripley, 1997)

$$Fr = \left(\frac{NDVI - NDVI_0}{NDVI_\infty - NDVI_0} \right)^2 , \qquad \text{(VI-4)}$$

where $NDVI_\infty$ is the NDVI of the surface 100% covered by green vegetation (or the NDVI of the vegetation end-member), and $NDVI_0$ is the NDVI of 100% bare soil surface (or the NDVI of the bare soil end-member).

Table VI-1 Common models of deriving fractional vegetation cover from pixel NDVI

Fr-NDVI models	$NDVI_0$	$NDVI_\infty$	Fr	Surface types	Remote sensing image	Reference
Fr=[N]	0.10 fitted value	0.66 fitted value	Estimated from temporal phonological observations	Vineyard, grass, wheat field, western Germany	AVHRR	Wittich & Hansing, 1995
Fr=[N]	0.04 estimated from GVI data (0.15°)	0.52 estimated from GVI data (0.15°)	No validation		AVHRR	Gutman & Ignatov, 1998
Fr=[N]*[N]	Estimated from scatter plot of remote sensed NDVI and surface temperature		Inversed from SVAT model	FIFE site in Kansas, U.S.A.; MONSOON'90 at Walnut Gulch in Arizona, U.S.A.	AVHRR, NS001	Gillies at al., 1997
$Fr=1-(1-[N])^m$ m=0.5~0.75, also referred as Fr=[N]*[N]	Relation estimated from a heat balance and a radiative transfer model					Choudhury et al., 1994
Fr=[N]*[N]	Derived from a radiative transfer model					Carlson & Ripley, 1997

Notes: $[N] = [(NDVI - NDVI_0)/(NDVI_\infty - NDVI_0)]$, where $NDVI_\infty$ is supposed to represent NDVI of the surface 100% covered by green vegetation, and $NDVI_0$ is the NDVI of 100% bare soil surface. Gillies et al. (1997) and Carlson & Ripley (1997) referred to Choudhury's (1994) results as Fr=[N]*[N], which could be more or less observed from Choudhury's data.

Without applying field data we already see some inconsistencies between the three *Fr* models. As you might imagine, with different levels of non-linearity, the three models are mathematically inconsistent. They are also parametrically or physically inconsistent. For example, except the extreme cases that NDVI = $NDVI_0$ or $NDVI_\infty$, for any NDVI $\subset$ ($NDVI_0$, $NDVI_\infty$) the linear NDVI model (3) and the quadratic NDVI model (4) cannot possibly hold simultaneously. In another example, if the linear reflectance model is accepted, i.e., the area-weighted linear combination of reflectance of each end-member in a pixel gives the pixel reflectance, the linear combination of NDVI of each end-member within a pixel will not give pixel NDVI (Asner and Heidebrecht, 2002). In short, the three fractional vegetation cover models are mathematically and physically different and mutually exclusive. Although the linear reflectance model is physically more explicable, the linear and quadratic NDVI models appear to have worked well in some cases (e.g., Wittich and Hansing, 1995; Gutman and Ignatov, 1998; and Gillies et al., 1997). The purpose of this paper is to test and compare these three mathematically and physically inconsistent *Fr* models for a semi-arid environment by analyzing a Landsat ETM+ image and comparing to *in situ* measurements.

2. Methodology

2.1 Study sites

The study sites were selected in Sevilleta National Wildlife Refuge (NWR), the major study area of the Sevilleta Long-Term Ecological Research (LTER) program (Hobbie et al., 2003). The Sevilleta NWR, located in Socorro County, New Mexico, has a hot, dry climate, and with an average annual precipitation of about 255 mm. Two types of vegetated surface, shrub land and woodland, with distinctive vegetation height and

canopy LAI,, were selected for this study. There were three study sites, each of 712.5m×427.5m (or 25×15 = 375 pixels of an ETM+ image): one shrub land site in a relatively flat area of the Refuge, and two woodland sites along the eastern slope of Los Pinos Mountains (Figure VI-1). The shrub site (Site 1) is covered with creosote shrub and bare soil, and the two woodland sites are covered by piñon, juniper, dry grass, and soil (referred to as Site 2 and Site 3). All study sites are within the coverage of one selected Landsat ETM+ image.

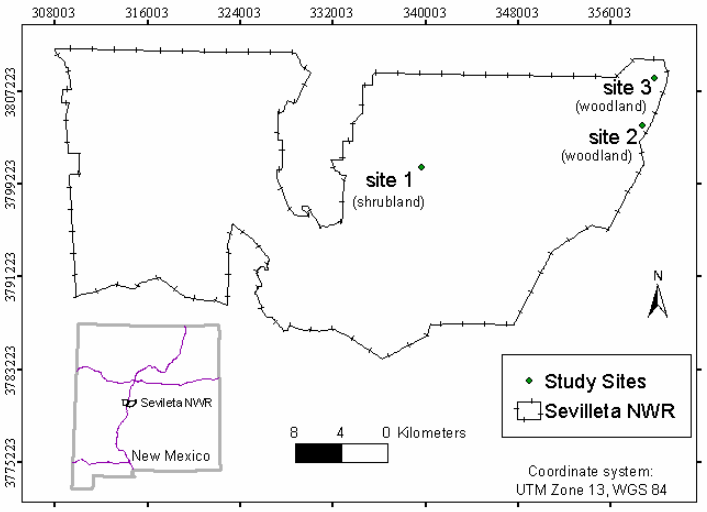

Figure VI-1 Index map of the study sites.

2.2 *Field measurement and satellite image processing*

The reflectance of all surface end-members (piñon, juniper, creosote shrub, dry grass, soils, and soils in shadow) encountered at the study sites was measured by a portable hyperspectral spectroradiometer (model FieldSpec©Pro FR, Analytical Spectral Devices, Inc., Boulder, CO) at the same season during which the Landsat ETM+ image was acquired. The spectroradiometer covers visible to mid-infrared wavelength regions (350-2500 nm), with a spectral resolution of about 3 nm at 700 nm in the visible and near-

infrared portion of the spectrum (350-1050 nm) and 10-12 nm in the short-wavelength infrared portion of the spectrum (1050-2500 nm). The sampling interval is 1.4 nm for 350 -1050 nm region and 2 nm for 1050-2500 nm region. Data collection in the whole 350 – 2500 nm spectral region is accomplished using three separate detectors: 512-channel silicon photodiode array for 350 -1050 nm, and two separate "graded index" InGaAs photodiodes for 1050 -2500nm. 2151 data points are obtained by the controlling software accounting for the overlap in wavelength intervals (oversampling of the spectrum). The field of view of the fore-optic sensor is 12°. Measurement was carried out under clear sky conditions and the fore-optic sensor was placed just above the canopy so that the field of view of the sensor covered as much leaf area as possible. The viewing direction of the sensor was in nadir. Spectral radiance data were collected for both canopy and a white reference panel so that the reflectance was obtained as the ratio of the radiance data of canopy to that of the reference panel for a specific wavelength. At each site, spectral reflectance measurement was conducted for all end-members. For each end-member, for instance creosote shrub, measurements were taken for several (3-5) individuals. For each individual, ~10 samples were taken. All individuals and samples were arbitrarily selected. The estimated mean of all measurements for each end-member was used as the end-member spectral signature.

To measure the fractional vegetation cover at the woodland sites, several cells (4 at Site 2 and 3 at Site 3) with the same size as an ETM+ pixel (28.5m × 28.5m) were arbitrarily selected. The maximum crown diameter of each individual tree within each cell was measured, and used to estimate crown area by vertical projection. The fractional vegetation cover of each cell was then calculated by summing crown areas and dividing

by the cell area. The shrub cover fraction of Site 1 was estimated by Kurc and Small (2004) from field aerial digital photos.

We lumped data for piñon and juniper at the woodland sites into one vegetation cover type. There is little difference in their spectral reflectance; especially when their reflectance is compared to other end-members. Using average reflectance of piñon and juniper should not lead to significant error in any of the *Fr* models. Moreover, the proportion of piñon and juniper at the woodland sites varied between pixels; it was difficult to distinguish the fractional vegetation cover of each species from the *Fr* models.

A Landsat ETM+ image was used for this study because its small pixel size (28.5×28.5 m^2) is appropriate for testing the *Fr* models with field measurements. A lower resolution image such as that of MODerate resolution Imaging Spectroradiometer (MODIS) might be usable, but a pixel of 1km × 1km is too big for ground measurement. The ETM+ image of path 33/row 36, acquired in June 16, 2002, before the local monsoon season, was used in this study to avoid disturbing surface reflectance with temporal changes of soil moisture (Karnieli et al. 2002). The radiance recorded in each pixel includes reflected energy from the surface target and diffusively scattered energy (path radiance) from the atmosphere. The dark-pixel-subtraction method (Crippen 1987) was applied to the ETM+ scene to remove the path radiance. The topography affects solar incident angle, and thus the radiance on the surface, resulting in an apparent surface spectral signature received at the remote sensing sensor deviated from a flat surface with same coverage. A digital elevation model (DEM) of 30m ×30m resolution was applied to correct for the effect of slope angle and aspect using an algorithm developed by Duffie and Beckman (1991). Finally, the spectral reflectance of each pixel was calculated from

the spectral radiance of the six visible and near-infrared (VNIR) bands of the Landsat 7 image (Marken & Barker, 1986; Landsat 7 Science Users Handbook, 2003).

2.3 *Shadow effect correction*

The fractional vegetation cover models described above assume a vertical projection of vegetation. However, the canopy projection is deformed because of the oblique satellite viewing angle (Figure VI-2b). The observed projected vegetation area is generally different from the vertically-projected area, which, if not corrected, can lead to errors in estimating *Fr*. The models also ignore the vegetation's solar shadow due to an oblique solar position (Figure VI-2a). The solar shadow reduces the solar illumination and thus influences the spectral reflectance (Figure VI-3). In effect the shadow becomes another end-member. Both effects should be considered in estimating fractional vegetation cover using spectral unmixing analysis. While solar shadow has previously been noted in fractional surface cover analysis (Adams, Smith, & Johnson, 1986; Smith et al., 1990a,b; Roberts, Smith, & Adams, 1993), the effect of a deformed canopy projection has not.

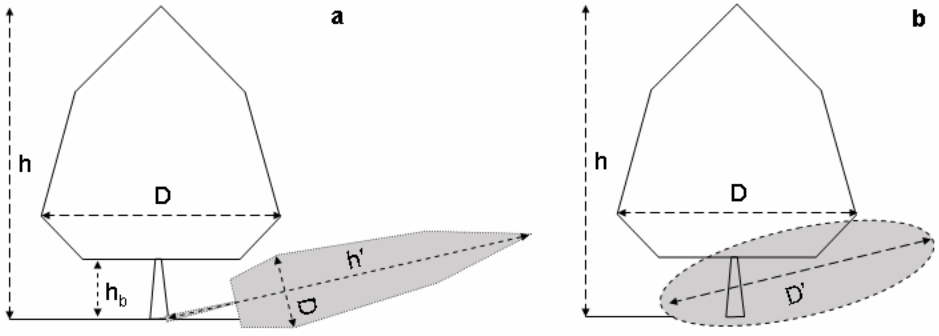

Figure VI-2 The tree shadow (a) caused by oblique solar position (solar elevation angle < 90^0), and the elliptic tree projection (b) on the surface caused by the oblique satellite remote sensing sensor.

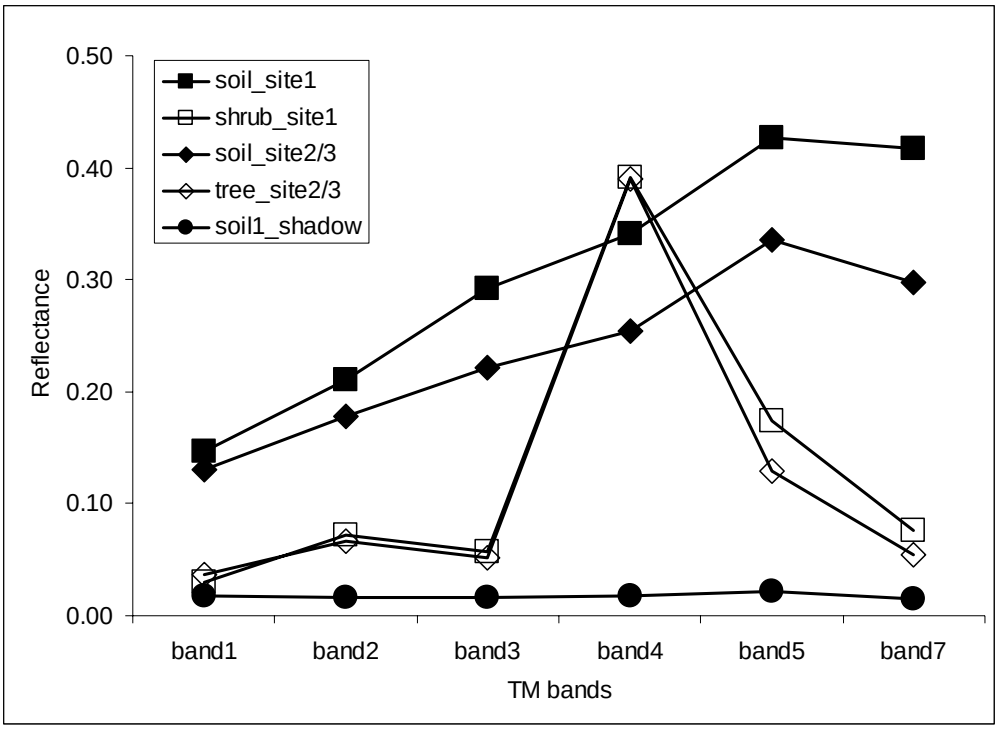

Figure VI-3 Field-measured reflectance of the surface end-members at six ETM+ bands.

With assumptions that (a) the solar shadow of the vegetation falls on inter-canopy space, (b) the vegetation crown has a shape between a triangle and a rectangle, (c) the sensor shadow, which is defined as the projection of the vegetation on the surface from the point of view of the sensor, has a ellipsoid shape, and (d) the solar shadow on the inter-canopy space does not overlap with the sensor shadow, we developed very simple algorithms to correct for these effects. The solar shadow factor (*SF*) of vegetation, which is defined as the ratio of the actual or effective shadow area of vegetation to the vertically projected canopy area, and the sensor projection factor (*PF*), which is defined as the ratio of the difference between the actual sensor projection area and the vertically projected area, relative to the vertically projected area, are given by (5) and (6), respectively. A

shadow or projection factor of zero indicates no correction. The corrections are (Figure VI-2a)

$$SF = \begin{cases} \dfrac{\frac{3}{4}\left(h\tan\alpha - \max(h_b\tan\alpha, \frac{D}{2})\right)D}{\pi\left(\frac{D}{2}\right)^2}, & \text{for } h\tan\alpha > D/2, \\ 0, & \text{for } h\tan\alpha \le D/2, \end{cases} \qquad \text{(VI-5)}$$

and (Figure VI-2b)

$$PF = \frac{\pi\left(\frac{D}{2}\right)\left(\frac{D}{2\cos\beta}\right) - \pi\left(\frac{D}{2}\right)^2}{\pi\left(\frac{D}{2}\right)^2} = \frac{1}{\cos\beta} - 1 \quad , \qquad \text{(VI-6)}$$

where α is the solar zenith (incident) angle when the ETM+ scene was taken, h is the vegetation height, h_b is the height of the trunk below the vegetation crown, β is the sensor viewing zenith angle, and D is the diameter of the vertical projection of the vegetation crown. For instance, considering MODIS scene h09v05 taken on June16th, 2002, the solar zenith angle ranges from 6.5° to 32.5°, with a mean of 19.6°, and the sensor zenith angle ranges from 0.03° to 65.3°, with a mean of 31.4°, significance of *PF* and *SF* varies from pixel to pixel for the MODIS image. On a site covered with vegetation of an equivalent height of 4 meters and a canopy diameter of 2 meters, correction factors *PF* and *SF* would be about 0.64 and 0.17, respectively, for the MODIS image with a solar zenith angle of 19.6°, and a sensor zenith angle of 31.4°, indicating significant corrections.

With its distinct spectral signature, the vegetation shadow becomes an additional end-member. With vegetation, vegetation shadow, and bare soil as end-members, the linear reflectance model (1) now takes the form

$$R_{\infty} \cdot Fr \cdot (PF + 1) + R_0 \left[1 - Fr \cdot ((PF + 1) + SF)\right] + R_{shadow}(Fr \cdot SF) = R_{pixel} \ , \quad \text{(VI-7)}$$

where R_0 is the spectral reflectance of the bare soil, R_{∞} is the spectral reflectance of the vegetation, and R_{shadow} is the spectral reflectance of the effective shadow. Similarly, NDVI models (3) and (4) should also be modified to account for shadow effects if necessary. However, our analysis and data show that shadow does not change the target NDVI significantly at our sites. Finally, the *SF* correction factor depends on the canopy geometry, specifically the canopy aspect ratio (*h/D*) for our study sites. For example, SF varies from 0, 0.15, 0.37, to 0.58 for an aspect ratio of 1, 1.5, 2, 2.5, respectively. Since the canopy aspect ratio is a function of both vegetation type and vegetation age, it is difficult to assign an accurate SF for the woodland sites where piñon and juniper have different canopy aspect ratios and the proportions of two vegetation types vary with pixels. For our purposes we again lumped piñon and juniper canopy data into one vegetation cover, with an equivalent canopy diameter of 2 meters estimated from field measurements of seven field pixels, and with an equivalent height of 4 meters estimated by eye.

2.4 *Modeling*

The linear reflectance model was used to obtain fractional vegetation cover by unmixing reflectance of each pixel into the area-weighted end-member reflectances. The

spectral reflectance of the pixel is derived from the atmospheric and topographic effect-corrected image. The spectral reflectance of six bands (3 visible and 3 near infrared) of the ETM+ image were employed to solve for the optimal *Fr* by a least squares algorithm. The model was applied with and without a shadow correction. Using field measurements for the end-members in (3) and (4), the linear and quadratic NDVI models were applied to estimate fractional vegetation cover. Pixel NDVI was calculated from the atmospheric and topographic effects-corrected pixel spectral reflectances. The results from the three models were then compared to the field measurements.

3. Results

The hyperspectral reflectances of surface end-members were measured on two types of surfaces (three study sites) in May, 2003, the same season as the acquired Landsat image. The reflectance was then resampled to match the six ETM+ bands, as shown in Figure VI-3. The tree spectral reflectance is the average reflectance of piñon and juniper at woodland sites. Since the spectral reflectance of dry grass (not shown) is close to that of the soil, and the dry grass cover is sparse at woodland sites, only soil spectral reflectance is used below. Correction factors for the shadow effect and the deformed vegetation projection are shown in Table VI-2. The calculated deformed projection factor (*PF*) for the ETM+ image is so low that the projection correction is negligible at all three sites. The NDVIs for end-members were calculated from the spectral reflectance data; they were 0.748 and 0.077 for the shrub and inter-canopy soil, respectively, at the shrub site, and 0.766 and 0.069 for the trees and inter-canopy soil, respectively, at the woodland sites. The soil-in-shadow NDVI was not significantly different from that of the soil in sun (we measured the soil at the shrub site, the relative difference is in the order of 10%).

Table VI-2 The dimensionless vegetation shadow-correction factor and deformed sensor projection-correction factor, and the associated parameters for the vegetation of the three study sites

	vegetation		solar position (degree)		sensor position (degree)		correction factors	
study sites	D[1] (m)	H[2] (m)	zenith	azimuth	zenith	azimuth	shadow (SF)	projection (PF)
Site 1-shrub	1	1	23.92	111.13	5.17	98.20	0.00	0.004
Site 2-woodland	2	4	23.92	111.13	3.68	98.20	0.37	0.002
Site 3-woodland	2	4	23.92	111.13	3.65	98.20	0.37	0.002

1: estimated based on field measurements

2: roughly estimated by eye

The fractional vegetation cover was calculated from the pixel spectral reflectances (for linear reflectance model) or NDVI (for two NDVI models), with the resulting statistics shown in Table VI-3. The linear reflectance model gives the largest *Fr*, while quadratic NDVI model gives the lowest. There is no significant shadow effect for the linear reflectance at Site 1 (the shrub site), because of the smaller vegetation (Table VI-2). With the larger vegetation at woodland Sites 2 and 3, the shadow effect is significant, with substantially lower estimated *Fr* from shadow-effect corrected linear reflectance model.

Table VI-3 The field measurements and statistics of fractional vegetation cover at the three sites for the linear reflectance model (without or with shadow-effect correction), linear NDVI model, and quadratic NDVI model

	statistics	field[1]	LR[2]	LRS[3]	LN[4]	QN[5]
Site 1-shurb	mean	0.3	0.306	0.306	0.117	0.014
	number of pixels	NA	375	375	375	375
	stand deviation		0.026	0.026	0.012	0.003
	minimum		0.227	0.227	0.081	0.007
	maximum		0.376	0.376	0.155	0.024
Site 2-woodland	mean	0.33	0.448	0.355	0.318	0.103
	number of pixels	4	375	375	375	375
	stand deviation		0.067	0.053	0.044	0.028
	minimum		0.285	0.226	0.201	0.040
	maximum		0.610	0.488	0.443	0.197
Site 3-woodland	mean	0.21	0.340	0.274	0.194	0.039
	number of pixels	3	375	375	375	375
	stand deviation		0.066	0.053	0.036	0.015
	minimum		0.174	0.139	0.083	0.007
	maximum		0.500	0.407	0.304	0.093

1: field measurement
2: linear reflectance model without shadow-effect correction
3: linear reflectance model with shadow-effect correction
4: linear NDVI model
5: quadratic NDVI model

The shadow correction is not shown for the two *Fr* NDVI models as there is no significant difference between soil NDVI in shadow and that in sunshine. At the shrub site, the linear reflectance model gives a mean fractional vegetation cover of 0.31, which agrees well with the shrub field measurement (*Fr* = 0.3) by Kurc and Small et al. (2004). Both linear and quadratic NDVI models significantly underestimate the actual fraction vegetation cover at this site. At the woodland sites, fractional vegetation cover of seven arbitrarily selected cells, four at Site 2 and three at Site 3, were measured in the field. The comparison of these seven field measurements to the model-derived *Fr* of respective pixels is shown in Figure VI-4. Without shadow-effect correction, the linear reflectance model significantly overestimates the actual *Fr*, the quadratic NDVI model strongly underestimates *Fr*, while the linear NDVI model gives the best estimation. With shadow-correction, the linear reflectance model estimates of *Fr* are still biased high, but much less than before the shadow-correction.

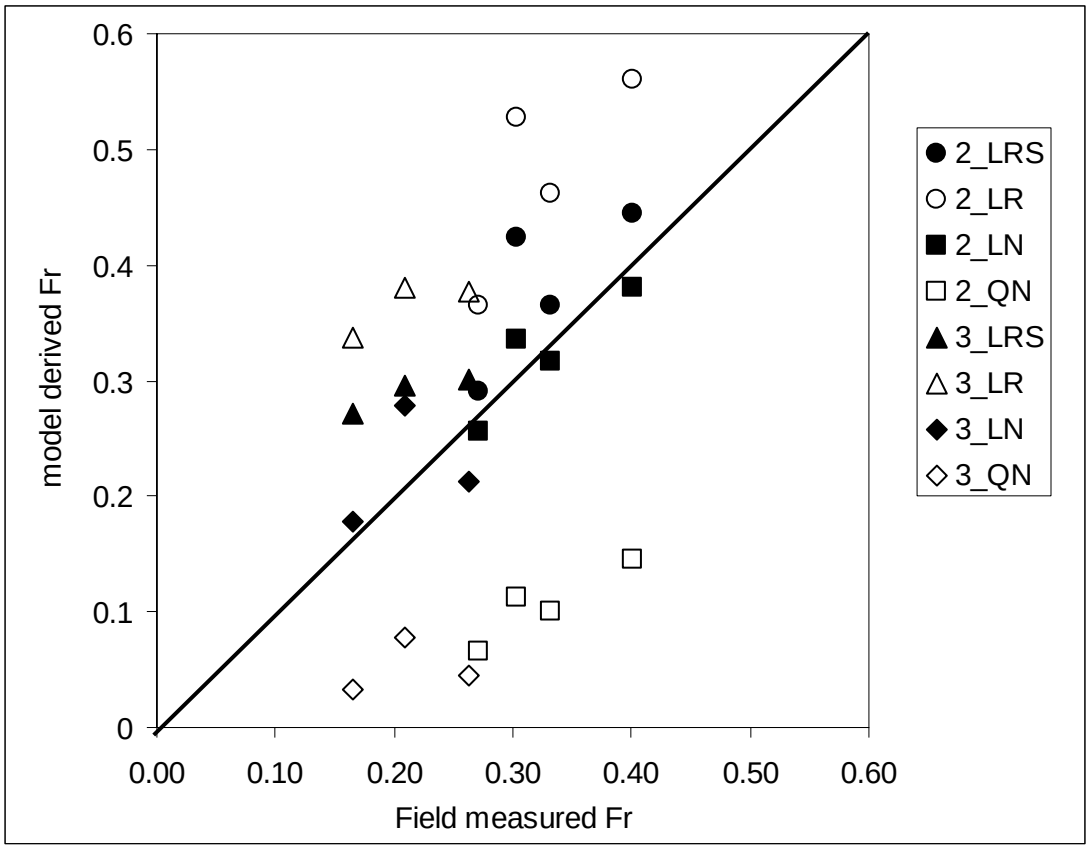

Figure VI-4 Comparison of model estimated *Fr* to the seven field measured *Fr* for the woodland sites, that is Site 2 and Site 3. (LR = linear reflectance model, LRS = linear reflectance model with shadow correction, LN = linear NDVI model, QN = quadratic NDVI model, 2 and 3 = site number).

4. Discussion

4.1 Model testing

The linear reflectance model is based on the assumption that the reflected radiant energy of a pixel is the simple sum of radiant energy reflected separately by the sub-pixel end-members. In other words, there is no radiometric interaction between end-members. When the vegetated surface is composed of spectrally separable and radiometrically isolated end-members, a mixed pixel can be simplified as a linear combination of end-members (Adams, Smith, & Johnson, 1986). However, some radiometric interaction

inevitably occurs between surface end-members, e.g., the vegetation and the soil in the inter-canopy space. This interaction increases the probability of photons being adsorbed by the surface, reducing the total surface reflectance. Without correction for these inter-member nonlinear effects, the linear reflectance model will overestimate the fractional cover of the end-member with the (overall) lower spectral reflectance. In the case of our two woodland sites, the fractional vegetation cover would be overestimated. Non-linear effects in the spectral mixture have been reported in a variety of papers (Roberts, Smith, & Adams, 1993; Borel & Gerstl, 1994; Ray & Murray, 1996). The good agreement between the linear reflectance model-derived *Fr* and in situ measurement at the shrub site (Site 1) demonstrates that these inter-member nonlinear effects were not very important at this site. This apparently stands in contrast to Ray & Murray's (1996) study in which a significant non-linear effect is reported for a similar creosote shrub area in the Mojave Desert.

Physically, reflectance on a surface is a nonlinear process because of multiple scattering. Non-linear spectral mixture occurs not only between end-members, but also within each end-member. Using a radiosity model Borel & Gerstl (1994) demonstrate that the vegetation above ground exhibits dramatically increased reflectance due to the nonlinear multi-scattering between the leaves and the substrate soil. The same phenomenon was revealed by Ray and Murray's (1996) experiments, where their nonlinear effect is mainly the multi-scattering between the creosote bush and the underlying substrate (a combination of soil, litter, and other organic matters). This underlying substrate is different from the inter-canopy space soil, one end-member in our models. This type of nonlinear effect is intra-member, and is already implicitly included

in the field measurements that we used to estimate the end-member spectral signatures. We believe that the difference in observed non-linear effects, between our study and Ray & Murray's, is primarily due to the difference of reflectance of creosote used in the unmixing analyses. The reflectance of the creosote used for our analysis is the measured reflectance on top of the creosote, which includes the overall absorption and scattering effects from the whole tree (leaves and branches above the ground surface) and the underlying layer of mixture of litter, roots, and soil. While, the reflectance of the creosote used in Ray & Murray's analysis only includes the absorption and scattering effects from the above ground biomass. The combined results of these two studies suggests that the major non-linear effect identified in Ray & Murray's study is mostly due to the interaction (absorption and scattering) between the above ground biomass and the ground surface covered by a creosote, rather than the radiative interaction between the creosote and the inter-creosote soil surface. In our study, this intra-member multi-scatting does not affect performance of the linear reflectance model because this nonlinear effect has already been implicitly included in the end-member's measured spectral reflectance. As long as the applied spectral reflectance represents the reflectance of the surface covered by the end-member, the linear reflectance model should give a reliable estimate of fractional vegetation cover. This is the physical basis of the model.

The vegetation shadow decreases the total spectral radiance by adding a new surface end-member with near zero spectral reflectance (Figure VI-3). There is no significant shadow effect at the shrub site (Site 1), mainly due to the limited height of the shrub (about 1 meter). However, shadow effects are clearly observed at the woodland sites (Sites 2 and 3) with their taller vegetation. The linear reflectance model estimation of *Fr*

at the woodland sites is significantly improved by adding shadow as an additional end member of approximately zero reflectance, further supporting the physical basis of that model (Figure VI-4). After the shadow-effect correction, the linear reflectance model still overestimates *Fr* compared to the field observation. Several reasons could explain this remaining *Fr* overestimation. First, with higher canopy LAI and taller tree height, radiometric interaction between the inter-canopy soil and the vegetation increases, and most of this interaction was probably not included in our field measurement. It was, however, viewed from the remote sensor. Second, radiometric multi-scattering occurs more frequently in piñon-juniper than in creosote, due to a much more complex canopy structure. The overall canopy spectral reflectance is different than the local spectral reflectance, as found, for example, in the difference of measured spectral reflectance at the leaf scale, branch, and canopy scales (Williams, 1991). Thus, the average of our multiple field point measurements may not be representative of the canopy spectral reflectance. Third, a portion of the canopy might be in shadow, an effect not be completely captured by our field point measurements. The 2nd and 3rd issues are related to nonlinearity in scaling the spectral reflectance from the local measurement to the whole canopy. Fourth, parameterization of the shadow model is only approximate. For example, at the woodland sites we used an equivalent maximum canopy diameter of 2 meters, slightly larger than what we measured in the field, and an estimated equivalent tree height of 4 meters. However, our parameterization likely overestimates shadow effects because piñon and juniper (especially juniper) often have a larger diameter-height ratio than we assumed. This cannot be the reason that the corrected linear reflectance model overestimates *Fr* at the two woodland sites, leaving the explanation to the nonlinear

spectral mixture between end-members and the nonlinear scaling effect from point field measurements to the canopy values.

In summary, the linear reflectance model is appropriate to estimate *Fr* on a surface where nonlinear inter-member spectral mixture effect is small, and the end-member spectral reflectance implicitly includes the intra-member nonlinear (spectral mixture and measurement scaling) effects reported by Borel & Gerstl (1994) and Ray and Murray (1996). The linear reflectance model is sensitive to environmental conditions, such as the shadow effect, varying soil spectral signatures, etc, and is undermined by degree of nonlinear spectral mixture if it is not implicitly included in the applied end-members' spectral signatures.

As a non-linear function of the reflectance, the NDVI of a pixel is not the linear combination of the NDVI of the subpixel end-members, making the physical interpretation of the linear and quadratic NDVI models difficult. The linear NDVI model underestimates *Fr* for the shrub site, while it gives surprisingly good estimates for the piñon-juniper woodland sites (Figure VI-4 and Table VI-3). The shadow effect on the reflectance of each band mostly cancels out when the ratio is taken in calculating the pixel NDVI, explaining why no significant difference was found between the shadow NDVI and the original soil NDVI. This suggests that the variation in performance of the linear NDVI model between the shrub site and the woodland sites is due to the site-specific characteristics other than the shadow effects. Two interesting site-dependent characteristics are the canopy leaf area index, which is over three for piñon and juniper while about one for the creosote shrub, and the vegetation height, about four meters for piñon and juniper while one meter for the shrub. Gutman and Ignatov (1998) provide a

function to adjust parameter values of linear NDVI model for situations with leaf area indexes lower than three. Application of this function for Site 1 (shrub) improves the linear NDVI model estimates of *Fr*, but they are still significantly underestimated (not shown). One possible reason for good performance of linear NDVI model at woodland sites is that the tall vegetation and larger canopy LAI increase the nonlinearity of spectral mixture at those sites, as we discussed above. This nonlinear spectral mixture is partially captured by NDVI, a nonlinear multi-band spectral transformation. Also, the nonlinear effect in scaling NDVI from point to whole canopy may be not as large as for the spectral reflectance. In summary, the linear NDVI model appears to perform well for surfaces covered by tall vegetation with high canopy LAI, but poor for short vegetation with low canopy LAI. The inconsistent performance of the linear NDVI model indicates that it is condition-specific, and suggests that the physics of the NDVI model may not be entirely appropriate for *Fr* estimation.

The quadratic NDVI model strongly underestimates *Fr* for all three sites (Figure VI-4 and Table VI-3). This indicates that the quadratic NDVI model is not appropriate for environments similar to our study sites. Actually, the quadratic NDVI model has never before been validated with field measured *Fr*. In the three papers that used the quadratic NDVI model, shown in Table VI-1, *Fr* was derived from either the SVAT model or a radiative transfer model.

4.2 Statistical relation of Fr and imaged-derived NDVI

Although the linear NDVI model provides good *Fr* estimates for the woodland sites, it performs poorly at the shrub site. We suggested physical reasons for this, and noted that the model may be condition specific. This implies that NDVI can be used in a purely

statistical approach to *Fr* estimation using site specific data. We tested linear and quadratic regressions between *Fr* and NDVI, without physically constraining parameter values, and proceeded to see if these regressions change with the spatial scale of the pixel and between vegetation types.

We first present regressions as a function of pixel size using only the data from the shrub site. We don't have actual field fractional coverage data for all 375 ETM+ pixels at this site. Instead we use a surrogate. With short shrub cover and a single species (creosote) on a very flat surface, and with the overall good agreement of the linear-reflectance-model results with the field measurement, it is reasonable to assume that the linear reflectance model gives reliable estimates of fractional vegetation cover for each pixel. This fractional coverage surrogate, from the 25×15 image of 28.5m ETM+ pixels, was upscaled (simple averaging) to a 8×5 image of 85.5m pixels (by dropping the eastern most column of 28.5m pixels) and to a 5×3 image of 142.5m pixels. We also upscaled to 285m pixels using simple averaging of overlapping domains to yield a 4×2 image of upscaled pixels (it was necessary to stay within the original site area to maintain homogeneous vegetation, and to overlap the 285m upscaled samples to get enough data for regression, although it is admittedly improper to regress correlated data). As shown in the first four rows of Table VI-4 there are statistically significant linear regressions between *Fr* and NDVI for all pixel sizes, although the coefficient of determination (R^2) is low. The performance of statistical *Fr* prediction functions improves when the pixel scale increases to 85m×85m and above.

We compared regressions between vegetation types by examining the woodland regression statistics for the seven field measured woodland *Fr* cells and their respective

~30m ETM+ pixel NDVIs, contrasting them with the regression for the shrubland ETM+ pixels (contrast first and last rows in Table VI-4). The woodland regression correlation is much better than that for the shrubland. For all cases, regardless of scale, including the quadratic terms does not significantly improve the regression and they are probably not needed.

Table VI-4 The linear and quadratic regressions between surrogate *Fr* (the shrub site) and image-derived NDVI for various pixel sizes, and between field-measured *Fr* and image-derived NDVI for the woodland sites

Surfaces	Pixel size meters (# of pixels)	Linear regression Fr=a*NDVI+b			Quadratic regression $Fr=c*NDVI^2+d*NDVI+e$				Contribution of the 2nd order term to the total variance
		a	b	R^2	c	d	e	R^2 (Adjusted R^2)	
Shrub land	~30*30 (375)	1.76	0.03	0.31	-24.7	9.4	-0.56	0.32 (0.32)	1%
	~90*90 (40)	2.79	-0.13	0.52	-132	43.4	-3.26	0.57 (0.56)	5%
	~150*150 (15)	3.19	-0.19	0.47	-526	166	-12.8	0.58 (0.55)	11%
	~300*300 (8)	4.22	-0.35	0.60	-1584	501	-39.3	0.66 (0.60)	6%
Woodland	~30*30 (7)	1.35	-0.08	0.74	5.36	-1.46	0.28	0.76 (0.71)	2%

It may be reasonable to apply fitted *Fr*-NDVI functions for fractional vegetation cover prediction at a surface with tall vegetation and high canopy LAI, and using NDVI derived from a low spatial resolution (or large pixel size) imagery, such as MODIS and Advanced Very High Resolution Radiometer (AVHRR) images (1 km × 1km). However, such fitted functions would be different from the previously described and often used theoretical linear NDVI and quadratic NDVI models, (3) and (4), and their coefficients would not necessarily have specific physical meaning. This is evident from the varying

regression coefficients with the changing pixel scales in Table VI-4. Instead of being derived from spectral reflectance measurement of surface end-members, these regression coefficients must be estimated from the calibration with many field-observed *Fr*'s for each site of interest. The regression between *Fr* and NDVI also depends on the vegetation characteristics. At the woodland sites in this study, tall vegetation and high canopy LAI increases the nonlinear spectral mixture, and the correlation between *Fr* and NDVI increases significantly (Table VI-4).

4.3 Why three different, non-complementary Fr models?

This discussion suggests that the linear reflectance model is the most reliable *Fr* model for the relatively sparse vegetation of a semi-arid environment, and is transferable between various vegetated surfaces as long as the nonlinearity of spectral mixture is small, or the nonlinear effects are captured in the applied end-member spectral signatures. However, the literature reports that both linear NDVI and quadratic-NDVI models have also been used to obtain fractional vegetation cover for this environment (Table VI-1). Why are such different and mutually exclusive models in use? Our results and discussion, and a review of the literature, suggests four explanations: (a) model performance depends on the spatial scale of the remote sensing data; (b) model parameters are obtained from different approaches, possibly deviating from their physical meaning as implied in the model structure; (c) some site-specific effects (e.g., shadow effects and nonlinear effects) are not corrected for in the models; and (d) surface spectral signatures derived from remote sensing images, from which pixel NDVI is typically calculated, are not corrected for atmospheric and topographic disturbance.

To examine whether scaling affects the performance of these three common models, the 375 pixels at each of the three sites were up-scaled from the normal ETM+ pixel size

(28.5×28.5 m^2) to 15 pixels of size 142.5×142.5 m^2. The reflectance of upscaled pixels at each site was obtained by the linear spectral mixture rule. The fractional vegetation cover was up-scaled in the same way. The upscale NDVI was calculated from the upscaled reflectance. Since field measurements of *Fr* were not available for every pixel of our study sites, the optimal *Fr* estimates, i.e., *Fr* estimated from the linear reflectance model for Site 1 and *Fr* derived from the linear NDVI model for Sites 2 and 3, were used as surrogates for fractional vegetation cover for each pixel. The three models were then applied with the upscaled pixel reflectance and NDVI to estimate the enlarged pixel *Fr*. The *Fr* obtained this way at an aggregated pixel is compared to the *Fr* upscaled directly and linearly from the *Fr* of the individual ETM+ pixels that constitute the aggregated pixel (Figures VI-5 and 6). The performance of the three models does not change significantly for the two different scales. Therefore, scaling does not appear to significantly affect the performance of the three models.

Consider different parameter estimate approaches. In other studies the NDVI of bare soil and 100% vegetation were estimated from the spectral signature of pixels with very large size (e.g., 0.15°) (Table VI-1), not from "direct measurement". At a large pixel scale, it is difficult to have a pure pixel with either 0% or 100% vegetation cover, leading to apparent $NDVI_0$ and $NDVI_\infty$ values that are different from their physical meaning. For example, Gutman & Ignatov (1998) applied a $NDVI_\infty$ of 0.52, much smaller than the 0.75 that we estimated from the field measurement. Derivation of *Fr* using these deviated values of $NDVI_0$ and $NDVI_\infty$ is not consistent with the NDVI model results that we describe in this paper. Similarly, as we discussed earlier, upscaling the local field

measurements to the canopy level may also lead to deviated end-member spectral signature, e.g., at the woodland sites in our study.

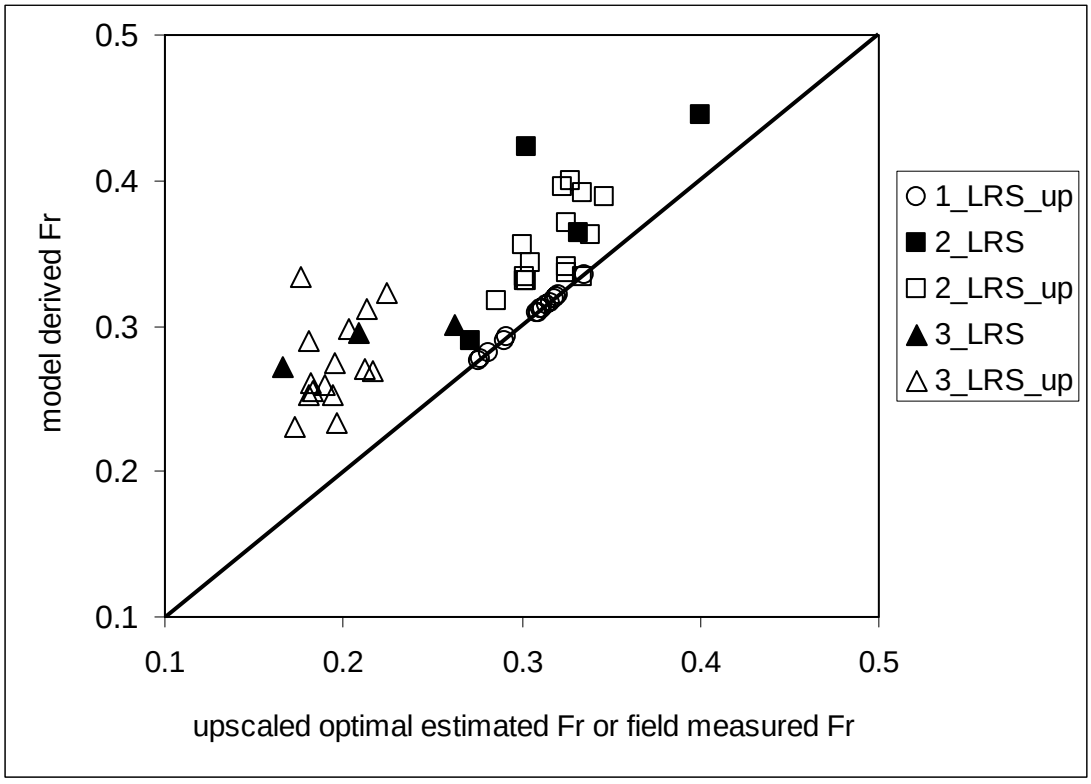

Figure VI-5 The performance of the shadow-effect-corrected linear reflectance model at three study sites at two pixel-scales. (#_LRS_up = the results of 15 synthetic large pixels (142.5×142.5 m^2) at each site, #_LRS = the results of normal ETM+ pixels, # (1, 2 or 3) = site number).

Failing to correct for site-specific effects may lead to malfunction of a model. In this study, the linear reflectance model without shadow correction for piñon-juniper sites significantly overestimates *Fr*. With the shadow correction, it performs better, but is still biased high for these sites. We earlier suggest that the tall vegetation and high canopy LAI at woodland sites may increase the radiometric interactions between the vegetation and the intra-canopy bare soil, as well as within the canopy, thus increasing the nonlinear spectral mixture. These nonlinear effects can be accounted for by the linear reflectance

model through the use of end-member spectral signatures that include the nonlinear effects. At the woodland sites, this can be achieved by measuring canopy reflectance and soil reflectance at a height above the canopy. But this does not completely solve the problem because the nonlinear effects on soil reflectance also depend on relative distance from the canopy, which is a function of *Fr*. Radiative transfer modeling could be used to better deal with the nonlinear spectral mixture. However, these models are difficult to conceptualize and parameterize for a vegetated surface. We also suggested that the nonlinear spectral mixture may also be responsible for the good performance of the linear NDVI model at the woodland sites. Further work is needed to test this hypothesis.

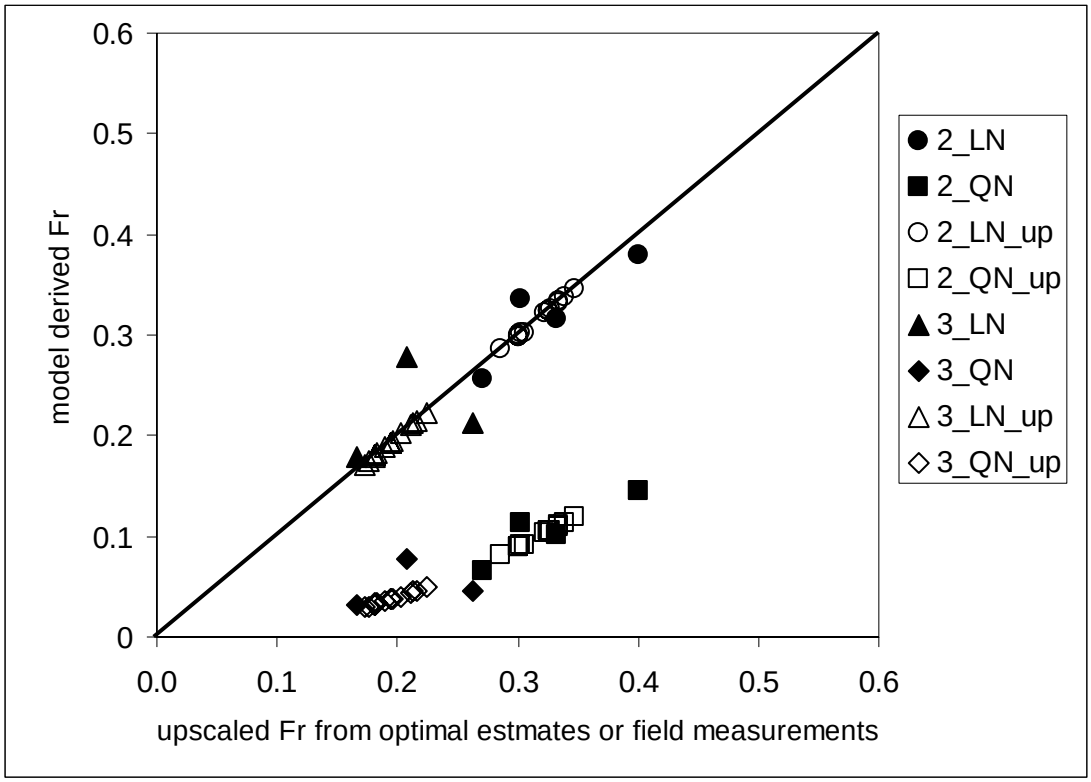

Figure VI-6 The performance of the linear and quadratic NDVI models at the two woodland sites at two pixel-scales. (LN = linear NDVI model, QN = quadratic NDVI model, #__up = the results of 15 synthetic large pixels (142.5×142.5 m^2) at each site, #_** = the results of normal ETM+ pixels, # (2 or 3) = the site number).**

Failing to correct for topographic and atmospheric disturbance in the apparent surface reflectance may also lead to malfunction of *Fr* models. For a linear NDVI model, Wittich & Hansing (1995) reported that un-corrected spectral signatures gave lower estimates of *Fr* than corrected spectral signatures. For their quadratic NDVI model, however, Carlson & Ripley (1997) showed that the estimated *Fr* was insensitive to atmospheric correction for both clear and hazy conditions. We compared the performance of the three *Fr* models in this paper with and without topographic and atmospheric corrections (Table VI-5). Failing to include atmospheric correction leads to significant *Fr* underestimates for both NDVI models, while the effect on the linear reflectance model is not as significant. The robust performance of the linear reflectance model is probably because all six bands are used to estimate *Fr* optimally. The topographic correction does not significantly change the model results at any of the three sites, of which two are sloped surfaces. However, we cannot exclude the topographic disturbance on *Fr* model performance because (a) both sloped surfaces are located in east slope of the Los Pinos Mountains in which two sites face to the morning sunshine when the Landsat 7 satellite passes over at 10:30 am or so local time, (b) only one ETM scene was used, (c) only mean pixel *Fr* was compared, and (d) the steepness of both sloped sites is small.

Table VI-5 Comparison of mean fractional vegetation cover for three sites from three Fr-models with radiance data without any correction, with atmospheric correction, and with both atmospheric and topographic correction, respectively

effects corrected	site 1(shrub)				site2 (woodland)				site3 (woodland)			
	field[1]	LRS[2]	LN[3]	QN[4]	field	LRS	LN	QN	field	LRS	LN	QN
atmospheric topographic	0.30	0.31	0.117	0.014	0.33	0.355	0.318	0.103	0.21	0.274	0.194	0.039
atmospheric	0.30	0.31	0.117	0.014	0.33	0.344	0.319	0.103	0.21	0.276	0.195	0.039
none	0.30	0.31	0.076	0.006	0.33	0.315	0.233	0.056	0.21	0.253	0.130	0.018

1: field measurement
2: linear reflectance model with shadow-effect correction
3: linear NDVI model
4: quadratic NDVI model

5. Conclusions

Fractional vegetation cover, *Fr*, was estimated for a Landsat ETM+ image of semi-arid central New Mexico, using three common models, and compared with ground measurements. The physically based linear reflectance model reliably estimates the fractional cover of short vegetation, where the nonlinear spectral mixture between end-members is small. Corrections (e.g., shadow-effect correction) are necessary when this model is applied to a complex surface with tall vegetation of high canopy LAI. Another advantage of this model is that the spectral signatures of all visible and near-infrared bands can be utilized in the calculation, and it is insensitive to the atmospheric radiometric disturbance. Results suggest that the strong physical basis of the linear reflectance model provides advantages over the other two models and make it is less site-dependent. However, nonlinear effects (both spectral mixture and scaling) within the end-members and between end-members, if not included in the applied end-member spectral signature, may lead to model malfunction.

The physical meaning of NDVI based models is much more difficult to interpret. The linear and quadratic relationships between *Fr* and NDVI are actually more fitting functions than physically robust relationships. Comparison of the model-derived *Fr* to ground measurements shows that the linear NDVI model can be used to estimate *Fr* on a surface with tall vegetation and high canopy LAI, where the nonlinear spectral mixture effect is significant. It is not sensitive to the vegetation shadow effect. But it performs poorly for short and low LAI vegetation, where the inter-member nonlinear spectral effect is not significant. The quadratic NDVI model did not perform well at any of the sites. The parameters in the two NDVI models are site-specific fitting numbers. This can be deduced from that the fact that both NDVI models strongly underestimated *Fr* of the low LAI and short vegetation surface when the physically-meaningful values were applied to the models.

Without constraints to the physical meaning of the parameters, there are statistically significant linear regressions between *Fr* and image-derived NDVI. The performance of the fitted Fr-NDVI functions improves when the pixel size increases, though these fitted functions and their coefficients would have to be estimated from the calibration with many field-observed *Fr*'s for each site of interest. Including quadratic terms did not significantly improve regressions; they are probably not needed.

References

Adams, J.B., Smith, M.O., and Johnson, P.E. (1986). Spectral mixture modeling: a new analysis of rock and soil types at the Viking Lander I site, *Journal of Geophysical Research*, 91(B8), 8098-8112.

Asner, G.P., and Heidebrecht, K.B. (2002). Spectral unmixing of vegetation, soil and dry carbon cover in arid regions: comparing multispectral and hyperspectral observations, *International Journal of Remote Sensing*, 23,3939-3958.

Borel, C. C., and Gerstl, S. A. W. (1994). Nonlinear spectra mixing models for vegetative and soil surfaces, *Remote Sensing of Environment*, 47, 403-416.

Carlson, T. N. and Ripley, D.A. (1997). On the relation between NDVI, fraction vegetation cover, and leaf area index, *Remote Sensing of Environment*, 62, 241-252.

Crippen, R.E. (1987) The regression intersection method of adjusting image data for band ratioing, *International Journal of Remote Sensing,* 8,137-155.

Choudhury, B.J., Ahmed, H.U., Idso, S.B., Reginato, R.J., and Daughtry, C.S.T. (1994). Relations between evaporation coefficients and vegetation indices studied by model simulations, *Remote Sensing of Environment*, 50,1-17.

Duffie,J.A. and Beckman, W.A. (1991). *Solar engineering of thermal processes*. John Wiley and Sons, NY.

Gertner, G., Wang, G., Fand S., and Anderson, A.B. (2002). Mapping and uncertainty of predictions based on multiple primary variables from joint co-simulation with Landsat TM image and polynomial regression, *Remote Sensing of Environment*, 83, 498-510.

Gillies, R.R, Carlson, T.N., Cui, J., Kustas, W.P., and umes, K.S. (1997). A verification of the 'triangle' method for obtaining surface soil water content and energy fluxes from remote measurements of the Normalized Difference Vegetation Index (NDVI) and surface radiant temperature, *International Journal of Remote Sensing,* 18,3145-3166.

Gutman, G. and Ignatov, A. (1998). The derivation of the green vegetation fraction from NOAA/AVHRR data for use in numerical weather prediction models, *International Journal of Remote Sensing*, 19,1533-1543.

Hobbie, J.E., Carpenter, S.R., Grimm, N.B., Gosz, J.R., and Seastedt, T.R. (2003). The US Long Term Ecological Research Program, *BioScience*, 53, 21-32.

Huete, A.R. (1986). Separation of soil-plant mixtures by factor analysis, *Remote Sensing of Environment*, 19, 237-251.

Karnieli, A., Gabai, A., Ichoku, C., Zaady, E. and Shachak, M. (2002). Temporal dynamics of soil and vegetation spectral responses in a semi-arid environment, *International Journal of Remote Sensing*, 23,4073-4087.

Kurc, S.A., and Small, E.E. (2004). Dynamics of evapotranspiration in semiarid grassland and shrubland during the summer monsoon season, central NM, *Water Resources Research*, in review.

Landsat 7 Science Users Handbook (2003). Landsat Project Science Office, NASA Goddard Space Flight Center in Greenbelt, Maryland, http://ltpwww.gsfc.nasa.gov/IAS/handbook/handbook_toc.html.

Markham,B.L., and Barker, J. L.(1986). Landsat MSS and TM post-calibration dynamic ranges, exoatmospheric reflectances and at-satellite temperatures, *EOSAT Landsat Tech. Notes* (Aug.), 3-8.

Ramsey, M.S., and Christensen, P. R. (1998). Mineral abundance determination: quantitative deconvolution of thermal emission spectra. *Journal of Geophysical Research* 103 (B1), 577-596.

Ray, T.W., and Murray, B.C. (1996). Nonlinear spectral mixing in desert vegetation, *Remote Sensing of Environment, 55*, 59-64.

Roberts, D.A. (1991). *Separating spectral mixtures of vegetation and soils*, Ph.D. thesis, University of Washington.

Roberts, D. A., Smith, M. O., and Adams, J. B. (1993). Green vegetation, nonphotosynthetic vegetation, and soils in AVIRIS data, *Remote Sensing of Environment, 44*(2-3), 255-269.

Roberts, D. A., Gardner, M., Church, R., Ustin, S., Scheer, G., & Green, R. O. (1998). Mapping chaparral in the Santa Monica Mountains using multiple endmember spectral mixture models, *Remote Sensing of Environment, 65*(3), 267-279.

Sabol, D. E., Adams, J. B., and Smith, M. O. (1992). Quantitative subpixel spectral detection of targets in multispectral images, *Journal of Geophysical Research*, 97, 2659-2672.

Smith, M.O., Ustin, S.L., Adams, J.B., and Gillespie, A.R. (1990a). Vegetation in deserts, I. A regional measure of abundance from multispectral images, *Remote Sensing of Environment*, 31, 1-26.

Smith, M.O., Ustin, S.L., Adams, J.B., and Gillespie, A.R. (1990b). Vegetation in deserts, II. Environmental influences on regional abundance, *Remote Sensing of Environment*, 31, 27-52.

Williams, D. L. (1991). A Comparison of spectral reflectance properties at the needle, branch, and canopy level for selected conifer species, *Remote Sensing of Environment*, 35(2-3), 79-93.

Wittich, K. P., and Hansing, O. (1995). Area-averaged vegetative cover fraction estimated from satellite data, *International Journal of Biometeorology*, 38, 209-215.

Zhou, X. and Li, S. (2003). Comparison between in situ and MODIS-derived spectral reflectance of snow and sea ice in the Amundsen Sea, Antarctica, *International Journal of Remote Sensing*, *24*(24), 5011-5032.

Appendix VII Sunrise and sunset hour angles for particular tilted surfaces

The incoming solar radiation to an arbitrary sloped surface depends on two variables. They are the solar incident angle (Equation 4.10), and the time during which the sun illuminates on the surface (Equation 4.12). The equation for solar incident angle on an arbitrary sloped surface is available from literature (Equation 4.11), while it is not available for daily solar illuminating hours. The appendix develops equations for calculating the daily solar illuminating hours on north-, east-, and west-facing slope surfaces.

North-facing surface

For tilted north-facing surface, the sunrise and sunset hour angles are symmetric. As shown in Figure VII-1, the sun should rise above the plane extended from the tilted surface so that the surface can see it. Thus, the sunrise or sunset hour angle corresponds to the situation where OB=CD , shown in the figure (γ_s is the solar azimuth angle, zero due to the south, east negative, and west positive; θ_z is the solar incident angle on horizontal surface, solar zenith angle).

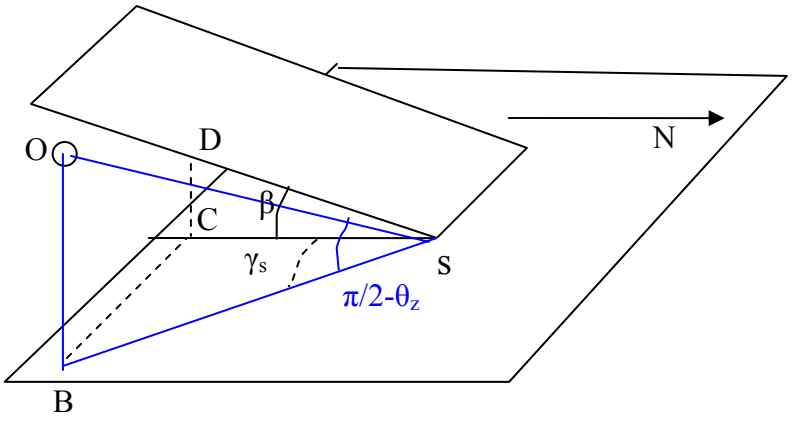

$$OB = \tan(\frac{\pi}{2} - \theta_z)AB$$
$$CD = \tan(\beta)AC$$
$$AC = \cos(\gamma_s)AB$$

Figure VII-1 Schematic diagram showing a north-facing slope and the solar position.

From the geometrics, we have

$$\tan(\pi/2 - \theta_z) = \tan\beta\cos\gamma_s \qquad \text{(VII-1)}$$

For this problem, the solar azimuth angle between $-\pi/2$ and $\pi/2$ is good enough. We adopt the formula from Braun and Mitchell [1983] [Duffie & Beckman, 1991, p16].

$$\sin\gamma_s = \frac{\sin\omega\cos\delta}{\sin\theta_z} \qquad \text{(VII-2)}$$

$$\cos\theta_z = \cos\phi\cos\delta\cos\omega + \sin\phi\sin\delta \qquad \text{(VII-3)}$$

In these three equations, the three unknowns are θ_z, γ_s, and ω. Other variables, latitude φ, slope angle β, and solar inclination angle δ, are known. The equations can be solved

numerically for sunset hour angle ω_s. The sunrise hour angle is negative of the sunset hour angle.

East- or west-facing surface

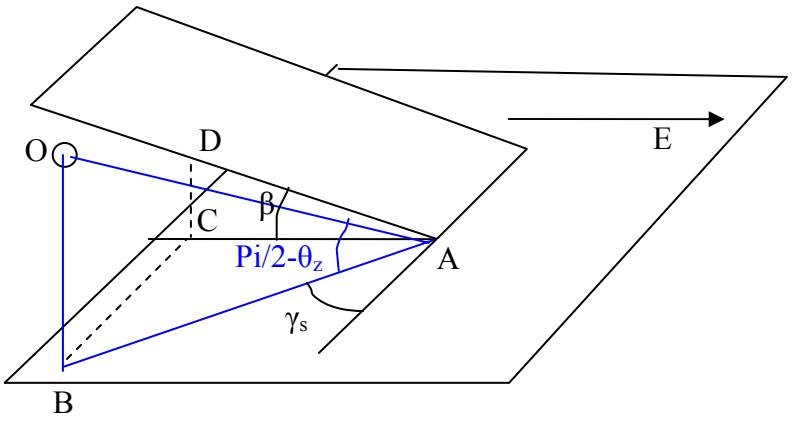

$$OB = \tan(\frac{\pi}{2} - \theta_z)AB$$
$$CD = \tan(\beta)AC$$
$$AC = \sin(\gamma_s)AB$$

Figure VII-2 Schematic diagram showing an east-facing slope and the solar position.

Similar to the north-facing surface, the sunrise and sunset hour angle of east-/west- facing surfaces can be solved from the geometrics (Figure VII-2).

$$\tan(\pi/2 - \theta_z) = \tan\beta \sin\gamma_s \qquad \text{(VII-4)}$$

With equations VII-2~4, we can solve for ω_s. For an east-facing slope, what we solve for here is the sunset hour angle, because solar azimuth angle is positive in the afternoon. The sunrise angle is approximately equal to that of a flat surface, i.e., $-\omega_{s0}$. For a west-facing slope, we solve for sunrise hour angle, with sunset hour angle equal to ω_{s0}.

References

Braun, J.E., and J.C. Mitchell (1983), Solar geometry for fixed and tracking surfaces, *Solar Energy*, 31, 439.

Duffie, J.A., and W.A. Beckman (1991), *Solar engineering of thermal processes*, New York, Wiley, 2nd edition, 919p.

Appendix VIII Derivation of TVET two-component equations

This appendix derives the major equations of the TVET model, which fills the gap between Equations (4.25 and 4.26) and Equations (4.27 and 4.28) in §4.4.5.

The total available energy for latent heating and sensible heating of the surface is first partitioned into two potions: the canopy part (A_s) and the inter-canopy bare soil part (A_c). A_s and A_c are further partitioned into latent heat and sensible heat, using the patch approach (§4.4.1). The energy balance equations:

$$A_c = Fr * (\lambda E_c + H_c) \qquad \text{(VIII-1)}$$

$$A_s = (1 - Fr) * (\lambda E_s + H_s) \qquad \text{(VIII-2)}$$

for cover $0 < Fr < 1$, where A is the available energy for sensible heating and latent heating; λE is the energy for transpiration; H is the energy used for heating the air; subscripts s and c represent the substrate soil and the vegetation, respectively; Fr is the fractional vegetation cover. Please note that in equations (VIII-1) and (VIII-2), the energy term ($Jm^{-2}day^{-1}$) on the left-hand site is a quantity evaluated over the total surface, while the energy terms on the right-hand site are quantities evaluated over the sub-component areas. The Fr term is used for unit conversion between the energy from the layer approach on the left-hand side and that for the patch approach on the right-hand side.

On each component surface, heat transfer equations are

$$H_c = \frac{1}{r_a^a + r_a^c} \rho_a c_p (T_0^c - T_z) \quad \text{(VIII-3)}$$

$$H_s = \frac{1}{r_a^a + r_a^s} \rho_a c_p (T_0^s - T_z) \quad \text{(VIII-4)}$$

where ρ_a is the density of the air, c_p is the specific heat capacity of the air, T_0^c is the temperature of the vegetation surface, T_0^s is the temperature of the soil surface, T_z is the temperature of the air at some reference height z, r_a is the aerodynamic resistances shown in Figure 4.2, while superscripts s and c represent the bare substrate soil and the vegetation, respectively. On each component surface, vapor transfer equations (from vegetation/substrate surface to the air stream at reference height) are:

$$\lambda E_c = \frac{1}{r_a^a} \frac{\rho_a c_p}{\gamma} (e_0^c - e_z) \quad \text{(VIII-5)}$$

$$\lambda E_s = \frac{1}{r_a^s + r_a^a} \frac{\rho_a c_p}{\gamma} (e_0^s - e_z) \quad \text{(VIII-6)}$$

where e_0 is the vapor pressure at the effective canopy surface, e_z is the vapor pressure at the reference height z, and γ is the psychrometric constant (= 66 Pa/K). Vapor transfer equation (from the bulk leaf stomata to the bulk vegetation surface) is

$$\lambda E_c = \frac{1}{r_s^c + r_a^c} \frac{\rho_a c_p}{\gamma} (e_s(T_0^c) - e_0^c) \quad \text{(VIII-7)}$$

where r_s^c is the intra-canopy aerodynamic resistance. Combining of (VIII-5) and (VIII-7) leads to the following equation for vapor transport:

$$\lambda E_c = \frac{1}{r_s^c + r_a^c + r_a^a} \frac{\rho_a c_p}{\gamma} (e_s(T_0^c) - e_z) \qquad \text{(VIII-8)}$$

Equation (VIII-8) requires the saturated vapor on the target (here the vegetation) surface. However, the temperature and vapor pressure (or air humidity) are measured at the reference height *z*. Penman [*1948*] used the following equation to connect saturated vapor pressure on the surface to that at the reference height.

$$e_s(T_0) = e_s(T_z) + \Delta(T_0 - T_z) \qquad \text{(VIII-9)}$$

where e_s is the saturated vapor pressure, Δ represents the slope of the saturated vapor pressure versus temperature curve. From (VIII-8), substituting (9), then (3), and then (1), we have

$$\lambda E_c = \frac{\frac{\Delta A_c}{Fr} + \frac{\rho_a c_p}{r_a^c + r_a^a}(e_s(T_z) - e_z)}{\Delta + \gamma(1 + \frac{r_s^c}{r_a^c + r_a^a})} \qquad \text{(VIII-10)}$$

Similarly, from (VIII-6), substituting (9), then (4), and then (2), we have

$$\lambda E_s = \frac{\frac{\Delta A_s}{1-Fr} + \frac{\rho_a c_p}{r_a^a + r_a^s}(e_s(T_z) - e_z)}{\Delta + \gamma} \qquad \text{(VIII-11)}$$

Since λE_c and λE_s in equations (VIII-10) and (11) are quantities evaluated over the sub-component areas, the equivalent values for the total surface area are adjusted to become:

$$PT = \frac{\Delta A_c + Fr\frac{\rho_a c_p}{r_a^c + r_a^a}(e_s(T_z) - e_z)}{\Delta + \gamma(1 + \frac{r_s^c}{r_a^c + r_a^a})} \qquad \text{(VIII-12)}$$

$$PE = \frac{\Delta A_s + (1-Fr)\frac{\rho_a c_p}{r_a^a + r_a^s}(e_s(T_z) - e_z)}{\Delta + \gamma} \qquad \text{(VIII-13)}$$

References

Penman, H.L. (1948), Natural evaporation from open water, bare soil, and grass. *Proceeding of Royal Society London*, Ser. A., 193, 120-146.

Appendix IX Stomatal resistance and Jarvis-type functions

Vegetation regulates transpiration rate via its stomata, in response to the environmental conditions. Jarvis-types functions are adopted to represent these stomatal behaviors. The mean leaf stomatal resistance is assumed to be a function of vegetation type and the environmental conditions, such as vapor pressure deficit and short-wave radiation, (IX-1) [*Jarvis, 1976; Stewart, 1988; Lhomme et al. 1998*].

$$r_{ST} = r_{ST\_\min} * f_1(D) * f_2(I'_{on}) * f_3(T) * f_4(\psi_l) \qquad \text{(IX-1)}$$

where r_{ST_min} is the minimum mean leaf stomatal resistance at optimal conditions; D is the vapor pressure deficit; G'_{on} is the incoming solar irradiance; T is the air temperature; and ψ_l is the leaf water potential.

In equation (IX-1), leaf water potential is related to soil water potential. The term $f_4(\psi_l)$ accounts for the effect of soil water condition on the stomatal resistance. Since we treat this effect by hydrological modeling in vadose zone, $f(\psi_l)$ is not included in the procedure to generate the atmospheric boundary condition, *PT*. Instead, the soil water potential effect on transpiration is regulated by the root-water-uptake model in HYDRUS. The function of $f_1(D)$ is suggested by Jarvis [*1976*], Stewart [*1988*], and Noilhan and Planton [*1989*], and is given in (IX-2) [*Lhomme et al. 1998*].

$$f_1(D) = \frac{1}{(1 - aD)} \qquad \text{for } 0 < D < 1/a \qquad \text{(IX-2)}$$

where a is an empirical coefficient, which is 0.06~0.08 for pine with D in g/kg, or (3.49~4.65)*10^{-4} Pa^{-1} for D in Pa [Stewart 1988]. Noilhan and Planton [*1989*] give the value of a for coniferous forest of 2.5 *10^{-4} Pa^{-1}.

The function of $f_2(I_{on}')$, equation (IX-3), is given by Stewart [*1988*], and Lhomme et al. [*1998*].

$$f_2(I'_{on}) = \frac{I'_{on} + c}{(1 + \frac{c}{1000}) * I'_{on}} \qquad \text{(IX-3)}$$

where I'_{on} is the solar irradiance on the surface during time of interest, in Wm^{-2}; c is empirical coefficient, about 100 for a pine forest in England [*Stewart, 1988*], and 400 for the Konsa Prairie in Kansas [*Stewart and Gay, 1989*]. These values were estimated from a short period of the daytime. Thus, they need to be adjusted when solar radiation is used in the equation.

The function of $f_3(T)$ is suggested by Dickinson [*1984*], Noilhan and Planton [*1989*], and Lhomme et al. [*1998*], and is given in equation (IX-4).

$$f_3(T) = \frac{1}{1 - k_T (T_x - T)^2} \qquad \text{(IX-4)}$$

where k_T=0.0016 and T_x=25^{0}C [*Lhomme et al. 1998*]. We also suggest a switch function to describe the dormancy of the vegetation due to the low temperature, while neglecting the temperature effect when it is above the dormancy temperature.

$$f_3(T) = 1 \qquad \text{for } T > T_d$$

$$f_3(T) = \infty \qquad \text{for } T \le T_d \qquad \text{(IX-5)}$$

where T_d is the temperature below which the vegetation becomes complete dormant.

References

Jarvis, P.G. (1976), The interpretation of leaf water potential and stomatal conductance found in canopies in the field, *Philos. Trans. R. soc. London, Ser*. B, 273, 593-610.

Lhomme, J.P., E. Elguero, A. Chehbouni, and G. Boulet (1998), Stomatal control of transpiration: Examination of Monteith's formulation of canopy resistance, *Water Resources Research*, 34, 2301-2308.

Noilhan, J. and S. Planton (1989), A simple parameterization of land surface processes for meteorological models, *Monthly Weather Review*, 117, 536-549.

Stewart, J.B. (1988), Modeling surface conductance of pine forest, *Agric. For. Meteorol.,* 43, 19-37.

Stewart, J.B., and L. W. Gay (1989), Preliminary modeling of transpiration from the FIFE site in Kansas, *Agric. For. Meteorol*., 48, 305-315.

Appendix X TVET MATLAB code

```
%*************************************************************************************
%      A Topography- and Vegetation-based surface energy partitioning algorithm for ET modeling      *
%                                   (TVET) version 1.0                                                *
%                                      By Huade Guan                                                  *
%                              Hydrology Program, New Mexico Tech                                     *
%                                      November, 2004                                                 *
%*************************************************************************************

%*************************************************************************************
% This MATLAB code is designed to generate atmospheric boundary conditions (PE,PT,                   *
% active water for infiltration) for near-surface hydrologic modeling on partially                   *
% vegetated sloped surfaces. The flux is adjusted perpendicular to the top boundadry,                 *
% the way that HYDRUS 2D treats the boundary conditions for sloped surface in HYDRUS.                 *
%                                                                                                     *
% The major features of TVET model are
% (1) Generating PE and PT separately based on surface topograpy and vegetation cover                 *
% (2) Considering slope steepness and aspect effects on surface available energy                      *
% (3) energy partition based on vegetation characteristics (coverage, structures, etc.)               *
% (4) rainfall interception, snow and snowmelt                                                        *
% (5) environmental contraint on vegetation transpiring                                               *
% (6) correction for site aridity                                                                     *
%                                                                                                     *
% The required input data, the number in () is the column number                                      *
% (1)year,(2)month or julian days, (3)day, not necessary if julian days provided                     *
% (4)daily precipitation in mm, (5)min.daily T in degC,(6)max. daily T. in degC                       *
% (7)daily mean windspeed(m/sec), if not available, use 2 m/sec.                                      *
% (8)daily sunshine hours (hours), or solarsolar radiation (J/m^2/day)                                *
% (9)relative humidity (%), or dew point (degC)                                                       *
```

```
% For those columns having two options, adjust switch parameter value to tell which                *
% data is provided.
% Two example input data 'input_type1.txt' and 'input_type2.txt' are provided                       *
% type1: julian day, RH, daily solar radiaiton used, note setting the swithes correctly             *
% type2: month and day, Tdew, and actual sunshine hour used, check the swithes.                     *
%                                                                                                   *
% Two functions (hillfunct, julian) are working together with this routine.                         *
%                                                                                                   *
% The output file pept_output.txt                                                                   *
% column (1~3) = input file, (4) PT (mm/day) for sloped surface                                     *
% (5) PE (mm/day) for sloped surface, (6) It, Interception (mm)                                     *
% (7) daily active water for infiltration                                                           *
%                                                                                                   *
% Some parameter values provided in this code have not been tested                                  *
% Any comments and questions, please contact hdguan@nmt.edu or jwilson@nmt.edu                      *
%***************************************************************************************************
```

Major routine

```
clear all;

% Input parameters
%-------------------------------------------------------------------------
% constant (usually not necessary to change)
   cp=1.013e3;                    %specific heat at constant pressure, in J/(kg*degC)
   eps=0.622;                     %ratio molecular weight of water vapor/dry air
   Gsc=1367;                      %solar constant, in J/(m^2*sec)
   sigma=5.6697*10^(-8);          % Stefan_Boltzmann constant in J/(k4m2sec)
   k=0.41;                        % von Karman constant
   rhop_a=1.292;                  % kg/m^3, density of air
```

```
   rhop_w=1000;                    % kg/m^3, density of water
   lamda_f=3.33e5;                 % latent heat of snow melt (J/kg)
%-------------------------------------------------------------
% site specific parameters  (indented lines are derivations, not necessarily changed)
   long=-107.1813;
   lat=33.9755;
   elev=3243;                      % meter above sea level
   slope=20;                       % slope angle in degree
      slpcrrct=cos(slope/180*pi);
   aspect=180;                     % surface azimuth angle, 0 due south, -90 due east, and 90 due west
   fr=0.5;                         % fractional vegetation cover
   alpha_v=0.20;                   % albedo of the vegetation,
   alpha_s=0.30;                   % albedo of the soil,
   alpha_sn=0.50;                  % albedo of snowcover
   swe=0;                          % initial the snow water equivalent
%-------------------------------------------------------------
% parameters for daily available energy (not used if measured solar radiation is available)
% don't change unless you have your own functions
   as=0.25;                        % Rns=(1-alpha)*Rs24*(as+bs*n/N)
   bs=0.50;
   G=0;                            % daily energy lost to the ground J/(m^2 day)
   swe1=2.0;                       % the threshold swe below which snow albedo linearly decreases to zero

%-------------------------------------------------------------
% vegetation parameters; (indented lines are derivations, not necessarily changed)
   Lc=5;                           % canopy leaf area index
      L=Lc*fr;                     % surface leaf area index
   h=5;                            % vegetation height
      d=0.67*h;                    % zero plane displacement, m (Shuttleworth, 1993).
      zm=0.123*h;                  % roughness length for momentum transfer, m
      zh=zm/2.0;                   % roughness length for heat and vapor transfer, m, for forest
```

```
                                % for grasses,/12.0, for crop /7.0, (Mo et al., 2004);

   zms=0.005;                   % rouhgness length for momentum transfer on the substrate, m
      zhs=0.1*zms;              % roughness length for heat and vapor transfer on the substrate, m
   z=h+2;                       % reference height at which windspeed, humidity is measured, m

   kc=0.4;                      % extinction coefficient of beer's law

% paramters for bulk stomatal resistance (estimated from Korner 1994)
    rST_min=180;                % mean minimum stomatal resistance for coniferous tree, sec/m
    %rST_min=210;               % for shrub
    %rST_min=130;               % for grass

% parameters for intra-canopy aerodaynamic resistance
   alpha_w=2.5;                 % wind-extinction coefficent Mo (2004) used 2.5
   alpha_0=0.005;               % coefficient with unit of ms^(-1/2)Mo (2004) used 0.005
   lw=0.03;                     % characteristic leaf width (m).
%-----------------------------------------------------------------
% switches (or flags)
   rht=2;                       % rht==1 , RH is used; or rht==2, T_dew is used; rht==0, T_dew=f(T_min) for D
   sundata=0;                   % sundata==0, daily sunshine hour data; ==1, daily solar radiation data J/m^2
   jorm=0;                      % the date in input file is in julian (column #2) for jorm==1, and in month and day for jorm==0

   sunt=1;                      % runt==1, solar radiation effect on rST, sunt==0, not effect on rST
   Tt=1;                        % Tt==1, temperature effect on rST; if only dormancy effect, Tt=1, and kT=0.
   VPDt=1;                      % VPDt==1, vapor pressure deficit effect on rST is on, otherwise VPDt=0;

   aridt=1;                     % do correction for site aridity,
                                % ==1 do Temesgen's correction, ==2 do Jensen's correction  ==0, no correction

% parameters for correction of site aridity
```

```
% don't change unless you have your own functions
   kx=0.6; kn=0.45; kd=0.55;          % for Temesgen's correction (0.7, 0.4, 0.6 for arid (semiarid) tropical climates)
                                      % (0.5, 0.5, and 0.5)for humid and semi-humid teperate climates
   kj=4; pret=0.5;                    % for Jensen's correction, pret is long term P/PET

% paramters for Jarvis functions
% don't change unless you have your own functions
                                      %rST=rST_min*f1(D)*f2(Rs_24)*f3(T)
   f1a=3.5e-4;                        % parameters for f1(d)=1/(1-aD), for coniferous trees, Pa-1
   f2c=100;                           % parameters for f2(Rsun)=(Rsun+c)/[(1+c/1000)*Rsun], caution: big uncertainty!
   kT=0;                              % parameters for f3(T)=1/[1-kT(Tx-T)^2], degC-1, make it zero to shut this function down
                                      % kT=0.00137, not recommended if aridt=1
   Tx=25;                             % degC
   Td=-2;                             % temperature for complete dormancy of the vegetation, make it -100 to shut down this function
%-----------------------------------------------
% parameters for interception and snowmelt
% don't change unless you have your own functions
   Imax=1;                            % the maximum interception in mm for the surface with L=1
   Tm=0;                              % temperature to initiate the snowmelt (degC)
   ksm=3.6;                           % empirical coefficient in Pm=ksm(Tmean-Tm), mm/(day degC)
   Tsnow=0;                           % temperature to partition precip into snow and rainfall
%-----------------------------------------------
% input daily weather data:
   %(column 1)year, (2)month or julian day, (3)day, (4)precip.(mm), (5)Tmin(degC), (6)Tmax
   %(7)windspeed(m/sec), (8)sunshine hour (hour) or solar radiation (J/m^2/day),
   %(9)humidity (relative humidity in %)or dew point

   meteo=load('input_type2.txt');
      days=size(meteo,1);             % the total number of the days

%************************** no inputs are required below this line ************************************
```

```
%-------------------------------------------------------------------------------------------------
% creat the matrix for daily on_site potential transpiration(PT 4) on_site potential evaporation(PE 5),
   %interceptionloss(It 6) and net precipitation into the ground-surface (P_active 7).

   PET=zeros(days, 8);              % year, month/J, day, PT, PE, It, PI
   pars=zeros(days, 17);            % Ritg, albedo, Rns, Rnl, Ait, Asm, As, Ac, raa, ras, rac, rsc, f1, f2, f3, MDD, ed

   Aloan=0; %swe=0;

% calculate PT and PE in for_loop
  for i=1:days
   PET(i, 1)=meteo(i,1); PET(i,2)=meteo(i,2); PET(i,3)=meteo(i,3);        % save the date for PT matrix
   if jorm==1
      J=meteo(i,2);
   else
      J=julian(meteo(i,1), meteo(i,2), meteo(i,3));                      % number of the day in the year 1~365/366
   end
   precip=meteo(i,4)*slpcrrct;                                           % daily precipitation in mm
   T_max=meteo(i,6);                                                     % daily maximum, in degree Celcius
   T_min=meteo(i,5);                                                     % daily minimum, in degreee Celcius
   RH=meteo(i,9)/100;                                                    % relative humidity
   T_dew=meteo(i,9);                                                     % dew point, degC
   uz=meteo(i,7);                                                        % average daily wind speed m/s
      uh1=log((h-d)/zm)/log((z-d)/zm)*uz;                                % uh(alpha) mean canopy windspeed with fr=1
   sun=meteo(i,8);                                  % actually duration of sunshine hour or daily solar radiation


 % obtain the correction for the effects of slope, aspect, and julian day

   [Ritg, itg0, N]=hillfunct(lat, long, slope, aspect, J);
```

```
% calculate saturation vapour pressure deficit for aridity correction
  % do the correction for site aridity if applicable
  MDD=0;                                                          % initialize MDD
  if rht==1                                                       % RH data
    es=(0.6108*exp(17.27*T_max/(T_max+237.3))+0.6108*exp(17.27*T_min/(T_min+237.3)))/2*1.0e3; %in Pa
    ea=RH*es;
    T_dew=237.3/(17.27/log(ea/610.8)-1);                          % obtain T_dew from RH data
    if aridt==1
      MDD=T_min-T_dew;
      if MDD>2
        T_maxa =T_max-kx*(MDD-2);
        T_mina =T_min-kn*(MDD-2);
        T_dewa =T_dew+kd*(MDD-2);
      else
        T_dewa=T_min-2;
        T_maxa=T_max;
        T_mina=T_min;
      end
    elseif aridt==2
      T_bias =kj*(1-sqrt(pret));
      T_maxa =T_max-T_bias;
      T_mina =T_min-T_bias;
      T_dewa =T_dew+T_bias;
    else
      T_maxa=T_max;
      T_mina=T_min;
      T_dewa=T_dew;
    end
  elseif rht==2                                                   % T_dew data
    if aridt==1
      MDD =T_min-T_dew;
```

```
        if MDD>2
            T_maxa =T_max-kx*(MDD-2);
            T_mina =T_min-kn*(MDD-2);
            T_dewa =T_dew+kd*(MDD-2);
        else
            T_dewa=T_min-2;
            T_maxa=T_max;
            T_mina=T_min;
        end
    elseif aridt==2
        T_bias=kj*(1-sqrt(pret));
        T_maxa =T_max-T_bias;
        T_mina =T_min-T_bias;
        T_dewa =T_dew+T_bias;
    else
        T_maxa=T_max;
        T_mina=T_min;
        T_dewa=T_dew;
    end
  elseif rht==0                                   % no RH or T_dew data, and aridity correction not applicable
    T_dewa=T_min-2;
    T_maxa=T_max;
    T_mina=T_min;
  end

% calculate VPD and other pars (after aridity correction)

    ea=0.6108*exp(17.27*T_dewa/(T_dewa+237.3))*1.0e3;  %in Pa

    % re-calculate es after the aridity correction
    es=(0.6108*exp(17.27*T_maxa/(T_maxa+237.3))+0.6108*exp(17.27*T_mina/(T_mina+237.3)))/2*1.0e3;
```

```
      ed=es-ea;                                          % vapor pressure deficit, in Pa
      Tmeana=(T_maxa+T_mina)/2;                          % in degC
      Tmean=(T_max+T_min)/2;                             % for snow and snowmelt, and Rnl, etc.

      P=1.013e5*((293-0.0065*elev)/293)^5.256;           % in Pa

      lamda=((2.501-(0.002361*T_maxa))+(2.501-(0.002361*T_mina)))/2*1.0e6;          % in J/kg

      gamma=(cp*P)/(eps*lamda);                          % psychrometric constant in Pa/degC

      % calculate the slope of saturation vapour pressure curve at T_mean
      delta=4098*es/(Tmeana+237.3)^2;                                               % in Pa/degC

%-------------------------------------------------------------------------
% calculate the net radiation
% net short wave radiation
  dr=1+0.033*cos(2*pi*J/365);
  if sundata==1
     Rsun=Ritg*sun;
  else
     Rsun=Ritg*itg0*((12*3600/pi)*Gsc*dr)*(as+bs*sun/N);
                                                     % daily incident solar radiation at the surface with actual sky J/(m^2day)
  end

% determine the surface albedo
   if swe==0
      snoww=0;
    elseif swe>swe1
      snoww=1;
    else
```

```
      snoww=swe/swe1;
   end
   % alpha= snoww*alpha_sn+(1-snoww)*(fr*alpha_v+(1-fr)*alpha_s);  %consider the snow covers vegetation as it covers the
ground
   alpha=alpha_v*fr+(1-fr)*(alpha_s*(1-snoww)+alpha_sn*snoww);        % neglect the effect of snow in the vegetation

   Rns=(1-alpha)*Rsun;                                                % dialy solar radiation absorbed by the surface J/(m^2day)

% net outgoing long wave radiation

   Rso=(0.75+0.00002*elev)*(Ritg*itg0*(12*3600/pi)*Gsc*dr);
                                                  %clear-sky solar radiation on the sloped surface in J/(m^2*day) Allen et al. 1998
   Rnl=(24*3600)*sigma*((T_max+273.16)^4+(T_min+273.16)^4)/2*(0.34-0.14*sqrt(ea/1000))*(1.35*Rsun/Rso-0.35);
   Rnl=max(Rnl,0);                                % force Rnl to be zero if it is negative
   A=Rns-Rnl-G-Aloan;                             % Available energy without interception and snowmelt correction
   A=max(A,0);                                    % force A to be zero if it is negative
%-------------------------------------------------------------------
% calculate the aerodynamic resistances

   raa1=log((z-d)/zm)*log((z-d)/zh)/(k^2*uz);        %raa(alpha), sec/m
   ras1=log(h/zms)*log(h/zhs)/(k^2*uh1);             % ras(alpha), sec/m
   ras0=log(h/zms)*log(h/zhs)/(k^2*uz);              % ras(0), sec/m
   raa0=log(z/zms)*log(z/zhs)/(k^2*uz)-ras0;         % raa(0), sec/m

   if L<=4
      raa=1/4*L*raa1+1/4*(4-L)*raa0;
      ras=1/4*L*ras1+1/4*(4-L)*ras0;
   else
      raa=raa1;
      ras=ras1;
   end
```

```
   uh=uz+(uh1-uz)*fr;                                    % mean canopy wind speed
   rac=alpha_w/(4*alpha_0*(1-exp(-alpha_w/2)))*(lw/uh)^0.5/Lc;          % intracanopy aerodynamic resistance

%------------------------------------------------------------------------
% calculate the bulk stomatal resistance (as function of vapor pressure)
% deficit and solar radiation, etc
   if VPDt==1
      if ed>0 & ed<1/f1a
         f1=1/(1-f1a*ed);
      elseif ed==0
         f1=1;
      else
         f1=1000;
      end
   else
      f1=1;
   end


   Gon=Rsun/(N*3600);                                    % N is the ideal sunshine hour of the day
   if sunt==1
      f2=(Gon+f2c)/[(1+Gon/1000)*Gon];                   % consider the solar radiation effect of rST
   else
      f2=1;                                              % not consider the Rsun effect
   end

   if Tt == 1 & Tmeana>=Td                               % not recommended if aridt=1
      f3=1/(1-kT*(Tx-Tmean)^2);
   elseif Tt==1 & Tmean<Td
      f3=1000;
   else
```

```
      f3=1;
   end

   if f3<0                                                    % due to f3 function
      f3=1000;
   end

   rST=rST_min*f1*f2*f3;

   rsc=rST/Lc;

%-------------------------------------------------------------------------
% corrected P and A for interception loss
  It=0; Ait=0; Aloan=0;
  if precip>0 & Tmean>Tsnow
     It=min(precip, L*Imax);                                  % in mm
     Ait=It/1000*lamda*rhop_w;                                % in J/(m^2 day)
     PET(i,6)=It;
     if A<Ait
        A=0; Aloan=Ait-A;                          % for situation not enough energy for evaporating intercepted water.
     end
     precip=precip-It;
  elseif precip>0 & Tmean <0
      swe=swe+precip;                                         % snowfall
      precip=0;                                               % no active rainfall
  end

%-------------------------------------------------------------------------
% partition available energy
   As=A*exp(-kc*L);                                           % J/(m^2 day)
   Ac=A-As;
```

```
% snow and snowmelt
   deltaw=0; Asn=0;
   %snowmelt
   if swe>0 & Tmean>Tm & As>0
      deltaw=ksm*(Tmean-Tm);
      deltaw=min(deltaw, swe);
      maxmelt=As/(lamda_f*rhop_w)*1000;                    % consider the constraint from available energy
      deltaw=min(deltaw, maxmelt);
      swe=swe-deltaw;
      Asn=deltaw/1000*lamda_f*rhop_w;
   end

   PET(i,7)=precip+deltaw;                                 % add the rainfall and snowmelt, mm/day
   As=As-Asn;

   PET(i,8)=swe;

%-------------------------------------------------------------------------
% calculate PT and PE

   PT=(delta*Ac+fr*24*3600*(rhop_a*cp)*ed/(rac+raa))/(delta+gamma*(1+rsc/(rac+raa)))/(lamda*rhop_w);
                                                           % in m/day
   PT=PT*1000;                                             % mm/day

   PE=(delta*As+(1-fr)*24*3600*(rhop_a*cp)*ed/(ras+raa))/(delta+gamma)/(lamda*rhop_w);
                                                           % in m/day
   PE=PE*1000;                                             % mm/day

   PET(i,4)=PT; PET(i,5)=PE;
```

```
   % save the parameter values
   pars(i,:)=[Ritg, alpha, Rns, Rnl, Ait, Asn, As, Ac, raa, ras, rac, rsc, f1, f2, f3, MDD,ed];
end

save pept_output.txt PET -ascii;
save pars_output.txt pars -ascii;

%****************************************** The End ***********************************************
```

Subroutine

```
function [rItg, itg0, N]=hill(lat, long, slope, aspect, J)

% This function calculates the ratio of solar radiation on sloped surface to that of flat surface, rItg
% integration of cos(theta) from -omigas to omigas (flat surface), itg0
% and ideal sunlight hours for flat surface, N
% The steepness upper limit for this function is 60 degree.

   Gsc=1367;                                                    % solar constant, in J/(m^2*sec)
   lat=lat/180*pi;
   long=long/180*pi;
   slope=slope/180*pi;
   aspdeg=aspect;

   dr=1+0.033*cos(2*pi*J/365);                                  % inverse relative distance Earth-Sun
   sdec=(23.45*pi/180)*sin(2*pi*(J+284)/365);                   % solar declination, delta in the equation
   omgs0=acos(-tan(lat)*tan(sdec));                             % sunset solar hour angle for flat surface
   N=24/pi*omgs0;
   itg0=2*omgs0*(sin(sdec)*sin(lat))+2*sin(omgs0)*(cos(sdec)*cos(lat));
                                                                % integration of cos(theta) from -omigas to omigas (flat surface)
```

```
if slope>0

  % Ra for south facing slope
  aspect=0;
  omgss=acos(-tan(lat-slope)*tan(sdec));
  omgss=min(omgss, omgs0);
  pts1=2*omgss*(sin(sdec)*sin(lat)*cos(slope)-sin(sdec)*cos(lat)*sin(slope)*cos(aspect));
  pts2=2*sin(omgss)*(cos(sdec)*cos(lat)*cos(slope)+cos(sdec)*sin(lat)*sin(slope)*cos(aspect));
  itgs=pts1+pts2;                                          % integration of cos(theta) from -omigas to omigas

  % Ra for north facing slope
  aspect=pi;
  % solve for sunrise/sunset hour angle
  if slope+(lat-sdec)>= pi/2
     omgsn=0;
  else
     adiff=1;
     guess=0;
     tolerance=0.001;
     while (adiff>tolerance)
        agms=guess;
        athtz=pi/2-atan(tan(slope)*cos(agms));
        aomgs=acos((cos(athtz)-sin(lat)*sin(sdec))/(cos(sdec)*cos(lat)));
        bgms=asin(sin(aomgs)*cos(sdec)/sin(athtz));
        adiff=abs(bgms-agms);
        guess=bgms*1/5+agms*4/5;
     end
     omgsn=aomgs;
  end
  ptn1=2*omgsn*(sin(sdec)*sin(lat)*cos(slope)-sin(sdec)*cos(lat)*sin(slope)*cos(aspect));
  ptn2=2*sin(omgsn)*(cos(sdec)*cos(lat)*cos(slope)+cos(sdec)*sin(lat)*sin(slope)*cos(aspect));
```

```
itgn=ptn1+ptn2;                                          % integration of cos(theta) from -omigas to omigas


% Ra for east facing slope
aspect=-pi/2;
% solve for sunset hour angle
   adiff=1;
   guess=0;
   tolerance=0.001;
   while (adiff>tolerance)
      agms=guess;
      athtz=pi/2-atan(tan(slope)*sin(agms));
      aomgs=acos((cos(athtz)-sin(lat)*sin(sdec))/(cos(sdec)*cos(lat)));
      bgms=asin(sin(aomgs)*cos(sdec)/sin(athtz));
      adiff=abs(bgms-agms);
      guess=bgms*1/5+agms*4/5;
   end
   omgse2=aomgs;
omgse1=-omgs0;
pte1=(omgse2-omgse1)*(sin(sdec)*sin(lat)*cos(slope)-sin(sdec)*cos(lat)*sin(slope)*cos(aspect));
pte2=(sin(omgse2)-sin(omgse1))*(cos(sdec)*cos(lat)*cos(slope)+cos(sdec)*sin(lat)*sin(slope)*cos(aspect));
pte3=(cos(omgse1)-cos(omgse2))*(cos(sdec)*sin(slope)*sin(aspect));
itge=pte1+pte2+pte3;


% Ra for west facing slope
aspect=pi/2;
omgsw1=-omgse2;                                          % from east facing slope sunset hour angle
omgsw2=omgs0;
ptw1=(omgsw2-omgsw1)*(sin(sdec)*sin(lat)*cos(slope)-sin(sdec)*cos(lat)*sin(slope)*cos(aspect));
ptw2=(sin(omgsw2)-sin(omgsw1))*(cos(sdec)*cos(lat)*cos(slope)+cos(sdec)*sin(lat)*sin(slope)*cos(aspect));
```

```
   ptw3=(cos(omgsw1)-cos(omgsw2))*(cos(sdec)*sin(slope)*sin(aspect));
   itgw=ptw1+ptw2+ptw3;


% do the interpolation
   if aspdeg>=-180 & aspdeg<-90
      itg=itgn*(-90-aspdeg)/90 + itge*(aspdeg+180)/90;
   elseif aspdeg>=-90 & aspdeg<0
      itg=itge*(-aspdeg/90)+itgs*(90+aspdeg)/90;
   elseif aspdeg>=0 & aspdeg<90
      itg=itgs*(90-aspdeg)/90 + itgw*aspdeg/90;
   else
      itg=itgw*(180-aspdeg)/90 + itgn*(aspdeg-90)/90;
   end

else
   itg=itg0;                                          % integration of cos(theta) from -omigas to omigas
end

rItg=itg/itg0;


% **** the end of the subroutine****
```

Appendix XI Slope steepness and aspect effects calculated from TVET model

One of the two major elements of the TVET model is accounting for the slope steepness and aspect effects on surface energy balance. A series of geometric functions are employed in the model to capture the effects. Since the solar position changes with latitude and with time in the year, the slope steepness and aspect effects vary consequently with latitude and time. Below are results calculated from the TVET model, which clearly show the model's capability to capture topographical, seasonal, and latitudinal effects on surface energy balance.

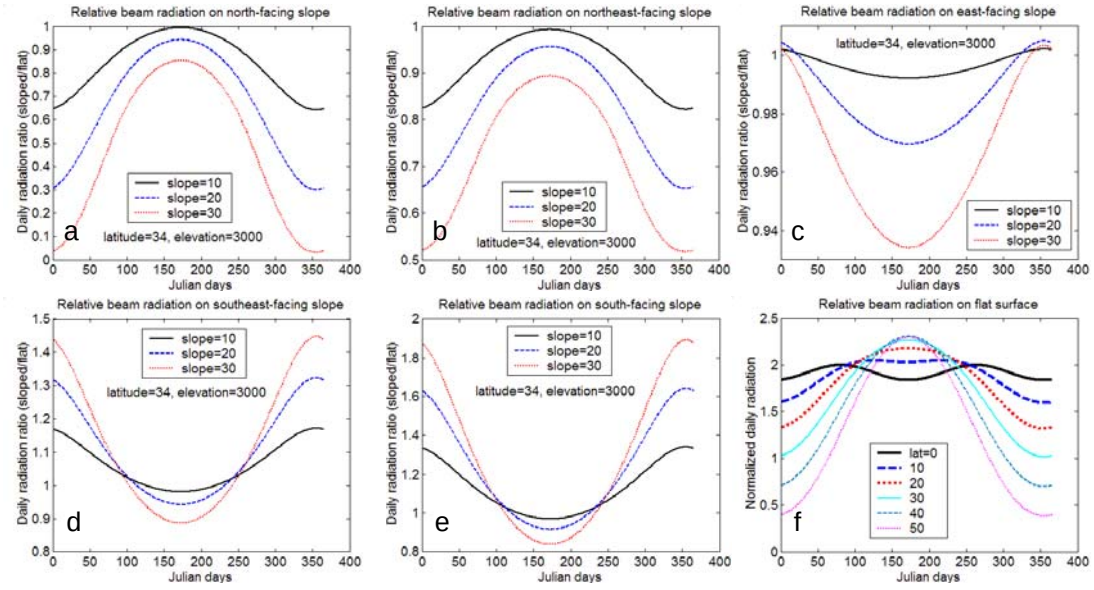

Figure XI-1 Relative daily in-coming solar radiation on the sloped surface (normalized by that of a flat surface) of three selected slope steepness (10, 20, and 30˚), and six aspects: north-facing (a), northeast-facing (b), east-facing (c), southeast-facing (d), south-facing(e), and west-facing(f), at latitude 34˚N, longitude 107˚W, and elevation 3000 m, as a function of Julian days in the year.

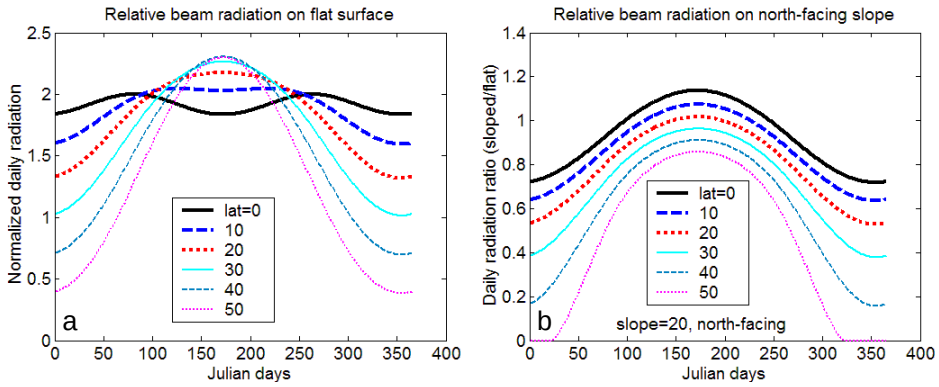

Figure XI-2 Relative daily beam radiation ($\int_{\omega\_sunrise}^{\omega\_sunset} \cos\theta \, d\omega$, of equation 4.13) on the flat surface (a), and relative daily beam radiation for a north-facing 20˚ slope normalized by that of a flat surface at various latitudes, as a function of Julian days in the year.

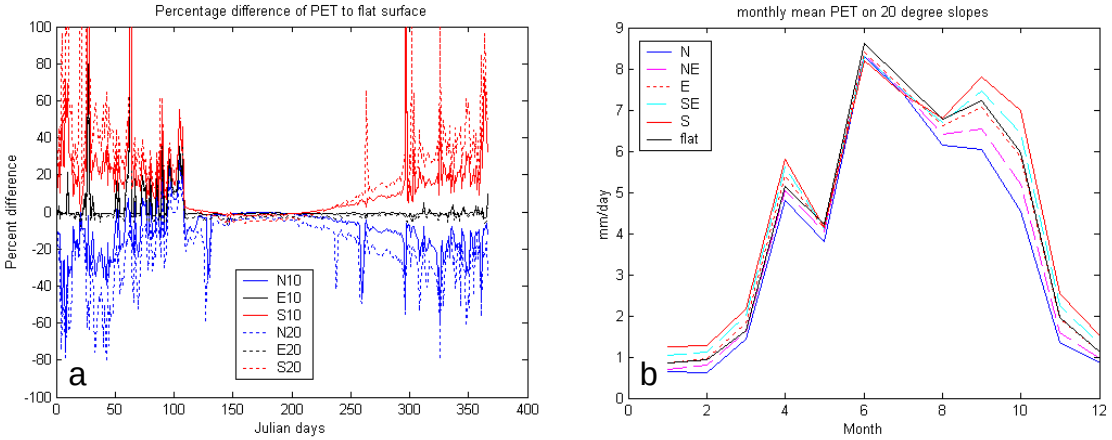

Figure XI-3 The percentage difference of PET to the flat suface for six sloped surfaces with different steepness and aspect, where N10 means north-facing 10˚ slope (a), and monthly mean daily PET for a 20˚ slope of various aspects (b), at a location (latitude 34˚N, longitude 107˚W, and elevation 3243 m) near South Baldy, Magdalena Mountains, central New Mexico, in 1992. The prescribed characteristics of the surface cover are *Fr = 0.5*, *Lc = 5*, and vegetation height *h = 5*.

Appendix XII Modeling evaporation using the HYDRUS code

In this appendix, I will examine (1) whether HYDRUS evaporation scheme can extract soil water below the first grid layer, (2) how sensitively the grid spacing and hCritA in the model affect the simulated E and T partitioning.

Physically, evaporation from soil surface experiences three stages [*Rassam et al., 2003*]. At stage 1, the soil surface is wet, evaporation goes at the potential rate. When the surface soil becomes drier and cannot provide water at the rate required by potential evaporative demand, the evaporation rate decrease below the potential rate. The stage 2 commences. In this stage, both transmission of liquid water in the shallow soil to the surface and soil vapor diffusion to the surface contributes to the evaporation. The liquid water transmission strongly depends on soil hydraulic properties, and the soil moisture content. With the soil water content decreasing, vapor diffusion contribution increases. When the transmission of liquid water to the soil surface stops, evaporation goes to the third stage, during which only vapor diffusion goes.

HYDRUS does not model vapor diffusion process. It implements a scheme to mimic the physical evaporation processes by applying a user-defined water potential "hCritA". When the surface soil water potential is above (wetter than) this value, evaporation is at its potential rate. At this situation, the surface boundary is constant flux which is defined by potential evaporation. When the surface soil water potential drops below this value, the boundary turns to constant pressure (i.e., hCritA). The evaporation is determined by water potential gradient of the surface grid layer and the layer below, and unsaturated hydraulic conductivity of the soil. This boundary condition is intended to

mimic situation of the dryer part of the stage 2 and stage 3. The value of "hCritA" is dependent of soil type, which significantly affects the simulated evaporation process. Rassam et al. [*2003*] suggest -500m for a sandy soil, and -1000m for a silty soil. Rassam et al. [2003] also show that the simulated evaporation is also sensitive to the grid size. If the grid cell is too coarse, evaporation is overestimated. Finer grid cell size is recommended [*Rassam et al., 2003*]. In the earlier simulations of E and T partitioning of Sevilleta sites, the 1D grid spacing is 1cm, and the "hCritA" for the loam soil is -1000m.

Simulation design

I chose the shrub site for the testing, using HYDRU1D. The soil column is 200 cm loam, with adjusted hydraulic conductivity based on Bhark's [*2002*] measurement. The original simulation is also listed below for easier comparison.

1) Shrubaa: original simulation, 1cm spacing, hCritA=-1000m
2) Shrubab: 1cm spacing, hCritA =-800m, or -500m, leading to numerical instability, large mass balance error, not shown in the results.
3) Shrubba: 0.2cm spacing, hCritA=-1000m
4) Shrubbb: 0.2cm spacing, hCritA=-750m.
5) Shrubbc: 0.2 cm spacing, hCritA=-750m, with only PE=total PET, PT=0

Results

First, lets look at whether HYDRUS1D evaporation scheme extracts soil water below the top grid layer in the column. If we assume HYDRUS can not extract soil water below the top grid layer, we would expect to see that most water infiltrate below the top

grid layer becomes recharge in the "shrubbc" run (no transpiration). Figure XII-1 shows how water infiltrates into the soil after the three rainfall events.

The annual total daily rainfall exceeding the daily potential ET for the study site is 12 cm. However, the simulated (shrubbc run) percolation is only 1.2 cm (Figure XII-2). This suggests that most soil water infiltrated below the top grid layer is extracted out of the soil column by the HYDRUS evaporation scheme.

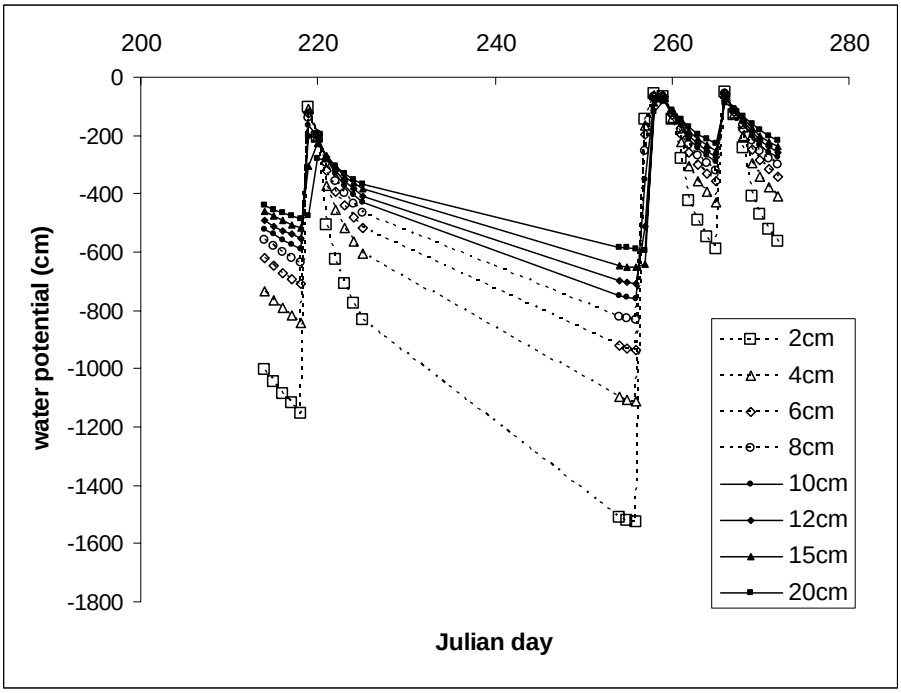

Figure XII-1 Simulated (Shrubbc run) soil water potentials at various depths responding to the three rainfall events for the shrub site.

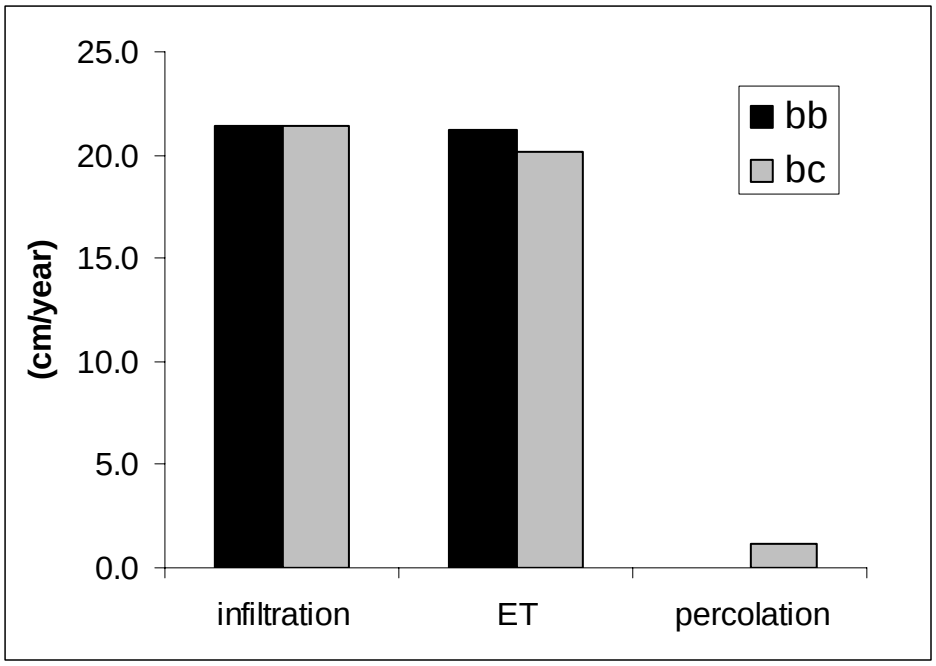

Figure XII-2 The simulated water fluxes at the shrub site of 2002 for simulations with different modeling settings: bb=0.2cm grid, -750m hCritA, PE and PT input, and bc=0.2cm grid, -750m hCritA, only PE (the amount equal to the sum of PE and PT of bb run), PT=0.

How is the simulated partitioning of E and T sensitive to the grid spacing, and the prescribed hCritA? The results (Figure XII-3) show that difference in grid spacing does lead to difference in simulated E and T partitioning. T fraction increases with finer spacing, consistent with what we discussed earlier (i.e., evaporation may be overestimated for coarser grid). But the difference is very small (~0.01 in fraction). This does not significantly affect the modeled E and T partitioning. The hCritA effect is negligible for the two types of grid spacing that are investigated.

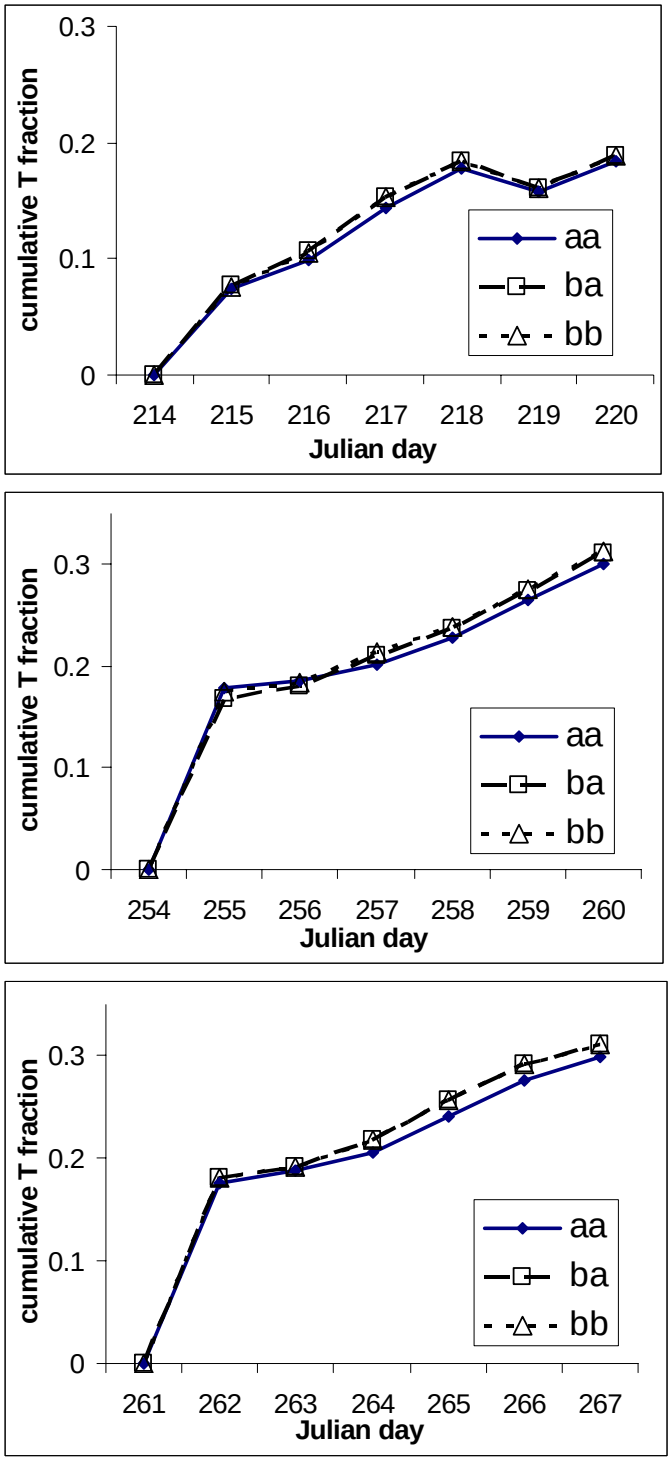

Figure XII-3 Simulated cumulative T fractions following three rainfall events at the shrub site from models with different settings: aa=1cm grid, -1000m hCritA, ba=0.2cm grid, -1000m hCritA, and bb=0.2cm grid, -750m hCritA.

References

Bhark, E. (2002), Water availability to vegetation across a semiarid shrubland and grassland ecotone, Sevilleta Wildlife Refuge, M.S. Thesis, New Mexico Institute of Mining and Technology, Socorro, New Mexico.

Rassam, D., J. Simunek, and M. Th. Van Genuchten (2003), Modeling variably saturated flow with HYDRUS-2D, 'ND Consult', Brisbane, Australia.

Appendix XIII TVET inputs for Sevilleta and Rio Grande riparian

Input parameters for Sevilleta creosotebush surface

```
%site specific parameters  (indented lines are derivations, not necessary changed)
   long=-106.6911;
   lat=34.3586;
   elev=1600;          % meter above sea level
   slope=0;            % slope angle in degree
      slpcrrct=cos(slope/180*pi);
   aspect=0;           % surface azimuth angle, 0 due south, -90 due east, and 90 due west
   fr=0.3;               % fractional vegetation cover
   alpha_v=0.15;            % albedo of the vegetation,
   alpha_s=0.30;            % albedo of the soil,
   alpha_sn=0.50;           % albedo of snowcover
   swe=0;                % initial the snow water equivalent
%-------------------------------------------------------------
% parameters for daily available energy and others
   as=0.25;              % Rns=(1-alpha)*Rs24*(as+bs*n/N)
   bs=0.50;                %(not used if measured solar radiation is availabe)

   G=0;                  % daily energy lost to the ground J/(m^2 day)
   swe1=2.0;               % the threshold swe below which snow albedo linearly decreases to zero

% correction for daily mean temperature, and relative humidity, this is
% removed in this version, refered to TVET_1st.
%-------------------------------------------------------------
%vegetation parameters;
```

```
   Lc=1.2;                  % canopy leaf area index
      L=Lc*fr;              % surface leaf area index
   h=1.0;                   % vegetation height
      d=0.67*h;             % zero plane displacement, m (Shuttleworth, 1993).
      zm=0.123*h;           % roughness length for momentum transfer, m
      zh=zm/7.0;            % roughness length for heat and vapor transfer, m,  for forest /2.0
                         % for grasses,/12.0, for crop /7.0, (Mo et al., 2004);

   zms=0.005;               % rouhgness length for momentum transfer on the substrate, m
      zhs=0.1*zms;       % roughness length for heat and vapor transfer on the substrate, m
   z=h+2;                   % reference height at which windspeed, humidity is measured, m

   kc=0.4;                  % extinction coefficient of beer's law

% paramters for bulk stomatal resistance
    %rST_min=180;        % mean minimum stomatal resistance for coniferous tree, sec/m
    rST_min=210;              % for shrub
    %rST_min=130;             % for grass

% parameters for intra-canopy aerodaynamic resistance
   alpha_w=2.5;              % wind-extinction coefficent Mo (2004) used 2.5
   alpha_0=0.005;            % coefficient with unit of ms^(-1/2)Mo (2004) used 0.005
   lw=0.02;                  % characteristic leaf width (m).
%-------------------------------------------------------------
%switches
   rht=1;                 % rht =1 , RH is used; or rht=2, T_dew is used; rht=0, T_dew=f(T_min) for D
   sundata=1;               % sundata=0, daily sunshine hour data; =1, daily solar radiation data J/m^2
   jorm=1;         % the date in input file is in julian (column #2) for jorm=1, and in month and day for jorm=0

   sunt=0;       % sunt=1, solar radiation effect on rST, sunt=0, not effect on rST
   Tt=1;        % Tt=1, temperature effect on rST; if only dormancy effect, Tt=1, and kT=0.
```

```
   VPDt=0;      % VPDt=1, vapor pressure deficit effect on rST is on, otherwise VPDt=0;

   aridt=1;                %do correction for site aridity,
         % ==1 do Temesgen's correction, ==2 do Jensen's correction  ==0, no correction

% Parameters for correction of site aridity
   kx=0.7; kn=0.4; kd=0.6;          % for Temesgen's correction (0.7, 0.4, 0.6 for arid (semiarid) tropical climates)
                          % (0.5, 0.5, and 0.5)for humid and semi-humid teperate climates
   kj=4; pret=0.5;                % for Jensen's correction, pret = long term P/PET

% paramters for Jarvis functions
   %rST=rST_min*f1(D)*f2(Rs_24)*f3(T)
   f1a=3.5e-4;                % parameters for f1(d)=1/(1-aD), for coniferous trees, Pa-1
   f2c=100;                   % parameters for f2(Rsun)=(Rsun+c)/[(1+c/1000)*Rsun], big uncertainty
   kT=0;                % parameters for f3(T)=1/[1-kT(Tx-T)^2], degC-1, make it zero to shut this function down
                          % kT=0.00137, not recommended if aridt=1
   Tx=25;                     % degC
   Td=-2;             % temperature for complete dormancy of the vegetation, make it -100 to shut down this function
%-----------------------------------------------
% parameters for interception and snowmelt
   Imax=1;                    % the maximum interception in mm for the surface with L=1
   Tm=0;                      % temperature to initiate the snowmelt (degC)
   ksm=3.6;                   % empirical coefficient in Pm=ksm(Tmean-Tm), mm/(day degC)
   Tsnow=0;                   % temperature to partition precip into snow and rainfall
```

Input parameters for Sevilleta grass surface

```
%vegetation parameters;
   Lc=1.2;                  % canopy leaf area index
      L=Lc*fr;              % surface leaf area index
   h=0.3;                   % vegetation height
      d=0.67*h;             % zero plane displacement, m (Shuttleworth, 1993).
      zm=0.123*h;           % roughness length for momentum transfer, m
      zh=zm/12.0;           % roughness length for heat and vapor transfer, m, for forest
                        % for grasses,/12.0, for crop /7.0, (Mo et al., 2004);

   zms=0.005;               % rouhgness length for momentum transfer on the substrate, m
      zhs=0.1*zms;          % roughness length for heat and vapor transfer on the substrate, m
   z=h+2;                   % reference height at which windspeed, humidity is measured, m

   kc=0.4;                  % extinction coefficient of beer's law

%seasonal-change par for grass
   Lc1=1.2;
   Lc2=1.0;
   Fr1=0.55;
   Fr2=0.4;
   h1=0.3;
   h2=0.2;
   rST_min1=130;
   rST_min2=5000;
   vg1=120;
   vg4=300;

% paramters for bulk stomatal resistance
    %rST_min=180;                % mean minimum stomatal resistance for coniferous tree, sec/m
```

```
    %rST_min=210;                % for shrub
    rST_min=130;                 % for grass

% parameters for intra-canopy aerodaynamic resistance
   alpha_w=2.5;                  % wind-extinction coefficent Mo (2004) used 2.5
   alpha_0=0.005;                % coefficient with unit of ms^(-1/2)Mo (2004) used 0.005
   lw=0.02;                      % characteristic leaf width (m).
%-------------------------------------------------------------
%switches
   rht=1;                    % rht =1 , RH is used; or rht=2, T_dew is used; rht=0, T_dew=f(T_min) for D
   sundata=1;                  % sundata=0, daily sunshine hour data; =1, daily solar radiation data J/m^2
   jorm=1;         % the date in input file is in julian (column #2) for jorm=1, and in month and day for jorm=0

   sunt=0;                    % runt=1, solar radiation effect on rST, sunt=0, not effect on rST
   Tt=1;                     % Tt=1, temperature effect on rST; if only dormancy effect, Tt=1, and kT=0.
   VPDt=0;                    % VPDt=1, vapor pressure deficit effect on rST is on, otherwise VPDt=0;

   aridt=1;                  %do correction for site aridity,
                        % ==1 do Temesgen's correction, ==2 do Jensen's correction  ==0, no correction

% Parameters for correction of site aridity
   kx=0.6; kn=0.45; kd=0.55;          % for Temesgen's correction (0.7, 0.4, 0.6 for arid (semiarid) tropical climates)
                           % (0.5, 0.5, and 0.5)for humid and semi-humid teperate climates
   kj=4; pret=0.5;                 % for Jensen's correction, pret = long term P/PET

% paramters for Jarvis functions
   %rST=rST_min*f1(D)*f2(Rs_24)*f3(T)
   f1a=3.5e-4;                   % parameters for f1(d)=1/(1-aD), for coniferous trees, Pa-1
   f2c=100;                      % parameters for f2(Rsun)=(Rsun+c)/[(1+c/1000)*Rsun], big uncertainty
   kT=0;                        % parameters for f3(T)=1/[1-kT(Tx-T)^2], degC-1, make it zero to shut this function down
                           % kT=0.00137, not recommended if aridt=1
```

```
   Tx=25;                    % degC
   Td=-2;            % temperature for complete dormancy of the vegetation, make it -100 to shut down this function
%-----------------------------------------------
% parameters for interception and snowmelt
   Imax=1;                   % the maximum interception in mm for the surface with L=1
   Tm=0;                     % temperature to initiate the snowmelt (degC)
   ksm=3.6;                  % empirical coefficient in Pm=ksm(Tmean-Tm), mm/(day degC)
   Tsnow=0;                  % temperature to partition precip into snow and rainfall
%-----------------------------------------------
```

Input parameters for cottonwood flooded site (Belen)

```
%site specific parameters  (indented lines are derivations, not necessary changed)
   long=-106.83;
   lat=34.5;
   elev=1500;          % meter above sea level

% time-dependent vegetation par (for 2002).
   kc=0.4;                % extinction coefficient of beer's law
   vg1=110;                % start to develp leaf
   vg2=125;                % full development
   vg3=285;                % start decidous phase
   vg4=300;                % stop decidous pahse
   Lc1=2.8;                % bulk Lc in summer
   Lc2=1.9;                % bulk Lc in winter
   h1=25;                 % tree height
   h2=5;                 % equivalent canopy height
   rST_min1=150;
   rST_min2=10000;           % dry leaf

% time-dependent vegetation par (for 2003)
       kc=0.4;                % extinction coefficient of beer's law
      vg1=85;                % start to develp leaf
      vg2=125;                % full development
      vg3=295;                % start decidous phase
      vg4=315;                % stop decidous pahse
      Lc1=2.8;                % bulk Lc in summer
      Lc2=1.9;                % bulk Lc in winter
      h1=25;                 % tree height
      h2=5;                 % equivalent canopy height
      rST_min1=150;
```

```
    rST_min2=10000;            % dry leaf

%time-dependent vegetation functions

  if J>=vg2 & J<=vg3
    Lc=Lc1;                    % canopy leaf area index
    h=h1;                      % vegetation height
    rST_min=rST_min1;
  elseif J<vg2 & J>=vg1
    Lc=Lc2+(Lc1-Lc2)*(J-vg1)/(vg2-vg1);
    h=h2+(h1-h2)*(J-vg1)/(vg2-vg1);
    rST_min=exp(log(rST_min2)+(log(rST_min1)-log(rST_min2))*(J-vg1)/(vg2-vg1));
  elseif J>vg3 & J<=vg4
    Lc=Lc1-(Lc1-Lc2)*(J-vg3)/(vg4-vg3);
    h=h2+(h1-h2)*(J-vg3)/(vg4-vg3);
    rST_min=exp(log(rST_min1)-(log(rST_min1)-log(rST_min2))*(J-vg3)/(vg4-vg3));
  else
    Lc=Lc2;
    h=h2;
    rST_min=rST_min2;
  end

% Aridity correction on, Jarvis functions off.
  kx=0.7; kn=0.4; kd=0.6;
%-------------------------------------------------------------------------------------------------
```

Input parameters for saltcedar flooded site (Bosque del Apache)

```
%site specific parameters  (indented lines are derivations, not necessary changed)
      long=-106.87;
      lat=34.27;
      elev=1430;          % meter above sea level
   % parameters for intra-canopy aerodaynamic resistance
      alpha_w=15;              % wind-extinction coefficent Mo (2004) used 2.5
      alpha_0=0.005;           % coefficient with unit of ms^(-1/2)Mo (2004) used 0.005
      lw=0.10;                 % characteristic leaf width (m).
% time-dependent vegetation par (for 2002).
       kc=0.4;                 % extinction coefficient of beer's law
      vg1=100;                 % start to develp leaf
      vg2=160;                 % full development
      vg3=255;                 % start decidous phase
      vg4=320;                 % stop decidous pahse
      Lc1=4.0;                 % bulk Lc in summer
      Lc2=2.4;                 % bulk Lc in winter
      h1=6.15;                  % tree height
      h2=3;                   % equivalent canopy height
      rST_min1=210;
      rST_min2=10000;            % dry leaf
% time-dependent vegetation par (for 2003)
      kc=0.4;                 % extinction coefficient of beer's law
      vg1=100;                 % start to develop leaf
      vg2=160;                 % full development
      vg3=260;                 % start deciduous phase
      vg4=330;                 % stop deciduous pahse
      Lc1=4.0;                 % bulk Lc in summer
      Lc2=2.4;                 % bulk Lc in winter
```

```
    h1=6.15;                % tree height
    h2=3;                   % equivalent canopy height
    rST_min1=210;
    rST_min2=10000;         % dry leaf

%time-dependent vegetation functions

  if J>=vg2 & J<=vg3
    Lc=Lc1;                 % canopy leaf area index
    h=h1;                   % vegetation height
    rST_min=rST_min1;
  elseif J<vg2 & J>=vg1
    Lc=Lc2+(Lc1-Lc2)*(J-vg1)/(vg2-vg1);
    h=h2+(h1-h2)*(J-vg1)/(vg2-vg1);
    rST_min=exp(log(rST_min2)+(log(rST_min1)-log(rST_min2))*(J-vg1)/(vg2-vg1));
  elseif J>vg3 & J<=vg4
    Lc=Lc1-(Lc1-Lc2)*(J-vg3)/(vg4-vg3);
    h=h2+(h1-h2)*(J-vg3)/(vg4-vg3);
    rST_min=exp(log(rST_min1)-(log(rST_min1)-log(rST_min2))*(J-vg3)/(vg4-vg3));
  else
    Lc=Lc2;
    h=h2;
    rST_min=rST_min2;
  end

% Aridity correction on, Jarvis functions off.
  kx=0.7; kn=0.4; kd=0.6;
%-------------------------------------------------------------------------------------------------------
```

Appendix XIV Input for HYDRUS 1D simulations of Sevilleta surfaces

This appendix includes root distribution, root-water-uptake model parameterization, and soil hydraulic properties for the simulations of two surfaces at Sevilleta NWR, central New Mexico. The root distribution is derived from the field study of Dr. Eric Small's research group [*Kurc and Small, 2004*] (Figures XIV-1 and 2. Because the simulations are used to test the TVET model by comparing the E and T partitioning from the simulations at a certain time (@ the sixth day) after a rainfall events to the isotopic study results, an close-to-realistic root-water-uptake model parameterization is important. The root-water-uptake model parameterization for the creosote shrub is derived from lab study by Pockman and Sperry [*2000*] (Appendix V) (Figure XIV-3). No rigorously estimated root-water-uptake model parameterization has been found in literature for the grass at the study site. I prescribe the parameterization in my subjective conception, which is intended to make the root-water-uptake behavior of the grass between that of the crops (from HYDRUS) and the creosotebush (Figure XIV-4). Based on Bhark [*2002*], the soil at the study site is sandy loam, based on the saturated hydraulic conductivity measurement. However, the default sandy loam parameters in HYDRUS leads to numerical instability, as discussed in Appendix V. As a result, I use loam parameters while keeping the hydraulic conductivity the measured value.

Root distribution

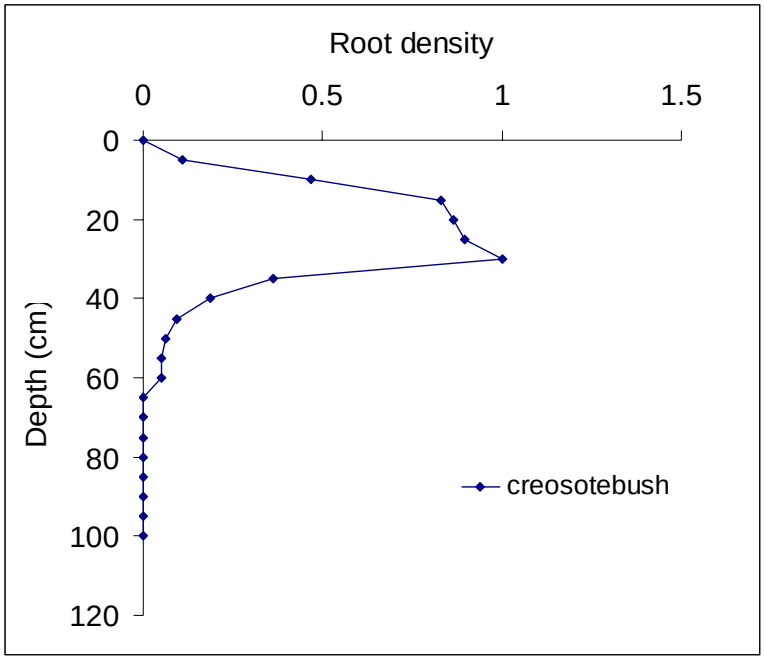

Figure XIV-1 Root distribution of creosotebush derived from Kurc and Small [*2004*].

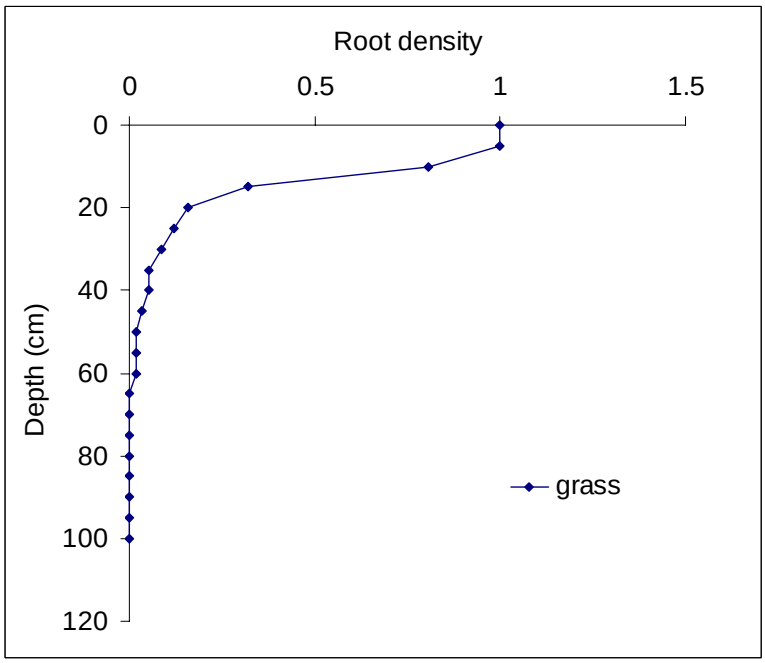

Figure XIV-2 Root distribution of grass derived from Kurc and Small [*2004*].

Root-water-uptake S-shape model parameters

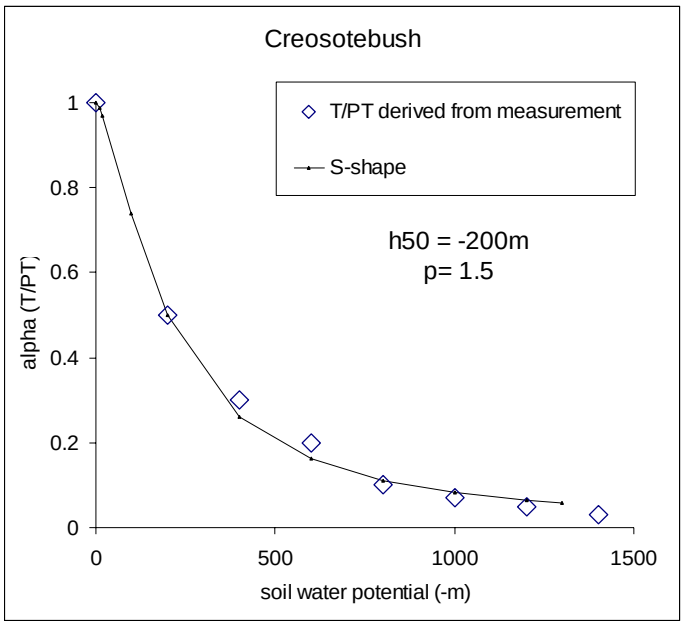

Figure XIV-3 The S-shape root-water-uptake model of creosotebush derived from Pockman and Sperry [*2000*].

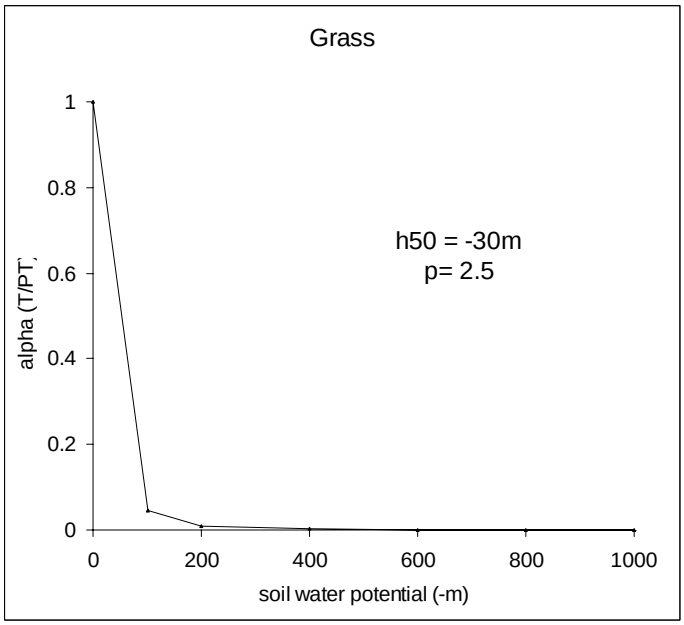

Figure XIV-4 The S-shape root-water-uptake model of the grass (subjective conceptualization that the grass should have the root-water-uptake capacity between crops with salinity constraint (the default S-shape model parameterization in HYDRUS) and the creosotebush)

Soil hydraulic properties

θ_r	θ_s	α 1/cm	n	K_s cm/day*
0.078	0.43	0.036	1.56	100

* According to Bhark [*2002*]

References

Kurc, S.A., and E.E. Small (2004), Dynamics of evapotranspiration in semiarid grassland and shrubland ecosystems during the summer monsoon season, central New Mexico, *Water Resources Research*, 40, W09305, doi: 10.1029/2004WR003068.

Pockman, W.T., and J. S. Sperry (2000), Vulnerbility to xylem cavitation and the distribution of Sonoran Desert vegetation, *American Journal of Botany*, 87(9), 1287-1299.

Bhark, E. (2002), Water availability to vegetation across a semiarid shrubland and grassland ecotone, Sevilleta Wildlife Refuge, M.S. Thesis, New Mexico Institute of Mining and Technology, Socorro, New Mexico.

Appendix XV Model settings for generic transient simulations with daily atmospheric boundary conditions

This appendix describes the model settings for HYDRUS 2D simulations of hypothetical hillslopes based on South Baldy, Magdalena Mountains, central New Mexico (Figure 5.11). The atmospheric boundary conditions for two aspect slopes with different vegetation cover, generated from the TVET model, are also included.

The model settings for different locations of the hillslope

Figure XV-1 shows the modeling settings of two sloping slices at two relative hillslope locations (topslope and midslope). The soil cover for two different thicknesses (30 cm, and 100 cm) overlying the bedrock are applied. For computation reasons, the slices are 20 cm wide. To mimic the conditions of a long slope, a continuous slope boundary, defined below, is prescribed at both sides of the soil layer for the midslope slice, and at the downslope side of the soil layer for the topslope slice.

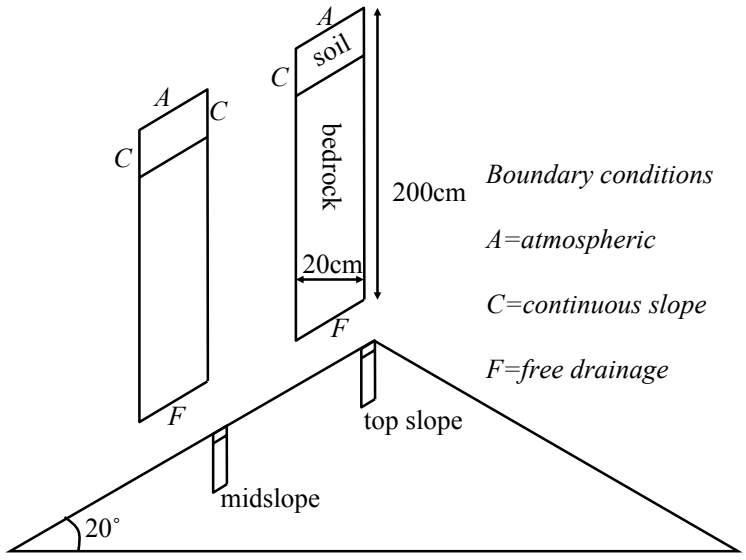

Figure XV-1 The model setting of two sloping slices at different relative hillslope locations.

In arid and semiarid regions, the water potential distribution depends on the depth below the ground surface for most of the year, because of the sporadic rainfall regime. With the assumption that the water potential is identical at the equi-depth line, the hydraulic gradient between A and B in Figure XV-2 near the vertical side boundary will be

$$J = \frac{Z_B - Z_A}{AB} = \sin\alpha \qquad \text{(XV-1)}$$

Since the prescribed gradient boundary condition at the vertical sides is perpendicular to the sides, the hydraulic gradient is corrected as

$$J_n = J\cos\alpha = \sin\alpha\cos\alpha = \frac{1}{2}\sin 2\alpha \qquad \text{(XV-2)}$$

This gradient also applies for the upslope side. With this boundary, we can simulate a long hillslope with a small sloping slice.

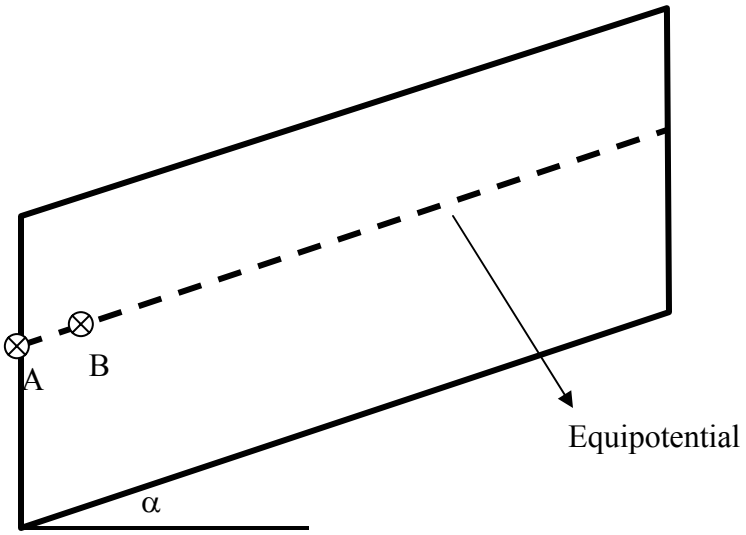

Figure XV-2 Schematic graph of the soil water potential distribution on a hypothetical slopes.

TVET generated atmospheric boundary conditions

The TVET model is used to generate atmospheric boundary conditions of the hypothetical hillslope with different aspects and vegetation coverage. Two aspects, north-facing and south-facing, and two fractional vegetation cover (50% and 5%) are applied. The vegetation is assumed to be conifer tree, with a canopy leaf area index of 5, a height of 5 meters, and a minimum stomatal resistance of 180 sm^{-1}. Site aridity correction and Jarvis-type functions are turned on. The daily atmospheric conditions (solar radiation, temperature, wind speed, relative humidity), observed at the Langmuir Lab near the South Baldy, are downloaded (and derived) from Sevilleta LTER website (http://sevilleta.unm.edu/research/local/climate/meteorology/summaries). The solar radiation is adjusted to account for the slope steepness and aspect effects for the two hypothetic slopes. Other climate conditions are assumed to be the same for the two slopes, and equal to the measurements. Figure XV-3 show the results with 50% tree coverage, and Figure XV-4 for 5% tree coverage. The TVET input file is also attached.

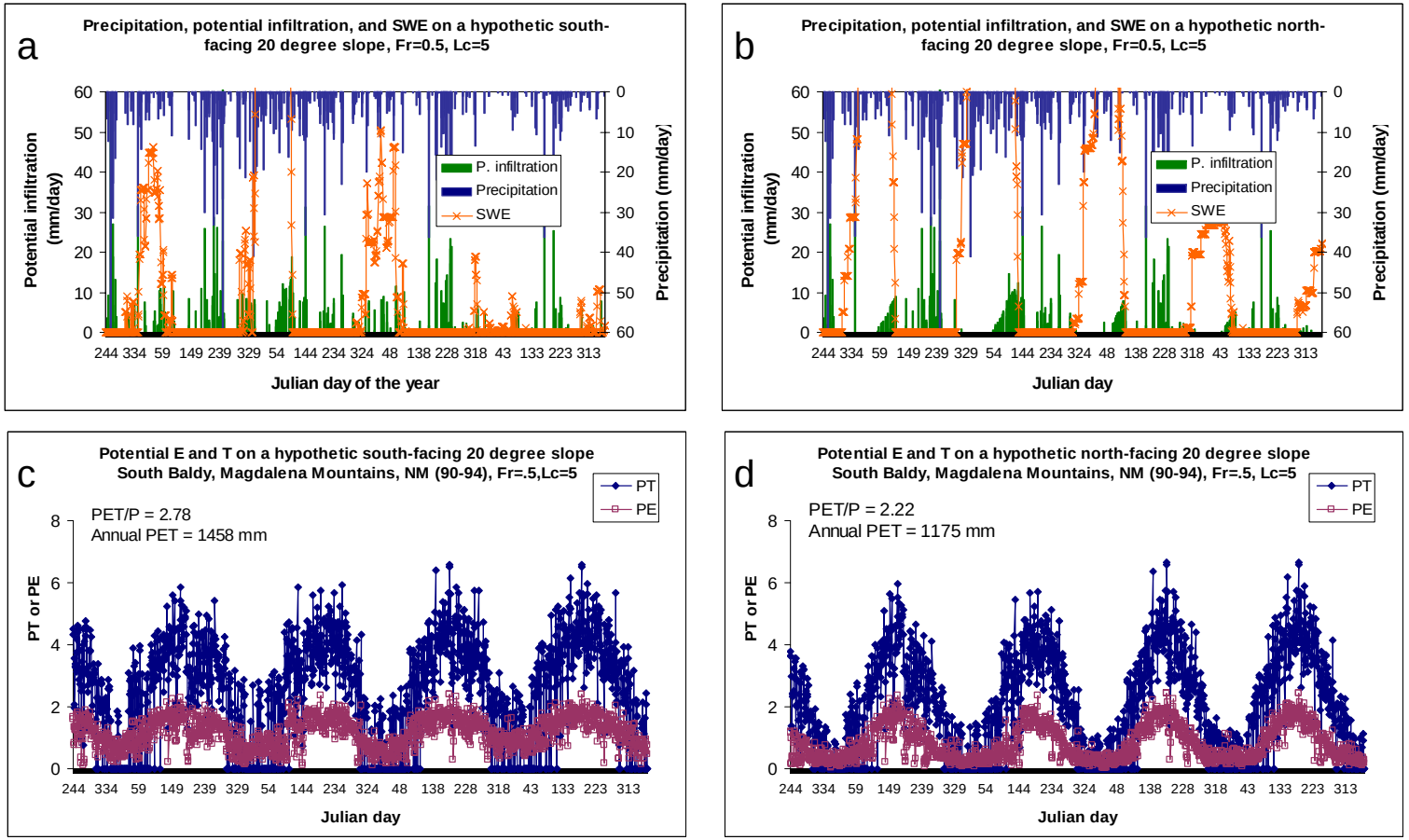

Figure XV-3 TVET generated atmospheric boundary conditions (active water for infiltration or potential infiltration, PE, and PT) for a south-facing 20 degree hillslope (a,c), and north-facing 20 degree hillslope (b,d) with 50% hypothetical conifer. The precipitation and snow water equivalent (SWE) are also shown (a,b).

413

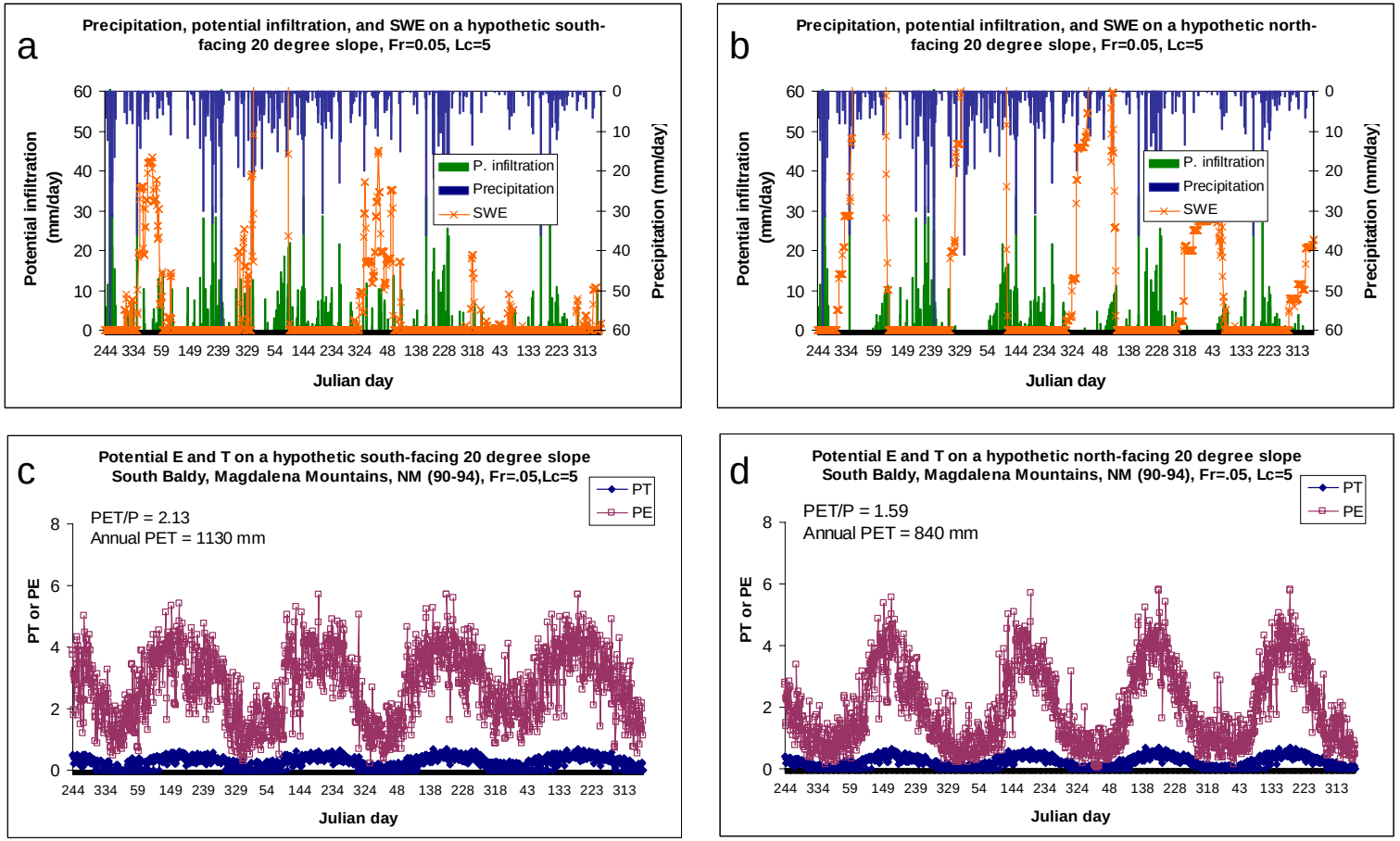

Figure XV-4 TVET generated atmospheric boundary conditions (active water for infiltration or potential infiltration, PE, and PT) for a south-facing 20 degree hillslope (a,c), and north-facing 20 degree hillslope (b,d) with 5% hypothetical conifer. The precipitation and snow water equivalent (SWE) are also shown (a,b).

414

TVET input parameters for South Baldy, Magdalena Mountains

```
%site specific parameters  (indented lines are derivations, not necessary changed)
   long=-107.1813;
   lat=33.9755;
   elev=3243;            % meter above sea level
   slope=20;             % slope angle in degree
      slpcrrct=cos(slope/180*pi);
   aspect = 0 or 180;
%vegetation parameters;
   Lc=5;                 % canopy leaf area index
   h=5;                  % vegetation height
   fr=0.5 or 0.05;

% paramters for bulk stomatal resistance
    rST_min=180;       % mean minimum stomatal resistance for coniferous tree, sec/m

% parameters for intra-canopy aerodaynamic resistance
   alpha_w=2.5;              % wind-extinction coefficent Mo (2004) used 2.5
   alpha_0=0.005;            % coefficient with unit of ms^(-1/2)Mo (2004) used 0.005
   lw=0.03;                  % characteristic leaf width (m).

%switches
   rht=1;                % rht =1 , RH is used; or rht=2, T_dew is used; rht=0,
         T_dew=f(T_min) for D
   sundata=1;            % sundata=0, daily sunshine hour data; =1, daily solar radiation data J/m^2
   jorm=1;               % the date in input file is in julian (column #2) for jorm=1, and in  month  and day for jorm=0

   sunt=1;               % runt=1, solar radiation effect on rST, sunt=0, not effect on rST
   Tt=1;                 % Tt=1, temperature effect on rST; if only dormancy effect, Tt=1, and kT=0.
   VPDt=1;               % VPDt=1, vapor pressure deficit effect on rST is on, otherwise VPDt=0;
```

415

```
   aridt=1;                %do correction for site aridity,
                           % =1 do Temesgen's correction, =2 do Jensen's correction =0, no correction

% Parameters for correction of site aridity
   kx=0.6; kn=0.45; kd=0.55;          % for Temesgen's correction (0.7, 0.4, 0.6 for arid
         (semiarid) tropical climates)
                            % (0.5, 0.5, and 0.5)for humid and semi-humid teperate climates
% paramters for Jarvis functions
   %rST=rST_min*f1(D)*f2(Rs_24)*f3(T)
   f1a=3.5e-4;             % parameters for f1(d)=1/(1-aD), for coniferous trees, Pa-1
   f2c=100;      % parameters for f2(Rsun)=(Rsun+c)/[(1+c/1000)*Rsun], big uncertainty
   kT=0;         % parameters for f3(T)=1/[1-kT(Tx-T)^2], degC-1, make it zero to shut this function down
                 % kT=0.00137, not recommended if aridt=1
   Tx=25;        % degC
   Td=-2;        % temperature for complete dormancy of the vegetation, make it -100 to shut down this function
%input daily weather data:
   meteo=load('daily46_3.txt');
      days=size(meteo,1);     % the total number of the days
%-------------------------------------------------------------------------------------------------------
```

416

Appendix XVI Model settings and input daily atmospheric boundary conditions for generic transient simulations

This appendix includes the list of simulation runs (Table XVI-1) for generic simulations based on South Baldy, Magdalena Mountains, central New Mexico, and the simulated cumulative water fluxes (Table XVI-2). A plot of dry root-zone soil duration for tuff slopes is also included.

Table XVI-1 The simulation runs

Simulation run	rock	aspect	Soil thickness	S-shape model parameters h50,p	boundary
with vegetation cover Fr=0.5					
ms20a	granite	south	100	500cm, 2	midslope
ms20b	tuff	south	100	500cm, 2	midslope
mn20a	granite	north	100	500cm, 2	midslope
mn20b	tuff	north	100	500cm, 2	midslope
ms20at	granite	south	30	500cm, 2	midslope
ms20bt	tuff	south	30	500cm, 2	midslope
mn20at	granite	north	30	500cm, 2	midslope
mn20bt	tuff	north	30	500cm, 2	midslope
ms20aE	granite	south	100	500cm, 2	topslope
ms20bE	tuff	south	100	500cm, 2	topslope
mn20aE	granite	north	100	500cm, 2	topslope
mn20bE	tuff	north	100	500cm, 2	topslope
ms20atE	granite	south	30	500cm, 2	topslope
ms20btE	tuff	south	30	500cm, 2	topslope
mn20atE	granite	north	30	500cm, 2	topslope
mn20btE	tuff	north	30	500cm, 2	topslope

Simulation run	rock	aspect	Soil thickness	S-shape model parameters h50,p	boundary
with vegetation cover Fr=0.05					
xs20a	granite	south	100	500cm, 2	midslope
xs20b	tuff	south	100	500cm, 2	midslope
xn20a	granite	north	100	500cm, 2	midslope
xn20b	tuff	north	100	500cm, 2	midslope
xs20at	granite	south	30	500cm, 2	midslope
xs20bt	tuff	south	30	500cm, 2	midslope
xn20at	granite	north	30	500cm, 2	midslope
xn20bt	tuff	north	30	500cm, 2	midslope
xms20aE	granite	south	100	500cm, 2	topslope
xms20bE	tuff	south	100	500cm, 2	topslope
xmn20aE	granite	north	100	500cm, 2	topslope
xmn20bE	tuff	north	100	500cm, 2	topslope
xms20atE	granite	south	30	500cm, 2	topslope
xms20btE	tuff	south	30	500cm, 2	topslope
xmn20atE	granite	north	30	500cm, 2	topslope
xmn20btE	tuff	north	30	500cm, 2	topslope

Table XVI-2 The simulated cumulative water fluxes (cm) over four simulated years

	infiltration	runoff	Evaporation[3]	transpiration	interflow	percolation
mn20at	184	2	52	101	6	9
mn20a	183	0	55	137	-19	8
mn20bt	186	0	48	89	-14	62
mn20b	183	0	54	125	-46	47
mn20atE	177	0	47	96	29	6
mn20aE	175	0	50	106	20	1
mn20btE	177	0	45	84	8	40
mn20bE	175	0	50	104	19	4
ms20at	185	1	72	106	-2	6
ms20a	183	0	73	125	-21	4
ms20bt	186	0	67	88	-11	42
ms20b	183	0	73	119	-26	16
ms20atE	177	0	65	94	16	3
ms20aE	175	0	68	97	11	0
ms20btE	177	0	63	83	5	26
ms20bE	175	0	68	97	11	1
xn20at[1]	206	1	145	24	11	16
xn20a[2]	204	0	151	28	-13	37
xn20bt	228	0	119	17	-18	109
xn20b	224	0	139	26	-89	143
xn20atE	217	0	127	23	61	10
xn20aE	215	0	127	26	60	6
xn20btE	217	0	113	17	11	77
xn20bE	215	0	148	28	25	16
xs20at	225	3	171	26	5	12
xs20a	224	0	175	32	-13	29
xs20bt	228	0	144	19	-14	78
xs20b	224	0	163	29	-51	80
xs20atE	217	0	151	25	37	7
xs20aE	215	0	150	29	35	3
xs20btE	217	0	136	18	8	56
xs20bE	215	0	148	28	25	16

Note

1,2: Because the HYDRUS cannot simulate completely saturated soil profile, input precipitation of two runs, xn20at and xn20a, has been truncated. Cumulative truncated input precipitation is 18.9 cm on sloped surface, or 20 cm on the equivalent level surface.

3: The evaporation does not include interception loss, which is 44.6 cm for the slope of Fr=0.5, and 6.3 cm for the slope of Fr=0.05.

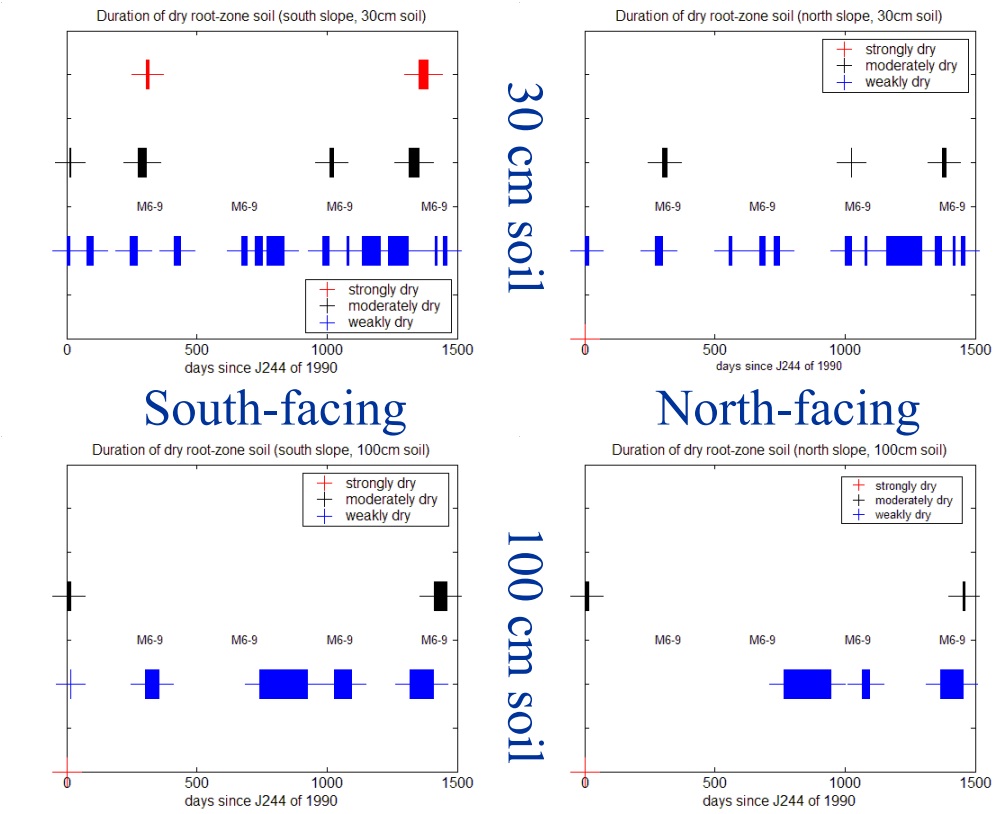

Figure XVI-1 The duration of dry root-zone soil for hypothetical slopes of 50% vegetation coverage (conifer trees), and of slope angle of 20˚, with two opposite slope orientations and two types of soil thickness. The bedrock is tuff. For the 30 cm soil, soil water potential at 20 cm depth is examined from the simulations. For the 100 cm soil, soil water potential at 40 cm depth is examined.

Appendix XVII TVET-generated daily atmospheric boundary conditions for a grass-covered south-facing slope

This appendix includes TVET generated atmospheric boundary conditions (Figure XVII-1) for a hypothetic south-facing slope with seasonal grass cover, based on South Baldy, Magdalena Mountains, central New Mexico. The grass is assumed to be active from May through October of the year, with a canopy leaf area index of 3, a height of 0.5 meter, and a minimum stomatal resistance of 130 sm^{-1}. The daily atmospheric conditions (solar radiation, temperature, wind speed, relative humidity), observed at the Langmuir Lab near the South Baldy, are downloaded (and derived) from Sevilleta LTER website. The solar radiation is adjusted to account for the slope steepness and aspect effects for the two hypothetic slopes. Other climate conditions are assumed to be the same for the two slopes, and equal to the measurements at the nearly weather station. The input parameters for TVET model are also included.

The TVET-generated atmospheric boundary conditions

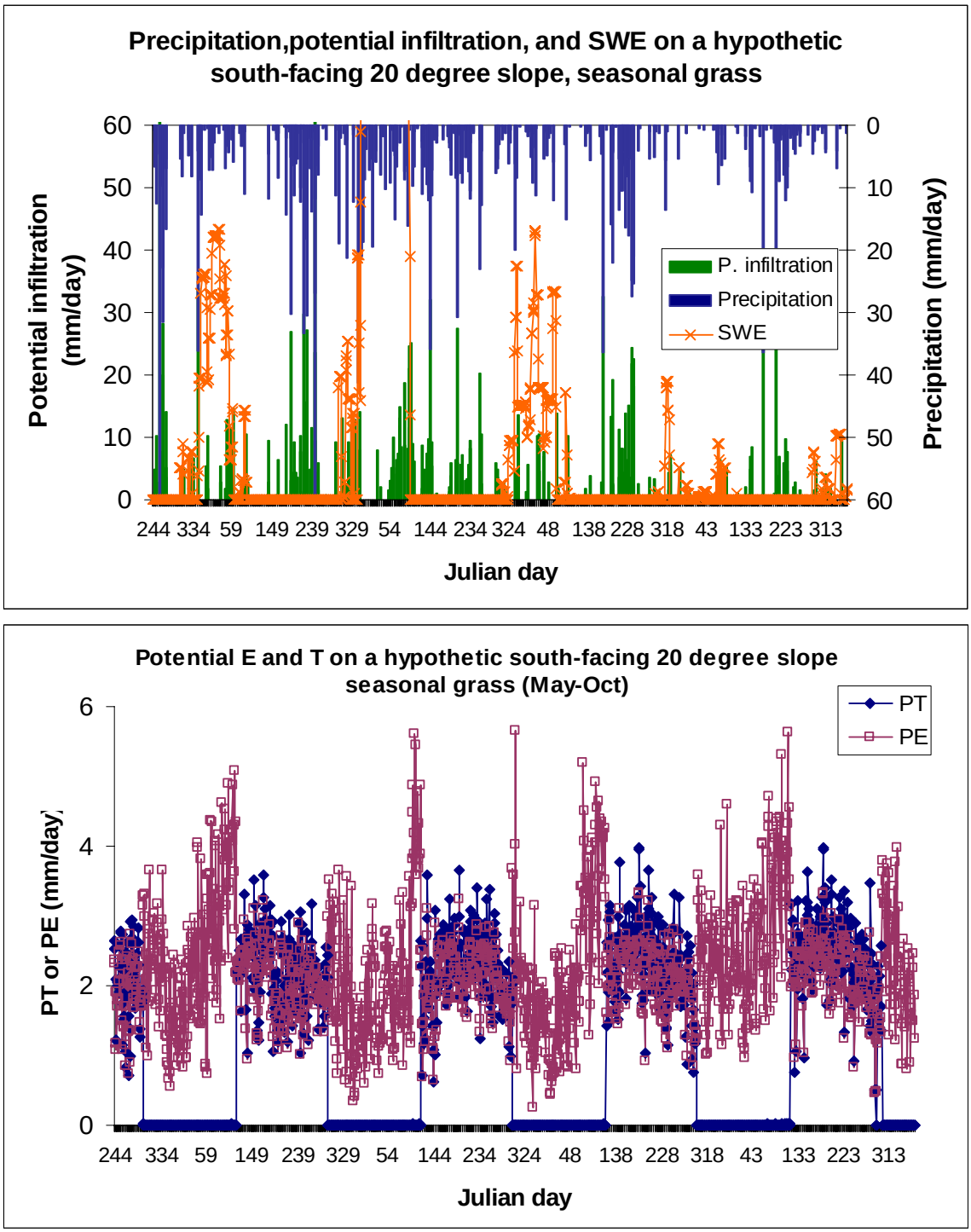

Figure XVII-1 TVET generated atmospheric boundary conditions: active water for infiltration (or potential infiltration), snow water equivalent (top), and PE and PT (bottom), for a south-facing 20 degree hillslope with 50% hypothetical seasonal grass.

TVET input parameters

```
%site specific parameters  (indented lines are derivations, not necessary changed)
   long=-107.1813;
   lat=33.9755;
   elev=3243;          % meter above sea level
   slope=20;            % slope angle in degree
      slpcrrct=cos(slope/180*pi);
   aspect=180;        % surface azimuth angle, 0 due south, -90 due east, and 90 due west
   fr=0.5;              % fractional vegetation cover
   alpha_v=0.20;           % albedo of the vegetation,
   alpha_s=0.30;           % albedo of the soil,
   alpha_sn=0.50;          % albedo of snowcover
   swe=0;               % initial the snow water equivalent
%-------------------------------------------------------------
%vegetation parameters;
   Lc=3;                % canopy leaf area index
      L=Lc*fr;          % surface leaf area index
   h=0.5;               % vegetation height
      d=0.67*h;         % zero plane displacement, m (Shuttleworth, 1993).
      zm=0.123*h;       % roughness length for momentum transfer, m
      zh=zm/7.0;        % roughness length for heat and vapor transfer, m, for forest
                     % for grasses,/12.0, for crop /7.0, (Mo et al., 2004);

   zms=0.005;           % rouhgness length for momentum transfer on the substrate, m
      zhs=0.1*zms;      % roughness length for heat and vapor transfer on the substrate,
m
   z=h+2;               % reference height at which windspeed, humidity is measured, m

   kc=0.4;              % extinction coefficient of beer's law

%seasonal-change par for grass
   Lc1=3;
   Lc2=0.5;
   Fr1=0.5;
   Fr2=0.2;
   h1=0.8;
   h2=0.3;
   rST_min1=130;
   rST_min2=5000;
   vg1=120;
   vg4=300;
   % change Fr for seasonal grass
      %time-dependent vegetation parameters;

   if J<vg1 | J>vg4
      Lc=Lc2;              % canopy leaf area index
```

```
   h=h2;                  % vegetation height
   rST_min=rST_min2;
   fr=Fr2;
else
   Lc=Lc1;                  % canopy leaf area index
   h=h1;                  % vegetation height
   rST_min=rST_min1;
   fr=Fr1;
end

      d=0.67*h;          % zero plane displacement, m (Shuttleworth, 1993).
      z=h+2;             % reference height at which windspeed, humidity is measured, m
      L=Lc*fr;             % surface leaf area index
      zm=0.123*h;           % roughness length for momentum transfer, m
      zh=zm/7.0;            % roughness length for heat and vapor transfer, m, for forest
      zms=0.005;          % rouhgness length for momentum transfer on the substrate, m
      zhs=0.1*zms;   % roughness length for heat and vapor transfer on the substrate, m
```

Appendix XVIII Vegetation controls on hydrologic processes

On the two hypothetical slopes based on South Baldy, Magdalena Mountains, central New Mexico (Figure 5.11), the local climate condition is quite different. The south-facing has an annual potential ET exceeding that of the north-facing slope by about half of the annual precipitation (Appendix XV). However, it is surprising that modeled percolation is similar for the two slopes with their current vegetation covers (§5.4.2.3). One possible explanation for the inconsistency between the climate forcing and the percolation on these two slopes is that vegetation modifies the local hydrologic system, leading to similar hydrologic state on the two slopes when an ecohydrological equilibrium is reached (Figure XVIII-1).

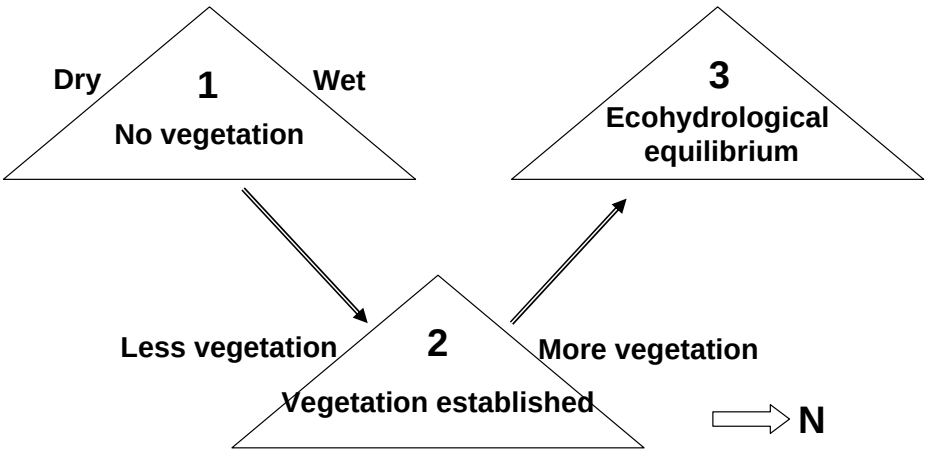

Figure XVIII-1 Schematic graph showing vegetation developed on the two opposite-aspect slopes with different local climatic conditions.

An ecohydrological equilibrium is a state at which the vegetation cover reaches its optimal stage for given environmental conditions (solar radiation, water supply, temperature, etc). At this stage, the limited environmental condition is optimally utilized

by the vegetation. In arid and semiarid regions of the southwestern United States, the limitation is soil water availability. For simple explanation, let's assume there was no vegetation initially on the two slopes (e.g., "1" in Figure XVIII-1). Both slopes have soil water to support vegetation. The north-facing slope has more available soil water because of less potential ET, leading to more vegetation developed on the north-facing slope ("2" in Figure XVIII-1). When both slopes reach ecohydrological equilibrium, there is no more water for additional vegetation. The hydrologic state becomes similar between two slopes ("3" in Figure XVIII-1). This could help explain similar percolation for the two slopes.

We can further hypothesize a local climate condition range (characterized by annual precipitation and potential ET) in which the vegetation will adapt itself to the climate conditions, and lead to a similar soil water state (Figure XVIII-2). Beyond this range, some other conditions (other than water) constrain vegetation development. For example, if the climate is too wet, the solar radiation becomes a constraint. The "elastic range" in Figure XVIII-2 may have several sub-ranges. Each responds to a specific ecosystem. The hydrologic states between ecosystems change slightly and abruptly. But within each ecosystem, the root-zone hydrologic state becomes uniform by naturally adjusted vegetation density. An example is the four vegetation belts (creosote shrub, grass, juniper, and ponderosa pine) in the central New Mexico [*Sandvig, 2005*].

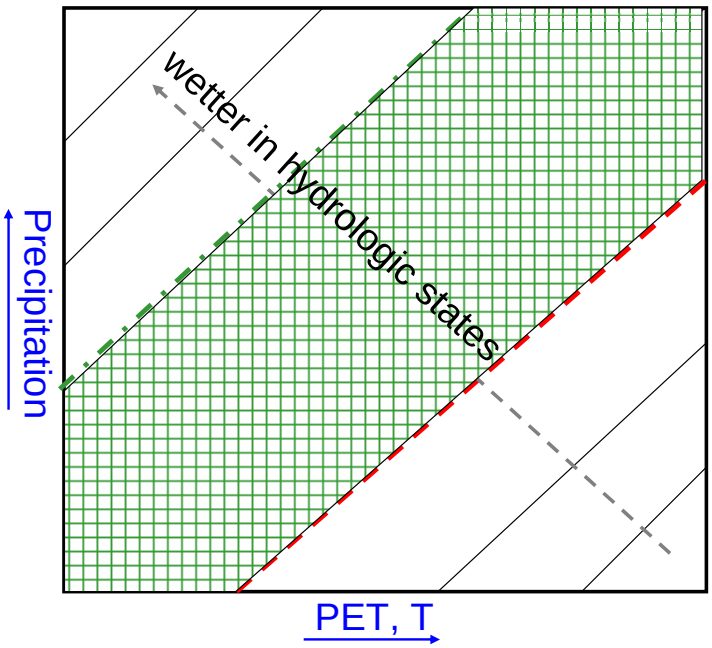

Figure XVIII-2 Schematic plot showing an "ecohydrologically elastic range" of the climate conditions, within which vegetation adapts itself to the climate conditions, leading to a similar hydrologic state. The diagonal lines represent equal soil hydrologic states. The shaded area represents the local climate condition range within vegetation brings the soil to one hydrologic state.

What can we do with the concept of ecohydrologically elastic range? First, we can use it to study terrestrial ecotones, and their responses to climate variability and change. An example is shown in Figure XVIII-3. Second, it provides an approach for basin-scale groundwater recharge maping based on remote sensing natural vegetation coverage [*Sandvig, 2005*]. Third, the ecohydrologically elastic range is useful to provide guidance for watershed vegetation controls. But first of all, we need to test this concept before its application.

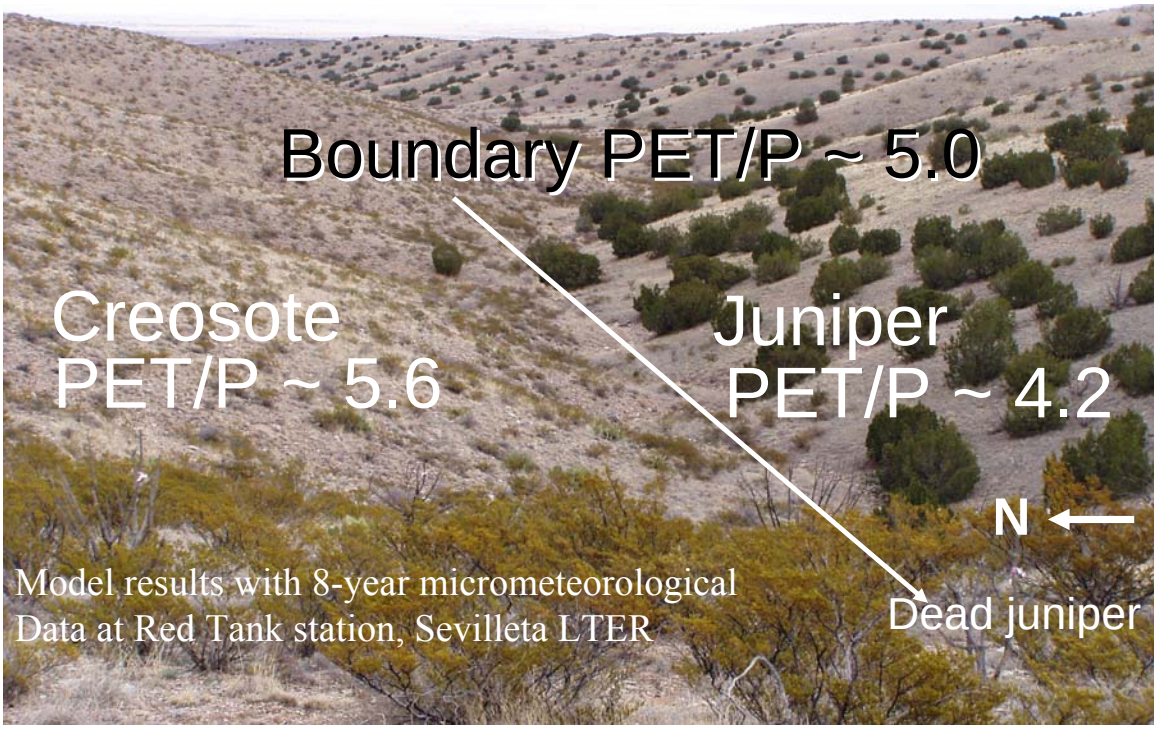

Figure XVIII-3 TVET estimated climate condition for the topography-induced ecotone in western Sevilleta LTER, central New Mexico, U.S.A. Slope aspect-modified climate conditions lead to different ecosystem. Juniper covers the north-facing slope, while creosotebush covers the south-facing slope. Using TVET model, the climate condition is estimated for each slope. The two topography-induced ecosystems meet at the head slope of the small drainage basin. This boundary is very sensitive to climate variability and change. For example, some east-facing slope juniper trees in the near field of the photograph died during the 1950's drought.

Reference

Sandvig, R. (2005), Ecohydrological controls on soil-moisture fluxes in arid vadose zones, Master Thesis, New Mexico Institute of Mining and Technology, Socorro, New Mexico.

Appendix XIX Model settings for generic transient simulations with minute-based atmospheric forcing

This appendix describes the model settings for HYDRUS 2D simulations of hypothetical hillslopes based on Los Alamos hillslope experimental site, northern New Mexico (§5.5 and Chapter 6).

The model settings for different locations of the hillslope

Figure XIX-1 shows the modeling settings of two sloping slices at two relative hillslope locations. The continuous slope boundary (Appendix XV) is prescribed at both sides of the soil layer for the midslope slice, and at the downslope side of the soil layer for the topslope slice.

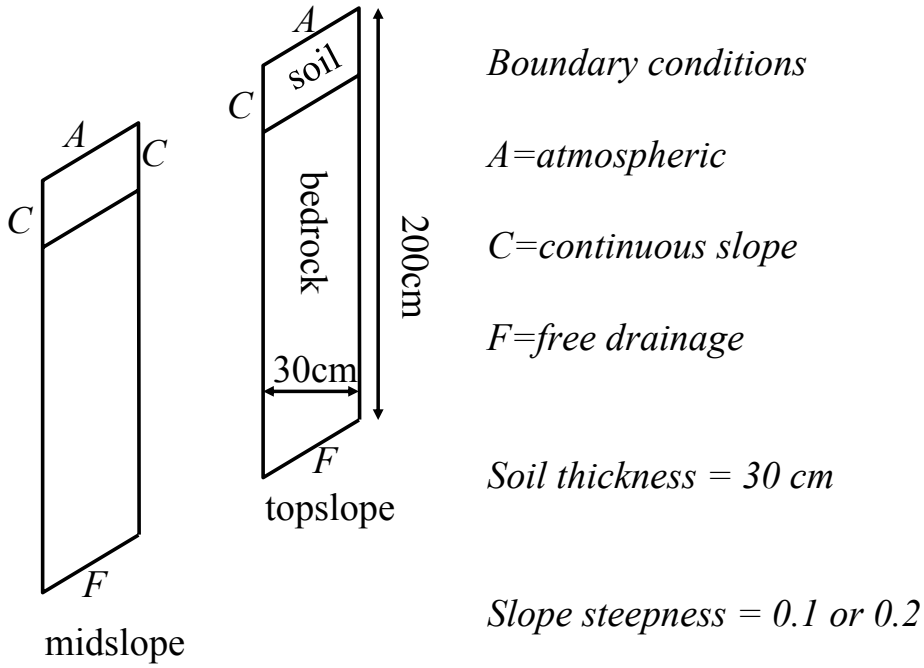

Figure XIX-1 Model setting of two sloping slices at different relative hillslope locations.

Appendix XX Generic transient simulation runs with minute-based temporal atmospheric forcing

This appendix includes the modeling runs (Table XX-1) of hypothetical hillslopes based on Los Alamos hillslope experimental site, northern New Mexico (Appendix XIX). The simulated runoff plots are also included.

Table XX-1 The generic transient simulation runs with minute-based atmospheric boundary conditions

runs with three atmospheric boundaries[1]			Local climate adjusting factor[2]	bedrock	slope location[3]
94 water year	95 water year	96 water year			
D4t1,2[4]	D5t1,2	D6t1,2	1	tuff	midslope
S4t1,2	S5t1,2	S6t1,2	0.75	tuff	midslope
M4t1,2	M5t1,2	M6t1,2	0.5	tuff	midslope
H4t1,2	H5t1,2	H6t1,2	0.35	tuff	midslope
ED4t1,2	ED5t1,2	ED6t1,2	1	tuff	topslope
ES4t1,2	ES5t1,2	ES6t1,2	0.75	tuff	topslope
EM4t1,2	EM5t1,2	EM6t1,2	0.5	tuff	topslope
EH4t1,2	EH5t1,2	EH6t1,2	0.35	tuff	topslope
D4g1,2	D5g1,2	D6g1,2	1	granite	midslope
S4g1,2	S5g1,2	S6g1,2	0.75	granite	midslope
M4g1,2	M5g1,2	M6g1,2	0.5	granite	midslope
H4g1,2	H5g1,2	H6g1,2	0.35	granite	midslope
ED4g1,2	ED5g1,2	ED6g1,2	1	granite	topslope
ES4g1,2	ES5g1,2	ES6g1,2	0.75	granite	topslope
EM4g1,2	EM5g1,2	EM6g1,2	0.5	granite	topslope
EH4g1,2	EH5g1,2	EH6g1,2	0.35	granite	topslope

Notes:

1. The atmospheric boundary condition is derived from high-temporal resolution micrometeorological measurement conducted at Los Alamos hillslope experiment site (Chapter 6)
2. Because of the elevation and terrain aspect effect, PET varies with locations. These factors are used to uniformly scale observed PET (without considering actual topography effects), to generate various climate conditions. With these conditions, the relationships of percolation and the climate condition are estimated from the hydrologic simulations. Later, in Chapter 7, the topography effects on percolation are investigated using the results from §5.5.
3. Two relative slope locations are simulated. Topslope has a no-flow boundary at the upper side, and a prescribed gradient at the lower side. Midslope has a prescribed gradient at both sides of the slope (Appendix XIX).
4. 1 and 2 represent the slope steepness of 0.1 and 0.2.

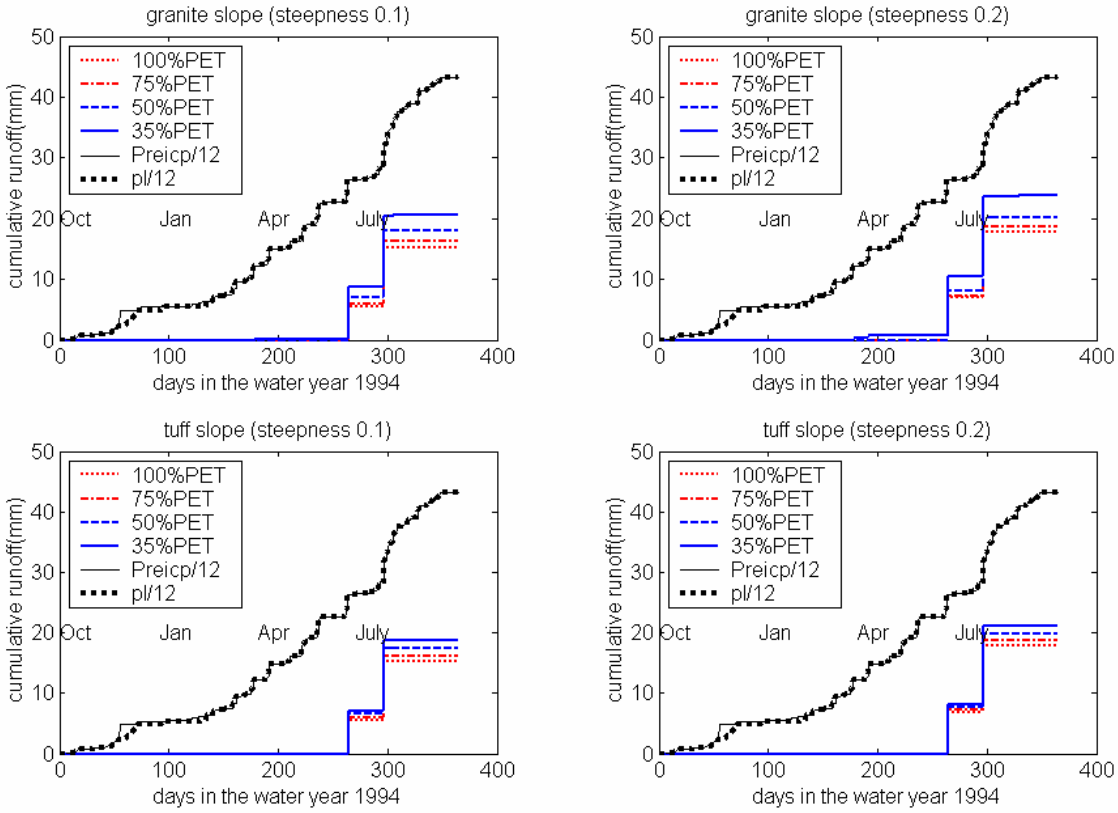

Figure XX-1 Simulated cumulative runoff (geometric mean of the topslope and midslope) under various synthetic climate conditions for the 1994 water year, together with the cumulative precipitation, and active water (pI, or rainfall + snowmelt), for two degrees of slope steepness, and two types of bedrock.

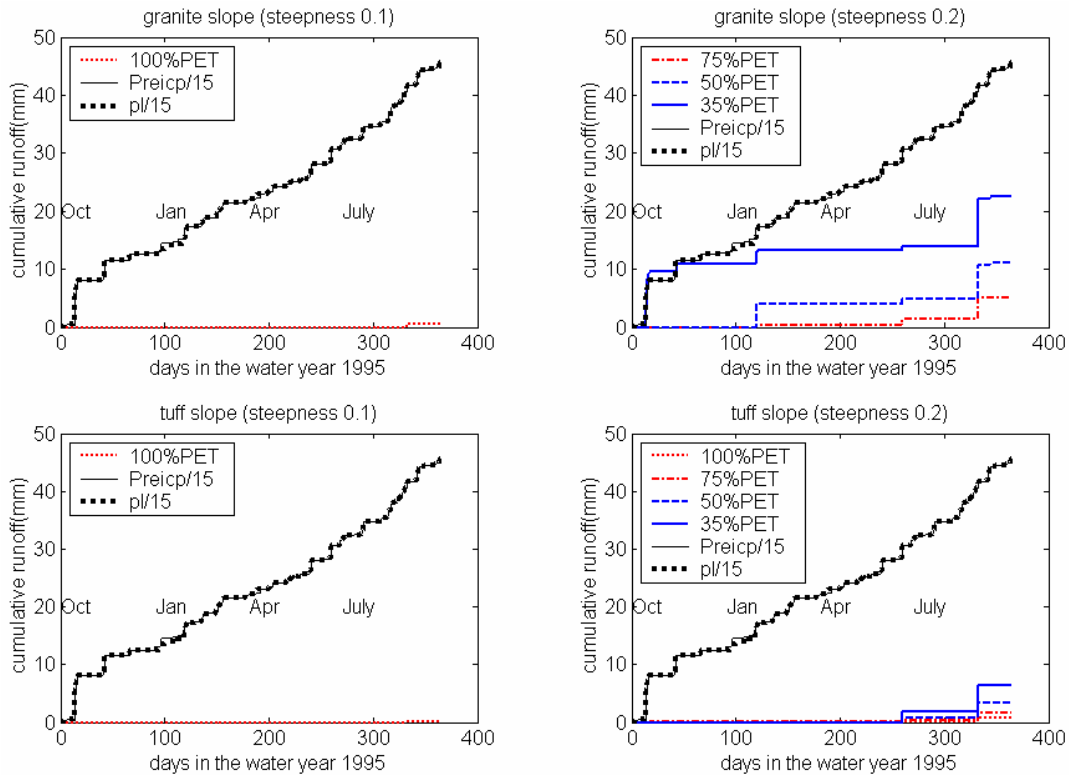

Figure XX-2 Same as 5.18, but for the 1995 water year. Some simulation runs are missed because of numerical stability problems of HYDRUS.

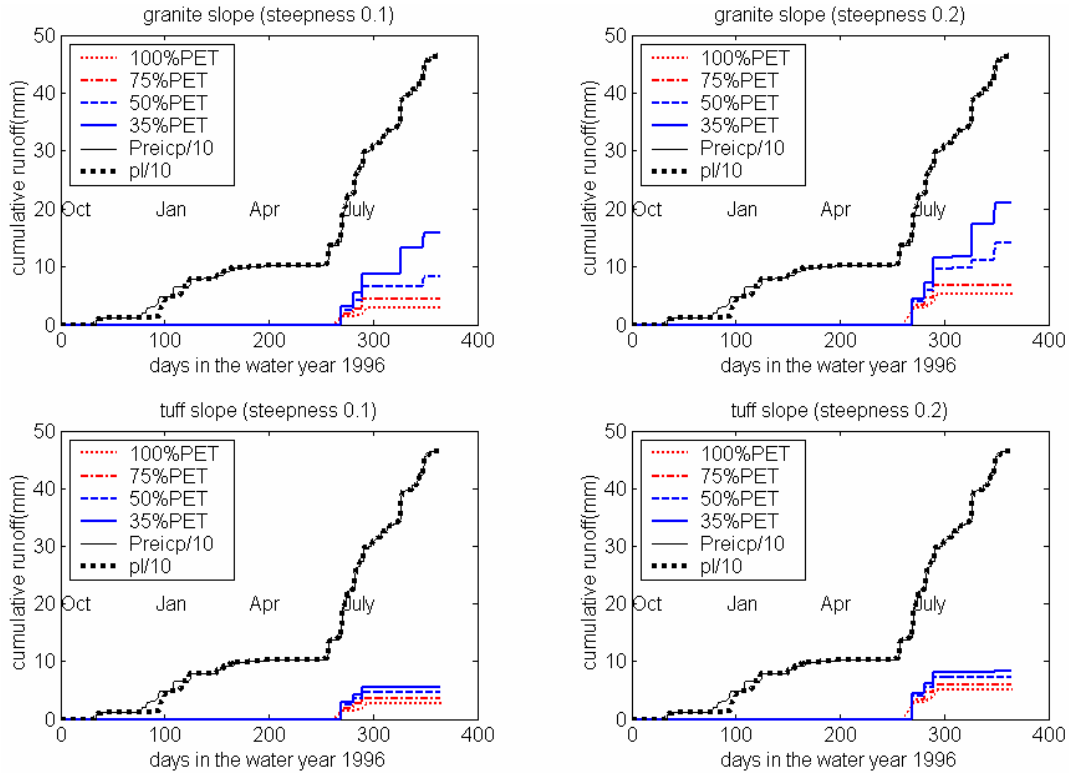

Figure XX-3 Same as Figure 5.18, but for the 1996 water year.

Appendix XXI Testing recharge-aridity index relationship with field-observation-based recharge estimates in a ponderosa pine ecosystem, central New Mexico

This appendix includes a testing of recharge-climate index relationship with a field study conducted by Sandvig [*2005*]. Using soil chloride profiles, Sandvig [*2005*] estimates the long-term mean recharge at the ponderosa pine sites (PET/P = 3.7), central New Mexico, is about 2.3 mm/yr. If the climate index can be used an indicator for recharge, we should expect similar percolation from the numerical simulations forced by a climatic boundary with aridity index of 3.7. Because no high-temporal-resolution climate data is available for this site, which is important to simulate recharge (§5.6.6.1), the three-year minute-time-step micrometeorological observations at Los Alamos, are rescaled for Sandvig's ponderosa pine site. Below is the modeling design to test whether the climate index approach is applicable to estimate recharge.

Simulation design

1) Rescale the PET time series to make PET/P ratio to be 3.7, similar to Renee's ponderosa pine site, for all three-year minutely based observations (original aridity index, 1994=2.62, 1995=1.83, and 1996=3.09).

2) Based on the soil profile description of Sandvig's [2005] two ponderosa pine sites (10 and 11), the model soil profile is composed of sandy-loam (0~30 cm depth), loam (30~70 cm), and silt (70~200 cm), with hydrologic properties shown in Table XXI-1. Although at 30~70 cm, clay content is usually high for the ponderosa pine site, the tree root increases the hydraulic conductivity of the bulk soil. This is why loam is prescribed at this depth interval.

3) The root distribution is prescribed in the top 70 cm of the profile, with relative density based on Los Alamos hillslope site observations (i.e, 0.65 at 0~30cm, and 0,35 at 30~70cm). The root-water-uptake model is prescribed as S-shape model (h50=-500, p=2), which was calibrated at the Los Alamos ponderosa pine site.
   Do 1D simulations with infiltration-excess runoff.

Table XXI-1 The hydrologic properties of soils for Sandvig's [2005] ponderosa pine sites

	Depth (cm)	θ_r	θ_s	α_1 (1/cm)	n_1	k (m^2)
Sandy loam	0~30	0.065	0.41	0.075	1.89	1.23×10^{-12}
loam	30~70	0.078	0.43	0.036	1.56	2.89×10^{-13}
Silt	70~200	0.034	0.46	0.016	1.37	6.94×10^{-14}

4) Two series of 1D simulations are conducted using HYDRUS1D. In first series, the simulations are conducted in equilibrium to individual year atmospheric forcing. In the second series, the simulations are conducted in sequence with initial condition inherited from the previous year.

Results

If the simulations are conducted in equilibrium with each individual year climatic conditions, the percolation is 0.7, 7.8, and 2.2 mm/yr for the hypothetic 1994, 1995 and 1996 water year (all having aridity index of 3.7). The mean annual percolation of the three-year results is 3.6 mm/yr, close to Sandvig's [2005] estimate (~2.3 mm/yr) for the ponderosa pine sites.

If the simulations are conducted with sequential initial condition (starting with the year 1996, having the moderate percolation among the three years), the percolation is 2.2, 3.9, and 5.2 mm/yr for the hypothetic 1994, 1995, and 1996 water years, respectively. The mean annual percolation of the three-year results is 3.9 mm/yr, also close to Sandvig's [*2005*] estimate (~2.3 mm/yr) for the ponderosa pine sites.

Conclusions and implications

The good agreement of the simulated average annual percolation to the estimates from field observations, gives some confidence of using climatic index approach for estimating recharge.

However, the variability of percolation in three individual years with the same aridity index indicates that in addition to the annual aridity index the recharge is also dependent of some other climatic characteristics. Thus, it is not appropriate to use the climate index approach to estimate recharge for a specific year. Nonetheless, the average annual percolation of the three-year results of both series simulations is close to the estimated long-term mean recharge based on field observations. This suggests that the climate index approach may be useful to estimate long-term mean recharge.

Reference

Sandvig, R. (2005), Ecohydrological controls on soil-moisture fluxes in arid vadose zones, Master Thesis, New Mexico Institute of Mining and Technology, Socorro, New Mexico.

Appendix XXII Parameterization of conceptual models for root macropore flow at the Los Alamos ponderosa hillslope site

This appendix includes the parameterization of different conceptual models representing the effect of root-induce macropore flow, based on the root macropore model developed in §4.7. For the anisotropic single continuum model, the calculation of saturated hydraulic conductivity exactly follows the root macropore model in §4.7, by using the observed root density profile (Table 6.2), and assuming a certain root perimeter aperture b_i (=2.7% D_i), and equivalent dip angle β (1, 15, and 30 degree). The tortuosity is assumed to be 2. The results are shown in Tables XXI-1~3. The advantage of this model is that it captures the directional preferential flow due to the root directions. The disadvantage is that the root macropore flow does not shut off when the soil becomes dry.

For the composite continuum model, root direction is not considered. With the observed root density profile (Table 6.2) and assumed root perimeter aperture b_i (=2.7% D_i), the bulk saturated hydraulic conductivity is calculated from Equations 4.55 and 4.51. With this bulk conductivity for each horizon and its matrix hydraulic properties (Tables 6.1 and 6.3), the composite function is estimated for each horizon (Table XXI-4).

Table XXII-1 The anisotropic saturated hydraulic conductivities (cm/min) for roots and the bulk soil horizons, assumed that root perimeter aperture is 2.7% of the root diameter, and the equivalent root dip angle of 1 degree relative to the surface (x direction parallel to the surface, and z direction perpendicular to the surface)

layers	Kx_root	Kz_root	K_matrix	Kx_bulk	Kz_bulk	Kx/Kz
A	1.095E+01	1.912E-01	4.500E-03	5.809E-02	5.414E-03	10.7
Bw	1.095E+01	1.912E-01	1.134E-04	5.372E-02	1.049E-03	51.2
Bt	1.093E+01	1.908E-01	1.500E-06	5.804E-02	1.015E-03	57.2
CB	1.705E-01	2.976E-03	1.824E-05	2.104E-05	1.829E-05	1.2

Table XXII-2 The anisotropic saturated hydraulic conductivities (cm/min) for roots and the bulk soil horizons, assumed that root perimeter aperture is 2.7% of the root diameter, and the equivalent root dip angle of 15 degrees relative to the surface (x direction parallel to the surface, and z direction perpendicular to the surface)

layers	Kx_root	Kz_root	K_matrix	Kx_bulk	Kz_bulk	Kx/Kz
A	1.058E+01	2.835E+00	4.500E-03	5.627E-02	1.836E-02	3.1
Bw	1.058E+01	2.835E+00	1.134E-04	5.190E-02	1.399E-02	3.7
Bt	1.056E+01	2.830E+00	1.500E-06	5.607E-02	1.502E-02	3.7
CB	1.647E-01	4.413E-02	1.824E-05	2.095E-05	1.897E-05	1.1

Table XXII-3 The anisotropic saturated hydraulic conductivities (cm/min) for roots and the bulk soil horizons, assumed that root perimeter aperture is 2.7% of the root diameter, and the equivalent root dip angle of 30 degrees relative to the surface (x direction parallel to the surface, and z direction perpendicular to the surface)

layers	Kx_root	Kz_root	K_matrix	Kx_bulk	Kz_bulk	Kx/Kz
A	9.487E+00	5.477E+00	4.500E-03	5.091E-02	3.129E-02	1.6
Bw	9.487E+00	5.477E+00	1.134E-04	4.655E-02	2.692E-02	1.7
Bt	9.470E+00	5.467E+00	1.500E-06	5.027E-02	2.902E-02	1.7
CB	1.477E-01	8.526E-02	1.824E-05	2.067E-05	1.964E-05	1.1

Table XXII-4 Parameterization of composite continuum model, representing the soil matrix and root-zone macropores, in units of cm and minute

Layers	$\alpha 1$ (1/cm)	$n1$	θ_s	θ_r	$\alpha 2$ (1/cm)	$n2$	$w2$	K_s cm/min
A	0.015	1.33	0.436	0.06	0.6	3	0.1	4.24E-2
Bw	0.017	1.14	0.388	0.06	6	3	0.1	3.80E-2
Bt	0.0045	1.15	0.398	0.08	6	3	0.1	4.11E-2
CB	0.016	1.11	0.469	0.06	0.6	3	0.03	2.02E-5
R	0.0014	1.42	0.276	0	0.0014	1.42	0	3.48E-3

Appendix XXIII Error transferred from precipitation to recharge estimates

This appendix shows how the bias in precipitation estimates, due to missing gauge observations at higher elevations, transfers to the recharge estimates. In §7.6, the precipitation estimates at high elevations are used to study climate variability effects on MBR. It is assumed that the bias in estimated precipitation at higher elevations with few gauges available is similar between ENSO + PDO categories. Here, I try to show that the precipitation bias linearly translates into the bias in recharge (percolation) between ENSO + PDO categories.

From Chapter 5, the percolation regression function has a general form shown in equation (XXIII-1).

$$y = a \exp(b \frac{PET}{P}) \qquad \text{(XXIII-1)}$$

Assumed that the bias in precipitation is δP, leading to a bias in recharge δy, let's find the relationship between δP and δy.

$$y+\delta y = a\exp(b\frac{PET}{P+\delta P})$$

$$y+\delta y = a\exp(b\frac{PET/P}{P/P+\delta P/P})$$

$$y+\delta y = a\exp(b\frac{PET}{P}\left(\frac{1}{1+\frac{\delta P}{P}}\right))$$

when δP/P is small, then a series approximation suggests that

$$\frac{1}{1+\frac{\delta P}{P}} \approx 1-\frac{\delta P}{P}$$

and

$$y+\delta y = a\exp\left[(b\frac{PET}{P})\left(1-\frac{\delta P}{P}\right)\right]$$

$$y+\delta y = \frac{y}{\exp\left(b\frac{PET}{P}\frac{\delta P}{P}\right)}$$

$$y+\delta y = y\left(1-b\frac{PET}{P}\frac{\delta P}{P}\right)$$

$$\delta y = y\left(-b\frac{PET}{P}\frac{\delta P}{P}\right)$$

$$\frac{\delta y}{y} = -b\frac{PET}{P}\left(\frac{\delta P}{P}\right)$$

Thus,

$$\frac{\delta y}{y} = -b\frac{PET}{P}\left(\frac{\delta P}{P}\right) \qquad \text{(XXIII-2)}$$

From equation (XXIII-2), the bias in percolation is linearly related to the bias in precipitation. In order to find whether the amount of bias in percolation cancels each other between climate conditions of ENSO + PDO categories, the bias of percolation due to a hypothetic 10% precipitation bias is calculated for all pixels above the elevation of

2700 m of the Jemez Mountains area. The percolation bias of El Nino + high PDO conditions is then compared to that of the long-term mean conditions. Of all pixels above 2700 m, the maximum difference is 4.8 mm, and the mean difference about 0.8 mm (averaged over all elevation pixels).